

Photoinduced Processes at Surfaces and in Nanomaterials

ACS SYMPOSIUM SERIES 1196

**Photoinduced Processes at
Surfaces and in Nanomaterials**

Dmitri Kilin, Editor

North Dakota State University

Fargo, North Dakota

and

University of South Dakota

Vermillion, South Dakota

**Sponsored by the
ACS Division of Computers in Chemistry**



American Chemical Society, Washington, DC

Distributed in print by Oxford University Press



Library of Congress Cataloging-in-Publication Data

Photoinduced processes at surfaces and in nanomaterials / Dmitri Kilin, editor,
North Dakota State University, Fargo, North Dakota, and University of South Dakota,
Vermillion, South Dakota ; sponsored by the ACS Division of Computers in Chemistry.
pages cm. -- (ACS symposium series ; 1196)

Includes bibliographical references and index.

ISBN 978-0-8412-3094-1 (alk. paper) -- ISBN 978-0-8412-3093-4 (alk. paper)

1. Photochemistry. 2. Photovoltaic power generation. 3. Electrochemistry. 4. Surface chemistry. 5. Nanostructured materials. I. Kilin, Dmitri, editor. II. American Chemical Society. Division of Computers in Chemistry.

QD708.2.P48 2015

660'.295--dc23

2015036678

The paper used in this publication meets the minimum requirements of American National Standard for Information Sciences—Permanence of Paper for Printed Library Materials, ANSI Z39.48n1984.

Copyright © 2015 American Chemical Society

Distributed in print by Oxford University Press

All Rights Reserved. Reprographic copying beyond that permitted by Sections 107 or 108 of the U.S. Copyright Act is allowed for internal use only, provided that a per-chapter fee of \$40.25 plus \$0.75 per page is paid to the Copyright Clearance Center, Inc., 222 Rosewood Drive, Danvers, MA 01923, USA. Republication or reproduction for sale of pages in this book is permitted only under license from ACS. Direct these and other permission requests to ACS Copyright Office, Publications Division, 1155 16th Street, N.W., Washington, DC 20036.

The citation of trade names and/or names of manufacturers in this publication is not to be construed as an endorsement or as approval by ACS of the commercial products or services referenced herein; nor should the mere reference herein to any drawing, specification, chemical process, or other data be regarded as a license or as a conveyance of any right or permission to the holder, reader, or any other person or corporation, to manufacture, reproduce, use, or sell any patented invention or copyrighted work that may in any way be related thereto. Registered names, trademarks, etc., used in this publication, even without specific indication thereof, are not to be considered unprotected by law.

PRINTED IN THE UNITED STATES OF AMERICA

Foreword

The ACS Symposium Series was first published in 1974 to provide a mechanism for publishing symposia quickly in book form. The purpose of the series is to publish timely, comprehensive books developed from the ACS sponsored symposia based on current scientific research. Occasionally, books are developed from symposia sponsored by other organizations when the topic is of keen interest to the chemistry audience.

Before agreeing to publish a book, the proposed table of contents is reviewed for appropriate and comprehensive coverage and for interest to the audience. Some papers may be excluded to better focus the book; others may be added to provide comprehensiveness. When appropriate, overview or introductory chapters are added. Drafts of chapters are peer-reviewed prior to final acceptance or rejection, and manuscripts are prepared in camera-ready format.

As a rule, only original research papers and original review papers are included in the volumes. Verbatim reproductions of previous published papers are not accepted.

ACS Books Department

Preface

This ACS Book presents studies of photoinduced processes in nanomaterials that fall into the category of basic research contributing to solar energy conversion. The book focuses on photophysical and photochemical processes at surfaces of semiconductor nanostructures that are related to photovoltaic and photocatalytic applications with a broader focus on time-resolved spectroscopic monitoring of related processes in photoactive materials. Changes of the composition, quantum confinement, size, shape, surface functionalization, doping, and relative spatial arrangements of nanocrystals, as well as the formation of semiconductor-to-metal nano-interfaces, tune the timescales of the relevant basic processes and properties of the materials. The book reports short, up-to-date reviews, recent experimental data, and computational results that all contribute to an atomistic description of electronic dynamics and charge transfer induced by optical excitations and lattice vibrations. Basic processes — such as light absorption, formation and evolution of charge transfer excitations, hot carrier relaxation, and reaction dynamics — all are perturbed by the environmental factors, such as lattice vibrations and solvent polarization, and are treated with different implementations of the "open system" approach. The merging of experimental and computational approaches allows for a holistic and coordinated effort to interpret, guide, and optimize the efficiency of photocatalytic and photovoltaic processes.

Chapters cover the tuning of optoelectronic properties of nanomaterials for energy application via the broad modification of morphological variables. Properties of nanostructures are tuned by varying their dimensionality from zero-dimensional quantum dots (Chapters 5 and 12) and one-dimensional nanorods (Chapter 10) to two-dimensional thin films (Chapters 2, 6, and 7) and mesoporous materials (Chapter 3). Additional tune-ability is achieved via sensitization by dyes (Chapters 1, 8, and 12), doping (Chapters 1, 5, 6, and 9), or deposition of metal clusters on semiconductor surfaces (Chapters 7 and 11). Although the main focus of the reported research is basic science, several chapters report noticeable advances in dye-sensitized solar cells (Chapters 1 and 8), semiconductor-based photovoltaics (Chapters 7, 9, and 10), sensing applications (Chapter 6), pharmaceutical applications (Chapter 12), and conversion of solar energy to chemical energy in a broad variety of photoelectrochemical cells for photocatalysis and water splitting (Chapters 3, 4, and 11). The contributions come from both an experimental community (Chapters 1, 3, 4, and 12) and a community of researchers dealing with computing electronic structure (Chapters 2, 5, and 6), nonadiabatic dynamics of excited states (Chapters 7, 8, 9, and 10), and modeling chemical reaction dynamics (Chapter 11).

1. King, Kern, and Parkinson (Chapter 1, *Sensitization of Single Crystal Substrates*) provide a starting point and a “system of coordinates” for other chapters dealing with the sensitization of single crystal wide-gap single crystal semiconductor surfaces by dyes, polymers, quantum dots, and doping (Chapters 2, 3, 4, and 8).
2. Giorgi and Yamashita (Chapter 2, *Electronic and Optical Properties of Low-Dimensional TiO₂: From Minority Surfaces to Nanocomposites*) focus on the confinement effect for ultra-thin titania films and their functionalization by graphene, as explored by electronic structure computations that reveal the excitonic nature of their optical spectra.
3. Mahoney, Rasalingam, and Koodali (Chapter 3, *Dye-sensitized and Doped TiO₂ Mesoporous Materials for Visible Light Induced Photocatalytic Hydrogen Evolution*) provide an overview of the benefits of doped mesoporous materials for visible light-induced photocatalytic hydrogen production: Sensitization of wide-gap semiconductors such as titania with dyes, quantum dots and doping by transition metals extends the response to visible light, while mesoporous morphology provides high surface-to-volume ratio, which collectively contributes to the efficiency of photocatalytic processes. This complements other chapters dealing with the effects of the confinement, morphology, and sensitization of nanomaterials for solar energy applications (Chapters 1, 2, and 4) and opens a call for the computational modeling of hydrogen evolution (Chapter 11).
4. Pillai et al. (Chapter 4, *Single Site Metal Ions on the Surface of TiO₂ Nanorods: A Platform for Theoretical and Experimental Investigation*) summarize the synthetic protocols for controlled deposition of transition metals on the surface of titania nanostructures and outline possible ways to characterize those nanomaterials for solar energy utilization, experimentally and computationally.
5. Proshchenko and Dahnovski (Chapter 5, *Transition Metal Doped Semiconductor Quantum Dots: Tunable Emission*) examine the modeling of transition metal doping in semiconductor quantum dots, covering the impact of crystal field splitting and many-electron effects onto the absorption and luminescence of such models.
6. Inerbaev et al. (Chapter 6, *Theoretical Modeling of Oxygen and Water Adsorption on Indium Oxide (111) Surface*) address the control of the optical properties of an indium oxide thin film by the surface adsorption of oxygen at different air humidity for sensor applications.
7. Micha (Chapter 7, *Density Matrix Treatment of Optical Properties in Photovoltaic Materials: Photoconductivity at a Semiconductor Surface*) focuses on metal clusters deposited on silicon surfaces. An overview of the practical implementations of the methods to describe the light-to-matter interaction, which are based on density operator techniques, paves the way to predict and interpret key observables in such nanostructures: photovoltage spectra, photocurrent, and photoconductivity. This chapter is closely connected to three subsequent chapters (Chapters 8, 9, and

10), which focus on perturbations by light, solvent, substrate, and lattice vibrations onto the evolution of excited states.

8. Bowman, Chan, and Jakubikova (Chapter 8, *Investigating Interfacial Electron Transfer in Highly Efficient Porphyrin-Sensitized Solar Cells*) explore the way in which electron transfer in dye-sensitized titania depends on the details of the anchoring group composition, the surface adsorption, and the binding pattern. This chapter provides an excellent companion to experimental chapters as well as an overview of one of the first practical methods for the atomistic modeling of electron transfer that is based on the survival probability concept.

9. Akimov and Prezhdo (Chapter 9, *Nonradiative Relaxation of Charge Carriers in GaN-InN Alloys: Insights from Nonadiabatic Molecular Dynamics*) provide an overview of hot carrier relaxation in indium-doped gallium nitride — a promising material for solar energy conversion. The authors review a commonly used method for atomistic modeling of relaxation based on Tully's surface-hopping algorithm and on-the-fly coupling along molecular dynamics trajectory. Prezhdo and Akimov highlight the importance of accounting for quantum decoherence effects, which are responsible for the precision of the computed rates of carrier relaxation.

10. Kryjevski (Chapter 10, *Toward First-principles Description of Carrier Relaxation in Nanoparticles*) focuses on the description of carrier relaxation due to phonon emission in semiconductor nanostructures, which is an important process in photo-excited nanostructures and is potentially relevant to photovoltaics. The chapter discusses an alternative to the on-the-fly procedure for computing electron–phonon interaction. Here, the electron–phonon interactions are treated perturbatively using the Keldysh technique, or non-equilibrium Green's function, including one- and two-phonon processes. Nanoparticle-specific electron–phonon couplings are given by derivatives of the electron–ion interaction along each normal mode of lattice vibrations.

11. Meng (Chapter 11, *Optical, Electronic and Catalytic Properties of Metal Nanoclusters by ab initio Molecular Dynamics Simulation: A Mini Review*) covers two classes of photoinduced processes related to metal nanoparticles: their ability to catalyze chemical reactions and their influence on excited state relaxation. These two classes of processes relate to the dynamics of inter-atomic distances for molecules adsorbed at metal cluster and to the dynamics of electronic excited states, respectively. In the first half of the chapter, Meng provides computational predictions of the efficiency of proton reduction and hydrogen evolution at the surface of metal and bimetal clusters, thus making connections to the experimental chapter on hydrogen generation (Chapter 3). In the second part of the chapter, Meng addresses the details of electronic excited state dynamics in metal clusters by combining the reduced density operator method, similar to the one described in Chapter 7 by Micha, and the on-the-fly procedure for nonadiabatic coupling, similar to the one used in Chapter 9 by Prezhdo and Akimov. The

reported methodology paves the way to compute such nonequilibrium observables as photoluminescence spectra.

12. Zenkevich and von Borczyskowski (Chapter 12, *Surface Photochemistry of “Quantum Dot – Porphyrin” Nanoassemblies: Exciton Relaxation Pathways and Singlet Oxygen Generation Generation*) provide experimental time-resolved data on energy transfer and electron transfer at the interface of semiconductor quantum dot and a sensitizing dye molecule. A range of time-resolved spectoscopical techniques allows for the coexistence of several pathways of photoexcitation to be identified: charge transfer, resonant energy transfer, and multi-electron Auger processes, thus providing new opportunities for the quantitative comparison of computational and experimental approaches.

In summary, complementary reviews on a broad variety of physical and chemical processes in functional nanostructures are presented to recognize recent achievements and to help explore open problems in order to coordinate experimental and computational efforts toward the further research of materials for renewable energy.

Dmitri Kilin

Department of Chemistry
University of South Dakota
Vermillion, South Dakota 57069
and
Department of Chemistry and Biochemistry
North Dakota State University
Fargo, North Dakota 58102

Editor's Biography

Dmitri Kilin

Dmitri Kilin is an assistant professor of computational chemistry at USD (University of South Dakota). Dr. Kilin has over ten years' experience in modeling of excited state dynamics in photoactive nanomaterials, including interfacial charge transfer and reaction dynamics and surface reactions at catalytic sites and interfaces of metal and semiconductor nanomaterials for photovoltaic and photocatalytic solar energy conversion. Dr. Kilin has published over 50 peer-reviewed publications in the area of electron dynamics. Recently, he has organized and co-organized several symposia at the American Chemical Society national meetings and the Pacificchem Congress.

Dmitri Kilin completed his undergraduate (1994) and masters degrees (1996) in Physics from Belarus State University (Minsk, Belarus) and received a doctoral degree from the Chemnitz University of Technology (Chemnitz, Germany) in 2000. After subsequent postdoctoral internships at research groups of Prof. Jeff Cina at the University of Oregon, Prof. Oleg Prezhdo at the University of Washington, and Prof. David Micha at the University of Florida, he joined the Department of Chemistry at the University of South Dakota as faculty. His current research interests are focused on modeling the photo-induced dynamic processes of charge transfer, nonradiative charge carrier relaxation, and surface reactions at catalytic sites and interfaces of metal and semiconductor nanomaterials for photovoltaic and photocatalytic solar energy conversion.

Chapter 1

Sensitization of Single Crystal Substrates

Laurie A. King,¹ Meghan E. Kern,¹ and B. A. Parkinson^{*}

Department of Chemistry and School of Energy Resources,
University of Wyoming, Laramie, Wyoming 82071

^{*}E-mail: bparkin1@uwyo.edu.

¹These authors contributed equally to this work.

Sensitizing large band gap semiconductors to subbandgap light began with the development of photography and has recently been applied to solar energy conversion. In this chapter we review work that employs single crystal semiconductor substrates, such as oxides, chalcogenides and pnictides, to investigate this important fundamental photoinduced interfacial electron transfer processes using sensitizers from dyes to polymers to quantum dots.

Early History of Dye Sensitization

In the 1830s artists began capturing the world around them using the newly developed photographic techniques. However, photography did not reach the masses until films containing grains of silver halides were developed. Silver halides are ionic semiconductors with band gaps ranging from 2.7 – 3.2 eV making them mostly insensitive to visible light (1). The optical absorption of visible light by dyes adsorbed on the multifaceted micron-sized grains of silver halides enables “sensitization” to visible light where photon absorption by the dye promotes an electron from the highest occupied molecular orbital (HOMO) to the lowest unoccupied molecular orbital (LUMO) that subsequently is injected into the silver halide producing a latent image or a reduced silver cluster. The reduced silver center in the grain is a nucleation site for subsequent development of the whole grain by chemical reduction by developers to produce a photographic negative. This photon multiplication process resulted in films sensitive enough to capture images with very little light using either fast shutter speeds or long exposures such as in astronomical applications (2).

Photosensitization of semiconductor electrodes began in the 1960s when Gerischer and Tributsch studied the ability of organic dyes to sensitize ZnO single crystals (3, 4). Unlike photography, where the electron is immediately trapped and reduces a Ag^+ center to Ag^0 , the photoexcited electron of the dye molecule is injected into the ZnO conduction band and can be drawn off as current. The oxidized dye can be regenerated by a reducing agent in an electrolyte to enable a continuous flow of photocurrent (Figure 1) whereas in photography the reducing agent (developer) further reduces Ag^+ around the Ag^0 nucleation sites to produce a dark area forming a negative image. Sensitizing semiconductor electrodes enabled continuous monitoring of the electron transfer reaction (current) with the additional advantage of being able to change the driving force for this interfacial reaction by adjusting the bias, semiconductor band positions and redox electrolyte. Subsequent work led to the establishment of the general principles of electron transfer processes in photosensitized systems. In particular, the alignment of the electron energy levels between sensitizer and the energy bands of the semiconductor were shown to control electron injection. For example, photocurrent was not measureable for dye sensitization of a metal (5). Examples of early sensitization studies include zinc oxide (n-type), copper oxide (p-type) (6), and gallium phosphide (GaP) (p-type) (7). These early studies led to work by Tributsch and Calvin on the photosensitization of ZnO single crystals with chlorophyll; the first direct link between solar energy conversion in nature and photoelectrochemistry (8, 9).

Throughout early dye sensitization experiments, the dyes were weakly bound to the single crystal surface by physisorption. To alleviate the problem of dye desorption experiments were typically performed with dye in solution and hence adsorbed dye is in dynamic equilibrium with dissolved dye. Spectral sensitization was demonstrated with dyes adsorbed again to ZnO (11) but also TiO_2 (12) and SrTiO_3 (13) single crystal surfaces. Further investigations with single crystal semiconductors led to developing greater insight into the fundamental process that dictate electron transfer at these interfaces. For example, the conduction band of a semiconductor can be shifted with respect to the dye LUMO by controlling the pH of solution (59 mV per unit of pH). To probe the effect this has on dye sensitized photoanodes, two dyes were selected such that the conduction band edge of SrTiO_3 at pH 4 approximately matched the LUMO level of the cyanine dyes. Indeed, a threshold for electron transfer was reached by increasing the pH of the electrolyte above 4 such that the conduction band of SrTiO_3 was moved above that of the dye LUMO (13).

Such early work with single crystals also led to the need for quantification of photosensitization driven electron transfer. There are two frequently reported efficiencies for photocurrent generation – incident photon current efficiency (IPCE), also known as the external quantum yield and absorbed photon current efficiency (APCE), also known as the internal quantum yield. Such spectral measurements enable the comparison between sensitizer absorbance and photocurrent generation. The early measurements of these efficiencies produced very low IPCEs and APCEs (<3% APCE) that were often attributed to recombination effects due to surface states that were unavoidable due to dangling bonds on the surface of the semiconductor crystals. In retrospect we now know

that many of the limitations were a result of surface contamination that either blocked the access of the dye to the surface or displaced it from the surface due to weak van der Waals or hydrophobic interactions.

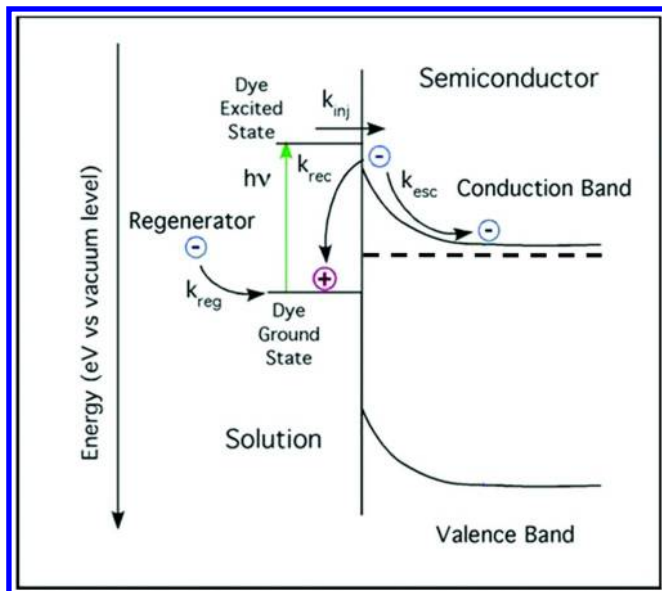


*Figure 1. Rate processes at a dye-sensitized single crystal electrode are depicted for electron transfer into an n-type semiconductor biased to produce a depletion layer. Excitation of an electron from the ground state of a dye at a specific energy to an excited state level results in electron transfer to the semiconductor conduction band with a rate k_{inj} . This charge is drawn off as current as the electrons escape the surface at a rate depicted as k_{esc} . The electrons at the semiconductor surface can also recombine (k_{rec}) with the oxidized dye in competition with reduction by the regenerator (k_{reg}). Reproduced with permission from Spitler, M. T. and Parkinson B. A. *Acc. Chem. Res.* **2009** 42(12) 2017-2029.*

Copyright (2009) American Chemical Society (10).

Dye Sensitization of van der Waal Surfaces

Early work on photoelectrochemical cells made from two dimensional layered transition metal dichalcogenide (TMD) semiconductor compounds, such as MoS_2 , MoSe_2 , SnS_2 and WSe_2 , produced devices with efficiencies of up to 12% were the most stable photoelectrochemical cells (14–21). Mark Spitler, an early pioneer of dye sensitization, arrived at the Solar Energy Research Institute (now called the National Renewable Energy Laboratory) on a sabbatical where one of the authors was working on the TMD photoelectrochemical properties of these layered materials. The two came together since it was realized that these materials might

be particularly attractive due the ease of cleaving layers to expose clean, inert and atomically flat surfaces. Band alignment dictates that due to their relatively small band gaps (1.1 – 1.2 eV) sensitization of MoS₂, MoSe₂ and WSe₂ is restricted to infrared absorbing dyes (21). An appropriate dye was selected (3,3'-diethyl-9,11:15,17-dineopentylene-2,2'-thiapentacarbocyanine), and gave astoundingly high photocurrent yields for a monolayer of dye with IPCE values of 4.4% and APCEs of virtually 100% (Figure 2) (14).

Indeed the signals were so high and background currents so low that they could be easily measured without the use of a lock-in amplifier that had traditionally been needed to extract the small photocurrent signals. Such unprecedented high IPCE values were accredited to the absence of interlayer dangling bonds, and hence lack of trap states that would otherwise lower electron injection efficiencies, and the absence of competition for adsorption sites from organic impurities. Additionally, the stability of their surfaces with respect to water, air or common solvents highlighted them as suitable semiconductors for sensitization.

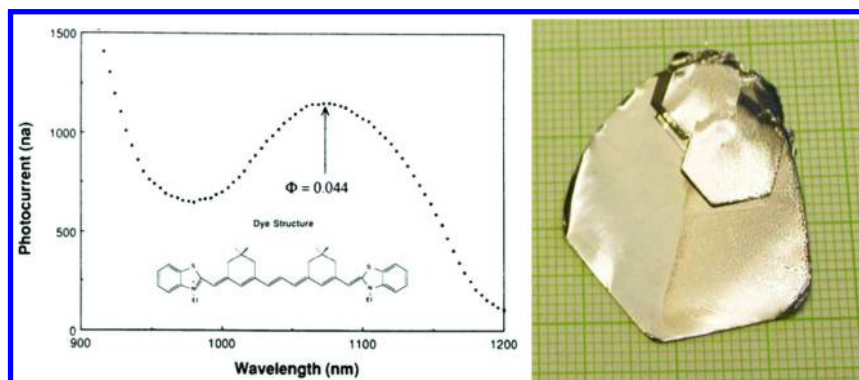
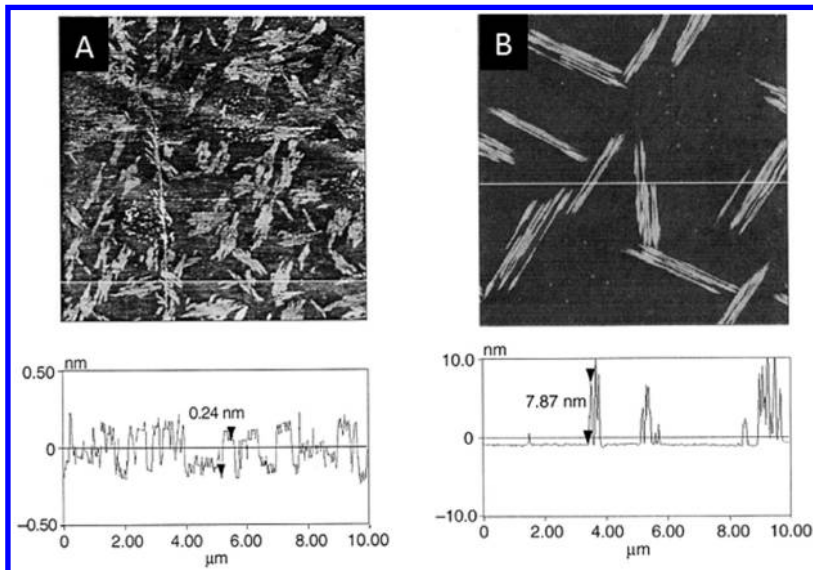


Figure 2. (left) Sensitized photocurrent response of a WSe₂ crystal by the infrared absorbing dye shown at the bottom left of the figure (3,3'-diethyl-9,11:15,17-dineopentylene-2,2'-thiapentacarbocyanine) with a remarkable IPCE value of 4.4% from a monolayer of dye. Reproduced with permission from Spitler, M. T. and Parkinson B. A. *Langmuir* 1986 2(5) 549-553.

Copyright (1986) American Chemical Society (14). (right) A very large WSe₂ crystal on centimeter/millimeter ruled graph paper showing the platelike morphology of these two dimensional materials. (see color insert)

Given the small band gaps of the TMD materials, dye sensitization was limited to unstable IR absorbing dyes, therefore new layered materials, such as SnS₂ with a band gap of 2.2 eV, were explored. SnS₂ was shown to be particularly stable and suitable for study with a broad range of sensitizing dyes (15). Large crystals were grown using the Bridgman method and could be controllably doped using chloride substitution for sulfur (22, 23). The large range of oxidation and

reduction potentials of the dyes that could sensitize SnS_2 led to the observation that lower IPCE values were measured when the potential of the dye HOMO approaches the energy of the conduction band (CB) of SnS_2 (15), implying that the rate of back reaction could be the controlling kinetic factor in the system. The rate of photoexcited electron injection in these materials was also measured to be extremely fast due to the intimate contact and thus strong electronic coupling between the dye and the semiconductor (19, 24).



*Figure 3. Tapping mode AFM images of the squaraine dye Bis(4-dimethylamino-2-dihydroxyphenyl)squarene (1-1 OHSQ) aggregates on SnS_2 prepared by a) dipping for 12 minutes, b) dropping 1 mL equivalent of dye solution and dried in ambient air. Height retraces are shown beneath. Reproduced from *Electrochim. Acta*, 45/28, Takeda, N. and Parkinson, B. A., The relationship between squaraine dye surface morphology and sensitization behavior on SnS_2 electrodes, 4559-4564, Copyright (2000), with permission from Elsevier (20).*

The atomically flat surfaces of the layered compounds make these materials ideal for morphological studies of the sensitizing dyes on the surface using scanning probe microscopies. For example, AFM studies of squaraine dyes enabled the larger scale structures of dye on a SnS_2 surface to be studied. Two routes were compared for dye sensitization: dipping (soaking the crystal in dye solution), and dropping (dropping and evaporating dye solution on the crystal). The resultant dye aggregates that populated the SnS_2 surface were found to be rod shaped, larger and high (approximately 14 nm) for the surface prepared by the dropping method. Aggregated surfaces from the dipping technique were conversely much smaller, particularly in height (approximately 2 nm), but were mostly in rod shapes (18, 20). These two distinct morphologies can be seen in

Figure 3. Figure 4a shows a IPCE spectrum taken at +0.7 V vs SCE together with the optical absorption spectrum obtained for a SnS_2 electrode sensitized by the dipping technique. The sensitized photocurrent-voltage curve, measured at 680 nm incident light, is shown in Figure 4b. The onset of anodic photocurrent was $\sim +0.1$ to 0.2 V more positive than E_{fb} of bare SnS_2 electrodes. The photocurrent increased as the positive bias increased and leveled off around $+0.55$ V vs SCE. After the introduction of the dye-sensitized solar cell (DSSC) (discussed below) photoetching of the SnS_2 single crystal was done to produce high surface area “parking garage” structures that yielded IPCE values of up to 30% (Figure 5) using methylene blue as a sensitizer (23). However there was no expansion of interest in SnS_2 sensitization since single crystals were not widely available and interest in dye sensitization of oxide semiconductors was revived by the DSSC.

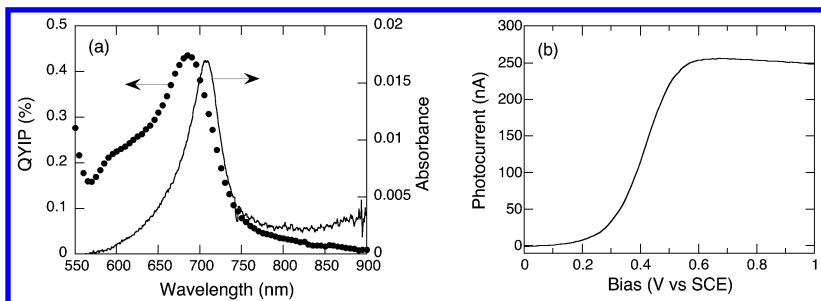


*Figure 4. (a) Vis-NIR absorption spectrum (solid curve) and photocurrent action spectrum obtained at $+0.7$ V vs SCE bias (symbol) for 1-IOHSQ on SnS_2 prepared by the dipping method ($8\mu\text{M}$ for 2min). Note that the absorption spectrum contains contributions from adsorbates on both sides of SnS_2 surface. (b) Photocurrent-voltage curve of the sample illuminated at 680nm ($104\mu\text{W}$). Reproduced with permission from Takeda, N. and Parkinson, B. A., *J. Am. Chem. Soc.* 2003 125(18) 5559-5571. Copyright (2003) American Chemical Society (18).*

During the period when SnS_2 was being studied, Michael Gratzel provoked world-wide interest in dye sensitization with the introduction of the DSSC where both IPCE and APCE values were very high and solar to electrical power conversion efficiencies were competitive with other emerging photovoltaic technologies (25). This breakthrough can be attributed to two innovations; firstly the usage of covalently bound dyes that strongly bound the dyes to the surface and promoted electronic coupling, and secondly, the sensitization of high surface area mesoporous TiO_2 electrodes that could then absorb all the incident light since a monolayer of even highly absorbing dyes can seldom absorb more than 3%. This work eventually lead to devices with power conversion efficiencies in excess of 12% and IPCEs approaching 100% (26). In a typical cell, 20 nm crystallites of anatase TiO_2 are sintered together to prepare a mesoporous network with typically 1000 times the surface area of a planar electrode. The high surface area of the porous cell architecture circumvents the inherent problem of producing

high efficiencies with sensitization of planar electrodes, namely, the low optical absorbance and photocurrent yields of monolayer dye coverage. The dye binding through carboxylate or phosphonate functional groups also removes the need to use excess dye in the electrolyte solution to prevent dye desorption. The unexpected electron lifetime in the high surface area porous network of TiO₂ that is bathed in oxidizing triiodide solution was also a key factor in the success of this solar cell architecture.

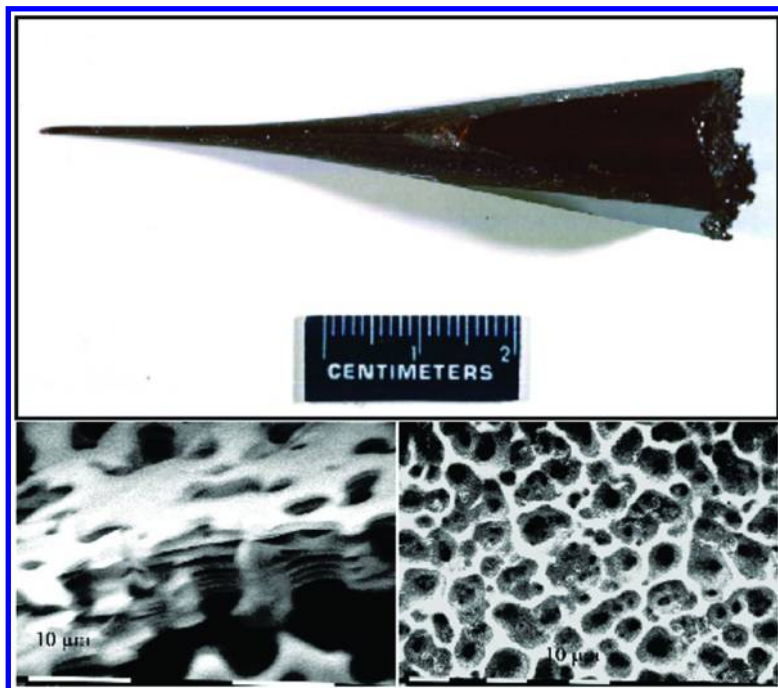


Figure 5. A photograph of a SnS₂ crystal that was grown using the Bridgman technique showing several cleavage planes from the twinned crystal (upper). Reproduced with permission from Sharp, L.; Soltz, D.; Parkinson, B. A.; Cryst. Growth Des. 2006 6(6) 1523-1527. Copyright (2006) American Chemical Society (22). Lower left shows a side view of the “parking garage” structure obtained from photoetching a SnS₂ crystal to obtain a high surface area. Lower right is a top view of the same photoetched crystal. Bottom reprinted from Sharp Thesis (23). (see color insert)

While both single crystal and mesoporous sensitized electrodes are electrochemical junctions that enable the extraction of photoexcited electrons from sensitizers, the physical mechanism/driving force for charge separation at the dye-semiconductor single crystal interface is different. As shown in Figure 1, the single crystals support the formation of a space charge field at the semiconductor electrolyte interface producing a Schottky-like junction where the band bending drives charge separation of the positive charge that remains in the

dye from the injected electron. Conversely, nano-sized crystallites are too small to support a depletion layer and therefore are reliant on concentration gradients of electrons between the surface and back contact to drive charge separation.

Following the introduction of DSSC technologies the research in dye sensitization rapidly expanded with thousands of researchers being engaged in the quest for achieving increased cell efficiencies perhaps due to the ease of fabrication and low cost of the components (27). Much of this work has, and continues to concentrate on the design of new sensitizers, new redox couples and electrolytes, techniques to prepare and modify the mesoporous films and attempts to manufacture and reduce the costs of this solar cell. Despite the significant increase in cell efficiencies and commercialization of this technology there remain significant advantages to utilizing well-characterized atomically flat single crystals for studying the sensitization process (10). Namely, the ability to conduct fundamental studies with structurally well-defined and clean surfaces. Obtainable insights include the deciphering of the role of dye adsorption geometries, sensitizer coverage and structure, the influence of crystal orientation and extent, benefit or detriment of sensitizer aggregation on sensitization yields. The remainder of this chapter will review the progress in both experimental protocols needed to work with semiconductor single crystal substrates and the fundamental understanding of the photoinjection process that may aid in the optimization of nanocrystalline sensitized solar cells.

Metal Oxide Dye Sensitization with Covalently Bound Dyes

Methods To Prepare Clean and Terraced Single Crystal Substrates

To enable the elucidation of sensitizer coverage and ensure reproducible photocurrent yields, it was necessary to develop techniques to prepare clean, atomically flat terraced surfaces that are detailed in the following sections.

Titanium Dioxide

Titanium dioxide (TiO_2), in the nanocrystalline anatase polymorph, remains the most commonly sensitized substrate in DSSCs. With a band gap of 3.2 eV anatase does not absorb visible light. It is known that to obtain high coverages of dyes on these nanocrystalline substrates that it is best to sensitize them immediately after sintering the nanocrystals to avoid competitive adsorption to binding sites by adventitious impurities. The high surface area of these scaffolds means that in this short time there is relatively little surface contamination, however this is not true for an oxide single crystal since the actual and geometric surface area are nearly the same.

Clean and terraced rutile (110) and (100) TiO_2 surfaces for photoelectrochemical studies were previously prepared by a chemical etching method (28, 29). Specifically, the crystals were submerged in HF, rinsed, dried and annealed at 550 – 900 °C in air. This route is indeed effective for obtaining atomically flat crystallographic surfaces since the material etches in a layer-by-layer fashion. However, for crystal surfaces with higher surface

energies, pits and channels have been observed due to selective crystallographic plane etching and increased etching at defects and impurities (30).

To alleviate the issues associated with a chemical etch, an alternative method was developed to prepare various surface orientations of all three polymorphs of TiO_2 (rutile, anatase and brookite) (31). A combination of manual polishing, ultrasonic cleaning and annealing was found to produce atomically flat surfaces. Dependent on the initial condition and roughness of an as received (commercially grown) or cut (natural crystal) surface, an appropriate polishing procedure must first be selected or developed. Alumina polishing grits and silica colloidal suspensions with a polishing pad are used for manual polishing. The polishing suspensions are used sequentially, stepping down in size until final polishing with $0.02\text{ }\mu\text{m}$ colloidal silica. The sample is ultrasonicated in H_2O between each step to remove excess polishing material. Subsequently, crystals are etched in HF to remove surface damage caused by polishing and any silica polishing agents that adhere to the surface. The crystals are then annealed in air for 7 – 16 hours at temperatures and times appropriate to each TiO_2 polymorph (31).

In addition to assisting the preparation of atomically flat crystal surfaces, HF-annealing treatment was shown to remove inactive/amorphous layers from polishing damage at the surface, enhancing dye sensitized photocurrent yields relative to only annealing (32).

UV Treatment/Cleaning of TiO_2

In our lab once an atomically flat, terraced TiO_2 surface has been prepared and confirmed by AFM the crystals are ready for sensitization. However, when crystals were sensitized without a subsequent cleaning treatment, irreproducible coverages and subsequent photocurrents were measured. A treatment was therefore developed to clean the surface directly prior to sensitization. Originally, an ultraviolet (UV) treatment was developed for single crystal anatase (101) TiO_2 (33). The treatment uses UV illumination of the TiO_2 crystal held at positive potential (depletion condition) for 5 – 20 min in HCl (anatase) or NaClO_4 (rutile) (34). The surface is subsequently rinsed with deionized water, dried and then submerged in the sensitizing solution as quickly as possible. The cleaning treatment was found to improve both the reproducibility and photocurrent efficiencies of dye sensitization. UV illumination of TiO_2 produces highly oxidizing holes in the TiO_2 valance band that form OH radicals at the electrolyte interface that oxidize residual organic impurities from the TiO_2 surface and perhaps activate the surface for dye binding (33). AFM images verified that multiple cleaning cycles did not change the surface morphology implying that the treatment does not etch the surface to produce a higher surface area that could be responsible for the higher photocurrents measured after such treatments. It does not eliminate the possibility of etching the surface in a layer-by-layer fashion but this is unlikely since it works on many low index surfaces of both anatase and rutile and no increase in pitting at defects is observed. The UV phototreatment led to reproducible IPCE yields for single crystal dye sensitization of up to 2% and APCEs approaching 100% (35). The UV treatment allowed for the measurement of isotherms for N3 and other dyes in a facile fashion whereas before the UV

cleaning procedure the dye coverages were lower and less reproducible and the crystal was soaked in the dye solution at every concentration for many hours before it was thought that equilibrium coverage was reached. Now when measuring an adsorption isotherm the UV-treatment is used between exposure of the crystal to the different dye concentrations and a point on the isotherm could be obtained in a few minutes. However, after many cycles of repeat sensitizing or long times periods, the surface photocurrents, and presumably the surface coverage of the dye, declines so a return to polishing and annealing is needed to rejuvenate the surface.

Doping Density

Not all crystals (naturally occurring or commercially grown) are doped to the optimum doping density for conductivity, or, indeed sensitization. In semiconductors, doping refers to electrically active impurity atoms or vacancies within the crystal. The doping determines the free carrier concentration of a material and in general, the higher doping density, the more conductive the crystal. Dependent on the dopant, electron donor impurities create states near the conduction band or electron acceptors near the valance band and therefore shift the Fermi level of the semiconductor. Mott-Schottky analysis is commonly utilized to determine the doping density and the flatband potential. These values are used to calculate the band positions of crystals in the electrolyte solution. Procedures for vacuum doping TiO_2 have been developed to prepare rutile and anatase crystals for sensitization (36). Vacuum-doping produces oxygen vacancies that increase the electron concentration in the conduction band of the TiO_2 . The process can be reversed by annealing in air or an oxygen containing environment.

Despite the many years of studying sensitization on single crystals, and the existence of a one dimensional Onsager model to explain the expected influence of the doping level of the semiconductor on the collection of photojected electrons (37), there were no systematic experimental tests of this theory. Therefore a systematic study with rutile (110) crystals with doping levels spanning from almost insulating (10^{15} cm^{-3}) to near degenerate (10^{20} cm^{-3}) TiO_2 single crystals was performed. A photograph of a series of rutile crystals after doping is shown in Figure 6. Dye sensitized photocurrent quantum yields and the shapes of the photocurrent voltage curves were measured (36). Three distinct regions of behavior in the current-voltage curves were identified corresponding to three ranges of doping densities as seen in Figure 7.

These regions were fit to an Onsager-based model for charge collection at a semiconductor electrode and revealed the role of physical parameters such as the space charge layer, diffusion, and rates of electron transfer on photocurrent yields. At the low doping density range, a slow rise of photocurrent was observed with increased potential. Across the intermediate range, a saturation level for photocurrents with applied bias was measured, as expected for Schottky barrier type behavior. Within the third region, highly-doped crystals, tunnelling currents were found to play significant role in dictating the photoresponse. The overall plot showing the IPCE dependence on doping density is shown in Figure 8. It is clear an optimal doping density is around $2 \times 10^{17} \text{ cm}^{-3}$ for both dyes. The lower

peak for N3 is a result of an extinction coefficient for this dye being $\sim 1/3$ that of G15. However, the equal values at low and high doping is a result of N3 being less susceptible to recombination processes.

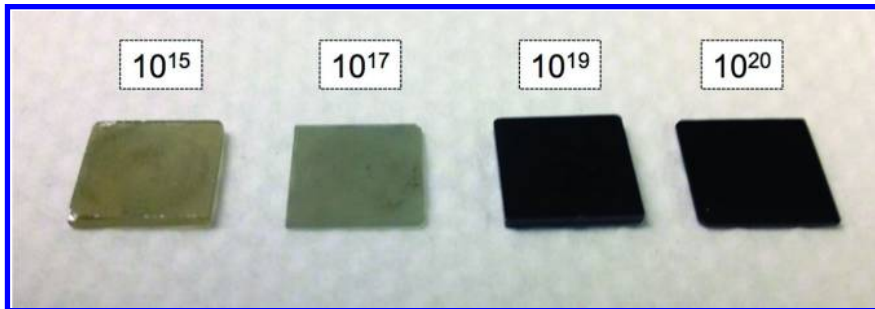


Figure 6. Photograph of rutile crystals prepared with a reductive doping procedure at high temperatures in varius atmospheres. (see color insert)

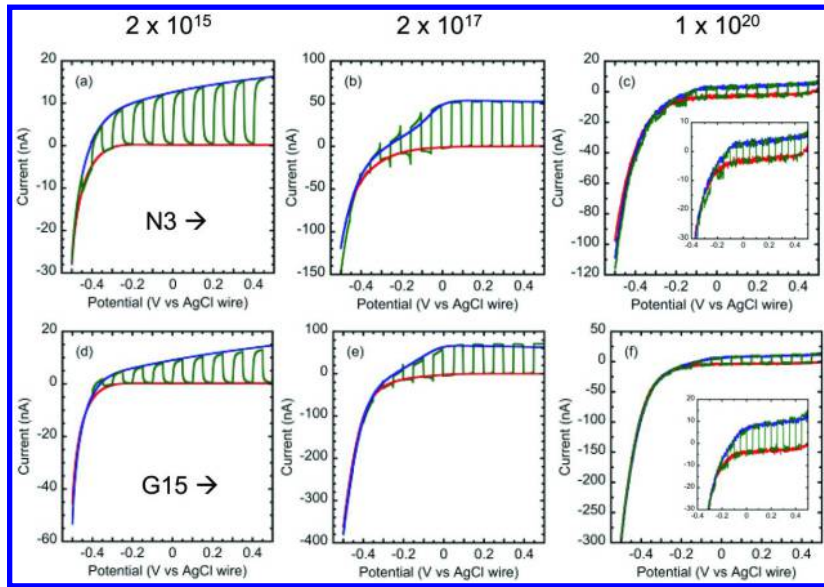


Figure 7. Current-voltage curves for N3 (a,b,c) and G15 (d,e,f) sensitized TiO_2 electrodes at doping levels of $2 \times 10^{15} \text{ cm}^{-3}$, $2 \times 10^{17} \text{ cm}^{-3}$, and $1 \times 10^{20} \text{ cm}^{-3}$, (a,d), (b,e), (c,f) respectively. Curves were measured in the dark (red), under 80 μW of 532 nm illumination (blue), and chopped (green). Permissions requested to reproduce from Watkins, K., Parkinson, B. A., and Spipler, M. T. *J. Phys. Chem. C* 2015, submitted (36).

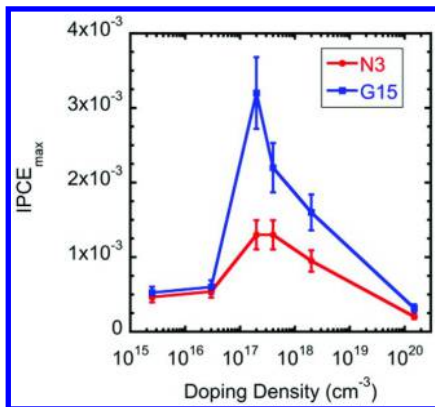


Figure 8. Plot of maximum IPCE values for N3 and G15 sensitized TiO_2 over a range of doping densities. Permissions requested to reproduce from Watkins, K., Parkinson, B. A., and Spitler, M. T. *J. Phys. Chem. C* 2015, submitted (36).

Single crystals of the rutile TiO_2 polymorph are available from commercial crystal growing labs. However single crystal anatase, the most commonly used polymorph in mesoporous DSSCs, is not. Techniques to grow large synthetic anatase TiO_2 have not to our knowledge been developed and to date, only one report of sensitization of synthetic crystals has been published (38). Therefore, natural sources of anatase crystals have been utilized for sensitization studies. Such crystals are sourced from sites in Norway, Pakistan and Brazil. While natural crystals have been sensitized successfully, the purity, doping densities and surface morphology are inherently uncontrollable. Finding a smooth terraced surface with an appropriate doping density can often require sorting through many natural crystals before a suitable crystal is found. Epilayers of anatase TiO_2 are therefore particularly appealing in order to circumvent and ultimately control the impurities that influence doping density and carrier mobilities of a semiconductor. Techniques have been developed to enable the growth of homoepitaxial layers of rutile-on-rutile and anatase-on-anatase such as molecular beam epitaxy (MBE) (39), pulsed laser deposition (PLD) (40) and, recently in our lab, atomic layer deposition (ALD) (41).

Despite the success of growing anatase-on-anatase to enable the control of the single crystal substrate doping density, an alternative route that does not require natural crystals was also desired. Anatase (001) heteroepitaxial layers have been grown on SrTiO_3 (100) crystals that has a lattice mismatch of 3%. CVD and MBE have both been used to prepare around 1 nm thick epitaxial layers (39, 42, 43). However, ALD produced layer-by-layer epitaxial growth up to 10 nm thick (44) as seen in Figure 9.

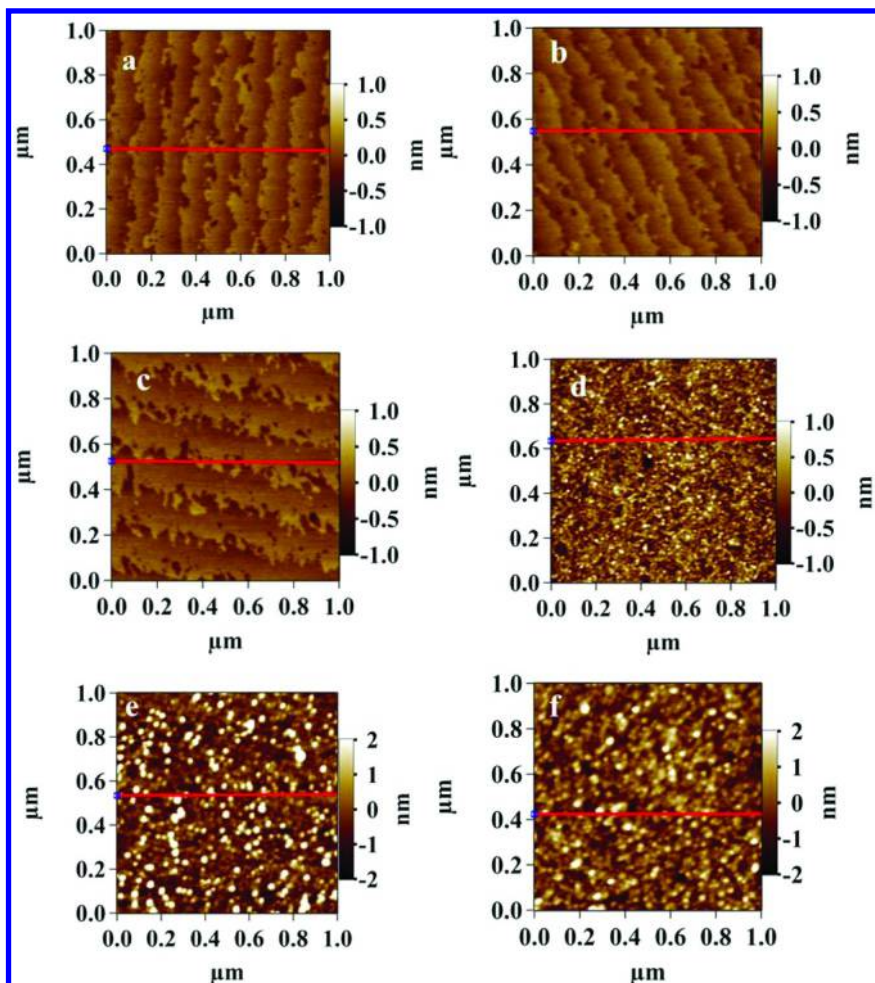


Figure 9. AFM images of pure (a) $\text{SrTiO}_3(100)$ and ALD deposited $\text{TiO}_2(100)$ films with different thicknesses : b) 6, c) 10, d) 14, e) 20, f) 32 nm. Reproduced with permission from Kraus, T.; Nepomnyashchii, A.; Parkinson, B. A.; *J. Vac. Sci. Technol., A*. **2015**, *33*, 01A135. Copyright 2014, American Vacuum Society (44).

The relevance of such epitaxially grown anatase layers for sensitization studies was confirmed by sensitizing them with both N3 and G15 dyes. Interestingly, photocurrent yields (IPCE) were found to be dependent on the thickness of the epilayer. Specifically, the IPCE photocurrent yields almost doubled when the epilayer thickness was increased from 5 nm to 10 nm, as shown in Figure 10. Within this region of layer-by-layer growth, the single crystal

surface area remains constant and therefore increased dye coverage cannot explain such enhanced yields. The doping level measured for the epilayer should produce a space charge layer thickness in the anatase film of about 20 nm, greater than the epilayer thickness. Therefore the electric field gradient between the highly doped more conductive SrTiO_3 substrate is much steeper resulting in a narrower potential barrier for the electron to tunnel through in the case of the 5 nm film. In comparison, the thicker, less steep potential barrier of the 10 nm layer, will have a higher recombination rate with absorbed photooxidized dye. For layers grown over 10 nm in thickness, the increased photocurrents can be accredited to the larger surface area due to nanocrystalline growth at the surface and hence more adsorbed dye coverage and higher IPCE (Figure 9d-f and Figure 10).

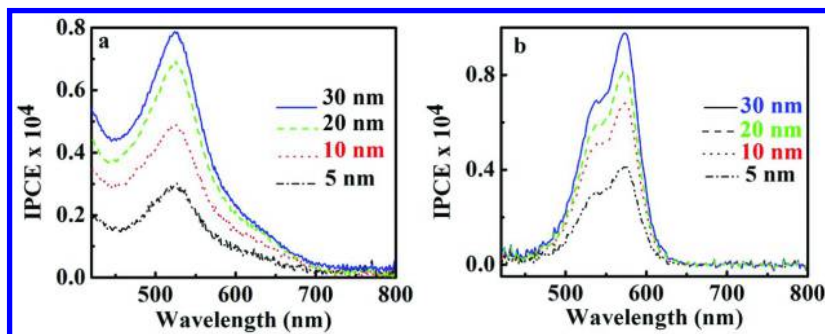


Figure 10. Dye sensitization of anatase TiO_2 (001) ALD layers grown on SrTiO_3 and sensitized by a) 1 mM N3 and b) 5×10^{-5} M G15. Reproduced with permission from Kraus, T.; Nepomnyashchii, A.; Parkinson, B. A.; J. Vac. Sci. Technol., A. 2015, 33, 01A135. Copyright 2014, American Vacuum Society (44).

Studies of Dye Binding Morphologies on TiO_2 Crystals

The ruthenium-based dye that was the most commonly used sensitizer for DSSCs is the complex *cis*-di(thiocyanato)-bis(2,2'-bipyridyl-4,4'-dicarboxylate) ruthenium (II), commonly known as N3 the structure is shown in Figure 11a. N3 has four carboxyl groups on the peripheral bipyridines through which the dye can bind to oxide surfaces. The advantages of N3 include its broad spectral absorbance range and its demonstrated stability in a DSSC. The visible absorption band is due to a metal-to-ligand charge transfer transition.

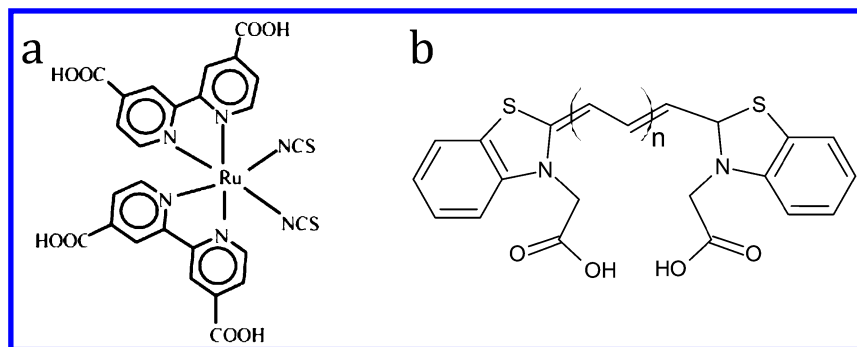


Figure 11. Molecular structure of a) N3 and b) generic thiacyanine dye sensitizers where G15 dye has $n = 1$ and R8 dye has $n = 2$.

Cyanine dyes are organic dyes where the HOMO-LUMO transition is from π to π^* orbitals. A general molecular structure for carboxylated thiacyanine dyes is shown in Figure 11b. Most cyanine dyes aggregate (33, 34, 36, 45–48) causing a shift in the absorbance, emission, reflectance or transmittance spectrum of a dye solution or in the solid state (49). The different geometric arrangements of dye monomers lead to either blue or red shifts that characterize them as H- or J- aggregates, respectively. H-aggregates are the consequence of parallel, dye molecules stacked plane-to-plane like a deck of cards such that the slippage angle is formed between the parallel transition dipoles is less than 55°. When the centers of the dye dipoles are stacked at an angle greater than 55° it is termed J-aggregation. J-aggregate absorption bands are typically sharper and have higher extinction coefficients than their corresponding monomer or H-aggregate peaks.

Dye Loading

As mentioned previously it is desireable to covalently attach the dye molecules to the semiconducting substrate. The majority of the investigated dyes use a carboxylate linkage but exact binding motif of carboxylate group to the uncoordinated Ti sites on the TiO₂ surface has been a contentious issue in the dye sensitization literature. The binding motif between dye and semiconductor could potentially adsorb in one of 3 orientations: unidentate, bidentate, or bridging fashion (50, 51). Ehret et al. showed that dye sensitization on nanocrystalline anatase is controlled by dye linkage at the carboxylic acid groups (52). Models have also been developed to simulate the binding interaction (53). In some cases, monomeric forms of dye are observed, while dimers have also been evidenced (54). Control over dye aggregation has been effectively demonstrated by adding antiaggregation coadsorbants to minimize dye-dye interactions (55).

Quantifying dye coverage at a single crystal surface provides important information regarding the dependence of dye attachment on the crystalline

semiconductor face, difference in dye geometry, binding motif, organization and aggregation. As described above, direct measurement of dye coverage is non trivial at a single crystal surface. Therefore, adsorption isotherms are typically measured by assuming that the measured IPCE is directly proportional to surface coverage. Hence, crystals are soaked in dye solutions over a range of concentrations and the IPCE is measured at each concentration. This is repeated until no increase in photocurrent is detected and close to a monolayer of dye coverage is then assumed. Adsorption isotherms have been measured this way for N3 (56) and cyanine dyes (33, 34) at various single low index crystal surfaces of TiO_2 . Sensitization from low concentration dye solutions led to low surface coverage in which the monomer dye dominates. With longer exposure times and higher concentrations the aggregated dye dominated the surface coverage. The initial rate of adsorption of dyes from solution onto single crystal substrates was found to be very fast and not resolved by the slow time scale of the measurements used. However, the second step was a slow adsorption step that was shown to fit a Langmuir kinetic model. The Langmuir isotherm model assumes that surface bound molecules do not interact. If aggregation at the surface, an attractive interaction, is considered in the Langmuir model, a steeper isotherm is predicted. Similar isotherms were observed for N3 and cyanine dyes.

Dye desorption rates have been measured for both N3 and dicarboxylated cyanine dyes. N3 has been shown to bind to the surface very strongly and minimal desorption occurs at a very slow rate (56). The little desorption that was observed was attributed to the loss of dye molecules bound by just one or two or three possible carboxylic acid binding groups. In the case of G15, a dicarboxylated cyanine dye, more than half of the adsorbed dye was lost in 20 minutes when utilizing hydroquinone as a regenerator in acetonitrile (46). It was speculated that the desorption was the replacement of G15 dye (most likely the G15 that was only bound by one carboxylate) with a surface bound quinone species. Along with the dye desorption process, a rearrangement of monomer into dimers or small aggregates was also observed. When KI was used as a regenerator very little change in the photocurrent over time was observed suggesting very little dye desorption.

Monitoring dye coverage as a function of metal oxide crystallographic plane for different dyes has been a particularly revealing experiment made possible by the utilization of oriented low index single crystal surfaces. Specifically, surface-dye combinations whereby the distance between Ti binding sites on the surface closely matched the distance between carboxylic acid binding groups on the dyes were found to have the highest dye loading and photocurrent yields (Figure 12). Experiments with N3 (56) and dicarboxylate thiacyanine dyes (33, 34) sensitized at different low-index TiO_2 polymorphs were performed to verify the importance of this effect named “lattice matching”. For example, the highest IPCE acquired for N3 was measured for anatase (101) and rutile (100) where comparing the distances between Ti binding sites and the modelled distances between two carboxylates on the N3 molecules was found to have the closest match. In contrast, the (001) faces had lower dye coverage and therefore lower IPCE values. This was accredited to geometric discrepancies between N3 carboxyl groups and the binding sites on the crystal face.

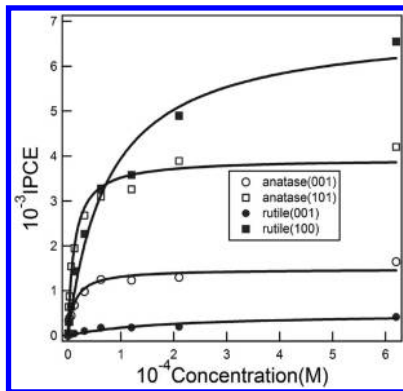


Figure 12. Isotherms for N3 adsorption onto the four TiO_2 crystal surfaces. Reproduced with permission of The Electrochemical Society from Lu, Y. et al. *J. Electrochem. Soc.* **2006** 153(8) E131-E137 (56).

The influence of lattice matching on dicarboxylated cyanine dye sensitization at single crystal surfaces was also probed. In these organic dyes a conjugated carbon chain separates two cyanine groups which have carboxylate “legs” that enable binding to the Ti surface sites. To probe the lattice matching model, a family of four structurally similar dyes were used to sensitize four different low index TiO_2 single crystal surfaces (34). Each dye was identical in structure apart from the carboxyl-carboxyl distance of the cyanine dye. A simple simulation was used to calculate the assumed parabolic probability of the intramolecular carboxyl-carboxyl separation distance with respect to the equilibrium length. The binding probability is highest for the dyes in which the difference between the carboxyl distance and that between the Ti binding sites on the different TiO_2 surfaces is the smallest. An example of the lattice matching is shown in Figure 13 for anatase TiO_2 and the thiacyanine dye R8. Photochronocoulometry was used to measure the actual surface coverage of dye and verified the influence of lattice matching on surface coverage. Indeed the lattice matching model used to simulate the projected surface coverage was found to match the correct surface coverage of each dye for each of the crystallographic faces.

AFM images reveal some of the differences in the binding of N3 and cyanine dyes on rutile surfaces (Figure 14). The N3 dye appears as dots in the AFM images broadened by tip interaction but showing a reasonable height whereas the cyanine dyes appear to be small aggregates on the surface and often larger higher structures that may be extended aggregates (white feature on right image) are seen. Whether these larger aggregates are electronically coupled to the surface and contributing to the sensitized photocurrent is not yet understood but will be discussed in the ATR section below.

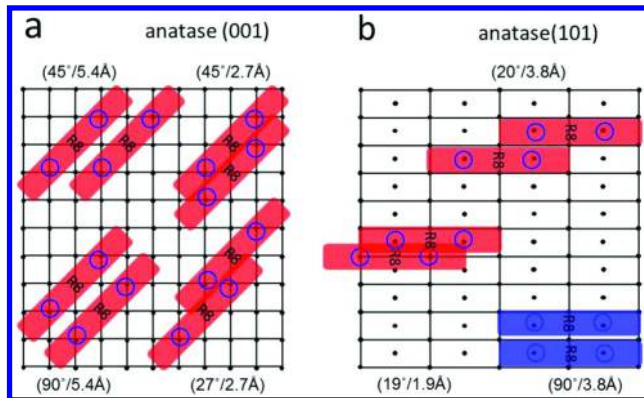


Figure 13. Possible surface bound confirmations for R8 on TiO₂ (a) anatase (001) and (b) anatase (101) that fall within the approximate parabolic binding probability of the intramolecular carboxyl-carboxyl separation distance with respect to the equilibrium length. The grids show surface unit cells for the crystallographic face with the dots corresponding to Ti binding sites. The long rectangles represent dye molecules, the two circles within the rectangle represent the approximate location of the two carboxylate binding groups. Dye binds to the TiO₂ surface as monomers (red) or H-aggregates (blue). The parentheses contain the slip angle and intermolecular distance between neighboring R8 molecules. Reproduced with permission from Choi, D.; Rowley, J. G.; Spitler, M. T.; Parkinson, B. A.; Langmuir 2013 29, 9410-9419. Copyright (2013) American Chemical Society (34).

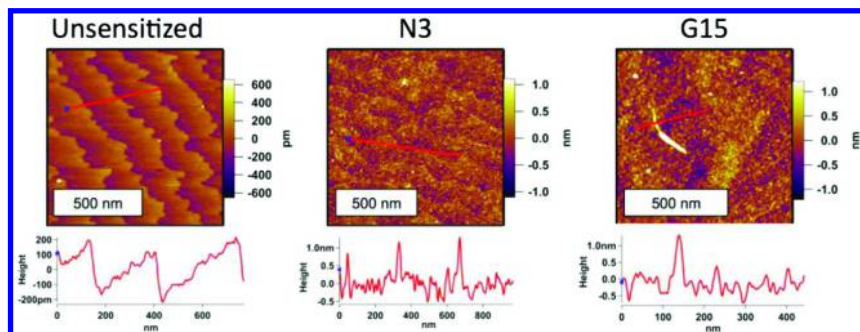


Figure 14. Representative AFM images of prepared atomically flat single crystal (110) rutile TiO₂ for clean, N3 sensitized, and G15 sensitized surfaces. Red lines show where the height traces are on the images. Monolayer dye coverage is evident from the underlying terraces still being visible. The spherical shape of N3 dye and the tendency of the flat G15 dye to aggregate is observed in the images. Permissions requested to reproduce from Watkins, K., Parkinson, B. A., and Spitler, M. T. J. Phys. Chem. C 2015, submitted (36).

A further study using the monocarboxylate merocyanine dye also demonstrated the importance of lattice spacing on photoelectrode efficiencies (57). Here, the conclusion was based on the IPCE and APCE comparisons between rutile (100) and (110) TiO_2 surfaces. APCE values were found to be almost identical for both surfaces. On the contrary, IPCE values were much larger for the (100) surfaces. It was calculated that the density of Ti sites on the (100) surface was approximately 1.44 times larger than that of the (110) surface. Therefore, it was concluded that the higher IPCE of (100) was due to increased dye loading due to the increased density of surface binding sites.

Other Single Crystal Substrates

Single crystals of ZnO , SrTiO_3 , and SnO_2 are other wide band gap semiconductor materials that have been used as substrates for sensitization. A significant amount of work has already been carried out on single crystal ZnO (47, 58–60). ZnO has a band gap of 3.4 eV, ideal for enabling selective excitation of QDs with high-energy photons avoiding absorption from the substrate, while also being optically transparent and still exhibiting high electronic conductivity (61). The amphoteric nature of ZnO and varying stabilities of different faces does not allow for the harsh cleaning procedures used for TiO_2 (discussed above) to be used. Currently, ZnO single crystals are polished with colloidal silica and annealed at 1000°C for a few hours. Preparation techniques for ZnO are currently being investigated to determine the most reproducible method for acquiring terraced surfaces. SrTiO_3 and SnO_2 have band gaps of 3.2 eV and 3.8 eV, respectively (62). SrTiO_3 is of interest due to its low cost while SnO_2 has a more negative conduction band edge than TiO_2 allowing for sensitization from other materials. Due to limited commercial availability of single crystal SnO_2 substrates, natural crystals of SnO_2 are currently being investigated to determine doping densities and preparation techniques.

Specialized Techniques for Single Crystal Sensitization Studies

Given the inherently low optical density of monolayer sensitizer coverage at single crystal surfaces, it is difficult to measure the absorption spectrum of a surface attached dye in a conventional manner. Therefore, more sensitive, specialized techniques have been employed to quantify surface adsorption. These include total attenuated reflection spectroscopy (ATR) and photochronocoulometry.

ATR was first implemented to study dye adsorption in Gerischer's laboratory in 1979 (63). In ATR spectroscopy, the crystal used for sensitization is fashioned into an attenuated reflection element (ARE) such that the crystal acts as a waveguide for the internally reflected probe beam. Signal amplification is achieved by the inherent nature of ATR and the multiple reflections within the crystal as dictated by the crystal size and angle of incidence of the probe beam. Measurement of the probe beam therefore enables simultaneous surface dye adsorption and photocurrent measurements to be monitored. The general setup for ATR measurements is shown in Figure 15.

ATR has been used for both non-carboxylated and carboxylated dye sensitization studies. Disparities (13, 64) and matches (13, 47) between the spectral shape of photocurrent yields and sensitizer absorbance have been observed for different dyes and concentrations. To explain such discrepancies the considerations go beyond simple molecular dye interactions with substrate semiconductors. Rather, a description that considers the different oxidation potentials of monomer and aggregate in combination with a hole-trapping scheme is required (13). The hole-trapping scheme model was originally established for photographic literature. In this model, the exciton of an aggregate is broken by trapping of the hole by either surface defects, or an adjacent monomer/aggregate (dependent on the H- or J- nature of the aggregate) and therefore leads to a differing ratio of aggregate to monomer in photocurrent efficiencies relative to the absorptance spectra.

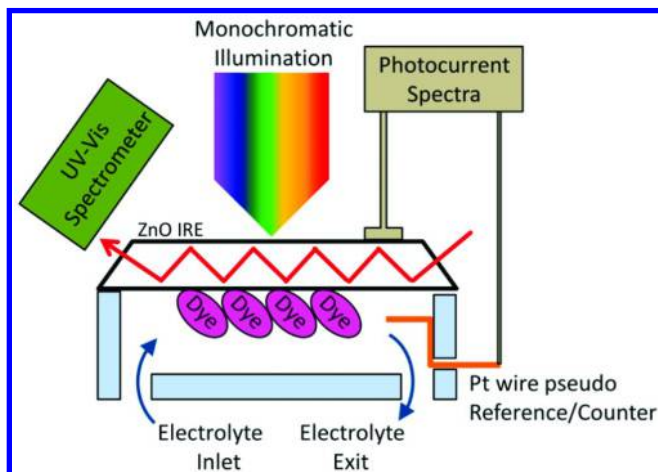


*Figure 15. Schematic of attenuated reflection spectroscopy typical setup used to monitor the dye on the surface of a large band gap metal oxide shaped into a prismatic internal reflection element. The crystal is used as one side to a flow cell enabling the electrolyte and dye to be exchanged. The setup allows a time-dependent spectral characterization of adsorption of the dye on the surface as well as an in-situ determination of IPCE. Reproduced with permission from Rowley, J. G. and Parkinson, B. A. *Langmuir* 2013 29(45) 13790-13796.*

Copyright (2013) American Chemical Society (47). (see color insert)

Deconvolution of cyanine dye spectra (absorptance and IPCE) with respect to the monomer and dimer (or aggregate) contributions, can be particularly challenging due to significant spectral overlap between species. Thermal aggravation shifts the equilibrium of dye monomer to dimer ratio in solution. Therefore, as a function of temperature, a dye solution spectra can be deconvoluted to separate the individual monomer and aggregate spectra (65). With regards to single crystal sensitization, the solution fit was used to fit and hence decipher the monomer to aggregate contributions to photocurrent and optical absorption

spectra (34, 47). An alternative route to decipher the monomer and dimer spectra is through studies over a certain concentration range (specific to each dye) as shown by their adherence to the law of mass action for the monomer-dimer equilibrium leading to the presence of an isobestic point when absorption spectra are normalized by solution concentration. This evidences the presence of two colored species in equilibrium. As the concentration of dye is increased further, the cyanine dye typically proceeds beyond the dimer to a more aggregated state. At this stage, the absorbance spectrum no longer passes through the same isobestic point. The ratio of concentrations of monomer and dimer can therefore be found by knowledge (or elucidation), or the molar extinction coefficient of pure monomer (54).

Chronocoulometry is the measurement of charge versus time in response to an applied potential and can be used, for example, to estimate electrode surface areas. Photochronocoulometry was first used to quantify adsorbed triiodide (I_3^-) at the surface of $MoSe_2$ electrodes (66). In this study, the photooxidation of adsorbed I_3^- and the resultant current was measured, therefore giving the number of species adsorbed at the electrode surface. More recently, photochronocoulometry has been developed to elucidate dye coverage of sensitized single crystals. In these measurements, light excites the dye (as it would in a conventional photocurrent measurement), but a lack of regenerator prevents the reduction of the photooxidized dye molecule. In this configuration, theoretically, one electron is injected into the semiconductor per dye molecule and hence summing the current and calculating the total charge injected gives the total number of molecules adsorbed at the surface (34, 48).

Very fundamental work by the late Frank Willig on sensitization of oxide crystals in UHV is of particular note since it was able to probe the entire density of states of both dye and semiconductor and the timescales of all of the often ultrafast processes occurring at the interface (67, 68). In one study, a comparison between organic chromophore (perylene) injecting electrons into a metal (Ag) and sensitization of titanium dioxide single crystals was probed by two-photon photoemission spectroscopy (2PPE) revealing the energy distribution of electrons injected into acceptor states. The two transfer times for Ag and TiO_2 were shown to be very similar despite the inherent differences in bulk density of states in the solid electrode. This was rationalized by the assumption that the active electronic acceptor state share localized electronic states on the surface of TiO_2 and are created in the vicinity of the bonds formed by the anchor groups of the organic chromophore, hence the similarity between the two systems (67).

Conjugated Polymers as Sensitizers

Conjugated polyelectrolytes (CPEs) are another sensitizer being explored for solar energy conversion due to their tunable band gap, large absorption cross section, stability, potentially low cost and charge transport properties (69, 70). An additional advantage of utilizing these materials as sensitizers is the ability to produce an environmentally friendly, lightweight and low-cost device (69, 70).

A study by Sambur et al. investigated the effect of surface coverage and morphology of poly(phenylene ethynylene) CPEs on the sensitized photocurrent yield on single crystal substrates (71). AFM studies revealed an increase in surface coverage of CPE as a function of both solution concentration and adsorption time. However, the degree of aggregation present on the surface was observed to vary as a function of solvent and was attributed to the solubility of the CPE. Well-solvated CPEs underwent surface limited growth where no further adsorption of CPE was observed with prolonged adsorption in even the most concentrated solution, whereas low solubility of the CPE led to the persistent growth of aggregates with increasing adsorption time. This suggests that in the case of low solubility, the chain-chain interactions between CPEs were driving the formation of an aggregated polymer network and increasing the thickness of the CPE layer. Corresponding IPCE spectra were found to be consistent with the CPE morphology. An increase in IPCE was observed with increasing both CPE concentration and adsorption time. However, when the CPE was adsorbed from low-solubility solution the IPCE was red shifted from that of the solution absorption indicative of aggregation of the polymer and consistent with the AFM images. APCE values for the different polymer morphologies revealed that exciton transport through thicker layers of CPE is not efficient as the IPCE values saturate while the polymer thickness increases thus decreasing the APCE.

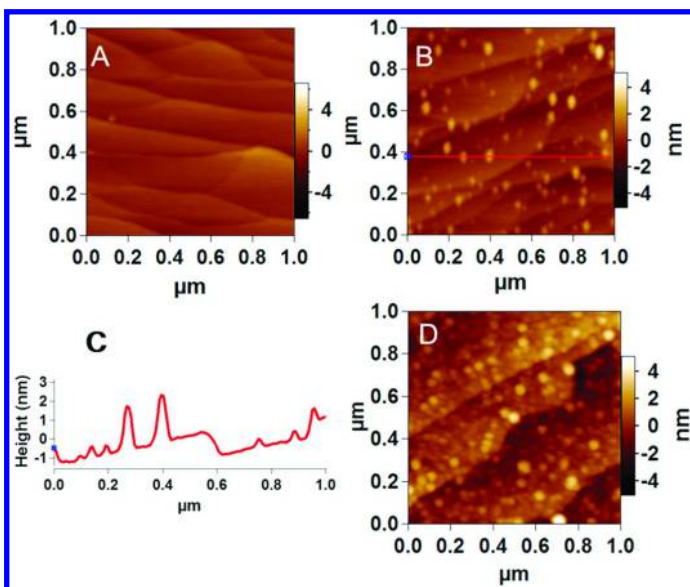


*Figure 16. Noncontact tapping mode AFM images of poly-1 deposited on a ZnO(0001) surface from DMF solutions of different concentrations with a dipping time of 5 min: (A) 0 (clean ZnO surface), (B) 6, and (D) 60 μ g/mL. (C) Cross section analysis along the red line in (B). Reproduced with permission from Zhu, X.; Nepomnyashchii, A.; Roitberg, A.; Parkinson, B. A.; Schanze, K. S.; *J. Phys. Chem. Lett.* 2013, 4, 3216-3220. Copyright (2013) American Chemical Society (73).*

The structure of the CPE can be not only used to tailor the HOMO-LUMO gap but also the structure-property relationship exhibited by the CPE (72). Through specifically designed syntheses, the degree of aggregation observed by the polymer in solution can be controlled. The attachment of a non-aggregating CPE was monitored by AFM to study the morphology of unaggregated polymer chains (73). The adsorption of the non-aggregating CPE to single crystal ZnO increased as a function of solution concentration. Submonolayer coverage of individual polymer chains was observed at low concentration of non-aggregating PCE and interestingly, monolayer coverages of individual polymer chains can still be observed at higher concentrations with no aggregation of the PCE (Figure 16). The size of the individual polymer chains measured by AFM were consistent with the size distribution obtained by GPC analysis.

Sensitized photocurrent was obtained from all concentrations of non-aggregating CPE solution tested, even the lowest coverage of non-aggregating polymer, indicating photoinduced electron transfer between the polymer and substrate (73). IPCE spectra measured as a function of solution concentration revealed behavior similar to the Langmuir adsorption isotherm where the photocurrent plateaued at high polymer surface coverage. These results correlated with the AFM images suggesting that the individual polymer chains are all strongly electronically coupled to the surface.

Quantum Dots as Sensitizers

Recently, quantum-confined semiconductor materials have been employed to absorb light and sensitize wide band gap semiconductors in place of molecular sensitizers but utilizing the same operational principles of the DSSC. Colloidal semiconductor nanocrystals with a diameter between 1-20 nm, often referred to as quantum dots (QDs), are one such set of materials. QDs are considered advantageous for use in solar energy conversion because of their potential stability (compared to dyes that can bleach but as yet not demonstrated), relatively simple synthesis and high absorption-cross sections (74–76). Additionally, their absorption edge can be tuned by varying the particle size allowing for utilization of much of the solar spectrum and matching their energy levels with various substrate semiconductors (75). QDs are also particularly attractive because, due to quantum confinement effects, they can exhibit a variety of phenomena such as hot electron injection and multiple excitation generation (MEG) that could be exploited to exceed the Shockley-Quieisser limit for a single gap photovoltaic solar energy converter (77). MEG is particularly attractive because it allows for more efficient harvesting of high-energy photons by creating multiple excited electrons instead of heat due to relaxation of the high energy carriers to the band edges.

Despite the advantages of employing QDs for solar energy conversion, to date devices exhibit low power conversion efficiencies when QDs are substituted for dyes in DSSCs (75). This is considered to be primarily due to a lack of knowledge of the surface chemistry of these materials that would lead to high coverages

of quantum dots that are all electronically coupled to the semiconductor. QDs are most commonly synthesized via the hot injection method that involves the use of organometallic precursors in the presence of a large excess of long chain organic surfactants (78, 79). The organic surfactants, that also serve as capping agents, are essential to control the growth to produce stable and monodisperse suspension of nanoparticles. The complexity of the surface chemistry and larger size of the QDs, in comparison to the dyes used for sensitization, make it difficult to control the formation of the sensitizer/metal oxide interface that in turn effects the efficiency of extraction of photogenerated charge. Fundamental studies of quantum dot-sensitized solar cells (QDSSCs) utilizing colloidal nanoparticles are then essential to elucidate the issues that limit the performance of these devices and again single crystal substrates are very useful for such fundamental studies.

Deposition of Colloidal Quantum Dots

QDs can be deposited on substrates by a variety of approaches such as: chemical bath deposition (CBD), successive ionic layer adsorption and reaction (SILAR), direct attachment by drop casting, spin coating methods or linker-assisted attachment via ligand exchange (80, 81).

QD formation by means of CBD (82–84) and SILAR (85, 86) involves the synthesis of the QDs directly on the substrate. Both methods utilize solutions of cationic and anionic precursors to form the QDs but do so in slightly different manners. For CBD, a substrate is immersed in a solution of both ionic precursors and the QDs subsequently form on the surface of the substrate. Whereas with the SILAR method, the substrate is sequentially cycled between solutions of each individual precursor until the desired QD coverage/size is achieved. While these deposition methods yield high QD coverages, minimal control over the growth of the QDs is possible, resulting in a broad size distribution of the QDs on the substrate. The lack of homogeneity of QD size distribution makes these methods less useful for fundamental studies of QD photosensitization since they are not routinely done on the single crystal substrates and so will not be further discussed in this chapter.

The deposition of QDs synthesized via the hot injection method onto metal oxide substrates is not trivial but has been used for sensitization on either crystals or nanocrystalline scaffolds but usually requires a ligand exchange procedure to remove the native surfactant and replace it with a bridging ligand. QDSSCs produced by this method are plagued by low and irreproducible QD coverage on the surfaces, even when using seemingly identical surface modification procedures, resulting in both low and irreproducible IPCE and APCE values. The most successful sensitizing molecular dyes contain carboxylate or phosphonate groups to tether the dye to the metal oxide surface resulting in the formation of a monolayer. Ligand exchange procedures are therefore frequently used to replace the native bulky surfactants with short chain molecules with the carboxylate functionality necessary for covalent attachment to the metal oxide substrate (58, 60, 71, 87–94). Bifunctional molecular linkers, such as mercaptoalkanoic acids, where the thiol functionality has an affinity for the QD and the carboxylate

functionality has an affinity for the substrate, are most commonly used for such ligand exchange reactions. Bifunctional molecular linkers are not only used to promote the binding of QDs to the substrate surface but also have been shown to enhance the electronic coupling at the QD/substrate interface that promotes electron injection (92, 95–98).

Attachment of QDs to substrates through the use of bifunctional linker molecules can be carried out by either an *ex situ* or *in situ* ligand exchange method. The *in situ* ligand exchange method involves first functionalizing the surface of the substrate with the bifunctional linker molecule and subsequently exposing the functionalized substrate to the synthesized QDs hoping that a ligand exchange happens between the QD and the surface-bound ligands (87, 89, 90, 92). One issue with the *in situ* method is that it often requires extensive purification procedures to remove excess organic surfactants that can inhibit binding to the linker-functionalized substrates or replace the surface bound ligands leading to low QD adsorption that limits efficient sensitization. In contrast, the *ex situ* ligand exchange method involves the replacement of the native capping agents with the bifunctional linker molecule prior to the adsorption of the QDs to the substrate (60, 92, 93). The benefit of this method is that, if properly done, it removes all of the organic surfactants that by their nature adsorb preferentially to the surface and insulate the QD from interactions with the surface. However, this method can be time-consuming and often results in QD suspensions that are stable for less than the time it takes to carry out the ligand exchange and surface binding procedures.

The influence of ligand exchange methods on QD attachment to TiO_2 single crystal substrates was studied using CdSe QDs prepared via a method reported by Peng et al. (99) that utilizes tri-*n*-octylphosphine (TOP) and tri-*n*-octylphosphine oxide (TOPO) as the capping agents (92). Rutile (101) TiO_2 single crystals were sensitized with CdSe QDs via the *in situ* method utilizing 3-mercaptopropionic acid (MPA) as the bifunctional linker molecule. IPCE spectra were measured for MPA-functionalized TiO_2 crystals sensitized with unwashed, dilute-unwashed, and thoroughly washed TOPO/TOP CdSe QDs (Figure 17). The highest photocurrent response was obtained for the crystal sensitized with the thoroughly washed sample of QDs where the IPCE spectrum mimicked the absorption spectrum of the suspension. No photocurrent response was obtained for the crystal that was sensitized with the unwashed QDs. However the dilute-unwashed sample did exhibit a smaller photocurrent response (~20% of the thoroughly washed sample). This result was attributed to the dynamic equilibrium between the QD surface and the amount of excess surfactant/ligand present within the suspension. The thoroughly washed sample where a majority of the excess surfactant was removed from the suspension allows for uncompetitive adsorption of MPA to vacant surface sites and ensures good electronic coupling to the surface. In the unwashed sample, the probability of MPA penetrating the TOPO/TOP shell to attach to a vacant surface state is minimal since any ligand desorbed from the surface is immediately replaced due to the high concentration of excess surfactant. However, in the case of the dilute-unwashed sample of QDs, the concentration of excess ligand is lower than the unwashed sample and vacant surface sites will not immediately be filled therefore allowing MPA to bind to the vacant sites.

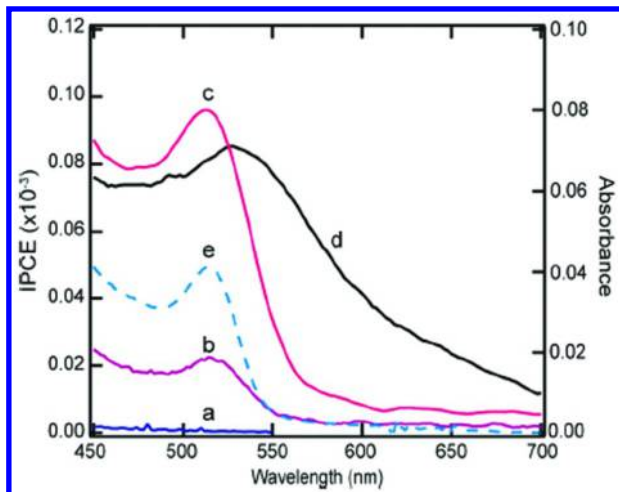


*Figure 17. IPCE spectra of (a) unwashed, (b) dilute, and (c) thoroughly washed TOP/TOPO-capped CdSe QDs adsorbed on an MPA-modified rutile (101) TiO_2 single crystal measured at short circuit in an acetonitrile electrolyte with $Co(dtb)_3^{2+}$ as a mediator. The IPCE spectrum of N3 dye (d) on the same unmodified TiO_2 crystal is shown for comparison. The solution absorbance spectrum of the TOP/TOPO-capped CdSe QDs in toluene (e) is also shown. Reproduced with permission from Sambur, J.; Riha, S. C.; Choi, D.; Parkinson, B. A.; *Langmuir* 2010 26(7) 4839-4847. Copyright (2010) American Chemical Society (92).*

AFM images of MPA-functionalized TiO_2 crystals sensitized with unwashed QDs show the presence of QDs on the surface (Figure 18); although the obtained coverage was not reproducible and a majority of the surface was covered by agglomerated QDs. This sample exhibited little or no photocurrent response perhaps due to the agglomeration of QDs hindering the electronic coupling between both other QDs and the substrate. Another factor that may contribute to irreproducibility of the photocurrent response, for electrodes prepared via the *in situ* ligand exchange method, is that the QDs are adsorbing to linker-modified surfaces from organic solvents. Under these conditions the thiol group on the bifunctional linker molecule remains protonated and no covalent bond is established between the QD and substrate. Instead, it is likely that when employing the *in situ* ligand exchange method, the QDs are physisorbed to the substrate and this weak interaction leads to irreproducible QD loadings and in turn irreproducible photocurrents that often decrease with time.

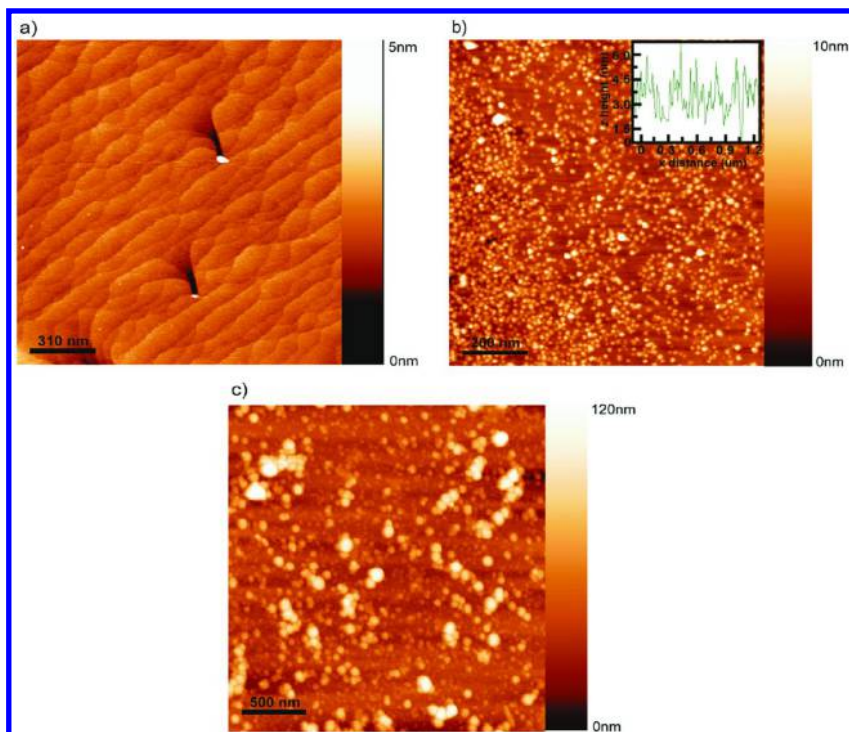


*Figure 18. AFM images of (a) bare rutile (110) TiO_2 , (b) rutile (110) crystal after modification with MPA and exposure to unwashed TOP/TOPO-capped QDs from toluene, and (c) more common regions showing QD agglomeration. Reproduced with permission from Sambur, J.; Riha, S. C.; Choi, D.; Parkinson, B. A.; *Langmuir* **2010** *26*(7) 4839-4847. Copyright (2010) American Chemical Society (92).*

Excess surfactant present in the QD suspensions can not only block the adsorption of the bifunctional linker molecule to vacant binding sites on the QD, but it can also competitively adsorb to the substrate surface. Phosphonates, such as TOPO and TOP, are commonly used capping agents for QD synthesis and are also known to bind more strongly than carboxylates to metal oxide substrates (100–102) and it is well established that long chain carboxylic acid molecules can readily displace short chain carboxylic acid monolayers on TiO_2 (103).

To probe the effect of excess surfactant on the *in situ* ligand exchange method, anatase (001) TiO_2 crystals were functionalized with TOPO, MPA, and TOP prior to the adsorption of N3. N3 was used for this study because it binds through carboxylate groups to the TiO_2 crystal surface similarly to MPA and is known to yield reproducible surface coverage on TiO_2 . Therefore, any difference in IPCE spectra between each modified TiO_2 surface can be attributed to differences in N3 binding caused by impurities present in QD suspensions. The IPCE spectra for N3 adsorbed to TOPO- and MPA-modified TiO_2 crystals was similar to previously reported values and indicating that TOPO and MPA did not inhibit binding of N3 to

TiO₂ (Figure 19). However, the IPCE spectrum for N3 adsorbed to TOP-modified TiO₂ was significantly lower in comparison indicating that the presence of TOP-impurities blocked the adsorption of N3.

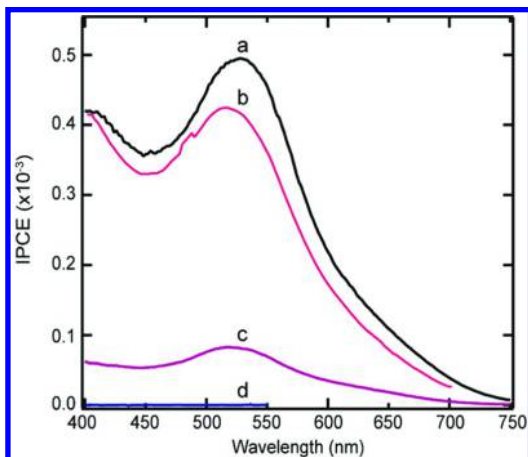


*Figure 19. IPCE spectra of (a) N3 on TOPO-modified, (b) MPA modified, and (c) TOP-modified TiO₂ surfaces on an anatase (001) TiO₂ single crystal measured at short circuit in an acetonitrile electrolyte with Co(dtb)₃²⁺ mediator. N3 photocurrent spectra for bare anatase (001) (d) surfaces were similar to those for MPA- and TOPO-modified TiO₂ surfaces. Reproduced with permission from Sambur, J.; Riha, S. C.; Choi, D.; Parkinson, B. A.; *Langmuir* 2010 26(7) 4839-4847. Copyright (2010) American Chemical Society (92).*

Differing from the *in situ* method of ligand exchange that is carried out in organic solvent, the formation of MPA-capped CdSe QDs, either by direct synthesis or *ex situ* ligand exchange, requires the QDs to be resuspended in water (pH>10). The high pH is necessary to deprotonate the thiol to promote thiolate-QD binding that stabilizes the suspension. Once a stable suspension is prepared, sensitizing the substrate with QDs can be straightforward with the carboxylate binding to the metal oxide substrate with suitable electronic coupling between the QD and substrate.

TOP/TOPO-capped CdSe QDs were *ex situ* ligand exchanged utilizing MPA as the bifunctional linker molecule (92). The obtained MPA-capped CdSe QDs required this time consuming procedure and yielded suspensions that were stable for only a few hours. In order to circumvent this stability issue, commercially synthesized MPA-capped CdSe QDs prepared utilizing the *ex situ* ligand exchange method were obtained (ON-MPA/CdSe). MPA-capped CdSe QDs were also synthesized in water following a synthesis reported by Chen et al. (104) (aq-MPA/CdSe) but this produced a suspension with a broad absorption spectrum, indicative of a large size distribution. Despite these challenges, the attachment and performance of the two methods to prepare MPA-capped CdSe QDs on single crystal substrates were compared.

Rutile (001) and anatase (001) single crystal substrates were exposed to aq-MPA/CdSe and ON-MPA/CdSe QD samples. Sensitized photocurrents mimicking the absorption spectra of the suspensions were obtained for both samples of QDs, however, the aq-MPA/CdSe QDs yielded no photocurrent response until further purification with isopropyl alcohol and resuspension in water (pH 10.5) presumably removing unreacted precursors. Interestingly, the photocurrent stability of the two samples was different despite the similar surface chemistry of the samples, as they both in principle should be capped completely with MPA. The photocurrent response from aq-MPA/CdSe was reproducible and stable over long periods of illumination in both aqueous sulfide/polysulfide electrolyte, a typical electrolyte for QDSSCs, and the bipyridyl cobalt mediator ($\text{Co}(\text{dtb})_3$) in acetonitrile, a common electrolyte for DSSCs.

The photocurrent response over the course of 15 h of the ON-MPA/CdSe on anatase (001) TiO_2 single crystals was stable for many hours with aqueous sulfide/polysulfide electrolyte (Figure 20), consistent with the results obtained for the aq-MPA/CdSe. In contrast the sensitized photocurrent for the ON-MPA/CdSe decayed immediately upon illumination in the cobalt mediator solution in acetonitrile. The stability of the photocurrent response for this sample could be extended by purging the cobalt mediator with nitrogen prior to measurements but quickly decayed upon exposure to air. Because the stability of both the ON-MPA/CdSe and aq-MPA/CdSe suspensions is the same prior to exposure to the TiO_2 crystal, the variance between the photocurrent stability in the presence of oxygen is presumably due to slight differences between the surface chemistry making one more prone to oxidation than the other.

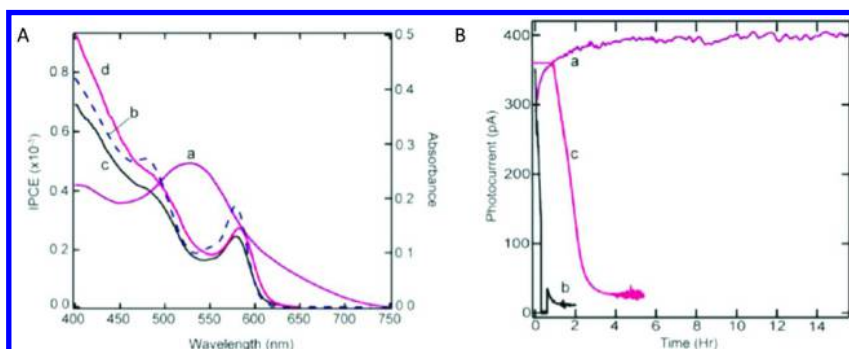


*Figure 20. (A) IPCE spectra of (a) N3 on an unmodified anatase (001) TiO_2 single crystal measured at short circuit in an acetonitrile electrolyte with a $\text{Co}(\text{dtb})_3^{2+}$ mediator. The solution absorbance spectrum in water (b) is compared with the IPCE spectrum of (c) ON-MPA/CdSe initially and (d) after 15 h illumination measured at short circuit in a sulfide/polysulfide electrode. Panel (B) shows the photocurrent versus time for ON-MPA/CdSe adsorbed on the same crystal in (a) sulfide/polysulfide electrolyte, and (b) unpurged and (c) purged $\text{Co}(\text{dtb})_3^{2+}$. Reproduced with permission from Sambur, J.; Riha, S. C.; Choi, D.; Parkinson, B. A.; *Langmuir* **2010** *26*(7) 4839-4847. Copyright (2010) American Chemical Society (92).*

Electronic Coupling

The collection of photoexcited electrons in solar energy conversion devices such as the QDSSC, relies on the efficient transfer of electrons from the QDs into the metal oxide substrate. The efficiency of this process is strongly influenced by both the delocalization of photogenerated excitons within the QDs and the strength of electronic coupling between the QDs and substrate that is influenced by the nature of the capping/bridging ligands (94). The exciton wave function confined in the QD can be extended from the QD core to the ligand molecule if the QD and capping ligands are electronically coupled by exchanging the insulating long-chain surfactant capping groups with smaller molecules (105).

The importance of electronic coupling in QD sensitization was evident when the effect of capping ligands on the electron transfer properties of QD-interfaces was studied (59). To systematically investigate this effect, rutile (110) TiO_2 and ZnO (0001) single crystal substrates were sensitized with CdSe QDs capped with oleic acid/TOPO (OA/TOPO-CdSe), 11-mercaptoundecanoic acid (MUA-CdSe), and MPA (MPA-CdSe) where MPA- and MUA-CdSe QDs were prepared via *ex situ* ligand exchange of OA/TOPO-CdSe. The insulating effect of long chain surfactants was apparent as no photocurrent was generated from OA/TOPO-CdSe on either substrate whereas both MPA- and MUA-CdSe yielded photocurrent response. MPA-CdSe exhibited IPCE values much larger than those obtained from MUA-CdSe on either substrate demonstrating that shorter chain bifunctional linker molecules have better electronic coupling between QDs and substrates than longer chain molecules and the rate of electron transfer through alkyl chains is known to increase with decreasing chain length (106), it was therefore likely that the differences observed in IPCE values between MPA-CdSe and MUA-CdSe were due to the length of the alkyl chain. This led to the systematic study of the effect the length of the bifunctional linker molecule on photocurrent yields (60). Photocurrent spectra were obtained for ZnO single crystal substrates sensitized with CdSe QDs capped with 4-mercaptopbenzoic acid (MBzA), 2-mercaptopacetic acid (MAA), MPA, 8-mercaptopoctanoic acid (MOA), and MUA. The results demonstrated the distance dependence of electron transfer through alkyl chains. As shown in Figure 21, IPCE values measured at the exciton peak wavelength increased as the length of the alkyl chain of the linker molecule was decreased demonstrating that longer chain linkers like MUA are not as effective at transporting charge as short chain linkers such as MPA and MAA that reduce carrier recombination. These results are consistent with an optical study of electron transfer from CdS QDs to TiO_2 nanoparticles (96).

Quantum Dot Stability

The low efficiencies of QDSSCs in comparison to DSSCs have led to the exploration of a variety of strategies to increase power conversion (81). One attractive method involves increasing the open circuit potential of the device by tuning the redox potential of the electrolyte; however, the stability of QDs in the presence of electrolyte is a major problem. A prime example of this is when

employing the iodide/triiodide (I^-/I_3^-) redox electrolyte commonly used for DSSCs as the regenerator for QDSSCs. Stability studies of QDSSC performance revealed that photocorrosion of metal chalcogenide QDs occurs in the presence of I^-/I_3^- as evident by the rapid decay of the photocurrent (107, 108).

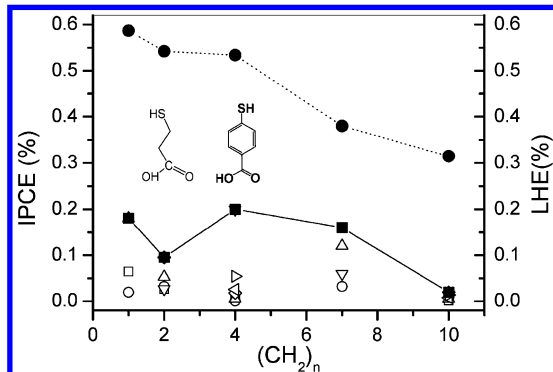


*Figure 21. Dependence of the IPCE values at the exciton peak on the $(-CH_2 -)$ units of molecular linkers on ZnO (0001). The molecular structures of MPA and MBzA are also shown. A solid line (left) connecting the highest values of IPCE for each MXA molecule is shown, the dashed line (right) corresponds to calculated light harvesting efficiency (LHE) values estimated for close-packed monolayers of CdSe QDs (2.62 nm diameter) with different MXA linkers. Reproduced with permission from Liang, Y.; Thorne, J. E.; Kern, M. E.; Parkinson, B. A., *Langmuir* 2014 30(42) 12551-12558. Copyright (2014) American Chemical Society (60).*

The corrosion process was investigated by continuous 532 nm illumination of MPA-capped CdSe QDs attached to TiO_2 single crystal substrate in aqueous KI electrolyte (109). IPCE spectra obtained before and after long-term illumination revealed not only a significant loss of photocurrent but also a substantial blue shift of the first exciton peak indicative of a decrease in the QD diameter (Figure 22a). Interestingly, the onset of photocurrent after extended illumination occurred at 530 nm, just above the incident photon energy. This effect was further probed using monochromatic illumination at different photon energies. For all incident photon energies examined, a decrease and blue shift of the IPCE spectra was observed and the onset of photocurrent after extended illumination was shifted to just above the energy of the incident photons (Figure 22b). These results revealed that photoelectrochemical corrosion of QDs occurred when the incident photon energy was greater than the band gap of the QDs but stopped when the photon energy was less than that of the QD band gap signifying a size-selective etching process.

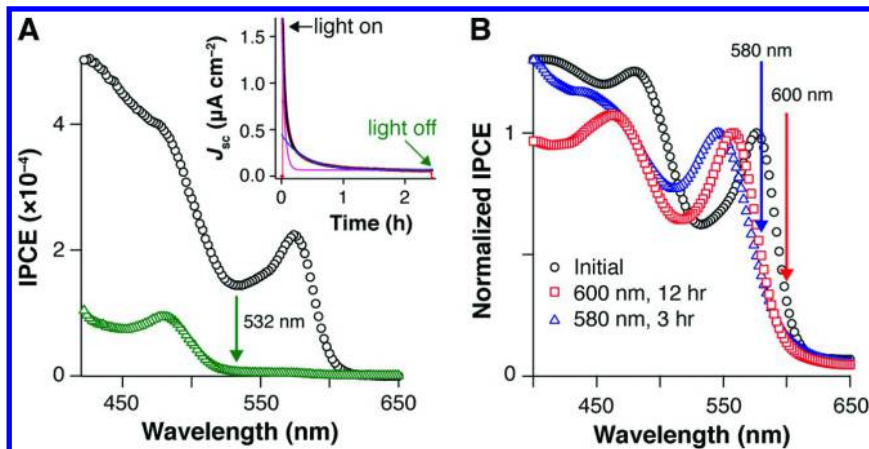


Figure 22. (A) IPCE spectra of MPA-capped CdSe QDs adsorbed on an anatase (001) measured before (black circles) and after (green triangles) 20 hours of $47.7 \mu\text{W cm}^{-2}$ (532 nm) in an aqueous iodide (0.25 M KI) electrolyte at short circuit vs Pt. The inset shows the short circuit photocurrent vs time (red dots) for the first 2 hours. The dashed black line represents a double exponential fit to the data and the individual components are represented as pink and blue lines. (B) IPCE spectra normalized to the maxima of the excitonic features measured on anatase (001) before (black circles) and after 12 hrs of continuous $30 \mu\text{W cm}^{-2}$ 600 nm illumination (red squares) and after an additional 3 hrs of continuous $30 \mu\text{W cm}^{-2}$ 580 nm illumination (blue triangles). Reproduced with permission from Sambur J. and Parkinson, B. A., ACS Appl. Mater. Interfaces 2014 ASAP, DOI: 10.1021/am507974h. Copyright (2014) American Chemical Society (109).

Core/shell QDs have been shown to prevent photocorrosion and enhance the stability of QDs in the presence of usually corrosive electrolytes. Photocurrent stability tests of MPA-capped CdSe and CdSe/ZnS QDs attached to TiO_2 crystals was performed in aqueous KI electrolyte (91). The photocurrent from the CdSe QDs decreased by half in minutes and 90% of the initial photocurrent signal was gone after only a few hours. Conversely, ~21% of the initial photocurrent signal remained for the CdSe/ZnS QDs after 20 hours of continuous illumination. Normalized IPCE spectra of CdSe/ZnS QDs before and after illumination exhibited similar shapes where a significant blue shift was observed for CdSe QDs consistent with photocorrosion by the electrolyte. Evidently the use of a stable, wide band gap shell material on the QD core can shield the core from photocorrosion and in turn improve device stability. It also suggests that the thin ZnS core layer may not be continuous on ~80% of the QDs as is usually suggested in the cartoons drawn to depict these core/shell structures.

Quantum Dots Absorbing in the near-IR

The use of lower band gap and or larger QDs can extend absorption of a device into the infrared region of the solar spectrum. The potential for device efficiencies that exceed the Shockley-Quiesser limit is another attractive feature of employing near-infrared (n-IR) QDs as sensitizers (110). The small band gaps allow for the production of multiple excitons at the higher photon energies in the visible range of the solar spectrum. Therefore, the realization of multiple exciton generation (MEG) and collection (MEC) as well as hot carrier injection is possible.

The extension of sensitized photocurrent into the n-IR was shown when ZnO single crystals were sensitized with PbS QDs (58). For electron transfer to occur, the energetic alignment between the sensitizer and the substrate must be thermodynamically favorable. Mott-Schottky analysis of ZnO single crystals revealed that the conduction band edge is at -4.77 eV. Because the intrinsic Fermi level of PbS is known to be approximately -4.7 eV with a nearly symmetric distribution of the conduction and valence band (111, 112), the energetic alignment of the ZnO/PbS interface should allow for the injection of electrons from all sizes of PbS QDs (Figure 23A).

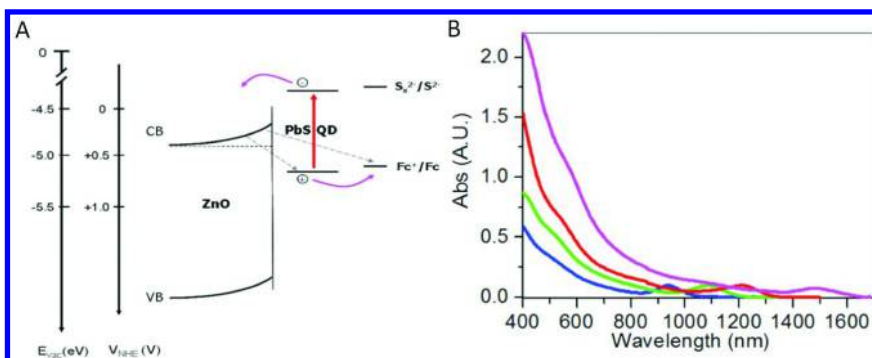


Figure 23. (A) Band alignment between ZnO single crystal electrodes, PbS QDs, and redox couples. The positions of the energy level are only shown relatively, not to scale. The dashed lines indicate back transfer or recombination of injected electrons. (B) UV-Vis spectra of various size PbS QDs in hexane solution. The diameters of the four different batches of PbS QDs are estimated to be 3.04 nm (blue curve), 3.62 nm (green curve), 4.16 nm (red curve), and 5.50 nm (magenta curve). Reproduced from *Phys. Status Solidi A*, 211/9, Liang, Y.; Novet, T.; Thorne, J.; Parkinson, B. A.; Photosensitization of ZnO single crystal electrodes with PbS quantum dots, 1954-1959, Copyright (2014), with permission from Wiley (58).

IPCE spectra measured for ZnO single crystals sensitized with PbS QDs ranging in size from 3.2-5.5 nm in diameter are shown in Figure 23B. Sensitized photocurrents extending into the n-IR region were obtained for all PbS QD

samples on ZnO confirming that electron injection from a wide distribution of PbS QD sizes into ZnO is indeed possible. IPCE spectra for each size of PbS QDs on ZnO exhibited slight red shifts from the absorption spectra of the suspensions suggesting enhanced electronic coupling between QDs and substrate or also between neighboring QDs. The largest size of PbS QDs tested (5.5 nm) resulted in sensitized photocurrent out to 1580 nm that may currently be the record for the longest wavelength sensitization achieved for dyes or QDs on oxide substrates.

Multiple Exciton Generation and Collection

The formation of multiple photogenerated carriers from the excess energy of absorbed high energy photons has been observed via indirect optical methods such as transient absorption and time-resolved photoluminescence for many suspensions of QD such as PbS, PbSe, InAs, nanocrystalline Si, as well as carbon nanotubes (77, 110). These methods rely on the detection of signatures of MEG such as Auger recombination and enhanced luminescence or decay rates. The minimum threshold energy necessary to induce MEG has been shown to be close to twice the band gap; however, the minimum energy measured to induce MEG within such materials has often been reported to be higher than this (110). While indirect measurements have proven MEG is possible in QDs, the collection of multiple carriers within QD-devices has only recently been shown (93, 113).

The first direct measurement of the production and collection of photocurrent from MEG was measured in a model single crystal sensitized photoanode (93). Four distinct sizes of PbS QDs (2.5, 3.1, 4.5, 9.9 nm corresponding to band gap energies of 1.39, 1.27, 0.96, and 0.85 eV, respectively) were attached to single crystal anatase (001) TiO₂. To efficiently extract multiple carriers generated within QDSSCs, the energetics of the interface must be such that the conduction band of the QD is more negative on the electrochemical scale than that of the conduction band of the semiconductor for dissociation of excitons into free carriers. Features consistent with the first excitonic band present in the absorption spectrum of the suspension were observed in the IPCE spectra for QDs 4.5 nm or smaller in diameter (Figure 24). No excitonic features were present in the IPCE spectrum of the 9.9 nm QD sample coinciding with the energetics of the conduction band of the QDs being more positive than that of the TiO₂. However, photocurrent response was detected for this sample at wavelengths <700nm indicative of hot injection from higher lying energy states in the QDs.

IPCE values obtained from steady-state short circuit photocurrents at various incident light intensities were converted to APCE by accounting for the light harvesting efficiency of the QDs on TiO₂. APCE values revealed quantum yields above unity were achieved for 4.5 nm PbS QDs where the onset of MEG for this system occurred at approximately 2.6 times the energy associated with the band gap of the QDs (Figure 25). A size-dependent MEC effect was observed, as APCE values for the 2.5 and 3.1 nm PbS QDs approached/exceeded unity however, they were within the range of experimental error for lower energy photocurrent measurements and could therefore not conclusively be considered MEC.

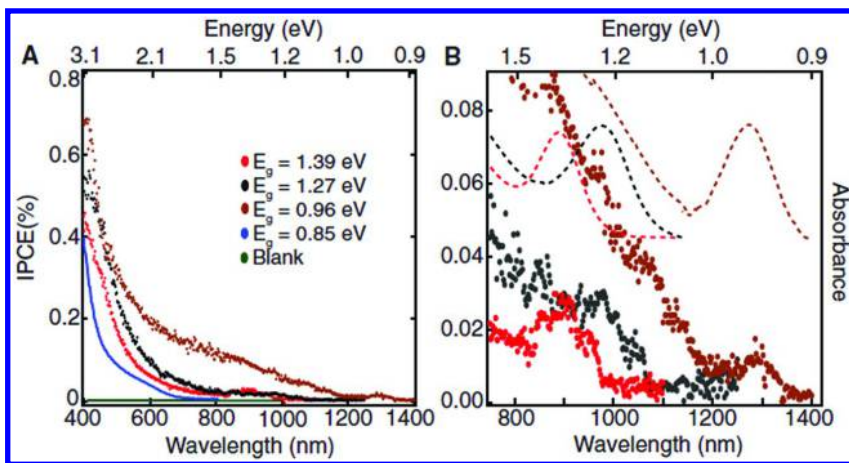


Figure 24. IPCE spectra of various band gap PbS QDs adsorbed on an anatase (001) electrode. Photocurrents were acquired in an aqueous electrolyte (0.5 M Na₂S and 0.01 M S in 0.1 M NaOH) at short circuit in a two-electrode configuration versus a platinum wire. (A) IPCE spectra for each QD size. The green trace represents the bare anatase (001) photocurrent response. (B) IPCE spectra displaying the near-IR region to compare the photocurrent (solid dots) and QD absorbance in water (dashed lines). From Sambur, J. B.; Novet, T.; Parkinson, B. A. Multiple Exciton Collection in a Sensitized Photovoltaic System. *Science* **2010**, *330*, 63–66 (93). Reproduced with permission from AAAS.

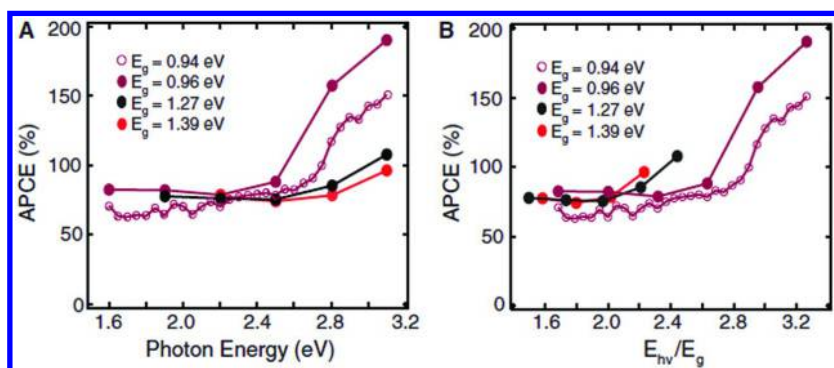


Figure 25. APCE values as a function of the illumination energy. (A) APCE versus the absolute incident photon energy. (B) APCE vs the incident photon energy divided by the QD band gap energy (indicating the multiples of the band gap). Adjustments that would increase the APCE because of solution absorption and reflection from the cell window and TiO₂ crystal were not performed. From Sambur, J. B.; Novet, T.; Parkinson, B. A. Multiple Exciton Collection in a Sensitized Photovoltaic System. *Science* **2010**, *330*, 63–66 (93). Reproduced with permission from AAAS.

Gallium Phosphide Sensitization

Gallium phosphide (GaP) has a band gap of (2.26 eV) and a higher carrier mobility than TiO_2 . Memming and Tributsch originally investigated the suitability of GaP for dye sensitization of both n- and p-type single crystals in 1971 (7) but there has been almost no work on this material until recently. The earlier study found that despite being under positive bias, both n- and p-type crystals gave cathodic sensitized photocurrents. A subsequent study was conducted with dye sensitization from the same dye, Rhodamine-B, again on both n- and p-type GaP. Intriguingly, both anodic and cathodic photocurrent on n- and p-type crystals respectively was observed post sensitization from the same dye as shown in Figure 26. Of particular interest was the n-type GaP sensitization whereby despite the LUMO position being lower than the conduction band of GaP, photosensitization (photocurrent) from the dye was measured (114). This led to the speculation of numerous possible mechanisms of electron injection including electron tunnelling, hot carrier injection, triplet-triplet annihilation, reductive quenching and energy transfer. It was, however, rationalized that the most likely mechanism for anodic sensitization was sensitized photoanodic decomposition of GaP. By this mechanism, anodic decomposition drives oxidation of GaP liberating electrons that are able to generate anodic current.

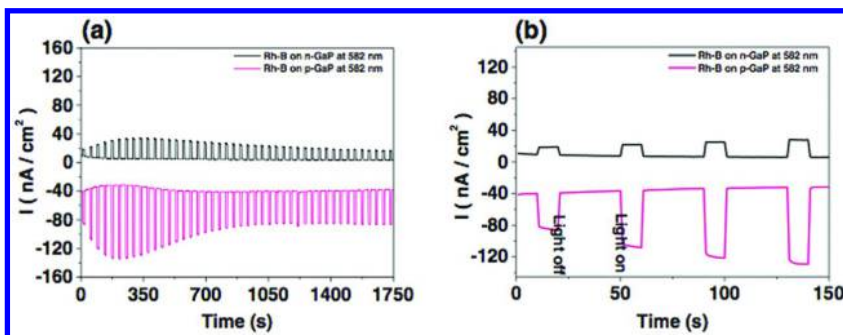


Figure 26. (a) Time dependence of the sensitized photocurrent response for n- and p-type GaP single crystals sensitized with Rhodamine-B dye and illuminated at 582 nm (3.9 μW) under -0.4 V (for n-type GaP) and 0 V (for p-type GaP) (vs. Ag/AgCl) applied. Photocurrent response on n-type GaP (black line) and on p-type GaP (pink line). (b) Expanded region from 0 sec to 150 sec, saw-tooth profile due to chopping of the illumination light. Reproduced with permission of The Electrochemical Society from Choi, D. et al. *J. Electrochem. Soc* 2012 159(11) H846-852 (114).

Work with GaP by the Maldonado group investigated the sensitization of p-GaP single crystals (100) with six different, non covalently bound triphenylmethane dyes in aqueous solution (115). The steady-state internal

quantum yield of the GaP sensitized photoanodes was found to be unusually high with values approaching 10%. These results were compared to a finite-difference model which determined that such high efficiencies were due to the presence of an internal electric field within the depletion layer at the p-GaP surface. In the same study it was also observed that the sensitized photocurrents measured in aerated solution were larger than those measured in deaerated solutions. The difference was variable for each of the six dyes tested, however, it was consistent within the subset of the triphenylmethane dyes.

Another study by the Maldonado group involved the adsorption of CdSe QDs to p-GaP (100) single crystals (116). Time-resolved photoluminescence decay measurements revealed an enhanced decay response for CdSe QDs deposited on GaP in comparison to CdSe QDs deposited on glass indicating the presence of an additional quenching pathway. Steady-state photoelectrochemical data showed an enhanced photocurrent response when CdSe-sensitized GaP was illuminated with sub-band gap monochromatic light. These results combined with external quantum efficiencies, mimicking the absorption spectrum of the CdSe suspension, confirm that sensitized hole injection to p-GaP single crystals from CdSe QDs is occurring.

Summary and Future Outlook for Single Crystal Sensitization

Since the original work on dye sensitization of semiconductor crystals almost fifty years ago there has been considerable progress in understanding this interesting and fundamental photoinduced interfacial electron transfer process. It has also produced a technology in the DSSC that may have a niche in future photovoltaic energy conversion but certainly became a cottage industry for thousands of researchers throughout the world who investigated variations of every aspect of this device. It was also useful in verifying that solar energy conversion device efficiencies can perform in excess of the Shockley-Quieser limit and that hot injection from higher QD states can produce photocurrent. It is expected that the field will continue to diversify the substrates, sensitizers and regenerators and employ more and more sophisticated techniques at even smaller spatial and time scales (24, 67) that will also have important implications on future solar energy conversion processes.

Acknowledgments

Most of the funding for the cited work where BAP was an author was through the U.S. Department of Energy, Office of Science, Basic Energy Sciences, Division of Chemical Sciences, Geosciences and Biosciences most recently through grant DE-FG03-96ER14625. We also thank Mark Spitler and Kevin Watkins for helpful comments.

References

1. Glaus, S.; Calzaferri, G. The Band Structures of the Silver Halides AgF, AgCl, and AgBr: a Comparative Study. *Photochem. Photobiol. Sci.* **2003**, *2*, 398–401.
2. Gerischer, H.; Bressel, B. Photoelectrochemical Studies of Dye Sensitization at Silver Chloride Single Crystals. *Ber. Bunsen-Ges. Phys. Chem.* **1985**, *89*, 1083–1087.
3. Gerischer, H.; Tributsch, H. Elektrochemische Untersuchungen Zur Spektralen Sensibilisierung Von ZnO-Einkristallen. *Ber. Bunsen-Ges. Phys. Chem.* **1968**, *72*, 437–445.
4. Tributsch, H.; Gerischer, H. Elektrochemische Untersuchungen Über Den Mechanismus Der Sensibilisierung Und Übersensibilisierung an ZnO-Einkristallen. *Ber. Bunsen-Ges. Phys. Chem.* **1969**, *73*, 251–260.
5. Gerischer, H. Electrochemical Techniques for the Study of Photosensitization. *Photochem. Photobiol.* **1972**, *16*, 243–260.
6. Schöppel, H. R.; Gerischer, H. Die Kathodische Reduktion Von Cu-I-Oxid-Elektroden Als Beispiel Für Den Mechanismus Der Reduktion Eines Halbleiter-Kristalls. *Ber. Bunsen-Ges. Phys. Chem.* **1971**, *75*, 1237–1239.
7. Memming, R.; Tributsch, H. Electrochemical Investigations on the Spectral Sensitization of Gallium Phosphide Electrodes. *J. Phys. Chem.* **1971**, *75*, 562–570.
8. Tributsch, H.; Calvin, M. Electrochemistry of Excited Molecules: Photo-Electrochemical Reactions of Chlorophylls. *Photochem. Photobiol.* **1971**, *14*, 95–112.
9. Tributsch, H. Reaction of Excited Chlorophyll Molecules at Electrodes and in Photosynthesis. *Photochem. Photobiol.* **1972**, *16*, 261–269.
10. Spitzer, M. T.; Parkinson, B. A. Dye Sensitization of Single Crystal Semiconductor Electrodes. *Acc. Chem. Res.* **2009**, *42*, 2017–2029.
11. Spitzer, M. T.; Calvin, M. Adsorption and Oxidation of Rhodamine B at ZnO Electrodes. *J. Chem. Phys.* **1977**, *67*, 5193–5200.
12. Spitzer, M. T.; Calvin, M. Electron Transfer at Sensitized TiO₂ Electrodes. *J. Chem. Phys.* **1977**, *66*, 4294–4305.
13. Sonntag, L. P.; Spitzer, M. T. Examination of the Energetic Threshold for Dye-Sensitized Photocurrent at Strontium Titanate (SrTiO₃) Electrodes. *J. Phys. Chem.* **1985**, *89*, 1453–1457.
14. Spitzer, M. T.; Parkinson, B. A. Efficient Infrared Dye Sensitization of van Der Waals Surfaces of Semiconductor Electrodes. *Langmuir* **1986**, *2*, 549–553.
15. Parkinson, B. A. Dye Sensitization of van Der Waals Surfaces of Tin Disulfide Photoanodes. *Langmuir* **1988**, *4*, 967–976.
16. Parkinson, B. A.; Spitzer, M. T. Recent Advances in High Quantum Yield Dye Sensitization of Semiconductor Electrodes. *Electrochim. Acta* **1992**, *37*, 943–948.
17. Chau, L. K.; Arbour, C.; Collins, G. E.; Nebesny, K. W.; Lee, P. A.; England, C. D.; Armstrong, N. R.; Parkinson, B. A. Phthalocyanine

Aggregates on Metal Dichalcogenide Surfaces: Dye Sensitization on Tin Disulfide Semiconductor Electrodes by Ordered and Disordered Chloroindium Phthalocyanine Thin Films. *J. Phys. Chem.* **1993**, *97*, 2690–2698.

- 18. Takeda, N.; Parkinson, B. A. Adsorption Morphology, Light Absorption, and Sensitization Yields for Squaraine Dyes on SnS_2 Surfaces. *J. Am. Chem. Soc.* **2003**, *125*, 5559–5571.
- 19. Lanzafame, J. M.; Miller, R. J. D.; Muenter, A. A.; Parkinson, B. A. Ultrafast Charge-Transfer Dynamics at Tin Disulfide Surfaces. *J. Phys. Chem.* **1992**, *96*, 2820–2826.
- 20. Takeda, N.; Parkinson, B. A. The Relationship Between Squaraine Dye Surface Morphology and Sensitization Behavior on SnS_2 Electrodes. *Electrochim. Acta* **2000**, *45*, 4559–4564.
- 21. Kam, K. K.; Parkinson, B. A. Detailed Photocurrent Spectroscopy of the Semiconducting Group VIB Transition Metal Dichalcogenides. *J. Phys. Chem.* **1982**, *86*, 463–467.
- 22. Sharp, L.; Soltz, D. Growth and Characterization of Tin Disulfide Single Crystals. *Cryst. Growth Des.* **2006**, *6*, 1523–1527.
- 23. Sharp, L. Photoelectrochemical Etching and Dye Sensitization of Bridgman Grown Single Crystal SnS_2 Photoanodes. Ph.D. Thesis, Colorado State University, Fort Collins, CO, 2002.
- 24. Willig, F.; Eichberger, R.; Sundaresan, N. S.; Parkinson, B. A. Experimental Time Scale of Gerischer's Distribution Curves for Electron-Transfer Reactions at Semiconductor Electrodes. *J. Am. Chem. Soc.* **1990**, *112*, 2702–2707.
- 25. O'Regan, B. C.; Grätzel, M. A Low-Cost, High-Efficiency Solar Cell Based on Dye-Sensitized Colloidal TiO_2 Films. *Nature* **1991**, *353*, 737–740.
- 26. Zhang, S.; Yang, X.; Numata, Y.; Han, L. Highly Efficient Dye-Sensitized Solar Cells: Progress and Future Challenges. *Energy Environ. Sci.* **2013**, *6*, 1443–1464.
- 27. Hardin, B. E.; Snaith, H. J.; McGehee, M. D. The Renaissance of Dye-Sensitized Solar Cells. *Nat. Photonics* **2012**, *6*, 162–169.
- 28. Nakamura, R.; Okamura, T.; Ohashi, N.; Imanishi, A.; Nakato, Y. Molecular Mechanisms of Photoinduced Oxygen Evolution, PL Emission, and Surface Roughening at Atomically Smooth (110) and (100) n- TiO_2 (Rutile) Surfaces in Aqueous Acidic Solutions. *J. Am. Chem. Soc.* **2005**, *127*, 12975–12983.
- 29. Nakamura, R.; Naomichi, O.; Akihito, I.; Takeo, O.; Yuji, M.; Hideomi, K.; Yoshihiro, N. Crystal-Face Dependence of Surface Band Edges and Hole Reactivity, Revealed by Preparation of Essentially Atomically Smooth and Stable (110) and (100) n- TiO_2 (Rutile) Surfaces. *J. Phys. Chem. B* **2005**, *109*, 1648–1651.
- 30. Tsujiko, A.; Kisumi, T.; Magari, Y.; Murakoshi, K.; Nakato, Y. Selective Formation of Nanoholes with (100)-Face Walls by Photoetching of n- TiO_2 (Rutile) Electrodes, Accompanied by Increases in Water-Oxidation Photocurrent. *J. Phys. Chem. B* **2000**, *104*, 4873–4879.

31. Lu, Y.; Jaeckel, B.; Parkinson, B. A. Preparation and Characterization of Terraced Surfaces of Low-Index Faces of Anatase, Rutile, and Brookite. *Langmuir* **2006**, *22*, 4472–4475.
32. Imanishi, A.; Suzuki, H.; Ohashi, N.; Kondoh, H.; Ohta, T.; Nakato, Y. Pretreatment Dependence of Adsorption Properties of Merocyanine Dye at Rutile (110) and (100) TiO_2 Surfaces Studied by C K-Edge NEXAFS. *J. Phys. Chem. C* **2009**, *113*, 17254–17261.
33. Ushiroda, S.; Ruzycki, N.; Lu, Y.; Spitler, M. T.; Parkinson, B. A. Dye Sensitization of the Anatase (101) Crystal Surface by a Series of Dicarboxylated Thiacyanine Dyes. *J. Am. Chem. Soc.* **2005**, *127*, 5158–5168.
34. Choi, D.; Rowley, J. G.; Spitler, M. T.; Parkinson, B. A. Dye Sensitization of Four Low Index TiO_2 Single Crystal Photoelectrodes with a Series of Dicarboxylated Cyanine Dyes. *Langmuir* **2013**, *29*, 9410–9419.
35. Fillinger, A.; Parkinson, B. A. The Adsorption Behavior of a Ruthenium-Based Sensitizing Dye to Nanocrystalline TiO_2 Coverage Effects on the External and Internal Sensitization Quantum Yields. *J. Electrochem. Soc.* **1999**, *146*, 4559–4564.
36. Watkins, K. J.; Spitler, M. T. Physical Models for Charge Transfer at Single Crystal Oxide Semiconductor Surfaces as Revealed by the Doping Density Dependence of Collection Efficiency of Dye Sensitized Photocurrents. *J. Phys. Chem. C* **2015**, submitted for publication.
37. Spitler, M. T. One Dimensional Onsager Model for Dye Sensitized Charge Injection Into Semiconductors. *J. Electroanal. Chem. Interfacial Electrochem.* **1987**, *228*, 69–76.
38. Kavan, L.; Gratzel, M.; Gilbert, S. E.; Klemenz, C.; Scheel, H. J. Electrochemical and Photoelectrochemical Investigation of Single-Crystal Anatase. *J. Am. Chem. Soc.* **1996**, *118*, 6716–6723.
39. Herman, G. S.; Gao, Y. Growth of Epitaxial Anatase (001) and (101) Films. *Thin Solid Films* **2001**, *397*, 157–161.
40. Yamamoto, Y.; Matsumoto, Y.; Koinuma, H. Homo-Epitaxial Growth of Rutile TiO_2 Film on Step and Terrace Structured Substrate. *Appl. Surf. Sci.* **2004**, *238*, 189–192.
41. Kraus, T. J.; Nepomnyashchii, A. B.; Parkinson, B. A. Templated Homoepitaxial Growth with Atomic Layer Deposition of Single-Crystal Anatase (101) and Rutile (110) TiO_2 . *ACS Appl. Mater. Interfaces* **2014**, *6*, 9946–9949.
42. Oropenza, F. E.; Zhang, K. H. L.; Regoutz, A.; Lazarov, V. K.; Wermeille, D.; Poll, C. G.; Egdell, R. G. Growth of Epitaxial Anatase Nano Islands on SrTiO_3 (001) by Dip Coating. *Cryst. Growth Des.* **2013**, *13*, 1438–1444.
43. Shimada, T.; Kaji, T.; Saiki, K. Electron Spectroscopy of Dye-Sensitized Anatase (001) Surfaces Under Illumination. *Mol. Cryst. Liq. Cryst.* **2006**, *455*, 317–325.
44. Kraus, T. J.; Nepomnyashchii, A. B.; Parkinson, B. A. Atomic Layer Deposition of Epitaxial Layers of Anatase on Strontium Titanate Single Crystals: Morphological and Photoelectrochemical Characterization. *J. Vac. Sci. Technol., A* **2015**, *33*, 01A135–01A135–6.

45. Nepomnyashchii, A. B.; Parkinson, B. A. Influence of the Aggregation of a Carbazole Thiophene Cyanoacrylate Sensitizer on Sensitized Photocurrents on ZnO Single Crystals. *Langmuir* **2013**, *29*, 9362–9368.

46. Lu, Y.; Spitzer, M. T.; Parkinson, B. A. Regenerator Dependent Photoinduced Desorption of a Dicarboxylated Cyanine Dye From the Surface of Single-Crystal Rutile. *Langmuir* **2007**, *23*, 11637–11642.

47. Rowley, J. G.; Parkinson, B. A. Simultaneous Measurement of Absorbance and Quantum Yields for Photocurrent Generation at Dye-Sensitized Single-Crystal ZnO Electrodes. *Langmuir* **2013**, *29*, 13790–13796.

48. Lu, Y.; Spitzer, M. T.; Parkinson, B. A. Photochronocoulometric Measurement of the Coverage of Surface-Bound Dyes on Titanium Dioxide Crystal Surfaces. *J. Phys. Chem. B* **2006**, *110*, 25273–25278.

49. Doja, M. Q. The Cyanine Dyes. *Chem. Rev.* **1932**, *11*, 273–321.

50. Allara, D. L.; Nuzzo, R. G. Spontaneously Organized Molecular Assemblies. 2. Quantitative Infrared Spectroscopic Determination of Equilibrium Structures of Solution-Adsorbed n-Alkanoic Acids on an Oxidized Aluminum Surface. *Langmuir* **1985**, *1*, 52–66.

51. Arnold, R.; Azzam, W.; Terfort, A.; Wöll, C. Preparation, Modification, and Crystallinity of Aliphatic and Aromatic Carboxylic Acid Terminated Self-Assembled Monolayers. *Langmuir* **2002**, *18*, 3980–3992.

52. Ehret, A.; Stuhl, L.; Spitzer, M. T. Spectral Sensitization of TiO₂ Nanocrystalline Electrodes with Aggregated Cyanine Dyes. *J. Phys. Chem. B* **2001**, *105*, 9960–9965.

53. Shklover, V.; Ovchinnikov, Y. E.; Braginsky, L. S.; Zakeeruddin, S. M.; Gratzel, M. Structure of Organic/Inorganic Interface in Assembled Materials Comprising Molecular Components. Crystal Structure of the Sensitizer Bis [(4, 4"-Carboxy-2, 2"-Bipyridine) (Thiocyanato)]Ruthenium (II). *Chem. Mater.* **1998**, *10*, 2533–2541.

54. West, W. The Dimeric State of Cyanine Dyes. *J. Phys. Chem.* **1965**, *69*, 1894–1903.

55. Wang, Z. S.; Cui, Y.; Dan-oh, Y.; Kasada, C.; Shinpo, A.; Hara, K. Thiophene-Functionalized Coumarin Dye for Efficient Dye-Sensitized Solar Cells: Electron Lifetime Improved by Coadsorption of Deoxycholic Acid. *J. Phys. Chem. C* **2007**, *111*, 7224–7230.

56. Lu, Y.; Choi, D.; Nelson, J.; Yang, O. B.; Parkinson, B. A. Adsorption, Desorption, and Sensitization of Low-Index Anatase and Rutile Surfaces by the Ruthenium Complex Dye N3. *J. Electrochem. Soc.* **2006**, *158*, E131–E137.

57. Imanishi, A.; Suzuki, H.; Ohashi, N.; Ohta, T.; Nakato, Y. Dye-Sensitized Photocurrents and Adsorption Properties of Merocyanine Dye at Atomically Flat Rutile (110) and (100) TiO₂ Surfaces. *Inorg. Chim. Acta* **2008**, *361*, 778–782.

58. Liang, Y.; Novet, T.; Thorne, J. E.; Parkinson, B. A. Photosensitization of ZnO Single Crystal Electrodes with PbS Quantum Dots. *Phys. Status Solidi A* **2014**, *211*, 1954–1959.

59. Shepherd, D. P.; Sambur, J. B.; Liang, Y.; Parkinson, B. A.; Van Orden, A. In Situ Studies of Photoluminescence Quenching and Photocurrent Yield in

Quantum Dot Sensitized Single Crystal TiO_2 And ZnO Electrodes. *J. Phys. Chem. C* **2012**, *116*, 21069–21076.

- 60. Liang, Y.; Thorne, J. E.; Kern, M. E.; Parkinson, B. A. Sensitization of ZnO Single Crystal Electrodes with CdSe Quantum Dots. *Langmuir* **2014**, *30*, 12551–12558.
- 61. Janotti, A.; Van de Walle, C. G. Fundamentals of Zinc Oxide as a Semiconductor. *Rep. Prog. Phys.* **2009**, *72*, 126501.
- 62. Robertson, J.; Xiong, K.; Clark, S. J. Band Gaps and Defect Levels in Functional Oxides. *Thin Solid Films* **2006**, *496*, 1–7.
- 63. Spitzer, M. T.; Lübke, M.; Gerischer, H. Studies of Dye Photooxidation at Semiconductor Electrodes Using Attenuated Total Reflection Techniques. *Ber. Bunsen-Ges. Phys. Chem.* **1979**, *83*, 663–666.
- 64. Kavassalis, C.; Spitzer, M. T. Photooxidation of Thiacyanine Dyes at Zinc Oxide Single-Crystal Electrodes. *J. Phys. Chem.* **1983**, *87*, 3166–3171.
- 65. Passier, R.; Ritchie, J. P.; Toro, C.; Diaz, C.; Masunov, A. E.; Belfield, K. D.; Hernandez, F. E. Thermally Controlled Preferential Molecular Aggregation State in a Thiacarbocyanine Dye. *J. Chem. Phys.* **2010**, *133*, 134508–134508–7.
- 66. Turner, J. A.; Parkinson, B. A. The Application of Chronocoulometry to the Study of Adsorption at the Semiconductor/Electrolyte Interface. *J. Electroanal. Chem.* **1983**, *150*, 611–617.
- 67. Gundlach, L.; Ernstorfer, R.; Willig, F. Dynamics of Photoinduced Electron Transfer From Adsorbed Molecules Into Solids. *Appl. Phys. A: Mater. Sci. Process.* **2007**, *88*, 481–495.
- 68. Gundlach, L.; Letzig, T.; Willig, F. Test of Theoretical Models for Ultrafast Heterogeneous Electron Transfer with Femtosecond Two-Photon Photoemission Data. *J. Chem. Sci. (Bangalore, India)* **2009**, *121*, 561–574.
- 69. Schanze, K. S.; Shelton, A. H. Functional Polyelectrolytes. *Langmuir* **2009**, *25*, 13698–13702.
- 70. Jiang, H.; Taranekar, P.; Schanze, K. S. Conjugated Polyelectrolytes: Synthesis, Photophysics, and Applications. *Angew. Chem., Int. Ed.* **2009**, *48*, 4300–4316.
- 71. Sambur, J. B.; Averill, C. M.; Bradley, C.; Shuttlefield, J.; Lee, S. H.; Reynolds, J. R.; Schanze, K. S.; Parkinson, B. A. Interfacial Morphology and Photoelectrochemistry of Conjugated Polyelectrolytes Adsorbed on Single Crystal TiO_2 . *Langmuir* **2011**, *27*, 11906–11916.
- 72. Xie, D.; Parthasarathy, A.; Schanze, K. S. Aggregation-Induced Amplified Quenching in Conjugated Polyelectrolytes with Interrupted Conjugation. *Langmuir* **2011**, *27*, 11732–11736.
- 73. Zhu, X.; Nepomnyashchii, A. B.; Roitberg, A. E.; Parkinson, B. A.; Schanze, K. S. Photosensitization of Single-Crystal ZnO by a Conjugated Polyelectrolyte Designed to Avoid Aggregation. *J. Phys. Chem. Lett.* **2013**, *4*, 3216–3220.
- 74. Nozik, A. J. Quantum Dot Solar Cells. *Phys. E (Amsterdam, Neth.)* **2002**, *14*, 115–120.

75. Hodes, G. Comparison of Dye-and Semiconductor-Sensitized Porous Nanocrystalline Liquid Junction Solar Cells. *J. Phys. Chem. C* **2008**, *112*, 17778–17787.
76. Semonin, O. E.; Luther, J. M.; Beard, M. C. Quantum Dots for Next-Generation Photovoltaics. *Mater. Today* **2012**, *15*, 508–515.
77. Beard, M. C.; Luther, J. M.; Semonin, O. E.; Nozik, A. J. Third Generation Photovoltaics Based on Multiple Exciton Generation in Quantum Confined Semiconductors. *Acc. Chem. Res.* **2013**, *46*, 1252–1260.
78. Murray, C. B.; Norris, D. J.; Bawendi, M. G. Synthesis and Characterization of Nearly Monodisperse CdE (E = Sulfur, Selenium, Tellurium) Semiconductor Nanocrystallites. *J. Am. Chem. Soc.* **1993**, *115*, 8706–8715.
79. Hughes, B. K.; Luther, J. M.; Beard, M. C. The Subtle Chemistry of Colloidal, Quantum-Confined Semiconductor Nanostructures. *ACS Nano* **2012**, *6*, 4573–4579.
80. Kamat, P. V. Quantum Dot Solar Cells. the Next Big Thing in Photovoltaics. *J. Phys. Chem. Lett.* **2013**, *4*, 908–918.
81. Jun, H. K.; Careem, M. A.; Arof, A. K. Quantum Dot-Sensitized Solar Cells—Perspective and Recent Developments: a Review of Cd Chalcogenide Quantum Dots as Sensitizers. *Renewable Sustainable Energy Rev.* **2013**, *22*, 148–167.
82. Chattarki, A. N.; Kamble, S. S.; Deshmukh, L. P. Role of pH in Aqueous Alkaline Chemical Bath Deposition of Lead Sulfide Thin Films. *Mater. Lett.* **2012**, *67*, 39–41.
83. Chang, C.-H.; Lee, Y.-L. Chemical Bath Deposition of CdS Quantum Dots Onto Mesoscopic TiO₂ Films for Application in Quantum-Dot-Sensitized Solar Cells. *Appl. Phys. Lett.* **2007**, *91*, 053503.
84. Niitsoo, O.; Sarkar, S. K.; Pejoux, C.; Rühle, S.; Cahen, D.; Hodes, G. Chemical Bath Deposited CdS/CdSe-Sensitized Porous TiO₂ Solar Cells. *J. Photochem. Photobiol., A* **2006**, *181*, 306–313.
85. Guijarro, N.; Lana-Villarreal, T.; Shen, Q.; Toyoda, T.; Gómez, R. Sensitization of Titanium Dioxide Photoanodes with Cadmium Selenide Quantum Dots Prepared by SILAR: Photoelectrochemical and Carrier Dynamics Studies. *J. Phys. Chem. C* **2010**, *114*, 21928–21937.
86. Santra, P. K.; Kamat, P. V. Mn-Doped Quantum Dot Sensitized Solar Cells: a Strategy to Boost Efficiency Over 5%. *J. Am. Chem. Soc.* **2012**, *134*, 2508–2511.
87. Watson, D. F. Linker-Assisted Assembly and Interfacial Electron-Transfer Reactivity of Quantum Dot-Substrate Architectures. *J. Phys. Chem. Lett.* **2010**, *1*, 2299–2309.
88. Nevins, J. S.; Coughlin, K. M.; Watson, D. F. Attachment of CdSe Nanoparticles to TiO₂ Via Aqueous Linker-Assisted Assembly: Influence of Molecular Linkers on Electronic Properties and Interfacial Electron Transfer. *ACS Appl. Mater. Interfaces* **2011**, *3*, 4242–4253.
89. Kern, M. E.; Watson, D. F. Influence of Solvation and the Persistence of Adsorbed Linkers on the Attachment of CdSe Quantum Dots to TiO₂ Via Linker-Assisted Assembly. *Langmuir* **2012**, *28*, 15598–15605.

90. Kern, M. E.; Watson, D. F. Linker-Assisted Attachment of CdSe Quantum Dots to TiO₂: Time- and Concentration-Dependent Adsorption, Agglomeration, and Sensitized Photocurrent. *Langmuir* **2014**, *30*, 13293–13300.

91. Sambur, J. B.; Parkinson, B. A. CdSe/ZnS Core/Shell Quantum Dot Sensitization of Low Index TiO₂ Single Crystal Surfaces. *J. Am. Chem. Soc.* **2010**, *132*, 2130–2131.

92. Sambur, J. B.; Riha, S. C.; Choi, D.; Parkinson, B. A. Influence of Surface Chemistry on the Binding and Electronic Coupling of CdSe Quantum Dots to Single Crystal TiO₂ Surfaces. *Langmuir* **2010**, *26*, 4839–4847.

93. Sambur, J. B.; Novet, T.; Parkinson, B. A. Multiple Exciton Collection in a Sensitized Photovoltaic System. *Science* **2010**, *330*, 63–66.

94. Liang, Y.; Thorne, J. E.; Parkinson, B. A. Controlling the Electronic Coupling Between CdSe Quantum Dots and Thiol Capping Ligands via pH and Ligand Selection. *Langmuir* **2012**, *28*, 11072–11077.

95. Hyun, B. R.; Zhong, Y.-W.; Bartnik, A. C.; Sun, L.; Abruña, H. D.; Wise, F. W.; Goodreau, J. D.; Matthews, J. R.; Leslie, T. M.; Borrelli, N. F. Electron Injection From Colloidal PbS Quantum Dots Into Titanium Dioxide Nanoparticles. *ACS Nano* **2008**, *2*, 2206–2212.

96. Dibbell, R. S.; Watson, D. F. Distance-Dependent Electron Transfer in Tethered Assemblies of CdS Quantum Dots and TiO₂ Nanoparticles. *J. Phys. Chem. C* **2009**, *113*, 3139–3149.

97. Dibbell, R. S.; Youker, D. G.; Watson, D. F. Excited-State Electron Transfer From CdS Quantum Dots to TiO₂ Nanoparticles via Molecular Linkers with Phenylene Bridges. *J. Phys. Chem. C* **2009**, *113*, 18643–18651.

98. Hines, D. A.; Kamat, P. V. Quantum Dot Surface Chemistry: Ligand Effects and Electron Transfer Reactions. *J. Phys. Chem. C* **2013**, *117*, 14418–14426.

99. Peng, Z. A.; Peng, X. Formation of High-Quality CdTe, CdSe, and CdS Nanocrystals Using CdO as Precursor. *J. Am. Chem. Soc.* **2001**, *123*, 183–184.

100. Mann, J. R.; Nevins, J. S.; Soja, G. R.; Wells, D. D.; Levy, S. C.; Marsh, D. A.; Watson, D. F. Influence of Solvation and the Structure of Adsorbates on the Kinetics and Mechanism of Dimerization-Induced Compositional Changes of Mixed Monolayers on TiO₂. *Langmuir* **2009**, *25*, 12217–12228.

101. Pawsey, S.; Yach, K.; Reven, L. Self-Assembly of Carboxyalkylphosphonic Acids on Metal Oxide Powders. *Langmuir* **2002**, *18*, 5205–5212.

102. Yan, S. G.; Prieskorn, J. S.; Kim, Y.; Hupp, J. T. In Search of the Inverted Region: Chromophore-Based Driving Force Dependence of Interfacial Electron Transfer Reactivity at the Nanocrystalline Titanium Dioxide Semiconductor/Solution Interface. *J. Phys. Chem. B* **2000**, *104*, 10871–10877.

103. Kern, M. E.; Watson, D. F. Influence of Dispersion Forces and Ordering on the Compositions of Mixed Monolayers of Alkanoic Acids on Nanocrystalline TiO₂ Films. *Langmuir* **2013**, *29*, 13797–13807.

104. Chen, X.; Hutchinson, J. L.; Dobson, P. J. Highly Luminescent Monodisperse CdSe Nanoparticles Synthesized in Aqueous Solution. *J. Mater. Sci.* **2009**, *44*, 285–292.

105. Frederick, M. T.; Weiss, E. A. Relaxation of Exciton Confinement in CdSe Quantum Dots by Modification with a Conjugated Dithiocarbamate Ligand. *ACS Nano* **2010**, *4*, 3195–3200.

106. Adams, D. M.; Brus, L.; Chidsey, C.; Creager, S. E.; Creutz, C.; Kagan, C. R.; Kamat, P. V.; Lieberman, M.; Lindsay, S.; Marcus, R.; Metzger, R. M.; Michel-Beyerle, M. E.; Miller, J. R.; Newton, M. D.; Rolison, D. R.; Sankey, O.; Schanze, K. S.; Yardley, J.; Zhu, X. Charge Transfer on the Nanoscale: Current Status. *J. Phys. Chem. B* **2003**, *107*, 6668–6697.

107. Ellis, A. B.; Kaiser, S. W.; Bolts, J. M.; Wrighton, M. S. Study of n-Type Semiconducting Cadmium Chalcogenide-Based Photoelectrochemical Cells Employing Polychalcogenide Electrolytes. *J. Am. Chem. Soc.* **1977**, *99*, 2839–2848.

108. Hodes, G.; Miller, B. Thermodynamic Stability of II–VI Semiconductor–Polysulfide Photoelectrochemical Systems. *J. Electrochem. Soc.* **1986**, *133*, 2177–2180.

109. Sambur, J. B.; Parkinson, B. A. Size Selective Photoetching of CdSe Quantum Dot Sensitizers on Single-Crystal TiO₂. *ACS Appl. Mater. Interfaces* **2014**, *6*, 21916–21920.

110. Beard, M. C. Multiple Exciton Generation in Semiconductor Quantum Dots. *J. Phys. Chem. Lett.* **2011**, *2*, 1282–1288.

111. Choi, J. J.; Lim, Y. F.; Santiago-Berrios, M. B.; Oh, M.; Hyun, B. R.; Sun, L.; Bartnik, A. C.; Goedhart, A.; Malliaras, G. G.; Abruna, H. D.; Wise, F. W.; Hanrath, T. PbSe Nanocrystal Excitonic Solar Cells. *Nano Lett.* **2009**, *9*, 3749–3755.

112. Leschikies, K. S.; Beatty, T. J.; Kang, M.-S.; Norris, D. J.; Aydil, E. S. Solar Cells Based on Junctions Between Colloidal PbSe Nanocrystals and Thin ZnO Films. *ACS Nano* **2009**, *3*, 3638–3648.

113. Semonin, O. E.; Luther, J. M.; Choi, S.; Chen, H.-Y.; Gao, J.; Nozik, A. J.; Beard, M. C. Peak External Photocurrent Quantum Efficiency Exceeding 100% via MEG in a Quantum Dot Solar Cell. *Science* **2011**, *334*, 1530–1533.

114. Choi, D.; Rowley, J. G.; Parkinson, B. A. Dye Sensitization of n and p Type Gallium Phosphide Photoelectrodes. *J. Electrochem. Soc.* **2012**, *159*, H846–H852.

115. Chitambar, M.; Wang, Z.; Liu, Y.; Rockett, A.; Maldonado, S. Dye-Sensitized Photocathodes: Efficient Light-Stimulated Hole Injection Into p-GaP Under Depletion Conditions. *J. Am. Chem. Soc.* **2012**, *134*, 10670–10681.

116. Wang, Z.; Shakya, A.; Gu, J.; Lian, S.; Maldonado, S. Sensitization of P-GaP with CdSe Quantum Dots: Light-Stimulated Hole Injection. *J. Am. Chem. Soc.* **2013**, *135*, 9275–9278.

Chapter 2

Electronic and Optical Properties of Low-Dimensional TiO₂: From Minority Surfaces to Nanocomposites

Giacomo Giorgi and Koichi Yamashita*

Department of Chemical System Engineering, School of Engineering,
The University of Tokyo, 7-3-1, Hongo, Bunkyo-ku, Tokyo, Japan and
CREST-JST, 7 Gobancho, Chiyoda-ku, Tokyo 102-0076, Japan

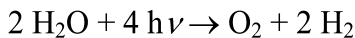
*E-mail: yamasita@chemsys.t.u-tokyo.ac.jp.

We present a review of our most recent work concerning the electronic and optical properties of several low-dimensional systems of anatase TiO₂. First, we describe the analysis of the (001) minority surface of anatase, for which we offer evidence of improved photoactivity as function of the reconstruction. We then describe the analysis of bilayers of anatase, (001)-oriented and lepidocrocite type, and confirm the experimentally reported excitonic nature of their optical spectra. The primary role that packing plays in the optical properties of such layered systems is also revealed. Finally, we focus on the structural and electronic features of nanocomposites formed by anatase (001)-oriented bilayers and graphene. Interesting differences between chemisorbed and physisorbed heterostructures are found.

Introduction

Modern photocatalysis era begins with the pioneering discovery of the Fujishima–Honda effect (1). After nanoparticles of TiO₂ rutile immersed in H₂O were exposed to a source of light, there was clear evidence of H₂ and O₂ evolution. Specifically, photocurrent flows from the Pt counter electrode to the TiO₂ electrode through an external circuit when the TiO₂ electrode is exposed to

light at energies just lower than the energy band gap of the semiconductor. The overall reaction scheme, i.e., the sum of the two half-reactions at the electrodes, is given by the following equation (2):



Improving on the initial discovery has represented, and still represents, one of the most studied chemical processes over the last four decades. Subsequently, further significant milestones have been achieved, and several reviews that shed light on the state-of-the-art of the mechanism of this reaction have been published. (For a full overview from a surface science perspective, e.g., see (3–5).) Motivation for the great interest in this arises from the fact that hydrogen production via photocatalytic water splitting represents a promising strategy for a clean, environmentally friendly, and affordable solar-to-energy process, for the production of H₂. It is thus the most viable alternative pathway to the polluting fossil-fuel-derived energy pathway.

The photovoltage required to achieve water photocatalysis is minimal (1.23 V). A further requirement to achieve efficient production of H₂ and O₂ from an ideal system is that the valence band maximum (VBM) (conduction band minimum [CBM]) level of the semiconductor must be more positive (negative) on the electrochemical scale than on the H₂O oxidation (reduction) level (6). Figure 1 shows a simplified scheme of the photocatalytic mechanism.

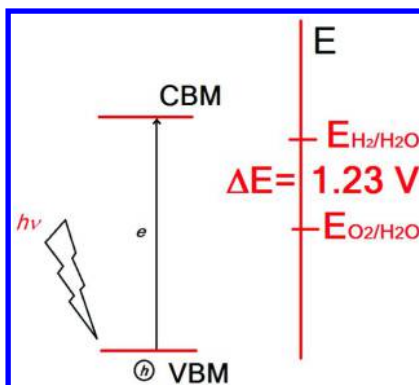


Figure 1. Schematic diagram of the photocatalytic mechanism: the electron (hole) at the CBM (VBM) favours H₂O reduction (oxidation) to form H₂ (O₂).

Photocatalysis is also used for the purification of air and water from pollutants (7–27). In a broader context, photocatalysis can be related to an artificial photosynthesis mechanism (28–31) because of the similarities with the natural process of photosynthesis, which governs biological activities on earth: both photocatalysis and photosynthesis take advantage indeed of solar light in order to produce chemical energy.

Of importance is that the two photocatalytic processes, i.e., that for hydrogen production and that for environmental purification, rely on different chemistries. In the latter case, only the VBM level is important because it is the holes that are responsible for pollutant degradation. On the other hand, for the former process, also the CBM level becomes important.

The band edge requirements for photocatalytic H_2O splitting are met by a large class of binary semiconductors, for example, SiC , CdS , GaP , oxide semiconductors such as TiO_2 (as mentioned), SrTiO_3 , CaTiO_3 , KTaO_3 , Ta_2O_5 , ZrO_2 (32, 33), perovskites (34, 35), and others. The impressive recent progress in computational methods now even enables computational screening for the prediction of the possible suitability of new materials for photocatalysis: materials experimentally known and materials still to be synthesized (36). Unfortunately, most of the known materials have disadvantages in photocatalysis, e.g., a too wide band gap, a corrosive nature and poor availability (which increases material cost), leading to unsuitability for efficient use in solar energy conversion. Because of its combination of chemical stability, low cost, wide availability, and highly oxidizing/reducing photogenerated carriers (32), TiO_2 is regarded as the best material to date for photocatalytic applications.

There remain some important issues that characterize this manifold material in light-to-energy conversion processes: a rapid carrier recombination, the possibility of a backward reaction and, most importantly, the fact that it mainly absorbs in the UV region, which represents only ~4% of the whole solar spectrum. In order to avoid the later drawback, much effort has been directed at improving the absorption onset towards the visible region. Modifications of TiO_2 have been experimentally performed and theoretically investigated (37, 38) in efforts to accomplish this. The following, in particular, have shown promising results: dye-sensitization (39–51) heterosemiconductor coupling (52–60), and doping (e.g., metal (61–63)/anion (64–69)).

The importance of doping TiO_2 to enhance its absorption towards the visible region was first recognized almost three decades ago (70, 71). The relevance of the process for the preparation of N-doped TiO_2 was again recognized later, and the photocatalytic activity of N-doped TiO_2 in the anatase form was widely investigated (72–74). Similarly, S-doped TiO_2 in the anatase form was also found to be photocatalytically active when sulfur atoms were substituted onto the oxygen sites (anion doping) (67, 68). Interestingly, S-doped TiO_2 was successfully produced with the S atoms substituted onto the titanium sites (cation doping). While the visible light absorbance of this form of S-cation-doped TiO_2 was higher than that of the N-, C-, or S-anion-doped forms, its photocatalytic activity was lower due to catalytic poisoning induced by the sulfate ions formed (75).

Dyes used in photovoltaics (76) also satisfy the characteristics required for efficient functioning in photocatalytic systems (e.g., see (77–81)). The electrons, once that the dye is excited, transfer to the TiO_2 CBM activating the H_2O splitting process. Several dyes have been tested on different substrates (82). Substantial efficiency improvement due to the presence of dyes has been recorded, but no conclusive results about the most suitable dyes have been obtained.

During the last decade, our group deeply investigated the photocatalytic-oriented applications of TiO_2 . In particular, we investigated its two most stable

polymorphs, rutile and anatase, in several morphological shapes, from bulk to surface (83) and nanosheets (NS) (84), and combined in heterostructures (85). We focused on the impact of defects (86), doping (87, 88), and dopant-defect mutual interactions (89, 90), with the aim of describing the relationship between atomic structure and photoresponsivity. This was done in efforts to predict viable procedures to optimize TiO_2 performances in photocatalytic applications.

We here want review our more recent theoretical results obtained for the 2D TiO_2 -derived systems (83, 84) and for the heterostructures formed by TiO_2 -derived NS and graphene (85).

From Bulk to Surface: Excitonic Effects on the Reactive Minority Surfaces of Anatase – A Combined Density Functional and Many Body Perturbation Theory Analysis

The surface of a semiconductor, it being the boundary region of the bulk and thus the access point for the light, has a significant effect on photocatalytic properties. Knowledge of the structural, electronic, and optical features of the surface enables us to better understand the photocatalytic properties of the material under investigation.

In this section, we focus particularly on the relationship between optical properties and the structure of minority surfaces of anatase, and aim to determine how the exciton spatial localization may impact on the photocatalytic activity.

It is well documented that the (photo)catalytic performances of TiO_2 are strongly influenced by the exposed surfaces (91, 92). In the case of anatase, the most stable surfaces are the (101) and the (100)/(010) (93). A reduced defect concentration characterizes the {001} facet compared with other facets of both anatase and rutile (94–96). This finding, in conjunction with enhanced reactivity (97, 98), makes the (001) minority surfaces extremely appealing for photocatalytic and photovoltaic applications. The {001} facet, in conjunction with the {101}, represents the main surface in nanocrystalline films (99). Importantly, the (001) surface impacts on the photoreactivity of anatase nanoparticles (98, 100). There is proof of the extremely localized nature of the exciton along the [001] direction in such nanosized systems, as reported by Chiodo *et al.* (101).

We performed excited-state calculations (102) of stoichiometric slab models to first obtain the quasi-particle (QP) energies (by means of Green's function based formalism, G_0W_0) and solved the Bethe–Salpeter equation (BSE) in efforts to describe the optical excitonic properties of the minority (001) surface.

Experimentally, a (1×1) periodicity is obtained according to the procedure reported by Hengerer *et al.* (103) and Herman *et al.* (104), while a (1×4) reconstruction appears after annealing under UHV (103, 105). Interestingly, from the (1×4) , once oxygen or air is introduced into the experimental chamber, the (1×1) is recovered (103).

After carrying on an investigation based on the screening of twelve non-metallic elements terminating the (001) reconstruction, Yang *et al.* (106) used hydrofluoric acid (HF) as a capping agent under hydrothermal conditions and then clearly demonstrated that fluorine is able to highly stabilize the {001}

facet and that, under such conditions, the $\{001\}$ is even energetically preferable to the $\{101\}$. Samples were obtained that exposed up to 47% (1×1) facets. Using 2-propanol as a synergistic capping agent and reaction medium, together with HF, 64% was reached in the case of high-quality anatase TiO_2 single-crystal NS (107).

While the (1×1) periodicity clearly represents the bulk cut of anatase along the $[001]$ direction (108, 109), more complex is the (1×4) reconstruction for which several structural models have been formulated. Using low-energy electron diffraction (LEED), X-ray photoelectron spectroscopy (XPS), and angle-resolved mass spectroscopy of recoiled ions analyses, Herman *et al.* (105) described such reconstruction on the basis of a micro-faceted surface that exposes (103) and $(1\ 03)$ surface planes. It is suggested that the (103) -like surfaces are lower in energy than the (001) surface. On the other hand, Hengerer *et al.* (103) suggested a missing oxygen row model for the (001) surface as explanation for the origin of the observed (1×4) pattern. Based on scanning tunnelling microscopy, XPS, reflection high-energy electron diffraction and LEED results, Liang (110) proposed an “added” and “missing” row model to account for such reconstruction. Further experimental findings indicated that the anatase (1×4) reconstruction is stoichiometric, exposing Ti^{4+} centred along the highest points on the structure, and does not expose fourfold coordinated Ti^{4+} . This feature is accounted for by Tanner *et al.* (111) who proposed a new model based on $\{101\}$ micro-facets, which is consistent with the experimental observations.

In our calculations, we also took into account the “ad molecule” model suggested by Lazzeri and Selloni (112). Here, rows of TiO_3 species periodically replace rows of surface-bridging oxygens of the parental (1×1) surface, strongly reducing (by $\sim 43\%$) the large surface tensile stress that characterizes the (1×1) , due to the $\text{Ti}-\text{O}-\text{Ti}$ angle at the surface ($\sim 150^\circ$), which is much wider than expected for a sp^2 hybridized O atom (112).

The two investigated reconstructions of the (001) surface are presented in Figure 2.

Concerning the computational details, our initial structures were all relaxed at the DFT-PBE level of calculation (113), along with a projector augmented wave (PAW) approach (114–116), as implemented in the VASP code (17, 118). Eight-atomic-layer (001) oriented slabs were considered. At these fixed geometries, we recalculated the occupied and 800 empty KS states (119) with norm-conserving pseudopotentials (120, 121), the results used then as input for the G_0W_0 and BSE calculations performed using the Yambo code (122). Full details of the calculations are available elsewhere (83).

Accordingly, we calculated the G_0W_0 gap correction for the $(001)-(1 \times 1)$ slab to be 1.8 eV (119, 122). The same gap correction was assumed for the $(001)-(1 \times 4)$ slab.

Results of the electronic properties of bulk anatase and the two surface reconstructions are quite similar; the only difference is the increase of a peak in the DOS of the two surface systems, which is not observed in the bulk case.

In the (1×1) case, the O p orbitals at the VBM overlap among themselves along the $[100]$ (x) direction because of their reduced hybridization with the subsurface Ti d orbitals, although their orientation is along the $[010]$ direction.

The different structure and electronic symmetry of the (1×4) surface does not allow for such chain-like hybridization and the VBM is mainly localized on the O p_x orbitals along the top of the ridge in the $[010]$ direction.

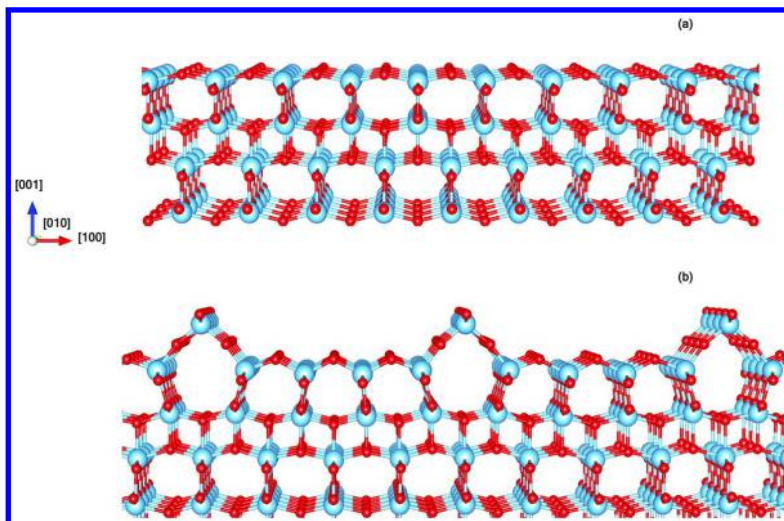


Figure 2. Top, (a): anatase TiO_2 (001) surface with (1×1) periodicity. Bottom, (b): same surface with (1×4) periodicity. [Online version, light blue: Ti atoms, red: O atoms]. The calculated energy difference between the two surfaces at PAW/PBE level is $\sim 0.43 \text{ J m}^{-2}$.

In Figure 3, the imaginary part of the macroscopic dielectric functions of the (1×1) and (1×4) models, calculated at the independent QP level, and after including the electron-hole interaction, are reported.

It is interesting to note that there is a strong similarity between the optical spectrum of bulk anatase and that of the (1×4) case (Figure 3d). For the (1×1) termination, optical structures (S_2 and S_3) are present below the first bulk absorption peak B_1 . This result clearly reflects the different nature of the VBM of the two reconstructions. In particular, the first direct exciton (S_1 in Figure 3c, S'_1 in Figure 3d) is at $\sim 3.2 \text{ eV}$ for the (1×1) case and at 3.5 eV for the (1×4) case, respectively; it results constituted by the mixing of vertical transitions at Γ , from VBM/VBM-1 states to CBM/CBM+1. The former two states have a strong surface character; the latter two are mainly localized on the Ti atoms of the slab. In the (1×1) , the S_2 and S_3 peaks derive from the mixing of IQP transitions at the Γ point from VBM and VBM-1, as in the S_1 case, to CBM/CBM+1/CBM+2. The peak B_1 (which corresponds to the first structure, referred to as B_1 in the inset, of the bulk spectrum for light polarized perpendicular to c) results from mixing transitions (at some k points near Γ , along the $\Gamma - J$ and $\Gamma - K$ directions)

from a few bands below to a few bands above the Fermi level. Surface termination for both the (1×1) and (1×4) cases induces an optical anisotropy in the (001) plane (see Figure 3), which is still related to the nature of the VBM of the two systems.

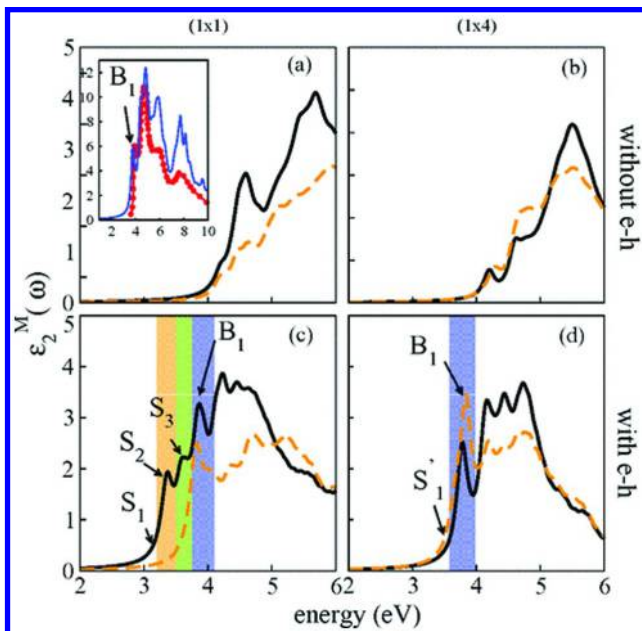


Figure 3. Macroscopic dielectric function $\varepsilon_2^M(\omega)$ for (1×1) (left column) and (1×4) - (001) (right column) cases. (a) and (b) Spectra calculated at IQP level. (c) and (d) As before, but calculated including the local-field effects and the electron-hole Coulomb attraction. Online version, the black solid (orange dashed) curves are for light polarized along the $[100]$ ($[010]$) direction. Inset (a): Bulk BSE (blue curve) and experimental (red diamonds, ref. (131)) spectrum for light polarized perpendicular to c . The arrows indicate the exciton energies under consideration. The widths of the orange (left), green (middle), and blue (right) boxes indicate the energetic windows where the excitonic eigenvalues are summed to plot the electron-hole distribution probabilities discussed in Figure 4. [Reprinted figure with permission from ref. (83). Copyright 2011 by the American Physical Society.]

For the (1×1) case, the optical structures S_2 and S_3 are completely polarized along the $[100]$ direction, while B_1 is slightly more intense for this light polarization. In the (1×4) case, however, an opposite anisotropy is observed for B_1 , hence the $[010]$ polarization is favoured. Both absorption and photoluminescence (PL) data are available for polycrystalline thin layers or nanostructures. This means that the reported optical properties often refer to

a mixture of crystalline orientations, and various phases (mainly anatase and rutile) are present in the experimental samples. There are some reports of optical spectra of thin films very similar to bulk anatase (123, 124). According to our predictions, these should correspond to the presence of the (1×4) reconstruction. A few reports of optical data of anatase thin films include absorption at energies 3.2 eV (125, 126).

To complete the experimental scenario, we now mention PL spectra of TiO_2 films prepared *via* dc reactive magnetron sputtering, where the presence of a band ranging from 2.8 to 3.1 eV is attributed to surface-trapped exciton emission (127). Other PL spectra (128) measured on fluorinated NS with dominant (001) facets are characterized by optical peaks around 2.6–3.1 eV. A very interesting feature derived from the calculations is the carrier spatial distribution, i.e., the most probable position that an electron and hole occupy in the surfaces after the photoexcitation process (Figure 4).

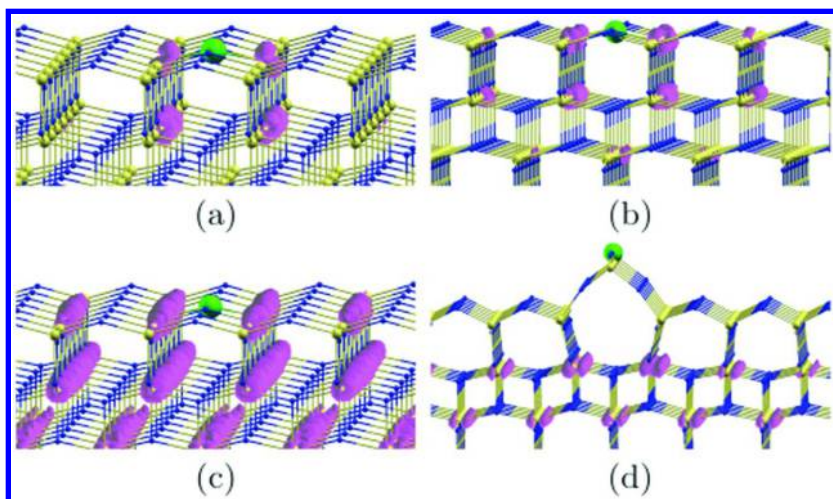


Figure 4. Two-body electron-hole pair correlation function for the main excitonic peaks (in Fig. 3) for the two investigated reconstructions. Online version, large, yellow (small, blue) spheres represent Ti (O) atoms in the (1×1) – (001) [panels (a)–(c)] and (1×4) – (001) [panel d] slabs. (a) Magenta isosurface (at 25% of its maximum value): probability of finding the electron when the hole position (green ball) is fixed near a given atomic site. All the excitons summed in the energetic window indicated by the orange area of Figure 3c around S_2 . (b) As in (a), but for excitons in the window indicated by the green area of Figure 3c around S_3 . (c) As in (a), but for excitons in the window indicated by the blue area of Figure 3c around B_1 . (d) As in (a), but at the (1×4) surface and summing over all the excitons in the window indicated by the blue area of Figure 3d around B_1 . [Reprinted figure with permission from ref. (83). Copyright 2011 by the American Physical Society.].

In the (1×1) model, the electron is mainly localized in the vicinity of the surface plane, mainly on the top of the two nearest neighbour Ti surface atoms along the [100] direction (Figure 4a). Fixing the hole position on one bridging oxygen at the surface, and summing over all the excitons related to the S_3 structure (green in Figure 3c), we observe that the electron has a nonzero probability to localize near other Ti surface atoms (Figure 4b). For higher energy excitons, close to B_1 (blue in Figure 3c), although the electron-hole spatial distribution results in more spread over the subsurface and bulk part of the slab, other Ti surface sites have a nonzero probability to host the electron (Figure 4c). For the (1×4) reconstruction, the exciton at the optical onset (S'_1), and all the excitons around B_1 (blue in Figure 3d), show a similar spatial behaviour. With the hole fixed near either a ridge surface oxygen or a bulk oxygen atom, the probability to find the electron is buried in the central part of the slab (Figure 4d). The two different reconstructions have different impacts on the photocatalytic performances of the minority (001) surface of anatase. For the (1×4) , the electrons are spread over the subsurface region when the hole is at the surface meaning reduced photocatalytic activity. In the (1×1) case, at variance, we can predict improved photocatalytic performance due to the observed net spatial separation between the photocarriers in addition to their concomitant presence at the surface (129). For excitation energies around 3.2–3.4 eV, the electron tends to be mainly on the two nearest-neighbour Ti atoms bound to the O 2c atom, where the hole is mainly localized. For higher excitation energies, other Ti surface atoms can be photoactivated, supporting the idea that Ti and O atoms involved in such photochemical reactions do not necessarily need to face each other, as they do in chemical reactions. This offers further evidence of the heterogeneous nature of the hydroxyl groups present at the surface (130).

From Surfaces to Nanosheets: Enhanced Excitonic Effects on Spatially Confined Systems

Directly related to (001) minority surfaces are anatase NS oriented along the same [001] direction. Such NS show improved performances in photochemistry due to their intrinsic enhanced exposed surface area (107, 132). TiO_2 bidimensional nanomaterials, other than the anatase-derived, have recently been synthesized and attracted much attention for their device-oriented applicability (see (133–135) and references therein). However, not much information is available on this class of low-dimensional materials; furthermore, most importantly, their photoexcited and structural properties are still largely unknown (136–140).

Using the same computational set-up employed for the previously investigated case of the surfaces (for full details, see (84)), here we calculated the optical properties of several TiO_2 -based NS; we similarly tried to relate them to structural and electronic properties. The inclusion of local-field effects and electron-hole interaction (see (102) and references therein) enabled us to focus on the reported excitonic nature of such TiO_2 NS, a behaviour widely documented for similar low-dimensional semiconducting materials, as in the case of single-walled carbon

nanotubes (141), silicon nanowires (142), boron nitride nanotubes (143), and others. Here we analysed the properties of pristine (001)-anatase bilayers and the lepidocrocite NS. This latter structure (144, 145) is related to the former by a barrierless phase transition associated with the gliding of the upper layer of a pristine (001)-anatase NS on top of a bottom one, which leads to considerable reduction in the tensile stress (146). The stability of the lepidocrocite NS is further enhanced by the fact that Ti atoms recover the sixfold coordination, as in the bulk of anatase. A lepidocrocite NS is only 0.18 eV/unit formula more unstable than bulk anatase (147).

We modelled three different isolated anatase-like NS: the first two, anatase-S and anatase-AS1, have the same lateral lattice parameter a as bulk anatase, they only differ in the nature of the Ti–O–Ti angle at the surface. In the case of the former, two identical and symmetric (S) Ti–O bonds (1.96 Å) at the surface are present. In the case of latter (Figure 5b), which is more stable since it is less stressed at the surface (148), two asymmetric (AS) bonds are present (1.74 and 2.24 Å).

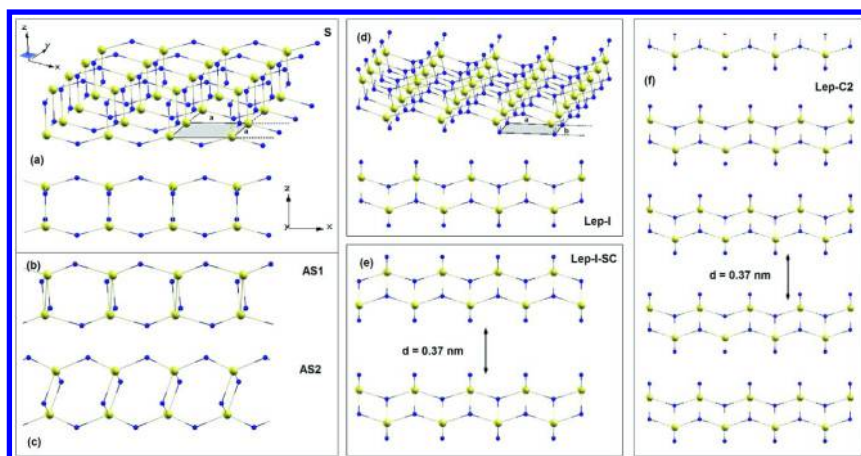


Figure 5. (a) Anatase-S: perspective view of the planar 2D infinite sheet (top); lateral view along the (100) direction (bottom). (b) Lateral view of anatase-AS1. (c) Lateral view of anatase-AS2. (d) Lepidocrocite-I sheet: perspective view of the 2D infinite sheet (top); lateral view along the (010) direction (bottom). (e) Isolated bilayer sheet, lepidocrocite-I-SC. (f) 3D packed atomic model (lepidocrocite-C2) where the distance between the periodic layers along the (001) direction is $d = 0.37$ nm. In (e) and (f), only the lateral view along the (010) orientation is shown. Online version, the gray region in (a) and (d) represents schematically the size of the fundamental cell in the xy plane. [Ti (O) atoms yellow (blue).] [Reprinted with permission from ref. (84). Copyright 2012 American Chemical Society.]

The last of these three structures (anatase-AS2, Figure 5c) is obtained via energy minimization with respect to the lattice parameter a , and keeping as constraint the squared geometry of the (001) surface (i.e., $a = b$) (146).

Finally, the isolated lepidocrocite-I sheet is obtained by minimizing the total energy with a , along (010), fixed to its bulk value, while varying the lattice parameter b along the (100) direction. See Figure 5d (146, 147). Following Sato (147), we also modelled an isolated double-sheet model (lepidocrocite-I-SC) in a stacked configuration (Figure 5e).

The optimized lattice parameters, the associated total energies, and the formation energies of the four isolated NSs are reported in Table 1.

Table 1. Optimized in-Plane Lattice Parameters (a and b), and Film Formation Energy (FE, eV) for the Four Isolated NS Here Considered

<i>Model</i>	<i>a</i>	<i>b</i>	<i>FE</i>
Anatase-S	3.78	3.78	0.896
Anatase-AS1	3.78	3.78	0.775
Anatase-AS2	3.51	3.51	0.580
Lepidocrocite-I	3.76	3.03	0.165

FE calculated according to the formula $FE = TE/n - E_{tot}(TiO_2)$, where TE is the total energy of the sheet, n is the number of TiO_2 units in the sheet, and $E_{tot}(TiO_2)$ is the energy per unit of TiO_2 in bulk anatase.

Besides considering the isolated layers, we likewise considered two models in the case of lepidocrocite (periodic also along the (001) direction) with different distances (d) between the layers: lepidocrocite-C1 ($d = 1.3$ nm) and lepidocrocite-C2 ($d = 0.37$ nm). (The latter is shown in Figure 5f). A periodic 3D arrangement of the lepidocrocite-I-SC case was also considered (lepidocrocite-SC).

Concerning the electronic properties of the four isolated NS investigated here (see Figure 6) we now report the direct and indirect minimum gaps, calculated at the single-particle DFT-KS level (PBE (113)). Moving from the anatase-S to lepidocrocite-I, the DFT gaps increase, and, because of the quantum confinement effect, they are larger than the gaps calculated at the same level, for rutile and anatase bulk compounds (101, 149). The relevance of the inclusion of a nonlocal and energy-dependent description for the exchange and correlation self-energy term is evident when looking at the corresponding GW gaps. They are much wider than the GGA-PBE gaps calculated here and those previously reported in the literature for similar nanostructured TiO_2 -based systems. Our GW-calculated gap of 5.6 eV for the lepidocrocite-I atomic model closely resembles previous results at the hybrid DFT level of calculation (150).

Interestingly, upon passing from anatase-S to lepidocrocite-I, the band gap changes character – it passes from indirect to direct. The three anatase models show, similar to the (001)-anatase surface (83, 108), M– indirect minimum gaps, while the lepidocrocite sheet has a direct minimum gap at Γ .

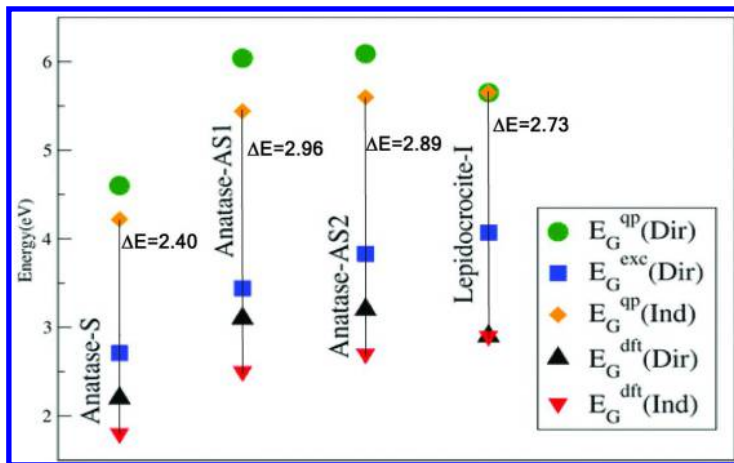


Figure 6. Energy values (eV) of the minimum direct (indirect) gaps (E_g) for the four isolated NS, calculated at different levels of theoretical approximation. Single-particle DFT-KS direct (indirect) gaps, within the GGA approximation: online version, inverted red triangles (black triangles). GW electronic direct (indirect) gaps: green dots (golden diamonds). BSE optical (excitonic) direct gaps: blue squares. The energy difference (E) between the minimal band gap calculated at DFT-KS level and that at the GW level is also reported. [Reprinted with permission from ref. (84). Copyright 2012 American Chemical Society.]

Before commencing with the discussion on the optical properties of the four isolated TiO_2 NS, it is important to observe that, as a result of the strong attractive electron-hole interaction associated with the structural reduced dimensions, the optical (BSE) gaps (blue squares in Figure 6) are > 1.5 eV smaller than the corresponding QP electronic gaps (green dots in Figure 6).

Consequently, the corresponding optical spectra for such systems have a clear excitonic nature in the UV-Vis region. Figure 7 shows the $\varepsilon_2(\omega)$, calculated at both at the independent QP and at the BSE levels of approximation. The excitonic nature of the optical spectra is evident by looking at the important differences between the independent QP curves and the BSE ones, where the electron-hole interaction and local-field effects are “switched on” in the calculation.

Once excitonic effects are included in the calculation, the anisotropic optical behaviour already found at the IQP level becomes even more evident. In close agreement with the case of the surfaces previously discussed (83), for all the NS, we predict a net optical anisotropy, as a function of the atomic orbital character (Ti and O) at the surface, with the (100) polarization preferred over the (010) polarization.

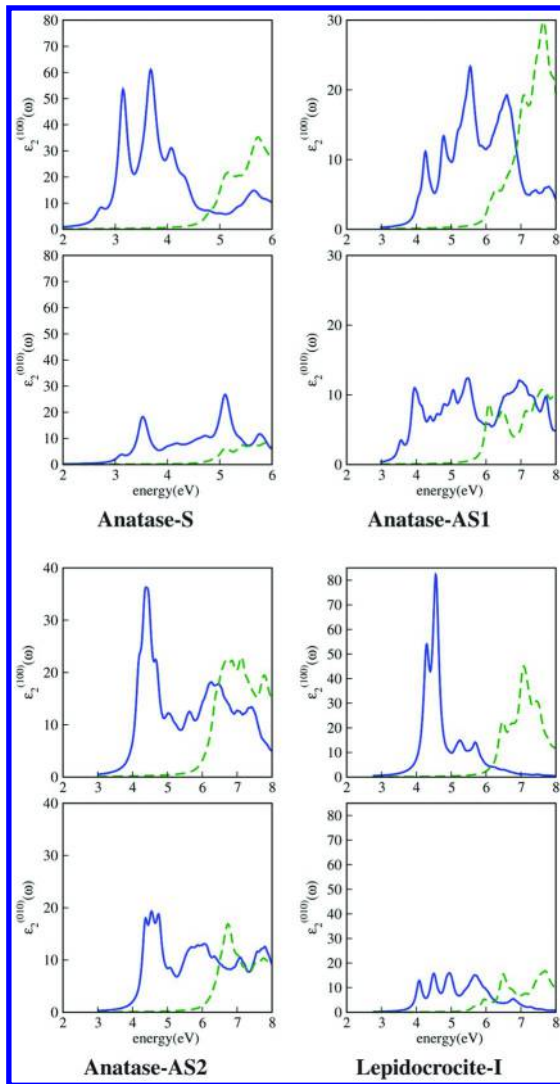


Figure 7. Imaginary part of the macroscopic dielectric functions, $\epsilon_2(\omega)$, of the four isolated NS, calculated at the IQP (online version, green) and BSE (blue) levels of approximation for the (100) (above) and (010) (below) light polarization.

The intensity was renormalized to the thickness of each NS. [Reprinted with permission from ref. (84). Copyright 2012 American Chemical Society.]

In the case of the previously analysed minority (001) surfaces, the increased stability of the (001)-(1 \times 4) reconstruction associated with the stress reduction is observable in the disappearance of the low energy peaks which, at variance, are typical of the more stressed (001)-(1 \times 1) surface. In the case of NS, we predict a very similar interplay between stress and electronic and optical properties.

Furthermore, for NS in the lepidocrocite structure, the final structure is more stable as a consequence of the recovered coordination (as in the anatase bulk) for Ti atoms. This fact supports the idea that the marked increase in the lower energy peaks is a consequence of the stress present in the atomic structure.

The optical spectra calculated at the BSE level further reveal that some optical peaks are present at lower energies for anatase-S and anatase-AS1 sheets, while the optical absorption of lepidocrocite-I and anatase-AS2 commences at higher energies (4 eV).

For the structure of lepidocrocite, which has been subject of optical measurements as a function of number of layers (151), we also considered the 3D packing; we studied electronic and optical properties of the 3D counterpart. Similarly, as reported earlier (147), we found that the 3D packing has little impact on the calculated electronic properties; the DFT band gap between the NS and their 3D counterparts was almost identical.

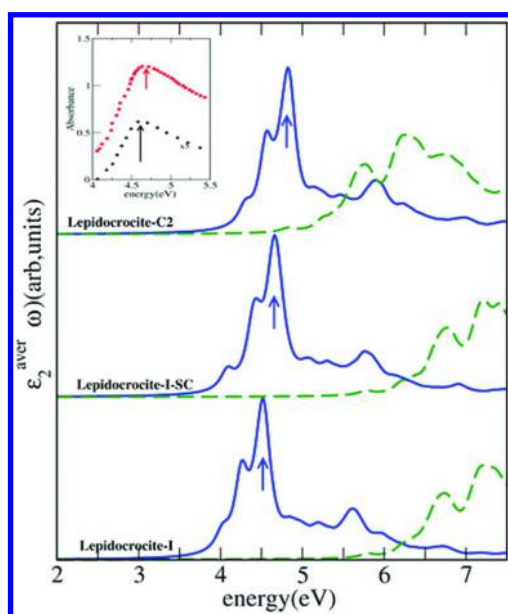


Figure 8. Role of packing effect on the lepidocrocite sheets optical response. Imaginary part of the theoretical dielectric functions calculated at the BSE (online version, blue) and IQP (green dashed) levels of approximation averaged over the three light polarizations. Inset: Zoom of the experimental absorbance spectra of ref. (153), corresponding to a deposition of 1 (bottom, black, scaled by a factor 5) and 10 (top, red) layers. [Reprinted with permission from ref. (84). Copyright 2012 American Chemical Society].

In the 3D counterparts, the inclusion of many-body effects changes the QP electronic gaps and the exciton binding energies: the QP electronic bandgap energy decreases by more than 1 eV when moving from isolated to 3D packed NS and the exciton binding energy correspondingly decreases from \sim 1.8 eV to <0.5 eV. The optical gaps remain around 4 eV in all atomic models.

Focusing further on this aspect, we show, in Figure 8, the imaginary part of the dielectric function calculated at the QP and BSE levels of approximation for the atomic models lepidocrocite-I, lepidocrocite-I-SC and lepidocrocite-C2. The blue shift due to the self-energy correction and the red shift due to the electron-hole attractive interaction almost compensate for each other, making the optical gaps, similarly to the shape of $\epsilon_2(\omega)$, calculated at the BSE level (Figure 8), very similar in the three cases. This finding is consistent with experimental observations (151–153), where no impact of the layer number on the energetic position of the main optical peaks is observed. Consistent with experimental data (see the inset in Figure 8), a small blue shift is observable when going from an isolated to a packed structure.

Analysis of the exciton spatial localization of the two different reconstructions reveals that the lowest energy exciton is a bright one, only present in isolated NS, while several dark excitons are present below the first bright one when 3D packed structures are considered. The reported extremely localized nature of the exciton for other semiconductor NS is confirmed here for the case of TiO_2 . For the anatase-S sheet, it is mainly distributed on first-neighbour Ti sites along the (010) direction, while for the anatase-AS2 (a very similar behaviour also holds for anatase-AS1) the electron prefers to localize on the first-neighbour Ti along the (100) direction. Similar localization on the nearest Ti atoms along the (100) direction also occurs in the lepidocrocite-I sheet. Finally, the extremely localized nature of the excitons observed when the packing effect in the lepidocrocite-C1 case is taken into account is consistent with experimental light absorption and luminescence measurements carried out on TiO_2 -based nanotubes by Bavykin *et al.* (154), which reveal an apparent 2D behaviour. In this case, the electron-hole couple, because of its high spatial localization, seems not to “feel” the curvature until very small diameters beyond which the tube nature prevails.

We thus observe that, in view of photocatalysis application, the excitonic nature of the main optical peaks clearly arises from the analysis of the theoretical spectra of isolated NS. Our analysis shows that the layer packing plays a primary role both in the electronic and the optical features of these nanosystems. Not secondarily, the enhanced surface area (compared to the bulk) in conjunction with the immediate co-presence of the photocarriers at the surface of such 2D systems, similarly to the case of the previously investigated (001)-1x1 surface, are fundamental prerequisites that highly improve the water-splitting process (155) even if, on the other hand, an enhanced exciton binding energy could, in principle, result in worsened photocatalytic performances.

The Emergence of New Optical Features in Titania/Graphene Nanocomposites

Nowadays, nanocomposites formed by graphene and titania are receiving particular attention for their possible applications in photocatalysis and photovoltaics (156–168). The idea of a material that is semiconducting (TiO_2) and, simultaneously, has excellent transport properties (graphene) is very appealing. Due to its large surface area, high transparency, flexible structure, and good electrical/thermal conductibility, graphene represents a material with superior characteristics in nanocompositing (169–176). It also exhibits excellent mobility of charge carriers and is expected to be able to slow the recombination of photogenerated electron-hole pairs, contributing to the improvement of the photocatalytic efficiency of the titania/graphene hybrid material.

Titania/graphene nanocomposites find their own device-oriented applicability according to the synthetic route that they undergo (177–180). For example, the incorporation of graphene in TiO_2 by means of hydrothermal hydrolysis of $\text{Ti}(\text{SO}_4)_2$ in an acidic suspension of graphene oxide (GO) followed by UV-assisted photocatalytic reduction affords TiO_2 -graphene nanocomposites with enhanced adsorption capacity towards azo dyes (181). The addition of small amounts of graphene (177, 179) to TiO_2 NS with exposed (001) facets gives a very high H_2 production rate; it exceeds the rate observed for samples constituted by only TiO_2 NS by more than 41 times. This result can be clearly ascribed to the ability of graphene sheets to efficiently separate the photogenerated charge carriers (177).

The term “graphene oxide” defines those materials with an insulating nature (181, 182) characterized by the presence of a highly heterogeneous number of oxidized terminations at the surface of graphene. Over the years, several models have been suggested for GO to disclose its structure. The nonstoichiometric amorphous model (183) has recently received much attention from the scientific community and is preferred to the lattice-based structure proposed earlier by Ruess (184). The similar chemical and physical properties that characterize reduced graphene oxide (RGO) and the pristine graphene layer make the reduction process probably the most studied for GO layers. This process allows the production of RGO, which is the most viable alternative to pristine graphene for large-scale applications.

We now analyse the electronic and optical properties of (001)-oriented anatase TiO_2 NS and graphene interfaces. The anatase (001)-oriented NS is considered in the assembling procedure of TiO_2 /graphene hybrids since the enhanced photoactivity reported for the NS TiO_2 systems oriented along the (001) direction (106, 185–187). Our modellization provides hybrids of both graphene- TiO_2 NS and GO- TiO_2 NS, i.e., a semimetal–semiconductor and an insulator–semiconductor hybrid, respectively.

As was done for the geometry optimizations in the cases of surfaces (83) and NS (84), we used the VASP code (117, 118), by means of the GGA-PBE functional (113), along with the projector augmented waves (PAW) approach (114–116). The electron wave functions are expanded on a plane-waves basis set with an energy cut-off of 500 eV.

Whereas the mechanical and thermodynamic properties are all calculated on the basis of a pure PBE approach, the electronic and optical properties are all discussed based on the PBE+U approach (188). In particular, for Ti we used $U_d = 4.0$ eV, i.e., the U value we required to open the band gap in bulk anatase to its experimental value (3.2 eV (189)). A $7 \times 9 \times 1$ Γ -centred k -point sampling of the Brillouin zone was used in the geometry optimization of all the investigated interfaces, while a $22 \times 24 \times 1$ one was used in the calculation of electronic and optical properties (the latter calculated at the random phase approximation (RPA) level).

The choice of a “simpler” (simpler than BSE) level of calculation, as RPA is, in the study of optical properties of our hybrid nanocomposites is clearly because of the computational burden associated with their prohibitive sizes. Nevertheless, in the case of pure NS (84), we have clearly demonstrated how the excitonic nature of such layered materials makes the spectra obtained at DFT level very similar to those obtained at BSE level.

Indeed, the electronic band gap opening induced by the QP correction is counterbalanced when the local and excitonic effects are included (BSE) in the calculation, with the overall result that the two induced shifts (by the two methods) tend to compensate for each other.

The area of our models ranges between 30.07 \AA^2 (**d**₂ model) and 30.74 \AA^2 (**w**₁ model). The rotation that transforms hexagonal graphene into tetragonal graphene, which in turn is able to better match the in-plane anatase (001)-oriented NS lattice parameters, is accompanied by an increase in the number of C atoms (from 2 to 4). In the case of the supercells of our heterostructures, 3×1 replicas of the initial tetragonal cell were used (**d**₁, **d**₂, **w**₁, and **w**₂ [d = dry, w = wet] models are all constituted by a 12 C atom layer of graphene). According to the geometrical rearrangement, the graphene topology of these supercells changes, with the Dirac cones (zero energy gap points) occurring at Γ and not, as in the biatomic standard hexagonal cell, at K (K').

We modelled the hybrids following the experimentally reported procedure. In particular, two physisorbed models (**d**₁, **d**₂) mimic the occurrence of a dry process (atomic layer deposition) (180). Whereas the first model (**d**₁) optimization leads to a bilayer still formed by graphene and TiO₂ NS, optimization of the second of these non-aqueous interfaces (**d**₂) shows the formation of a topological defect of the same class of the Stone–Wales defects in the graphene subunit, with the subsequent formation of C_{n=6} rings (190–193). The high concentration of such defects due to the reduced area of the interface is more consistent with the study of predicted new 2D metallic carbon allotropes for which more specific metallic properties are reported (194). Similarly, we modelled two chemisorbed systems (**w**₁ and **w**₂, see Figure 9) for which the moisture of the aqueous environment is accounted for by including H₂O molecules anchored on the TiO₂ NS. Water molecules are thus split by the high-energy (001) surface that favours their dissociative adsorption (195). The anatase subunit will be hydroxylated at both the surfaces, while GO is considered in assembling these aqueous interfaces (177). Figure 9 shows the lateral and top view of the four models considered in our work.

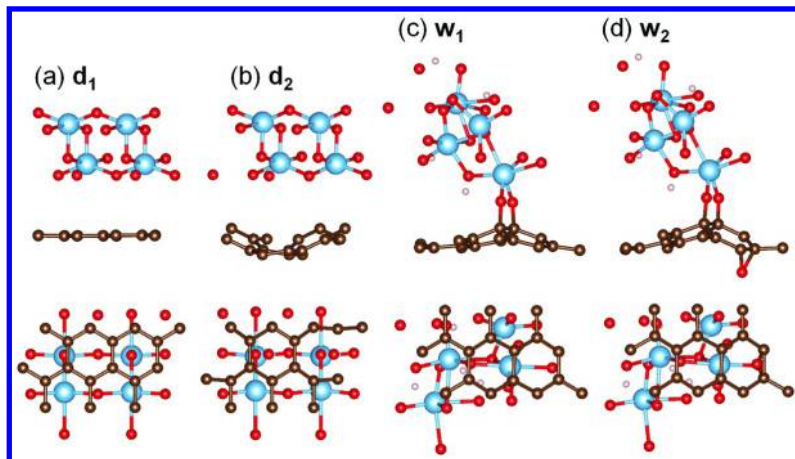


Figure 9. Lateral and top views of graphene-TiO₂ bilayer nanocomposite models. (a) first “dry” model (d₁), (b) second “dry” model (d₂), (c) first “wet” model (w₁), and (d) second “wet” model (w₂). Online version: brown: C atoms; light blue (large): Ti atoms; red: O atoms. [Reprinted with permission from ref. (85).

Copyright 2014 WILEY-VCH Verlag GmbH & Co. KGaA, Weinheim].

We performed a preliminary analysis of the stress present at the interfaces and found that, generally, the TiO₂ (001)-oriented NS contributes more than the graphene layer does to the final amount of stress. The w₁ model is characterized by a chelating region where Ti is bound via two O atoms to the two nearest neighbour C atoms. In this case, we considered as precursors for the interface a hydrated TiO₂ bilayer and GO. In assembling such a model, we considered one O atom as part of a TiO₂ NS and the other of a GO layer. The second wet model (w₂) is still characterized by the presence of direct chemical bonds between the two layers forming the interface, but with an enhanced number of O atoms in the GO side arranged in epoxidic fashion. As for w₁, the formation of the chemical bonds induces a net stabilization of the system, leading to a stress-released nanocomposite (compared to the dry models) due to the enhanced flexibility offered by the Ti–O–Ti bond rupturing induced by the reactive H₂O molecule. The Ti–O–C bond lengths are different in the two models: the average length of the Ti–O bond is 1.831 Å (w₁) and 1.829 Å (w₂) and that of the O–C bond is 1.435 Å (w₁) and 1.425 Å (w₂), suggesting that the hybrid formation is facilitated by the oxidized environment. The slightly shorter distances optimized for the w₂ model indicate a stronger interaction between the graphene part and TiO₂ NS compared to for the w₁ model. The band structures of the investigated models are reported in Figure 10. The CBM of TiO₂ NS and CBM of graphene are at (almost) the same energy level near Γ in Figure 10a. From a comparison of the experimental results for TiO₂ thin films and graphene (195, 196), the CBM level of TiO₂ is expected to be located very close to the band edges (CBM/VBM) of graphene, which is in good agreement with our band calculation for the d₁ model. VBM-1, VBM, CBM, and CBM+2 are localized in the *p* orbitals of graphene

C atoms, while CBM+1 and CBM+3 are in the Ti d orbital of the TiO_2 bilayer. Results of the \mathbf{d}_2 model charge density distribution are similar to those of \mathbf{d}_1 . VBM and CBM are mainly localized on graphene, and such localization holds along the band edges of the hybrid (from VBM-2 to CBM+1). The instability of \mathbf{d}_2 is further witnessed by the electrostatic potential profile analysis (not reported here); \mathbf{d}_2 quantum wells are indeed shallower than \mathbf{d}_1 .

Analysis of workfunction and charge transfer (197–199) reveals that the presence of the chemical bond induces charge delocalization over an entire hybrid system. The presence of an additional electronegative O atom on the GO layer induces the reduction of charge flow between layers for the \mathbf{w}_2 model, compared to the \mathbf{w}_1 one. Such charge transfer is responsible for electron (hole) accumulation in TiO_2 NS (graphene).

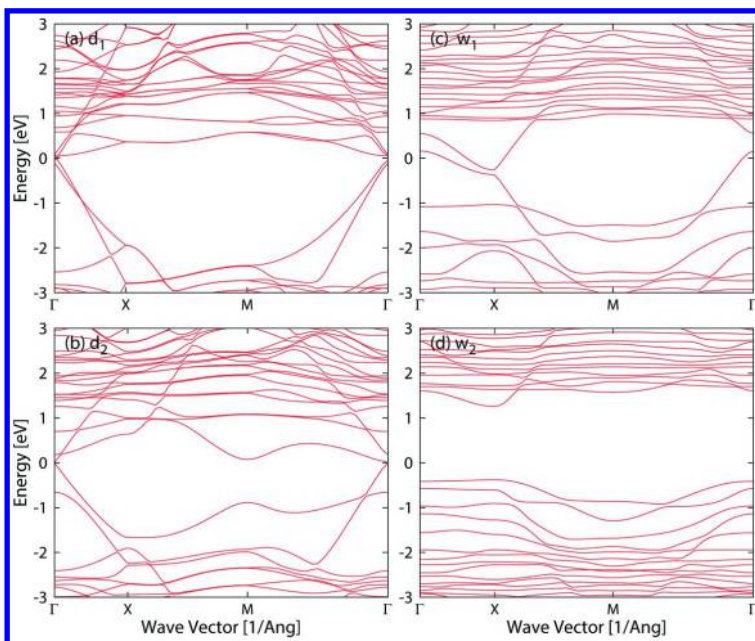


Figure 10. Band structures of (a) \mathbf{d}_1 , (b) \mathbf{d}_2 , (c) \mathbf{w}_1 , and (d) \mathbf{w}_2 at PBE+U level. ($\Gamma=0.0, 0.0, 0.0$; $X=0.5, 0.0, 0.0$; $M=0.5, 0.5, 0.0$). [Reprinted with permission from ref. (85). Copyright 2014 WILEY-VCH Verlag GmbH & Co. KGaA, Weinheim].

The VBM-1 of \mathbf{w}_1 comprises chelating O $2p$ orbitals, while the VBM and CBM comprise the mixing of C $2p$, Ti $3d$, and $2p$ orbitals of the chelating O atoms. The Dirac point (200) of the \mathbf{w}_1 model is only qualitatively observed. The position of the two cones is shifted and they no longer lie on the point. The valence edge is still on Γ while the CBM is observed on X of the Brillouin zone, i.e., at the Γ point the Fermi level crosses the VBM, as a consequence of the hole-doped conditions (p -type doping). Moving towards the X point, we observe the inversion of such

a trend; here the Fermi level crosses the CBM, clearly revealing electron excess associated with *n*-type doping. Concerning the **w**₂ model, its VBM consists of C and O 2p orbitals of the atoms of the anchoring group, while the CBM is localized in the 3d orbitals of Ti.

The band profile of the **w**₂ interface system is much more complex and very different from other interface models, with a clear band gap opening (1.64 eV at PBE+U level). The presence of the chemical bond therefore has a dual role: it enhances the electronic coupling between the two layers and induces noticeable modifications in the electronic features of the final wet systems. Furthermore, an oxidized environment, like that of **w**₂, where the GO layer is still present, further impacts on the band structure shape of the final hybrid: system has indeed completely different electronic features compared to the other investigated hybrids. Such a result is mainly because of the replacement of the graphene layer with a GO one and the nature of the oxidizing functionality present in GO itself.

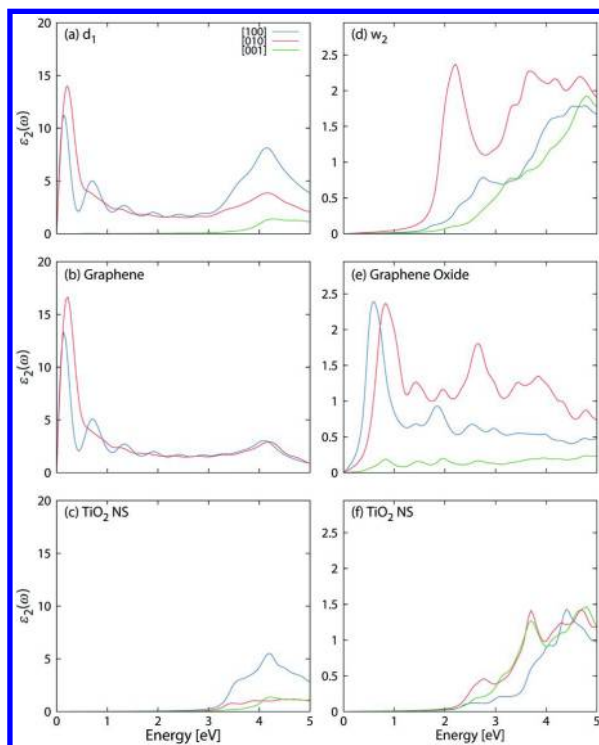


Figure 11. The imaginary part of the dielectric function for the: (a) *d*₁ system, (b) graphene, and (c) TiO_2 bilayer. Likewise, for the (d) *w*₂ hybrid, (e) graphene oxide, and (f) the hydrated TiO_2 NS. Online version, blue and red are the two ordinary rays (E_x, y), i.e. along the [100] and [010] directions, respectively, and green is the extraordinary ray (E_z , [001]). [Reprinted with permission from ref. (85). Copyright 2014 WILEY-VCH Verlag GmbH & Co. KGaA, Weinheim].

To analyse the role of the chemical bond on such systems further, we investigated and compared the dielectric functions (2) of a physisorbed (**d**₁) and a chemisorbed (**w**₂) model. The spectrum of the **d**₁ hybrid system and the two components, graphene and TiO₂ NS, are shown in Figure 11a, b, and c. The shape of the **d**₁ spectrum closely resembles the sum of those of its separate constituents: graphene and TiO₂ NS. The peak below 1.0 eV is associated with an intra-graphene local excitation. At variance, the absorption in the UV region is due to the sum of still one intra-graphene local excitation plus an intra-TiO₂ NS local one. The peak that disappears near 0.2 eV is expected to be because of the slight hybridization effect of graphene and TiO₂ NS, as deduced from the analysis of the charge density distribution (not reported here). From the same analysis, the VBM and CBM of graphene and CBM of TiO₂ NS are slightly hybridized around Γ with some $\text{VBM}_g \rightarrow \text{CBM}_{\text{TiO}_2}$ electron transfer. Therefore, the joint density of states between VBM and CBM of graphene decreases and, accordingly, the intra-graphene local excitation peak decreases. Moreover, in order to improve the $\text{CBM}_{\text{TiO}_2} \rightarrow \text{CBM}_g$ excitation flow, better alignment between these two band levels is highly desirable. Likewise, the spectra of **w**₂, GO, and the hydrated TiO₂ layered precursor are shown in Figure 11d, e, and f.

The **w**₂ spectrum shows a strong and anisotropic peak at ~2.0 eV, suggesting that this hybrid system absorbs at wavelengths longer than TiO₂ NS. This new absorption peak is the result of the GO/TiO₂ NS hybridization. Analysis of the frontier orbitals shows that the O 2p orbitals of the anchoring O atoms and the C 2p orbitals of GO are shared between VBM-1, VBM, and CBM. Therefore, a key role is clearly played by these orbitals in the increase of the observed anisotropic peak. This new longer wavelength region absorption for the **w**₂ hybrid system thus involves 2p orbitals of the anchoring O atoms, GO C 2p orbitals, and Ti 3d orbitals from the CBM TiO₂ NS. The absorption at ~2.0 eV is the sum of the excitations between the VBM-1/VBM and the CBM states. The orbital composition suggests that this longer wavelength region absorption would involve mainly GO localized VBM-1/VBM and GO and TiO₂ hybridized CBM.

Such excitation therefore seems to be associated with the electron localization in the conduction region (mainly constituted by TiO₂) and the hole localization in the valence region (mainly formed by GO orbitals). In other words, this absorption could favour the excitonic couple separation between TiO₂ NS and the GO layer, potentially leading to significantly reduced charge recombination. Such behaviour has been reported, experimentally, in the assembling procedure of a hybrid titania/graphene photoanode in solar cells, where graphene addition enhances the photovoltaic performance of dye-sensitized solar cells (201). The signature peaks around 0.5~1.0 eV in the spectrum of GO are not observed in that of **w**₂, indicating the paramount relevance of the chemical bond on the optical properties, similarly to the electronic ones, of the final hybrid system formed by GO and TiO₂ NS.

In this final section, we have focused on the structural, electronic, and optical properties of several graphene/TiO₂ NS and GO/TiO₂ NS hybrids, offering proof of the fact that the presence of a chemical bond between the organic and the inorganic layers has a great impact on the electronic and optical properties of the final nanocomposite. In particular, the GO/TiO₂ chemisorbed system results of a

higher photoresponsivity in the visible region, while the physisorbed system does not enhance the photoresponsivity in the visible region, and a better alignment between the CBM of the two components, is beneficial for the TiO₂ to graphene electron transfer.

Acknowledgments

Authors want to thanks Prof. Maurizia Palummo (University “Tor Vergata”, Rome, Italy), Prof. Angel Rubio (Universidad del País Vasco UPV/EHU, San Sebastian, Spain) Dr. Letizia Chiodo (Istituto Italiano di Tecnologia, Italy) and Yasuyuki Masuda (Showa Denko K.K., Japan) for the support and the always very fruitful and stimulating scientific discussions.

References

1. Fujishima, A.; Honda, K. Electrochemical Photolysis of Water at a Semiconductor Electrode. *Nature* **1972**, *238*, 37–38.
2. Hashimoto, K.; Irie, H.; Fujishima, A. TiO₂ photocatalysis: a historical overview and future prospects. *Jpn. J. Appl. Phys.* **2005**, *44*, 8269–8285.
3. Linsebigler, A. L.; Lu, G.; Yates, J. T. Photocatalysis on TiO₂ Surfaces: Principles, Mechanisms, and Selected Results. *Chem. Rev.* **1995**, *95*, 735–758.
4. Henderson, M. A. A surface science perspective on TiO₂ photocatalysis. *Surf. Sci. Rep.* **2001**, *66*, 185–297.
5. Agrios, A.; Pichat, P. State of the art and perspectives on materials and applications of photocatalysis over TiO₂. *J. Appl. Electrochem.* **2005**, *35*, 655–663.
6. Ashokkumar, M. An overview on semiconductor particulate systems for photoproduction of hydrogen. *Int. J. Hydrogen Energy* **1998**, *23*, 427–438.
7. Ravelli, D.; Dondi, D.; Fagnoni, M.; Albini, A. Photocatalysis. A multi-faceted concept for green chemistry. *Chem. Soc. Rev.* **2009**, *38*, 1999–2011.
8. Hoffmann, M. R.; Martin, S. T.; Choi, W.; Bahnemann, D. W. Environmental Applications of Semiconductor Photocatalysis. *Chem. Rev.* **1995**, *95*, 69–96.
9. Fujishima, A.; Zhang, X.; Tryk, D. A. TiO₂ photocatalysis and related surface phenomena. *Surf. Sci. Rep.* **2008**, *63*, 515–582.
10. Mills, A.; Davies, R. H.; Worsley, D. Water purification by semiconductor photocatalysis. *Chem. Soc. Rev.* **1993**, *22*, 417–425.
11. Wold, A. Photocatalytic Properties of Titanium Dioxide (TiO₂). *Chem. Mater.* **1993**, *5*, 280–283.
12. Ljubas, D. Solar photocatalysis—a possible step in drinking water treatment. *Energy* **2005**, *30*, 1699–1710.
13. Alfano, O. M.; Bahnemann, D.; Cassano, A. E.; Dillert, R.; Goslich, R. Photocatalysis in water environments using artificial and solar light. *Catal. Today* **2000**, *58*, 199–230.

14. Bhatkhande, D. S.; Pangarkar, V. G.; Beenackers, A. Photocatalytic degradation for environmental applications – a review. *J. Chem. Technol. Biotechnol.* **2002**, *77*, 102–116.
15. Hufschmidt, D.; Liu, L.; Selzer, V.; Bahnemann, D. Photocatalytic water treatment: fundamental knowledge required for its practical application. *Water Sci. Technol.* **2004**, *49*, 135–140.
16. Romero, M.; Blanco, J.; Sanchez, B.; Vidal, A.; Malato, S.; Cardona, A. I.; Garcia, E. Solar photocatalytic degradation of water and air pollutants: challenges and perspectives. *Sol. Energy* **1999**, *66*, 169–182.
17. Zhao, J.; Chen, C.; Ma, W. Photocatalytic degradation of organic pollutants under visible light irradiation. *Top. Catal.* **2005**, *35*, 269–278.
18. Herrmann, J. M.; Guillard, C.; Pichat, P. Heterogeneous photocatalysis : an emerging technology for water treatment. *Catal. Today* **1993**, *17*, 7–20.
19. Kabra, K.; Chaudhary, R.; Sawhney, R. L. Treatment of Hazardous Organic and Inorganic Compounds through Aqueous-Phase Photocatalysis: A Review. *Ind. Eng. Chem. Res.* **2004**, *43*, 7683–7696.
20. Konstantinou, I. K.; Albanis, T. A. TiO₂-assisted photocatalytic degradation of azo dyes in aqueous solution: kinetic and mechanistic investigations: A review. *Appl. Catal., B* **2004**, *49*, 1–14.
21. Peral, J.; Domenech, X.; Ollis, D. F. Heterogeneous Photocatalysis for Purification, Decontamination and Deodorization of Air. *J. Chem. Technol. Biotechnol.* **1997**, *70*, 117–140.
22. Paz, Y. Preferential photodegradation—why and how? *C. R. Chim.* **2006**, *9*, 774–787.
23. Fu, X.; Zeltner, W. A.; Anderson, M. A. In *Semiconductor Nanoclusters, Studies in Surface Science and Catalysis*; Kamat, P. V., Meisel, D., Eds.; Elsevier: Amsterdam, 1996; Vol. 103, pp 445–461.
24. Legrini, O.; Oliveros, E.; Braun, A. M. Photochemical Processes for Water Treatment. *Chem. Rev.* **1993**, *93*, 671–698.
25. Pirkanniemi, K.; Sillanpää, M. Heterogeneous water phase catalysis as an environmental application: a review. *Chemosphere* **2002**, *48*, 1047–1060.
26. Zhao, J.; Yang, X. D. Photocatalytic oxidation for indoor air purification: A literature review. *Build. Environ.* **2003**, *38*, 645–654.
27. Sun, Q.; Xu, Y. Evaluating Intrinsic Photocatalytic Activities of Anatase and Rutile TiO₂ for Organic Degradation in Water. *J. Phys. Chem. C* **2010**, *114*, 18911–18918.
28. Bard, A. J.; Fox, M. A. Artificial Photosynthesis: Solar Splitting of Water to Hydrogen and Oxygen. *Acc. Chem. Res.* **1995**, *28*, 141–145.
29. Meyer, T. J. Chemical approaches to artificial photosynthesis. *Acc. Chem. Res.* **1989**, *22*, 163–170.
30. Graetzel, M. Artificial photosynthesis: water cleavage into hydrogen and oxygen by visible light. *Acc. Chem. Res.* **1981**, *14*, 376–384.
31. Gust, D.; Moore, T. A.; Moore, A. L. Solar Fuels via Artificial Photosynthesis. *Acc. Chem. Res.* **2009**, *42*, 1890–1898.
32. Fujishima, A.; Rao, T. N.; Tryk, D. A. Titanium dioxide photocatalysis. *J. Photochem. Photobiol., C* **2000**, *1*, 1–21.

33. Kudo, A.; Kato, H.; Tsuji, I. Strategies for the Development of Visible-light-driven Photocatalysts for Water Splitting. *Chem Lett.* **2004**, *33*, 1534–1539.
34. Yang, M.; Oró-Solé, J.; Rodgers, J. A.; Belén Jorge, A.; Fuertes, A.; Attfield, J. P. Anion order in perovskite oxynitrides. *Nat. Chem.* **2011**, *3*, 47–52.
35. Fuertes, A. Synthesis and properties of functional oxynitrides – from photocatalysts to CMR materials. *Dalton Trans.* **2010**, *39*, 5942–5948.
36. Castelli, I. E.; Olsen, T.; Datta, S.; Landis, D. D.; Dahl, S.; Thygesen, K. S.; Jacobsen, K. W. Computational screening of perovskite metal oxides for optimal solar light capture. *Energy Environ. Sci.* **2012**, *5*, 5814–5819.
37. Girish Kumar, S.; Gomathi Devi, L. Review on Modified TiO₂ Photocatalysis under UV/Visible Light: Selected Results and Related Mechanisms on Interfacial Charge Carrier Transfer Dynamics. *J. Phys. Chem. A* **2011**, *115*, 13211–13241.
38. Daghrir, R.; Drogui, P.; Robert, D. Modified TiO₂ For Environmental Photocatalytic Applications: A Review. *Ind. Eng. Chem. Res.* **2013**, *52*, 3581–3599.
39. Pan, L.; Zou, J.-J.; Zhang, X.; Wang, L. Water-Mediated Promotion of Dye Sensitization of TiO₂ under Visible Light. *J. Am. Chem. Soc.* **2011**, *133*, 10000–10002.
40. Bamwenda, G. R.; Tsubota, S.; Nakamura, T.; Haruta, M. Photoassisted hydrogen production from a waterethanol solution: a comparison of activities of Au-TiO₂ and Pt-TiO₂. *J. Photochem. Photobiol., A* **1995**, *89*, 177–189.
41. Sakthivel, S.; Shankar, M. V.; Palanichamy, M.; Arabindoo, B.; Bahnemann, D. W.; Murugesan, V. Enhancement of photocatalytic activity by metal deposition: characterization and photonic efficiency of Pt, Au and Pd deposited on TiO₂ catalyst. *Water Res.* **2004**, *38*, 3001–3008.
42. John, M. R.; Furgals, A. J.; Sammells, A. F. Hydrogen Generation by Photocatalytic Oxidation of Glucose by Platinized *n*-TiO₂ Powder. *J. Phys. Chem.* **1983**, *87*, 801–805.
43. Li, F. B.; Li, X. Z. The enhancement of photodegradation efficiency using Pt-TiO₂ catalyst. *Chemosphere* **2002**, *48*, 1103–1111.
44. Jin, S.; Shiraishi, F. Photocatalytic activities enhanced for decompositions of organic compounds over metal-photodepositing titanium dioxide. *Chem. Eng. J.* **2004**, *97*, 203–211.
45. Subramanian, V.; Wolf, E. E.; Kamat, P. Catalysis with TiO₂/Gold Nanocomposites: Effect of Metal Particle Size on the Fermi Level Equilibration. *J. Am. Chem. Soc.* **2004**, *126*, 4943–4950.
46. Tseng, I. H.; Wu, J. C. S.; Chou, H. Y. Effects of sol-gel procedures on the photocatalysis of Cu/TiO₂ in CO₂ photoreduction. *J. Catal.* **2004**, *221*, 432–440.
47. Subramanian, V.; Wolf, E. E.; Kamat, P. V. Semiconductor-Metal Composite Nanostructures, to What Extent Do Metal Nanoparticles Improve the Photocatalytic Activity of TiO₂ Films? *J. Phys. Chem. B* **2001**, *105*, 11439–11446.

48. Kim, S.; Choi, W. Dual Photocatalytic Pathways of Trichloroacetate Degradation on TiO_2 : Effects of Nanosized Platinum Deposition on Kinetics and Mechanism. *J. Phys. Chem. B* **2002**, *106*, 13311–13317.

49. Subramanian, V.; Wolf, E. E.; Kamat, P. V. Green Emission to Probe Photoinduced Charge Events in ZnO -Au Nanoparticles, Charge Distribution and Fermi-Level Equilibration. *J. Phys. Chem. B* **2003**, *107*, 7479–7485.

50. Jakob, M.; Levanon, H.; Kamat, P. V. Charge Distribution between UV-Irradiated TiO_2 and Gold Nanoparticles: Determination of Shift in the Fermi Level. *Nano. Lett.* **2003**, *3*, 353–358.

51. Tseng, I. H.; Chang, W. C.; Wu, J. C. S. Photoreduction of CO_2 using sol-gel derived titania and titania-supported copper catalysts. *Appl. Catal., B* **2002**, *37*, 37–48.

52. Xiang, Q.; Yu, J.; Jaroniec, M. Synergetic Effect of MoS_2 and Graphene as Cocatalysts for Enhanced Photocatalytic H_2 Production Activity of TiO_2 Nanoparticles. *J. Am. Chem. Soc.* **2012**, *134*, 6575–6578.

53. Hu, Y.; Tsai, H.-L.; Huang, C.-L. Effect of brookite phase on the anatase–rutile transition in titania nanoparticles. *J. Eur. Ceram. Soc.* **2003**, *23*, 691–696.

54. Fu, X.; Clark, L. A.; Yang, Q.; Anderson, M. A. Enhanced Photocatalytic Performance of Titania-Based Binary Metal Oxides: $\text{TiO}_2/\text{SiO}_2$ and $\text{TiO}_2/\text{ZrO}_2$. *Environ. Sci. Technol.* **1996**, *30*, 647–653.

55. Cui, H.; Dwight, K.; Soled, S.; Wold, A. Surface Acidity and Photocatalytic Activity of $\text{Nb}_2\text{O}_5/\text{TiO}_2$ Photocatalysts. *J. Solid State Chem.* **1994**, *115*, 187–191.

56. Moret, M. P.; Zallen, R.; Vijay, D. P.; Desu, S. B. Brookite-rich titania films made by pulsed laser deposition. *Thin Solid Films* **2000**, *366*, 8–10.

57. Zorn, M. E.; Tompkins, D. T.; Zeltner, W. A.; Anderson, M. A. Photocatalytic oxidation of acetone vapor on $\text{TiO}_2/\text{ZrO}_2$ thin films. *Appl. Catal., B* **1999**, *23*, 1–8.

58. Papp, J.; Soled, S.; Dwight, K.; Wold, A. Surface Acidity and Photocatalytic Activity of TiO_2 , WO_3/TiO_2 , and $\text{MoO}_3/\text{TiO}_2$ Photocatalysts. *Chem. Mater.* **1994**, *6*, 496–500.

59. Shehukin, D.; Poznyak, S.; Kulak, K.; Pichat, P. $\text{TiO}_2\text{-In}_2\text{O}_3$ photocatalysts: preparation, characterisations and activity for 2-chlorophenol degradation in water. *J. Photochem. Photobiol., A* **2004**, *162*, 423–430.

60. Vinodgopal, K.; Kamat, P. V. Enhanced Rates of Photocatalytic Degradation of an Azo Dye Using $\text{SnO}_2/\text{TiO}_2$ Coupled Semiconductor Thin Films. *Environ. Sci. Technol.* **1995**, *29*, 841–845.

61. Ghosh, A. K.; Maruska, H. P. Photoelectrolysis of Water in Sunlight with Sensitized Semiconductor Electrodes. *J. Electrochem. Soc.* **1977**, *124*, 1516–1522.

62. Choi, W.; Termin, A.; Hoffmann, M. R. The Role of Metal Ion Dopants in Quantum-Sized TiO_2 : Correlation between Photoreactivity and Charge Carrier Recombination Dynamics. *J. Phys. Chem.* **1994**, *98*, 13669–13679 and references therein.

63. Yamashita, H.; Harada, M.; Misaka, J.; Takeuchi, M.; Ichihashi, Y.; Goto, F.; Ishida, M.; Sasaki, T.; Anpo, M. Application of ion beam techniques for

preparation of metal ion-implanted TiO_2 thin film photocatalyst available under visible light irradiation: metal ion-implantation and ionized cluster beam method. *J. Synchrotron Radiat.* **2001**, *8*, 569–571.

64. Morikawa, T.; Asahi, R.; Ohwaki, T.; Aoki, K.; Taga, Y. Band-Gap Narrowing of Titanium Dioxide by Nitrogen Doping. *Jpn. J. Appl. Phys.* **2001**, *40*, L561–L563.
65. Torres, G. R.; Lindgren, T.; Lu, J.; Granqvist, C.-G.; Lindquist, S.-E. Photoelectrochemical Study of Nitrogen-Doped Titanium Dioxide for Water Oxidation. *J. Phys. Chem. B* **2004**, *108*, 5995–6003.
66. Sakthivel, S.; Kisch, H. Photocatalytic and Photoelectrochemical Properties of Nitrogen-Doped Titanium Dioxide. *Chem. Phys. Chem.* **2003**, *4*, 487–490.
67. Ohno, T.; Mitsui, T.; Matsumura, M. Photocatalytic Activity of S-doped TiO_2 Photocatalyst under Visible Light. *Chem. Lett.* **2003**, *32*, 364–365.
68. Umebayashi, T.; Yamaki, T.; Itoh, H.; Asai, K. Band gap narrowing of titanium dioxide by sulfur doping. *Appl. Phys. Lett.* **2002**, *81*, 454–456.
69. Umebayashi, T.; Yamaki, T.; Tanaka, S.; Asai, K. Visible Light-Induced Degradation of Methylene Blue on S-doped TiO_2 . *Chem. Lett.* **2003**, *32*, 330–331.
70. Sato, S. Photocatalytic activity of NO_x -doped TiO_2 in the visible light region. *Chem. Phys. Lett.* **1986**, *123*, 126–128.
71. Noda, H.; Oikawa, K.; Ogata, T.; Matsuki, K.; Kamata, H. Preparation of Titanium(IV) Oxides and Its Characterization. *Nippon Kagaku Kaishi* **1986**, *8*, 1084–1090.
72. Asahi, R.; Ohwaki, T.; Aoki, K.; Taga, Y. Visible-Light Photocatalysis in Nitrogen-Doped Titanium Oxides. *Science* **2001**, *293*, 269–271.
73. Sakatani, Y.; Okusako, K.; Koike, H.; Ando, H. Development of a Visible Light Responsive TiO_2 Photocatalyst. *Photocatalysis* **2001**, *4*, 51–54.
74. Ihara, T.; Ando, M.; Sugihara, S. Preparation of visible light active TiO_2 photocatalysis using wet method [in Japanese]. *Photocatalysis* **2001**, *5*, 19.
75. Irie, H.; Watanabe, Y.; Hashimoto, K. Carbon-doped Anatase TiO_2 Powders as a Visible-light Sensitive Photocatalyst. *Chem. Lett.* **2003**, *32*, 772–773.
76. O'Regan, B.; Graetzel, M. A low-cost, high-efficiency solar cell based on dye-sensitized colloidal TiO_2 films. *Nature* **1991**, *353*, 737–740.
77. Jana, A. K. Solar cells based on dyes. *J. Photochem. Photobiol., A* **2000**, *132*, 1–17.
78. Gurunathan, K. Photobiocatalytic production of hydrogen using sensitized $\text{TiO}_2\text{-MV}^{2+}$ system coupled Rhodopseudomonas Capsulata. *J. Mol. Catal. A: Chem.* **2000**, *156*, 59–67.
79. Argazzi, R.; Iha, N. Y. M.; Zabri, H.; Odobel, F.; Bignozzi, C. A. Design of molecular dyes for application in photoelectrochemical and electrochromic devices based on nanocrystalline metal oxide semiconductors. *Coord. Chem. Rev.* **2004**, *248*, 1299–1316.
80. Polo, A. S.; Itokazu, M. K.; Iha, N. Y. M. Metal complex sensitizers in dye-sensitized solar cells. *Coord. Chem. Rev.* **2004**, *248*, 1343–1361.

81. Park, Y.; Lee, S.-H.; Kang, S. O.; Choi, W. Organic dye-sensitized TiO_2 for the redox conversion of water pollutants under visible light. *Chem. Commun.* **2010**, *46*, 2477–2479.
82. Gurunathan, K.; Maruthamuthu, P.; Sastri, V. C. Photocatalytic hydrogen production by dye-sensitized Pt/SnO_2 and $\text{Pt/SnO}_2/\text{RuO}_2$ in aqueous methyl viologen solution. *Int. J. Hydrogen Energy* **1997**, *22*, 57–62.
83. Giorgi, G.; Palummo, M.; Chiodo, L.; Yamashita, K. Excitons at the (001) surface of anatase: Spatial behavior and optical signatures. *Phys. Rev. B* **2011**, *84*, 073404–4.
84. Palummo, M.; Giorgi, G.; Chiodo, L.; Rubio, A.; Yamashita, K. The Nature of Radiative Transitions in TiO_2 -Based Nanosheets. *J. Phys. Chem. C* **2012**, *116*, 18495–18503.
85. Masuda, Y.; Giorgi, G.; Yamashita, K. DFT study of anatase-derived TiO_2 nanosheets/graphene hybrid materials. *Phys. Status Solidi B* **2014**, *251*, 1471–1479.
86. Kamisaka, H.; Yamashita, K. Theoretical Study of the Interstitial Oxygen Atom in Anatase and Rutile TiO_2 : Electron Trapping and Elongation of the r (O–O) Bond. *J. Phys. Chem. C* **2011**, *115*, 8265–8273.
87. Kamisaka, H.; Adachi, T.; Yamashita, K. Theoretical study of the structure and optical properties of carbon-doped rutile and anatase titanium oxides. *J. Chem. Phys.* **2005**, *123*, 084704–9.
88. Kamisaka, H.; Mizuguchi, N.; Yamashita, K. Electron trapping at the lattice Ti atoms adjacent to the Nb dopant in Nb-doped rutile TiO_2 . *J. Mater. Sci.* **2012**, *47*, 7522–7529.
89. Kamisaka, H.; Suenaga, T.; Nakamura, H.; Yamashita, K. DFT-Based Theoretical Calculations of Nb- and W-Doped Anatase TiO_2 : Complex Formation between W Dopants and Oxygen Vacancies. *J. Phys. Chem. C* **2010**, *114*, 12777–12783.
90. Kamisaka, H.; Hitosugi, T.; Suenaga, T.; Hasegawa, T.; Yamashita, K. Density functional theory based first-principle calculation of Nb-doped anatase TiO_2 and its interactions with oxygen vacancies and interstitial oxygen. *J. Chem. Phys.* **2009**, *131*, 034702–10.
91. Liu, G.; Yang, H. G.; Pan, J.; Yang, Y. Q.; Lu, G. Q.; Cheng, H.-M. Titanium Dioxide Crystals with Tailored Facets. *Chem. Rev.* **2014**, *114*, 9559–9612.
92. De Angelis, F.; Di Valentin, C.; Fantacci, S.; Vittadini, A.; Selloni, A. Theoretical Studies on Anatase and Less Common TiO_2 Phases: Bulk, Surfaces, and Nanomaterials. *Chem. Rev.* **2014**, *114*, 9708–9753.
93. Diebold, U. The surface science of titanium dioxide. *Surf. Sci. Rep.* **2003**, *48*, 53–229 and references therein.
94. Ho, C.-H.; Tsai, M.-C.; Wong, M.-S. Characterization of indirect and direct interband transitions of anatase TiO_2 by thermoreflectance spectroscopy. *Appl. Phys. Lett.* **2008**, *93*, 081904–3.
95. Thomas, A. G.; Flavell, W. R.; Kumarasinghe, A. K.; Tsoutsou, D.; Khan, N.; Chatwin, C.; Rayner, S.; Smith, G. C.; Stockbauer, R. L.; Warren, S.; Johal, T. K.; Patel, S.; Holland, D.; Taleb, A.; Wiame, F. Comparison of the electronic structure of anatase and rutile single-crystal surfaces using

resonant photoemission and x-ray absorption spectroscopy. *Phys. Rev. B* **2007**, *75*, 035105–12.

- 96. Cheng, H.; Selloni, A. Surface and subsurface oxygen vacancies in anatase TiO_2 and differences with rutile. *Phys. Rev. B* **2009**, *79*, 092101–4.
- 97. Selloni, A. Crystal growth: Anatase shows its reactive side. *Nat. Mater.* **2008**, *7*, 613–615.
- 98. Gong, X. Q.; Selloni, A. Reactivity of Anatase TiO_2 Nanoparticles: The Role of the Minority (001) Surface. *J. Phys. Chem. B* **2005**, *109*, 19560–19562.
- 99. Burnside, S. D.; Shklover, V.; Barbé, C.; Comte, P.; Arendse, F.; Brooks, K.; Grätzel, M. Self-Organization of TiO_2 Nanoparticles in Thin Films. *Chem. Mater.* **1998**, *10*, 2419–2425.
- 100. Vittadini, A.; Selloni, A.; Rotzinger, F. P.; Grätzel, M. Structure and Energetics of Water Adsorbed at TiO_2 Anatase 101 and 001 Surfaces. *Phys. Rev. Lett.* **1998**, *81*, 2954–2957.
- 101. Chiodo, L.; Garcia-Lastra, J. M.; Iacomino, A.; Ossicini, S.; Zhao, J.; Petek, H.; Rubio, A. Self-energy and excitonic effects in the electronic and optical properties of TiO_2 crystalline phases. *Phys. Rev. B* **2010**, *82*, 045207–12.
- 102. Onida, G.; Reining, L.; Rubio, A. Electronic excitations: density-functional versus many-body Green's-function approaches. *Rev. Mod. Phys.* **2002**, *74*, 601–659.
- 103. Hengerer, R.; Bolliger, P.; Erbudak, M.; Grätzel, M. tructure and stability of the anatase TiO_2 (101) and (001) surfaces. *Surf. Sci.* **2000**, *400*, 162–169.
- 104. Herman, G. S.; Gao, Y.; Tran, T. T.; Osterwalder, J. X-ray photoelectron diffraction study of an anatase thin film: TiO_2 (001). *Surf. Sci.* **2000**, *447*, 201–211.
- 105. Herman, G. S.; Sievers, M. R.; Gao, Y. Structure Determination of the Two-Domain (1×4) Anatase TiO_2 (001) Surface. *Phys. Rev. Lett.* **2000**, *84*, 3354–3357.
- 106. Yang, H. G.; Sun, C. H.; Qiao, S. Z.; Zou, J.; Liu, G.; Smith, S. C.; Cheng, H. M.; Lu, G. Q. Anatase TiO_2 single crystals with a large percentage of reactive facets. *Nature* **2008**, *453*, 638–641.
- 107. Yang, H. G.; Liu, G.; Qiao, S. Z.; Sun, C. H.; Jin, Y. J.; Smith, S. C.; Zou, J.; Cheng, H. M.; Lu, G. Q. Solvothermal Synthesis and Photoreactivity of Anatase TiO_2 Nanosheets with Dominant {001} Facets. *J. Am. Chem. Soc.* **2009**, *131*, 4078–4083.
- 108. Hua, Z.; Songyuan, D.; Kongjia, W. First-Principles Investigation of (001) Surface of TiO_2 . *Plasma Sci. Technol.* **2004**, *6*, 2467–2474.
- 109. Hussain, A.; Gracia, J.; Nieuwenhuys, B. E.; Niemantsverdriet, J. W. Chemistry of O- and H-Containing Species on the (001) Surface of Anatase TiO_2 : A DFT Study. *ChemPhysChem* **2010**, *11*, 2375–2382.
- 110. Liang, Y.; Gan, S.; Chambers, S. A.; Altman, E. I. Surface structure of anatase TiO_2 (001): Reconstruction, atomic steps, and domains. *Phys. Rev. B* **2001**, *63*, 235402–7.
- 111. Tanner, R. E.; Liang, Y.; Altman, E. I. Structure and chemical reactivity of adsorbed carboxylic acids on anatase TiO_2 (001). *Surf. Sci.* **2002**, *506*, 251–271.

112. Lazzeri, M.; Selloni, A. Stress-Driven Reconstruction of an Oxide Surface: The Anatase $\text{TiO}_2(001)$ -(1×4) Surface. *Phys. Rev. Lett.* **2001**, *87*, 266105–4.
113. Perdew, J. P.; Burke, K.; Ernzerhof, M. Generalized Gradient Approximation Made Simple. *Phys. Rev. Lett.* **1996**, *77*, 3865–3868. *Phys. Rev. Lett.* **1996**, *78*, 1396Erratum.
114. Blöchl, P. E. Projector augmented-wave method. *Phys. Rev. B* **1994**, *50*, 17953–17979.
115. Kresse, G.; Joubert, J. From Ultrasoft Pseudopotentials to the Projector Augmented Wave Method. *Phys. Rev. B* **1999**, *59*, 1758–1775.
116. Blöchl, P. E.; Först, C. J.; Schimpl, J. Projector Augmented Wave Method: Ab-Initio Molecular Dynamics with Full Wave Functions. *Bull. Mater. Sci.* **2003**, *26*, 33–41.
117. Kresse, G.; Hafner, J. *Ab initio* molecular dynamics for liquid metals. *Phys. Rev. B* **1993**, *47*, 558–561.
118. Kresse, G.; Furthmüller, J. Efficient iterative schemes for *ab initio* total-energy calculations using a plane-wave basis set. *Phys. Rev. B* **1996**, *54*, 11169–11186.
119. Gonze, X.; Beuken, J.-M.; Caracas, R.; Detraux, F.; Fuchs, M.; Rignanese, G.-M.; Sindic, L.; Verstraete, M.; Zerah, G.; Jollet, F.; Torrent, M.; Roy, A.; Mikami, M.; Ghosez, Ph.; Raty, J.-Y.; Allan, D. C. First-principles computation of material properties: the ABINIT software project. *Comput. Mater. Sci.* **2002**, *25*, 478–492.
120. Mikami, M.; Nakamura, S.; Kitao, O.; Arakawa, H.; Gonze, X. First-Principles Study of Titanium Dioxide: Rutile and Anatase. *Jpn. J. Appl. Phys.* **2000**, *39*, L847–L850.
121. Troullier, N.; Martins, J. L. Efficient pseudopotentials for plane-wave calculations. *Phys. Rev. B* **1991**, *43*, 1993–2006.
122. Marini, A.; Hogan, C.; Grüning, M.; Varsano, D. yambo: An *ab initio* tool for excited state calculations. *Comput. Phys. Commun.* **2009**, *180*, 1392–1403.
123. Hasan, M. M.; Haseeb, A. S. M. A.; Saidur, R.; Masjuki, H. H. Effects of annealing treatment on optical properties of anatase TiO_2 thin films. *Int. J. Chem. Biomol. Eng.* **2008**, *1*, 93–97.
124. Wang, Z.; Helmersson, U.; Käll, P.-O. Optical properties of anatase TiO_2 thin films prepared by aqueous sol–gel process at low temperature. *Thin Solid Films* **2002**, *405*, 50–54.
125. Liu, B.; Zhao, X.; Wen, L. The structural and photoluminescence studies related to the surface of the TiO_2 sol prepared by wet chemical method. *Mater. Sci. Eng., B* **2006**, *134*, 27–31.
126. Wong, M.; Hsu, S.; Rao, K. K.; Kumar, C. P. Influence of crystallinity and carbon content on visible light photocatalysis of carbon doped titania thin films. *J. Mol. Catal. A: Chem.* **2008**, *279*, 20–26.
127. Liu, B.; Wen, L.; Zhao, X. The photoluminescence spectroscopic study of anatase TiO_2 prepared by magnetron sputtering. *Mater. Chem. Phys.* **2007**, *106*, 350–353.
128. Xiang, Q. J.; Lv, K. L.; Yu, J. G. Pivotal role of fluorine in enhanced photocatalytic activity of anatase TiO_2 nanosheets with dominant (001)

facets for the photocatalytic degradation of acetone in air. *J. Appl. Catal., B* **2010**, *96*, 557–564.

129. Ni, M.; Leung, M. K. H.; Leung, D. Y. C.; Sumathy, K. A review and recent developments in photocatalytic water-splitting using TiO_2 for hydrogen production. *Renewable Sustainable Energy Rev.* **2007**, *11*, 401–425.
130. Hadjiiivanov, K. I.; Klissurski, D. G. Surface Chemistry of Titania (Anatase) and Titania-supported Catalysts. *Chem. Soc. Rev.* **1996**, *25*, 61–69.
131. Hosaka, N.; Sekiya, T.; Kurita, S. Optical Properties of Single-Crystal Anatase TiO_2 . *J. Phys. Soc. Jpn.* **1997**, *66*, 877–880.
132. Han, X.; Kuang, Q.; Jin, M.; Xie, Z.; Zheng, L. Synthesis of Titania Nanosheets with a High Percentage of Exposed (001) Facets and Related Photocatalytic Properties. *J. Am. Chem. Soc.* **2009**, *131*, 3152–3153.
133. Chen, X.; Mao, S. S. Titanium Dioxide Nanomaterials: Synthesis, Properties, Modifications, and Applications. *Chem. Rev.* **2007**, *107*, 2891–2959.
134. Bavykin, V.; Friedrich, J. M.; Walsh, F. C. Protonated Titanates and TiO_2 Nanostructured Materials: Synthesis, Properties, and Applications. *Adv. Mater.* **2006**, *18*, 2807–2824.
135. Riss, A.; Elser, J. E.; Bernardi, J.; Diwald, O. Stability and Photoelectronic Properties of Layered Titanate Nanostructures. *J. Am. Chem. Soc.* **2009**, *131*, 6198–6202 and references therein.
136. Mogilevsky, G.; Chen, Q.; Kulkarni, H.; Kleinhammes, A.; Mullins, W. M.; Wu, Y. Layered Nanostructures of Delaminated Anatase: Nanosheets and Nanotubes. *J. Phys. Chem. C* **2008**, *112*, 3239–3246.
137. Mogilevsky, G.; Chen, Q.; Kleinhammes, A.; Wu, Y. The structure of multilayered titania nanotubes based on delaminated anatase. *Chem. Phys. Lett.* **2008**, *460*, 517–520.
138. Ma, R.; Bando, Y.; Sasaki, T. Nanotubes of lepidocrocite titanates. *Chem. Phys. Lett.* **2003**, *380*, 577–582.
139. Vittadini, A.; Sedona, F.; Agnoli, S.; Artiglia, L.; Casarin, M.; Rizzi, G. A.; Sambi, M.; Granozzi, G. Stability of TiO_2 Polymorphs: Exploring the Extreme Frontier of the Nanoscale. *ChemPhysChem* **2010**, *11*, 1550–1557.
140. Hart, J. N.; Parker, S. C.; Lapkin, A. A. Energy Minimization of Single-Walled Titanium Oxide Nanotubes. *ACS Nano* **2009**, *3*, 3401–3412.
141. Spataru, C. D.; Ismail-Beigi, S.; Benedict, L. X.; Louie, S. G. Excitonic Effects and Optical Spectra of Single-Walled Carbon Nanotubes. *Phys. Rev. Lett.* **2004**, *92*, 077402–4.
142. Bruno, M.; Palummo, M.; Marini, A.; Del Sole, R.; Ossicini, S. From Si Nanowires to Porous Silicon: The Role of Excitonic Effects. *Phys. Rev. Lett.* **2007**, *98*, 036807–4.
143. Wirtz, L.; Marini, A.; Rubio, A. Excitons in Boron Nitride Nanotubes: Dimensionality Effects. *Phys. Rev. Lett.* **2006**, *96*, 126104–4.
144. Grey, I. E.; Li, C.; Madsen, I. C.; Watts, J. A. The stability and structure of cesium titanate ($\text{Cs}_x[\text{Ti}_{2-x/4}\square_{x/4}]\text{O}_4$) $0.61 < x < 0.65$. *J. Solid State Chem.* **1987**, *66*, 7–19.
145. Orzali, T.; Casarin, M.; Granozzi, G.; Sambi, M.; Vittadini, A. Bottom-Up Assembly of Single-Domain Titania Nanosheets on (1×2)-Pt(110). *Phys. Rev. Lett.* **2006**, *97*, 156101–4.

146. Vittadini, A.; Casarin, M. *Ab initio* modeling of TiO₂ nanosheets. *Theor. Chem. Account*. **2008**, *120*, 551–556.

147. Sato, H.; Ono, K.; Sasaki, T.; Yamagishi, A. First-Principles Study of Two-Dimensional Titanium Dioxides. *J. Phys. Chem. B* **2003**, *107*, 9824–9828.

148. Lazzeri, M.; Vittadini, A.; Selloni, A. Structure and energetics of stoichiometric TiO₂ anatase surfaces. *Phys. Rev. B* **2001**, *63*, 155409–9.

149. Lawler, H. M.; Rehr, J. J.; Vila, F.; Dalosto, S. D.; Shirley, E. L.; Levine, Z. H. Optical to UV spectra and birefringence of SiO₂ and TiO₂: First-principles calculations with excitonic effects. *Phys. Rev. B* **2008**, *78*, 205108–8.

150. Szieberth, D.; Ferrari, A. M.; Noel, Y.; Ferrabone, M. Ab initio modeling of TiO₂ nanotubes. *Nanoscale* **2010**, *2*, 81–89.

151. Sasaki, T.; Watanabe, M. Semiconductor Nanosheet Crystallites of Quasi-TiO₂ and Their Optical Properties. *J. Phys. Chem. B* **1997**, *101*, 10159–10161.

152. Shibata, T.; Sakai, N.; Fukuda, K.; Ebina, Y.; Sasaki, T. Photocatalytic properties of titania nanostructured films fabricated from titania nanosheets. *Phys. Chem. Chem. Phys.* **2007**, *9*, 2413–2420.

153. Akatsuka, K.; Haga, M.; Ebina, Y.; Osada, M.; Fukuda, K.; Sasaki, T. Construction of Highly Ordered Lamellar Nanostructures through Langmuir–Blodgett Deposition of Molecularly Thin Titania Nanosheets Tens of Micrometers Wide and Their Excellent Dielectric Properties. *ACS Nano* **2009**, *3*, 1097–1106.

154. Bavykin, D. V.; Gordeev, S. N.; Moskalenko, A. V.; Lapkin, A. A.; Walsh, F. C. Apparent Two-Dimensional Behavior of TiO₂ Nanotubes Revealed by Light Absorption and Luminescence. *J. Phys. Chem. B* **2005**, *109*, 8565–8569.

155. Ni, M.; Leung, M. K. H.; Leung, D. Y. C.; Sumathy, K. A review and recent developments in photocatalytic water-splitting using TiO₂ for hydrogen production. *Renewable Sustainable Energy Rev.* **2007**, *11*, 401.

156. Wang, W. S.; Wang, D. H.; Qu, W. G.; Lu, L. Q.; Xu, A. W. Large Ultrathin Anatase TiO₂ Nanosheets with Exposed {001} Facets on Graphene for Enhanced Visible Light Photocatalytic Activity. *J. Phys. Chem. C* **2012**, *116*, 19893–19901.

157. Hu, Y. H.; Wang, H.; Hu, B. Thinnest Two-Dimensional Nanomaterial—Graphene for Solar Energy. *ChemSusChem* **2010**, *3*, 782–796.

158. Bai, S.; Shen, X. Graphene–inorganic nanocomposites. *RSC Adv.* **2012**, *2*, 64–98.

159. Peining, Z.; Nair, A. S.; Shengjie, P.; Shengyuan, Y.; Ramakrishna, S. Facile Fabrication of TiO₂–Graphene Composite with Enhanced Photovoltaic and Photocatalytic Properties by Electrospinning. *ACS Appl. Mater. Interfaces* **2012**, *4*, 581–585.

160. Shen, J.; Yan, B.; Shi, M.; Ma, H.; Li, N.; Ye, M. One step hydrothermal synthesis of TiO₂-reduced graphene oxide sheets. *J. Mater. Chem.* **2011**, *21*, 3415–3421.

161. Morales-Torres, S.; Pastrana-Martínez, L. M.; Figueiredo, J. L.; Faria, J. L.; Silva, A. M. T. Design of graphene-based TiO_2 photocatalysts—a review. *Environ. Sci. Pollut. Res.* **2012**, *19*, 3676–3687.
162. Williams, G.; Seger, B.; Kamat, P. V. TiO_2 -Graphene Nanocomposites. UV-Assisted Photocatalytic Reduction of Graphene Oxide. *ACS Nano* **2008**, *2*, 1487–1491.
163. Zhang, Y.; Tang, Z.-R.; Fu, X.; Xu, Y.-J. TiO_2 -Graphene Nanocomposites for Gas-Phase Photocatalytic Degradation of Volatile Aromatic Pollutant: Is TiO_2 -Graphene Truly Different from Other TiO_2 -Carbon Composite Materials? *ACS Nano* **2010**, *4*, 7303–7314.
164. Liang, Y.; Wang, H.; Sanchez Casalongue, H.; Chen, Z.; Dai, H. TiO_2 nanocrystals grown on graphene as advanced photocatalytic hybrid materials. *Nano Res.* **2010**, *3*, 701–705.
165. Akhavan, O.; Ghaderi, E. Photocatalytic Reduction of Graphene Oxide Nanosheets on TiO_2 Thin Film for Photoinactivation of Bacteria in Solar Light Irradiation. *J. Phys. Chem. C* **2009**, *113*, 20214–20220.
166. Zhang, Y.; Tang, Z.-R.; Fu, X.; Xu, Y.-J. Engineering the Unique 2D Mat of Graphene to Achieve Graphene- TiO_2 Nanocomposite for Photocatalytic Selective Transformation: What Advantage does Graphene Have over Its Forebear Carbon Nanotube? *ACS Nano* **2011**, *5*, 7426–7435.
167. Xiang, Q.; Yu, J.; Jatoniec, M. Graphene-based semiconductor photocatalysts. *Chem. Soc. Rev.* **2012**, *115*, 782–796.
168. Fan, W.; Lai, Q.; Zhang, Q.; Wang, Y. Nanocomposites of TiO_2 and Reduced Graphene Oxide as Efficient Photocatalysts for Hydrogen Evolution. *J. Phys. Chem. C* **2011**, *115*, 10694–10701.
169. Geim, A. K.; Novoselov, K. S. The rise of graphene. *Nat. Mater.* **2007**, *6*, 183–191.
170. Neto, A. H. C.; Guinea, F.; Peres, N. M. R.; Novoselov, K. S.; Geim, A. K. The electronic properties of graphene. *Rev. Mod. Phys.* **2009**, *81*, 109–162.
171. Novoselov, K. S.; Geim, A. K.; Morozov, S. V.; Jiang, D.; Katsnelson, M. I.; Grigorieva, I. V.; Dubonos, S. V.; Firsov, A. A. Two-dimensional gas of massless Dirac fermions in graphene. *Nature* **2005**, *438*, 197–200.
172. Geim, A. K. Graphene: Status and Prospects. *Science* **2009**, *324*, 530–534.
173. Novoselov, K. S.; Jiang, Z.; Zhang, Y.; Morozov, S. V.; Stormer, H. L.; Zeitler, U.; Maan, J. C.; Boebinger, G. S.; Kim, P.; Geim, A. K. Room-Temperature Quantum Hall Effect in Graphene. *Science* **2007**, *315*, 1379.
174. Morozov, S. V.; Novoselov, K. S.; Katsnelson, M. I.; Schedin, F.; Elias, D. C.; Jaszczak, J. A.; Geim, A. K. Giant Intrinsic Carrier Mobilities in Graphene and Its Bilayer. *Phys. Rev. Lett.* **2008**, *100*, 016602–4.
175. Nair, R. R.; Blake, P.; Grigorenko, A. N.; Novoselov, K. S.; Booth, T. J.; Stauber, T.; Peres, N. M. R.; Geim, A. K. Fine Structure Constant Defines Visual Transparency of Graphene. *Science* **2008**, *320*, 1308.
176. Meyer, J. C.; Geim, A. K.; Katsnelson, M. I.; Novoselov, K. S.; Booth, T. J.; Roth, S. The structure of suspended graphene sheets. *Nature* **2007**, *446*, 60–63.

177. Xiang, Q.; Yu, J.; Jaroniec, M. Enhanced photocatalytic H₂-production activity of graphene-modified titania nanosheets. *Nanoscale* **2011**, *3*, 3670–3678.
178. Liu, S.; Liu, C.; Wang, W.; Cheng, B.; Yu, J. Unique photocatalytic oxidation reactivity and selectivity of TiO₂–graphene nanocomposites. *Nanoscale* **2012**, *4*, 3193–3200.
179. Chen, C.; Cai, W.; Long, M.; Zhou, B.; Wu, Y.; Wu, D.; Feng, Y. Synthesis of Visible-Light Responsive Graphene Oxide/TiO₂ Composites with p/n Heterojunction. *ACS Nano* **2010**, *4*, 6425–6432.
180. Meng, X.; Geng, D.; Liu, J.; Li, R.; Sun, X. Controllable synthesis of graphene-based titanium dioxide nanocomposites by atomic layer deposition. *Nanotechnology* **2011**, *22*, 165602–10.
181. Dreyer, D. R.; Park, S.; Bielawski, C. W.; Ruoff, R. S. The chemistry of graphene oxide. *Chem. Soc. Rev.* **2010**, *39*, 228–240.
182. He, H.; Riedl, T.; Lerf, A.; Klinowski, J. Solid-State NMR Studies of the Structure of Graphite Oxide. *J. Phys. Chem.* **1996**, *100*, 19954–19958.
183. Lerf, A.; He, H.; Forster, M.; Klinowski, J. Structure of Graphite Oxide Revisited. *J. Phys. Chem. B* **1998**, *102*, 4477–4482.
184. Ruess, G. Über das Graphitoxyhydroxyd (Graphitoxyd). *Monatsh. Chem.* **1946**, *76*, 381–417.
185. Liu, S.; Yu, J.; Jaroniec, M. Anatase TiO₂ with Dominant High-Energy {001} Facets: Synthesis, Properties, and Applications. *Chem. Mater.* **2011**, *23*, 4085–4093.
186. Liu, C.; Yang, S. Synthesis of Angstrom-Scale Anatase Titania Atomic Wires. *ACS Nano* **2009**, *3*, 1025–1031.
187. Yang, X. H.; Li, Z.; Liu, G.; Xing, J.; Sun, C.; Yang, H. G.; Li, C. Ultra-thin anatase TiO₂ nanosheets dominated with {001} facets: thickness-controlled synthesis, growth mechanism and water-splitting properties. *Cryst. Eng. Commun.* **2011**, *13*, 1378–1383.
188. Dudarev, S. L.; Botton, G. A.; Savrasov, S. Y.; Humphreys, C. J.; Sutton, A. P. Electron-energy-loss spectra and the structural stability of nickel oxide: An LSDA+U study. *Phys. Rev. B* **1998**, *57*, 1505–1509.
189. Tang, H.; Berger, H.; Schmid, P. E.; Levy, F.; Burri, G. Photoluminescence in TiO₂ anatase single crystals. *Solid State Commun.* **1993**, *87*, 847–850.
190. Stone, A. J.; Wales, D. J. Theoretical studies of icosahedral C₆₀ and some related species. *Chem. Phys. Lett.* **1986**, *128*, 501–503.
191. Ivanovskii, A. L. Graphene-based and graphene-like materials. *Russ. Chem. Rev.* **2012**, *81*, 571–605.
192. Kotakoski, J.; Krasheninnikov, A. V.; Kaiser, U.; Meyer, J. C. From Point Defects in Graphene to Two-Dimensional Amorphous Carbon. *Phys. Rev. Lett.* **2011**, *106*, 105505–4.
193. Banhart, F.; Kotakoski, J.; Krasheninnikov, A. V. Structural Defects in Graphene. *ACS Nano* **2011**, *5*, 26–41.
194. Wang, X.-Q.; Li, H.-D.; Wang, J.-T. Structural stabilities and electronic properties of planar C₄ carbon sheet and nanoribbons. *Phys. Chem. Chem. Phys.* **2012**, *14*, 11107–11111.

195. Gong, X. Q.; Selloni, A.; Vittadini, A. Density Functional Theory Study of Formic Acid Adsorption on Anatase $\text{TiO}_2(001)$: Geometries, Energetics, and Effects of Coverage, Hydration, and Reconstruction. *J. Phys. Chem. B* **2006**, *110*, 2804–2811.
196. Wang, Y.; Chen, X.; Zhong, Y.; Zhu, F.; Loh, K. P. Large area, continuous, few-layered graphene as anodes in organic photovoltaic devices. *Appl. Phys. Lett.* **2009**, *95*, 063302–3.
197. Tang, W.; Sanville, E.; Henkelman, G. A grid-based Bader analysis algorithm without lattice bias. *J. Phys. Condens. Matter* **2009**, *21*, 084204–7.
198. Sanville, E.; Kenny, S. D.; Smith, R.; Henkelman, G. Improved grid-based algorithm for Bader charge allocation. *J. Comput. Chem.* **2007**, *28*, 899–908.
199. Henkelman, G.; Arnaldsson, A.; Jónsson, H. A fast and robust algorithm for Bader decomposition of charge density. *Comput. Mater. Sci.* **2006**, *36*, 354–360.
200. Goerbig, M. O. Electronic properties of graphene in a strong magnetic field. *Rev. Mod. Phys.* **2011**, *83*, 1193–1243.
201. Fan, J.; Liua, S.; Yu, J. Enhanced photovoltaic performance of dye-sensitized solar cells based on TiO_2 nanosheets/graphene composite films. *J. Mater. Chem.* **2012**, *22*, 17027–17036.

Publication Date (Web): October 16, 2015 | doi:10.1021/bk-2015-1196.ch003

Chapter 3

Dye-Sensitized and Doped TiO₂ Mesoporous Materials for Visible Light-Induced Photocatalytic Hydrogen Evolution

Luther Mahoney, Shivatharsiny Rasalingam, and Ranjit T. Koodali*

Department of Chemistry, University of South Dakota,
Vermillion, South Dakota 57069

*E-mail: Ranjit.Koodali@usd.edu.

Intense research in solar energy conversion has been devoted in recent years due to concerns of growing energy demands and increasing threats to the quality of human life from problems from climate change. In response to these needs, a variety of new materials have been developed and explored for harnessing solar energy. Mesoporous materials have been used as photocatalysts for water splitting reactions. Among the materials explored, titanium dioxide has been the most widely studied material; however, it lacks activity in the visible region of the solar spectrum. Thus, efforts have been directed towards extending the response to the visible portion and these include coupling with small band gap semiconductors, doping, and sensitizing with dyes. In this work, we have doped mesoporous titania with transition metal ions and have used dyes for visible light induced hydrogen generation.

Introduction

Porous semiconductor materials have great potential in lowering our dependence on fossil and nuclear energy by utilizing solar energy input (1). The solar energy striking the Earth's surface for one hour could provide the energy to supply all the world population's need for one year (2). However, designing materials with an optimal band gap energy that models the solar spectrum on Earth has been challenging (3). Stable semiconductors made of metal oxides, such

as titanium dioxide, have relatively large band gap energies, and can only exploit the UV spectrum of solar radiation. However, metal sulfides like CdS can absorb visible light, but these materials lack stability under solar illumination. Therefore, the challenge facing the world population includes developing renewable energy sources that will sustain the future generations (4). It has been shown previously that doping metal ions in TiO_2 matrices can shift the absorption spectrum to longer wavelength of light (5). In addition, the metal doped TiO_2 materials with high porosities (large pore sizes and pore volume) and high surface areas may adsorb several dye molecules significantly compared to non-porous materials. Thus, using mesoporous doped-titania materials that contains dye molecules may afford opportunities for designing a visible light photocatalyst for solar water splitting reaction. This chapter details the opportunities and challenges towards this efforts.

Importance of Water Splitting Reaction

Currently, the world is facing energy challenges because the fossil fuel production cannot keep pace with the demand (4, 6). The world energy consumption is projected to increase in coming years leading to the terawatt challenge to power the future generations (2). Therefore, typical conventional fossil fuel production will not be able to keep pace at a reasonable cost in coming years. Furthermore, the environmental costs affected by using fossil fuels include climate change, reduced life expectancy, and higher health care costs because of associated increased pollution levels (7). The energy and environmental challenges will require renewable energy that harnesses abundant sunlight (8). Solar energy using sunlight to split water into hydrogen and oxygen appears to be an optimal fuel energy source for fuel cells. Hydrogen combined with oxygen gas produces only water as an innocuous by-product. Fuel cell may be used to produce electricity with greater efficiencies compared with the internal combustion engine (9). Therefore, the conversion of water into hydrogen and oxygen gases using sunlight provides an avenue to obtain clean energy that will be sustainable for coming generations. We will review potential means of splitting water using TiO_2 based semiconductors that are coupled to low band gap semiconductors such as CdS, doped with metals, and sensitized by dyes, in the following section.

Water Splitting Using Visible Light

In this section, we will review attempts to extend the visible light response of titania based materials.

Coupled Semiconductors

Coupled semiconductors, such as CdS/ TiO_2 , take the positive aspects of visible light active semiconductor (CdS) and the benefits of the wide band gap material (TiO_2). However, such composite materials still needs to have a sacrificial electron donor source to minimize photocorrosion. Lianos and co-workers compared the H_2 evolution efficiency using ethanol-water mixture

with sulfide and sulfite as hole scavenging agents (10). They found that an optimal loading of 33% CdS on TiO₂ produced the largest hydrogen yield under visible light illumination. The crystallinity of TiO₂ at this loading of CdS was not compromised, and further increase of CdS decreased the crystallinity of TiO₂ and reduced the activity for hydrogen evolution. The hole scavenging agents alone were noted to produce little hydrogen at identical loadings of CdS on TiO₂. Furthermore, Pt was added to the CdS/TiO₂ system to increase the visible light hydrogen evolution rate in the same study. In contrast to alcohols as electron donors, dye molecules have been considered as poor donors due to their stable aromatic structures. Stengl and Kralova have studied model Orange II dye solutions for environmental remediation and hydrogen production using TiO₂/ZnS/CdS composite material (11). They employed two irradiation source wavelengths of 365 nm (UVA) and 400 nm (visible light). The UVA light degraded the Orange II dye at a rapid rate compared to the visible light illumination because the TiO₂ was activated under UVA in addition to the metal sulfide semiconductors. Orange II dye has been indicated to be challenging to degrade due to the presence of stable resonance structures. The yield of hydrogen obtained using Orange II was lower compared to ethanol-water mixture as expected. The main goal of this study was to photodegrade the Orange II dye to innocuous products with the added benefit of hydrogen production. Sigmund and co-workers noted the positive benefit of the coupled semiconductors, such as CdS/TiO₂, for efficient hydrogen production due to the greater charge separation occurring among the two materials (12). This system has shown better efficiency than either CdS or TiO₂ alone towards hydrogen production with model polluted waters in the presence of electron donors. However, CdS in CdS/TiO₂ still undergoes photocorrosion, limiting its utility. To overcome these challenges, doped semiconductor systems using metal or non-metals have been explored for splitting water under visible light illumination, and this is discussed in the next subsection.

Doped TiO₂ Photocatalysts

Metal ions have been incorporated on the surface or in the lattice (bulk) of TiO₂ (3, 5, 12, 13). The surface doping forms a solid solution with essentially no expansion of the unit cell upon increasing the dopant content in the photocatalyst (14). The bulk or lattice doping tend to usually increase the recombination rate of the charge carriers compared with surface doping for solar hydrogen evolution. Reddy and co-workers studied Fe doped TiO₂ for visible light hydrogen production either on the surface or in the bulk. They found that the 0.5 wt.% surface doping of Fe produced 1700 μ mole H₂/h/g catalyst. In contrast, 0.5 wt% lattice doping in TiO₂ gave only 500 μ mole H₂/h/g catalyst (15). These researchers suggest that the lattice doped Fe³⁺ ions in TiO₂ act to promote recombination of the electron-hole pairs. However, the Fe³⁺ ions on the surface in Fe-TiO₂ act as trap states, thereby minimizing electron-hole recombination and increasing hydrogen production. In another study, doping in the bulk was found to increase the activity. In this study, a dye was used for degradation and for generation of

hydrogen suggesting that mechanistic differences may account for the differences in the activity trends for production of hydrogen in the presence and absence of dyes (13). Fan and co-workers studied Fe-Ni-TiO₂ photocatalyst for solar hydrogen production using ethanol-water mixture under visible light, and they obtained higher photocatalytic activity compared with the individually doped Fe-TiO₂ or Ni-TiO₂ materials. Furthermore, Fan and co-workers compared the activities of Fe lattice doped TiO₂ and surface bound Ag-TiO₂ and found that Ag-TiO₂ showed higher activity compared to Fe-TiO₂ (16). These researchers only saw a positive effect with bulk metal doping when two different metal ions, such as Fe and Ag, were co-doped on TiO₂. The metal dopant appears to facilitate either charge separation or recombination depending on its location.

Sun and co-workers studied four different methods for reducing copper oxide on TiO₂, and they noted that the chemical reduction method led to higher solar hydrogen evolution results compared to wet impregnation, sol-gel, or photodeposition (17). These researchers indicate dispersion of the copper species as one of the factors affecting the hydrogen evolution rate.

Another approach to extend the visible light response is by doping with non-metals, but this discussion is beyond the scope of this chapter. The next section will explore the avenues for water splitting using dye-sensitized TiO₂.

Dye-Sensitized TiO₂ Photocatalysts

Visible light water splitting using dye-sensitized TiO₂ have been reported in literature. Chatterjee studied six different dyes adsorbed onto Degussa P-25 TiO₂ material for water-splitting (18). The six dyes studied included cationic (thionine, methylene blue (MB), nile blue A, and safranine O), anionic (eosin Y, EY), and hybrid (rhodamine B, RhB). Visible light hydrogen evolution was completed using triethanolamine (TEOA)-water mixture for 15 hour time period, which produced 600 to 1500 μ mole H₂. There seemed to be no correlation between dye adsorption and hydrogen production efficiency. Rather, different electron transfer mechanism for the two classes of dyes was indicated to be the main reason for the trends seen in hydrogen evolution. EY had the highest visible light hydrogen value of 1500 μ mole H₂; likewise, RhB produced 1117 μ mole H₂ evolution under visible light illumination. Safranine O, a cationic dye, evolved 622 μ mole H₂, and these three dyes were among the most active; the high efficiency was explained by three step mechanism that involved direct injection of electrons from the dyes to the conduction band edge of TiO₂. The other dyes thionine (318 μ mole H₂), MB (320 μ mole H₂), and nile blue A (MB) (462 μ mole H₂) evolved comparatively lower amount of H₂ on account of a four step mechanism, that involved injection of electrons from the reduced form of the dye, which posed some kinetic barriers.

Cheng and co-workers used a novel ruthenium based dye comprised of two rings and compared this with N3 dye that has only one macrocycle ring on P-25 TiO₂ host material (19). These researchers discovered that the two ring structure produced almost double the amount of hydrogen (1420 μ mole H₂ in a 6 h) upon visible light illumination; the single bipyridyl macrocycle ring produced 803 μ mole H₂ in the same period. The researchers indicated the reason for increased

visible light hydrogen evolution from the two ring based dye was due to enhanced charge injection kinetics. In this regard, doping of metal ion onto the dye-coupled semiconductor system can further increase the efficiency of visible light induced water splitting.

Various types of electron donors have been used as sacrificial reagents for the regeneration of the dye. The most used electron donor is TEOA for dye-sensitized water splitting. Other sacrificial reagents studied in dye-sensitized water splitting include diethanolamine (DEA), triethylamine (TEA), ethylenediaminetetraacetic acid (EDTA), and methanol. Notably, TEOA has been used widely due to its high reducing ability. Rogach and co-workers noted the much greater reducing ability of sulfite and TEOA in comparison with EDTA and methanol (20). These researchers indicated that sodium sulfite has a larger reducing ability, so it will be able to remove the generated holes rapidly. The trend observed in the activity for hydrogen production was sulfite > TEOA > EDTA > methanol, and it was explained by the reduction potential of the sacrificial agents. The other electron donor reported in literature would include NaI. Arakawa and co-workers used I⁻ (in acetonitrile solvent) for visible light dye-sensitized water splitting using a merocyanine dye (21). The yield of hydrogen was shown to be dependent on the ratio of acetonitrile to water, and the larger amounts of acetonitrile increased the overall yield of solar hydrogen. Lu and co-workers studied EY dye-sensitized water-splitting using CuO/TiO₂ photocatalysts (22). The difference in the H₂ yield between DEA (127 μ mole H₂/10 h) and TEOA (116 μ mole H₂/10 h) may be from the increased pH associated with TEOA. The pH influences in the H₂ production *via* changing the oxidation-reduction potential of the semiconductor was also evidenced by the work of Ray and co-workers (23). In their study, they noticed that the pH affects the interaction of the dye molecule and the electron donor. In short, the choice of the sacrificial reagent is important in visible light dye-sensitized hydrogen evolution reaction because of its ability to donate electrons to the oxidized dye molecules. The next section will elaborate on systems involving the use of dyes and metal doped TiO₂ photocatalysts.

Dye-Sensitized and Doped TiO₂ Photocatalysts

Platinum has been the most widely used element as a dopant because of its ability to form a heterojunction (Schottky barrier) with TiO₂, and because of its role as a co-catalyst to facilitate the production of hydrogen. The two dyes most studied for water splitting with TiO₂ are EY and Ru(dcbpy)₂(NCS)₂ (N719), where (dcbpy=2,2'-bipyridyl-4,4'-dicarboxylic acid). Arakawa and co-workers studied platinum doped TiO₂ materials with five types of xanthene dyes: EY, merbromine, 2',7'-dichlorofluorescein, RhB, and rhodamine 6G (24). These researchers used four different TiO₂ (P-25, anatase, rutile, and amorphous) that were photodeposited with Pt. The use of EY with Pt-TiO₂ photocatalyst produced hydrogen with a quantum yield of 10%. Furthermore, recycling studies indicated that in the second photocatalytic run, the activity of EY coupled Pt-TiO₂ system was 90% of the original activity after replenishing with TEOA. Boßmann and co-workers examined the hydrogen evolution using

Pt loaded P-25 TiO₂ and a series of Ru-based dye sensitizers. Ru(bpy)₃²⁺ sensitizer gave the highest hydrogen evolution in conjunction with an electron relay 3,3'-dimethyl-propyl-viologen-sulfonate, (MPVS) and TEOA (25). The dye containing the simpler bipyridyl rings produced the greatest hydrogen evolution rate, which may be due to tight binding of carboxylic acid groups attaching to the surface of TiO₂ *via* Ti-OH (titanol) groups to form stable metal ester bonds. A later study by Peng and co-workers examined three ruthenium dyes, N719, Ru(bpy)₂(him)₂-NO₃ (him=imidazole), and Ru₂(bpy)₄L₁-PF₆ (L₁= μ -4,4'-azo-benzene carboxylic acid) using Pt-loaded TiO₂ (26). Their results for visible water splitting showed that the binuclear Ru dye, Ru(bpy)₂(him)₂-NO₃ showed the highest activity among the three dyes examined in the study. They attributed the marked improvement of the binuclear Ru dye to the reduced back electron transfer from two metal centers, increased “antenna effect” by the larger molecular area, and the weaker binding to the TiO₂ host material. To prove that weaker binding of dyes to titania prevent back electron transfer, these researchers used Ru(bpy)₂(him)₂-NO₃ dye. This Ru dye had increased visible light hydrogen evolution compared with the standard Ru N719 dye. Furthermore, the stability of the binuclear Ru dye was similar to the N719 dye. Comparison of later research by Li and co-workers, using other Ru dyes such as N3 and Z907 for visible light hydrogen evolution reveals the need for the dye structure to be bound to the host TiO₂ material but not very strongly (27). The modulation of the charge transfer *via* Ru dye binding interactions to TiO₂ host was further studied by Fan and co-workers with a novel mononuclear dye [RuL(bpy)₂](PF)₂ (L=2-hydroxyl-5-(imidazo[4,5-f]-1,10-phenanthrolin) benzoic acid), that has carboxylic acid and hydroxyl groups (28). This dye produced 386 μ mole of H₂ after 3 hours of visible light illumination. The Ru(bpy)₃²⁺ dye on a composite Al₂O₃/TiO₂/Pt material produces more hydrogen than over Pt-loaded TiO₂. Choi and co-workers used this composite material to produce approximately 100 μ mole of H₂ compared to 50 μ mole of H₂ using only Pt-loaded TiO₂ (29).

Even though the Ru dyes show higher visible light hydrogen evolution, metal free dyes have the advantage of lower cost. Lu and co-workers employed EY and RhB and adsorbed them onto Pt-loaded TiO₂ (22). These researchers studied the effect of both anionic and hybrid dye for visible light water splitting as function of pH, transition metal oxide loaded on TiO₂, platinum loading, and sacrificial reagents. The anionic dye, EY had greater hydrogen evolution using three sacrificial reagents studied: DEA, EDTA, and TEA. A pH of 14 produced the largest visible light hydrogen evolution activity of 127 μ mole H₂ in 10 h using EY and DEA. The optimal CuO loading on TiO₂ was found to be 1.0 wt.%, whereas the optimum Pt loading obtained was 1 wt.%. The same Pt-loaded CuO/TiO₂ material using RhB dye produced only 7.4 μ mole H₂ in a 10 h time span under identical reaction conditions. This suggests that the degree of binding of the dye to the host material appears to be critical. In addition, the influence of the sacrificial reagent may also play a role in changing the pH value and ability to donate electrons to the excited dye molecules, as shown by Lu and co-workers' in their study with EY and RhB dyes. Sreethawong and co-workers also discovered that a basic pH of 11.5 was favorable for producing hydrogen using EY dye on Pt-loaded TiO₂ under visible light illumination (30). The Pt loading was 0.6 wt.%

and the sacrificial reagent used was DEA. These two parameters were similar to the study by Lu and co-workers (22). Other studies using EY dye employed a pH value of 7 with TEOA as the sacrificial reagent and Pt loadings of 0.5 wt.% (31, 32). The functionalization of the surface of TiO₂ using phosphoric acid enabled the EY-TiO₂ photocatalyst to produce approximately 280 μ mole of H₂ in 5 h (31). EY was used as the sensitizer to explore the role of faceting in Pt/TiO₂ photocatalysts. Pt/TiO₂ exhibited higher activity since Pt{111} possessed a higher Fermi energy level and has lower activation energy for hydrogen generation (32, 33).

Mixed oxide systems have also been explored. The two research works on Pt-loaded TiO₂-ZrO₂, used EY dye. Sreethawong and Yoshikawa made Pt-loaded TiO₂-ZrO₂ using a sol-gel synthesis followed by photodeposition of Pt to obtain an optimal value of 0.5 wt.% loading (34). These researchers discovered that a Zr/Ti molar ratio of 95 gave the optimal photocatalytic activity, and the anatase TiO₂ phase was retained even at calcination temperatures as high as 800 °C. The Pt loading range used was from 0 to 1 wt.%, and DEA was chosen as the sacrificial reagent. Chavadej and co-workers further optimized this system by using EY at a pH of 11.6 and completing the synthesis with platinum salt, thereby avoiding the photodeposition step (35). The resulting photocatalyst was also heat treated at 800 °C. However, both of these studies using Pt-TiO₂-ZrO₂ produced little hydrogen under visible light illumination. In another study, Sreethawong and co-workers utilized Ag, Ni, and Cu doped TiO₂, using EY dye as the sensitizer (30). These researchers found the following trend EY-Pt-TiO₂ > EY-Ag-TiO₂ >> EY-Ni-TiO₂ > EY-Cu-TiO₂ for hydrogen evolution under visible light irradiation. Therefore, EY and Pt loaded TiO₂ have been the main dye and metal studied in TiO₂ systems in the past for visible light hydrogen activity. A study by Du and co-workers attempted to break the trend in using Pt-TiO₂ photocatalysts, and these researchers used Cu, Co, Ni, and Fe as the dopant (36). The EY sensitized Ni(OH)₂ system produced approximately 40 μ mole H₂ in 5 hours. The trend in activity of hydrogen using EY dye under visible light radiation was found to be Ni(OH)₂ > Cu(OH)₂ >> Co(OH)₂ >>> Fe(OH)₃. The metal oxides CoO_x and NiO_x had relatively small hydrogen activity of 5 to 7 μ mole of H₂ in 5 h with the least activity from the non-doped TiO₂. Other than Lu and co-workers' work (22), RhB dye-sensitized water splitting reaction has not been largely explored. The only dedicated study reported for transition metal doped RhB dye visible light water splitting used Co-TiO₂ (37). This study employed P-25 TiO₂ impregnated with Co(NO₃)₂ and DEA as the sacrificial reagent for producing hydrogen. These researchers obtained approximately 50 μ mole H₂ in 6 h of visible light illumination.

In this work, we have set out to explore hydrogen production from dye-sensitized and transition metal doped (transition metal = Co, Ni, and Zn) under visible light illumination and compared its activity with non-doped titania. The mesoporous materials were synthesized by the sol-gel evaporation-induced self-assembly (EISA). The following experimental section will discuss various characterization techniques that include powder XRD, nitrogen physisorption, Diffuse Reflectance Spectroscopy (DRS), zeta potential, and transmission electron microscopy (TEM).

Experimental Section

The evaporation-induced self-assembly (EISA) synthetic methodology has been used to synthesize the non-doped and doped mesoporous TiO_2 materials in this study (38, 39). In a typical synthesis, first the cationic surfactant (cetyltrimethylammonium bromide) was dissolved in an absolute ethanol solution to obtain a clear colorless solution. The titania precursor, titanium isopropoxide, absolute ethanol, and concentrated HCl were mixed separately and the metal precursors, such as $\text{Co}(\text{NO}_3)_2 \cdot 6\text{H}_2\text{O}$, $\text{Ni}(\text{NO}_3)_2 \cdot 6\text{H}_2\text{O}$, or $\text{Zn}(\text{NO}_3)_2 \cdot 6\text{H}_2\text{O}$ were then added into the titania precursor solution mixture. Finally, the surfactant solution and the metal containing solutions were mixed together followed by addition of deionized water ($18 \text{ M}\Omega \text{ cm}$ resistivity) to initiate the hydrolysis under stirring for a period of time. A 0.5 wt.% metal loading was chosen for the three metal doped materials because it was found to be the optimal. The homogeneous solutions were placed onto four Petri dishes and placed in an oven and heated from room-temperature to 60°C at $1^\circ\text{C}/\text{minute}$ and held for a half-day in the oven. The resulting films were extracted with a spatula, and the amorphous flakes were then ground finely followed by calcination at 500°C for 6 h at heating rate of $3^\circ\text{C}/\text{minute}$.

The powder X-ray diffraction (XRD) was completed using Rigaku Ultima IV instrument, and nitrogen adsorption analysis was done using a Quantachrome NovaWin 2200e instrument. The UV-Vis and diffuse reflectance spectroscopy (DRS) analysis was completed with a Cary 100 Bio instrument, and the Harrick praying mantis attachment was used for DRS studies. Zeta potential measurements were completed using a Malvern Nano ZS-90 zetasizer. The TEM analysis was completed using a FEI Tecnai G² Spirit instrument at an acceleration voltage of 120 kV to study the structure morphology of samples with the microscope objective of 50x. The visible light hydrogen evolution reactions were carried out with an Oriel light source and a SRI 8610 C gas chromatograph (GC) was used for analyzing hydrogen.

Results and Discussion

Physico-Chemical Characterization

The mesoporous materials prepared in this study have been characterized by a variety of techniques and these are discussed in this section. The low-angle XRD pattern (Figure 1A) exhibits a broad reflection peak at $2\theta \approx 2^\circ$, which is an indication of the presence of mesoporosity in these materials.

The XRD patterns in Figure 1A perhaps represents wormhole phase indicated by the relative large FWHM value of the highest intense peak (38). Figure 1B shows the high angle reflections; however, the peaks are found to be broad due to the amorphous nature of uncalcined TiO_2 materials (40). In addition, the peak positions of the transition ion containing mesoporous materials are slightly different from the non-doped mesoporous titania indicating a change

in the d spacing and pore sizes on addition of the dopant ions. The high angle XRD patterns for the calcined TiO_2 materials depicted in Figure 2 show that the significant sharp peaks could be indexed to the anatase phase of titania only.

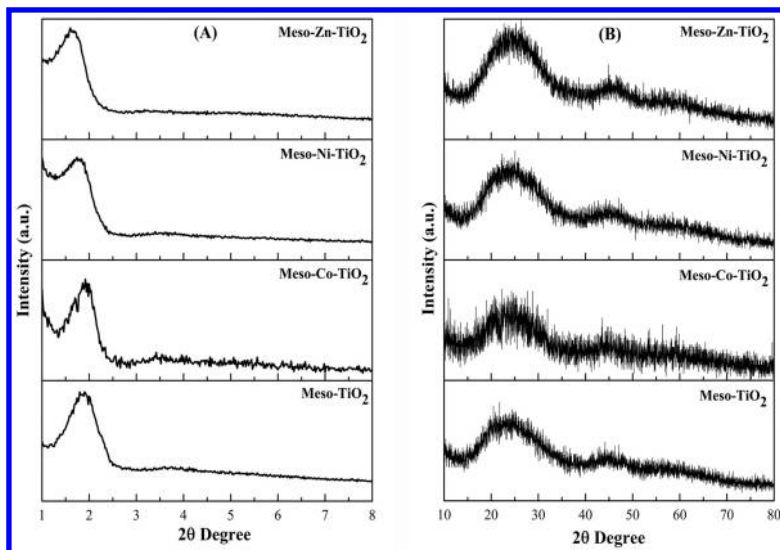


Figure 1. Powder X-ray diffractogram of as-synthesized mesoporous titania materials, (A) low angle and (B) High angle regions.

All the TiO_2 materials exhibit peaks at $2\theta = 25.4^\circ, 37.9^\circ, 48.2^\circ, 54.1^\circ, 55.1^\circ, 62.6^\circ, 68.9^\circ, 70.4^\circ$, and 75.1° which correspond to the anatase phase d -spacings of $d_{101}, d_{004}, d_{200}, d_{105}, d_{211}, d_{204}, d_{116}, d_{220}$, and d_{213} respectively. The crystallite size of mesoporous titanium dioxide materials was calculated using Halder-Wagner method derived from the Debye-Scherrer equation for three selected peaks with 2θ angles 25.3° (d_{101}), 48.14° (d_{200}), and 62.80° (d_{213}). Table 1 exemplifies the structural properties of the mesoporous titanium dioxide materials. It is noteworthy to mention here that the addition of metal ion marginally lowers the crystallite size of the materials, and it was noted to be similar among the doped TiO_2 materials. In addition, similar lattice constants of $a \approx 3.78 \text{ \AA}$ and $c \approx 9.50 \text{ \AA}$ and comparable unit cell volume of around 136 \AA^3 were obtained with all the materials using the whole-pattern-powder-fitting Rigaku software, and these results are consistent with previously reported mesoporous TiO_2 materials (41, 42). The ionic radii of Ti^{4+} is 0.745 \AA , whereas that of Ni^{2+} , Co^{2+} , and Zn^{2+} are 0.83 \AA , 0.89 \AA , and 0.88 \AA respectively and larger than that of Ti^{4+} (40). The unit cell volume of the Co- and Zn-doped titania are relatively larger than that of the non-doped titania. Because the ionic radii of Co^{2+} and Zn^{2+} are relatively higher than that of Ti^{4+} , the increase in unit cell volume on doping with these ions suggest that Co^{2+} and Zn^{2+} ions are perhaps doped in the bulk (lattice) of the mesoporous material in accordance with previous results (43). In contrast, doping with Ni^{2+} ions decreases the unit cell volume suggesting the formation of a solid solution, *i.e.* the Ni^{2+} are located on the surface of the mesoporous titania.

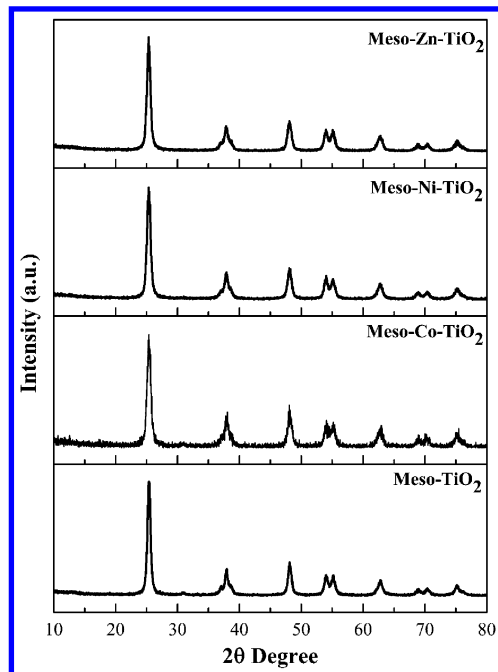


Figure 2. Powder X-ray diffractogram of calcined mesoporous titanium dioxides.

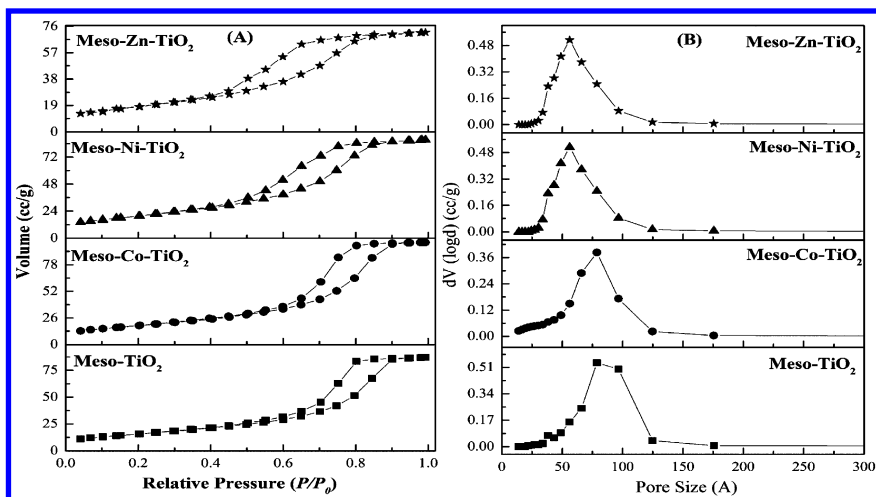


Figure 3. Nitrogen adsorption-desorption isotherms of mesoporous titanium dioxide. The insets show the pore size distribution.

Table 1. Structural Properties of the Mesoporous Titanium Dioxide Materials

Sample	SA (m^2/g)	PV (cm^3/g)	PD (\AA)	Crystallite size (nm)	$B_g(eV)$	IEP	Lattice constant (\AA)		Unit cell volume (\AA^3)
							a	c	
Meso-TiO ₂	57	0.13	79.0	13 \pm 1	3.18	6.50	3.7855	9.5042	136.20
Meso-Co-TiO ₂	67	0.15	61.0	10 \pm 1	2.31	8.04	3.7873	9.5037	136.32
Meso-Ni-TiO ₂	73	0.14	57.0	11 \pm 1	2.64	9.59	3.7846	9.5014	136.09
Meso-Zn-TiO ₂	67	0.11	39.0	11 \pm 1	2.82	9.82	3.7871	9.5094	136.39

SA, PV, and PD refer to specific surface area, pore volume, and pore diameter respectively. B_g refers to band gap energy and IEP refers to isoelectric point.

The N_2 adsorption-desorption isotherm and pore-size-distribution (PSD) plots of the mesoporous titanium dioxide materials are shown in Figure 3(A-D). All the materials exhibit type IV isotherms with H_2 hysteresis loop, which are characteristic for mesoporous materials, where a multilayer adsorption at low pressures followed by capillary condensation at higher pressures takes place (44–46). By applying the Brunauer-Emmett-Teller (BET) equation within the relative pressure P/P_0 range of 0.05–0.30, the surface area of the mesoporous titania materials were calculated. The surface areas were obtained to be 57, 67, 73, and 67 m^2/g for Meso-TiO₂, Meso-Co-TiO₂, Meso-Ni-TiO₂, and Meso-Zn-TiO₂, respectively. The surface area of doped titania were found to be slightly higher than that of the non-doped TiO₂. The pore volume of the materials was obtained at the highest relative pressure $P/P_0 \approx 0.99$, and it was observed that the pore volume of the mesoporous materials lies in a narrow range between 0.11 and 0.15 cm^3/g . The pore size distribution was determined by applying the Barrett-Joyner-Halenda (BJH) equation to the desorption isotherm.

The insets in Figure 3 illustrate the pore size distribution of the corresponding materials. It was observed that the pore size was centered near 80 Å for the non-doped TiO₂, and it seems to be shifted to lower pore sizes for the doped mesoporous titanium dioxide materials.

The absorbance spectra of doped mesoporous titanium dioxide materials extend slightly into the visible region. Meso-Ni-TiO₂ and Meso-Zn-TiO₂ materials exhibited relatively small absorption between 400 and 550 nm, while Meso-Co-TiO₂ material showed broader absorption peaks up to 700 nm in the absorbance spectra (not shown here). The extended absorption observed for the metal doped mesoporous TiO₂ materials in the visible region can be considered to involve d-d transitions of the metal ions and/or the excitation of the electron from the dopant ions to the conduction band of titania. In addition, oxygen vacancies could also be created because the metal ion dopants have an oxidation state different from that of Ti⁴⁺ (40).

Band gap energies of the materials were calculated by the Tauc-plot, which is translation of corresponding absorbance spectra for the solid mesoporous titania materials *via* Kubelka-Munk function. Figure 4 depict the Tauc plot of the calcined mesoporous titania materials. The band gap was found to be 3.18 eV for the non-doped Meso-TiO₂ material; whereas the band gaps were estimated to be 2.31, 2.64, and 2.82 eV for Meso-Co-TiO₂, Meso-Ni-TiO₂, and Meso-Zn-TiO₂ respectively.

The characteristic morphological features of the photocatalysts were examined by using transmission electron microscopy (TEM). Figure 5 depicts a representative TEM image of the non-doped mesostructured TiO₂ material.

To understand the surface charge of the mesoporous TiO₂ materials, zeta potential measurements were carried out. The pH of the TiO₂-electrolyte (KNO₃ in deionized water) suspension was adjusted by the addition of appropriate amounts of HNO₃ and KOH. The variation of zeta potential *vs.* pH is shown in Figure 6. It can be clearly seen from the titration curves that the isoelectric point (IEP) or the point of zero charge (pzc), has shifted to higher pH values for the doped-TiO₂ materials. In particular, Meso-Ni-TiO₂ and Meso-Zn-TiO₂ have IEP values close to pH of 10 than the Meso-Co-TiO₂ material. Table 1 lists the IEP values and they vary from 6.50 for the non-doped TiO₂ to 9.82 for Meso-Zn-TiO₂.

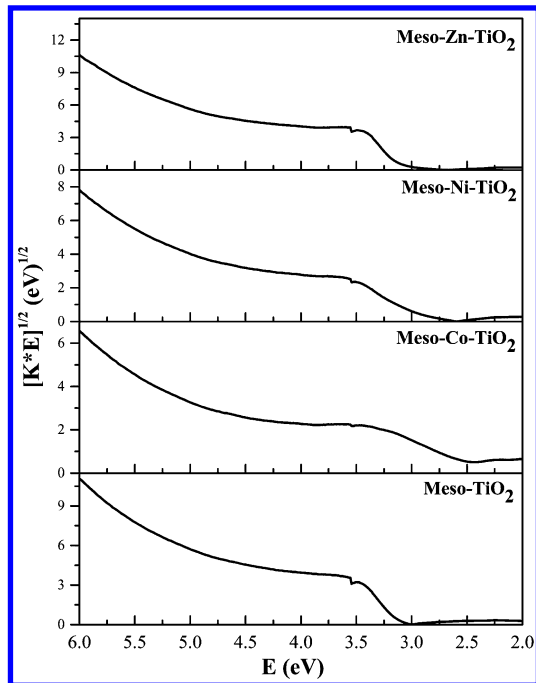


Figure 4. Diffuse reflectance spectra (Tauc Plots) of calcined mesoporous titanium dioxide.

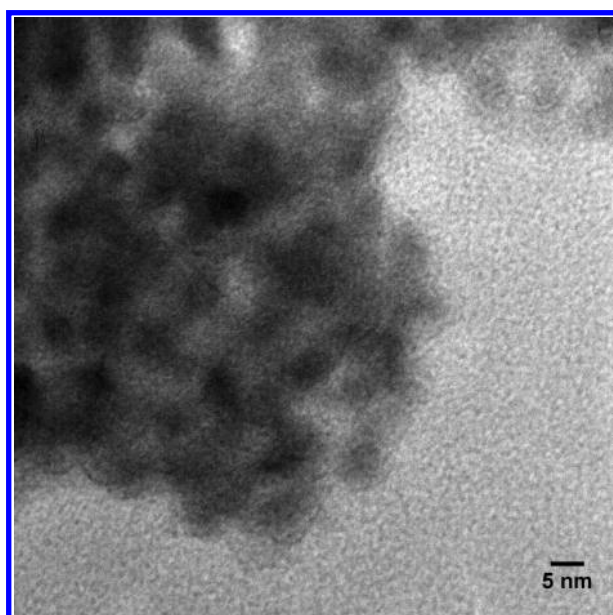


Figure 5. Representative transmission electron microscope image of mesostructured titania.

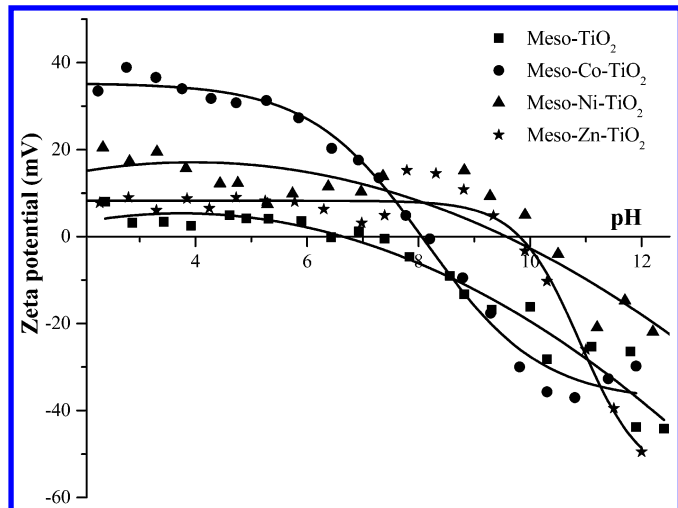
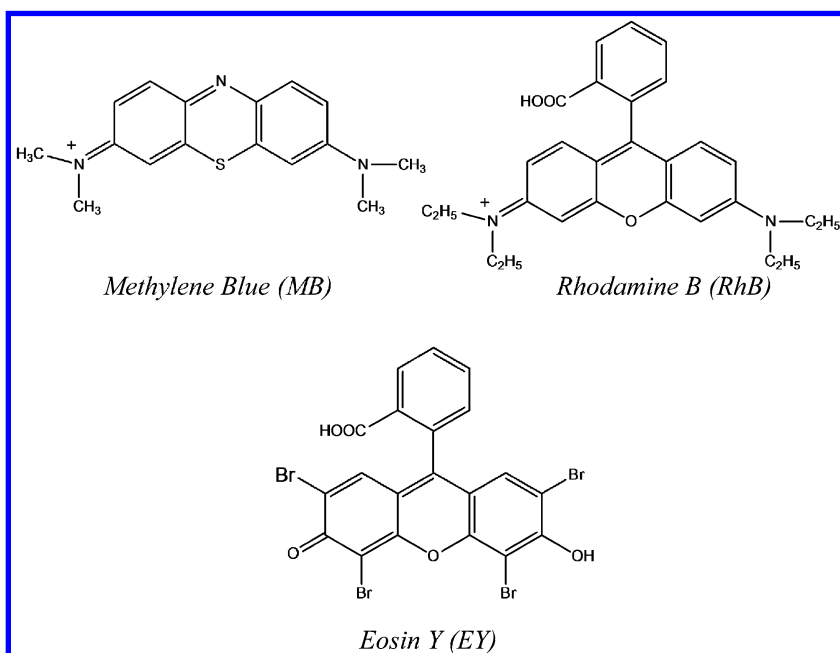


Figure 6. Variation of zeta potential vs. pH for mesoporous titanium dioxide.



Scheme 1. Structures of the Dye Molecules

The surface hydroxyl groups on the mesoporous materials were determined by acid-base titrations. The experiments indicate that the Meso-TiO₂ material has a surface hydroxyl group value of 2.84 mmole/g, whereas all the doped mesoporous TiO₂ materials have values lying in a narrow range of 1.22 to 1.27 indicating that doping has affected the surface hydroxyl group density significantly. In the next section, the results from the photocatalytic experiments will be discussed.

Photocatalytic Studies

The non-doped Meso-TiO₂ material was evaluated for water splitting with three commercial dyes: RhB, EY, and MB and using TEOA as the sacrificial reagent. RhB could be considered as a hybrid dye (which consists of both negative and positive charges) at relatively basic pH, whereas EY has an anionic functional group, and MB has cationic functional group. Scheme 1 depicts the chemical structures of the three dye molecules used in this study.

The hybrid dye, RhB exhibited the highest visible light hydrogen evolution compared to EY or MB dyes. Figure 7 depicts the amount of H₂ evolved during the visible light water splitting using three different dyes and the non-doped mesoporous TiO₂ photocatalyst. The yields of hydrogen were found to be 15.1 μ mole H₂/g for RhB sensitized TiO₂; 8 μ mole H₂/g with EY sensitized TiO₂, and 3 μ mole H₂/g of TiO₂ for MB sensitized TiO₂. Adsorption studies of these three dyes were carried out in the presence of TEOA. The amount of RhB, EY, and MB adsorbed were found to be 1.12, 0.43, and 3.83 μ mole/g respectively.

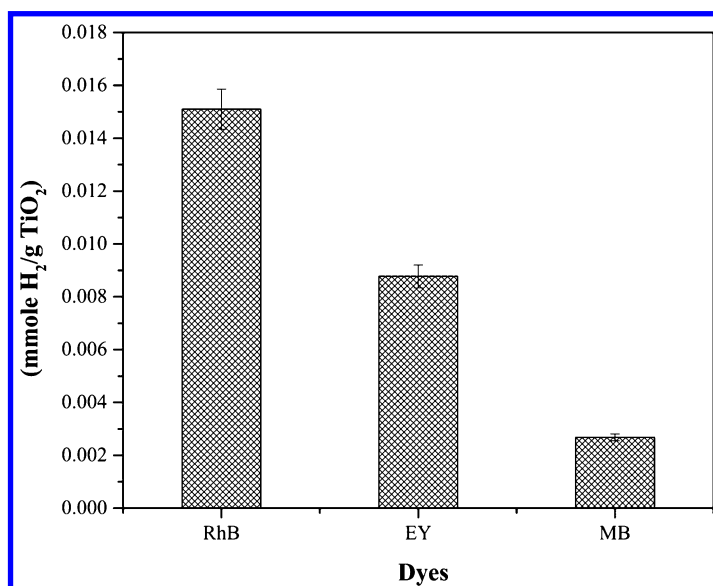


Figure 7. H₂ evolution from dye-sensitized mesoporous titania. RhB, EY, and MB refers rhodamine B, eosin Y, and methylene blue respectively.

Even though MB adsorbed three times higher than RhB, the MB sensitized TiO_2 photocatalyst showed the least activity. It has been suggested that MB tends to aggregate and form multilayers (47). This leads to the formation of an insulation layer that slows the rate of electron injection to titania. This is why, MB-sensitized TiO_2 shows lower activity. The lower activity of EY-sensitized system in comparison to the RhB sensitized system may be explained by the lower amount of EY adsorbed onto mesoporous TiO_2 . Therefore, RhB dye was explored further for visible light hydrogen evolution using the metal doped TiO_2 materials.

The following section will present the H_2 evolution results using these catalysts which will be followed by discussion to understand the trends observed in the activities of hydrogen. Figure 8 shows the visible light hydrogen evolution activity of all the mesoporous material sensitized by RhB. The photocatalytic activity is found to decrease in the order $\text{Meso-Ni-TiO}_2 \sim \text{Meso-TiO}_2 \gg \text{Meso-Zn-TiO}_2 > \text{Meso-Co-TiO}_2$.

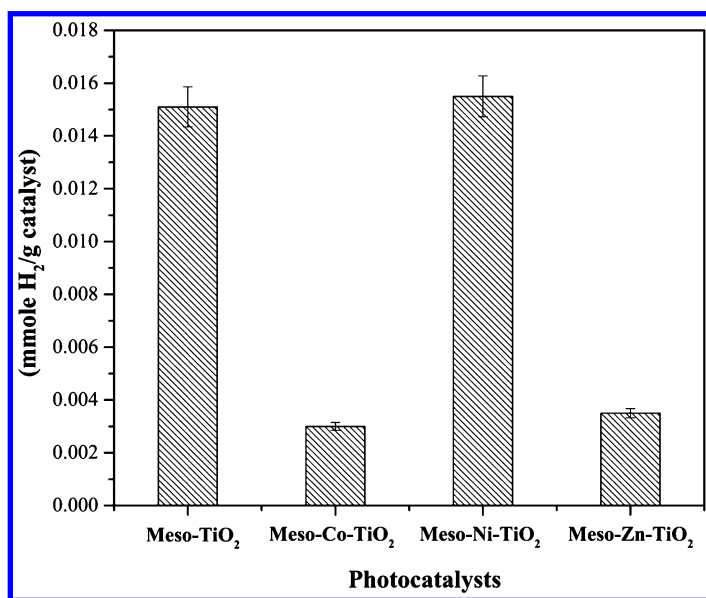


Figure 8. H_2 evolution from doped and non-doped mesoporous titania using RhB dye.

The activity of the photocatalysts depend on a number of properties such as crystallinity, crystallite size, surface area, surface hydroxyl groups, porosity, and amount of dye adsorbed. In dye-sensitized photocatalytic systems, the adsorption of dyes is a prerequisite. Efficient electron transport from the dye to the photocatalyst takes places, if the dyes are adsorbed effectively on the surface (48). Table 2 shows the amount of RhB adsorbed in the presence of TEOA

over the mesoporous materials. It seems that the amount of RhB adsorbed is relatively low for Meso-Co-TiO₂ and Meso-Ni-TiO₂ and higher for Meso-TiO₂ and Meso-Zn-TiO₂. The surface areas and the pore volumes of the mesoporous materials are similar. The amount of RhB adsorbed over Meso-Zn-TiO₂ may be higher due to the relatively lower pore diameter that prevents desorption of the dye suggesting that there is an optimal pore size to retain the dyes. Also, the pzc of a suspension containing TEOA and the photocatalyst was evaluated. The values of pzc were found to be relatively constant at – 30 mV for all the suspensions. This suggests that the surface charge of the mesoporous materials are similar. The density of surface hydroxyl groups was found to be twice as high as the doped-TiO₂ materials. Thus, the adsorbed of RhB may be favored on the non-doped mesoporous material through H-bonding interactions between them.

Table 2. Amount of Rhodamine B Adsorbed in the Presence of TEOA and the Hydrogen Yields

<i>Samples</i>	<i>Amount adsorbed</i> ($\mu\text{mol/g}$)	<i>H₂ yield</i> ($\mu\text{mole/g}_{\text{catalyst}}$)
Meso-TiO ₂	1.12	15.1
Meso-Co-TiO ₂	0.74	3.00
Meso-Ni-TiO ₂	0.90	15.5
Meso-Zn-TiO ₂	1.40	3.50

The amount of hydrogen evolved as indicated in Table 2 seems to suggest no correlation with the amount of RhB adsorbed. Thus, we have to examine other factors that may affect the photocatalytic activity. The crystallinity and the crystallite size of titania are all similar; hence, these cannot be reasons for differences in activity. The surface areas of the mesoporous materials lie in a narrow range and this may not account for the differences in photocatalytic activities. In comparing the activity, the photocatalytic activity of Meso-Zn-TiO₂ and Meso-Co-TiO₂ are significantly lower. The powder XRD results indicate that the Co²⁺ and Zn²⁺ are doped into the lattice of titania (perhaps in interstitial positions because of the relatively large size difference in the ionic radii). Doping of TiO₂ with alervalent cations of lower valence is expected to decrease the rate of hydrogen production because of a reduction in the capacity of the space charge region to separate the electron-hole pair (49). A similar mechanism may be in operation here with the dopant ions (Co²⁺ and Zn²⁺) in the bulk serving as electron trap centers. Thus, Meso-Zn-TiO₂ and Meso-Co-TiO₂ materials show lower activity in comparison to the non-doped TiO₂ material. On the other hand, doping with Ni²⁺, results in the formation of a solid solution, *i.e.*, the Ni²⁺ ions are located on the surface of the mesoporous titania. Although the density of surface hydroxyl groups are modulated by deposition of Ni²⁺ ions, the amount of RhB

adsorbed is similar on Meso-TiO₂ and Meso-Ni-TiO₂. Thus, the Meso-Ni-TiO₂ exhibits similar activity as Meso-TiO₂ and hence doping with Ni²⁺ ions is not detrimental to the production of hydrogen.

Conclusions

The EISA synthesis route was successfully utilized to synthesize the non-doped and metal-doped mesoporous TiO₂ materials. The surface area and the surface hydroxyl groups were found to be similar in all the metal-doped TiO₂ materials, while changes were noticed in the textural properties such as pore sizes. Whole powder pattern fitting suggest that Co²⁺ and Zn²⁺ ions are introduced into the bulk, whereas Ni²⁺ ions are probably located on the surface. The location of the dopant ions has a dramatic effect in photocatalytic evolution of hydrogen using RhB as the sensitizer.

References

1. Kudo, A.; Miseki, Y. Heterogeneous photocatalyst materials for water splitting. *Chem. Soc. Rev.* **2009**, *38*, 253–278.
2. Lewis, N. S.; Nocera, D. G. Powering the planet: Chemical challenges in solar energy utilization. *Proc. Natl. Acad. Sci. U.S.A.* **2006**, *103*, 15729–15735.
3. Maeda, K. Photocatalytic water splitting using semiconductor particles: History and recent developments. *J. Photochem. Photobiol., C* **2011**, *12*, 237–268.
4. Armaroli, N.; Balzani, V. The future of energy supply: Challenges and opportunities. *Angew. Chem., Int. Ed.* **2007**, *46*, 52–66.
5. Hoffmann, M. R.; Scot, M. T.; Wonyong, C.; Detlef, B. W. Environmental Applications of Semiconductor Photocatalysis. *Chem. Rev.* **1995**, *95*, 69–96.
6. Omer, A. M. Energy use and environmental impacts: A general review. *J. Renewable Sustainable Energy* **2009**, *1*, 053101–053130.
7. Archer, D.; Eby, M.; Brovkin, V.; Ridgwell, A.; Cao, L.; Mikolajewicz, U.; Caldeira, K.; Matsumoto, K.; Munhoven, G.; Montenegro, A.; Tokos, K. Atmospheric lifetime of fossil fuel carbon dioxide. *Annu. Rev. Earth Planet. Sci.* **2009**, *37*, 117–134.
8. Armaroli, N.; Balzani, V. The hydrogen issue. *ChemSusChem* **2011**, *4*, 21–36.
9. Winter, M.; Brodd, R. J. What Are batteries, Fuel Cells, and Supercapacitors? *Chem. Rev.* **2004**, *104*, 4245–4270.
10. Daskalaki, V. M.; Antoniadou, M.; Li Puma, G.; Kondarides, D. I.; Lianos, P. Solar Light-Responsive Pt/CdS/TiO₂ Photocatalysts for Hydrogen Production and Simultaneous Degradation of Inorganic or Organic Sacrificial Agents in Wastewater. *Environ. Sci. Technol.* **2010**, *44*, 7200–7205.
11. Štengl, V.; Králová, D. TiO₂/ZnS/CdS nanocomposite for hydrogen evolution and Orange II dye degradation. *Int. J. Photoenergy* **2011**, *2011*, 532578:1–532578:14.

12. Mohamed, R. M.; McKinney, D. L.; Sigmund, W. M. Enhanced nanocatalysts. *Mater. Sci. Eng., R* **2012**, *73*, 1–13.
13. Pelaez, M.; Nolan, N. T.; Pillai, S. C.; Seery, M. K.; Falaras, P.; Kontos, A. G.; Dunlop, P. S. M.; Hamilton, J. W. J.; Byrne, J. A.; O’Shea, K.; Entezari, M. H.; Dionysiou, D. D. A review on the visible light active titanium dioxide photocatalysts for environmental applications. *Appl. Catal., B* **2012**, *125*, 331–349.
14. Leung, D. Y. C.; Fu, X.; Wang, C.; Ni, M.; Leung, M. K. H.; Wang, X.; Fu, X. Hydrogen production over titania-based photocatalysts. *ChemSusChem* **2010**, *3*, 681–694.
15. Reddy, J.; Lalitha, K.; Reddy, P.; Sadanandam, G.; Subrahmanyam, M.; Kumari, V. Fe/TiO₂: A visible light active photocatalyst for the continuous production of hydrogen from water splitting under solar irradiation. *Catal. Lett.* **2014**, *144*, 340–346.
16. Sun, T.; Liu, E.; Fan, J.; Hu, X.; Wu, F.; Hou, W.; Yang, Y.; Kang, L. High photocatalytic activity of hydrogen production from water over Fe doped and Ag deposited anatase TiO₂ catalyst synthesized by solvothermal method. *Chem. Eng. J.* **2013**, *228*, 896–906.
17. Xu, S.; Ng, J.; Zhang, X.; Bai, H.; Sun, D. D. Fabrication and comparison of highly efficient Cu incorporated TiO₂ photocatalyst for hydrogen generation from water. *Int. J. Hydrogen Energy* **2010**, *35*, 5254–5261.
18. Chatterjee, D. Effect of excited state redox properties of dye sensitizers on hydrogen production through photo-splitting of water over TiO₂ photocatalyst. *Catal. Commun.* **2010**, *11*, 336–339.
19. Veikko, U.; Zhang, X.; Peng, T.; Cai, P.; Cheng, G. The synthesis and characterization of dinuclear ruthenium sensitizers and their applications in photocatalytic hydrogen production. *Spectrochim. Acta, Part A* **2013**, *105*, 539–544.
20. Vaneski, A.; Schneider, J.; Susha, A. S.; Rogach, A. L. Colloidal hybrid heterostructures based on II–VI semiconductor nanocrystals for photocatalytic hydrogen generation. *J. Photochem. Photobiol., C* **2014**, *19*, 52–61.
21. Abe, R.; Sayama, K.; Arakawa, H. Efficient hydrogen evolution from aqueous mixture of I[−] and acetonitrile using a merocyanine dye-sensitized Pt/TiO₂ photocatalyst under visible light irradiation. *Chem. Phys. Lett.* **2002**, *362*, 441–444.
22. Jin, Z.; Zhang, X.; Li, Y.; Li, S.; Lu, G. 5.1% Apparent quantum efficiency for stable hydrogen generation over eosin-sensitized CuO/TiO₂ photocatalyst under visible light irradiation. *Catal. Commun.* **2007**, *8*, 1267–1273.
23. Chowdhury, P.; Gomaa, H.; Ray, A. K. Factorial design analysis for dye-sensitized hydrogen generation from water. *Int. J. Hydrogen Energy* **2011**, *36*, 13442–13451.
24. Abe, R.; Hara, K.; Sayama, K.; Domen, K.; Arakawa, H. Steady hydrogen evolution from water on Eosin Y-fixed TiO₂ photocatalyst using a silane-coupling reagent under visible light irradiation. *J. Photochem. Photobiol., A* **2000**, *137*, 63–69.

25. Dürr, H.; Boßmann, S.; Beuerlein, A. Biomimetic approaches to the construction of supramolecular catalysts: titanium dioxide—platinum antenna catalysts to reduce water using visible light. *J. Photochem. Photobiol. A* **1993**, *73*, 233–245.
26. Peng, T.; Ke, D.; Cai, P.; Dai, K.; Ma, L.; Zan, L. Influence of different ruthenium(II) bipyridyl complex on the photocatalytic H₂ evolution over TiO₂ nanoparticles with mesostructures. *J. Power Sources* **2008**, *180*, 498–505.
27. Li, J.; E, Y.; Lian, L.; Ma, W. Visible light induced dye-sensitized photocatalytic hydrogen production over platinized TiO₂ derived from decomposition of platinum complex precursor. *Int. J. Hydrogen Energy* **2013**, *38*, 10746–10753.
28. Zheng, H.-Q.; Yong, H.; Ou-Yang, T.; Fan, Y.-T.; Hou, H.-W. A new photosensitive coordination compound [RuL(bpy)₂](PF₆)₂ and its application in photocatalytic H₂ production under the irradiation of visible light. *Int. J. Hydrogen Energy* **2013**, *38*, 12938–12945.
29. Kim, W.; Tachikawa, T.; Majima, T.; Choi, W. Photocatalysis of Dye-Sensitized TiO₂ Nanoparticles with Thin Overcoat of Al₂O₃: Enhanced Activity for H₂ Production and Dechlorination of CCl₄. *J. Phys. Chem. C* **2009**, *113*, 10603–10609.
30. Sreethawong, T.; Junbua, C.; Chavadej, S. Photocatalytic H₂ production from water splitting under visible light irradiation using Eosin Y-sensitized mesoporous-assembled Pt/TiO₂ nanocrystal photocatalyst. *J. Power Sources* **2009**, *190*, 513–524.
31. Liu, X.; Li, Y.; Peng, S.; Lu, G.; Li, S. Modification of TiO₂ with sulfate and phosphate for enhanced eosin Y-sensitized hydrogen evolution under visible light illumination. *Photochem. Photobiol. Sci.* **2013**, *12*, 1903–1910.
32. Cui, E.; Lu, G. Modulating Photogenerated Electron Transfer and Hydrogen Production Rate by Controlling Surface Potential Energy on a Selectively Exposed Pt Facet on Pt/TiO₂ for Enhancing Hydrogen Production. *J. Phys. Chem. C* **2013**, *117*, 26415–26425.
33. Paola, A. D.; Ikeda, S.; Marci, G.; Ohtani, B.; Palmisano, L. Transition metal doped TiO₂: physical properties and photocatalytic behaviour. *Int. J. Photoenergy* **2001**, *3*, 171–176.
34. Sreethawong, T.; Yoshikawa, S. Impact of Pt loading methods over mesoporous-assembled TiO₂-ZrO₂ mixed oxide nanocrystal on photocatalytic dye-sensitized H₂ production activity. *Mater. Res. Bull.* **2012**, *47*, 1385–1395.
35. Kokporka, L.; Onsuratoom, S.; Puangpetch, T.; Chavadej, S. Sol-gel-synthesized mesoporous-assembled TiO₂-ZrO₂ mixed oxide nanocrystals and their photocatalytic sensitized H₂ production activity under visible light irradiation. *Mater. Sci. Semicond. Process.* **2013**, *16*, 667–678.
36. Yan, Z.; Yu, X.; Zhang, Y.; Jia, H.; Sun, Z.; Du, P. Enhanced visible light-driven hydrogen production from water by a noble-metal-free system containing organic dye-sensitized titanium dioxide loaded with nickel hydroxide as the cocatalyst. *Appl Catal., B* **2014**, *160–161*, 173–178.

37. Le, T. T.; Akhtar, M. S.; Park, D. M.; Lee, J. C.; Yang, O. B. Water splitting on Rhodamine-B dye sensitized Co-doped TiO₂ catalyst under visible light. *Appl. Catal., B* **2012**, *111–112*, 397–401.
38. Cassiers, K.; Linssen, T.; Meynen, V.; Van Der Voort, P.; Cool, P.; Vansant, E. F. A new strategy towards ultra stable mesoporous titania with nanosized anatase walls. *Chem. Commun.* **2003**, 1178–1179.
39. Grosso, D.; Cagnol, F.; Soler-Illia, G.; Crepaldi, E.; Amenitsch, H.; Brunet-Bruneau, A.; Bourgeois, A.; Sanchez, C. Fundamentals of mesostructuring through evaporation-induced self-assembly. *Adv. Funct. Mater.* **2004**, *14*, 309–322.
40. Choi, J.; Park, H.; Hoffmann, M. R. Effects of Single Metal-Ion Doping on the Visible-Light Photoreactivity of TiO₂. *J. Phys. Chem. C* **2010**, *114*, 783–792.
41. Hongo, T.; Yamazaki, A. Thermal influence on the structure and photocatalytic activity of mesoporous titania consisting of TiO₂(B). *Microporous Mesoporous Mater.* **2011**, *142*, 316–321.
42. Lin, Y.-C.; Liu, S.-H.; Syu, H.-R.; Ho, T.-H. Synthesis, characterization and photocatalytic performance of self-assembled mesoporous TiO₂ nanoparticles. *Spectrochim. Acta, Part A* **2012**, *95*, 300–304.
43. Ranjit, K. T.; Viswanathan, B. Photocatalytic reduction of nitrite and nitrate ions over doped TiO₂ catalysts. *J. Photochem. Photobiol., A* **1997**, *107*, 215–220.
44. Sing, K. S. W.; Everett, D. H.; Haul, R. A. W.; Moscou, L.; Pierotti, R. A.; Rouquerol, J.; Siemieniewska, T. Reporting physisorption data for gas/solid systems with special reference to the determination of surface area and porosity. *Pure Appl. Chem.* **1985**, *57*, 603–619.
45. Sing, K. The use of nitrogen adsorption for the characterisation of porous materials. *Colloids Surf., A* **2001**, *187–188*, 3–9.
46. Sing, K.; Williams, R. Physisorption Hysteresis Loops and the Characterization of Nanoporous Materials. *Adsorpt. Sci. Technol.* **2004**, *22*, 773–782.
47. Pitigala, P.; Senevirathna, M. K. I.; Perera, V. P. S.; Tennakone, K. Dye-multilayer semiconductor nanostructures. *C. R. Chim.* **2006**, *9*, 605–610.
48. Bubacz, K.; Tryba, B.; Morawski, A. W. The role of adsorption in decomposition of dyes on TiO₂ and N-modified TiO₂ photocatalysts under UV and visible light irradiations. *Mater. Res. Bull.* **2012**, *47*, 3697–3703.
49. Karakitsou, K. E.; Verykios, X. E. Effects of Altervalent Cation Doping of Titania on Its Performance as a Photocatalyst for Water Cleavage. *J. Phys. Chem.* **1993**, *97*, 1184–1189.

Chapter 4

Single Site Metal Ions on the Surface of TiO₂ Nanorods - A Platform for Theoretical and Experimental Investigation

Saravanakumar T. Pillai,¹ Tom Fischer,¹ Tyler T. Clikeman,¹ Jennifer Esbenshade,² Catherine Berdanier,¹ Heather Rohwer,¹ Mark Jastram,¹ Wonjun Kang,¹ Choumini Balasanthiran,¹ Charles S. Spanjers,³ Talgat Inerbaev,⁴ Dmitri S. Kilin,¹ Robert M. Rioux,^{3,5} and James D. Hoefelmeyer^{*,1}

¹Department of Chemistry, University of South Dakota, 414 E. Clark Street, Vermillion, South Dakota 57069

²Department of Chemistry, Messiah College, One College Avenue, Mechanicsburg, Pennsylvania 17055

³Department of Chemistry, The Pennsylvania State University, 165 Fenske Laboratory, University Park, Pennsylvania 16802-4400

⁴Physical and Technical Department, L. N. Gumilyov Eurasian National University, Munaitpasov St. 5, 010008, Astana, Kazakhstan

⁵Department of Chemical Engineering, The Pennsylvania State University, 165 Fenske Laboratory, University Park, Pennsylvania 16802-4400

*E-mail: jhoefelm@usd.edu.

We demonstrate attachment of first-row transition metal ions to the surface of TiO₂ nanorods. The metallated TiO₂ nanorods were characterized with TEM, powder XRD, UV-visible, XAS, XPS, ICP-AES elemental analysis, and energy-dispersive X-ray spectroscopy. The materials can be readily studied using computational methods to provide valuable theoretical insight to the electron structure properties as well as charge-carrier dynamics. The materials are a testbed in which a feedback loop of computational and experimental results could guide the project toward the ultimate goal of creating optimized photocatalysts for solar energy utilization.

Introduction

This proceedings paper is based on the oral presentation having the same title given at the Fall 2013 National Meeting of the American Chemical Society in Indianapolis, IN on September 8, 2013. This paper is an account of the oral presentation and latest developments as of the presentation date. The work spans a period of approximately six years, with no less than five of the contributing authors having been undergraduate students upon making their contributions to the project.

The ultimate motivation for this work is the need to develop low-cost, high-performance materials for solar fuels catalysis (1–3). A well-known strategy for photocatalysis is the use of semiconductor materials (4, 5). Irradiation of a semiconductor with photon energy greater than its bandgap leads to light absorption and formation of a highly delocalized and energetic exciton. The exciton will dissipate energy while the electron and hole become localized. The lowest energy states for the electron and hole are at the surface sites, so charge carriers tend to migrate in random electron hopping events until they reach the surface. At the surface, the electron and hole can be utilized as reducing and oxidizing equivalents in chemical reactions. Thus, photocatalysis can be used to drive endergonic chemical reactions, and is a means to capture light energy and store it in reactive chemical bonds; the prototypical example being splitting of water to hydrogen and oxygen. Along the way, the electron and hole can recombine whereby the energetic state formed as a result of photon absorption becomes lost as light or heat. The recombination mechanism is competitive with surface chemical reactions.

There are a huge range of possible semiconductor materials, and among this set, various limitations may reduce the number of materials for study. Requirements include such factors as abundance/cost, toxicity, stability, match of band-edge potentials to desired electron transfer reactions, and match of bandgap to visible photon energy (6). No single material meets all of the requirements. So, material combinations or modifications that alter the properties of a material (especially at the surface) are methods to overcome the limitations of pure single-phase materials. In our work, we select TiO_2 as a scaffold semiconductor material with the intent to attach components to the surface to enhance its utility as a visible light photocatalyst. TiO_2 is earth abundant and has low toxicity. TiO_2 can be prepared in a wide range of morphology, as much is known about synthetic techniques for high surface area TiO_2 that yield diverse structures such as nanocrystals, ordered mesoporous materials, aerogels, and nanotube arrays (7). The band edge potentials of bulk anatase TiO_2 (anatase is the most abundant polymorph of nano- or high surface area TiO_2 due to the stability of the {101} facet) are approximately +3.0 V for the upper valence band and -0.2 V for the lower conduction band (vs SHE). For comparison, proton reduction occurs at 0.0 V and water oxidation occurs at +1.23 V. Thus the valence band holes are strongly oxidizing and there is large overpotential to drive water oxidation; however, conduction band electrons that relax to the band edge are not strongly reducing. The overpotential for proton reduction is lower than ideal. This was evident in the well-known Fujishima-Honda experiment in which the photoelectrochemical cell consisted of a TiO_2 photoelectrode and a Pt electrode immersed in aqueous

cells (8). Irradiation of the photoelectrode with UV radiation led to bandgap excitation and electron transfer from TiO_2 to Pt through a Cu wire (attached to In-sputtered TiO_2 with Ag paste). The electrochemical potential at the Pt electrode was very close to the potential of the proton reduction half-reaction. Without overpotential to drive the reaction, H_2 evolution was slow. Meanwhile, at the TiO_2 photoelectrode, electron transfer from water to fill electron vacancies led to oxygen evolution. However, the thermodynamically favorable reaction was very slow since the TiO_2 surface is a poor catalyst for electron transfer from water.

Despite its limitations, TiO_2 can be modified in many ways that improve its performance in visible light photocatalysis. An important problem to tackle is the conduction band edge potential. It is well established that quantum confinement occurs in semiconductor nanocrystals with dimension smaller than the Bohr exciton radius (9–11), which is ~1 nm in TiO_2 (12). Sub-nanometer thin anatase TiO_2 ‘nanosheets’ that present {001} facets exhibit greatly blue-shifted UV-vis absorption spectrum indicating larger bandgap (3.8 eV) (13). The valence band edge potential was shifted by +480 mV while the conduction band edge potential was shifted by -120 mV (14). Thus, upon confinement, the conduction band edge potential still does not provide large overpotential versus SHE. The ‘nanosheets’ are oxide rich and have net negative charge.

There has been much effort in the preparation of doped TiO_2 materials, including nanoparticles. Doping with non-metals has been reported to improve visible light absorption. Dopants include F, N, C, S, and P that replace O atoms in the crystal (15). Non-metal dopants introduce new states in the bandgap region of pure TiO_2 . The states tend to appear near to the valence band. Doping with metal ions also leads to new states in the bandgap region of TiO_2 . The energy of the new states is characteristic of the dopant ion introduced into the crystal. A theoretical study of first-row transition metal ion dopants in TiO_2 shows the appearance of new metal 3d states that appear near the conduction band for vanadium (early in the metal series) and the new states fall lower in energy moving toward the late first-row metals (16). Perhaps non-intuitively, new states associated with Ni-doping appear in the valence band.

Interestingly, the charge carriers in photoexcited TiO_2 tend to migrate to specific facets. In rutile, holes apparently migrate selectively to the (011) facet, as evidenced by deposition of PbO_2 on those surfaces; whereas electrons apparently migrate selectively to the (110) facet, as evidenced by deposition of Pt on those surfaces (17). A similar phenomenon was observed in anatase crystallites in which holes migrated to the (001) facet while electrons migrated to the (101) facet (18). Potentially shape selection in TiO_2 nanocrystals could be used to manage charge carriers in photocatalysis.

There has been a vast amount of investigation to make improvements based on the TiO_2 based photoelectrochemical cell and a huge range of new materials and combinations has been investigated. The pursuit of new solar fuels catalyst materials that can potentially absorb sunlight and efficiently catalyze formation of fuel/oxidizer combinations is alluring and is often called artificial photosynthesis due to its similarities to natural photosynthesis. Photo-induced electron transfer in artificial photosynthesis systems was recently summarized (19). Schemes include molecular triad, dye-sensitized solar cell (DSSC), semiconductor photocatalyst,

coupled DSSC to water oxidation and proton reduction catalyst, and tandem water-splitting cell. Sensitization has been a major strategy to improve visible light absorption of TiO_2 .

A seminal work in coupling sensitized semiconductor particles with catalysts was the colloidal photocatalyst system design in Prof. Gratzel's laboratory. The colloidal photocatalyst consisted of Ru(IV)-doped TiO_2 with adsorbed Pt particles and $\text{Ru}(\text{bpy})_3^{2+}$ sensitizer (20). The doping level of Ru(IV) (as RuO_2) was 0.1%, which presumably led to distribution of Ru(IV) within the particle and on the surface. The TiO_2 particles were anatase with diameter of $\sim 47\text{ nm}$. At the low doping level Ru(IV) were most likely isolated sites despite the description of ' RuO_2 ' domains in the system. The Ru(IV)-doped TiO_2 particles were added to a dispersion of colloidal platinum and sonicated for several minutes. The colloidal Pt/ RuO_2 - TiO_2 particles were subjected to UV irradiation. Evolution of H_2 and O_2 in the expected stoichiometry was observed. The UV photons induced bandgap excitation of the semiconductor, followed by electron transfer from the TiO_2 conduction band to Pt and from Ru(IV) to the TiO_2 valence band. The Pt domain catalyzed H_2 evolution while the highly oxidized Ru sites catalyzed O_2 evolution. The reaction was completely suppressed with a 400nm cutoff filter. Visible light photocatalysis was demonstrated in the presence of sensitizer and electron relay, $\text{Ru}(\text{bpy})_3^{2+}$ derivatives and methylviologen, respectively. With the cutoff filter in place, irradiation with the Xe lamp led to water splitting with quantum yield of H_2 near 5%. Later studies in which the Pt/ RuO_2 - TiO_2 catalyst was prepared via irradiation of aqueous colloidal (20nm) TiO_2 in the presence of RuO_4 and H_2PtCl_6 showed high activity for water splitting under bandgap excitation; however, the quantum yield of 5% under visible light irradiation in the presence of sensitizer and electron relay was never again matched (21). More importantly, the mechanism of Pt/ RuO_2 - TiO_2 catalyst in the presence of $\text{Ru}(\text{bpy})_3^{2+}$ and methylviologen (MV^{2+}) was demonstrated. The MV^{2+} relay accepts an electron from the excited sensitizer, and then donates the electron to Pt or the TiO_2 conduction band. The oxidized $\text{Ru}(\text{bpy})_3^{3+}$ species was found to be a selective electron acceptor for RuO_2 .

More recently, heteronanoocrystals can be prepared with increasingly reliable methods (22–27). In the Gratzel colloidal photocatalyst, a potential issue is whether there is a robust interface between the sensitized TiO_2 particle and the catalyst particles. In well-defined heteronanoocrystals this issue is resolved. While the number of examples of heteronanoocrystals is rapidly increasing with greater number of materials combinations, we decided to focus on semiconductor nanorods with metal nanoparticles attached to the tips. It is known that in nanorods charge carriers can migrate longitudinally with low energy loss. This directional conductivity might be important in charge separation. A second reason for the choice to use tipped nanorod morphology lies in the desire to ultimately produce a hierarchical photocatalyst system based on self-assembly. We have proposed to develop block-copolymer/heteronanoocrystal nanocomposite materials in which nanorods would serve as membrane-spanning units (28). In such a system, several advantages were envisioned: separation of reducing and oxidizing catalyst sites on opposite sides of a membrane, potential to favorably utilize a pH gradient across the membrane, self-assembly of nanoscale components, well-defined

heteronanocrystals, and possible scale-up. In this grand artificial photosynthesis scheme, a sensitized catalyst-tipped semiconductor nanorod heteronanocrystal could mimic the roles of photosystem II in natural photosynthesis.

There are several examples of selective nucleation of nanocrystals on semiconductor nanorod tips. The first demonstration of the concept was selective nucleation of Au on the tips of CdSe nanorods (29). The high surface free energy of the nanorod tips, and other defect sites on the nanorod initiate nucleation of the metal, which is followed by nanocrystal growth. Furthermore, prolonged heating of the dumbbell structure led to intra-rod Ostwald ripening and formation of one-sided metal-tipped Au-CdSe nanorods (30). Since the initial discovery of selective nucleation of nanocrystals on nanorod tips, other groups have reproduced the phenomenon. Co-TiO₂ dumbbell structures were synthesized upon decomposition of Co₂(CO)₈ in the presence of TiO₂ nanorods (31). The interface between Co and TiO₂ was present in more than one epitaxial configuration. Selective nucleation of Pt, Pd, or PtPd bimetallic particles on CdS nanorods led to dumbbell structures (32). The growth of Co on the tips of CdSe nanorods was demonstrated (33).

In order to prepare catalyst-tipped semiconductor nanorod heteronanocrystal based on TiO₂, it was imperative to learn to prepare rod-shaped TiO₂ nanocrystals. A variety of procedures can be found in the literature (34–40). Generally, rod-shape TiO₂ nanocrystals are relatively straightforward to prepare, and reported procedures are reproducible. The most common phase is *anatase*, with elongation along the *c*-axis that is clearly observed in transmission electron micrographs and powder X-ray diffraction data. The nanocrystals are typically stabilized with fatty acid molecules that strongly passivate the {101} facets and contribute to the anisotropy during nanocrystal growth. The nanocrystals disperse readily in non-polar solvents, and the dispersions can be stable for years. UV-visible absorption is strong in the UV region, with the onset of absorption blue-shifted by ~100 nm compared to the bulk solid.

Results and Discussion

We initially prepared rod-shape anatase TiO₂ according to the method reported by the Li group (35). In the synthesis, Ti(OBu)₄ and linoleic acid are combined in cyclohexane at elevated temperature and pressure in a Parr digestion bomb to yield the linoleic acid stabilized nanocrystal product that can be easily purified with precipitation/redispersion steps. The linoleic acid stabilized nanocrystals are susceptible to photodecomposition, as dispersions in hexanes left in ambient light precipitated from solution. The reaction yielded ~100 mg batches of nanocrystals; however, after size-selective precipitation to obtain uniform high-aspect ratio nanocrystals, the mass was typically ~70 mg. The *anatase* nanocrystals were elongated along the *c*-axis and presented {101} facets. We were able to use a 120 kV TEM to resolve the {101} and {004} lattice fringes and index individual nanocrystals.

We attempted alternate procedures to obtain rod shape TiO₂ nanocrystals. Starting from much more reactive TiCl₄ and oleylamine, it is possible to obtain

anatase nanorods (36). In the literature, it is reported that the nanorods grow along the *c*-axis, as is commonly observed for other rod-shape *anatase* samples; however, on close inspection of the authors' HRTEM data, it is clear that the nanorods actually grow along the *a*-axis. We are able to reproduce this observation. Interestingly, the reactive combination of TiCl₄ and oleylamine at different ratio leads to *brookite* phase rod-shape TiO₂ nanocrystals that grow along the *c*-axis (37). We were able to reproduce this observation in our laboratory as well.

While we have built-up significant expertise, and inventory, on synthesis of TiO₂ nanorods, it was apparent that we could benefit from a simpler synthesis route and larger scale. The procedure reported by Hyeon works quite well (40). We are able to reproduce the oleic acid stabilized rod shape *anatase* TiO₂ nanocrystal with [001] growth in 10 gram scale. The unprocessed product consists of broad distribution of aspect ratio nanocrystals. Workup in our lab yields a small fraction (5-10%) of nanocrystals with aspect ratio of 1-2, a small fraction (10-20%) of nanocrystals with intermediate aspect ratio of 2-6, and a large fraction (~70%) of high aspect ratio nanorods. The dispersions of oleic acid stabilized nanocrystals in hexanes are stable indefinitely, even in ambient light. So, the oleic acid stabilizer is more stable than the linoleic acid stabilizer. The latter can oxidize more easily due to the position of a -CH₂- between two C=C bonds that can lead to delocalized radicals over five carbon atoms. Due to the large scale, ease of synthesis (only two reactants), good reproducibility, and good stability of the sample, we prefer to use the method developed by Hyeon.

Over the course of our work on rod shaped TiO₂ nanocrystals, we've checked several procedures in the literature and confirmed their reproducibility. We prepared *anatase* with [001] growth direction using linoleic acid or oleic acid stabilizer, *anatase* with [100] growth direction using oleylamine stabilizer, *brookite* with [001] growth direction using oleylamine stabilizer, have learned to scale up from 10s of mg to 10 grams of nanocrystal product, and have learned how to perform ligand exchange reactions. The number of cycles of precipitation/redispersion that a sample can be subjected to depends on the affinity of the ligand to the nanocrystal surface. We note that oleylamine stabilized TiO₂ was much less stable than oleic acid stabilized TiO₂, such that the former could typically survive only three cycles before irreversible precipitation while the latter could survive six cycles. After enough successive cycles, it is presumed that most of the stabilizing ligand is removed (34). The samples can be redispersed if the ligand is added again. Alternatively, a new stabilizing ligand could be added, which is a method for ligand exchange. In particular, phosphonates and -enediols bind very tightly to the TiO₂ surface.

Following the preparation of TiO₂ nanorods, we began experiments to observe whether selective nucleation of metals on the tips occurs. Our initial experiment was to decompose Pt(acac)₂ in the presence of the linoleic acid stabilized TiO₂ nanorods. We performed the reaction with temperature, reaction time, and UV light as variables. While Pt nanoparticles formed quite readily in the experiments, there was no evidence for selective nucleation. We observed dispersions of Pt and TiO₂ nanocrystals together. The variables of the experiment only gave varying morphology and size of the Pt nanoparticles.

After this setback, we were inspired by the report of selective nucleation of Co on the tips of TiO_2 nanorods (31), and aimed to reproduce the result. It was our hope to utilize the Co- TiO_2 heteronanocrystal as a photocatalyst. In the reported experiment $\text{Co}_2(\text{CO})_8$ was decomposed in the presence of oleylamine stabilized TiO_2 nanorods formed from TiCl_4 . We performed the experiment numerous times and were unable to observe any nucleation of Co particles on the surface of TiO_2 . Upon varying conditions of the reaction, we could observe three outcomes: precipitation of cobalt metal, solution nucleation of cobalt nanoparticles not attached to TiO_2 , or formation of blue dispersions. The blue color suggested the presence of tetrahedral Co^{2+} and we observed that the blue color was always found with the colloid. That is, if the colloid was precipitated from solution the precipitate was blue (no color in the supernatant), and if the colloid was redispersed the dispersion was blue. The result was reproduced multiple times in the lab, and we believed the material was a surface modified TiO_2 nanocrystal with Co^{2+} ions attached to the surface.

We followed up with careful observation and analysis of the sample in order to fully understand the material. First, we established a mass balance of cobalt in the reaction based on the amount of $\text{Co}_2(\text{CO})_8$ injected. After the reaction, we observed a black precipitate and a blue reaction mixture. The precipitate was separated, dried, and identified as amorphous cobalt according to powder X-ray diffraction. Its mass accounted for half of the cobalt injected into the reaction. The remaining blue reaction mixture was subjected to precipitation/redispersion cycles until the supernatant was colorless (2 or 3 cycles sufficed). The supernatant was pink initially, suggesting octahedral Co^{2+} as molecular species. The precipitate was pale blue in color and readily redispersed in hexanes, suggesting a nanocrystal product that retained a significant amount of cobalt. Energy-dispersive X-ray spectroscopy and elemental analysis of the sample indicated ~7% cobalt by weight, which accounted for ~25% of the total cobalt added. The striking feature of the sample was its blue color. This is in stark contrast to the coloration of TiO_2 samples doped with Co^{2+} that appear light brown or tan in color (41, 42). UV-vis spectra show broad absorbance feature from ~500-650 nm and very much resembled data reported for cobalt-doped ZnO nanocrystals (43). Interestingly, the cobalt-doped ZnO sample possessed both internal and surface dopant sites and presented broad spectroscopic features. Upon growth of a ZnO shell that entombed all cobalt dopants in a forced tetrahedral geometry, the spectroscopic features became sharper. The UV-vis data from the cobalt modified TiO_2 sample had broad absorbance features and suggested surface cobalt species.

It had been reported that surface cobalt could be removed from cobalt-doped TiO_2 nanocrystals (42). The procedure led exclusively to cobalt atoms located within the nanocrystal with identical geometry. The protocol was to extract with trioctylphosphine oxide at 90°C for 1 hour to remove all surface cobalt species. For AOT capped TiO_2 nanocrystals (AOT = sodium bis(2-ethylhexyl) sulfosuccinate), the procedure achieved complete removal of surface cobalt. However, with our oleylamine stabilized Co- TiO_2 , the procedure was ineffective for removal of surface cobalt. We subjected the material to harsh treatment with excess trioctylphosphine oxide at 250°C for 14 hours, and found ~70% of the cobalt was removed while the remaining nanocrystal material was tan in color.

(suggesting internal cobalt). We had to determine whether this internal cobalt was already present in the sample before the trioctylphosphine procedure or if the procedure actually led to migration of cobalt from the surface to within the nanocrystal. To this end, we treated a new sample of the Co-TiO₂ nanorods with dimethylglyoxime (DMG), which is well-known to form a stable tetradentate macrocycle with cobalt ion (44). After mixing DMG with the Co-TiO₂ for 10 minutes at room temperature, it was found that all of the cobalt was removed from the nanocrystals. This result provides evidence that our synthetic method led to exclusively surface cobalt and that the trioctylphosphine protocol under forcing conditions actually led to diffusion of cobalt atoms into the nanocrystal.

TEM and powder XRD data of the Co-TiO₂ samples showed that the crystal phase was *brookite* and that the crystal was anisotropic (elongated along the *c*-axis). TEM specifically showed the presence of rod shape nanocrystals with fairly uniform dimensions and no evidence of other phases. There was no evidence of any crystalline phases due to cobalt, which is consistent with atomically dispersed species.

In order to provide further evidence that the cobalt was indeed on the surface of the nanocrystal and to learn more details about its geometry and electronic structure, we performed X-ray absorption spectroscopy (XAS) and X-ray photoelectron spectroscopy (XPS). The XAS data for several standards (cobalt metal, CoO, Co₃O₄, CoAl₂O₄) and the Co-TiO₂ sample were compared. At the Co L_{III}-edge energy the Co-TiO₂ gave an absorption edge consistent with Co²⁺ oxidation state. A pre-edge feature was located that was a useful diagnostic of the cobalt geometry. In tetrahedral cobalt (CoAl₂O₄) the pre-edge feature is intense whereas in octahedral environments (CoO) this feature has much lower intensity due to selection rules. The pre-edge feature of the Co-TiO₂ sample had intensity inconsistent with only tetrahedral or octahedral species, and its intensity was best modeled as arising from roughly equal parts tetrahedral and octahedral cobalt. Consistent with this finding, modeling of the EXAFS data showed an average coordination number of 5 that is best explained by equal contribution of tetrahedral and octahedral cobalt. Furthermore, the EXAFS data showed no long-range back-scattering interactions that strongly suggest a disordered environment about cobalt that is most consistent with cobalt atoms located on the surface of the nanocrystal. For example cobalt phosphate thin films show no long-range order whereas bulk cobalt phosphate does (45). The XPS data at the Co 2p binding energies was consistent with Co²⁺ oxidation state. Also consistent with this assignment were the presence of strong shake-up peaks. Furthermore, the energy separation of the Co 2p_{3/2} and Co 2p_{1/2} peaks (~5.3 eV) was intermediate in comparison with values typical for tetrahedral (5.0 eV) and octahedral (6.0 eV) complexes that suggested contributions from both geometries.

With the assignment of Co²⁺ firmly established based on spectroscopic data, an explanation as to the mechanism of its formation was required since the starting precursor was a source of Co⁰. The information may be found in Cotton and Wilkinson's text (46). It is known that in the presence of Lewis bases, the Co₂(CO)₈ cluster undergoes a heterolytic cleavage of the Co-Co bond to yield Co(CO)₄⁻ and CoL₅⁺ complexes. The tetracarbonylcobaltate(-1) complex is stable; however, it likely undergoes oxidative addition to form additional Co⁺

species. The Co^+ complexes tend to be unstable and undergo disproportionation to equal equivalents of Co^0 and Co^{2+} (47–49). These points are important and consistent with our observation of ~50% cobalt as metallic precipitate and ~50% as Co^{2+} (roughly equally distributed between free species in solution and ions attached to the TiO_2 nanocrystals). Furthermore, this mechanism presents an alternative to the selective nucleation mechanism that is required to form heteronanoocrystals. Our work was recently reported in a full paper (50).

The Co^{2+} decorated *brookite* TiO_2 nanocrystals were studied as visible light photocatalyst for the decomposition of 5,8-dihydroxynaphthoquinone. A sample of *brookite* TiO_2 nanocrystals was studied for comparison. In the presence of both samples, we observed reduction in the absorbance of 5,8-dihydroxynaphthoquinone with time. The Co^{2+} modified sample showed initial turnover frequency of $2.1 \pm 0.2 \times 10^{-2} \text{ s}^{-1}$ versus $1.3 \pm 0.1 \times 10^{-3} \text{ s}^{-1}$ for the *brookite* sample. The results were encouraging, but somewhat surprising to us. While TiO_2 is an active photocatalyst for visible light decomposition of dyes, it has been shown that activity was greatly lowered in the presence of aqueous metal ions (51). In the dye-sensitized scheme, visible light excites the dye, an excited electron is injected to the conduction band of TiO_2 that subsequently combines with O_2 to generate reactive oxygen species (i.e., superoxide), and these oxidize the dye. It was concluded that metal ions were effective scavengers of conduction band electrons that presented a competitive pathway to the formation of reactive oxygen species.

While we have found a new way to attach Co^{2+} to the surface of *brookite* TiO_2 nanocrystals and found the material could be an active visible light photocatalyst, we desire to expand the scope and utility of the system. It was highly desirable to move away from the use of TiCl_4 and $\text{Co}_2(\text{CO})_8$ in favor of a simpler synthesis, to scale up the yield of material, and to expand to a broader set of metal ions that could be attached to the surface of the TiO_2 nanocrystal. We began by borrowing the large-scale synthesis of rod-shaped *anatase* TiO_2 nanocrystals reported in the literature (40). As mentioned earlier in the paper, this method works quite well. With this material, we were able to develop a new method for the attachment of first-row transition metal ions to the surface of the TiO_2 nanocrystals (52). The method uses inexpensive metal chloride hydrates as precursors. In the presence of oleylamine, the metal ions are transferred in the non-polar synthesis medium and adsorb to the surface of the TiO_2 nanocrystals. The reaction is self-limiting, and the surface of the nanocrystal could be titrated. The method is applicable for the first row transition metal ions Cr^{3+} , Mn^{2+} , Fe^{2+} , Co^{2+} , Ni^{2+} , and Cu^{2+} .

Interestingly, a check of the newly derived *anatase* Co^{2+} - TiO_2 sample as catalyst for visible light decomposition of 5,8-dihydroxynaphthoquinone revealed substantially lower activity when compared to the *anatase* TiO_2 sample without adsorbed Co^{2+} ions. This result seems more consistent with previous observations (51), but is inconsistent with our observation of increased activity of *brookite* Co^{2+} - TiO_2 versus *brookite* TiO_2 . One obvious question might be whether the TiO_2 phase is a key in the difference in observations. More broadly and more importantly, our discovery of simple, large-scale self-limiting reactions to attach transition metal ions to the surface of nanocrystals could open new opportunities for investigation.

It became apparent to us that the M^{n+} -TiO₂ system was an excellent platform for computational study, and that we had an opportunity to generate theoretical outputs that could be compared with experimental data. This interaction is highly desirable in that theoretical methods can be improved, deeper understanding of experimental results can be achieved, and predictions may be possible that drive experimental work (ideally in the most fruitful directions). The initial computational models include electronic structure and charge-carrier dynamics in wet *anatase* TiO₂ nanostructures in which one of the surface Ti atoms is replaced with a transition metal (53, 54). Nanostructures of TiO₂ were cleaved from the *anatase* phase structure of titania downloaded from the U.S. Naval Research Laboratory Center for Computational Materials Science database. A simulation cell was established with periodic boundary conditions to construct various 1D and 2D nanostructures. A vacuum layer of 8 Å was added to the simulation cell to prevent spurious interactions between periodic replicas. The surface of TiO₂ was simulated with one monolayer of adsorbed water. This model could be modified to approximately represent the M^{n+} -TiO₂ materials upon replacing one Ti atom at top and bottom surfaces with a metal atom.

We atomistically compute the electron-to-lattice vibration coupling using the response of the excited state transition electron density to nuclear elongations. The electronic states are recalculated for each atomic configuration along molecular dynamics trajectory, produced during the simulation, to compute the “on-the-fly” nonadiabatic couplings between the electronic and nuclear degrees of freedom (55). These couplings determine dissipative transitions between electronic states and enter electron dynamics through solving the relevant Liouville-von-Neumann equation for a reduced density matrix (56). This approach scales well, noticeably reduces the required numerical resources, and substantially speeds up the computational procedure while still maintaining the precision associated with atomistic calculations for photoinduced non-equilibrium states of materials. Our method is justified by convergence of the results with those obtained at higher computational cost by the current state-of-the-art “surface hopping” methodology (57–60).

We focus on charge transfer dynamics, and the effects of inorganic functionalization of the surface. The main observables to explore are rate of charge transfer, direction of charge transfer, rate of charge transfer, and lifetime of charge transfer excitation. Preliminary results were obtained for anatase TiO₂ structures of different dimensionality: 0D (solvated ions, titanium hydroxide) (61), 1D (nanowires, bare and functionalized) (62, 63), 2D (thin films) (54, 64, 65), and 3D bulk (66). Control of charge transfer amount, direction, rate, and lifetime may be achieved through functionalizing different surfaces <100> (54, 64), <001> (65), and <101> (67) with transition metal or lanthanide ions. As an ultimate level of progress our group will explore transition metal clusters on the surface of TiO₂ substrate in the aqueous environment (67).

Being that the computational model is modular, we expect this to be a versatile platform to test various ideas related to the M^{n+} -TiO₂ materials, including effects of concentration of surface metal ions on electronic structure and surface reactions, effects of different metal ions, modeling reaction mechanisms on the surface, and changing atomic geometry of the metal ions. Once these relationships can be

established, it may become possible to compute the properties of new materials combinations to guide experimental work in the development of highly active photocatalyst materials.

Conclusions

Motivated to develop new low-cost, high performance nanostructured materials for solar fuels catalysis, new methods were discovered to attach transition metal ions to the surface of nanocrystals. The latest synthetic methodology could potentially allow a wide range of new materials to be prepared. Computational methods are being utilized in order to understand the electronic structure and charge-carrier dynamics in the M^{n+} -TiO₂ nanomaterials.

Acknowledgments

This work was supported by the National Science Foundation (CHE-0840507, CHE-0722632, CHE-0213320, EPS-0903804, DGE-0903685) and by the U.S. Department of Energy under Contract Nos. DE-FG02-08ER64624, DE-EE00000270, DE-AC02-05CH11231, and allocation Awards 85213 and 86185 “Computational Modeling of Photocatalysis and Photoinduced Charge Transfer Dynamics on Surfaces”. Portions of this research (preparation of TiO₂ nanorods and selective nucleation experiments; STP, TF, TTC, JE, CB, and JDH) were conducted at the Center for Nanophase Materials Sciences, which is a DOE Office of Science User Facility. Beamline X19A is supported, in part, by US DOE Grant No. DE-FG02-05ER15688. CSS acknowledges the National Science Foundation Graduate Research Fellowship under Grant No. DGE-070756 and RMR acknowledges the Air Force Office of Scientific Research (AFOSR, No. FA9550-12-1-0204) for financial support of this research. The authors acknowledge computational resources of USD High Performance computational facilities cosponsored by South Dakota IDeA Networks of Biomedical Research Excellence NIH 2 P20 RR016479 and operated by Douglas Jennewein.

References

1. Eisenberg, R.; Nocera, D. G. *Inorg. Chem.* **2005**, *44*, 6799–6801.
2. Lewis, N. S.; Nocera, D. G. *Proc. Natl. Acad. Sci. U.S.A.* **2006**, *103*, 15729–15735.
3. Nocera, D. G. *Daedalus* **2006**, 112–115.
4. Chen, X.; Shen, S.; Guo, L.; Mao, S. S. *Chem. Rev.* **2010**, *110*, 6503–6570.
5. Di Valentin, C.; Selloni, A. *J. Phys. Chem. Lett.* **2011**, *2*, 2223–2228.
6. Kudo, A.; Miseki, Y. *Chem. Soc. Rev.* **2009**, *38*, 253–278.
7. Chen, X.; Mao, S. S. *Chem. Rev.* **2007**, *107*, 2891–2959.
8. Fujishima, A.; Honda, K. *Nature* **1972**, *238*, 37–38.
9. Brus, L. E. *J. Chem. Phys.* **1983**, *79*, 5566–5571.
10. Brus, L. E. *J. Chem. Phys.* **1984**, *80*, 4403–4409.
11. Brus, L. E. *J. Chem. Phys.* **1986**, *90*, 2555–2560.

12. Monticone, S.; Tufeu, R.; Kanaev, A. V.; Scolan, E.; Sanchez, C. *Appl. Surf. Sci.* **2000**, *162*, 565–570.
13. Sasaki, T.; Watanabe, M. *J. Phys. Chem. B* **1997**, *101*, 10159–10161.
14. Sakai, N.; Ebina, Y.; Takada, K.; Sasaki, T. *J. Am. Chem. Soc.* **2004**, *126*, 5851–5858.
15. Asahi, R.; Morikawa, T.; Ohwaki, T.; Aoki, K.; Taga, Y. *Science* **2001**, *293*, 269–271.
16. Umebayashi, T.; Yamaki, T.; Itoh, H.; Asai, K. *J. Phys. Chem. Solids* **2002**, *63*, 1909–1920.
17. Ohno, T.; Sarukawa, K.; Matsumura, M. *New J. Chem.* **2002**, *26*, 1167–1170.
18. Wang, X.; Li, R. G.; Xu, Q.; Han, H. X.; Li, C. *Acta Phys. Chim. Sin.* **2013**, *29*, 1566–1571.
19. McConnell, I.; Li, G.; Brudvig, G. W. *Chem. Biol.* **2010**, *17*, 434–447.
20. Borgarello, E.; Kiwi, J.; Pelizzetti, E.; Visca, M.; Gratzel, M. *Nature* **1981**, *289*, 158–160.
21. Duonghong, D.; Borgarello, E.; Gratzel, M. *J. Am. Chem. Soc.* **1981**, *103*, 4685–4690.
22. Costi, R.; Saunders, A. E.; Banin, U. *Angew. Chem., Int. Ed.* **2010**, *49*, 4878–4897.
23. Cozzoli, P. D.; Pellegrino, T.; Manna, L. *Chem. Soc. Rev.* **2006**, *35*, 1195–1208.
24. Wang, C.; Xu, C.; Zeng, H.; Sun, S. *Adv. Mater.* **2009**, *21*, 3045–3052.
25. Donega, C. D. *Chem. Soc. Rev.* **2011**, *40*, 1512–1546.
26. Carbone, L.; Cozzoli, P. D. *Nano Today* **2010**, *5*, 449–493.
27. Buck, M. R.; Bondi, J. F.; Schaak, R. E. *Nat. Chem.* **2012**, *4*, 37–44.
28. Hoefelmeyer, J. D. In *Solar Photocatalysis*, 1st ed.; Suib, S. L., Ed.; In New and Future Developments in Catalysis; Elsevier: Amsterdam, Netherlands, 2013.
29. Mokari, T.; Rothenberg, E.; Popov, I.; Costi, R.; Banin, U. *Science* **2004**, *304*, 1787–1790.
30. Mokari, T.; Sztrum, C. G.; Salant, A.; Rabani, E.; Banin, U. *Nat. Mater.* **2005**, *4*, 855–863.
31. Casavola, M.; Grillo, V.; Carlino, E.; Giannini, C.; Gozzo, F.; Pinel, E. F.; Garcia, M. A.; Manna, L.; Cingolani, R.; Cozzoli, P. D. *Nano Lett.* **2007**, *7*, 1386–1395.
32. Habas, S. E.; Yang, P.; Mokari, T. *J. Am. Chem. Soc.* **2008**, *130*, 3294–3295.
33. Maynadie, J.; Salant, A.; Falqui, A.; Respaud, M.; Shaviv, E.; Banin, U.; Soulantica, K.; Chaudret, B. *Angew. Chem., Int. Ed.* **2009**, *48*, 1814–1817.
34. Cozzoli, P. D.; Kornowski, A.; Weller, H. *J. Am. Chem. Soc.* **2003**, *125*, 14539–14548.
35. Li, X. L.; Peng, Q.; Yi, J. X.; Wang, X.; Li, Y. *Chem.-Eur. J.* **2006**, *12*, 2383–2391.
36. Seo, J. W.; Jun, Y. W.; Ko, S. J.; Cheon, J. *J. Phys. Chem. B* **2005**, *109*, 5389–5391.
37. Buonsanti, R.; Grillo, V.; Carlino, E.; Giannini, C.; Kipp, T.; Cingolani, R.; Cozzoli, P. D. *J. Am. Chem. Soc.* **2008**, *130*, 11223–11233.

38. Jun, Y. W.; Casula, M. F.; Sim, J. H.; Kim, S. Y.; Cheon, J.; Alivisatos, A. P. *J. Am. Chem. Soc.* **2003**, *125*, 15981–15985.
39. Joo, J.; Kwon, S. G.; Yu, T.; Cho, M.; Lee, J.; Yoon, J.; Hyeon, T. *J. Phys. Chem. B* **2005**, *109*, 15297–15302.
40. Koo, B.; Park, J.; Kim, Y.; Choi, S.-H.; Sung, Y.-E.; Hyeon, T. *J. Phys. Chem. B* **2006**, *110*, 24318–24323.
41. Choi, J.; Park, H.; Hoffman, M. R. *J. Phys. Chem. C* **2010**, *114*, 783–792.
42. Bryan, J. D.; Heald, S. M.; Chambers, S. A.; Gamelin, D. R. *J. Am. Chem. Soc.* **2004**, *126*, 11640–11647.
43. Radovanovic, P. V.; Norberg, N. S.; McNally, K. E.; Gamelin, D. R. *J. Am. Chem. Soc.* **2002**, *124*, 15192–15193.
44. Jameson, D. L.; Grzybowski, J. J.; Hammels, D. E.; Castellano, R. K.; Hoke, M. E.; Freed, K.; Basquill, S.; Mendel, A.; Shoemaker, W. J. *J. Chem. Ed.* **1998**, *75*, 447–450.
45. Kanan, M. W.; Yano, J.; Surendranath, Y.; Dinca, M.; Yachandra, V. K.; Nocera, D. G. *J. Am. Chem. Soc.* **2010**, *132*, 13692–13701.
46. Cotton, F. A.; Wilkinson, G.; Murillo, C. A.; Bochmann, M.; Grimes, R. *Advanced Inorganic Chemistry*; New York: Wiley, 1999; Vol. 5, pp 833–834.
47. Stanghellini, P. L.; Rossetti, R.; Mentasti, E.; Pelizzetti, E. *Inorg. Chim. Acta* **1977**, *25*, 7–14.
48. Stanghellini, P. L.; Rossetti, R.; Mentasti, E.; Pelizzetti, E. *Inorg. Chim. Acta* **1977**, *22*, 19–22.
49. Buriez, O.; Cannes, C.; Nedelev, J.-Y.; Perichon, J. *J. Electroanal. Chem.* **2000**, *495*, 57–61.
50. Kang, W.; Spanjers, C. S.; Rioux, R. M.; Hoefelmeyer, J. D. *J. Mater. Chem. A* **2013**, *1*, 7717–7728.
51. Chen, C.; Li, X.; Ma, W.; Zhao, J.; Hidaka, H.; Serpone, N. *J. Phys. Chem. B* **2002**, *106*, 318–324.
52. Balasanthiran, C.; Hoefelmeyer, J. D. *Chem. Comm.* **2014**, *50*, 5721–5724.
53. Zhang, Y.; Kilin, D. S. *Int. J. Quantum Chem.* **2012**, *112*, 3867–3873.
54. Inerbaev, T.; Hoefelmeyer, J. D.; Kilin, D. S. *J. Phys. Chem. C* **2013**, *117*, 9673–9692.
55. Hammes-Schiffer, S.; Tully, J. C. *J. Chem. Phys.* **1994**, *101*, 4657–4667.
56. Kilin, D. S.; Micha, D. A. *J. Phys. Chem. Lett.* **2010**, *1*, 1073–1077.
57. Tully, J. C. *J. Chem. Phys.* **2012**, *137*, 22A301.
58. Akimov, A. V.; Neukirch, A. J.; Prezhdo, O. V. *Chem. Rev.* **2013**, *113*, 4496–4565.
59. Nelson, T.; Fernandez-Alberti, S.; Roitberg, A. E.; Tretiak, S. *Acc. Chem. Res.* **2014**, *47*, 1155–1164.
60. Fernandez-Alberti, S.; Kleiman, V. D.; Tretiak, S.; Roitberg, A. E. *J. Phys. Chem. A* **2009**, *113*, 7535–7542.
61. Vogel, D. J.; Kilin, D. S. *MRS Proc.* **2014**, *1647*, mrsf13-1647-gg08-07.
62. Huang, S.; Kilin, D. S. *Mol. Phys.* **2013**, *112*, 539–545.
63. Huang, S. P.; Kilin, D. S. *J. Chem. Theory Comput.* **2014**, *10*, 3996–4005.

64. Jensen, S.; Kilin, D. In *Nanotechnology for Sustainable Energy*; He, H., Burghaus, U., Qiao, S., Eds.; ACS Symposium Series 1140; American Chemical Society: Washington, DC, 2013; pp 187–218.
65. Zhang, Y.; Qiu, C.; Kilin, D. S. *Mol. Phys.* **2013**, *112*, 441–452.
66. Huang, S.; Kilin, D. S. *MRS Proc.* **2014**, *1659*, mrsf13-1659-ss06-04.
67. Huang, S.; Inerbaev, T. M.; Kilin, D. S. *J. Phys. Chem. Lett.* **2014**, *5*, 2823–2829.

Chapter 5

Transition Metal-Doped Semiconductor Quantum Dots: Tunable Emission

Vitaly Proshchenko and Yuri Dahnovsky*

Department of Physics and Astronomy/3905, 1000 E. University Avenue,
University of Wyoming, Laramie, Wyoming 82071

*E-mail: yurid@uwy.edu.

In this work we theoretically prove the effect of a dual luminescence discovered by Gamelin and co-workers for CdSe quantum dots (QDs) doped by a Manganese impurity (*Nano Lett.* **2008**, *8*, 1197). In this effect one line corresponds to light emission from CdSe conduction band while the second emission because of the presence of an Mn impurity with the very slow relaxation time of 0.1 – 1.0 ms. The second line disappears for quantum dots with diameters $D \geq 3.3$ nm and therefore, the luminescence becomes tunable by a QD size. Since the oscillator strength for the second line is very small, there is no computational methods and resources that allow for calculations within the traditional approaches. The other reason that makes the computations even more difficult is a high degeneracy of the energy states. In this case one should use ab initio multi-configuration computational methods. To overcome this problem we propose four assumptions where (1) a QD optical gap is independent of an Mn impurity at small concentrations; (2) we combine electronic structure calculations for medium size CdSe QDs with the effective mass calculations for medium and large QD sizes and match them in the medium size region assuming that the optical gap based on assumption 1 is independent of Mn even for larger QDs; (3) we cut an MnSe₄ fragment out of Cd₂₃MnSe₂₄, Cd₃₁MnSe₃₂, and Cd₈₁MnSe₈₂ QDs and check whether an electronic structure of these fragments quantitatively explains a mechanism the

second, slow relaxation emission in the experiments; and (4) the slow luminescence energy is independent of a QD size. We have proved all these assumptions theoretically and found that the critical size of a quantum dot is 3.2 nm (the experimental value is 3.3 nm) and the luminescence energy is 2.3 eV versus the experimental value 2.1-2.2 eV. We also study different QDs doped by Mn. They are CdS, ZnS, and ZnSe. For the slow relaxation line the emission energies are higher for ZnS and CdS QDs while the transition energy is lower for ZnSe quantum dots. We find that for a ZnS QD there is no critical size. Thus such luminescence is not tunable. In addition we predict how this energy depends on the length of an Mn-Se chemical bond. Such a prediction could be useful for CdSe nanocrystals different than Würtzite.

I. Introduction

It has been understood for a long time that materials systems combining the tunability of semiconductors due to their quantum size effects offer the flexibility of physics properties that can be useful to achieve high efficiency performance of solar cells (1–34). Another important feature that can change physics properties of semiconductor nanocrystals combining with the size effects, is doping with transition metal (TM) impurities. TM dopants can be efficient in photovoltaic energy conversion (35–39), nanospintronics and spin-photonics, (40), magneto optical and magneto-electronic properties (41–52), and giant Zeeman effect (53). Photoluminescence properties become unusual if nanocrystals are doped by Mn atoms. In this case one observes dual or single emission, thus tunable, depending on a $\text{Cd}_{n-x}\text{-Mn}_x\text{-Se}_n$ quantum dot (QD) size (54–56). The experiments show that there are two emission lines for small QDs and a single emission line for larger sizes. If two light transitions take place, the luminescence with the lower energy lives much longer than the fast luminescence with a life-time about 0.1–1.0 ms for CdSe nanocrystals (54). The higher energy line has a short life-time within a nanosecond range. For larger sizes the emission life-time is also short, about several nanoseconds. The light emission is schematically shown in Figure 1. The red line stands for the excited state 4T_1 of an Mn atom in a crystals field with T_d symmetry. Two emission lines are shown by the black arrows.

As mentioned above the long-living emission disappears for larger QDs. In this work we explain this effect. The difficulty of a theoretical description is due to small oscillator strengths, that are 10^6 times smaller than for the first emission line. It is practically impossible to calculate oscillator strengths for such a transition. Such a small oscillator strength is because this transition is forbidden by a spin. Nevertheless, the luminescence takes place due to a small spin-orbit interaction as suggested in Refs. (40, 54–56). However there is a way how to provide reliable theoretical description of the effect under study. To do this would require to make some physical assumptions and prove them computationally.

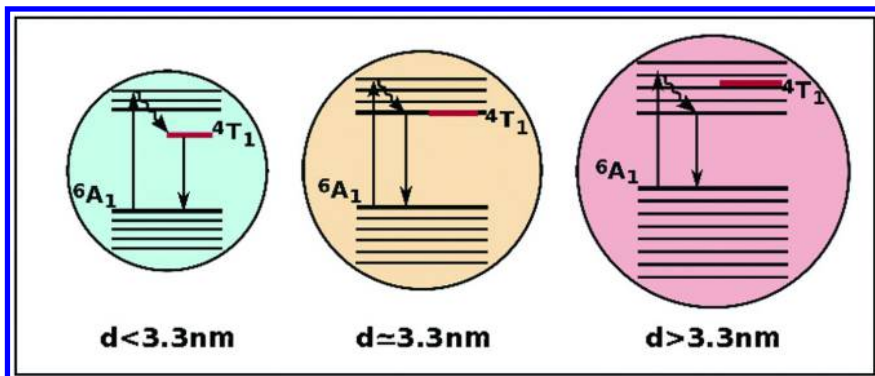


Figure 1. Emission of light for three different size QDs. For $d < 3.3$ nm there are two emission lines, for $d = 3.3$ nm the slow relaxation emission line disappears and for $d > 3.3$ nm there is only one emission line.

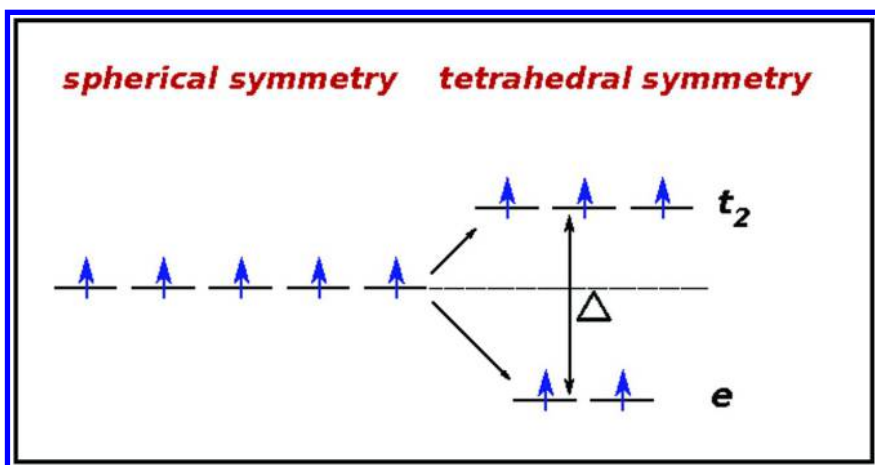


Figure 2. Splitting of the five-fold-degenerate energy levels in the spherical symmetry into two levels due to a tetrahedral ligand field. The upper level is triply degenerate while lower one is doubly degenerate (57).

II. Ligand Field Approach

In an isolated Mn atom in spherical symmetric configuration five electrons are placed on 3d unoccupied orbitals in accordance with the Hund's rule. Thus the total spin of the atom is $S = 5/2$ ($L = 0$) with the multiplicity $M = 6$. As soon as an Mn atom is located in a quantum dot, the spherical symmetry of the orbitals, 6S , descends to the symmetry of a crystal field. In our particular case the

symmetry of a QD is close to the symmetry of the tetrahedron, T_d . Thus, instead of five degenerate levels of a free atom, the five electrons are placed to the twice degenerate level, e ($d_{x^2-y^2}$ and d_{z^2}) and the triply degenerate level t_2 (d_{xy} , d_{yz} , and d_{zx} orbitals) (57). In a tetrahedral environment the e -level is below the t_2 -one as shown in Figure 2.

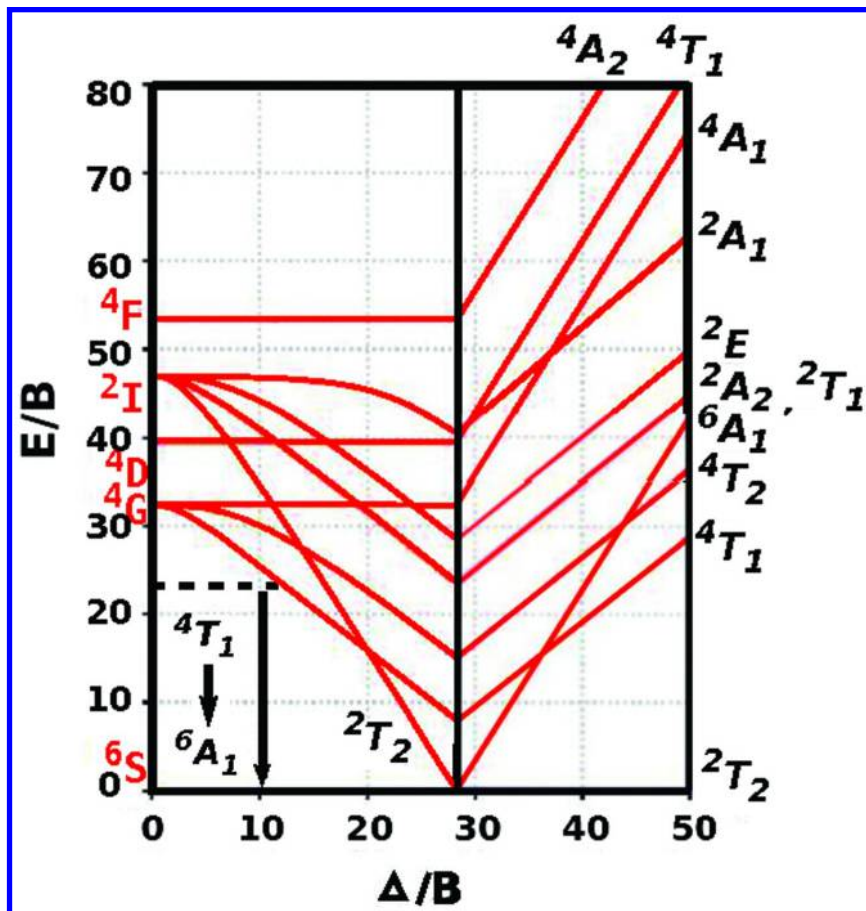


Figure 3. Ligand-field energy level diagram for tetrahedral symmetry. The luminescence takes place from the lowest 4T_1 level to the 6A_1 ground state (for the details see Ref. (57)).

The energy splitting between these two levels is Δ . The symmetry of the ground state can be easily found from the product $(t_2)^3(e)^2$. It is 6A_1 where “6” denotes the multiplicity of the state. The excited state for a tetrahedron configuration is determined by a spin flip where two electrons with the opposite spins are placed at one of the e -degenerate levels with $d_{x^2-y^2}$ or d_{z^2} orbitals. The total configuration of the total electronic state can be found from the product $(t_2)^2(e)^3$ and turns out to be 4T_1 , where “4” stands for the multiplicity of the

state. Then the transition takes place from the excited 4T_1 to the ground 6A_1 state as depicted in Figure 2. This transition is forbidden by spin. However, it is experimentally observed due to small spin-orbit interaction. This is the main reason of a very slow radiation transition. A schematic picture of electronic levels for a molecule with the tetrahedral symmetry with five d-electrons is shown in Figure 3 (see (57)).

It follows from the calculations that there is no exact tetrahedral symmetry for an Mn atom placed in the center of a QD. However, the chemical bond lengths and angles between the bonds are very close to the ones in T_d symmetry. The energy levels are not triply and doubly degenerate any longer but they group in the sets around the two energy levels, t_2 and e with very small differences between the energies in each group.

III. Calculation Plan

In this work we would like to theoretically understand the origin of two luminescence lines taking place in a $\text{Cd}_{n-x}\text{-Mn}_x\text{-Se}_n$ quantum dot (40, 54–56). If one increases a QD size, the second line disappears at the critical diameter and higher, $D > 3.3$ nm. For smaller QDs with two emission lines, one luminescence is very fast while the second emission line takes place with the much longer relaxation time of 0.1–1.0 ms (40, 54–56). The latter luminescence is spin forbidden but still takes place due to the small spin-orbit interaction. For this emission, $h\nu = 2.1 - 2.2$ eV (40, 54–56). The fast luminescence is obviously a transition from the conduction to valence band. As it was suggested by Gamelin and co-workers, this luminescence is determined by a CdSe QD and independent of an Mn impurity at small concentrations (40, 54–56). The second, slow relaxation transition is determined by an Mn atom surrounded by Se atoms composing a tetrahedral fragment with the approximate T_d symmetry. All these assumptions are not obvious and have to be computationally verified. There are computational difficulties in this problem. First, the second emission because of very slow relaxation, has an extremely small oscillator strength, that is 10^6 times smaller than that of for an allowed transition in the dipole approximation. Apparently, such a weak optical transition cannot be calculated even by the standard fast computational methods such as TDDFT, CIS, DFT etc. Second, electronic structure calculations cannot be performed for CdSe QDs doped by Mn atoms with the critical and larger diameters because of large number of atoms in a QD to prove a disappearance of the second, slow emission. Furthermore, an Mn impurity surrounded by Se atoms with tetrahedral symmetry has degenerate electronic states that cannot be calculated in the single configuration approximation. In this particular case one should use multi-configuration computational methods that appear to be very slow and therefore cannot be applied to a QD with the realistic number of atoms. All these difficulties make this problem unrealistic for electronic structure calculations by modern computational methods.

Nevertheless we believe that this computational problem can be resolved if one employs some approximations based on a physical picture of the processes taking place. Thus we propose the following plan for calculations that drastically simplifies computations. This plan includes the following approximations that we verify from the quantum chemical calculations.

Assumption 1

An Mn impurity does not change an optical gap and therefore, one can study only CdSe QD without Mn atoms for optical gap calculations. This assumption allows us to employ a size dependence of optical gap for larger QDs calculated in the effective mass including exciton effect approximation (see e.g. (5, 6, 19, 20)).

Assumption 2

As soon as assumption 1 is proved, we conclude that the slow emission transition is due to the presence of an Mn atom in a CdSe QD. Thus we cut the smallest fragment with an Mn atom out of $\text{Cd}_{n-x}\text{-Mn}_x\text{-Se}_n$ quantum dot as shown in Figure 4.

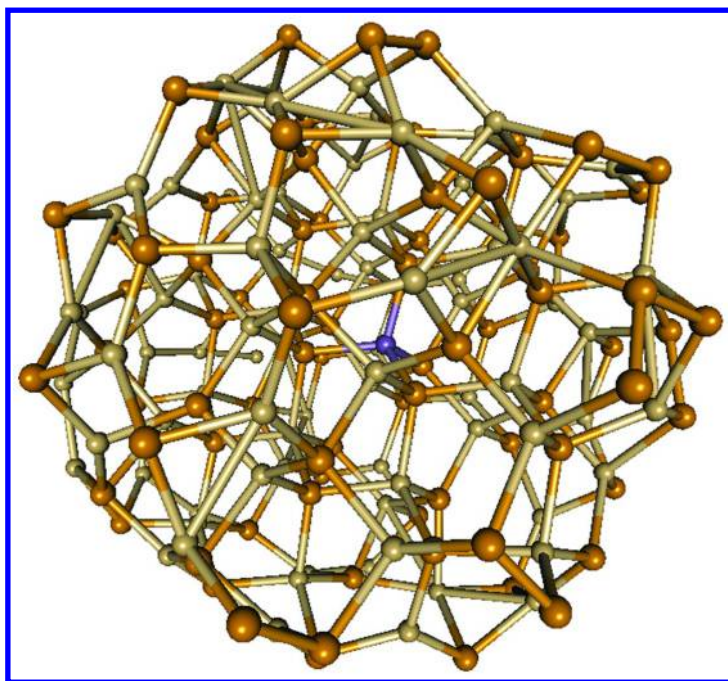


Figure 4. $\text{Cd}_{n-x}\text{-Mn}_x\text{-Se}_n$ quantum dot where $n = 82$ with the Mn atom (purple) in the center of the quantum dot.

This fragment includes the Se nearest-neighbor atoms. As shown in Figure 5 this fragment resembles a configuration with tetrahedral symmetry.

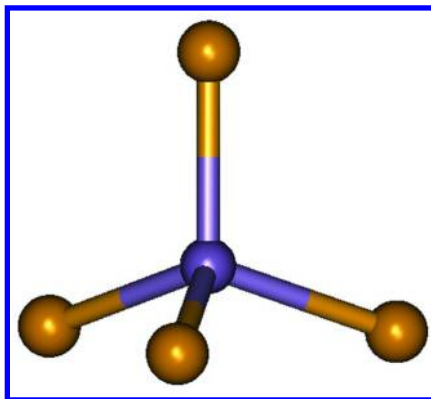


Figure 5. MnSe_4 fragment in the tetrahedral symmetry configuration.

Assumption 3

Since the fragment described in assumption 2 does not strictly possesses T_d symmetry, we prove that an energy structure and geometry of the fragment are very close to a fragment with the tetrahedral symmetry. Then we will use only the symmetric configuration of a fragment because calculations are much faster in the multi-configuration approach. In addition, it becomes possible to classify electronic states in accordance with T_d symmetry.

Assumption 4

It was experimentally observed that a second luminescence line does not depend on a QD size (40, 54–56). We verify this observation in our calculations.

IV. Computational Details

Since the calculation plan has been outlined, we specify computation details for each step. To find electronic structures of various quantum dots we use the Gaussian-09 software package (58). First, all spherical CdSe QDs were cut out from a Würzite bulk structure and optimized by the DFT method with a B3LYP exchange-correlation functional and LANL2dz basis set. For a Mn doped CdSe QD geometry optimization we also use the same method, unrestricted functional and basis set. Optical spectrum calculations for doped and undoped CdSe QDs have been performed by TDDFT. An exchange-correlation functional has been chosen to agree with the ab initio CISD calculations that includes electron correlations. The best fit turns out to be CAM-B3LYP. In Figure 6 we demonstrate how the TDDFT optical spectrum for $(\text{CdSe})_{10}$ fits the CISD one. The discrepancy between the CISD and TDDFT methods is less than 0.1eV for the optical spectrum.

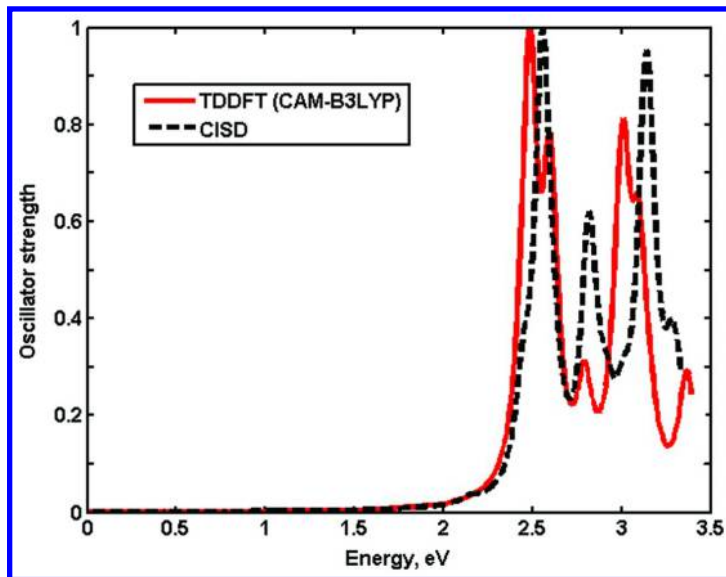


Figure 6. Optical spectrum for $(\text{CdSe})_{10}$ calculated by CISD (black line) and TDDFT (red line).

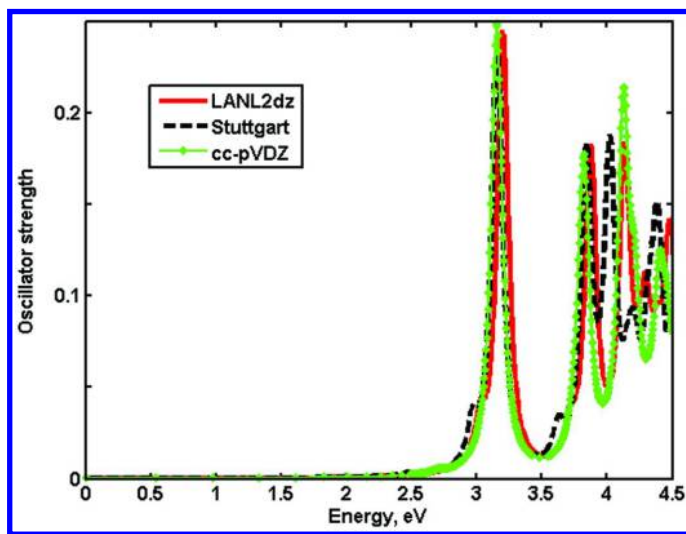


Figure 7. Optical spectra for $(\text{CdSe})_{10}$ calculated by the CIS method with different basis sets: LANL2dz (the red line), Stuttgart (the black line), and cc-pVDZ (the green line).

We have tested several basis sets for Cd and Se: LANL2dz, Stuttgart, and cc-pVDZ; and for Mn: LANL2dz, 6-31G+*, and cc-pVDZ. The choice of a working basis set is based on the two criteria: (a) the maximum agreement with the largest basis set cc-pVDZ and (b) the shortest time of calculations. Such a basis set has appeared to be a LANL2dz one for Cd and Se, and 6-31G+* for Mn. The choice of an exchange-correlation functional and basis sets have been employed for $\text{Cd}_{10}\text{Se}_{10}$ and $\text{Cd}_9\text{Mn}_1\text{Se}_{10}$ QDs. As shown in Figure 7 optical spectrum calculated in LANL2dz, Stuttgart, and cc-pVDZ basis sets has demonstrated almost no discrepancy for the CIS calculations. For further calculations we have chosen a LANL2dz basis set.

In order to calculate an optical gaps for large QDs we use the DFT method with an additional program (58, 59) that allows us to find the oscillator strengths for optical transitions between unoccupied and occupied states. In this work we are only interested in the lowest energy transitions that determines an optical gap. For these calculations we have tried various exchange-correlation functionals: B3LYP, PBEPBE1, CAM-B3LYP, and a LANL2dz basis set. It turned out that the best agreement with the optical gap calculations in the effective mass approximation (5, 6, 19, 20) is provided by the B3LYP exchange-correlation functional.

For an MnSe_4 fragment electronic structure calculations we have considered within the multi-configuration approach provided by the SAC-CI method. The multi-configuration Slater determinants employ the spin orbitals found from ROHF calculations. In these calculations T_d symmetry has remained unchanged for both ground ($M = 6$) and excited ($M = 4$) states. The energy difference between these states determines the luminescence energy for the slow relaxation emission.

V. Results and Discussions

In section III we have laid out the plan of calculations with some assumptions that we prove in this section. The assumptions that we have made are based on the impossibility of modern computational resources and methods to do calculations for large size quantum dots with the multi-configuration basis sets. However, some physical observations might be helpful to solve the problem under consideration.

Assumption 1

According to this assumption we have to verify an optical gap of a $\text{Cd}_{n-x}\text{Mn}_x\text{Se}_n$ QD to be independent of an Mn impurity. For large quantum dot we use other computational methods such as the effective mass approximation for nanocrystals (5, 6, 19, 20). This method provides excellent results for CdSe QDs without Mn doping. If we calculate optical gaps for intermediate size QDs using electronic structure methods and then match them with the optical gaps that are found in the effective mass approach, then it becomes proved that both methods work seamlessly for the intermediate and large size QDs. In Figures 8 and 9 we demonstrate how the optical gap (in this case it is a peak) depends on the presence of an Mn impurity. From these Figures we conclude that the optical gap remains

unchanged if a QD is doped by an Mn atom. In Figure 8 we have taken a $\text{Cd}_{16}\text{Se}_{16}$ and $\text{Cd}_{15}\text{Mn}_1\text{Se}_{16}$ quantum dot. To make sure that the optical gap is the same for doped and undoped quantum dots we have provided the results of the same calculations but for the larger QDs, i. e., $\text{Cd}_{24}\text{Se}_{24}$ and $\text{Cd}_{23}\text{Mn}_1\text{Se}_{24}$ as shown in Figure 9. Thus, we conclude that assumption 1 is proved. The calculations have been done by TDDFT with the exchange correlation functional to agree with the CISD results as described in Figure 6.

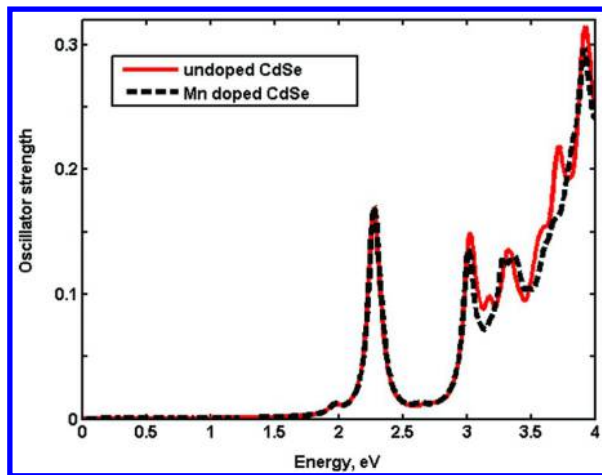


Figure 8. Optical spectra for $\text{Cd}_{16}\text{Se}_{16}$ (the red line) and $\text{Cd}_{15}\text{Mn}_1\text{Se}_{16}$ (the black line) calculated by TDDFT method with CAM-B3LYP exchange-correlation functional.

Assumption 2

As soon as assumption 1 is proved we are able now to calculate electronic structures for intermediate size quantum dots doped by Mn atoms. We know now that an Mn impurity does not affect the optical gap but it determines the slow relaxation luminescence. Assumption 2 states that instead of QD calculations with an Mn atom for intermediate sizes we can cut out a fragment, MnSe_4 and study an optical spectrum of this fragment. We prove that a geometry and energy levels are independent of a QD size. As soon as we prove the latter statement for medium size QDs, we become confident that the spectrum is even more independent of a QD size because at larger sizes the Mn geometry is less and less dependent on the increase of a QD diameter seamlessly with the results found by the quantum chemistry methods used for the intermediate size QDs. The optical gap calculated in the effective mass approximation (5, 6, 19, 20) for large and intermediate sizes is presented by the black solid line in Figure 10.

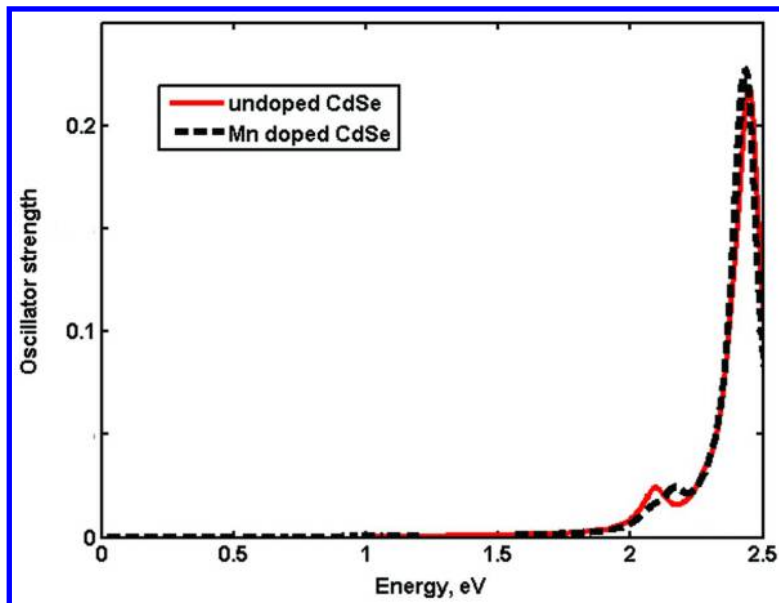


Figure 9. Optical spectra for $\text{Cd}_{24}\text{Se}_{24}$ (the red line) and $\text{Cd}_{23}\text{Mn}_1\text{Se}_{24}$ (the black line) calculated by TDDFT method with CAM-B3LYP exchange-correlation functional.

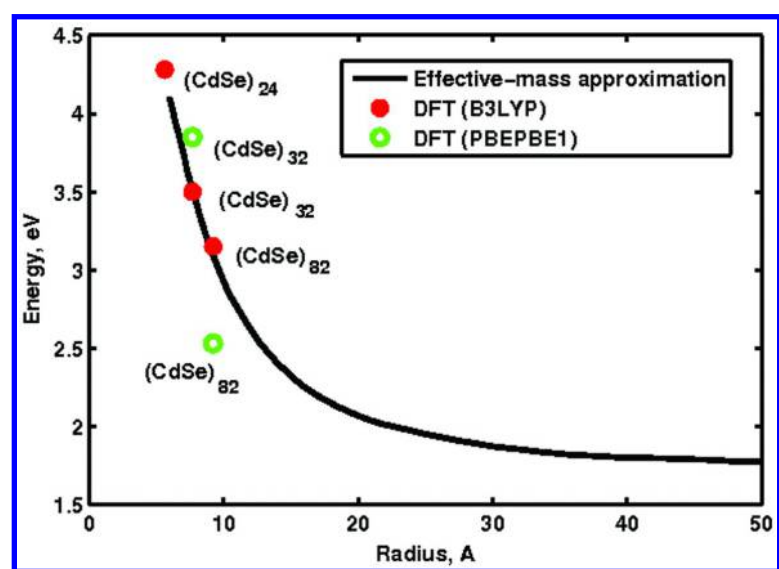


Figure 10. Size-dependence of optical gap for CdSe QDs calculated in the effective-mass approximation (the black line) and DFT with B3LYP (the filled dots) and PBE0PBE1 (the hollow dots) exchange-correlation functionals.

We have presented the DFT calculations of optical gaps for different size QDs, $\text{Cd}_{24}\text{Se}_{24}$, $\text{Cd}_{32}\text{Se}_{32}$, and $\text{Cd}_{82}\text{Se}_{82}$ using the additional original program that allows us to find oscillator strengths (59, 60). The exchange-correlation functional has been selected to match the optical gaps in the intersection region with the gaps predicted from the effective mass approximation. In Figure 10 we demonstrate the calculations of optical gaps employing the B3LYP (red) and PBE/PBE1 (green) exchange-correlation functional. It becomes clear that the results found with B3LYP provide the best match. We have also tested CAM-B3LYP exchange-correlation functional (it is not shown in Figure 10) where the values of optical gaps are too far from the effective mass predictions. Thus, doped by Manganese $\text{Cd}_{24}\text{Se}_{24}$, $\text{Cd}_{32}\text{Se}_{32}$, and $\text{Cd}_{82}\text{Se}_{82}$ QDs can be safely used for further calculations making sure that gap values will be unaffected by an Mn impurity for larger size QDs.

Assumption 3

The next step is to cut an MnSe_4 fragment out of the QDs of three different sizes: $\text{Cd}_{23}\text{MnSe}_{24}$, $\text{Cd}_{31}\text{MnSe}_{32}$, and $\text{Cd}_{81}\text{MnSe}_{82}$. As shown in Figure 11 single electron energy states are almost unchanged and independent of the QD size. The calculations have been performed by DFT with the UB3LYP exchange-correlation functional. In Figure 11 we also demonstrate a tetrahedral symmetry fragment (see Figure 5) with the energy levels close to the one with a realistic asymmetric cut. For the T_d fragment three t_2 single electron levels are degenerate while the lower e single electron state is doubly degenerate (57). We have found that the discrepancy between t_2 levels in the asymmetric fragment is about 0.06 eV and for e -levels is only 0.03 eV. Such a difference is negligibly small and therefore, we can use a T_d symmetric fragment for the further calculations.

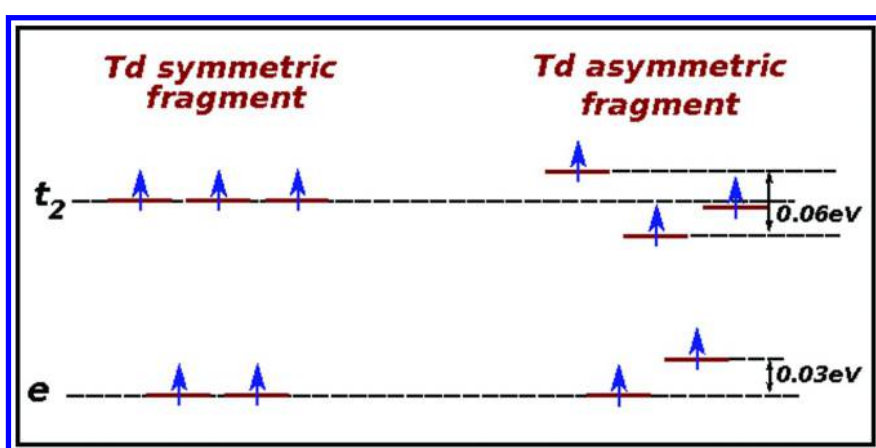


Figure 11. Single electron energy states for symmetric and asymmetric T_d fragment cut out from $\text{Cd}_{31}\text{Mn}_1\text{Se}_{32}$.

Now we are ready to find energy states for the symmetric fragment. In these calculations we are interested in the ground state with the symmetry 6A_1 ($M = 6$) and the excited state with the symmetry 4T_1 ($M = 4$). The latter state implies that there is a spin flip for one electron. Because of the high degeneracy of single electron states, one has to use a calculation method that includes a multi-configuration basis set. We employ the SAC-CI method. In the SAC-CI calculations we keep the T_d symmetry of the fragment unchanged during the computations. The basis set Slater determinants are built up from wave functions found in the restricted open shell Hartree-Fock calculations. From these calculations we have determined the energy difference between the excited ($M = 4$) and ground ($M = 6$) states that is 2.3 eV for the symmetric fragment cut out of the $\text{Cd}_{31}\text{MnSe}_{32}$ QD.

Assumption 4

We have also conducted the calculations for the two other size QDs and found that their luminescence energy remains unchanged. It proves that the slow relaxation luminescence is independent on a QD size and can be extended to larger size QDs where the electronic structure calculations are unrealistic but the effective mass approximation is valid (see Figure 10). Thus assumption 4 has been proved.

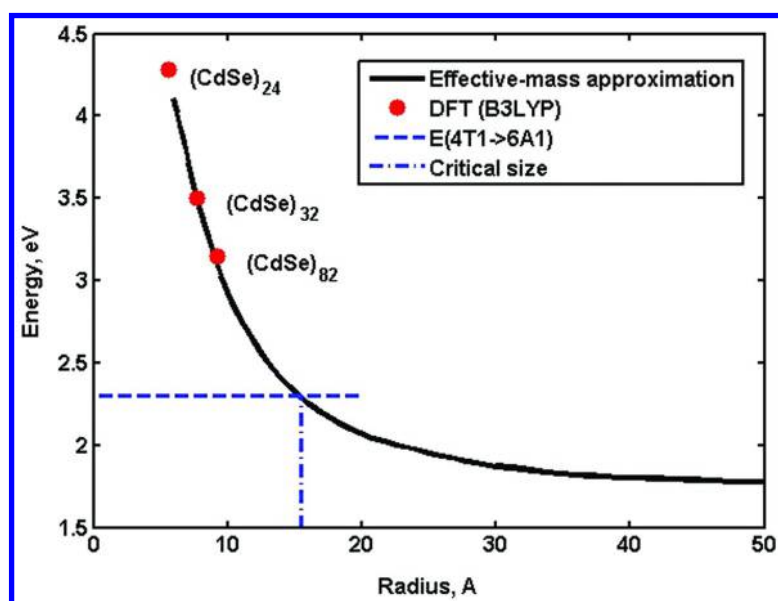


Figure 12. Crossing point between the energy difference $\Delta E = E(^4T_1) - E(^6A_1)$ and the optical gap curve from Figure 10 determines the critical size for a QD ($D = 3.2 \text{ nm}$) where the slow relaxation luminescence disappears from the emission spectrum.

Because an optical gap is independent of the presence of Mn dopants (assumption 1) and the slow relaxation luminescence energy for the T_d symmetric fragment is also independent of a QD size, we can find the critical size of a quantum dot where the second, slow relaxation emission line just disappears from the luminescence spectrum. The crossing point between the line with $\Delta E = 2.3$ eV and the optical gap curve determines the critical size QD with the diameter $D = 3.2$ nm. This result confirms the experimental value $D = 3.3$ nm found by Gamelin and co-worker in Refs. (40, 54–56) as shown in Figure 12.

Besides CdSe quantum dots we have also studied CdS, ZnS, and ZnSe QDs. Different materials give us different luminescence energies for a slow relaxation luminescence line. The luminescence energies are presented in Table 1.

Table 1

<i>Nanocrystal</i>	<i>Bond length (Å)</i>	<i>Energy (eV)</i>
CdSe	2.60	2.30
CdS	2.46	2.65
ZnSe	2.56	2.24
ZnS	2.44	2.60

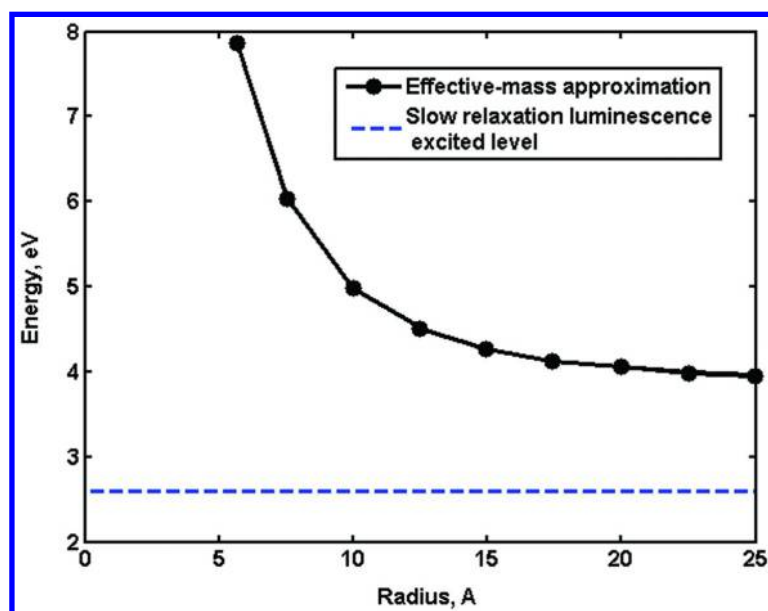


Figure 13. Size dependences for ZnS optical gap excited state MnS_4 fragment. There is no crossing between the lines indicating that the slow relaxation luminescence line never disappears.

As it is seen from Table 1, the emission energy is higher for QDs with *S* (Sulfur) than *Se* (Selenium). The slow relaxation emission energy is lower for ZnSe than for CdSe QDs. To find the critical diameter where the second, slow relaxation luminescence line disappears from the spectrum we have found that it is never disappears for ZnS QDs as shown in Figure 13. Indeed, the slow relaxation luminescence excited state energy never crosses the ZnS optical gap curve found in the effective mass approximation (61). It means that the luminescence is not tunable.

It is interesting to predict how the energy difference ΔE depends on the length of *Mn-Se* chemical bond. In Figure 14 we demonstrate such a dependence, the longer the chemical bond, the larger ΔE . This theoretical dependence can be useful if one studies crystal structures rather different than a Würzite structure.

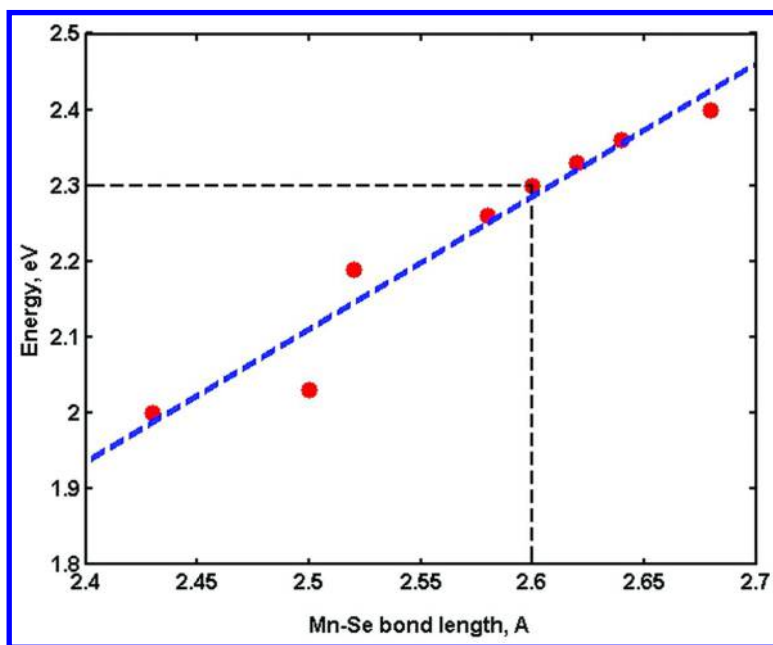


Figure 14. Energy difference $\Delta E = E(^4T_1) - E(^6A_1)$ dependence on a Mn-Se bond length. For Mn-Se bond length equals 2.6 Å the $\Delta E = 2.3$ eV.

VI. Conclusions

In this work we have theoretically studied a dual luminescence effect taking place in CdSe, CdS, ZnS, and ZnSe quantum dots doped by a Manganese impurity. Experimentally dual luminescence was discovered by Gamelin and co-workers (40, 54–56) for CdSe QDs where two emission lines took place, one line is with the fast relaxation while the second is slow with the relaxation time of 0.1 – 1.0 ms. The second emission line disappears at some critical size QD and then only

a single emission line remains at larger size QDs. Thus luminescence becomes tunable. The difficulty of a theoretical explanation of the effect is based on a very small oscillator strength, that is about 10^6 times lesser than a usual dipole oscillator strength. Therefore, it becomes impossible to find an optical transition within the conventional computational methods. The other reason that makes this problem even more computationally difficult is a high degeneracy of energy states. Indeed, five-fold-degenerate levels for $3d$ Mn electrons with a spherical symmetry are split in two levels because of a ligand field where the highest level is triply degenerate while the lowest is doubly degenerate. Computationally it becomes a problem because the standard computational methods such as DFT, TDDFT, CIS etc. use a single Slater determinant basis set. The theory recommends in this case to employ a multi-configuration basis set. Therefore, the problem becomes even more difficult for electronic structure calculations of medium and large size quantum dots. To explain the experimental dependencies (40, 54–56) we have proposed a computational scheme where we have made four assumption presented in section III. These assumptions are: (1) a QD optical gap is independent of an Mn impurity at small concentrations; (2) we combine electronic structure calculations for medium size CdSe QDs with the effective mass calculations for medium and large size QDs and match them in the medium size intersection region; (3) we cut an MnSe_4 fragment out of $\text{Cd}_{23}\text{MnSe}_{24}$, $\text{Cd}_{31}\text{MnSe}_{32}$, and $\text{Cd}_{81}\text{MnSe}_{82}$ QDs and check whether electronic structures of these fragments explain the second, slow relaxation emission in the experiments; and (4) the slow luminescence line is independent of a QD size (40, 54–56). We have computationally proved that all assumptions are correct. According to the calculations presented in this work we have proved *assumption 1*. The results are presented in Figures 8 and 9 where we have found that the optical gaps for QDs $\text{Cd}_{16}\text{Se}_{16}$ (the red line) and $\text{Cd}_{15}\text{MnSe}_{16}$ with an Mn impurity are independent of Mn at small concentrations. Then we have proved *assumption 2*. We have tried several exchange-correlation functionals for DFT to match the optical gap size dependence found in the effective mass approximation for large and intermediate size CdSe QDs (5, 6, 19, 20). Such an approach allows us to do calculations with an Mn impurity for intermediate size QDs and extend them to larger sizes. The results of the computations are presented in Figure 10 where we have shown that B3LYP provides the best match. To prove *assumption 3* we have cut an MnSe_4 fragment out of the three QDs of different sizes: $\text{Cd}_{23}\text{Mn}_1\text{Se}_{24}$, $\text{Cd}_{31}\text{Mn}_1\text{Se}_{32}$, and $\text{CdMn}_1\text{Se}_{82}$ and found that the energy levels with unpaired spins are independent of the QD sizes. This result can be extended to the larger sizes in accordance with *assumption 2* as shown in Figure 10. The asymmetric and symmetric versions of the fragments provide very close single electron energy levels as shown in Figure 11. In this case the electronic structure calculations for a tetrahedral fragment have been performed within the SAC-CI method. The calculations reveal that the energy difference between the excited ($M = 4$) and ground ($M = 6$) states is 2.3 eV for the symmetric fragment cut out of the $\text{Cd}_{31}\text{Mn}_1\text{Se}_{32}$ QD. This result confirms the experimental value that is 2.1–2.2 eV (40, 54–56). We have also found the QD critical size, at which the second emission line disappears. This size is 3.2 nm from the calculations. The experimental value is 3.3 nm (40, 54–56) (see Figure 12). In addition, we have made some predictions for a critical size with the length of an *Mn-Se* bond as shown in Figure 14. The

longer the bond length, the larger the slow luminescence energy. This prediction could be useful for a different nanocrystal structures rather than Würtzite. We have also studied different QDs with an Mn impurity. The luminescence energies are presented in Table 1. The luminescence emission line can have both higher and lower energies than for CdSe QD. For example, the energy is higher for CdS and ZnS quantum dots while for ZnSe QDs it is lower. For some QDs such as ZnS, we have not found the disappearance of the slow relaxation luminescence line. As shown in Figure 13 the optical gap curve never crosses the excited state energy line with the 4T_1 symmetry.

Acknowledgments

This work was supported by a grant No. DEFG02-10ER46728 from the Department of Energy to the University of Wyoming and the University of Wyoming School of Energy Resources through its Graduate Assistantship program.

References

1. Akimov, A. V.; Neukirch, A. J.; Prezhdo, O. V. *Chem. Rev.* **2013**, *113*, 4496–4565.
2. Gleiter, H. *Adv. Mater.* **1992**, *4*, 474–481.
3. Lehmann, V.; Gosele, U. *Adv. Mater.* **1992**, *4*, 114–116.
4. Sailor, M. J.; Kavanagh, K. L. *Adv. Mater.* **1992**, *4*, 432–434.
5. Efros, A. L.; Efros, A. L. *Sov. Phys.- Semicond.* **1982**, *16*, 772–775.
6. Efros, A. L.; Kharchenko, V. A.; Rosen, M. *Solid State Commun.* **1995**, *93*, 281–284.
7. Brus, L. E. *J. Chem. Phys.* **1983**, *79*, 5566–5571.
8. Rossetti, R.; Ellison, J. L.; Gibson, J. M.; Brus, L. E. *J. Chem. Phys.* **1984**, *80*, 4464–4469.
9. Weller, H.; Koch, U.; Gutierrez, M.; Henglein, A. *Ber. Bunsen-Ges. Phys. Chem.* **1984**, *88*, 649–656.
10. Fojtik, A.; Weller, H.; Koch, U.; Henglein, A. *Ber. Bunsen-Ges. Phys. Chem.* **1984**, *88*, 969–977.
11. Brus, L. E. *IEEE J. Quantum Electron.* **1986**, *22*, 1909–1914.
12. Henglein, A. *Top. Curr. Chem.* **1988**, *143*, 113–180.
13. Henglein, A. *Chem. Rev.* **1989**, *89*, 1861–1873.
14. Brus, L. E. *J. Appl. Phys.* **1991**, *53*, 465–474.
15. Wang, Y.; Herron, N. *J. Phys. Chem.* **1991**, *95*, 525–532.
16. Henglein, A. *Labor 2000* **1992**, *110*–121.
17. Weller, H. *Angew. Chem.* **1993**, *105*, 43–55.
18. Banyai, L.; Koch, S. W. *Semiconductor Quantum Dots*; World Scientific: Singapore, 1993, Vol. 2, pp 397–453.
19. Yoffe, A. D. *Adv. Phys.* **1993**, *42*, 173–262.
20. Yoffe, A. D. *Adv. Phys.* **2001**, *50*, 1–208.

21. Piryatinski, A.; Velizhanin, K. A. *J. Chem. Phys.* **2010**, *133*, 084508–084519.
22. Kilina, S.; Velizhanin, K. A.; Ivanov, S.; Prezhdo, O. V.; Tretiak, S. *ACS Nano* **2012**, *6*, 6515–6524.
23. Kilina, S.; Kilin, D.; Prezhdo, V. V.; Prezhdo, O. V. *J. Phys. Chem. C* **2011**, *115*, 21641–21651.
24. Prezhdo, O. V. *Acc. Chem. Res.* **2009**, *42*, 2005–2016.
25. Neukirch, A. J.; Hyeon-Deuk, K.; Prezhdo, O. V. *Coord. Chem. Rev.* **2014**, *263*, 161–181.
26. Kilina, S. V.; Kilin, D. S.; Prezhdo, O. V. *ACS Nano* **2009**, *3*, 93–99.
27. Kilina, S. V.; Craig, C. F.; Kilin, D. S.; Prezhdo, O. V. *J. Phys. Chem. C* **2007**, *111*, 4871–4878.
28. Kilina, S. V.; Neukirch, A. J.; Habenicht, B. F.; Kilin, D. S.; Prezhdo, O. V. *Phys. Rev. Lett.* **2013**, *110*, 180404–180406.
29. Kilina, S. V.; Ivanov, S.; Klimov, V. I.; Tretiak, S. *J. Am. Chem. Soc.* **2009**, *131*, 7717–7726.
30. Fischer, S. V.; Crotty, A. M.; Kilina, S. V.; Ivanov, S. A.; Tretiak, S. *Nanoscale* **2012**, *4*, 904–914.
31. Nguyen, K. A.; Pachter, R.; Day, P. R. *Chem. Theory Comput.* **2013**, *9*, 3581–3596.
32. Proshchenko, V.; Dahnovsky, Yu. *Chem. Phys. Lett.* **2014**, *595*–596, 250–255.
33. Proshchenko, V.; Dahnovsky, Yu. *Phys. Chem. Chem. Phys.* **2014**, *16*, 7555–7561.
34. Pimachev, A.; Dahnovsky, Yu. *J. App. Phys.* **2014**, *115*, 043705–043706.
35. Serpone, N.; Lawless, D.; Disder, J.; Hermann, J. M. *Langmuir* **1994**, *10*, 643–652.
36. Kudo, A.; Sekizawa, M. *Chem. Commun.* **2000**, 1371–1371.
37. Jaramillo, T. F.; Baek, S.-H.; Kleiman-Shwarsstein, A.; Choi, K.-S.; Stucky, G. D.; McFarland, E. W. *J. Comb. Chem.* **2005**, *7*, 264–271.
38. Liu, W. K.; Sally, G. M.; Gamelin, D. R. *J. Chem. Phys. B* **2005**, *109*, 14486–14495.
39. Osterloch, F. E. *Chem. Mater.* **2008**, *20*, 35–54.
40. Beaulae, R.; Arecher, P. L.; Ochsenbein, S. T.; Gamelein, D. R. *Adv. Funct. Mater.* **2008**, *18*, 3873–3891.
41. Norris, D. J.; Yao, N.; Charnock, F. T.; Kennedy, T. A. *Nano Lett.* **2001**, *1*, 3–7.
42. Hoffman, D. M.; Meyer, B. K.; Ekimov, A. I.; Merkulov, I. A.; Efros, Al. L.; Rosen, M.; Counio, G.; Gacoin, T.; Boilot, J. P. *Solid State Commun.* **2000**, *114*, 547–550.
43. Radovanovic, P. V.; Gamelin, D. R. *Proc. SPIE-Int. Soc. Opt. Eng.* **2002**, *4809*, 51–61.
44. Schwartz, D. A.; Norberg, N. S.; Nguyen, Q. P.; Parker, J. M.; Gamelin, D. R. *J. Am. Chem. Soc.* **2003**, *125*, 13205–13218.
45. Norberg, N. S.; Kittilstved, K. R.; Amonette, J. E.; Kukkadapu, R. K.; Schwartz, D. A.; Gamelin, D. R. *J. Am. Chem. Soc.* **2004**, *126*, 9387–9398.
46. Norberg, N. S.; Gamelin, D. R. *J. Appl. Phys.* **2006**, *99*, 08M104–3.

47. Norberg, N. S.; Dalpian, G. M.; Chelikowsky, J. R.; Gamelin, D. R. *Nano Lett.* **2006**, *6*, 2887–2892.
48. Norberg, N. S.; Parks, G. L.; Salley, G. M.; Gamelin, D. R. *J. Am. Chem. Soc.* **2006**, *128*, 13195–13203.
49. Archer, P. I.; Santangelo, S. A.; Gamelin, D. R. *J. Am. Chem. Soc.* **2007**, *129*, 9808–9818.
50. Archer, P. I.; Santangelo, S. A.; Gamelin, D. R. *Nano Lett.* **2007**, *7*, 1037–1043.
51. Beaulac, R.; Archer, P. I.; Liu, X.; Lee, S.; Salley, G. M.; Dobrowolska, M.; Furdyna, J. K.; Gamelin, D. R. *Nano Lett.* **2008**, *8*, 1197–1201.
52. Bussian, D. A.; Crooker, S. A.; Yin, M.; Brynda, M.; Efros, Al. L.; Klimov, V. I. *Nat. Mater.* **2009**, *8*, 35–40.
53. Furdyna, J. K.; Kossut, J. *Diluted Magnetic Semiconductors*. In *Semiconductors and Semimetals*; Willardson, R. K., Beer, A. C., Eds.; Academic Press: New York, 1988; Vol 25, pp 183 – 254.
54. Vlaskin, V. A.; Beaulac, R; Gamelin, D. R. *Nano Lett.* **2009**, *9*, 4376–4382.
55. Vlaskin, V. A.; Jansen, N.; Rijssen, J.; Beaulac, R.; Gamelin, D. *Nano Lett.* **2010**, *10*, 3670–3674.
56. Beaulac, R.; Ochesenbein, S. T.; Gamelin, D. In *Nanocrystals Quantum Dots*; Klimov, V., Ed.; CRC Press: New York, 2010; pp 397–453.
57. Cotton, F. A. *Chemical Applications of Group Theory*; Wiley, New York, 1990; Vol. 9.
58. M. J. Frisch, G. W. Trucks, H. B. Schlegel, G. E. Scuseria, M. A. Robb, J. R. Cheeseman, G. Scalmani, V. Barone, B. Mennucci, G. A. Petersson, H. Nakatsuji, M. Caricato, X. Li, H. P. Hratchian, A. F. Izmaylov, J. Bloino, G. Zheng, J. L. Sonnenberg, M. Hada, M. Ehara, K. Toyota, R. Fukuda, J. Hasegawa, M. Ishida, T. Nakajima, Y. Honda, O. Kitao, H. Nakai, T. Vreven, J. A. Montgomery, Jr., J. E. Peralta, F. Ogliaro, M. Bearpark, J. J. Heyd, E. Brothers, K. N. Kudin, V. N. Staroverov, R. Kobayashi, J. Normand, K. Raghavachari, A. Rendell, J. C. Burant, S. S. Iyengar, J. Tomasi, M. Cossi, N. Rega, J. M. Millam, M. Klene, J. E. Knox, J. B. Cross, V. Bakken, C. Adamo, J. Jaramillo, R. Gomperts, R. E. Stratmann, O. Yazyev, A. J. Austin, R. Cammi, C. Pomelli, J. W. Ochterski, R. L. Martin, K. Morokuma, V. G. Zakrzewski, G. A. Voth, P. Salvador, J. J. Dannenberg, S. Dapprich, A. D. Daniels, Ö. Farkas, J. B. Foresman, J. V. Ortiz, J. Cioslowski, and D. J. Fox *Gaussian 09*, Revision A.1; Gaussian, Inc.: Wallingford, CT, 2009.
59. Bour, P. Institute of Organic Chemistry and Biochemistry, Prague, Czech Republic, 2012.
60. Pimachev, A. *DFT transition dipole moment and oscillator strength program*; University of Wyoming: Laramie, WY, 2013.
61. Vatankhah, C.; Ebadi, A. *Res. J. Recent Sci.* **2013**, *2*, 21–24.

Chapter 6

Theoretical Modeling of Oxygen and Water Adsorption on Indium Oxide (111) Surface

Talgat Inerbaev,^{*,1} Ryoji Sahara,² Hiroshi Mizuseki,³
Yoshiyuki Kawazoe,^{4,5} and Takashi Nakamura⁶

¹Gumilyov Eurasian National University,
Astana, Mirzoyan str. 2, 010008, Kazakhstan

²Research Center for Strategic Materials, National Institute for Materials
Science, Tsukuba, Ibaraki, 305-0047, Japan

³Center for Computational Science, Korea Institute of Science and
Technology, Seoul, 136-791, Republic of Korea

⁴New Industry Creation Hatchery Center, Tohoku University,
Sendai, 980-8579, Japan

⁵Institute of Thermophysics, Siberian Branch of the Russian Academy of
Sciences, Lavrentyev Avenue, Novosibirsk 630090, Russia

⁶Institute of Multidisciplinary Research for Advanced Materials,
Tohoku University, Sendai, 980-8577, Japan

*E-mail: inerbaev_tm@enu.kz.

Indium oxide is one of the basic oxides, and has been extensively studied due to its prominent applications in solar cells, optoelectronics, gas sensors and possesses some interesting chemical and structural peculiarities. In recent years, significant efforts have been made to fabricate these materials as nanosized particles. However, the surface structure and reactivity become increasingly important to the overall material properties as the particle size is reduced. We present a density functional theory (DFT) study of the water and oxygen molecules interaction with stoichiometric and defective (111) In_2O_3 (IO) surfaces. It is found that water environment destabilizes IO surface with respect to formation of oxygen vacancies. Single water molecule barrierlessly dissociates at all the oxygen vacancy sites except one position with the lowest defect formation energy where water dissociation energy is calculated to be 0.41eV. This should lead to increase of free

electrons concentration up to some critical temperature where water dissociation heals surface defects. Another one effect that decreases eliminates free charge carriers is molecular oxygen chemisorption on surface oxygen vacant sites. O_2 species are adsorbed as peroxide ions that (i) decreases free electrons concentration and (ii) lead to appearance of extrapeaks in optical adsorption spectra. Combination of these factors governs free electrons concentration, i.e. conductivity of nanostructured IO.

1. Introduction

Indium oxide, In_2O_3 , (IO) is a technologically important material. Tin-doped IO is one of the most widely used transparent conducting oxides because of its two main properties, its electrical conductivity and optical transparency (1). IO has been suggested as a highly sensitive gas sensor toward various target gases among different metal oxides (2–4). The gas sensing mechanism of metal oxide based sensors is mainly attributed to the oxidation/reduction properties which are controlled by the surface. In case of bulk and thin film oxides, changes in grain size, porosity, thickness and stoichiometry affect the gas sensing properties. In case of nanostructures, the possibility of control the crystallinity and stoichiometry during the nanocrystals growth process allows manipulate of these critical parameters and tailor materials with desired gas sensing properties (5–7).

Fundamental understanding of IO surface properties is critical to rational advances in gas sensors design, electronic work function modification, etc. (8, 9) The IO (111) surface is lowest in energy and therefore the most abundant crystal face in thermodynamic equilibrium (10–12).

It was theoretically found that a metal-insulator transition is achievable in indium oxide surfaces through oxygen loss due to the drastic lowering of defect reaction energy and the creation of delocalized donor states (12). It was shown for IO that the energy required to form an oxygen vacancy decreases towards the (111) surface, where the coordination environment is lowered. That can result in a metal-insulator transition where donor sites are produced at chemically reduced extended defects.

It was theoretically found that a metal-insulator transition is achievable in indium oxide surfaces through oxygen loss due to the drastic lowering of defect reaction energy and the creation of delocalized donor states (12). It was shown for IO that the energy required to form an oxygen vacancy decreases towards the (111) surface, where the coordination environment is lowered. That can result in a metal-insulator transition where donor sites are produced at chemically reduced extended defects.

Recent experimental findings reveal that IO's thin films conducting properties depend on the external conditions. Oxidizing and reducing effects of the gas interactions with the (111) IO surface in all cases were accompanied by a corresponding behavior, i.e., a decrease or increase in photoemission response (8). Spectral dependencies of photocurrent have revealed some peaks near photon

energy 2.9 eV that is about 0.5 eV smaller than the fundamental optical band gap of IO. The appearance of a peak near 2.9 eV under oxidizing conditions, and subsequent disappearance of this peak under reducing conditions were noted (4). Similar feature was found after exposure of nanocrystalline IO in humid air at sufficiently high temperature of 400 °C. Dark conductivity of heated IO film exposed in humid air was found to be more than order of magnitude larger at temperature range 200-300 °C than the same value measured for dry air exposed samples. Following measurement of dark conductivity during cooling was found to be much smaller in humid air than in dry air (4). Taking into consideration that IO film conductivity is driven by surface oxygen vacancies (12, 13), it could be hypothesized that these experimental results are to be explained by IO film surface modification during its exposition under different environmental conditions, i.e. humidity and oxidation conditions of atmosphere.

First-principles study of O₂ and H₂O adsorption on oxygen- and metal-terminated (100) IO and tin-doped IO was carried out (14). It was found that dissociative chemisorption of O₂ and H₂O is facile on the metal-terminated oxide surfaces. O₂ chemisorption is energetically more favorable than H₂O dissociative chemisorption until the metal-terminated surfaces are saturated by chemisorbed O₂ dimers, at which point the surfaces become virtually identical to the O-terminated surfaces and the dissociative chemisorption of H₂O becomes the energetically preferred process. Recent density functional theory (DFT) studies reveal that the most thermodynamically stable (111) IO surface is almost chemically inert with respect to oxygen, but dissociation of the molecules is possible on the small fraction of the total surface area (10). It was recently shown that nonequilibrium optoelectronic properties at surfaces and interfaces are efficiently predicted using density matrix approach combined with electronic structure computations providing observables ranging from photovoltage (15), and photo-luminescence spectra (16) to photoinduced current density and photoconductivity (17).

In present study we report the results of DFT modeling of water and oxygen adsorption on perfect and defective (111) IO surfaces. It is found that adsorption of single molecular layer of water destabilizes surface with respect to oxygen vacancy formation. Dissociation barrier for water molecule adsorbed on the oxygen vacancy site becomes much smaller than the corresponding value for water molecule adsorbed by stoichiometric IO surface. At the same time, it is found that delocalized donor states in reduced IO slab are eliminated by O₂ molecule chemisorption on the surface vacant site. This leads to appearance of extra bright optical transitions from O2p states localized on peroxide ion to In4d states.

2. Computation Details

All calculations are based on DFT method within the local density approximation (LDA) as it is implemented in VASP software package (18). The semicore *d*-states of In atoms are explicitly treated as valence states through the projector-augmented wave method (19) and cutoff energy value equal to 400 eV.

The Brillouin zone was sampled at the Γ -point only. The convergence criteria for the electronic structure and the geometry were 10^{-4} eV and 10^{-3} eV/Å, respectively. Since in DFT the localization of d -electrons is underestimated, the semiempirical invariant Dudarev's et al. version of LDA+ U approach is employed to fix this shortcoming (20). The self-interaction parameter U was selected to be equal to 7 eV according to Ref. (21).

In_2O_3 (111) slabs were constructed using the standard hexagonal setting. The (111) slabs contain six trilayers with stoichiometric composition. Each trilayer consists of 24 oxygen and 16 indium ions resulting in a total number of 240 ions for the stoichiometric case and surface area of 165.76 Å². All atomic configurations were optimized by conjugated-gradient method. Effect of water environment was modeled by taking into consideration eight water molecules adsorbed on each side of IO slab that corresponds to 0.5 molecular layer of adsorbed water. We limit ourselves by this case since at higher water coverage H_2O molecules were found to be spontaneously dissociated even on stoichiometric IO surface. Comparison with experiment shows that limited case qualitatively describes the effect of water adsorption on IO surface stability. In practice, equilibrium water coverage of surface is expected to be dependent on the external conditions. For more accurate quantitative description of IO interaction with water at different H_2O partial pressure and external temperature is required. The latter one varies in experiment in range 300-1000 °C (4, 13), further investigations using technique employed, for example, in Ref. (22), are to be carried out. Configurations with one surface oxygen vacancy and one adsorbed O_2 molecule adsorbed by defective IO slab were examined.

Binding energies between IO slab and adsorbed species were calculated as:

$$E_{ads} = E(slab) + E(specie) - E(slab + specie) \quad (1)$$

where $E(\text{slab+specie})$, $E(\text{slab})$, and $E(\text{specie})$ are the energy of the IO slab with adsorbed specie, energy of the bare slab, and the energy of adsorbed molecule in the gas phase, respectively. PBE+ U method using LDA+ U geometries was employed in this case.

Transition states were determined using the climbing image nudged elastic band method (23) for configuration with one water molecule adsorbed. The convergence criteria for the transition state image was an absolute tangent force less than 0.05 eV/Å.

The defect formation energies was be evaluated as described in Ref. (24) taking into consideration a correction term to align the electrostatic potential with the same value of perfect lattice (25): where $E(D, q)$ and $E(P)$ denote the total energies of the unit cell containing a defect with the charge q and the perfect crystal lattice, respectively. n_O indicates the number of oxygen atoms that have been removed from the perfect surface, and the μ_O is the oxygen chemical potential. E_F is a Fermi level referenced to the valence-band maximum. We also take into consideration a correction term V_{corr} , to align the electrostatic potential with the same value of perfect lattice (25). The oxygen chemical potential is selected to

be equal to energy of O-atom in an O₂ molecule and equal to -5.227 eV. This corresponds to extreme O-rich conditions. Doubly charged surfacevacancies were considered in this study.

$$E_{def} = E(D, q) - E(P) + \mu_O n_O + q(E_F + V_{corr}) \quad (2)$$

Optical absorption spectra $\alpha(\omega)$ were calculated by summation over all electronic transitions from $|i\rangle$ to $|j\rangle$ Kohn-Sham states generated from projected augmented wave DFT calculations

$$\alpha(\omega) = \sum_{ij} f_{ij} \delta(\epsilon_{ij} - \hbar\omega) (\rho_{ii}^{eq} - \rho_{jj}^{eq}) \quad (3)$$

Here equilibrium occupation of i th KS orbital ρ_{ii}^{eq} is determined by Fermi-Dirac distribution, $\rho_{ii}^{eq} = 0, i > HO$, $\rho_{ii}^{eq} = 1, i < LU$ (26, 27). Thus, nonzero signal is obtained only for transitions between occupied and unoccupied orbitals. Interestingly, absorption at low transition energies and thus, optical conductivity, increases in two limits (a) additional occupied/unoccupied orbitals are contributed due to surface defects and (b) additional transitions become available due to photoinduced change of equilibrium occupation $\rho_{ii}^{eq} \rightarrow \rho_{ii}^{excited}(\Omega)$ as was recently shown in Ref. (28). Actual calculations were carried out in momentum space similar to procedure (29, 30). The dimensionless oscillator strength was evaluated using transition dipole D_{ij} that was calculated as a matrix element of electric dipole moment operator between Kohn-Sham orbitals of states $|i\rangle$ and $|j\rangle$; m_e and e are the electron mass and electron charge, respectively. Actual calculations were carried out in momentum space.

$$f_{ij} = \frac{8\pi^2}{3} \frac{m_e \epsilon_{ij}}{\hbar^2 e^2} |D_{ij}|^2 \quad (4)$$

3. Results and Discussion

The upper IO (111) surface structure is shown in Figure 1. Defect formation energies for both bare surface and water covered surfaces for different positions of formed oxygen vacancies are summarized in Table 1. Calculations reveal that oxygen atoms at highly coordinated sites could be easily removed from IO surface to create a surface vacancy. Our DFT calculation results are in a good agreement with data obtained in Ref. (12). Differences between values of E_{def} for bare surface that in some cases reach value up to approximately 0.35 eV presented here and reported in Ref. (12) are associated with differences in employed calculation methods.

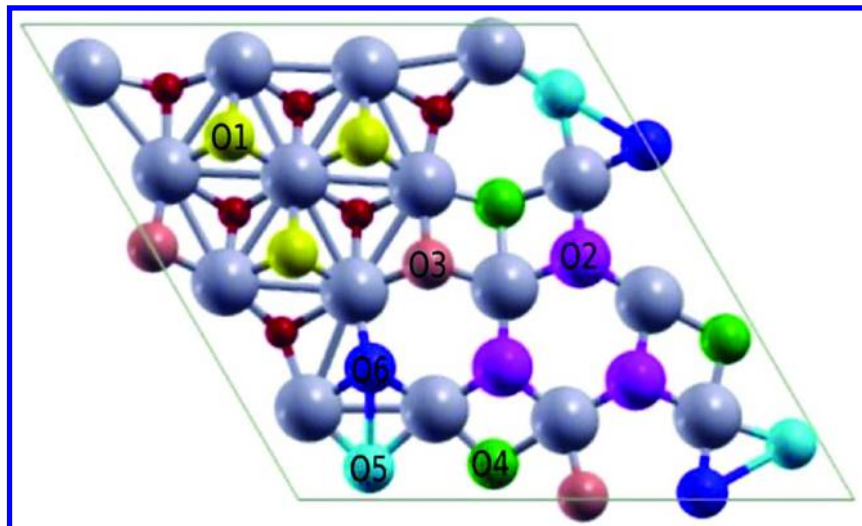


Figure 1. Top view on (111)-terminated IO surface. The first 6 inequivalent oxygens are labeled from the topmost atom.

Table 1. Calculated Surface Oxygen Vacancy Formation Energies for Bare and H₂O Covered (111) IO Surface. Oxygen Positions Are Denoted According to Figure 1. Data in Parentheses Are from Ref. (12).

Defect E_{def} (eV)	Defect E_{def} (eV)
	Bare Water
O1(Bare)	0.61 (0.95)
O2(Bare)	1.50 (1.29)
O3(Bare)	1.79 (1.57)
O4(Bare)	1.57 (1.93)
O5(Bare)	2.03 (2.04)
O6(Bare)	2.32 (2.27)
	Bare Water
	0.20
	1.19
	1.32
	1.37
	2.16
	2.27

We found that E_{def} depends on two main factors. First factor is the total coordination number of oxygen ion, while the second one is the coordination of the nearest neighboring indium atoms (12). Our data indicate that effect of water adsorption leads to decrease of E_{def} values for high-coordinated surface O-atoms. The same effect of easier surface oxygen vacancy creation in the presence of water with respect to removing an oxygen ion from dry surface was found during investigation ceria (111) surface (31).

Calculated oxygen vacancy formation energy at O1 position is extremely low and such vacancies are to be observed at low temperatures. Concentration of surface oxygen vacancies can be indirectly estimated from charge carrier concentration measurements assuming that each vacancy creates 2 conduction electrons. In our slab model with one surface vacancy charge carrier concentration is $7 \times 10^{20} \text{ cm}^{-3}$. Room temperature experiments reveal that in IO films charge carrier concentration is $2 \times 10^{18} \text{ cm}^{-3}$ and this value increases to around $1.5 \times 10^{19} \text{ cm}^{-3}$ in ultrahigh vacuum conditions, i.e. oxidation conditions. IO film thickness is one more parameter which determines its conductivity at some fixed temperature and oxygen partial pressure (13). In humid atmosphere at room temperature conductivity of IO film is approximately 2 times larger than in dry atmosphere and this ratio increases to 100 with heating to $\sim 250^\circ\text{C}$ (4). Thereby, our results at least qualitatively reproduce experimental dependence of IO thin film properties as a function of oxygen partial pressure and atmosphere humidity.

Oxygen molecule adsorption energy at perfect IO (111) surface was calculated to be equal to 0.15 eV while this value for O_2 adsorbed at the surface oxygen vacancy site becomes larger and equal to 2.37 eV. Adsorption energy of O_2 is by stoichiometric surface is not changed due to water adsorption and equal to 0.14 eV. At the same time adsorption energy of O_2 at defect site is slightly increases when water molecules are adsorbed as well and $E_{ads}=2.56 \text{ eV}$. Calculations reveal that adsorbed oxygen molecule is not spin-polarized, and the O-O interatomic distance is 1.504 Å, which matches with structure of O_2^{-2} molecule (32). Calculated stretching frequency of peroxide cation is found to be equal to 909 cm^{-1} that is typical for O_2^{-2} ion that exhibits this frequency in the $740 - 930 \text{ cm}^{-1}$ (33). Using the same computational parameters the stretching frequency for neutral O_2 molecule was found to be equal to 1645 cm^{-1} . This is in a good agreement with previously experimentally measured (1556 cm^{-1}) and theoretically calculated (1737 cm^{-1}) values of this feature (34, 35).

Surface oxygen vacancy formation leads to transition of IO from non-metallic to metallic state (12, 13). Our calculations are in agreement with recent finding of Lany et.al (13) that the surface carrier sheet density dominates the conductivity of IO thin films. Calculated electronic density of states for stoichiometric and defective IO (111) surfaces are shown in Figure 2. Highest occupied (HO) and lowest unoccupied (LU) Kohn-Sham orbitals for these surfaces are shown in Figure 3(a,b,c,d) using VASP Data viewer software (36). Calculations reveal that a single surface vacancy leads to appearance of two free electrons in the system which are localized mainly on the topmost slab layers. Such charge distribution is typical for a number of orbitals below HO and above LU orbitals. It is seen that occupied orbitals are localized that makes stoichiometric IO slab non-conducting. At the same time delocalization of LU orbitals allows the photo-induced electronic conductivity. Oxygen vacancy injects electrons to the topmost 3 trilayers in agreement with recent experimental findings (37) and dark surface conductivity is observed. Adsorption of molecular oxygen at vacancy leads to charge redistribution from IO to O_2^{-2} and there is a O_2^{-2} ion adsorbed on IO (111) surface. As a result there are no more conduction electrons in IO slab

and system becomes non-metallic (see Figure 3(e)). But adsorbed O_2^{-2} molecular ion significantly influences on the photo-induced conductivity.

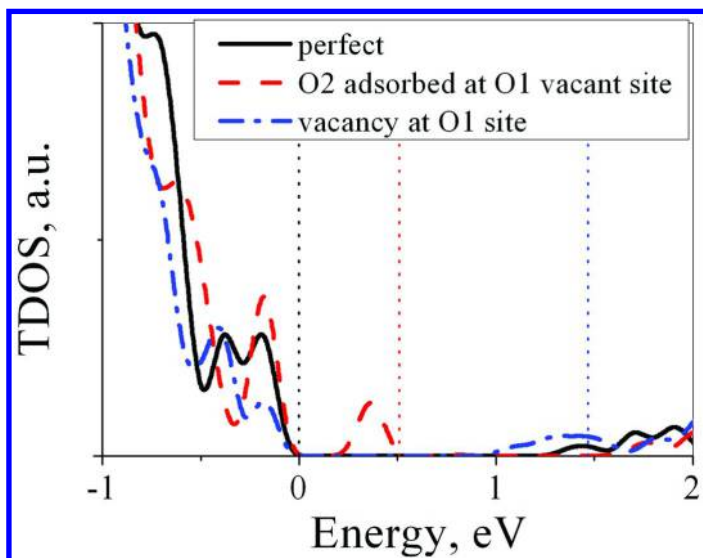


Figure 2. Total density of states for stoichiometric (black), defective with oxygen vacancy at O1 site (blue) and O_2 molecule adsorbed at O1 vacant site (red) (111) IO surface. Highest occupied energy levels for each system are shown by vertical dotted lines with corresponding color.

Calculated linear optical adsorption spectra are presented in Figure 4. It is seen that for stoichiometric IO slab optical adsorption starts at energy approximately equal to 1.6 eV. Presence of O_2^{-2} ion on non-stoichiometric surface leads to appearance extra adsorption peak at photon energy about 0.5 eV. This result is in qualitative agreement with experimentally observed shift in optical adsorption spectra of dry air deposited IO films (4).

Similar to the stoichiometric ceria(111) surface (38), three adsorbed structures: no-H-bonds configuration, one-H-bond configuration, and two-H-bonds configuration were taken into consideration. Starting from these initial geometries, a final stable configuration for the adsorbed H_2O molecule is reached, which has the one-H-bond structure. Water binds on stoichiometric IO (111) surface in either molecular or dissociated form. In agreement with those results, water molecules are found to be dissociated when they are adsorbed on surface sites where fivefold indium and threefold oxygen are found in close proximity. When water molecules are adsorbed on surface sites where either fivefold indium and fourfold oxygen or sixfold indium and threefold oxygen are close to each other.

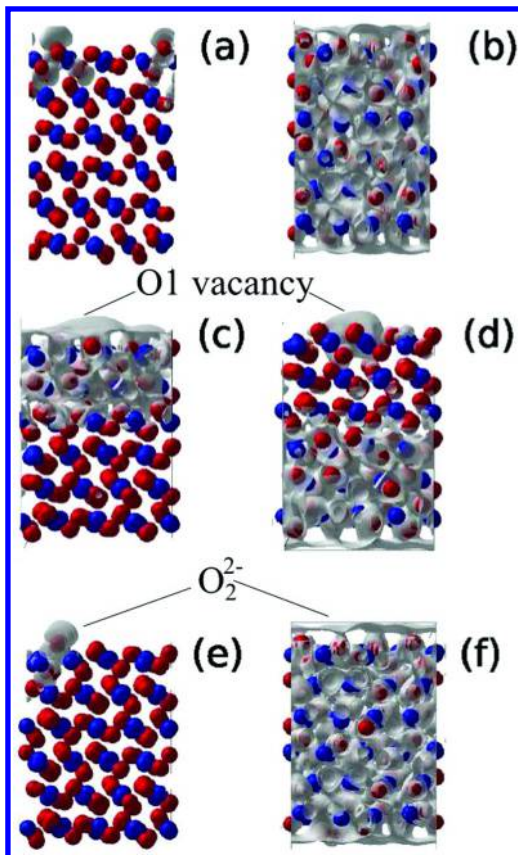


Figure 3. Partial charge density (visualized with VASP Data viewer software, (36) isosurface value = 2) of HO (a, c, e) and LU (b, d) and LU+4 (f) Kohn-Sham orbitals for stoichiometric (a, b) surface with oxygen vacancy (O1) (c, d) and O₂ molecule adsorbed on surface oxygen vacancy (O1) (e, f). Red and blue spheres represent oxygen and indium atoms, respectively. (a) HO orbital of stoichiometric slab is localized indicating that it is non-conductive. (c) Surface oxygen vacancy injects 2 free electrons into the IO slab which are delocalized and make IO film conductive. (e) Adsorbed O₂ molecule turns to O₂²⁻ state and eliminates effect of oxygen vacancy on IO film conduction properties. (b, d, f) All systems in excited states have delocalized orbitals which provide non-zero photoconductivity of IO film.

Here we also examined single water molecule dissociation on defective IO (111) surface. A water molecule adsorbed on the surface defect at O1 position is in metastable state with dissociation barrier of 0.41 eV. Corresponding values for metal- and oxygen-terminated (100) surfaces were calculated to be 0.39 and 0.61 eV, respectively (14). Water adsorbed on all other oxygen vacancy sites dissociates barrierlessly. After water dissociation hydroxyl group fills surface

vacancy position and H-atom is adsorbed by neighboring surface oxygen ion. Such structure is still conductive due to doping of IO by adsorbed hydrogen atoms. The pictures for HO and LU orbitals are qualitatively the same with Figure 3(c,d) and not shown here. But such structure is expected to be unstable since hydrogen adsorption energy was calculated to be equal to 0.13 eV. It is expected that hydrogen atoms will be detached from the IO surface that now becomes defectiveness. Such surface structure healing leads to elimination of effect O-vacancy doping (12) and makes structure non-conducting.

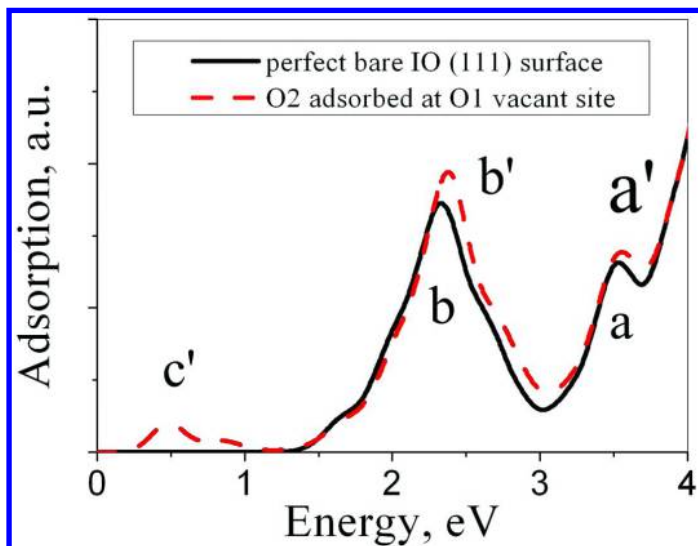


Figure 4. Linear optical adsorption spectra of bare stoichiometric (black) (111) IO surface and (111) IO surface with O₂ adsorbed on surface oxygen vacancy (dashed red). Bare surface shows a, b features. Reduced surface with adsorbed O₂ molecule demonstrates a', b' and c' features. Energies and intensities of a, a' and b, b' peaks coincide while c' is contributed by oxygen molecule chemisorption.

Summarizing, interaction of IO (111) surface with humid and dry air at elevated temperature takes place as it following. In wet air interaction of IO film with water results to formation an abundant amount of surface oxygen vacancies at O1 sites that leads to increase of free electron concentration that in turns increases the IO film's conductivity. Surface oxygen vacancies formed at other sites are healed through barrierless water dissociation. After some critical temperature water molecules dissociate on O1 vacant sites. This phenomenon leads to decrease of free electron concentration. Another one source of free electrons elimination is molecular oxygen adsorption at vacant sites. In dry air oxygen vacancies formation is less then in humid air. At the same time, adsorbed oxygen molecules partially eliminate effect of vacancies on conduction electrons concentration. As a result, conductivity after deposition in humid air is larger than the same value measured in dry air.

4. Conclusion

DFT study of the water and oxygen molecules interaction with stoichiometric and defective (111) IO surfaces was carried out. We found that there are a few competing phenomena which determine IO properties. One the one hand, water environment makes IO (111) surface unstable with respect to oxygen vacancies formation. It leads to easier surface oxygen vacancies formation in humid air that in turns increases free electron concentration, i.e. electric conductivity. On the other hand, at water molecules dissociate on surface vacancies and form stoichiometric IO surface with two adsorbed H-atoms. Since binding energy of adsorbed hydrogen atoms with IO surface is small they easily leave the surface and resulting effect is a healing of defective IO (111) surface. O₂ molecule is weakly physisorbed on stoichiometric surface while it is strongly bounded with surface vacant site. This adsorption is accompanied with transition of two free electrons from IO to oxygen molecule that now transformed to peroxide anion. Both water dissociation and oxygen chemisorption phenomena lead to decrease of free electron concentration in IO film. Taking into consideration all of these effects is essential for fundamental understanding IO-based gas sensors operating principles in different environment.

Acknowledgments

We would like to thank the Center for Computational Materials Science, Institute for MaterialsResearch, Tohoku University for their continuous support of the SR16000 M1 supercomputingsystem. One of the authors (Y. K.) thanks the Russian Mega Grant project no.14.B25.31.0030 “New energy technologies and energy carriers” for supporting the present research.

References

1. *Handbook of transparent conductors*; Ginley, D. S.; Hosono, H.; Paine, D. C., Eds.; Springer: New York, 2011 vol. XIV, 534 p.
2. Roush, C. S.; Hedge, M.; Govindaraj, A.; Rao, C. N. R. *Nanotechnology* **2007**, *18*, 205504.
3. Neri, G.; Bonavita, A.; Micali, G.; Rizzo, G.; Callone, E.; Carturan, G. Resistive CO gassensors based on In₂O₃ and InSnO_x nanopowders synthesized via starch-aided sol-gel processfor automotive applications. *Sens. Actuators, B* **2008**, *132*, 224–233.
4. Brinzari, V.; Ivanov, M.; Cho, B. K.; Kamei, M.; Korotcenkov, G. Photoconductivity in In₂O₃ nanoscale thin films: interrelation with chemisorbed-type conductometric response towards oxygen. *Sens. Actuators, B* **2010**, *148*, 427–438.
5. Gurlo, A.; Ivanovskaya, M.; Barsan, N.; Schweizer-Berberich, M.; Weimar, U.; Göpel, W.; Dièguez, A. Grain size control in nanocrystalline In₂O₃ semiconductor gas sensors. *Sens. Actuators, B* **1997**, *44*, 327–333.

6. Korotcenkov, G.; Brinzari, V.; Stetter, J. R.; Blinov, I.; Blaja, V. The nature of processes controlling the kinetics of indium oxide-based thin film gas sensor response. *Sens. Actuators, B* **2007**, *128*, 51–63.
7. Korotcenkov, G. Gas response control through structural and chemical modification of metal oxide films: state of the art and approaches. *Sens. Actuators, B* **2005**, *107*, 209–232.
8. Brinzari, V.; Korotcenkov, G.; Ivanov, M.; Nehasil, V.; Matolin, V.; Mašek, K.; Kamei, M. Valence band and band gap photoemission study of (111) In_2O_3 epitaxial films under interactions with oxygen, water and carbon monoxide. *Surf. Sci.* **2007**, *601*, 5585–5594.
9. Walsh, A.; Catlow, C. R. A. Structure, stability and work functions of the low index surfaces of pure indium oxide and Sn-doped indium oxide (ITO) from density functional theory. *J. Mater. Chem.* **2010**, *20*, 10438–10444.
10. Agoston, P.; Albe, K. Thermodynamic stability, stoichiometry, and electronic structure of bcc- In_2O_3 surfaces. *Phys. Rev. B* **2001**, *84*, 045311.
11. Zhang, K. H. L.; Walsh, A.; Catlow, C. R. A.; Lazarov, V. K.; Egdell, R. G. Surface energies control the self-organization of oriented In_2O_3 nanostructures on cubic zirconia. *Nano Lett.* **2010**, *10*, 3740–3746.
12. Walsh, A. Surface oxygen vacancy origin of electron accumulation in indium oxide. *Appl. Phys. Lett.* **2011**, *98*, 261910.
13. Lany, S.; Zakutayev, A.; Mason, T. O.; Wager, J. F.; Poeppelmeier, K. R.; Perkins, J. D.; Berry, J. J.; Ginley, D. S.; Zunger, A. Surface origin of high conductivities in undoped In_2O_3 thin films. *Phys. Rev. Lett.* **2012**, *108*, 016802.
14. Zhou, C.; Li, J.; Chen, S.; Wu, J.; Heier, K. R.; Cheng, H. First-principles study on water and oxygen adsorption on surfaces of indium oxide and indium tin oxide nanoparticles. *J. Phys. Chem. C* **2008**, *112*, 14015–14020.
15. Inerbaev, T.; Hoefelmeyer, J.; Kilin, D. Photoinduced charge transfer from titania to surface doping site. *J. Phys. Chem. C* **2013**, *117*, 9673–9692.
16. Chen, J.; Schmitz, A.; Inerbaev, T.; Meng, Q.; Kilina, S.; Tretiak, S.; Kilin, D. First-Principles Study of *p-n* Doped Silicon Quantum Dots: Charge Transfer, Energy Dissipation, and Time-Resolved Emission. *J. Phys. Chem. Lett.* **2013**, *4*, 2906–2913.
17. Han, Y.; Micha, D. A.; Kilin, D. S. *Ab initio* study of the photocurrent at the Au/Si metalsemiconductornanointerface. *Mol. Phys.* **2015**, *113*, 327–335.
18. Kresse, G.; Joubert, J. From ultrasoft pseudopotentials to the projector augmented-wave method. *Phys. Rev. B* **1999**, *59*, 1758–1775.v.
19. Blöchl, P. E. Projector augmented-wave method. *Phys. Rev. B* **1994**, *50*, 17953–17979.
20. Dudarev, S. L.; Botton, G. A.; Savrasov, S. Y.; Humphreys, C. J.; Sutton, A. P. Electron-energy-loss spectra and the structural stability of nickel oxide: an LSDA+U study. *Phys. Rev. B* **1998**, *57*, 1505–1509.
21. Erhart, P.; Klein, A.; Egdell, R. G.; Albe, K. Band structure of indium oxide: indirect versus direct band gap. *Phys. Rev. B* **2007**, *75*, 153205.
22. Zasada, F.; Piskorz, W.; Cristol, S.; Paul, J.-F.; Kotarba, A.; Sojka, Z. Periodic density functional theory and atomistic thermodynamic studies of

cobalt spinel nanocrystals in wet environment: molecular interpretation of water adsorption equilibria. *J. Phys. Chem. C* **2010**, *114*, 22245–22253.

23. Henkelman, G.; Uberuaga, B. P.; Jonsson, H. A climbing image nudged elastic band method for finding saddle points and minimum energy paths. *J. Chem. Phys.* **2000**, *113*, 9901–9904.
24. Janotti, A.; Van de Walle, C. G. Oxygen vacancies in ZnO. *J. Appl. Phys.* **2005**, *87*, 122102.
25. Van de Walle, C. G.; Neugebauer, J. First-principles calculations for defects and impurities: applications to III-nitrides. *J. Appl. Phys.* **2005**, *95*, 3851–3879.
26. Kilin, D. S.; Tsemekhman, K.; Prezhdo, O. V.; Zenkevich, E. I.; von Borczyskowski, C. *Ab initio* study of exciton transfer dynamics from a core-shell semiconductor quantum dot to a porphyrin-sensitizer. *J. Photochem. Photobiol. A* **2007**, *190*, 342–351.
27. Ramirez, J. J.; Kilin, D. S.; Micha, D. A. Electronic structure and optical absorbance of doped amorphous silicon slabs. *Int. J. Quantum Chem.* **2012**, *112*, 300–313.
28. Kilin, D.; Tsemekhman, K.; Kilina, S.; Balatski, A.; Prezhdo, O. Photo induced conductivity of porphyrin-gold composite nanowire. *J. Chem. Phys. A* **2009**, *113*, 4549–4556.
29. Vazhappilly, T.; Micha, D. A.; Kilin, D. S. Photoabsorbance and photovoltage of crystalline and amorphous silicon slabs with silver adsorbates. *J. Phys. Chem. C* **2012**, *116*, 25525–25536.
30. Kryjevski, A.; Kilin, D.; Kilina, S. Amorphous silicon nanomaterials: quantum dots versus nanowires. *J. Renewable Sustainable Energy* **2013**, *5*, 043120.
31. Molinari, M.; Parker, S. C.; Sayle, D. C.; Islam, M. S. Water adsorption and its effect on the stability of low index stoichiometric and reduced surfaces of ceria. *J. Phys. Chem. C* **2010**, *114*, 7073–7082.
32. Che, M.; Tench, A. J. Characterization and reactivity of molecular-oxygen species on oxide surfaces. *Adv. Catal.* **1983**, *32*, 1–148.
33. Suzuki, M.; Ishiguro, T.; Kozuka, M.; Nakamoto, K. Resonance Raman-spectra, excitation profiles, and infrared-spectra of $[\text{Co}(\text{salen})]_2\text{O}_2$ in the solid-state. *Inorg. Chem.* **1981**, *20*, 1993–1996.
34. Nakamoto, K. *Infrared and Raman spectra of inorganic and coordination compounds*, 3rd ed.; Wiley: New York, 1978.
35. Laasonen, K.; Car, R.; Lee, C.; Vanderbilt, D. Implementation of ultrasoft pseudopotentials in *ab initio* molecular-dynamics. *Phys. Rev. B* **1991**, *43*, 6796–6799.
36. *VASP Data Viewer*, URL <http://vaspview.sourceforge.net> (accessed Aug 19, 2011).
37. Zhang, K. H. L.; Egddell, R. G.; Offi, F.; Iacobucci, S.; Petaccia, L.; Gorovikov, S.; King, P. D. C. Microscopic origin of electron accumulation in In_2O_3 . *Phys. Rev. Lett.* **2013**, *110*, 056803.
38. Henderson, M. A.; Perkins, C. L.; Hengelhard, M. H.; Thevuthasan, S.; Peden, C. H. F. Redox properties of water on the oxidized and reduced surfaces of CeO_2 (111). *Surf. Sci.* **2003**, *526*, 1–18.

Chapter 7

Density Matrix Treatment of Optical Properties in Photovoltaic Materials: Photoconductivity at a Semiconductor Surface

David A. Micha*

Departments of Chemistry and of Physics Quantum Theory Project,
University of Florida, Gainesville, Florida 32611, U.S.A.

*E-mail: micha@qtp.ufl.edu.

Starting from the equations of motion of the reduced density matrix for a semiconductor slab excited by light and subject to an applied voltage, a derivation is given of the Drude-Lorentz photoconductance in terms of parameters which can be obtained from first principles calculations of electronic structure and dynamics. Systems of interest are surfaces of semiconductors containing adsorbates or dopants. A first application is given for the mobility of photoexcited electrons for silver clusters adsorbed on a silicon slab bounded by Si(111), forming a nanostructured surface. Changes in photomobility due to adsorption of a silver cluster versus photon excitation energies show that the adsorbates increase mobilities for visible and UV light absorption.

Introduction

The density operator combines quantum mechanics and statistical mechanics to provide a complete description of photoinduced phenomena in extended systems such as semiconductor slabs and nanostructures, including not only the quantal nature of electronic transitions, but also the statistical effects resulting from an excited localized atomic structure, such as an adsorbed cluster, interacting with a medium containing other electrons and atomic cores (1–3). Exchanging energy with the medium vibrational and electronic excitations (phonons and excitons) leads to fluctuation and dissipation effects which can be incorporated

in the equation of motion of a reduced density operator with terms involving dissipative and fluctuation rates.

The effects of externally applied light and electrical voltage, as they appear in photovoltaics and photocatalytic phenomena, can be incorporated in the treatment of both localized regions and media to provide results for light absorbance and for photoinduced mobilities (or photomobilities) in the case of semiconductors. There are scientific and technical motivations for doing research in this subject. Among them are interest in efficient capture of sunlight by materials, photoinduced production of electricity and fuels, photoinduced biological phenomena, and materials for storage of gaseous fuels (4–6).

As examples of the theoretical and computational treatments, we have published a number of papers on light absorbance, photovoltages, and dielectric functions for slabs of silicon, both crystalline and amorphous (7–13). This has been done for slabs with clean surfaces and also for nanostructured surfaces where clusters of silver atoms have been adsorbed, and for slabs where atoms of group III and V have been included as dopants, in atomic models constructed from ab initio electronic structure calculations of structures and bonding. The density operator treatment can also be developed for calculations of photomobilities, and some first derivations of the theory and results for silicon compounds are presented in this contribution.

There are some experiments in the literature showing that adsorption of silver on silicon increases its light absorbance, one of the steps needed to increase the efficiency of photovoltaic and photocatalytic devices. Among the earlier ones relating to light absorption, one has measured surface-plasmon enhanced light absorption in Si solar cells made of a Si wafer with adsorbed Ag nanoparticles of increasing size. The measurements provided the percentage of absorption enhancement as function of the Ag coverage (14). A recent measurement dealt with enhanced optical absorption of amorphous Si films by addition of Ag nanostructures. Light absorbance was measured for Ag clusters of increasing size (Ag nanoparticles of diameter 10 to 100 nm labelled Ag1 to Ag6) adsorbed on amorphous Si of increasing thickness. Absorption values were dependent on light wavelength, nanoparticle size, and film thickness. It was found that absorption is enhanced for optimal nanoparticle sizes, with measured reflection decreasing (or equivalently absorbance increasing) by 11 % for light of wavelength between 900 and 1200 nm (15). Increased absorption of light by these treated surfaces show the same trend as in our calculations with adsorbed clusters of Ag atoms. Experiments have been performed and results published also on mobilities following light absorption at interfaces of microcrystals of Si with amorphous Si and have provided some measured values of photomobilities of electrons and holes (16). Our first results appear to give similar magnitudes for surface photomobilities in our related systems.

This chapter focuses on photoexcitation of nanostructured semiconductor surfaces, and in particular silicon slab surfaces nanostructured with periodically adsorbed metal clusters subject to photoexcitation by visible and near infrared light, and with created photocurrent extracted with a voltage field. This is illustrated in Figure 1 below, where a semiconductor slab is shown in grey and adsorbed metal clusters in blue.

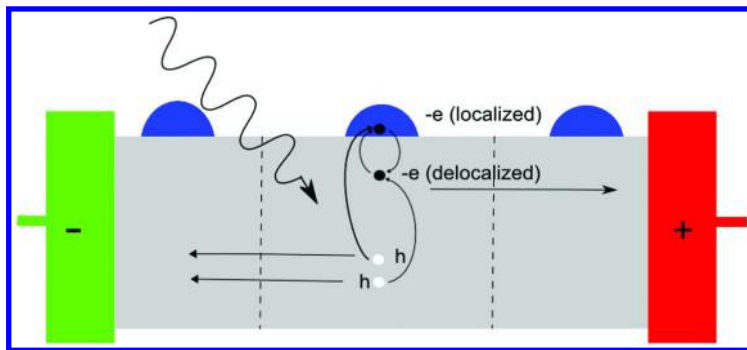


Figure 1. Pictorial representation of a semiconductor slab (grey) with adsorbed metal clusters (blue) undergoing photoexcitation by visible and near infrared light. This creates holes in the slab and electrons delocalized in the slab and localized at the adsorbates. Charged carriers are extracted by application of a voltage potential difference between electrodes, or by electric fields created by regions with p- and n-dopants, shown with positive and negative signs. From ref. (27).

To describe these physical systems and their properties it is convenient to model it as a primary region of interest involving active particles and degrees of freedom, and in contact with a secondary region containing a medium made up of electrons and atomic cores. In our case, a primary (p-) system is composed of electrons in photoactive states, adsorbed atoms, and their neighbors, undergoing localized vibrational motions. A secondary (s-) system or medium is composed of fluctuating electronic densities and vibrating atoms, alternatively described in terms of excitons and phonons.

Electrons in the p-region are activated by light absorption and undergo transitions from occupied states in the valence energy band (VB) to unoccupied states in a conduction band (CB). Adsorbed species and dopants add states near and inside the band gap of the semiconductor and also participate in the transitions. The range of energy levels involved in photoexcitation is shown schematically in Figure 2.

The interaction of electronic and ionic motions in a p-region of interest, and its behavior while interacting with a medium or s-region, lead to complex dynamics. Related fluctuation and dissipation phenomena require a treatment combining electronic structure and non-equilibrium statistical mechanics. Furthermore the absorption of light induced quantum transition between electronic states, so that the dynamics and statistical mechanics must be done within a quantum theory. This can best be described by density matrices instead of wavefunctions. A density operator for the whole system provides a starting point, which can be followed by construction of a reduced density operator (RDOp) for the primary region, formally discharging s-degrees of freedom by taking a trace over s-variables of electrons and ions (2). This is described in some detail in what follows.

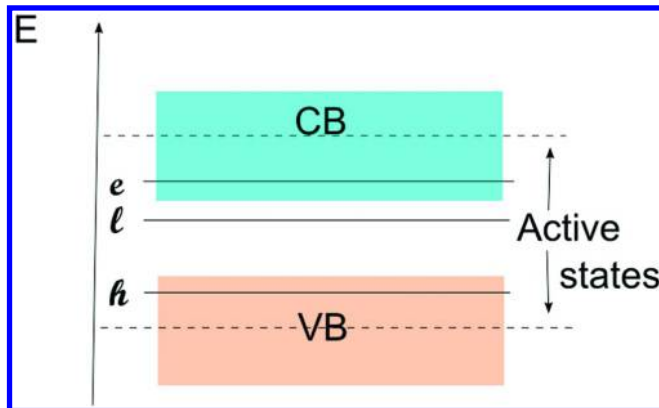


Figure 2. Schematic representation of energy levels activated by light absorption in a semiconductor, as treated in what follows. Electrons (*e*) are promoted to the conduction band (CB) leaving behind holes (*h*) in the valence band (VB). Localized (*l*) electron levels appear due to the presence of adsorbates or dopants. The range of active energy levels can be increased in calculations to verify convergence of calculated properties.

Nanostructured Semiconductor Surfaces

Light absorption can excite electrons in semiconductors with a sufficiently small energy band gap, or semiconductors containing dopants which create additional energy levels in band gaps. The most extensively studied semiconductor compounds are silicon based, with addition of group III or V dopants (17–19). We have modeled structures and optical properties of crystalline and amorphous silicon slabs with surface bonds passivated by hydrogen bonds (c-Si:H and a-Si:H) in slabs limited by the (111) surface for crystals, both pure and with dopants. In addition, and we have published results for Si slabs containing silver atom clusters of several sizes, which we have found to increase the light absorbance of surfaces, a factor important in photovoltaic devices. What follows concentrates on surfaces of Si with a periodic lattice of adsorbed Ag clusters, forming a nanostructured surface. The theoretical treatment however is quite general and can be applied to a variety of semiconductors, with dopants and, or with adsorbates.

Metal clusters have optical properties that can be controlled with their size and shape (20, 21). Adsorbed on semiconductor surfaces, they create photovoltages when they absorb steady visible light. These adsorbates provide pathways for electron transfer and electronic charge separation, of interest in photovoltaics. One of the issues is how long charge separation lasts, and our modeling has helped identify structures and mechanisms with long lasting separation of charges. Photocurrents can be extracted with applied voltages for those charges. Figure 3 shows a supercell of a slab containing four Si layers and with a Ag₃ adsorbed cluster, one of several similar systems with up to 20 layers we have studied. The slab structure is generated by periodically translating the supercell along x- and

y-directions, with the slab surfaces perpendicular to a z-axis. The supercell has an orthorhombic symmetry, and its reciprocal space, also orthorhombic, has a Brillouin zone with axes along wavenumber k directions x, y, and z with an origin labelled as the Γ point and going to X, Y, and Z points in reciprocal space.

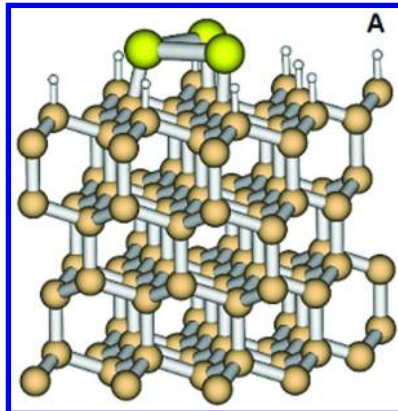


Figure 3. A c - SiAg_3H supercell with four Si layers. Structures have been studied with up to 20 layers and up to 37 Ag atoms in each cluster, giving increased thickness and cluster sizes which lead to varying light absorption. Reproduced with permission from ref. (8). Copyright 2009 American Chemical Society.

The early experimental work inspired our theoretical treatment of optical properties of Si slabs with adsorbed Ag clusters using density matrix methods for dissipative dynamics, and computational calculations of photovoltages. The observation that metal clusters of silver adsorbates have been observed to enhance the optical properties of semiconductors and can be controlled by their size and shape has been confirmed by our earlier modeling.

Modeling Optical and Conductivity Properties at Surfaces

Small metal clusters with $N_A < 4^3$ atoms behave like molecules in their measured optical properties and in relaxation phenomena, and must be described starting from their atomic composition. We have used a reduced density matrix (RDM) approach combined with ab initio electronic structure calculations from *ab initio* density functional treatments (DFT) (19). These provided atomic conformations, electronic structure, and optical properties of nanostructured surfaces, for small Ag clusters with $N_A=1, 2, 3, 4$, adsorbed on Si slabs of varying thickness, and for a large cluster with 37 Ag atoms. Introducing basis

sets of Kohn-Sham (K-S) electronic orbitals to expand quantum operators, the equation of motion (EOM) for the density operator is transformed into coupled differential equations for density matrix elements dependent on the time variable. Photoelectron dynamics is obtained from electronic state populations which follow from either steady state or relaxing solutions for the RDM, with diagonal elements giving populations and off-diagonal elements giving quantum coherences.

Light absorption leading to electronic excitation can be assumed to happen while electrons maintain their initial momentum $\hbar\vec{k}$. In most cases a good description of absorbance can be obtained using a basis set of electrons with zero momentum (at the Γ point of the Brillouin zone). But calculations of photoconductivity require an extension to include states with non-zero momentum. Orbitals in nanostructured slabs are shaped by the effective electronic potential where the first term is the potential of the pure a-Si or c-Si slabs, the second is the electronic perturbation around the adsorbed atoms, and the last term is a shift in potential energy change due to lattice distortions around the adsorbates. This gives

$$\hat{U}^{KS} = \hat{U}_0^{KS} + \hat{U}_{ads}^{KS} + \hat{U}_{dist}^{KS}$$

Electronic Bloch orbitals and energies with electron wavevector \vec{k} and band index j for the Brillouin zone of supercells have been obtained using atomic pseudopotentials, with periodic boundary conditions. They can be written as linear combinations of plane waves with reciprocal grid wavevectors, in the form

$$\varphi_{\vec{k}j}(\vec{r}) = \exp(i\vec{k} \cdot \vec{r}) \sum_{|\vec{G} + \vec{k}| < G_{cut}} C_{\vec{k}j, \vec{G}} \cdot \exp(-i\vec{G} \cdot \vec{r})$$

Solutions to the K-S equations provide these states and related energy levels. Electronic density of states (EDOS) are calculated from sums over Lorentzians, as shown below, where $w = 0.02\text{--}0.10$ eV is an estimated orbital energy width due to coupling with excitons and thermal vibrations of the lattice.

$$D(\varepsilon) = \sum_{\vec{k}} (w/\pi) [w^2 + (\varepsilon - \varepsilon_{\vec{k}j})^2]^{-1}$$

Most results in what follows have been obtained with the *Vienna Ab-initio Simulation Package (VASP)* (22), the Perdew-Wang 91 (PW91/PW91) GGA density functional (23), and core electrons of heavy atoms handled with Vanderbilt ultra-soft (US) pseudopotentials. The PBE (24) and HSE (25) functionals have also been used with norm conserving atomic pseudopotentials provided also by the Quantum Espresso software package.

Light absorbance can be obtained from orbitals generated for the valence and conduction bands of the slabs, at fixed electron wavevector after calculation of electric transition dipoles appearing in the expression for the light absorption as shown in the equations below.

$$\vec{D}_{ij} = \sum_{|\vec{G}|, |\vec{G}'| < \vec{G}\text{-cutoff}} C_{i,\vec{G}}^* \vec{D}_{\vec{G},\vec{G}'} C_{j,\vec{G}'} \quad , \quad \text{transition dipole for fixed } \vec{k}$$

$$\alpha(\hbar\Omega_L) = \sum_{I=(ij)} f_I \delta_\sigma(\hbar\Omega_L - \hbar\omega_I), \quad \text{absorbance}, \quad \delta_\sigma(\hbar\omega) = \sigma / [\pi(\sigma^2 + \hbar^2\omega^2)]$$

$$f_{ij} = \left| \vec{D}_{ij} \right|^2 \left(\frac{4\pi \cdot m_e v_{ij}}{3e^2 \hbar} \right), \quad \text{oscillator strength}$$

Here transitions are labelled by $I=(ij)$, light has frequency Ω_L and m_e is the electron mass.

Several treatments of photoconductivity are available in the literature with models of varying details and with parameters such as effective masses and relaxation times obtained from experiment or independent calculations (17, 18). Among them are physical kinetics models (the Drude-Lorentz model for semiconductors), using local electron densities and currents. A more detailed treatment follows from the Boltzmann equation approach, a traditional treatment for near thermal equilibrium conductivity, including effective masses and transport relaxation times independently obtained. The electronic Green's functions (propagator) treatment is general in principle and has been developed for near thermal equilibrium conductivity, but is quite difficult to implement computationally for electronically excited systems.

Calculation of the electronic photoconductivity starting from atomic structure is quite challenging and has required in our case to develop a new treatment using the RDM. This can be used to derive descriptions near and far from equilibrium, kinetics models and expressions for equation parameters. Some aspects are described in the next Section.

Density Operator Approach

The Liouville-vonNeumann (L-vN) equation for a primary (p-) region coupled to a dissipative secondary (s-) region of an infinite system, both interacting with light, involves the total Hamiltonian for the regions and light in interaction, given by

$$\hat{H} = \hat{H}_p + \hat{H}_s + \hat{H}_{ps} + \hat{H}_{pl} + \hat{H}_{sl}$$

The reduced density operator $\hat{\rho}$ refers to the p-region and involves an average over an statistical distribution in the s-region, obtained formally by taking the trace of the DOp $\hat{\Gamma}$ of the whole system over the s-variables,

$$\hat{\rho}(t) = \overline{tr_s[\hat{\Gamma}(t)]}$$

Doing this for the EOM of the whole system leads to the RDM EOM,

$$\frac{\partial \hat{\rho}}{\partial t} = -\frac{i}{\hbar} [\hat{F}_p + \hat{F}_{pl}, \hat{\rho}(t)] - \hat{\mathcal{R}}_p \hat{\rho}(0) - \frac{1}{\hbar^2} \int_0^t dt' \hat{\mathcal{M}}_p(t, t') \hat{\rho}(t')$$

where the first term contains effective hamiltonians, and the second and third terms contain a fluctuation (averaging to zero over initial variables) and a dissipative superoperator (including a delay) in the p-region. They can be obtained from the time-correlation functions of the s-region (1-3).

Dissipative rates from fast electronic motions and slow atomic motions are usually separated into fast and slow terms,

$$\hat{\mathcal{M}}_p(t, t') = \hat{\mathcal{M}}_p^{(el)}(t, t') + \hat{\mathcal{M}}_p^{(at)}(t, t')$$

Fast (instantaneous) electronic dissipation is due to electronic fluctuations (excitons) in the medium and is described by the Lindblad rate expression constructed from transition rates between vibronic states in the p-region induced by interactions with the s-region. Slow (delayed) dissipation is due to atomic lattice vibrations. The slow dissipation due to vibrational motions (phonons) can be obtained for bilinear couplings of p- and s-regions in terms of time-correlation functions of s-region displacements and the time evolution operator of the p-region. For measurement times long compared with TCF relaxation times, it can be obtained from the Redfield approximation for dissipative rates, which gives differential equations containing only the RDop at time t (1-3).

The RDop is yet a many-electron object with all the position and spin variables of electrons in the p-region. To proceed, it is convenient to further reduce the treatment introducing effective one-electron operators. These can then be expanded in a basis set of vibronic-light field states composed of one-electron states times vibrational states for the atoms in the p-region. Equations for the one-electron density operator and a given atomic configuration $\{Q\}$ follow from the contraction

$$\rho^{(1)}(x; x') = \text{tr}_{N-1} [\rho(x, X^{N-1}; x', X^{N-1})]$$

RDM elements are obtained in a basis set of K-S orbitals satisfying the equation $\hat{F}^{KS} \phi_{\bar{k}j} = \varepsilon_{\bar{k}j} \phi_{\bar{k}j}$ and given by

$$\rho_{\bar{k}j, \bar{k}'j'} = \langle \phi_{\bar{k}j} | \hat{\rho}^{(1)} | \phi_{\bar{k}'j'} \rangle$$

This is yet a function of atomic position variables and of photon variables, and must be expanded to include vibrational states of the lattice and photon field states. For photoinduced transitions involving only one photon absorption or emission, it is sufficient to construct one-photon and no-photon states as in

$$\{|a\rangle\} = \{|\vec{k}j\rangle \otimes |n_{\bar{k}\sigma}\rangle\}, \text{ electron-photon field basis set}$$

$$|n_{\bar{k}\sigma}\rangle = |1_{\bar{k}\sigma}\rangle, \text{ one photon in occ states}; = |\theta_{\bar{k}\sigma}\rangle, \text{ no photons in unocc states}$$

$$\{|\alpha\rangle\} = \{|\vec{k}j\nu_j\rangle \otimes |n_{\bar{k}\sigma}\rangle\}, \text{ vibronic-field basis set}$$

Expansion of operators with this choice of photon states gives the same results as working in the rotating wave approximation (RWA) for the equation of motion of the RDM (3). Vibrational matrix elements of an operator \hat{A} can be obtained in the Frank-Condon approximation as

$$\langle \alpha | \hat{A} | \alpha' \rangle = \langle \alpha | \alpha' \rangle_{FC} \langle \vec{k}j | \hat{A}(Q_{ave}) | \vec{k}'j' \rangle$$

Working in this basis set the RDM EOM can be derived for long times compared to the relaxation times in the s-region as given by their exciton and phonon time-correlation functions. Under these conditions the form of the dissipative rates take the Redfield form. To simplify, the equations are given below for matrices in the basis set of purely one-electron states, for fixed atomic positions and fixed electronic wavevectors, and in a rotating frame where terms oscillating with the light frequency have been eliminated, as in the rotating wave approximation (RWA) (8).

$$\begin{aligned} \frac{d\tilde{\rho}_{jj}}{dt} &= \frac{i}{2} \sum_k \Omega_{jk} (\tilde{\rho}_{kj} - \tilde{\rho}_{jk}) - \gamma_{jj} (\tilde{\rho}_{jj} - \tilde{\rho}_{jj}^{(eq)}) , \text{ population change} \\ \frac{d\tilde{\rho}_{jk}}{dt} &= -i\Delta_{jk} \tilde{\rho}_{jk} - i\Omega_{jk} (\tilde{\rho}_{kk} - \tilde{\rho}_{jj}) - \gamma_{jk} (\tilde{\rho}_{jk} - \tilde{\rho}_{jk}^{(eq)}) , j \neq k , \text{ coherence change} \\ \gamma_{jj} &= \sum_{k \neq j} \kappa_{jk} , \quad \gamma_{jk} = \sum_l (\kappa_{jl} + \kappa_{lk}) / 2 + \gamma_{jk}^0 , \text{ relaxation rates} \\ \kappa_{jk} &= \hbar^{-2} |V_{jk}|^2 J(\omega_{jk}) f_{BE}(\omega_{jk}, T) , \text{ state-to-state transition rate} \end{aligned}$$

The symbols here are

$$\begin{aligned} E(t) &= E_0 \cos(\Omega_L t + \phi) : \text{Applied light field} \\ \Omega_{jk} &= -D_{jk} E_0 : \text{Rabi frequency} , \quad \Delta_{jk} = \Omega_L - \omega_{jk} : \text{Detuning frequency} \\ \hbar\omega_{jk} &: \text{Electronic excitation energy} \\ J(\omega) &: \text{Vibrational frequency density} \\ V_{jk} &: \text{Medium-induced electronic transition} \\ f_{BE}(\omega, T) &: \text{Thermal distribution of frequencies} \end{aligned}$$

These coupled differential equations can be solved numerically for any given external light field. In particular, for steady light excitation it is possible to concentrate on steady state solutions obtained by setting the left hand side of the EOM equal to zero:

$$\begin{aligned} &\text{Steady state solution for light of frequency } \Omega_L \\ &\frac{d\tilde{\rho}_{jk}}{dt} = 0 \rightarrow \tilde{\rho}_{jk}^{(ss)}(\Omega_L) \quad (\text{in a rotating frame}) \end{aligned}$$

This solution provides populations of excited states given by its diagonal elements, and also a way for calculating electronic current averages. Explicit solutions for the matrix elements in terms of the Rabi frequency and state-to-state transition rates are given in ref. (8).

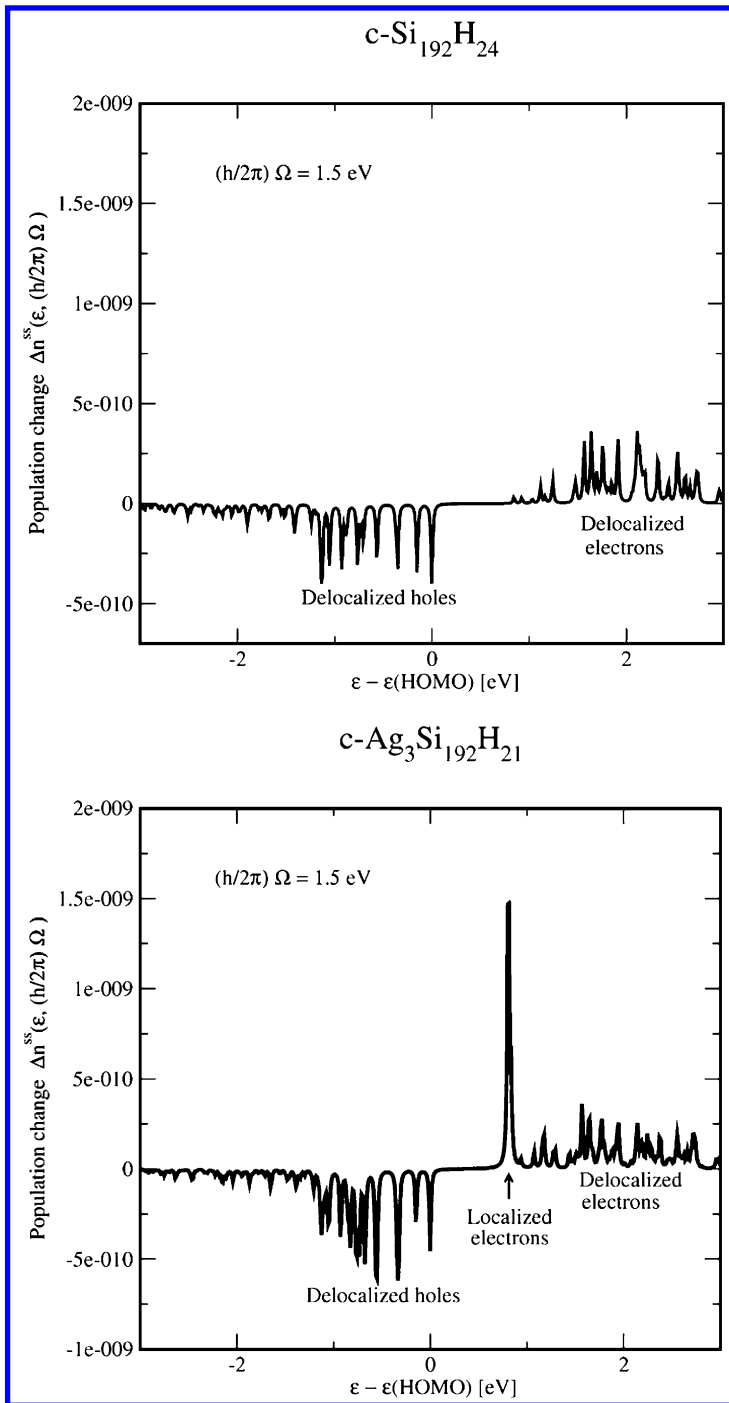


Figure 4. The top panel gives photoinduced population changes in a supercell for a Si slab with eight layers, at a photon energy of 1.5 eV, versus the energy of electronic orbitals with reference to the HOMO energy. It shows only delocalized electrons and holes created by light absorption. The lower panel gives similar results but with a Ag cluster adsorbate. There is a pronounced localized population of electrons at the cluster, and a larger population of delocalized holes, as compared with the top panel. Results were obtained with the PW91 density functional for electron band states at the Γ point of the Brillouin zone for an octahedral supercell. From ref. (26), previously unpublished.

Charge Carriers at Photoexcited Surfaces

Light absorbed at a Si surface induces excitation of both short lived and long lived many-electron states $I=G, E, F, \dots$. It is possible to separate a direct mechanism where light absorption to an excited electronic state E is rapidly followed by emission back to the ground electronic state as in $G \rightarrow E \rightarrow G$, from an indirect mechanism where a final long-lasting charge separation state F is formed, as in $G \rightarrow E \rightarrow F$. Electrons and holes are created by direct or indirect photoexcitation, but only the long lasting states allow enough time for extraction of a photovoltaic current by application of an external voltage (9, 12). When this is done, electrons and holes driven by an electric potential can flow through the slab lattice or jump between sites at its surface, or between dopant sites.

Standard treatments of conductivity have been extensively developed for charge transport near thermal equilibrium, and must be extended to account for photoexcitation. Among these are semiempirical treatment like the Drude model containing parameters for effective masses, transport relaxation times, and dielectric constants; extension of the Boltzmann transport equation to include the Boltzmann phase space distribution of a photoexcited system, including relaxation times for photoexcited charges; and more fundamental treatments using the Kubo formulation with time-correlation of fluxes, but with averages over photoexcited populations instead of thermal populations (3, 17, 18).

The long lasting charge separation states can be found from the steady state solutions for the RDM and this can provide the average of charge fluxes J_s at the slab surface during photoexcitation. For steady state light of frequency Ω_L and voltage of frequency ω_V , we can write in terms of matrix elements of a velocity operator between Bloch states (17),

$$\begin{aligned}
 \left\langle \left\langle \hat{\vec{J}}_S \right\rangle \right\rangle_{\omega_V} &= n_e \sum_{\vec{k}_s, j} \left\langle \vec{k}_s j \left| \hat{\vec{v}} \right| \vec{k}_s j \right\rangle \bar{\rho}_{jj}^{(ss)}(\vec{k}_s, \vec{k}_s; \Omega_L, \omega_V) \\
 &= n_e \sum_{\vec{k}_s, j} \hbar^{-1} (d\varepsilon_j / d\vec{k}_s) \bar{\rho}_{jj}^{(ss)}(\vec{k}_s, \vec{k}_s; \Omega_L, \omega_V) \\
 \left\langle \left\langle \hat{\vec{J}}_S \right\rangle \right\rangle_{\omega_V}^{(tot)} &= \vec{J}_e(\Omega_L, \omega_V) + \vec{J}_h(\Omega_L, \omega_V)
 \end{aligned}$$

where the total flux average contains electron and hole contributions.

Of special interest here is a comparison of the densities of photoinduced charge carriers without and with adsorbed Ag. The diagonal elements of the steady state RDM solutions provide changes in populations relative to the equilibrium values as shown below.

$$\Delta N_{\vec{k}j}^{(ss)} = \tilde{\rho}_{\vec{k}j, \vec{k}j}^{(ss)}(\hbar\Omega_L) - \tilde{\rho}_{\vec{k}j, \vec{k}j}^{eq}$$

These population changes have been obtained in calculations done for photons of energy 1.5 eV, and are shown below in two panels of Figure 4 at the Γ point in the Brillouin zone (wavevector $k=0$) of an octahedral supercell in the Si slab. They are given for a photon source with intensity corresponding to a black body at 5,800 K. As seen by comparison, the effects of adding Ag are to create localized electrons and to increase the density of delocalized holes. These results are from DFT calculations with VASP PW91 (26).

Derivation of a Drude-Lorentz Photoconductivity Equation

A useful treatment of photoconductivity can be based on the equations for the average momentum p of charge carriers u (electrons or holes). They can be derived starting from the EOM of the RDM and constructing the averages $\langle p \rangle_u = \text{tr}(\hat{p} \hat{\rho}_u)$. We employ the one-electron RDOp EOM for the p-region of a nanostructured $\text{Ag}_N\text{Si:H}$ slab interacting with quantized light, and with an electrical voltage (due to electrodes or to n- and p-dopant regions) and containing dissipative rates from s-region electronic excitations (excitons) and atomic lattice vibrations (phonons).

For semiconductors, the light field \vec{E}_L of frequency ω_L leading to excitation is the local field obtained from the dielectric function of the medium (a Si slab with adsorbed clusters). It interacts with the p-region as described by the EOM for the one-electron RDM including the Redfield dissipative rate, in

$$\frac{\partial \hat{\rho}^{(1)}}{\partial t} = -\frac{i}{\hbar} \left[\hat{F}^0 + \hat{H}_{pL} + \hat{H}_{pV}(t), \hat{\rho}^{(1)}(t) \right] - \hat{\mathcal{R}} \hat{\rho}^{(1)}(t)$$

$$\hat{\mathcal{R}} = \hat{\mathcal{R}}^{(el)} + \hat{\mathcal{R}}^{(at)}$$

where the dissipative rate superoperator contains two terms, with (el) from electron-exciton coupling and (at) from electron-phonon coupling. We include the (el) dissipative rate in the eq. for the steady state RDM, and consider the (at) rate when we calculate the transport relaxation rate for electronic conductivity.

The basis set of one-electron states for electrons of given momentum $\hbar\vec{k}$ and in a vibronic state $|j\mathbf{v}_j\rangle$ for electronic orbital j form an expansion set of states $|\vec{k}j\mathbf{v}_j\rangle$ used to transform the operator equation above into a matrix of coupled differential equations to be solved for stationary light excitation. In an isolated p-region and in the absence of electronic spin-orbit coupling, light absorption leads to a vertical excitation where the electron momentum does not change. In a medium, this transition is perturbed by lattice phonons and excitons which produce a relaxation of the photoexcited state. The electron momentum operator can be written as a sum of its average value plus a collision induced term, as

$$\hat{\vec{p}} = \langle \vec{p}(t) \rangle + \Delta \hat{\vec{p}}, \quad \langle \vec{p}(t) \rangle = \text{tr}[\hat{\vec{p}} \hat{\rho}^{(1)}(t)]$$

and the density operator here can be written as a sum of a steady state term incorporating electronic dissipation in the medium, due to excitons, plus a correction coming from atomic vibrations in the medium and leading to collisional relaxation of charge transport, as shown below.

$$\hat{\rho}^{(1)}(t) = \hat{\rho}^{(se)} + \hat{\rho}'(t)$$

$$0 = -\frac{i}{\hbar} \left[\hat{F}^0 + \hat{H}_{pL}, \hat{\rho}^{(se)} \right] - \hat{\mathcal{R}}^{(el)} \hat{\rho}^{(se)}$$

Here the steady state solution is found as in Ref. (8) and contains linearly the local light field. Returning to the EOM for the RDOp which includes also the electric field from an applied voltage, the EOM for the average momentum is then

$$\frac{d\langle \vec{p} \rangle}{dt} = N_{el}^* c_{el} \vec{E}_V(t) - \frac{\langle \vec{p} \rangle}{\tau} + \Delta \vec{F}_{coll}(t) \xrightarrow{\text{time ave.}} \frac{d\langle \vec{p} \rangle}{dt} = N_{el}^* c_{el} \vec{E}_V(t) - \frac{\langle \vec{p}(t) \rangle}{\tau}$$

with a transport relaxation time τ and a random collision force in parameters

$$1/\tau = \text{tr}[\hat{\mathcal{R}}^{(at)} \hat{\rho}^{(se)}]$$

$$\Delta \vec{F}_{coll}(t) = -N_{el}^* \text{tr}[\Delta \hat{\vec{p}}_1 \hat{\mathcal{R}}^{(at)} \hat{\rho}^{(se)}]$$

and with the random collision force averaging to zero over times large compared with the relaxation time, as shown above. The result is a simple differential equation for the average momentum, but with explicit expressions for the equation parameters in terms of the supermatrices that describe electronic and vibrational dissipation. These can be obtained from *ab initio* electronic structure calculations as done by us before for light absorption (8, 13). The electrical current of a charged carrier (here an electron) is just the velocity times electron density per unit volume, or

$$\vec{J}(t) = c_{el} \langle \vec{p}(t) \rangle / (m_{el} V_{Sl})$$

and its Fourier transform for an oscillating applied voltage gives the conductivity coefficient σ from

$$\begin{aligned} \tilde{J}(\omega_V) &= \sigma(\omega_V) \tilde{E}_V(\omega_V) , \\ \sigma(\omega_V) &= (N_{el}^* / V_S) (c_{el}^2 \tau / m_{el}) / (1 - i\omega_V \tau) = \sigma' + i\sigma'' \end{aligned}$$

These equations apply separately to photoexcited electrons (e) and holes (h), so that the total photoconductivity is their sum. The conductivities can alternatively be expressed in terms of mobilities μ , usually measured in semiconductors, multiplying carrier concentrations. The equations are shown below, with asterisks indicating properties changed by light absorption.

Photoinduced population of carriers $u = e, h$: $\Delta N_{ku}^{(ss)}(\hbar\Omega_L) = \sum_{j \in B_u} [\tilde{\rho}_{kj, \bar{k}j}^{ss}(\hbar\Omega_L) - \tilde{\rho}_{kj, \bar{k}j}^{eq}(\hbar\Omega_L)]$

$\sigma^* = n_e^* c_e \mu_e^* + n_h^* c_h \mu_h^*$ *photoconductivity for an applied voltage field $E_{V,x}$*

$n_u^* = \Delta N_u^{(ss)} / V_{SC}$, $\mu_u^* = \bar{v}_{u,x} / E_{V,x} = c_u \tau_{ux} / m_u^*$ *: photomobility*

Here the effective masses in the mobilities can be also calculated, from the second derivatives of Bloch energies with respect to electron wavevectors.

The above equations provide all the information needed to obtain mobilities from first principle electronic structure and molecular dynamics calculations. The equations also provide a way to estimate the changes in conductance due to changes in atomic structure, and in the present application they can be used to estimate how the addition of a Ag cluster to a Si slab would change the conductance. The most important change is in the photoinduced populations of carrier states, and to estimate these we can use the mobilities of electrons and holes available from the literature for bulk Si, of values 1350 cm²/(Vs) and 480 cm²/(Vs) for electrons and holes, respectively (27). The following Figure 5 gives the relative change $\Delta_C \sigma^* / \sigma(Si) = [\sigma(Ag_3Si) - \sigma(Si)] / \sigma(Si)$ due to addition of the cluster to a slab with eight layers of Si and all Si dangling surface bonds saturated by H atoms or the three Ag atoms on top positions, versus photon energies. The carrier populations came as before from density functional calculations using periodic boundary conditions, atomic pseudopotentials, and the PW91 functional. It is seen that adding a Ag cluster increases photoconductivity in the region of

visible and UV light, with both electron and hole contributions increasing after photoexcitation. In this figure, photon energies have been scaled dividing by the band gap EBG= 0.84 eV on all plots and population changes have been scaled by 1.50e-10 charge carriers in the pure Si supercell volume (28).

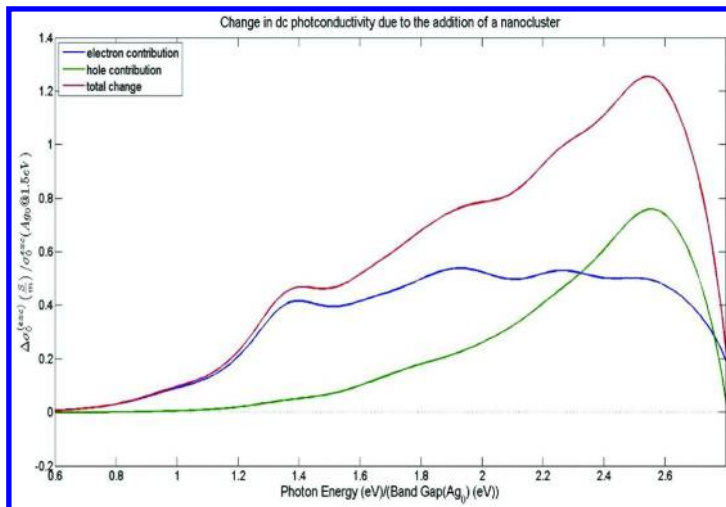


Figure 5. Relative changes to the photoconductance $\Delta_C\sigma^/\sigma(Si) = [\sigma(Ag_3Si) - \sigma(Si)]/\sigma(Si)$ due to addition of a Ag cluster to a slab with eight layers of Si versus photon energies. It is seen that adding a Ag cluster increases photoconductivity in the region of visible and UV light, with both electron and hole contributions increasing after photoexcitation. From ref. (28), previously unpublished.*

Conclusion

A combination of density matrix methods for dissipative dynamics and ab initio electronic structure methods for many-atom systems provide insight and useful results on optical properties and photoconductivity of Si slabs with adsorbed Ag clusters. Similar treatments could be applied to structures with dopants and to quantum dots of related elements. , and on quantum dots of similar compounds.

The present treatment extends our previous work by now adding energy band states with a range of electron wavevectors. This allows consideration of conductivity effects driven by applied voltages, which may come from regions of n- and p-dopants, or from the application of external voltages. A Drude –Lorentz model has been derived from the reduced density matrix equations of motion, that provides a differential equation for the charge carrier momenta and also computational expressions for equation parameters in terms of quantities that can be obtained from ab initio electronic structure and molecular dynamics.

Here the first results of our Drude-Lorentz model are shown comparing pure Si slabs and slabs with adsorbed Ag clusters. They indicate that adsorption of a cluster leads to large increases of photoconductivity.

Acknowledgments

The author thanks Drs. Tijo Vazhappilly and Robert Hembree for generating results for figures 4 and 5. This work has been partly supported by grants NSF CHE1011967 and CHE-1445825. Computer support was provided by the High Performance Computer facility of the University of Florida.

References

1. May, V.; Kuhn, O. *Charge and Energy Transfer Dynamics in Molecular Systems*; Wiley-VCH: Berlin, 2000.
2. Micha, D. A. From few-atom to many-atom quantum dynamics. *Adv. Quantum Chem.* **2002**, *41*, 139.
3. Nitzan, A. *Chemical Dynamics in Condensed Phases*; Oxford Univ. Press: Oxford, England, 2006.
4. Alivisatos, A. P. Semiconductor clusters, nanocrystals, and quantum dots. *Science* **1996**, *271*, 933–937.
5. Kamat, P. V. Quantum dot solar cells. Semiconductor nanocrystals as light harvesters. *J. Phys. Chem.* **2008**, *112*, 18737–18753.
6. Nozik, A. J. Nanoscience and Nanostructures for Photovoltaics and Solar Fuels. *Nano Lett.* **2010**, *10*, 2735–2741.
7. Micha D. A.; Leathers, A. S. Reduced density matrix equations for combined instantaneous and delayed dissipation in many-atom systems, and their numerical treatment. In *Energy Transfer Dynamics in Biomolecular Systems*; Burghardt, I., May, V., Micha, D. A., Bittner, E. R., Eds.; Springer-Verlag: Berlin, 2009; pp 363.
8. Kilin, D. S.; Micha, D. A. Surface Photovoltage at Nanostructures on Si Surfaces: Ab Initio Results. *J. Phys. Chem. C* **2009**, *113*, 3530–3542.
9. Leathers, S.; Micha, D. A.; Kilin, D. S. Direct and indirect electron transfer at a semiconductor surface with an adsorbate: Theory and application to Ag₃Si(111):H. *J. Chem. Phys.* **2010**, *132*, 114702–1.
10. Kilin, D. S.; Micha, D. A. Relaxation of Photoexcited Electrons at a Nanostructured Si(111) Surface. *J. Phys. Chem. Lett.* **2010**, *1*, 1073–1077.
11. Micha, D. A. Density matrix treatment of non-adiabatic photoinduced electron transfer at a semiconductor surface. *J. Chem. Phys.* **2012**, *137*, 22A521.
12. Hembree, R. H.; Micha, D. A. Photoinduced Electron Transfer at a Si(111) Nanostructured Surface: Effect of Varying Light Wavelength, Temperature, and Structural Parameters. *J. Chem. Phys.* **2013**, *138*, 184708.
13. Vazhappilly, T.; Micha, D. A. Computational Modeling of the Dielectric Function of a Silicon Slab with Varying Thickness. *J. Phys. Chem. C* **2014**, *118*, 4429–4430.
14. Pillai, S.; Catchpole, K. R.; Trupke, K.; Green, M. A. Surface plasmon enhanced silicon solar cells. *J. Applied Phys.* **2007**, *101*, 093105.
15. Zhou, B.; Li, D.-S.; Xiang, L.-L.; Yang, D.-R. Enhanced optical absorption of amorphous silicon films by Ag nanostructures. *Chin. Phys. Lett.* **2010**, *27*, 737303.

16. Juska, G.; Nekrasas, N.; Arlauskas, K.; Stuchlik, J.; Fejfar, A.; Kocka, J. Photogenerated carriers in micro-c-Si:H/a-Si:H multilayers. *J. Non-Crystalline Solids* **2004**, *338-340*, 353.
17. Ashcroft N. W.; Mermin, N. D. *Solid State Physics*; Thomson: London, 1976.
18. Callaway, J. *Quantum Theory of the Solid State*, 2nd ed.; Academic Press: San Diego, California, 1991.
19. Martin, R. M. *Electronic Structure*; Cambridge University Press: Cambridge, England, 2004.
20. Malinsky, M.; Kelly, K.; Schatz, G.; VanDuyne, R. P. Nanosphere Lithography: Effect of Substrate on the Localized Surface Plasmon Resonance Spectrum of Silver Nanoparticles. *J. Phys. Chem. B* **2001**, *105*, 2343–2350.
21. Link, S.; ElSayed, M. A. Optical properties and ultrafast dynamics of metallic nanocrystals. *Ann. Rev. Phys. Chem* **2003**, *54*, 331–366.
22. Hafner, J. Ab initio simulation of materials using VASP: Density functional theory and beyond. *J. Comput. Chem.* **2008**, *29*, 2044–2078.
23. Perdew, J. P.; Wang, Y. Accurate and simple analytical representation of the electron gas correlation energy. *Phys. Rev. B* **1992**, *45*, 13244.
24. Perdew, J. P.; Burke, K.; Ernzenhof, M. Generalized gradient approximation made simple. *Phys. Rev. Lett.* **1996**, *77*, 3865–3868.
25. Heyd, J.; Scuseria, G. E.; Ernzerhof, M. Hybrid functionals based on a screened Coulomb potential. *J. Chem. Phys.* **2003**, *118*, 8207.
26. Vazhappilly, T.; Micha, D. A. Non-adiabatic dissipative photoexcitation of silicon nanostructured surfaces; Sanibel Symposium Poster, St. Simons Island, GA, 2013.
27. Kittel, C. *Introduction to Solid State Physics*, 8th ed.; John Wiley: New York, 2005.
28. Hembree, R. H.; Vazhappilly, T.; Micha, D. A. Time-dependent photoconductivity at nanostructured silicon surfaces from a dissipative kinetics model; Sanibel Symposium Poster, St. Simons Island, GA, 2013.

Chapter 8

Investigating Interfacial Electron Transfer in Highly Efficient Porphyrin-Sensitized Solar Cells

David N. Bowman,¹ Jonathan Chan,^{2,3} and Elena Jakubikova^{*,1}

¹Department of Chemistry, North Carolina State University,
Raleigh, North Carolina 27695-8204, United States

²William G. Enloe High School,
Raleigh, North Carolina, 27610, United States

³Current address: Department of Chemistry, University of North Carolina,
Chapel Hill, North Carolina 27599-3290, United States

*E-mail: ejakubi@ncsu.edu.

The YD2-*o*-C8 complex based on zinc tetraphenylporphyrin (ZnTPP) is among the most efficient sensitizers for DSSCs to date, reaching over 12% in power conversion efficiency when paired with an organic co-sensitizer on a TiO₂ surface. To understand the link between the structure and light-harvesting properties of ZnTPP dyes, four sensitizers based on ZnTPP are investigated, with a systematic addition of structural features found in YD2-*o*-C8. Density functional theory (DFT) and time-dependent DFT are utilized to obtain the ground and excited state electronic structure of each chromophore. Quantum dynamics simulations are also employed to investigate interfacial electron transfer between the electronically excited ZnTPP dyes and the TiO₂ semiconductor. Overall, we find that substitution of the strongly coupled ethynyl bridged benzoic acid and diarylamine at the *meso* position of the porphyrin ring have the most significant impact on the absorption properties and IET efficiencies of Zn TPP based dyes. The addition of the alkoxy groups and long chain alkanes onto the *meso* substituted phenyl groups to produce YD2-*o*-C8 have little impact on the ground and excited state properties of the sensitizer. The structural modifications that do not impact the

chromophore electronic structure are, however, likely to impact intermolecular interactions (chromophore-chromophore and chromophore-electrolyte). Overall, our results shed light on the origins of the sensitization efficiency of the YD2-*o*-C8 dye and support the conclusions of previous experimental and computation work on this system.

1. Introduction

Dye-sensitized solar cells (DSSCs) offer an attractive alternative to crystalline silicon solar cells thanks to their low cost and versatility. Since the seminal work of O'Regan and Grätzel (1), which brought DSSCs into the arena of viable photovoltaics, a large body of research has accumulated regarding understanding fundamental photophysical processes in and optimizing power conversion efficiencies (PCE) of these devices (2–4). Conventional DSSCs utilize visible light absorbing dyes which undergo efficient interfacial electron transfer (IET) into a semiconductor network that is typically composed of a sintered anatase TiO₂ nanoparticles (3). Following IET, the conduction band electrons are collected at the photo-sensitized anode, passed through a work load, and returned to the oxidized dye via a redox shuttle (typically I⁻/I₃⁻) to regenerate the photoactive chromophore (3).

Historically, Ru-polypyridines have been the most extensively studied and utilized sensitizers in DSSCs due to their favorable absorption properties and efficient IET (5). Ru-based sensitizers remained the most efficient for nearly two decades until recently engineered *meso*-substituted push-pull Zn-porphyrin sensitizers were utilized to produce devices with PCEs of 12–13% (6, 7). This is of significant scientific importance, particularly because the new paradigm involves sensitizers based entirely on earth-abundant elements (8). In 2011, Grätzel and coworkers developed the highly-tailored push-pull Zn-porphyrin sensitizer YD2-*o*-C8 ([5,15-bis(2,6-dioctoxyphenyl)-10-(bis(4-hexylphenyl)amino)-20-(4-carboxyphenylethynyl)porphyrinato] Zinc (II), **5** in Figure 1), which reached a DSSC PCE of 12.3%, when utilized with an organic donor-acceptor co-sensitizer and a *tris*-2,2'bipyridine Co^(II/III) redox shuttle (7). By 2014, Grätzel and coworkers had further engineered SM315 as their best push-pull porphyrin sensitizer to date (6). This complex, relative to YD2-*o*-C8, has a benzothiadiazole anchoring group (rather than benzoic acid) and slight modifications to the bulky amine donor. Devices incorporating SM315 reached a new landmark PCE of 13.0% without a co-sensitizer (6).

Since the development of YD2-*o*-C8, a large amount of experimental (9–15) and computational (16–23) research has been performed to investigate the sensitization capabilities of this complex as well as multiple analogs. Computational studies have helped to establish fundamental structure-property relationships for Zn porphyrin sensitizers. Electron donor and acceptor groups *meso*-substituted on the same molecular axis (creating a push-pull system) are fundamentally important for tuning visible light absorption and the energetic

positioning and localization of excited states which facilitate IET (19–23). The choices of donor and acceptor groups that lead to efficient sensitization appear to be highly flexible, providing for a large unexplored chemical space available for device optimization. The long alkyl and alkoxy chains are also of fundamental importance, although not to the photophysics of the chromophore. These bulky groups significantly hinder dye aggregation (8), and the alkoxy groups on the phenyl substituents (perpendicular to push-pull axis) appear to hinder recombination (15).

In this work, we utilize a combination of density functional and quantum dynamics methodologies to study the impact of various functional groups, present in YD2-*o*-C8, on the ground state, absorption properties, and IET process in dye-TiO₂ assemblies by systematically constructing the full sensitizer from zinc tetraphenylporphyrin (**1**), as shown in Figure 1. Starting from the parent (complex **1**), addition of the ethynyl linked benzoic acid electron acceptor (complex **2**) is considered first, followed by the addition of a diaryl amine electron donor at the opposite *meso* position (complex **3**), and addition of methoxy groups to the phenyl rings perpendicular to the push-pull axis (complex **4**). Finally, the full YD2-*o*-C8 structure (**5**) is considered. This work validates the applicability of our methodology to push-pull zinc porphyrin sensitizers, and is able to determine IET rates for the YD2-*o*-C8 dye-TiO₂ system that have good agreement with experiment (24).

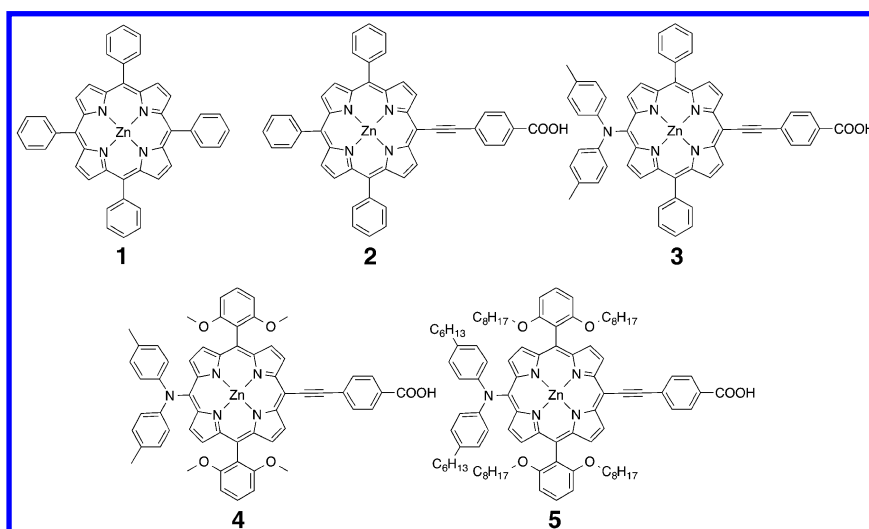


Figure 1. Systematically modified Zn(II) porphyrins investigated in this work. The most highly engineered structure is YD2-*o*-C8 (**5**).

2. Methods

2.1. Molecular Structure and Absorption Spectra

Complexes **1–5** were optimized in vacuum employing the B3LYP functional (25, 26). Hybrid functionals, such as B3LYP, are known to provide accurate geometries (27) as well as the absorption spectra in a good agreement with the experimental results (28). The LANL2TZ+ effective core potential and associated basis set was used for the Zn atom (29, 30), all other atoms (C, N, O, and H) were described using the 6-31G* basis set (31–33).

Time-dependent DFT (TD-DFT) (34–36) calculations at the CAM-B3LYP (37) level of theory were employed to obtain the 30 lowest-energy singlet excitations for all complexes. This method has proved useful for accurately reproducing the electronic absorption spectra of the target system, namely complex **5**, which contains charge transfer excitations (16). Solvent effects (acetonitrile) were included in the TD-DFT calculations by means of the polarizable continuum model (PCM) (38). The UV-vis absorption spectra were simulated by convoluting the stick spectra composed of the δ -functions associated with the excitation energies times the oscillator strength with a Lorentzian line shape, with half-width-at-half-maximum (hwhm) set to 0.08 eV. The excitations were characterized utilizing natural transition orbital (NTO) analysis (39). Excitations in the visible region of the absorption spectrum ($\lambda > 325$ nm) with oscillator strength greater than 0.01 were used to identify the donor states for interfacial electron transfer simulations. The Gaussian 09 software suite was utilized for all molecular calculations (40).

2.2. Slab Model Optimization

Periodic systems (bulk anatase and nanoparticle slab models) were optimized using the Vienna Ab initio Simulation Package (VASP) (41–44) employing the PBE exchange-correlation functional (45, 46) with Projector Augmented-Wave method (47, 48). A pure functional (PBE) was chosen over a hybrid functional (B3LYP) due to the computational cost considerations. Note that utilization of PBE and B3LYP functionals results in nearly identical Ti–O and Ti–C bond lengths (49). The plane wave basis set expansion was cutoff at 500 eV for all periodic boundary condition (PBC) calculations. The anatase TiO₂ unit cell was optimized with $(13 \times 13 \times 13)$ *k*-point sampling, which resulted in a tetragonal lattice with lattice vectors $a = b = 3.81$ Å, $c = 9.77$ Å.

The optimized unit cell of bulk anatase was used to construct a slab model of the (101) surface. Linker models consisting of benzoic acid attached to the anatase (101) surface via a monodentate and a bridging bidentate attachment were constructed. The top two layers of Ti and top four layers of O were relaxed along with the linker models, keeping the remainder of the slab frozen at bulk geometry, using a $(5 \times 3 \times 1)$ *k*-point sampling. The supercell volume was kept fixed with lattice vectors $a = 15.25$ Å, $b = 10.49$ Å, $c = 26.00$ Å.

Optimized linker models were then used to perform a constrained optimization of complexes **2–5**, keeping the linker and half of the aryl ring on the linker side (three carbon and two hydrogen atoms) frozen at the surface geometry.

Calculations were done employing the Gaussian 09 software package (40) at the B3LYP/LANL2TZ+,6-31G* level of theory. Following the constrained optimization, complexes **2-5** were aligned onto the surface using the linker geometry as a reference (50).

2.3. Interfacial Electron Transfer Simulations

Quantum dynamics simulations, in which the time-dependent electronic wave function, $|\Psi(t)\rangle$, is propagated according to the extended Hückel (EH) model Hamiltonian, were used to investigate interfacial electron transfer in all dye-TiO₂ assemblies (51–57). The methodology is described in detail in Reference (51).

The initial states for the IET simulations, $|\Psi(0)\rangle$, were created based on the results of the TD-DFT calculations for complexes **2-5**. Kohn-Sham (KS) orbitals populated by the visible light excitations were matched to virtual EH orbitals of the complexes **2-5** by visual inspection. These EH particle states then served as the initial states for the IET simulations of the entire dye-TiO₂ systems, and were evolved in time according to the time-dependent Schrödinger equation. Survival probability, or the probability that at time t the electron is still localized in the dye, was determined by projecting the time-evolved electronic wave function of the dye-TiO₂ system onto the atomic orbitals of the dye at each simulation step.

All quantum dynamics simulations were run for 2 ps with a step-size of 0.1 fs in vacuum at a frozen geometry. PBC with the super cell of 31.46 Å × 30.49 Å dimensions parallel to the slab and the cell height was altered to provide a sufficient vacuum layer above the dye (34.00 Å for **2**, 38.00 Å for **3-4**, and 45.00 Å for **5**). A k -point sampling of (1 × 1 × 1) was utilized in all quantum dynamics calculations. In order to avoid artificial recurrences in the electron-transient populations, absorbing potentials (i.e., imaginary terms to the diagonal elements of the Hamiltonian) were assigned to the bottom layer of Ti atoms.

Survival probabilities obtained from the IET simulations were fit to a linear combination of exponential functions according to the following expression,

$$P(t) = \sum_{i=1}^N c_i e^{-\alpha_i t}, \quad N = 1 - 3 \quad (1)$$

with the constraint that $P(t = 0) = 1$ satisfied by

$$\sum_{i=1}^N c_i = 1, \quad N = 1 - 3 \quad (2)$$

Goodness of each fit was determined by requiring that the coefficient of determination, R^2 , be greater than 0.95. The fit with the smallest N satisfying this condition was chosen for further analysis. In some cases IET was not observed and exponential fitting was not possible. The characteristic IET times were then calculated as the expectation values of the survival probabilities according to

$$\tau_{IET} = \langle t \rangle = \frac{\int_0^\infty t P(t) dt}{\int_0^\infty P(t) dt} \quad (3)$$

3. Results and Discussion

3.1. Ground State Structures

Average Zn-N bond lengths and relevant porphyrin-phenyl dihedral angles are summarized in Table 1 for the crystal structure (58) of **1** and the B3LYP optimized structures of complexes **1-5**. The chosen computational approach results in an overall accurate structure of the parent complex, with slight overestimation of Zn–N bond lengths (1.8 %) and underestimation of porphyrin-phenyl dihedral angles (6.1 %). Thanks to the structural similarity among all complexes investigated, one can assume that optimized structures for complexes **2-5** possess similar level of accuracy. Table 1 also lists relevant geometric parameters for **2-5** and includes the porphyrin-phenyl dihedral angle across the ethynyl bridge (see Figure 1). The approximately coplanar arrangement of the ethynyl phenyl moiety relative to the porphyrin macrocycle indicates that significant electronic mixing between the porphyrin and phenyl groups may be possible.

3.2. Absorption Spectra

Calculated absorption spectra for complexes **1-5** are shown in Figure 2. All of the significant transitions in the visible region are π to π^* in nature. A number of observations regarding the perturbations introduced by systematic additions of functional groups to **1** in building the target complex **5** can be made. First, the most dramatic change is a red-shift of both Q and Soret bands upon addition of the ethynyl-benzoic acid linker, which move from 375 nm to 400 nm and 550 nm to 585 nm, respectively. An increase in the intensity of the Q band by an order of magnitude is also observed for complexes **2-5** relative to **1**, as shown in Figure 2. These changes to the absorption profile are both desirable for harvesting of lower energy photons and capturing a larger portion of the solar spectrum.

The bathochromic shift of both Q and Soret bands can be understood in terms of the electronic structure of the substituted dyes. A significant decrease in the LUMO energy occurs due to the delocalization of this orbital onto the linker group. The linker ring is nearly coplanar with the porphyrin macrocycle (see Table 1), and the delocalization can clearly be observed in the relevant orbitals shown in Figure 3. The TD-DFT analysis shows that LUMO and LUMO+1 are the primary unoccupied orbitals involved in significant transitions, with oscillator strength greater than 0.01, shown in Figure 2. Clearly, LUMO+1 is not significantly perturbed by the linker addition (see Figure 3) as it lacks the proper symmetry to mix with the π -symmetry orbitals of the linker subunit.

Table 1. Experimentally Known Geometric Parameters of 1 (Average Zn–N Bond Length and Average Absolute Porphyrin-Phenyl Dihedral Angles) along with Those Calculated at the B3LYP/LANL2TZ+,6-31G* Level of Theory for Complexes 1–5. The Porphyrin-Phenyl Dihedral Angles Across the Ethynyl Bridge Are Also Given for Complexes 2–5. Absolute Value (Magnitude) of Dihedral Angles Is Reported.

<i>Geometric Parameter</i>	<i>Experimental</i> (58)	<i>Calculated</i>				
	<i>1</i>	<i>1</i>	<i>2</i>	<i>3</i>	<i>4</i>	<i>5</i>
Avg. Zn–N bond length [Å]	2.032	2.069	2.071	2.070	2.069	2.069
Avg. porph.-phenyl dihedral angle [deg.]	75.3	70.7	69.2	70.6	92.1	79.6
Porph.-phenyl dihedral angle, across ethynyl [deg.]	–	–	-0.5	-2.8	-1.7	-1.1

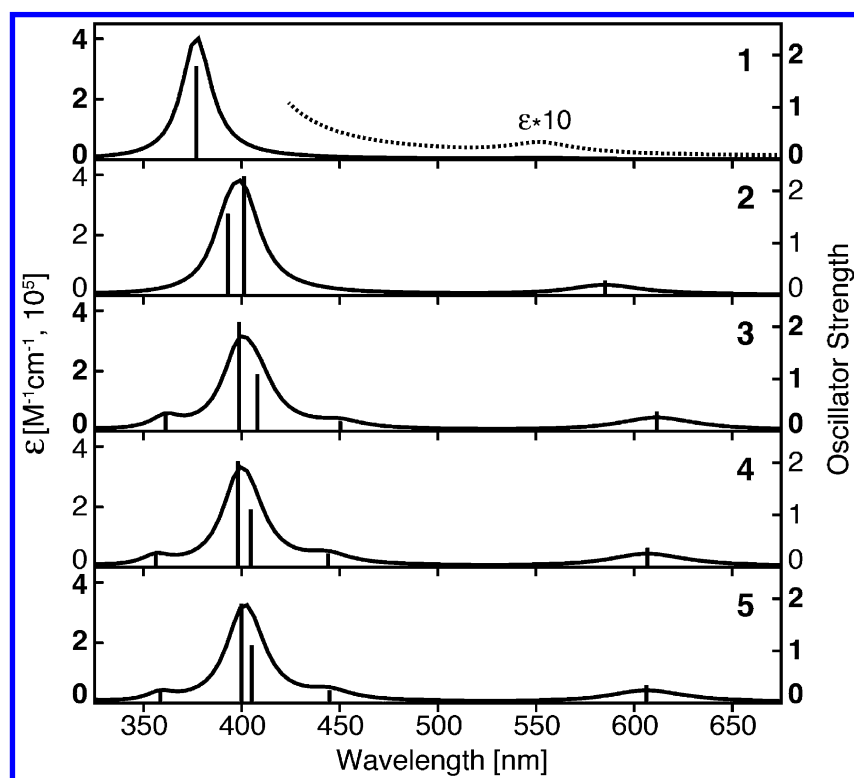


Figure 2. Calculated excitations for complexes 1–5 at the CAM-B3LYP/LANL2TZ+,6-31G level of theory. To generate the broadened spectra a Lorentzian broadening with hwhm = 0.08 eV was used.*

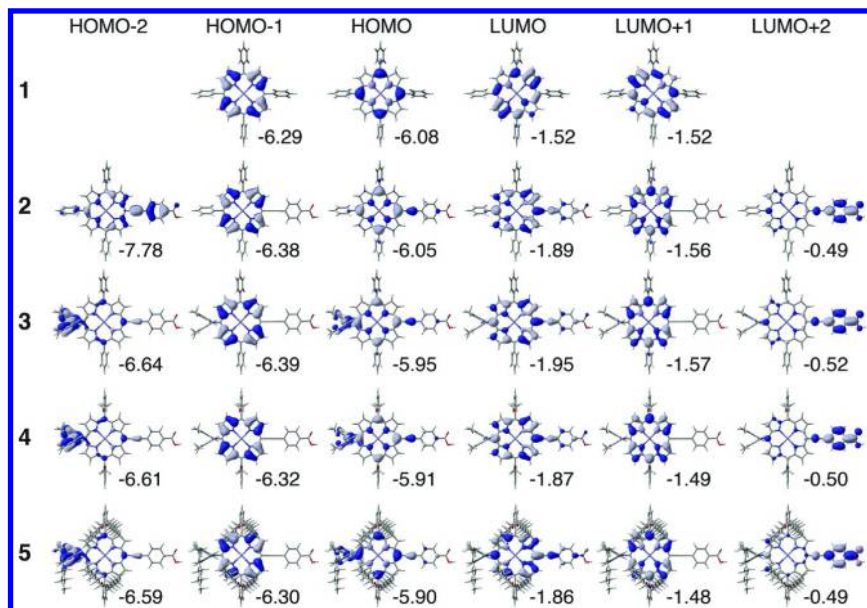


Figure 3. Kohn-Sham HOMO-1 through LUMO+1 of **1** and HOMO-2 through LUMO+2 of **2-5** at the CAM-B3LYP/LANL2TZ+,6-31G* level of theory, with orbital energies in eV. These are the relevant particle states that are populated from visible light excitation in the Q and Soret band. The isovalue shown is 0.03 electron/Å³.

The spectrum is also significantly altered upon substitution of the di-*p*-tolylamine electron donor group in complex **3**. With this structural modification, two shoulders appear on each side of the Soret band (compare UV-vis spectra of complexes **1** and **2** with **3-5**, Figure 2). These excitations are charge transfer in nature, with the occupied orbitals involved in the transitions containing electron density that is primarily localized on the donor group. This can clearly be seen by comparing the natural transition orbitals of **1** and **3** shown in Figures 4 and 5, respectively. A slight red-shift of the Q band is also observed, going from 585 nm in **2** to 610 nm in **3**. This can be rationalized on the basis that the HOMO of **3** is slightly destabilized in comparison to the HOMO of **2**, due to orbital interactions between the porphyrin ring and the di-*p*-tolylamine group. The two most intense peaks in the Soret band of complexes **3-5** become somewhat more charge transfer in nature (see Figure 5), due to contributions from HOMO-2 localized on di-*p*-tolylamine moiety, when compared to complex **2**. Overall, these changes to the absorption characteristics should be beneficial for light harvesting, as they improve absorption across the visible region and the new excitations neighboring the Soret band result in an initially charge separated state. The bathochromic shifts and broadening of the Soret band are consistent with the experimentally determined spectra of **1** (59) and **5** (7).

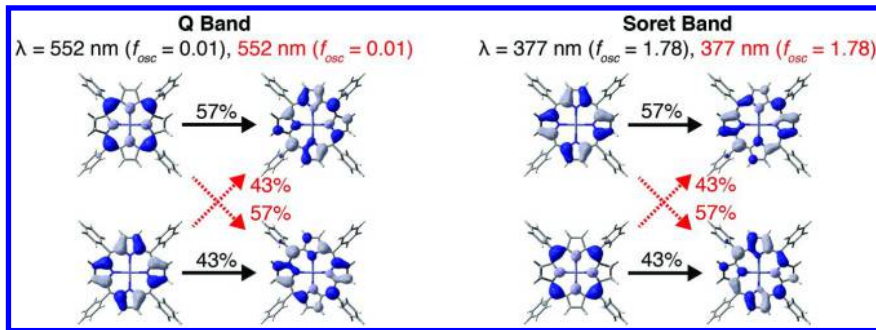


Figure 4. Natural transition orbitals for excitations in the *Q* and Soret regions of 1. Hole is pictured to the left, with particle to the right of the arrow. The percent contribution of the particle-hole pairs are shown. The horizontal (solid) and diagonal (dashed) sets of arrows represent two distinct transitions, which are degenerate. The isovalue shown is 0.03 electron/Å³.

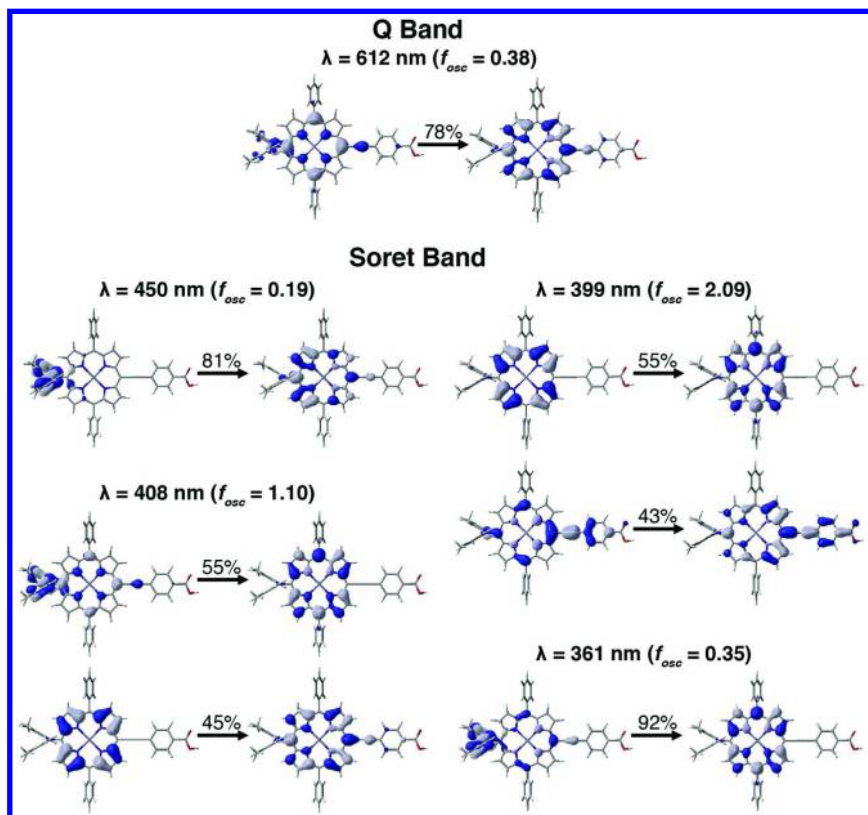


Figure 5. Natural transition orbitals for excitations in the *Q* and Soret regions of 3. Hole is pictured to the left, with particle to the right of the arrow. The percent contribution of the particle-hole pairs are shown over the arrow. The isovalue shown is 0.03 electron/Å³.

Finally, the addition of *ortho*-alkoxy groups to the remaining phenyl groups in going from **3** to **4** and further decoration with long alkane chains to produce **5** do not have any significant impact on the calculated absorption properties of the chromophore. These modifications occur on phenyl groups that are highly decoupled from the porphyrin macrocycle and contain no visible light absorbing moieties. No significant changes in orbital structure, orbital energy, excitation peak positions, or excitation composition are observed for **4** and **5** relative to **3**.

3.3. Dye-Nanoparticle Assemblies

The chromophore-TiO₂ assemblies used to perform IET simulations were constructed based on benzoic acid binding models, as described in section 2.2. Previously published results suggest that the two most stable binding modes of a carboxylic acid on the anatase (101) surface are the monodentate attachment, with a hydrogen bond between a surface oxygen and the hydroxyl group, and a bridging bidentate attachment, in which deprotonated carboxylate forms two Ti–O bonds (see Figure 4) (60–64).

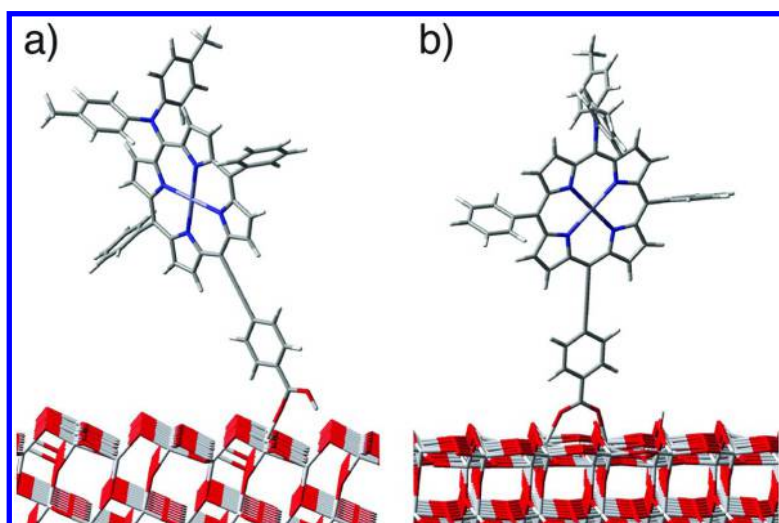


Figure 6. Assemblies of anatase (101) sensitized with complex **3**, with the chromophore anchored to TiO₂ via (a) monodentate carboxylic acid binding mode or (b) bridging bidentate carboxylate binding mode.

Following the dye alignment, the final constructed slab models position the chromophore nearly perpendicular to the semiconductor surface. Example attachments for **3**-TiO₂ in both the monodentate carboxylic acid and bidentate carboxylate attachment modes are shown in Figure 6. Due to the symmetry of the

sensitizers and the coplanarity of the porphyrin with the benzoic acid linker, only one orientation of attachment was considered for each binding mode (180° rotation around the carboxylic acid-phenyl bond is considered an equivalent assembly). In total, four sensitizers (**2–5**) were modeled in two different linker attachment modes resulting in eight unique dye-TiO₂ assemblies for IET simulations.

For the dye-semiconductor assemblies, a density of states (DOS) plot assists in analysis of the electronic structure of the full system. A DOS plot for **5**-TiO₂ with a monodentate attachment mode is shown in Figure 7 along with the discrete energy level of complexes **2–5**, calculated at the extended Hückel level of theory. It is apparent from Figure 7 that all of the relevant low-lying LUMOs of chromophores **2–5** lie at the approximately same energy level and will couple with the same set of the acceptor states localized on the TiO₂ slab. Note that the HOMO energy level is significantly destabilized in complexes **3–5**, relative to **2**. This is consistent with the results obtained at the DFT level of theory (see Figure 3) and with the observed bathochromic shift in the simulated UV-vis spectra. Based on the DOS alone, there are no significant differences between chromophores that would impact their relative sensitization capabilities.

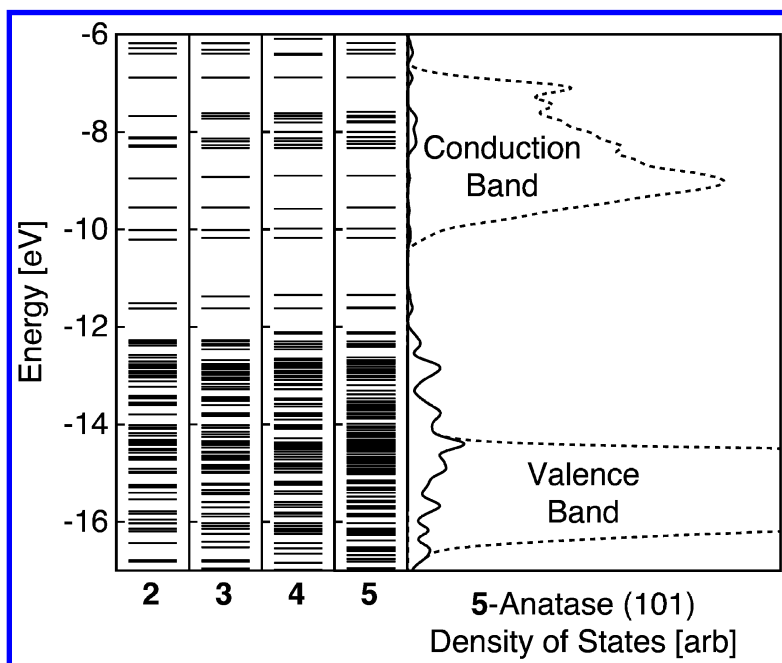


Figure 7. Extended Hückel energy levels (left) of chromophores **2–5**. Density of states for **5**-TiO₂ anatase (101) slab model (right) shows the total density of states (dashed line), and the projected density of states of the adsorbate (solid line). All assemblies shown have a monodentate carboxylic acid binding mode.

3.4. Interfacial Electron Transfer Simulations

For all complexes investigated, the LUMO-LUMO+2 were found to be the relevant orbitals populated upon visible light absorption. These KS orbitals (see Figure 3) were matched to orbitals at the extended Hückel level of theory, shown in Figure 8. The relevant extended Hückel particle states serve as initial electron wave packets, completely localized on the chromophore, which evolve under the time-dependent Schrödinger equation. The survival probability, or fractional percentage of electron remaining on the dye, is calculated at each simulation step (example results for the IET simulations in **5**-TiO₂ assemblies are shown in Figure 9) and fitting via exponential functions allows for calculation of the expectation value of the characteristic IET time.

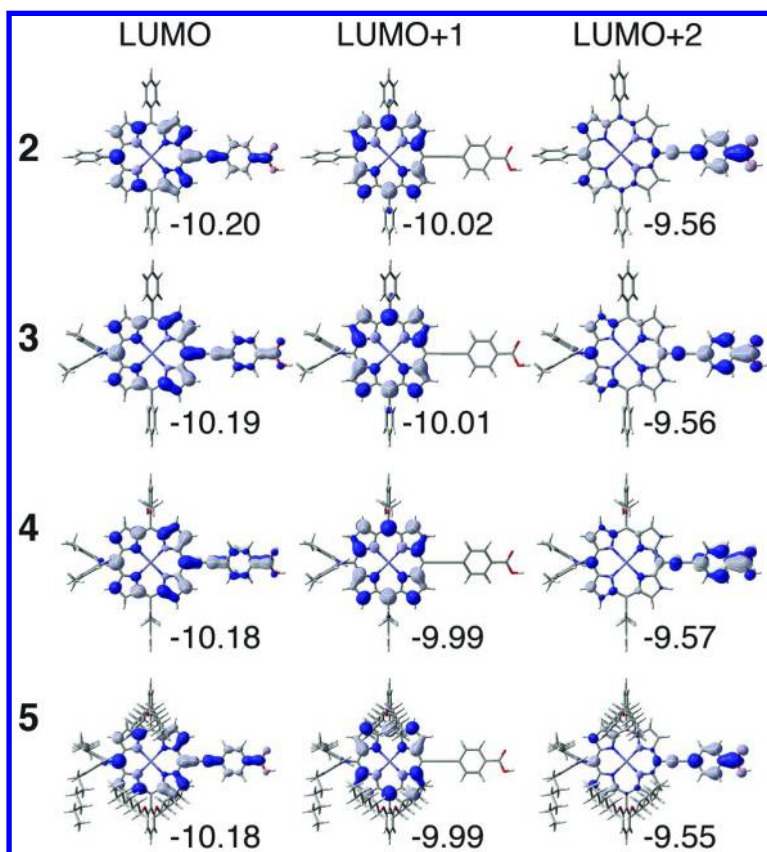
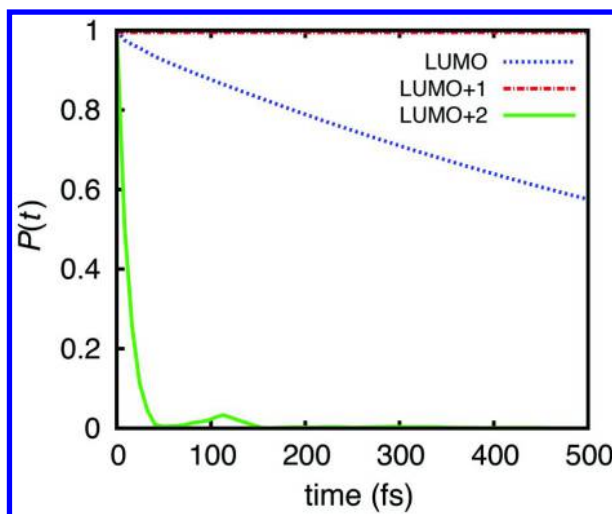


Figure 8. Extended Hückel LUMO through LUMO+2 of **2-5** at the monodentate carboxylic acid surface attachment geometry, with orbital energies in eV. The isovalue shown is 0.03 electron/Å³.

The calculated characteristic IET times for all the investigated models are given in Table 2. Interestingly, complexes **2–5** have essentially the same rate of IET for a given attachment mode. This is not entirely surprising, as the orbital localization and energies are not significantly different for any of the complexes (see Figures 3 and 7). We also find that the ordering of the states by the IET time is consistent across all complexes and attachment modes: LUMO+2 < LUMO << LUMO+1. Two factors are responsible for this trend: (1) delocalization of a particular initial state onto the linker group, and (2) energetic alignment of an initial state with the TiO_2 acceptor states. The LUMO+2 clearly has a large amount of electron density on the linker (primarily benzoic acid localized, see Figure 7) and is energetically aligned with a large number of acceptor states (i.e., DOS of TiO_2 at that particular energy level is large), leading to the rapid IET observed. For LUMO, there is some electron density delocalization onto the linker but the density of the TiO_2 acceptor states is lower at that particular energy level than for the other states (see Figure 7). For LUMO+1, there is approximately zero electron density on the linker group and therefore IET does not occur on the timescale of the excited state lifetime (~ 0.1 ns) (7). The computed characteristic IET times obtained for the states capable of sensitization are in line with those obtained from the experimental studies for the same YD2-*o*-C8 dye- TiO_2 system (24).



*Figure 9. Survival probability, $P(t)$, versus time for the **5**- TiO_2 assemblies, in which LUMO, LUMO+1, or LUMO+2 were chosen as the initial state for the simulations. The dye **5** (YD2-*o*-C8) was attached to anatase (101) slab via the monodentate carboxylic acid binding mode.*

The characteristic IET times highlighted in bold in Table 2 are below the expected excited state lifetime (~ 100 ps), indicating that sensitization is possible from LUMO and LUMO+2 for monodentate attachment, and LUMO+2 for bidentate attachment. Due to the LUMO and LUMO+1 having the predominant contributions to the TD-DFT excitations, and a relatively long characteristic IET

time for LUMO+1 initial state, we expect the majority of IET to occur upon population of the LUMO orbital. Note that the IET in dye-TiO₂ assemblies with monodentate carboxylic acid attachment is more efficient than the IET in assemblies with the bidentate attachment. This trend has been observed before in our work on sensitization capabilities of various metal polypyridine complexes, and is attributed to differences in the orbital overlap with TiO₂ acceptor states (56, 57, 65, 66).

Table 2. Characteristic Interfacial Electron Transfer Times into Anatase TiO₂ Determined for the LUMO–LUMO+2 Initial States of the Chromophores. Times under the Expected Excited State Lifetime of 0.1 ns Are Bolded. Results for Monodentate and Bidentate Carboxylic Acid Attachment Mode Are Shown.

Model	Monodentate			Bidentate		
	LUMO	LUMO+1	LUMO+2	LUMO	LUMO+1	LUMO+2
2-TiO₂	1.1 ps	>10 ns	11.5 fs	136.2 ps^b	>10 ns	51.1 fs^a
3-TiO₂	936.1 fs	>10 ns ^b	11.4 fs	183.9 ps^b	>10 ns ^c	42.3 fs^a
4-TiO₂	806.5 fs	>10 ns ^b	11.3 fs	145.3 ps^b	>10 ns ^c	47.8 fs^a
5-TiO₂	921.5 fs	>10 ns ^b	11.4 fs	178.4 ps^b	>10 ns ^c	41.8 fs

^a double exponential fit, ^b triple exponential fit, ^c exponential fit not possible.

The sensitization capabilities of complexes **2–5** do not differ significantly based on the characteristic IET times alone, and overall we find little difference in comparing complexes **3–5**. However, addition of the electron donating diarylamine group in going from **2** to **3** results in two new charge transfer transitions and general increase in charge transfer character to the Soret band (see Figure 5). The higher-energy charge transfer excitation (360 nm) primarily populates LUMO+1 and will not lead to the IET according to our model (see Table 2), though this may change with the inclusion of molecular motion. The lower energy charge transfer excitation (450 nm) has significant contribution from both LUMO and LUMO+2 and should therefore lead to a relatively rapid IET.

Overall, our results are consistent with the conclusions obtained by Yella et al. in their work on tailoring porphyrin sensitizers to produce YD2-*o*-C8 (7). Addition of the electron-donating group significantly impacts the sensitization capabilities of the porphyrin dyes, due to additional charge transfer nature of the Soret band excitations. Addition of the alkoxy and long alkyl chains to the sensitizer does not significantly impact the rate of the IET, but is expected to hinder dye aggregation and assist in the interactions with the Co(II/III) electrolyte. Because our simulations consider only single chromophores in vacuum, any chromophore-chromophore, chromophore-electrolyte, and chromophore-solvent interactions are neglected.

The computational model utilized in this work can be easily extended to include molecular motion or electron-hole coupling (52, 67–69). It is, however, useful even in its most basic form for rapidly screening a large number of push-pull dyes for their relative sensitization capabilities. Including the electron hole coupling is expected to generally increase the IET time (67) and inclusion of molecular motion may allow transient IET pathways to open up on the ps time scale (vibrational time scale) which will generally decrease the IET time (52) for slowly injecting states. Overall, we consider the model employed in this work to be an adequate approximation for comparing relative sensitization capabilities of a class of related complexes and for reproducing experimentally observed IET time scales.

4. Conclusions

This work focused on investigation of the ground and excited state electronic structure of substituted zinc porphyrins, with the goal to characterize sensitization capabilities of the highly efficient YD2-*o*-C8 dye. Substitution of the ethynyl bridged benzoic acid linker at the *meso* position of the porphyrin macrocycle has a significant impact on the electronic structure of the chromophore, resulting in: (1) delocalization of the π^* LUMO over the linker group, (2) lowering of the LUMO energy relative to the LUMO of **1**, and (3) presence of a new benzoic acid localized molecular orbital (LUMO+2) in the frontier energy region. Subsequently, a bathochromic shift is observed for both Q and Soret bands due to the stabilization of the LUMO orbital. Further tailoring of the chromophore by addition of a diarylamine donor group on the same molecular axis as the ethynyl bridged benzoic acid results in addition of new charge transfer excitations and modification of the Soret band that now displays a partial charge transfer character. All of these changes should facilitate the IET process following the visible light absorption. The addition of alkoxy groups and long chain alkyl groups to the periphery of the scaffold is not found to significantly impact the photophysical properties of Zn porphyrin dyes.

The IET simulations on dye-TiO₂ assemblies, where dye represents complexes **2–5**, were performed to estimate the time scale of electron transfer into (101) anatase, when the chromophores are attached via a carboxylic acid linker in either a monodentate or bridging bidentate mode. The calculated characteristic IET times for all complexes were found to be essentially equivalent, with the monodentate binding arrangement resulting in significantly faster IET than the bidentate mode. Our computational results support the conclusions of Yella et al. (7), who proposed that the addition of the electron donor group assists in facilitating IET. Our results also indicate that further modifications by alkoxy and alkyl chains on the periphery of the chromophore do not significantly impact the ground or excited state electronic structure of the porphyrin-based dyes. These synthetic modifications, as suggested (7), are more likely to impact chromophore-chromophore and chromophore-electrolyte interactions which were not considered in this model.

Acknowledgments

This research was supported by the U.S. Department Of Education Graduate Assistantship In Areas Of National Need (GAANN) Fellowship Program at North Carolina State University (D.N.B), as well as the Project SEED Program of the North Carolina Section of the American Chemical Society (J. C.). We gratefully acknowledge Prof. Victor S. Batista (Yale University) for providing us with a copy of the code for the IET simulations (IETsim). We would also like to thank the Chemistry Department and High Performance Computing Center at North Carolina State University for use of their facilities and computational resources.

References

1. O'Regan, B.; Grätzel, M. A low-cost, high-efficiency solar cell based on dye-sensitized colloidal TiO_2 films. *Nature* **1991**, *353*, 737–740.
2. Clifford, J. N.; Martinez-Ferrero, E.; Viterisi, A.; Palomares, E. Sensitizer molecular structure-device efficiency relationship in dye sensitized solar cells. *Chem. Soc. Rev.* **2011**, *40*, 1635–1646.
3. Hagfeldt, A.; Boschloo, G.; Sun, L.; Kloo, L.; Pettersson, H. Dye-sensitized solar cells. *Chem. Rev.* **2010**, *110*, 6595–6663.
4. Hardin, B. E.; Snaith, H. J.; McGehee, M. D. The renaissance of dye-sensitized solar cells. *Nat. Photonics* **2012**, *6*, 162–169.
5. Bomben, P. G.; Robson, K. C. D.; Koivisto, B. D.; Berlinguette, C. P. Cyclometalated ruthenium chromophores for the dye-sensitized solar cell. *Coord. Chem. Rev.* **2012**, *256*, 1438–1450.
6. Mathew, S.; Yella, A.; Gao, P.; Humphry-Baker, R.; Curchod, B. F.; Ashari-Astani, N.; Tavernelli, I.; Rothlisberger, U.; Nazeeruddin, M. K.; Grätzel, M. Dye-sensitized solar cells with 13% efficiency achieved through the molecular engineering of porphyrin sensitizers. *Nat. Chem.* **2014**, *6*, 242–247.
7. Yella, A.; Lee, H.-W.; Tsao, H. N.; Yi, C.; Chandiran, A. K.; Nazeeruddin, M. K.; Diau, E. W.-G.; Yeh, C.-Y.; Zakeeruddin, S. M.; Grätzel, M. Porphyrin-sensitized solar cells with cobalt (II/III)-based redox electrolyte exceed 12 percent efficiency. *Science* **2011**, *334*, 629–634.
8. Li, L.-L.; Diau, E. W.-G. Porphyrin-sensitized solar cells. *Chem. Soc. Rev.* **2013**, *42*, 291–304.
9. Luo, J.; Xu, M.; Li, R.; Huang, K.-W.; Jiang, C.; Qi, Q.; Zeng, W.; Zhang, J.; Chi, C.; Wang, P. N-annulated perylene as an efficient electron donor for porphyrin-based dyes: Enhanced light-harvesting ability and high-efficiency Co(II/III)-based dye-sensitized solar cells. *J. Am. Chem. Soc.* **2013**, *136*, 265–272.
10. Di Nunzio, M. R.; Cohen, B.; Pandey, S. S.; Hayase, S.; Piani, G.; Douhal, A. Spectroscopy and dynamics of YD2-*o*-C8 in solution and interacting with alumina nanoparticles electrode. *J. Phys. Chem. C* **2014**, *118*, 11365–11376.
11. Yella, A.; Mai, C. L.; Zakeeruddin, S. M.; Chang, S. N.; Hsieh, C. H.; Yeh, C. Y.; Grätzel, M. Molecular engineering of push–pull porphyrin dyes for highly efficient dye-sensitized solar cells: The role of benzene spacers. *Angew. Chem., Int. Ed.* **2014**, *126*, 3017–3021.

12. Lan, C.-M.; Wu, H.-P.; Pan, T.-Y.; Chang, C.-W.; Chao, W.-S.; Chen, C.-T.; Wang, C.-L.; Lin, C.-Y.; Diau, E. W.-G. Enhanced photovoltaic performance with co-sensitization of porphyrin and an organic dye in dye-sensitized solar cells. *Energ. Environ. Sci.* **2012**, *5*, 6460–6464.
13. Wang, Y.; Chen, B.; Wu, W.; Li, X.; Zhu, W.; Tian, H.; Xie, Y. Efficient solar cells sensitized by porphyrins with an extended conjugation framework and a carbazole donor: From molecular design to cosensitization. *Angew. Chem., Int. Ed.* **2014**, *53*, 10779–10783.
14. Kurotobi, K.; Toude, Y.; Kawamoto, K.; Fujimori, Y.; Ito, S.; Chabera, P.; Sundström, V.; Imahori, H. Highly asymmetrical porphyrins with enhanced push–pull character for dye-sensitized solar cells. *Chem.–Eur. J.* **2013**, *19*, 17075–17081.
15. Yi, C.; Giordano, F.; Cevey-Ha, N. L.; Tsao, H. N.; Zakeeruddin, S. M.; Grätzel, M. Influence of structural variations in push–pull zinc porphyrins on photovoltaic performance of dye-sensitized solar cells. *ChemSusChem* **2014**, *7*, 1107–1113.
16. Ju, M.-G.; Liang, W. Computational insight on the working principles of zinc porphyrin dye-sensitized solar cells. *J. Phys. Chem. C* **2013**, *117*, 14899–14911.
17. Hsu, H.-Y.; Chiang, H.-C.; Hu, J.-Y.; Awasthi, K.; Mai, C.-L.; Yeh, C.-Y.; Ohta, N.; Diau, E. W.-G. Field-induced fluorescence quenching and enhancement of porphyrin sensitizers on TiO₂ films and in PMMA films. *J. Phys. Chem. C* **2013**, *117*, 24761–24766.
18. Santhanamoorthi, N.; Lo, C.-M.; Jiang, J.-C. Molecular design of porphyrins for dye-sensitized solar cells: A DFT/TDDFT study. *J. Phys. Chem. Lett.* **2013**, *4*, 524–530.
19. Ørnsø, K. B.; Garcia-Lastra, J. M.; Thygesen, K. S. Computational screening of functionalized zinc porphyrins for dye sensitized solar cells. *Phys. Chem. Chem. Phys.* **2013**, *15*, 19478–19486.
20. Shalabi, A.; El Mahdy, A.; Assem, M.; Taha, H.; Abdel Halim, W. Theoretical characterisation of highly efficient dye-sensitised solar cells. *Mol. Phys.* **2014**, *112*, 22–34.
21. Karthikeyan, S.; Lee, J. Y. Zinc-porphyrin based dyes for dye-sensitized solar cells. *J. Phys. Chem. A* **2013**, *117*, 10973–10979.
22. Zhang, X.; Chen, Q.; Sun, H.; Pan, T.; Hu, G.; Ma, R.; Dou, J.; Li, D.; Pan, X. Theoretical design and screening of alkyne bridged triphenyl zinc porphyrins as sensitizer candidates for dye-sensitized solar cells. *Spectrochim. Acta A* **2014**, *118*, 564–571.
23. Zhang, X.; Du, Y.; Chen, Q.; Sun, H.; Pan, T.; Hu, G.; Ma, R.; Sun, Y.; Li, D.; Dou, J. Theoretical screening of novel alkyne bridged zinc porphyrins as sensitizer candidates for dye-sensitized solar cells. *Spectrochim. Acta A* **2014**, *133*, 514–520.
24. Piatkowski, P.; Martin, C.; di Nunzio, M. R.; Cohen, B.; Pandey, S. S.; Hayase, S.; Douhal, A. Complete photodynamics of the efficient YD2-*o*-C8 based solar cell. *J. Phys. Chem. C* **2014**, *118*, 29674–29687.
25. Becke, A. D. Density-functional thermochemistry. III. The role of exact exchange. *J. Chem. Phys.* **1993**, *98*, 5648–5652.

26. Stephens, P.; Devlin, F. Ab initio calculation of vibrational absorption and circular dichroism spectra using density functional force fields. *J. Phys. Chem.* **1994**, *98*, 11623–11627.
27. Bowman, D. N.; Jakubikova, E. Low-spin versus high-spin ground state in pseudo-octahedral iron complexes. *Inorg. Chem.* **2012**, *51*, 6011–6019.
28. Laurent, A. D.; Jacquemin, D. TD-DFT benchmarks: A review. *Int. J. Quantum Chem.* **2013**, *113*, 2019–2039.
29. Hay, P. J.; Wadt, W. R. Ab initio effective core potentials for molecular calculations. Potentials for K to Au including the outermost core orbitals. *J. Chem. Phys.* **1985**, *82*, 299–310.
30. Roy, L. E.; Hay, P. J.; Martin, R. L. Revised basis sets for the LANL effective core potentials. *J. Chem. Theory Comput.* **2008**, *4*, 1029–1031.
31. Hehre, W. J.; Ditchfie, R; Pople, J. A. Self-consistent molecular-orbital methods .XII. Further extensions of Gaussian-type basis sets for use in molecular-orbital studies of organic-molecules. *J. Chem. Phys.* **1972**, *56*, 2257–2261.
32. Harihara, P. C.; Pople, J. A. Influence of polarization functions on molecular-orbital hydrogenation energies. *Theor. Chim. Acta* **1973**, *28*, 213–222.
33. Franci, M. M.; Pietro, W. J.; Hehre, W. J.; Binkley, J. S.; Gordon, M. S.; Defrees, D. J.; Pople, J. A. Self-consistent molecular-orbital methods. XXIII. A polarization-type basis set for 2nd-row elements. *J. Chem. Phys.* **1982**, *77*, 3654–3665.
34. Bauernschmitt, R.; Ahlrichs, R. Treatment of electronic excitations within the adiabatic approximation of time dependent density functional theory. *Chem. Phys. Lett.* **1996**, *256*, 454–464.
35. Casida, M. E.; Jamorski, C.; Casida, K. C.; Salahub, D. R. Molecular excitation energies to high-lying bound states from time-dependent density-functional response theory: Characterization and correction of the time-dependent local density approximation ionization threshold. *J. Chem. Phys.* **1998**, *108*, 4439–4449.
36. Stratmann, R. E.; Scuseria, G. E.; Frisch, M. J. An efficient implementation of time-dependent density-functional theory for the calculation of excitation energies of large molecules. *J. Chem. Phys.* **1998**, *109*, 8218–8224.
37. Yanai, T.; Tew, D. P.; Handy, N. C. A new hybrid exchange–correlation functional using the coulomb-attenuating method (CAM-B3LYP). *Chem. Phys. Lett.* **2004**, *393*, 51–57.
38. Scalmani, G.; Frisch, M. J. Continuous surface charge polarizable continuum models of solvation. I. General formalism. *J. Chem. Phys.* **2010**, *132*.
39. Martin, R. L. Natural transition orbitals. *J. Chem. Phys.* **2003**, *118*, 4775–4777.
40. Frisch, M. J. T.; Trucks, G. W.; Schlegel, H. B.; Scuseria, G. E.; Robb, M. A.; Cheeseman, J. R.; Scalmani, G.; Barone, V.; Mennucci, B.; Petersson, G. A.; Nakatsuji, H.; Caricato, M.; Li, X.; Hratchian, H. P.; Izmaylov, A. F.; Bloino, J.; Zheng, G.; Sonnenberg, J. L.; Hada, M.; Ehara, M.; Toyota, K.; Fukuda, R.; Hasegawa, J.; Ishida, M.; Nakajima, T.; Honda, Y.; Kitao, O.; Nakai, H.; Vreven, T.; Montgomery, J. A.; Peralta, J. E. Jr; Ogliaro, F.; Bearpark, M.; Heyd, J. J.; Brothers, E.; Kudin, K. N.; Staroverov, V. N.; Keith,

T.; Kobayashi, R.; Normand, J.; Raghavachari, K.; Rendell, A.; Burant, J. C.; Iyengar, S. S.; Tomasi, J.; Cossi, M.; Rega, N.; Millam, J. M.; Klene, M.; Knox, J. E.; Cross, J. B.; Bakken, V.; Adamo, C.; Jaramillo, J.; Gomperts, R.; Stratmann, R. E.; Yazyev, O.; Austin, A. J.; Cammi, R.; Pomelli, C.; Ochterski, J. W.; Martin, R. L.; Morokuma, K.; Zakrzewski, V. G.; Voth, G. A.; Salvador, P.; Dannenberg, J. J.; Dapprich, S.; Daniels, A. D.; Farkas, O.; Foresman, J. B.; Ortiz, J. V.; Cioslowski, J.; Fox, D. J. *Gaussian 09*, revision B.02; Gaussian, Inc.: Wallingford, CT, 2010.

- Kresse, G.; Hafner, J. Ab initio molecular dynamics for liquid metals. *Phys. Rev. B* **1993**, *47*, 558–561.
- Kresse, G.; Hafner, J. Ab initio molecular-dynamics simulation of the liquid-metal-amorphous-semiconductor transition in germanium. *Phys. Rev. B* **1994**, *49*, 14251–14269.
- Kresse, G.; Furthmüller, J. Efficiency of ab-initio total energy calculations for metals and semiconductors using a plane-wave basis set. *Comput. Mat. Sci.* **1996**, *6*, 15–50.
- Kresse, G.; Furthmüller, J. Efficient iterative schemes for ab initio total-energy calculations using a plane-wave basis set. *Phys. Rev. B* **1996**, *54*, 11169–11186.
- Perdew, J.; Burke, K.; Ernzerhof, M. Generalized gradient approximation made simple. *Phys. Rev. Lett.* **1996**, *77*, 3865–3868.
- Perdew, J.; Burke, K.; Ernzerhof, M. Errata: Generalized gradient approximation made simple. Generalized gradient approximation made simple [phys. Rev. Lett. 77, 3865 (1996)]. *Phys. Rev. Lett.* **1997**, *78*, 1396.
- Blochl, P. E. Projector augmented-wave method. *Phys. Rev. B* **1994**, *50*, 17953–17979.
- Kresse, G.; Joubert, D. From ultrasoft pseudopotentials to the projector augmented-wave method. *Phys. Rev. B* **1999**, *59*, 1758–1775.
- Jensen, K. P.; Roos, B. O.; Ryde, U. Performance of density functionals for first row transition metal systems. *J. Chem. Phys.* **2007**, *126*, 014103–014114.
- Kabsch, W. A discussion of the solution for the best rotation to relate two sets of vectors. *Acta Crystallogr. A* **1978**, *34*, 827–828.
- Rego, L. G.; Batista, V. S. Quantum dynamics simulations of interfacial electron transfer in sensitized TiO₂ semiconductors. *J. Am. Chem. Soc.* **2003**, *125*, 7989–7997.
- Abuabara, S. G.; Rego, L. G. C.; Batista, V. S. Influence of thermal fluctuations on interfacial electron transfer in functionalized TiO₂ semiconductors. *J. Am. Chem. Soc.* **2005**, *127*, 18234–18242.
- Abuabara, S. G.; Cady, C. W.; Baxter, J. B.; Schmuttenmaer, C. A.; Crabtree, R. H.; Brudvig, G. W.; Batista, V. S. Ultrafast photooxidation of Mn(II)-terpyridine complexes covalently attached to TiO₂ nanoparticles. *J. Phys. Chem. C* **2007**, *111*, 11982–11990.
- McNamara, W. R.; Snoeberger, R. C., III; Li, G.; Schleicher, J. M.; Cady, C. W.; Poyatos, M.; Schmuttenmaer, C. A.; Crabtree, R. H.; Brudvig, G. W.; Batista, V. S. Acetylacetone anchors for robust functionalization of TiO₂

nanoparticles with Mn(II)-terpyridine complexes. *J. Am. Chem. Soc.* **2008**, *130*, 14329–14338.

55. Jakubikova, E.; Snoeberger, R. C., III; Batista, V. S.; Martin, R. L.; Batista, E. R. Interfacial electron transfer in TiO₂ surfaces sensitized with Ru(II)–polypyridine complexes. *J. Phys. Chem. A* **2009**, *113*, 12532–12540.
56. Bowman, D. N.; Blew, J. H.; Tsuchiya, T.; Jakubikova, E. Elucidating band-selective sensitization in iron(II) polypyridine-TiO₂ assemblies. *Inorg. Chem.* **2013**, *52*, 8621–8628.
57. Bowman, D. N.; Blew, J. H.; Tsuchiya, T.; Jakubikova, E. Correction to elucidating band-selective sensitization in iron(II) polypyridine-TiO₂ assemblies. *Inorg. Chem.* **2013**, *52*, 14449–14449.
58. Byrn, M. P.; Curtis, C. J.; Hsiou, Y.; Khan, S. I.; Sawin, P. A.; Tendick, S. K.; Terzis, A.; Strouse, C. E. Porphyrin sponges: Conservative of host structure in over 200 porphyrin-based lattice clathrates. *J. Am. Chem. Soc.* **1993**, *115*, 9480–9497.
59. Barnett, G. H.; Hudson, M. F.; Smith, K. M. Concerning mesotetraphenylporphyrin purification. *J. Chem. Soc., Perkin Trans. I* **1975**, 1401–1403.
60. Leon, C. P.; Kador, L.; Peng, B.; Thelakkat, M. Characterization of the adsorption of Ru-bpy dyes on mesoporous TiO₂ films with UV-vis, Raman, and FTIR spectroscopies. *J. Phys. Chem. B* **2006**, *110*, 8723–8730.
61. Nilsing, M.; Persson, P.; Ojamae, L. Anchor group influence on molecule–metal oxide interfaces: Periodic hybrid DFT study of pyridine bound to TiO₂ via carboxylic and phosphonic acid. *Chem. Phys. Lett.* **2005**, *415*, 375–380.
62. Labat, F.; Adamo, C. Bi-isonicotinic acid on anatase (101): Insights from theory. *J. Phys. Chem. C* **2007**, *111*, 15034–15042.
63. Hirva, P.; Haukka, M. Effect of different anchoring groups on the adsorption of photoactive compounds on the anatase (101) surface. *Langmuir* **2010**, *26*, 17075–17081.
64. Vittadini, A.; Selloni, A.; Rotzinger, F. P.; Gratzel, M. Formic acid adsorption on dry and hydrated TiO₂ anatase (101) surfaces by DFT calculations. *J. Phys. Chem. B* **2000**, *104*, 1300–1306.
65. Bowman, D. N.; Mukherjee, S.; Barnes, L. J.; Jakubikova, E. Linker dependence of interfacial electron transfer rates in Fe(II)–polypyridine sensitized solar cells. *J. Phys.: Condens. Matter* **2015** in press.
66. Mukherjee, S.; Bowman, D. N.; Jakubikova, E. Cyclometalated Fe(II) complexes as sensitizers in dye-sensitized solar cells. *Inorg. Chem.* **2014**, *54*, 560–569.
67. Hoff, D. A.; da Silva, R.; Rego, L. G. C. Coupled electron–hole quantum dynamics on D–π–A dye-sensitized TiO₂ semiconductors. *J. Phys. Chem. C* **2012**, *116*, 21169–21178.
68. Rego, L. G. C.; Abuabara, S. G.; Batista, V. S. Model study of coherent quantum dynamics of hole states in functionalized semiconductor nanostructures. *J. Chem. Phys.* **2005**, *122*, 154709.
69. Rego, L. G. C.; Abuabara, S. G.; Batista, V. S. Coherent optical control of electronic excitations in functionalized semiconductor nanostructures. *Quantum Inf. Comput.* **2005**, *5*, 318–334.

Chapter 9

Nonradiative Relaxation of Charge Carriers in GaN-InN Alloys: Insights from Nonadiabatic Molecular Dynamics

Alexey V. Akimov* and Oleg V. Prezhdo

Department of Chemistry, University of Southern California,
Los Angeles, California 90089

*E-mail: alexvakimov@gmail.com.

The nonradiative relaxation of charge carriers in GaN and In-doped GaN is investigated using nonadiabatic molecular dynamics. Notable differences in relaxation timescales in these materials are attributed to the density of electronic states and symmetry of the systems. Disperse density of states of the system with In atoms results in stronger coupling of electronic states and faster relaxation. The distribution of intraband gaps was found important for defining the order of slow/fast relaxation phases in multiexponential energy loss kinetics. The role of electronic decoherence has been found to be of great significance. It not only slows down the relaxation kinetics, but also changes the behavior to single-exponential one and emphasizes the role of energy gaps. The qualitative behavior of the computed timescales is in good agreement with available experimental data.

1. Introduction

Group III nitrides have been attracting an increased interest in the research community for many years. GaN, InN, and their alloys and derived materials have been successfully applied in photocatalysis (1–4), optoelectronics (5, 6), and as blue and green light-emitting diodes (7–9). This interest can be attributed to the small tunable gap (10, 11) corresponding to visible light absorption. The materials also show strong photoluminescence, which can be tuned by the level of dopant

element. They can be synthesized in a wide variety of nanoscale forms, including quantum dots, nanowires, discs and thin layers.

Experimental studies of carrier dynamics in (Ga,In)N ternary phases and in GaN have been performed by various groups. For example, Lioudakis et al. (12, 13) found that the hot electron relaxation times in GaN decreased as the percentage of In in the material is increased. In particular, for practically pure GaN ($\text{In}_{0.07}\text{Ga}_{0.93}\text{N}$) the relaxation time was estimated to be ca. 25 ps, while in $\text{In}_x\text{Ga}_{1-x}\text{N}$ with $x = 0.89 - 0.43$ it varied in the range from 0.4 to 1.4 ps, depending on composition. On the other hand, the studies of $\text{In}_{0.17}\text{Ga}_{0.83}\text{N}$ reveal that the initial ultrafast relaxation within the free-carrier states occurs on the timescale of 30 ps, while further relaxation down to the localized edge states occurs with the slower rate – within ca. 170 ps, depending on the irradiation intensity. Moreover, these effects occur only if the laser fluence is greater than the threshold of 3.68 mJ/cm^2 . Then a stimulated emission peak is observed. For smaller fluence, only a spontaneous emission can be triggered. You et al. (14) observed the stimulated emission due to recombination in $\text{In}_{0.20}\text{Ga}_{0.80}\text{N}$ nanowires to be on the 1.5 ps timescale. They also found slower kinetics rates, attributing two disparate timescales to shallow and deep localized exciton states. Upadhyá et al. (15) reported the multiexponential carrier relaxation kinetics in GaN nanowires, with the characteristic timescales ranging from 1-3 ps (initial) to 8-26 ps (middle) and to over ns (late). Many works concluded that excitation dynamics in (Ga,In)N materials is very complex with possible contributions from fluence rates, phonon bottleneck, deep and shallow defect states, and many-body electron-electron interactions, and Auger processes. The latter was especially pronounced in pure InN leading to a non-standard dependence of the hot electron relaxation times on the electron density. The dominant role of the Auger recombination was proposed for that material (16).

Despite the large number of useful experimental studies, there has been no computational modeling of the exciton relaxation dynamics in (Ga,In)N systems reported so far. In this work, we aim to provide such a theoretical study, and link the electronic structure properties of the materials to their quantum nonadiabatic kinetics. Specifically, we undertake the simplest modeling of spontaneous relaxation of various excited states in GaN and $\text{In}_{0.5}\text{Ga}_{0.5}\text{N}$ systems via nonadiabatic transitions. The consideration of external perturbation and effects of laser intensity, as well as many-particle interactions, is beyond the scope of this work and will be investigated in future studies.

2. Methodology

2.1. Computational Details

To study the relaxation dynamics of the charge carriers in bulk gallium nitride, GaN, and in its alloy with indium nitride, $\text{In}_x\text{Ga}_{1-x}\text{N}$, we have considered the minimal, yet sufficiently large simulation cells (Figure 1). In the case of the In-doped system, we have distributed several In atoms in the unit cell, placing them at random positions (Figure 1b).

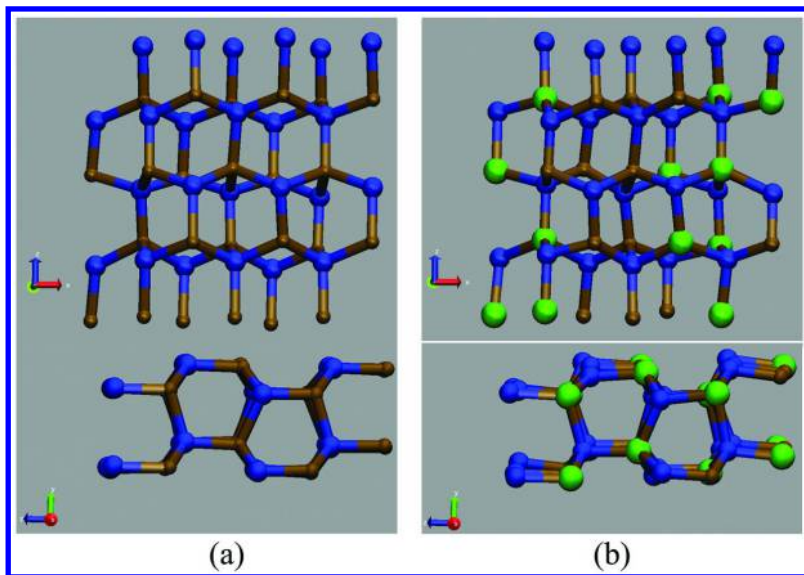


Figure 1. Molecular structure of the GaN (a) and InN:GaN (b) used in this work. Atom colors: ochre – Ga, green – In, blue – N. Periodic images are not shown for clarity.

First, we optimize the crystal structure of the considered systems, including a variation of the unit cell parameters. The resulting configurations are shown in Figure 1. All ab initio calculations are carried out using the Quantum Espresso package (17). The core electrons of the atoms are described by the pseudopotentials of ultrasoft type (18), while the valence electrons are represented by the converged plane wave basis. The satisfactory convergence is achieved with the kinetic energy cutoff of 40 Ry on the plane waves and 400 Ry on the electronic density. The dispersive interactions are accounted for with the semi-empirical terms (DFT-D) (19, 20). All computations are performed using only a gamma-point. This approximation helps accelerating the calculations significantly and simplifies the implementation of the nonadiabatic molecular dynamics (NA-MD) scheme. The approximation is accurate because the simulation cell size is sufficiently large, so the Brillouin zone integration is well approximated by only the central point. The interaction of electronic states corresponding to different crystal momentum, k , may have certain effects, but of the higher order.

The optimized structures are used as the starting points for the ab initio adiabatic (Born-Oppenheimer) molecular dynamics simulations. The evolution of each system is integrated for ca. 4-5 ps using the Verlet algorithm (21) with the time step of 1 fs. The lattice parameters are fixed to the optimized values. The temperature of 300 K is maintained with the Andersen thermostat (22). Initial 350 fs of the computed trajectories are considered the equilibration (thermalization) period and are not included in the analysis. The wavefunctions at adjacent

MD time steps are used to compute the nonadiabatic couplings numerically as described by Hammes-Schiffer and Tully (23).

The nonadiabatic molecular dynamics simulations have been performed using the PYXAID package (24, 25). The nonadiabatic couplings and the eigenenergies of the KS orbitals define the Hamiltonian in the time-dependent Schrodinger equation (TD-SE). The latter is solved in the adiabatic basis along the computed ground state trajectories – the approach known as the classical path approximation (CPA). The solution of the TD-SE defines the hopping probabilities between all pairs of states. Finally, the populations of all states and the average energy of the system are computed as the function of the time delay after the excitation of the system into a particular state with specific initial energy. The detailed description of the surface hopping procedure has been presented many times, so we refer the reader to the corresponding papers (23, 26–30). In addition to the standard fewest switches surface hopping (FSSH) technique we explore the effects of the decoherence by using the recently developed decoherence-induced surface hopping technique (DISH) (31).

3. Results and Discussion

3.1. The Electronic Structure of GaN and $\text{In}_{0.5}\text{Ga}_{0.5}\text{N}$

To understand the electronic structure of GaN and $\text{In}_{0.5}\text{Ga}_{0.5}\text{N}$, we compute the projected densities of states (pDOS) for both systems. The results for both systems are presented in Figure 2.

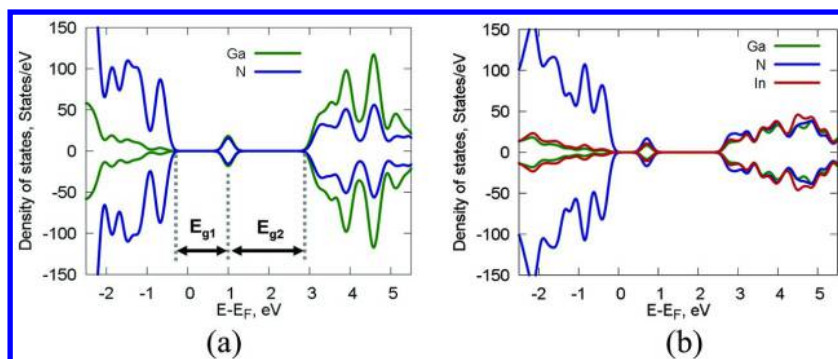


Figure 2. Partial densities of states of GaN (a) and $\text{In}_{0.5}\text{Ga}_{0.5}\text{N}$ (b) systems.

One of the distinctive features of all pDOS shown in Figure 2 is the presence of the state, located approximately $E_{g1}=0.8\text{--}1.0$ eV above the VB edge and $E_{g2}=1.8\text{--}2.0$ eV below the quasi-continuous part of the CB. The state is likely to be the band edge of the CB. Thus, the fundamental gap is defined by the quantity E_{g1} while the E_{g2} gap is an intraband gap.

The main distinctive feature between the pDOSs of GaN and $\text{In}_{0.5}\text{Ga}_{0.5}\text{N}$ is the difference of the quasi-continuous parts of their CB. The pDOS for GaN shows three intense peaks, relatively well separated from each other. Thus, the density of states is well localized in energy scale, and the average energy difference between the pairs of the adjacent energy levels is rather large. Therefore, it is expected that the relaxation kinetics should slow down – the effect observed in the experiment and also found in our NA-MD calculations, as will be discussed later. On the contrary, the CB of the $\text{In}_{0.5}\text{Ga}_{0.5}\text{N}$ is more disperse in energy scale, leading to smaller energy spacing between states and eventually to faster relaxation kinetics.

Finally, it is worth noting that the CB of both materials is separated by a gap located approximately 4.2 eV above the Fermi energy. This gap is well observed in GaN and is less pronounced in $\text{In}_{0.5}\text{Ga}_{0.5}\text{N}$. As we will show later, the presence of this intraband gap plays a crucial role in defining distinct excitation-energy-dependent relaxation regimes.

3.2. Energy Relaxation in GaN and $\text{In}_{0.5}\text{Ga}_{0.5}\text{N}$

Energy relaxation kinetics in GaN calculated within the FSSH-CPA framework is presented in Figure 3. The initial excitation energies are chosen in a 6.0 eV window, which corresponds to excitation of an electron from the HOMO to one of the first 20 unoccupied orbitals. The average energy of the excited system is defined by the populations of the KS states of the material and is zero for the ground state, for which there are no electrons excited. The energy of the first excited state in the single particle picture is equal to the HOMO-LUMO gap. Pictorially this excitation level corresponds to the energy of the state 1 (as denoted in the figure) at the moment of excitation ($t = 0$ fs). The values of the fundamental gap obtained from the DFT calculations are 1.6 eV for GaN and 1.07 for $\text{In}_{0.5}\text{Ga}_{0.5}\text{N}$. The absolute values are underestimated as a result of the delocalization error of DFT. However, the qualitative trend in the value of the energy gaps of $\text{In}_x\text{Ga}_{1-x}\text{N}$ compounds is captured reasonably well, providing the basis for a qualitative comparative analysis of the energy relaxation rates in these systems.

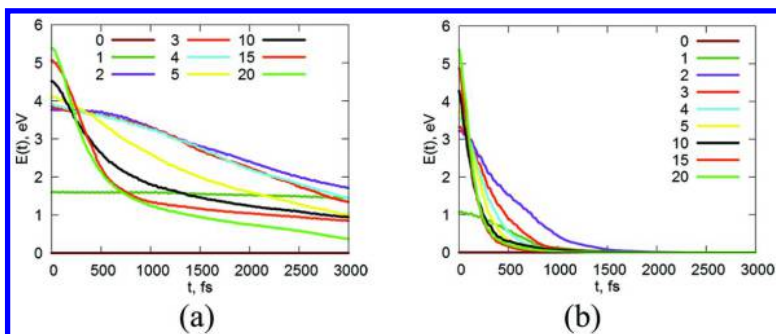


Figure 3. Relaxation kinetics in GaN (a) and $\text{In}_{0.5}\text{Ga}_{0.5}\text{N}$ (b) systems.

The energy relaxation in GaN is best described by a two-exponential decay kinetics. The energy relaxation in $\text{In}_{0.5}\text{Ga}_{0.5}\text{N}$ also follows the two-exponential behavior, in general. However, it appears almost as the mono-exponential kinetics, because of the overall faster dynamics. Depending on the initial excitation energy, one of the two relaxation regimes is possible. Pictorially the regimes can be identified by the order of the slow and fast phases of relaxation. This order defines the “bowing” direction.

For the excitation energies higher than 4.2 eV, an initial ultrafast relaxation is observed for both GaN and $\text{In}_{0.5}\text{Ga}_{0.5}\text{N}$. The energy decays to the level slightly below the CB for GaN and almost to the ground state energy level in case of In-doped GaN. This behavior indicates that the higher energy states in these materials are strongly coupled to the chosen ground state via nonadiabatic transitions. The relaxation rates decrease as time progresses, indicating that the low-energy excited states are weakly coupled to the ground state. Thus, the CB edge states may serve as the bottleneck for electron-hole recombination. The difference of the coupling magnitudes between distinct excited states and the ground state may be the reason for the difference in the timescales of spontaneous and stimulated emission observed in GaN-InN alloys. It can also explain the existence of the stimulated recombination in these systems. Namely, once the system is excited to higher energy states (stimulation) the direct coupling to the ground state increases, leading to fast and efficient recombination (and emission). On the contrary, spontaneous emission from the low-energy states may be significantly slower. This result is especially pronounced if decoherence effects are considered.

As we will discuss next, the system composition can strongly affect the properties of these states and notably affect the dynamics. The relaxation dynamics of the CB edge level (state 1 in Figure 3) is strikingly different in the two systems. One can observe that there is practically no transition out of this state – the energy level remains constant for the duration of the simulation, 3 ps (Figure 3a). On the contrary, the energy of the lowest excitation in $\text{In}_{0.5}\text{Ga}_{0.5}\text{N}$ decays to zero during the first 1 ps of simulation (Figure 3b). This result can be best understood if one considers symmetry of the two systems. The atom arrangement in pure GaN is relatively uniform and periodic, leading to more regular wavefunctions. As a result, such states have negligible nonadiabatic coupling because the corresponding operator is even. In the case of $\text{In}_{0.5}\text{Ga}_{0.5}\text{N}$ with the random position of In atoms, there is no any symmetry-based expectation regarding the nature of the KS orbitals. It is thus not surprising that two subsequent orbitals are coupled via a non-zero nonadiabatic coupling matrix element. The difference in the dynamics of the CB edge states leads to differences in the relaxation kinetics of the higher-energy state. Specifically, since high energy states may partially relax to the CB edge state, the dynamics of the latter defines the existence of the slow relaxation phase in the two-exponential kinetics. The edge state in GaN is stable to further relaxation, so the slow phase of the two-exponential kinetics is clearly observable in this case. On the contrary, the edge state of $\text{In}_{0.5}\text{Ga}_{0.5}\text{N}$ relaxes itself, so it has only a minor effect on the long-time dynamics in this material, making the overall curve appear almost as a single-exponential one.

Finally, for the excitation energies below 4.2 eV, but above the CBE, the initial relaxation is relatively slow while the second phase is faster. This behavior can be attributed to weaker coupling of these states to the ground state wavefunction, yet not negligible as for the CB edge state. The acceleration in the second phase can be attributed to a larger energy gap: If the short-time kinetics occurs in the dense manifold of the quasicontinuous states, in the longer run the transitions involve hops across the intra-gap E_{g2} , leading to faster dynamics.

The results of the simulation of the charge carrier relaxation in GaN and $\text{In}_{0.5}\text{Ga}_{0.5}\text{N}$ presented in Figure 3 reflect only the electronic structure effects and does not account for any system-bath interaction. As we have shown above, many effects in energy relaxation dynamic can be understood in terms of magnitudes of nonadiabatic couplings, intra- or inter-band energy gaps, and structural symmetry. In general, the results of the simulations are in agreement with the experimental observation of Lioudakis et al (13), who showed that the relaxation dynamics in Indoped GaN is faster than in pure GaN. To understand this observation together with the results of our simulation, one needs to resort to the analysis of the couplings in the two systems. The presence of the atoms of different type (In and Ga as opposed to only Ga) randomly distributed in the simulation cell increases the internal disorder and makes the CB states more dispersed on the energy scale (e.g. compare panels (a) and (b) in Figure 2). The random distribution of the dopant atoms leads to less regular wavefunctions, which are more responsive to vibrations of various atoms. Finally, indium atoms are notably larger than Ga atoms. As a consequence, the valence electrons are more diffuse, and their overlap with the valence electrons of other atoms is larger than for Ga atom. The large orbital overlap enhances the nonadiabatic couplings between the CB states and, hence, increases the relaxation rates.

3.3. Effect of the Decoherence Correction

Although the trend in the computed relaxation times obtained with the FSSH method agrees with the experimental results qualitatively, the rate magnitudes are notably underestimated. The contrast between the experimental and theoretical results is larger for the GaN system, where the intrinsic relaxation kinetics is slower. The relaxation time, computed for this material is approximately 3 ps (Figure 3a), while experimental works report the value of ca. 25 ps. for almost pure GaN (13). On the contrary, in the $\text{In}_{0.5}\text{Ga}_{0.5}\text{N}$ system the relaxation is practically complete on the time scale of ca. 0.5 ps (Figure 3b) – in better agreement with the corresponding experimental value of ca. 1.4 ps (13). Yet, the difference is not negligible.

The discrepancy between the theoretical and experimental time scales arises because of the increased importance of electronic decoherence. The latter is negligible if the intrinsic electronic transition is ultrafast and proceeds on the timescale of ca. 10-100 fs. Only a few atomic vibrations can occur on such a short timescale, and they have a minor impact on the evolution of the electronic sub-system. On the other hand, if the electron relaxation process is intrinsically slow and proceeds on the timescale of more than 1 ps, the number of the nuclear vibrations and the number of the stochastic collisions with the environment is

large. These stochastic interactions are seen by the quantum subsystem as noise, causing electronic wavefunctions to lose their coherence. Thus, it is expected that the role of the electron-phonon interaction is important for the intrinsically slow electronic transitions.

In the previous section, we have discussed only the electronic structure effects on the excitation energy relaxation in GaN and In-doped GaN. To assess the importance of the effects of decoherence, we perform the NA-MD calculations using the DISH method (31), which accounts for the decoherence caused by the stochastic environment. The results of such simulations for both GaN and $\text{In}_{0.5}\text{Ga}_{0.5}\text{N}$ systems are presented in Figure 4.

As a general trend, the inclusion of decoherence slows down excitation energy decay for all systems (Figure 4) in comparison to the overcoherent FSSH description (Figure 3). Quantitatively the effect of the decoherence correction is larger for the intrinsically slower electron relaxation processes, namely for the GaN system, as it is expected. Second, the kinetics is well described by a single exponential decay law for all initial excitation energies. This effect can be understood from the following point. The decoherence occurs on the timescale of ca. 5-30 fs, which defines the frequency with which the propagated wavefunction collapses onto a pure electronic state. Since the intrinsic energy relaxation dynamics occurs on a much longer timescale, the details of the population transfer are destroyed by often wavefunction collapses and are not reflected in the energy relaxation curves in Figure 4.

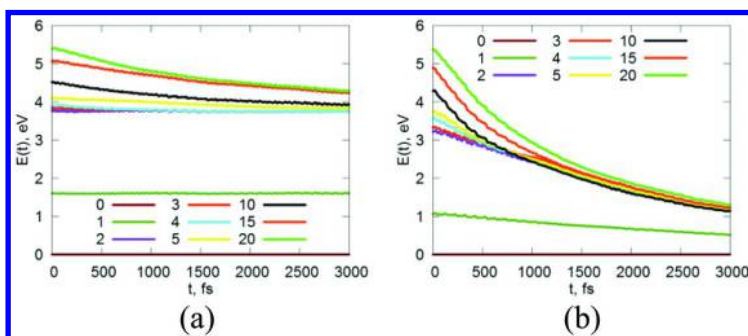


Figure 4. Relaxation kinetics in GaN (a) and in $\text{In}_{0.5}\text{Ga}_{0.5}\text{N}$ (b), computed with the decoherence effects accounted for via the DISH algorithm.

In addition to being significantly slower, the energy relaxation dynamics computed with the inclusion of decoherence effects qualitatively differs from that computed without decoherence effects. In GaN the CB edge state does not decay into the ground state, similar to the FSSH result. As we have discussed earlier, this is a purely electronic structure effect and decoherence does not introduce

any new features. On the opposite, the high energy states in GaN relax only to the intraband edge positions (Figure 4a), not to the ground state, as predicted by simple FSSH (Figure 3a). This effect originates from the existence of the large E_{g2} gap. The electronic states separated by larger gaps show smaller decoherence times (decoherence occurs faster), and the electronic transitions are suppressed to the larger extent. In general, we can differentiate relaxation curves into the groups, which correspond to the groups of states separated by notable energy gaps. For instance, the excitations in GaN with the energy above 5 eV decay to the level defined by the intraband gap at ca. 4.2 eV.

As in the fully coherent FSSH description, the relaxation dynamics in $In_{0.5}Ga_{0.5}N$ differs significantly from that in GaN. First, it occurs at much smaller timescales, but in better agreement with experiment as compared to the FSSH results. Second, the CB edge state relaxes to the ground state, similar as it predicted by the FSSH description. Thus, this result remains valid, indicating that the role of coherences is only in slowing down the kinetics. It also supports the earlier explanation of larger electron-hole recombination probability in this material in view of increased disorder and larger orbital overlaps. The grouping of the states depending on the nearby intraband gap is also observed in $In_{0.5}Ga_{0.5}N$. However, unlike GaN, there are only two notable gaps, E_{g1} and E_{g2} , leading to only two groups of relaxation curves. The smaller subgroup observed in GaN is not resolved in $In_{0.5}Ga_{0.5}N$, because the higher energy states are more disperse, so there is no well-identified intraband gap.

4. Conclusions

In this work we have studied the nonadiabatic relaxation dynamics in GaN and In-doped GaN using the combination of electronic structure calculations and atomistic nonadiabatic molecular dynamics. We have identified the importance of intraband gaps in determining the relaxation kinetics. In the fully coherent FSSH description, the energy gaps within the CB lead to multi-exponential kinetics. The asymmetry and increased disorder of molecular and electronic structures lead to increased nonadiabatic couplings and faster relaxation rates, as in In-doped GaN. On the contrary, the highly regular structure of GaN leads to slower relaxation dynamics. We also found that taking the decoherence effects into account results in significantly slower relaxation dynamics. In addition, the bi-exponential decay law observed in simulations without decoherence correction is changed to the single exponential decay law, reflecting the rate-determining effect of the system-bath (decoherence) interactions. From the quantitative point of view, the effect of decoherence is larger for the intrinsically slower electronic transitions. The decay times obtained from the simple FSSH scheme of the NA-MD calculation are on the order of 0.5 and 3.0 ps for $In_{0.5}Ga_{0.5}N$ and GaN, respectively. These values change to ~3.0 ps and ~20 ps in the DISH scheme. The latter are in a much better agreement with the experimental time scales for the relaxation processes in these materials.

References

1. Maeda, K.; Teramura, K.; Lu, D.; Takata, T.; Saito, N.; Inoue, Y.; Domen, K. Photocatalyst Releasing Hydrogen from Water. *Nature* **2006**, *440*, 295–295.
2. Yoshida, M.; Hirai, T.; Maeda, K.; Saito, N.; Kubota, J.; Kobayashi, H.; Inoue, Y.; Domen, K. Photoluminescence Spectroscopic and Computational Investigation of the Origin of the Visible Light Response of $(\text{Ga}_{1-x}\text{Zn}_x)(\text{N}_{1-x}\text{O}_x)$ Photocatalyst for Overall Water Splitting. *J. Phys. Chem. C* **2010**, *114*, 15510–15515.
3. Ohno, T.; Bai, L.; Hisatomi, T.; Maeda, K.; Domen, K. Photocatalytic Water Splitting Using Modified GaN:ZnO Solid Solution under Visible Light: Long-Time Operation and Regeneration of Activity. *J. Am. Chem. Soc.* **2012**, *134*, 8254–8259.
4. Zhang, H.; Wu, D.; Tang, Q.; Liu, L.; Zhou, Z. ZnO–GaN Heterostructured Nanosheets for Solar Energy Harvesting: Computational Studies Based on Hybrid Density Functional Theory. *J. Mater. Chem. A* **2013**, *1*, 2231–2237.
5. Lähnemann, J.; Hauswald, C.; Wölz, M.; Jahn, U.; Hanke, M.; Geelhaar, L.; Brandt, O. Localization and Defects in Axial (In,Ga)N/GaN Nanowire Heterostructures Investigated by Spatially Resolved Luminescence Spectroscopy. *J. Phys. D: Appl. Phys.* **2014**, *47*, 394010.
6. Zhou, X.; Lu, M.-Y.; Lu, Y.-J.; Jones, E. J.; Gwo, S.; Gradečák, S. Nanoscale Optical Properties of Indium Gallium Nitride/Gallium Nitride Nanodisk-in-Rod Heterostructures. *ACS Nano* **2015**, *9*, 2868–2875.
7. Kim, H.-M.; Cho, Y.-H.; Lee, H.; Kim, S. I.; Ryu, S. R.; Kim, D. Y.; Kang, T. W.; Chung, K. S. High-Brightness Light Emitting Diodes Using Dislocation-Free Indium Gallium Nitride/Gallium Nitride Multiquantum-Well Nanorod Arrays. *Nano Lett.* **2004**, *4*, 1059–1062.
8. Qian, F.; Gradečák, S.; Li, Y.; Wen, C.-Y.; Lieber, C. M. Core/Multishell Nanowire Heterostructures as Multicolor, High-Efficiency Light-Emitting Diodes. *Nano Lett.* **2005**, *5*, 2287–2291.
9. Lin, H.-W.; Lu, Y.-J.; Chen, H.-Y.; Lee, H.-M.; Gwo, S. InGaN/GaN Nanorod Array White Light-Emitting Diode. *Appl. Phys. Lett.* **2010**, *97*, 073101.
10. Wu, J.; Walukiewicz, W.; Yu, K. M.; Ager, J. W.; Haller, E. E.; Lu, H.; Schaff, W. J. Small Band Gap Bowing in $\text{In}_{1-x}\text{Ga}_x\text{N}$ Alloys. *Appl. Phys. Lett.* **2002**, *80*, 4741–4743.
11. Pereira, S.; Correia, M. R.; Monteiro, T.; Pereira, E.; Alves, E.; Sequeira, A. D.; Franco, N. Compositional Dependence of the Strain-Free Optical Band Gap in $\text{In}_x\text{Ga}_{1-x}\text{N}$ Layers. *Appl. Phys. Lett.* **2001**, *78*, 2137–2139.
12. Lioudakis, E.; Othonos, A.; Dimakis, E.; Iliopoulos, E.; Georgakilas, A. Ultrafast Carrier Dynamics in $\text{In}_x\text{Ga}_{1-x}\text{N}$ (0001) Epilayers: Effects of High Fluence Excitation. *Appl. Phys. Lett.* **2006**, *88*, 121128.
13. Lioudakis, E.; Othonos, A.; Iliopoulos, E.; Tsagaraki, K.; Georgakilas, A. Femtosecond Carrier Dynamics of $\text{In}_x\text{Ga}_{1-x}\text{N}$ Thin Films Grown on GaN (0001): Effect of Carrier-Defect Scattering. *J. Appl. Phys.* **2007**, *102*, 073104.
14. You, G.; Guo, W.; Zhang, C.; Bhattacharya, P.; Henderson, R.; Xu, J. Excitation Dependent Two-Component Spontaneous Emission and Ultrafast

Amplified Spontaneous Emission in Dislocation-Free InGaN Nanowires. *Appl. Phys. Lett.* **2013**, *102*, 091105.

15. Upadhyay, P. C.; Li, Q.; Wang, G. T.; Fischer, A. J.; Taylor, A. J.; Prasankumar, R. P. The Influence of Defect States on Non-Equilibrium Carrier Dynamics in GaN Nanowires. *Semicond. Sci. Technol.* **2010**, *25*, 024017.
16. Tsai, T.-R.; Chang, C.-F.; Gwo, S. Ultrafast Hot Electron Relaxation Time Anomaly in InN Epitaxial Films. *Appl. Phys. Lett.* **2007**, *90*, 252111.
17. Gianozzi, P.; Baroni, S.; Bonini, N.; Calandra, M.; Car, R.; Cavazzoni, C.; Ceresoli, D.; Chiarotti, G. L.; Cococcioni, M.; Dabo, I.; Dal Corso, A.; de Gironcoli, S.; Fabris, S.; Fratesi, G.; Gebauer, R.; Gerstmann, U.; Gougaud, C.; Kokalj, A.; Lazzeri, M.; Martin-Samos, L.; Marzari, N.; Mauri, F.; Mazzarello, R.; Paolini, S.; Pasquarello, A.; Paulatto, L.; Sbraccia, C.; Scandolo, S.; Sclauzero, G.; Seitsonen, A. P.; Smogunov, A.; Umari, P.; Wentzcovitch, R. M. QUANTUM ESPRESSO: A Modular and Open-Source Software Project for Quantum Simulations of Materials. *J. Phys. - Condens. Matter* **2009**, *21*, 395502.
18. Vanderbilt, D. Soft Self-Consistent Pseudopotentials in a Generalized Eigenvalue Formalism. *Phys. Rev. B* **1990**, *41*, 7892–7895.
19. Grimme, S. Semiempirical GGA-Type Density Functional Constructed with a Long-Range Dispersion Correction. *J. Comput. Chem.* **2006**, *27*, 1787–1799.
20. Barone, V.; Casarin, M.; Forrer, D.; Pavone, M.; Sambi, M.; Vittadini, A. Role and Effective Treatment of Dispersive Forces in Materials: Polyethylene and Graphite Crystals as Test Cases. *J. Comput. Chem.* **2009**, *30*, 934–939.
21. Verlet, L. Computer “Experiments” on Classical Fluids. I. Thermodynamical Properties of Lennard-Jones Molecules. *Phys. Rev.* **1967**, *159*, 98–103.
22. Andersen, H. C. Molecular Dynamics Simulations at Constant Pressure And/or Temperature. *J. Chem. Phys.* **1980**, *72*, 2384–2393.
23. Hammes-Schiffer, S.; Tully, J. C. Proton Transfer in Solution: Molecular Dynamics with Quantum Transitions. *J. Chem. Phys.* **1994**, *101*, 4657–4667.
24. Akimov, A. V.; Prezhdo, O. V. The PYXAID Program for Non-Adiabatic Molecular Dynamics in Condensed Matter Systems. *J. Chem. Theory Comput.* **2013**, *9*, 4959–4972.
25. Akimov, A. V.; Prezhdo, O. V. Advanced Capabilities of the PYXAID Program: Integration Schemes, Decoherence Effects, Multiexcitonic States, and Field-Matter Interaction. *J. Chem. Theory Comput.* **2014**, *10*, 789–804.
26. Tully, J. C. Molecular Dynamics with Electronic Transitions. *J. Chem. Phys.* **1990**, *93*, 1061–1071.
27. Fabiano, E.; Keal, T. W.; Thiel, W. Implementation of Surface Hopping Molecular Dynamics Using Semiempirical Methods. *Chem. Phys.* **2008**, *349*, 334–347.
28. Craig, C.; Duncan, W.; Prezhdo, O. Trajectory Surface Hopping in the Time-Dependent Kohn-Sham Approach for Electron-Nuclear Dynamics. *Phys. Rev. Lett.* **2005**, *95*, 163001.

29. Drukker, K. Basics of Surface Hopping in Mixed Quantum/Classical Simulations. *J. Comput. Phys.* **1999**, *153*, 225–272.
30. Nelson, T.; Fernandez-Alberti, S.; Chernyak, V.; Roitberg, A. E.; Tretiak, S. Nonadiabatic Excited-State Molecular Dynamics: Numerical Tests of Convergence and Parameters. *J. Chem. Phys.* **2012**, *136*, 054108.
31. Jaeger, H. M.; Fischer, S.; Prezhdo, O. V. Decoherence-Induced Surface Hopping. *J. Chem. Phys.* **2012**, *137*, 22A545.

Chapter 10

Toward First-Principles Description of Carrier Relaxation in Nanoparticles

Andrei Kryjevski*

Department of Physics, North Dakota State University,
Fargo, North Dakota 58108, U.S.A.
*E-mail: andrei.kryjevski@ndsu.edu.

Using an atomistic-level technique for the electron-phonon interactions in a nanoparticle where density functional theory (DFT) is combined with the non-equilibrium Green's function (NEGF) approach we derive expressions for the transition rates between Kohn-Sham states due to phonon emission, including one-and two-phonon contributions. The electron-phonon interaction is derived starting from the original microscopic problem. Application to a nanometer-sized nanorod $\text{Si}_{38}\text{H}_{42}$ has indicated importance of the multi-phonon processes due to presence of the soft surface phonon modes.

Introduction

The ability to predict heat loss of photoexcited charge carriers in a nanoparticle from simulations is important for the potential technological applications of nanomaterials. For example, fast carrier relaxation is desirable in lasers and other light emitting devices, but in, e.g., photovoltaics one aims to minimize the carrier heat loss rate as it limits the solar cell efficiency (1). For instance, carrier relaxation due to phonon emission is one of the main processes competing with the carrier multiplication, or multiple exciton generation mechanism (MEG) relevant to the third-generation photovoltaics (2, 3). It is understood that conclusions about MEG efficiency in a nanoparticle can only be made by comparing MEG with the carrier cooling rates due to phonon emission (3). For this and other reasons dissipative processes in photoexcited nanoparticles have received a great deal of attention (4–6).

Very generally, in a confined few nm-sized system one expects a mismatch between discrete electronic levels and phonon energies allowing carrier energy loss only via less effective multi-phonon processes resulting in a decrease of the relaxation rates in strongly confined nanoparticles, such as quantum dots (QDs), compared to the bulk – the so-called phonon bottleneck (4). There are several experimental studies that either confirm (e.g. (7), for the case of core-shell CdSe QD, in lead chalcogenide nanocrystals (8)) or disprove (e.g. (9–11),] also for CdSe) existence of this phenomenon in nanoparticles.

Theoretically, several detailed explanations of the carrier relaxation slowdown based on model treatment of electronic structure have been proposed (12–14). Several mechanisms for avoiding the phonon bottleneck, e.g., Auger mechanism (15, 16), electron and hole scattering (17), effectiveness of multi-phonon processes (18–20) have been investigated using empirical models.

A DFT-based many-body quantum mechanics approach has been used to study electron-phonon coupling in periodic and nanoscale structures (21–28). The time-domain DFT (tdDFT) approach includes non-adiabatic coupling of electronic and ionic subsystems in the molecular dynamics (MD) DFT simulations at finite temperature, which allows one to study dissipation processes numerically (29). It has been used to study dye-TiO₂ electron transfer (30), hot carrier cooling in CdSe and PbSe QDs (31–34). These studies have shown no evidence of phonon bottleneck. Another DFT-based approach to electron relaxation is based on the reduced density matrix formalism implemented in the Kohn-Sham (KS) orbital basis (35, 36).

Currently carrier relaxation dependence on the nanoparticle's morphology is still an important unsettled issue that needs comprehensive investigation using atomistic level high-precision methods.

Here, we present some results of a more detailed and less computationally demanding than, e.g., tdDFT and reduced density matrix approach to dissipative phenomena in semiconductor nanoparticles where one combines DFT with the Keldysh technique, which is the finite temperature real time formalism of many-body quantum mechanics (37). It is sometimes referred to as the non-equilibrium Green's function method (NEGF). In this atomistic approach electron density is coupled to the individual ions oscillating around their equilibrium positions, which naturally incorporates both acoustic and optical phonons. Phonon frequencies ω_v and mode decompositions U_{1v} needed for this approach can be computed in the standard DFT software, such as VASP (Vienna ab-initio simulation program) (38).

In this work we present expressions for the transition rates R_{sj} between a pair of KS states $|s\rangle$ and $|j\rangle$ in a semiconductor nanoparticle including one-and two-phonon processes. This extends recent work on the bulk Si where one-phonon processes have been studied (39). Using R_{sj} rates various quantities relevant for the description of dynamics of photoexcited nanoparticles, such as lifetimes and energy dissipation rates of photoexcited carriers, and exciton relaxation times, can be computed. In particular, for the same nanoparticle efficiency of MEG and electron energy relaxation can be compared (3).

The method is applied to calculate R_{sj} rates in a nm-sized nanorod (Si₃₈H₄₂). The results are discussed in Section **Preliminary Results**. The calculation has

shown importance of the soft surface phonon modes associated with the motion of the ligands (hydrogen atoms in this case) (32).

Finally, we emphasize that in this work the formalism is derived from the original microscopic problem and all the approximations made are clearly stated.

Electron Hamiltonian in the Basis of Kohn-Sham Orbitals

Dynamics of electrons and ions in a nanoparticle is governed by the following microscopic Hamiltonian

$$H = \int d\mathbf{x} \psi_\alpha^\dagger(\mathbf{x}) \left(-\frac{\hbar^2}{2m} \nabla^2 + V_{eN}(\mathbf{x}, \mathbf{R}) \right) \psi_\alpha(\mathbf{x}) + V_C + H_N, \quad (1)$$

where

$$V_{eN} = \sum_{I=1}^{N_i} v(\mathbf{x}, \mathbf{R}_I), \quad v(\mathbf{x}, \mathbf{R}_I) \simeq -\frac{Z_I e^2}{|\mathbf{x} - \mathbf{R}_I|}, \quad (2)$$

$$V_C = \int d\mathbf{x} d\mathbf{y} \psi_\alpha^\dagger(\mathbf{x}) \psi_\beta^\dagger(\mathbf{y}) \frac{e^2}{2|\mathbf{x} - \mathbf{y}|} \psi_\beta(\mathbf{y}) \psi_\alpha(\mathbf{x}), \quad (3)$$

$$H_N = \sum_{I=1}^{N_i} \frac{P_I^2}{2M_I} + V_{NN}, \quad V_{NN} \simeq \frac{1}{2} \sum_{I \neq J} \frac{Z_I Z_J e^2}{|\mathbf{R}_I - \mathbf{R}_J|}, \quad (4)$$

where $\psi_\alpha(\mathbf{x})$ is the electron annihilation operator, α, β are the spin indices; ψ and ψ^\dagger obey canonical anticommutation relations $\{\psi_\alpha(\mathbf{x}), \psi_\beta^\dagger(\mathbf{y})\} = \delta_{\alpha\beta} \delta(\mathbf{x} - \mathbf{y})$, $\{\psi_\alpha(\mathbf{x}), \psi_\beta(\mathbf{y})\} = 0$. In the above, e , m are the electron charge and mass, respectively, and $Z_I |e|$, M_I are the I^{th} ion charge and mass, respectively. V_C is the bare Coulomb interaction between electrons; $\{\mathbf{P}_I, \mathbf{R}_I\}$, $I=1, \dots, N_i$, are the momentum and position operators of the ions obeying canonical commutation relations. In the actual DFT simulations the microscopic ion-electron Coulomb potential is replaced by a pseudopotential $v(\mathbf{x}, \mathbf{R}_I)$ felt by the valence electrons explicitly included in the DFT simulations (e.g. (40, 41)). As indicated in the equation above, in the first approximation for $v(\mathbf{x}, \mathbf{R}_I)$ one uses Coulomb potential. As discussed in the following, it is to be augmented by the medium screening.

The electromagnetic field Hamiltonian, electron-photon coupling, relativistic corrections (spin-orbit coupling, fine structure, *etc.*) have been omitted in this calculation. They can be included as necessary.

Note that adiabatic approximation has not been made.

Alternatively, the problem of electronic motion in the presence of ions can be formulated in the path integral formalism (e.g. (42),) as

$$\begin{aligned}
 Z &= \int \prod_{I=1}^{N_i} d\mathbf{R}_I \exp\left(\frac{i}{\hbar} \mathbf{S}_I\right), \quad \mathbf{S}_I = \int_{-T/2}^{T/2} dt \left(\sum_{I=1}^{N_i} \frac{M_I \dot{\mathbf{R}}_I^2}{2} - V_{NN} - E_{gs}(\mathbf{R}_I) \right), \\
 \exp\left(\frac{-iE_{gs}T}{\hbar}\right) &= \int D\psi D\psi^\dagger \exp\left(\frac{i}{\hbar} \mathbf{S}_e\right), \\
 \mathbf{S}_e &= \int_{-T/2}^{T/2} dt \left(\int d\mathbf{x} \left[\psi_\alpha^\dagger(\mathbf{x}, t) \left(i\hbar \frac{\partial}{\partial t} + \frac{\hbar^2}{2m} \nabla^2 - V_{eN}(\mathbf{x}, \mathbf{R}_I) \right) \psi_\alpha(\mathbf{x}, t) \right] - V_C \right), \quad (5)
 \end{aligned}$$

where Z is the statistical sum, T is the time span over which the system's dynamics is considered, which is assumed to be much longer than any intrinsic dynamical time scale.

Path integral formulation of this problem makes it clear that for given instantaneous ion positions $\{\mathbf{R}_I\}$ one can “integrate the electrons out” by doing functional integration over the fermion fields ψ, ψ^\dagger . This produces ground state energy of the electrons $E_{gs}(\mathbf{R}_I)$. It is important to note that $E_{gs}(\mathbf{R}_I)$ is independent of the ions' momenta: the electrons only “know” about the instantaneous ion positions, and not their momenta which are included in the ions' kinetic term. Of course, viewed from another angle, this is precisely what DFT does at each step of geometry optimization.

Then, the effective Hamiltonian for the ions is

$$H_{ion} = \sum_{I=1}^{N_i} \frac{P_I^2}{2M_I} + \mathcal{E}(\mathbf{R}_I), \quad \mathcal{E}(\mathbf{R}_I) = E_{gs}(\mathbf{R}_I) + V_{NN}. \quad (6)$$

Assuming the ion positions $\{\mathbf{R}_I^0\}$ corresponding to the energy minimum have been found (by, e.g., the DFT geometry relaxation procedure) so that

$$\left(\frac{\partial \mathcal{E}}{\partial \mathbf{R}_I} \right)_0 = 0 \quad (7)$$

we set $\mathbf{R}_I = \mathbf{R}_I^0 + \mathbf{r}_I$, where \mathbf{r}_I are small deviations from the equilibrium positions. This leads to the standard Hamiltonian for small oscillations around equilibrium

$$H_{atom} = \sum_{I=1}^{N_i} \frac{P_I^2}{2M_I} + \sum_{I,J=1}^{N_i} \frac{\omega_{aI,bJ}^2}{2} r_{aI} r_{bJ} + \mathcal{E}(\mathbf{R}_0), \quad \omega_{aI,bJ}^2 = \left(\frac{\partial^2 \mathcal{E}}{\partial R_{aI} \partial R_{bJ}} \right)_0, \quad a, b = x, y, z. \quad (8)$$

Introduction of the normal modes and subsequent quantization results in

$$H_{ph} = \sum_{\alpha=1}^{3N_i-6} \hbar \omega_\alpha \left(c_\alpha^\dagger c_\alpha + \frac{1}{2} \right), \quad [c_\alpha, c_\beta^\dagger] = \delta_{\alpha,\beta}, \quad (9)$$

where ω_α are the normal frequencies, c_α is the annihilation operator of a phonon of the mode α . Note that the modes corresponding to the translation and rotational motion of the nanoparticle as a whole have been excluded (43–45).

But integrating out the electrons without the appropriate source terms (see, e.g. (42),) would discard all the information about the electron-phonon interactions. So, in order to study phonon-electron coupling one should treat dynamics of electrons and ions explicitly starting from the Hamiltonian (1). Note that $\psi_\alpha^\dagger(\mathbf{x}) V_{eN}(\mathbf{x}, \mathbf{R}) \psi_\alpha(\mathbf{x})$ is the only term in the original Hamiltonian (1) that

explicitly couples electron and atomic motion. So, set $\mathbf{R}_I = \mathbf{R}_I^0 + \mathbf{r}_I$ in (1) and expand V_{eN} to the first order in \mathbf{r}_I . Also, add and subtract the harmonic potential energy term

$$\sum_{I,J=1}^{N_i} \frac{1}{2} \omega_{IaJb}^2 r_{aI} r_{bJ}$$

to Eq. 1. This results in

$$H = H_{el}(\mathbf{R}_I^0) + H_{ph} + H_{e-ph} + \dots, \quad (10)$$

$$H_{ph} = \sum_{\alpha=1}^{3N_i} \hbar \omega_{\alpha} \left(c_{\alpha}^{\dagger} c_{\alpha} + \frac{1}{2} \right), \quad (11)$$

$$H_{e-ph} = - \int_{\mathbf{x}} n(\mathbf{x}) \sum_{I=1}^{N_i} Z_I e^2 \left(\frac{\partial v(\mathbf{x}, \mathbf{R})}{\partial \mathbf{R}_I} \right)_0 \cdot \mathbf{r}_I, \quad (12)$$

$$H_{el}(\mathbf{R}_0) = \int d\mathbf{x} \psi_{\alpha}^{\dagger}(\mathbf{x}) \left(-\frac{\hbar^2}{2m} \nabla^2 + V_{eN}(\mathbf{x}, \mathbf{R}_I^0) \right) \psi_{\alpha}(\mathbf{x}) + V_C, \quad (13)$$

$$n(\mathbf{x}) = \psi_{\alpha}^{\dagger}(\mathbf{x}) \psi_{\alpha}(\mathbf{x}), \quad \mathbf{r}_I = \sqrt{\frac{\hbar}{2\omega_{\nu} M_I}} \mathbf{U}_I^{\nu} (c_{\nu}^{\dagger} + c_{\nu}), \quad (14)$$

where \mathbf{U}_I^{ν} are the normal mode decompositions, ω_{ν} are the phonon frequencies. Note that the ... terms neglected in Eq. (10) above are not relevant to the electron-phonon coupling.

In the above we have neglected the $O(r_I^2)$ contribution to, e.g., H_{e-ph} of Eq. (12)-(27). The rational for this is that, as discussed below, typically the ion-electron interaction $v(\mathbf{x}, \mathbf{R})$ is strongly screened (44, 45). This suppresses the magnitude of second derivative of $v(\mathbf{x}, \mathbf{R})$, which results in $|\partial v(\mathbf{x}, \mathbf{R}_I)/\partial \mathbf{R}_I| > |\partial^2 v(\mathbf{x}, \mathbf{R}_I)/\partial \mathbf{R}_I^2|$. Also, the $O(r_I^2)$ term will not contribute to the KS transition rates at the one-and two-phonon level, which are the main objective of this work. Full investigation of the role of the neglected quadratic term is left for future work.

Let us recall that the KS equation of the orbital-based DFT (46, 47) reads

$$\left(-\frac{\hbar^2}{2m} \nabla^2 + V_{eN}(\mathbf{x}, \mathbf{R}_I^0) \right) \phi_i(\mathbf{x}) + \int_{\mathbf{x}'} V_{eff}(\mathbf{x}, \mathbf{x}') \phi_i(\mathbf{x}') = \epsilon_i \phi_i(\mathbf{x}), \quad (15)$$

where

$$V_{eff} = \int d\mathbf{x}' \frac{en(\mathbf{x}')}{|\mathbf{x} - \mathbf{x}'|} + \frac{\delta E_{xc}[n(\mathbf{x})]}{e \delta n(\mathbf{x})}, \quad (16)$$

where $\{\phi_i(\mathbf{x})\}$ and ϵ_i are the KS orbitals and energies, respectively, and $E_{xc}[n(\mathbf{x})]$ is the exchange-correlation functional; $n(\mathbf{x})$ is the ground state electron density. Depending on the structure's type the label i may include both band number,

lattice wave vector and spin label. In this work we will consider only spin non-polarized states so that each KS state is doubly degenerate with $\phi_{i\uparrow}(\mathbf{x}) = \phi_i(\mathbf{x})$. The potential $V_{\text{eff}}(\mathbf{x})$ depends on $\{\phi_i(\mathbf{x})\}$ and, so, Eq. (15) has to be solved self-consistently. Once $\{\phi_i(\mathbf{x})\}$ have been found, the ground-state energy, $E_{\text{gs}}(\mathbf{R}^0)$, and the ground state electron density can be computed.

To facilitate DFT-based calculations one proceeds by introducing $a_{i\alpha}$, the annihilation operator of a fermion in the i^{th} KS state and spin projection α . The relation between the two bases is standard (45, 48)

$$\psi_{\alpha}(\mathbf{x}) = \sum_i \phi_i(\mathbf{x}) a_{i\alpha}. \quad (17)$$

Now let us substitute $\psi_{\alpha}(\mathbf{x})$, $\psi_{\alpha}(\mathbf{x})^{\dagger}$ from Eq. (17) into (10); add and subtract V_{eff} term of Eq. (15) to and from the kinetic term of Hamiltonian (10) and use Eq. (15). Then in terms of $a_{i\alpha}$, $a_{i\alpha}^{\dagger}$ Hamiltonian (10) takes the form

$$H = H_0 + H_{ph} + H_C + H_{e-ph} - H_V + \dots, \quad (18)$$

where

1.

$$H_0 = \sum_{i\alpha} \epsilon_i a_{i\alpha}^{\dagger} a_{i\alpha}, \quad (19)$$

where a and a^{\dagger} obey the canonical anticommutation relations $\{a_{i\alpha}, a_{j\beta}^{\dagger}\} = \delta_{ij}\delta_{\alpha\beta}$, $\{a_{i\alpha}, a_{j\beta}\} = 0$.

2. The electron-phonon coupling term, takes the form

$$H_{e-ph} = g_{ij}^{\nu} a_{i\alpha}^{\dagger} a_{j\alpha} (c_{\nu}^{\dagger} + c_{\nu}), \quad (20)$$

$$g_{ij}^{\nu} = - \sum_{I=1}^{N_i} Z_I e^2 \sqrt{\frac{\hbar}{2\omega_{\nu} M_I}} \int_{\mathbf{x}} \phi_i^*(\mathbf{x}) \phi_j(\mathbf{x}) \left(\frac{\partial \mathbf{v}(\mathbf{x}, \mathbf{R})}{\partial \mathbf{R}_I} \right)_0 \cdot \mathbf{U}_I^{\nu}. \quad (21)$$

3. The Coulomb interaction takes the form

$$H_C = \frac{1}{2} \sum_{ijkl} \sum_{\alpha, \beta} V_{ijkl} a_{i\alpha}^{\dagger} a_{j\beta}^{\dagger} a_{k\beta} a_{l\alpha},$$

$$V_{ijkl} = \int d\mathbf{x} d\mathbf{y} \phi_i^*(\mathbf{x}) \phi_j^*(\mathbf{y}) \frac{e^2}{|\mathbf{x} - \mathbf{y}|} \phi_k(\mathbf{y}) \phi_l(\mathbf{x}). \quad (22)$$

4. The last term includes the effective potential acting on the KS fermions and prevents double-counting of electron interactions. This is the result of subtracting of $V_{\text{eff}}(\mathbf{x})$ from the kinetic term.

$$H_V = \sum_{ij} a_{i\alpha}^{\dagger} \left(\int d\mathbf{x} d\mathbf{x}' \phi_i(\mathbf{x})^* V_{\text{eff}}(\mathbf{x}, \mathbf{x}') \phi_j(\mathbf{x}') \right) a_{j\alpha}. \quad (23)$$

It is important to note that without any loss of generality instead of the equilibrium \mathbf{R}_i^0 in Eq. (15) one could use $\mathbf{R}_i(t)$, *i.e.*, the ion trajectories from some simulation of the ion thermal motion. Then the KS energies and eigenfunctions would become time-dependent. Indeed, time dependence would be introduced in the leading order Hamiltonian Eq. (19). But, by the same token, without loss of generality one is allowed to use $\epsilon_i(\mathbf{R}_0)$, $\varphi_i(\mathbf{x}; \mathbf{R}_i^0)$ instead, which is more technically convenient. So, in this work we use the “equilibrium” KS basis $\epsilon_i(\mathbf{R}_0)$, $\varphi_i(\mathbf{x}; \mathbf{R}_i^0)$.

Formally, here we work to the leading order in H_V , H_C terms. This corresponds to the simplest independent particle approximation where an excited electron or a hole occupies a specific KS state. This is only for simplicity, of course. Inclusion of electrostatic interaction effects in the single-particle energy corrections (GW) and of the exciton effects using Bethe-Salpeter equation is important for precision calculations. It is left for future work. On the other hand, in order to describe one- and two-phonon emission processes we need to include perturbative corrections up to the fourth order in H_{e-ph} .

Recall that the self-energy function Σ appears in the propagator’s denominator shifting the zero-order single-particle energy due to interactions (44, 45). Specifically, in our case

$$\int_{-\infty}^{\infty} dt e^{i\omega t} \langle \Omega | T a_s(t) a_s^\dagger(0) | \Omega \rangle = \frac{i}{\omega - (\epsilon_s + \Sigma_s(\omega))}, \quad (24)$$

where $|\Omega\rangle$ is the system’s ground state, T is the time-ordering symbol, the KS energies ϵ_s are shifted to have zero at the mid-gap (44, 45). In the presence of interactions the single-particle energies, which now can be complex indicating possibility of decaying into other states, are given by the roots of

$$\omega - (\epsilon_s + \Sigma_s(\omega)) = 0. \quad (25)$$

Then in our approximation the transition rate between KS states s and j due to phonon emission is

$$\mathbf{R}_{sj} = -\text{Im} \Sigma_s^{ph}(\omega) \Big|_{\omega=\epsilon_s/\hbar}, \quad (26)$$

where $\Sigma_s^{ph}(\omega)$ is the contribution to s^{th} KS state self-energy from the electron-phonon interactions. The contributions to $\text{Im} \Sigma_s^{ph}(\omega)$ will come from the processes where the phonon(s) are emitted by a KS particle or hole, interact with the thermal phonon ensemble, and then are re-absorbed again by the same KS quasiparticle. The one- and two-phonon processes relevant to this work are shown in Figure 1.

It is well known that screening in the electron-phonon interaction term, such as Eq. (21), is important. This is because typically the phonons involve lower energies and longer wavelengths than those of the electrons. So, in the following the Coulomb potential in the electron-phonon coupling Eq. (21) will be treated as screened (44, 45).

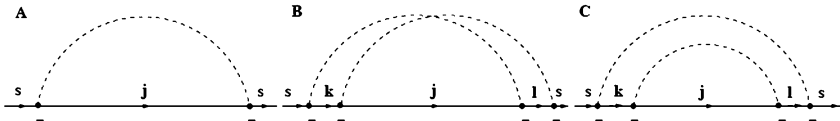


Figure 1. Feynman diagrams relevant for the s^{th} KS state self-energy calculations. The thin solid lines are the KS propagators, dashed line is the v^{th} phonon propagator; electron-phonon coupling \tilde{g}_{ji}^v are at the vertices; $-$ indices are specific to the Keldysh technique. A depicts leading order single phonon emission; B,C are relevant for the two phonon emission processes.

It turns out transition rates R_{sj} are dominated by the diagrams in Figure 1, A and C, respectively. The calculations are done using standard techniques of the Keldysh approach to perturbation theory of many-body quantum mechanics (37). Expressions for transition rate R_{sj} between KS states $|s\rangle$ and $|j\rangle$ due to one- and two-phonon processes are

$$\begin{aligned}
 R_{sj} &= R_{sj}^{1ph} + R_{sj}^{2ph}, \\
 R_{sj}^{1ph} &= \sum_{\nu} \frac{1}{\hbar^2} |\tilde{g}_{sj}^{\nu}|^2 \pi (\theta_s \theta_j [(n_{\nu} + 1) \delta(\omega_s - \omega_j - \omega_{\nu}) + n_{\nu} \delta(\omega_j - \omega_s - \omega_{\nu})] + \\
 &\quad + \theta_{-s} \theta_{-j} [(n_{\nu} + 1) \delta(\omega_j - \omega_s - \omega_{\nu}) + n_{\nu} \delta(\omega_s - \omega_j - \omega_{\nu})]), \\
 R_{sj}^{2ph} &= \sum_{\mu\nu k} \frac{\theta_s \theta_k \theta_j}{\hbar^4} |\tilde{g}_{sk}^{\mu}|^2 |\tilde{g}_{kj}^{\nu}|^2 \pi ([\mathcal{P}_{\gamma}(\omega_s - \omega_k - \omega_{\mu})]^2 \times \\
 &\quad ([n_{\nu}(n_{\mu} + 1) + 1] \delta(\omega_s - \omega_j - \omega_{\mu} - \omega_{\nu}) + [n_{\nu}(n_{\mu} + 1)] \delta(\omega_s - \omega_j - \omega_{\mu} + \omega_{\nu})) + \\
 &\quad + [\mathcal{P}_{\gamma}(\omega_s - \omega_k + \omega_{\mu})]^2 n_{\nu} n_{\mu} (\delta(\omega_s - \omega_j + \omega_{\mu} - \omega_{\nu}) + \delta(\omega_s - \omega_j + \omega_{\mu} + \omega_{\nu}))) + \\
 &\quad + \sum_{\mu\nu k} \frac{\theta_{-s} \theta_{-k} \theta_{-j}}{\hbar^4} |\tilde{g}_{sk}^{\mu}|^2 |\tilde{g}_{kj}^{\nu}|^2 \pi ([\mathcal{P}_{\gamma}(\omega_s - \omega_k + \omega_{\mu})]^2 \times \\
 &\quad ([n_{\nu}(n_{\mu} + 1) + 1] \delta(\omega_s - \omega_j + \omega_{\mu} + \omega_{\nu}) + [n_{\nu}(n_{\mu} + 1)] \delta(\omega_s - \omega_j + \omega_{\mu} - \omega_{\nu})) + \\
 &\quad + [\mathcal{P}_{\gamma}(\omega_s - \omega_k - \omega_{\mu})]^2 n_{\nu} n_{\mu} (\delta(\omega_s - \omega_j - \omega_{\mu} + \omega_{\nu}) + \delta(\omega_s - \omega_j - \omega_{\mu} - \omega_{\nu}))), \\
 n_{\nu} &= \left(\exp \left[\frac{\hbar \omega_{\nu}}{k_B T} \right] - 1 \right)^{-1}, \tag{27}
 \end{aligned}$$

where ω_{ν} is the v^{th} phonon energy, ω_s is the s^{th} KS state energy, T is temperature, and where

$$\delta(x) = \frac{\gamma}{x^2 + \gamma^2}, \quad \mathcal{P}_{\gamma}(x) = \frac{x}{x^2 + \gamma^2}. \tag{28}$$

Small width parameter $\gamma \simeq 0.01\text{eV}$, which is the typical phonon energy separation, has to be introduced when calculating properties of smaller nanoparticles, such as the $\text{Si}_{38}\text{H}_{42}$ nanorod considered in this work. The summation notations are

$$\sum_i \theta_i = \sum_{i \geq LU}, \quad \sum_i \theta_{-i} = \sum_{i \leq HO} \tag{29}$$

with HO and LU defined as the highest occupied and lowest unoccupied KS levels. So, a θ_i factor under sum restricts KS index i to the $i \geq LU$ range, θ_{-i} to the $i \leq HO$ range. As discussed above, the electron-ion potential is the static random phase approximation (RPA) screened Coulomb (45). So, the electron-phonon couplings in the above rate expressions are

$$\tilde{g}_{ij}' = \sum_{I=1}^{N_i} \frac{4\pi i Z_I e^2}{V} \sqrt{\frac{\hbar}{2\omega_\nu M_I}} \sum_{\mathbf{p}} \frac{\rho_{ji}^*(\mathbf{p}) (\mathbf{p} \cdot \mathbf{U}_I^\nu) e^{-i\mathbf{p} \cdot \mathbf{R}_I}}{p^2 - \Pi(0, \mathbf{p}, -\mathbf{p})}, \quad \rho_{ij}(\mathbf{p}) = \sum_{\mathbf{k}} \phi_i^*(\mathbf{k} - \mathbf{p}) \phi_j(\mathbf{k}), \quad (30)$$

where

$$\Pi(\omega, \mathbf{k}, \mathbf{p}) = \frac{8\pi e^2}{V\hbar} \sum_{ij} \rho_{ij}(\mathbf{k}) \rho_{ji}(\mathbf{p}) \left(\frac{\theta_{-j}\theta_i}{\omega - \omega_{ij} + i\gamma} - \frac{\theta_j\theta_{-i}}{\omega - \omega_{ij} - i\gamma} \right) \quad (31)$$

is the RPA polarization insertion (see, e.g. (45)). Note that here we use the “diagonal”, or uniform medium, screening approximation which is a significant technical simplification (49).

Note the expressions above include both processes of phonon emission and absorption, as they should. The one-phonon rate expressions resemble Fermi Golden Rule generalized to the finite temperature case. However, derivation of the two-phonon rates required full use of the Keldysh technique.

To determine, e.g., carrier cooling times one uses R_{sj} as an input for the Boltzmann equation for the KS state occupation numbers (see, e.g. (26)).

Preliminary Results

We have studied phonon emission in the $\text{Si}_{38}\text{H}_{42}$ which is a 1 nm-sized hydrogen-passivated nanorod with the diamond core structure (Figure 2, (a)). The optimized geometry and electronic structure have been obtained using VASP DFT program (38) with the PBE exchange correlation functional (50, 51) along with the projector augmented-wave (PAW) pseudopotentials (38, 41).

The results for electron density of states (DOS) in the single-particle sector and the phonon DOS are shown in Figure 3, (a) and (b), respectively. Note that the highest phonon energy corresponding to the Si–H bond stretching mode is ~ 0.27 eV. Therefore, presence of ~ 0.4 eV sub-gap in the electron spectrum (marked by an arrow in Figure 3, (a)) suggests relevance of multi-phonon processes in this nanoparticle since, e.g., an excited hole can only relax past this sub-gap by emitting at least two phonons.

The results for the one-phonon emission rates for $\text{Si}_{38}\text{H}_{42}$ are shown in Figure 2, (b). The oscillations of the rates are due to strongly non-uniform DOS, both electron and phonon, which is due to the quasi-discrete nature of the levels in this small nanoparticle. The $R_{sj}(\epsilon)$ curve in larger nanoparticles is expected to be much smoother. The two-phonon contributions have turned out to be of the same order as the one-phonon ones, which is contrary to general expectations. This is clearly due to the contributions of the low-energy phonon modes associated with the surface and ligand vibrations (the low-energy part in Figure 3, (b)). As mentioned in Section I, this is a known feature of the smaller nanoparticles where surface effects are more significant.

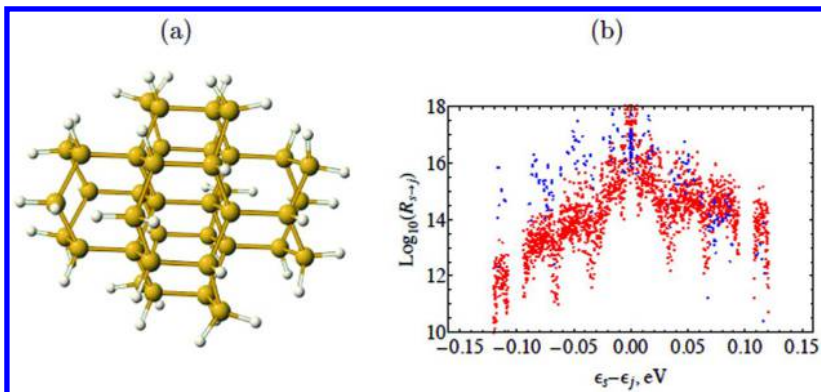


Figure 2. (a): Atomistic model of the $\text{Si}_{38}\text{H}_{42}$ nanorod with the crystalline core structure. (b): Particle and hole transition rates R_{sj} due to one-phonon emission in $\text{Si}_{38}\text{H}_{42}$ at $T = 300$ K. Particle state rates are in red, holes are in blue (color online).

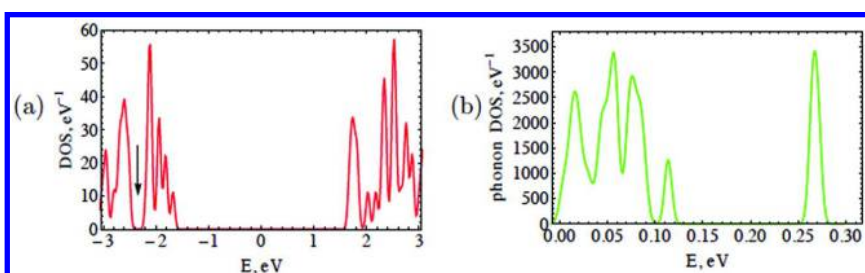


Figure 3. Single particle density of states (a) and phonon density of states (b) for $\text{Si}_{38}\text{H}_{42}$ nanorod. (Used 0.05 eV Gaussian broadening.)

This method will have better applicability to larger nanoparticles where surface phonon modes are relatively unimportant, or for the configurations where the nanoparticle is embedded into a solid matrix.

Conclusions and Discussion

Using an atomistic-level technique for the electron-phonon interactions in a nanoparticle where DFT is combined with the Keldysh method, or non-equilibrium Green's function (NEGF) approach, we have derived expressions for the transition rates between Kohn-Sham states due to phonon emission, including one- and two-phonon contributions. The method has been used to calculate R_{sj} rates in $\text{Si}_{38}\text{H}_{42}$ which is a nm-sized nanorod (See Figure 2, (a)).

The calculation has shown importance of the soft surface phonon modes associated with the motion of ligands (hydrogens in this case) (32).

One important application of this technique will be to check whether the phonon bottleneck is present in somewhat larger nanoparticles where, on one hand, a mismatch between discrete electronic levels and phonon energies is still present, and, on the other, where the surface mode contribution is relatively unimportant.

As mentioned in the Introduction, in this atomistic approach electron density is coupled to the motion of individual ions and naturally incorporates both acoustic and optical phonons. Normal frequencies ω_v and mode decompositions U_{vI} , which are needed for this approach are available in the standard DFT packages. This calculation requires about $6N_i$ DFT iterations, where N_i is the number of ions in the nanoparticle. However, in general, it will take many more DFT runs to simulate chaotic thermal motion of N_i atoms in tdDFT or in the reduced density matrix approaches.

Another important advantage of this approach is that single particle energy corrections (via, e.g., GW approximation) and the exciton effects can be systematically incorporated to calculate the observable, such as relaxation rate of an exciton rather than that of a KS state. Note that such method improvements would be challenging in the tdDFT or in the reduced density matrix approaches. More generally, the role of multi-phonon processes (18–20) and of the anharmonicity effects will be studied by comparing the results of our technique against the results benchmarked by other methods, such as tdDFT (31–33).

Acknowledgments

The author acknowledges use of computational resources of the Center for Computationally Assisted Science and Technology (CCAST) at North Dakota State University, and NERSC No. DE-AC02-05CH11231, allocation Award 86185 for providing computational resources, and financial support for method development from the NSF grant CHE-1413614.

References

1. Shockley, W.; Queisser, H. *J. Appl. Phys.* **1961**, *32*, 510–519.
2. de Boer, W.; de Jong, E.; Timmerman, D.; Gregorkiewicz, T.; Zhang, H.; Buma, W. J.; Poddubny, A.; Prokofiev, A.; Yassievich, I. *Phys. Rev. B* **2013**, *88*, 155304–155319.
3. Stewart, J.; Padilha, L.; Bae, W.; Koh, W.; Pietryga, J.; Klimov, V. *J. Phys. Chem. Lett.* **2013**, *4*, 2061–2068.
4. Nozik, A. *Annu. Rev. Phys. Chem.* **2001**, *52*, 193–231.
5. Nozik, A.; Beard, M.; Luther, J. M.; Law, M.; Ellingson, R.; Johnson, J. *Chem. Rev.* **2010**, *110*, 6873–6890.
6. Beard, M.; Luther, J.; Nozik, A. *Nat. Nanotechnol.* **2014**, *9*, 951–954.
7. Pandeyand, A.; Guyot-Sionnest, P. *Science* **2008**, *322*, 929–932.
8. Geiregat, P.; Delerue, C.; Justo, Y.; Aerts, M.; Spoor, F.; Van Thourhout, D.; Siebbeles, L.; Allan, G.; Houtepen, A.; Hens, Z. *ACS Nano* **2015**, *9*, 778–788.

9. Klimov, V.; McBranch, D. *Phys. Rev. Lett.* **1998**, *80*, 4028–4031.
10. Schaller, R.; Pietryga, J.; Goupalov, S.; Petruska, M.; Ivanov, S.; Klimov, V. *Phys. Rev. Lett.* **2005**, *95*, 196401–196406.
11. Zidek, K.; Abdellah, M.; Zheng, K. *Sci. Rep.* **2014**, *4*, 1933–1968.
12. Benisty, H.; Sotomayor-Torr'es, C.; Weisbuch, C. *Phys. Rev. B* **1991**, *44*, 10945–10948.
13. Bockelmann, U.; Bastard, G. *Phys. Rev. B* **1990**, *42*, 8947–8951.
14. Benisty, H. *Phys. Rev. B* **1995**, *51*, 13281–13293.
15. Bockelmann, U.; Egeler, T. *Phys. Rev. B* **1992**, *46*, 15574–15577.
16. Efros, A.; Kharchenko, V.; Rosen, M. *Solid State Commun.* **1995**, *93*, 281–284.
17. Vurgaftman, I.; Singh, J. *Appl. Phys. Lett.* **1994**, *64*, 232–234.
18. Inoshita, T.; Sakaki, H. *Phys. Rev. B* **1992**, *46*, 7260–7263.
19. Inoshita, T.; Sakaki, H. *Phys. Rev. B* **1997**, *56*, R4355–R4358.
20. Sercel, P. *Phys. Rev. B* **1995**, *51*, 14532–14541.
21. Mauri, F.; Zakharov, O.; de Gironcoli, S.; Louie, S.; Cohen, M. *Phys. Rev. Lett.* **1996**, *77*, 1151–1154.
22. Liu, A.; Quong, A. *Phys. Rev. B* **1996**, *53*, R7575–R7579.
23. Bauer, R.; Schmid, A.; Pavone, P.; Strauch, D. *Phys. Rev. B* **1998**, *57*, 11276–11282.
24. Baroni, S.; de Gironcoli, S.; Dal Corso, A.; Giannozzi, P. *Rev. Mod. Phys.* **2001**, *73*, 515–562.
25. Sjakste, J.; Vast, N.; Tyuterev, V. *Phys. Rev. Lett.* **2007**, *99*, 236405–236501.
26. Noffsinger, J.; Kioupakis, E.; Vande Walle, C.; Louie, S.; Cohen, M. *Phys. Rev. Lett.* **2012**, *108*, 167402–167407.
27. Gonze, X.; Boulanger, X.; Cote, M. *Ann. Phys.* **2011**, *523*, 168–178.
28. Frederiksen, T.; Paulsson, M.; Brandbyge, M.; Jauho, A. *Phys. Rev. B* **2007**, *75*, 205413–205422.
29. Craig, C.; Duncan, W.; Prezhdo, O. *Phys. Rev. Lett.* **2005**, *95*, 163001–163006.
30. Duncan, W.; Prezhdo, O. *Annu. Rev. Phys. Chem.* **2007**, *58*, 143–184.
31. Kilina, S.; Kilin, D.; Prezhdo, O. *ACS Nano* **2009**, *3*, 93–99.
32. Kilina, S.; Craig, C.; Kilin, D.; Prezhdo, O. *J. Phys. Chem. C* **2007**, *111*, 4871–4878.
33. Bao, H.; Habenicht, B.; Prezhdo, O.; Ruan, X. *Phys. Rev. B* **2009**, *79*, 235306–235317.
34. Chen, J.; Schmitz, A.; Kilin, D. *Int. J. Quantum Chem.* **2012**, *112*, 3879–3888.
35. Inerbaev, T.; Hoefelmeyer, J. D.; Kilin, D. *J. Phys. Chem. C* **2013**, *117*, 9673–9692.
36. Chen, J.; Schmitz, A.; Inerbaev, T.; Meng, Q.; Kilina, S.; Tretiak, S.; Kilin, D. *J. Phys. Chem. Lett.* **2013**, *4*, 2906–2913.
37. Lifshitz, E. M.; Pitaevskii, L. P. *Physical Kinetics*, 1st ed.; Pergamon Press: New York, 1981.
38. Blöchl, P. E. *Phys. Rev. B* **1994**, *50*, 17953–17979.
39. Bernardi, M.; Vigil-Fowler, D.; Lischner, J.; Neaton, J.; Louie, S. *Phys. Rev. Lett.* **2014**, *112*, 257402–257407.

40. Kresse, G.; Furthmüller, J. *Phys. Rev. B* **1996**, *54*, 11169–11186.
41. Kresse, G.; Joubert, D. *Phys. Rev. B*, **59**, 1758–1775199.
42. Negele, J.; Orland, H. *Quantum Many-Particle Systems*, 1st ed.; Addison-Wesley: Reading, MA, 1988.
43. Landau, L. D.; Lifshitz, E. M. *Statistical Physics Part 1*, 1st ed.; Pergamon Press: Oxford, 1980.
44. Abrikosov, A.; Gorkov, L.; Dzyaloshinski, I. *Methods of Quantum Field Theory in Statistical Physics*; Prentice-Hall: Englewood Cliffs, NJ, 1963.
45. Fetter, A. L.; Walecka, J. D. *Quantum Theory of Many-Particle Systems*; McGraw-Hill: New York, 1971.
46. Kohn, W.; Sham, L. J. *Phys. Rev.* **1965**, *140*, A1133–A1138.
47. Kümmel, S.; Kronik, L. *Rev. Mod. Phys.* **2008**, *80*, 3–60.
48. Mahan G. *Many-Particle Physics*, 2nd ed.; Plenum: New York, NY, 1993.
49. Kryjevski, A.; Kilin, D. *Mol. Phys.* Submitted for publication; arXiv:1411.6161.
50. Perdew, J.; Burke, K.; Ernzerhof, M. *Phys. Rev. Lett.* **1996**, *77*, 3865–3868.
51. Perdew, J.; Burke, K.; Ernzerhof, M. *Phys. Rev. Lett.* **1997**, *78*, 1396–1396.

Chapter 11

Optical, Electrical, and Catalytic Properties of Metal Nanoclusters Investigated by ab initio Molecular Dynamics Simulation: A Mini Review

Qingguo Meng*

Shenyang Institute of Automation, Chinese Academy of Sciences,
Guangzhou, China 511458

*E-mail: mengqingguo@gz.sia.cn.

Metal nanoclusters (e.g. Pt, Pd, and Au) have been those of the most valuable catalysts that have been used in many catalytic fields of hydrogenation, fuel-cell technologies, and water splitting photo-catalytically, etc. In this mini review, the previous works from our group about the optical, electrical and catalytic properties of metal nanoclusters, such as Pt_{13} , Pd_{13} , and Au_{13} , have been reviewed. Ab initio molecular dynamics simulation (AIMD) at a DFT (Density Functional Theory) level has been applied to simulate the catalytic properties. The results show that Pt_{13} and Pd_{13} nanocluster present interesting hydrogen reduction and molecular H_2 desorption on the surface of the metal nanoclusters. An elementary hydrogen evolution mechanism on the metal nanocluster was established as $\text{H}_{\text{ads}}^+ + \text{H}_{\text{ads}}^+ + 2\text{e}^- + \text{M}_{\text{ads}} \rightarrow [\text{M}_{\text{ads}}-\text{H}_{\text{ads}}-\text{H}_{\text{ads}}] \rightarrow \text{H}_2 + \text{M}$ ($\text{M} \sim \text{metal}$). On the other hand, an Au nanocluster, which is protected by organic thiolate groups, was investigated by ab initio electron dynamics (AIED) calculation. The comparison between the protected and unprotected Au nanoclusters clarifies the contributions from Au core and organic thiolate ligands to the optical and electronic properties, such as photoexcitation, electron/hole relaxation, and energy dissipation, etc.

Keywords: Metal nanocluster; DFT method; Hydrogen desorption; Thiolated Au nanocluster; Surface reaction; Photocatalysis

Introduction

Metallic nanostructures represent promising research interests in the field of nanomaterials, such as catalysis (1, 2), sensing (3, 4), optics (5), therapeutics (6), and diagnostics (7), hydrogen storage (8), hydrogen purification (9) and photo-catalytic water-splitting (10) etc. Most of these applications depend largely on the unique optical and electronic properties of metals when their sizes are confined to nanoscale dimensions. These properties change dramatically with the length scale from nanoparticles, sub-nanostructure, and quantum confined nanoclusters with discrete electronic orbitals and HOMO-LUMO energy gaps. For example, metal nanocluster and nanoparticles (e.g. Pt, Pd and Au) are industrially very important catalysts, such as fuel cell to generate hydrogen energy (11), which is drawing great attention as a future source of clean energy (12, 13). Theoretical studies on the chemisorption of hydrogen have been performed and are reviewed in many publications (14–16). The electronic structures of Pt_{13} clusters in icosahedral and cubic symmetry were quite often studied by the first principle calculations, and the calculated energies were in good agreement with experimental hydrogen-metal binding energies (17). Dissociative adsorption of hydrogen molecules on Pd clusters was reported (18) and compared with that on infinite Pd (111) surface. The weak Pd–H energy allows the chemisorbed H atoms to react with other adsorbates or two H atoms reacts together to form H_2 molecule (19, 20). Small Pd nanoclusters deposited on solid supporting surfaces, such as MgO (21) or TiO_2 (22, 23), were also theoretically studied since it was believed to be responsible for the majority of catalytic activity. The behavior characteristic to the clusters comes from a large fraction of surface atoms and the discrete nature of electronic states, which makes the electronic state of the cluster quite different from those of the bulk structure (24, 25). Metal clusters with an appropriate size would be an excellent representation of the metal nanoparticles (26). The 13-atom clusters have drawn much attention because it can form closed-shell icosahedral structure (27, 28) and are considered as being representative of highly dispersed metal catalysts (29–31).

Au nanocluster (32), which is different from Pt or Pd nanoclusters, are protected by organic thiolate group (–SR). They have attracted intense research interests recently due to their unique electronic, optical and catalytic properties (33–35). They are composed of very few Au atoms in the center core with the size less than 1 nm, and as a result they show “molecule-like” optical transitions in the absorption and emission spectra (36). The small-sized thiolate protected Au nanoclusters exhibit exceptional stability and size dependent HOMO-LUMO gap. Quite a few of thiolate protected Au nanoclusters with different core size and thiolate groups have been successfully synthesized and isolated (37, 38). Studies on the interface between Au nanostructures and the organic

molecules or semiconductors benefit the applications for the nano-electronics (39). Aikens, *et.al* studied the structural, electronic and optical properties of the thiolate-protected $\text{Au}_{38}(\text{SR})_{24}$ ($\text{R}=\text{CH}_3$ and C_6H_{13}) cluster (40) and the origin of discrete optical absorption spectra of $\text{Au}_{25}(\text{SH})_{18}$ nanoparticles (41) by Time Dependent Density Functional Theory (TDDFT) computations. Häkkinen, *et.al* carried out the DFT computations on a $\text{Au}_{144}(\text{SR})_{60}$ cluster with an icosahedral Au_{114} core with 30 RS-Au-SR units as ligand and yielded an excellent fit of the structure factor to the experimental X-ray scattering structure factor (42). The optical absorption spectrum of Au_{24} nanocluster protected by the mixed ligands of phosphine and thiolate was theoretically reproduced and interpreted (43). Most interestingly, ultrafast luminescence dynamics of thiolate protected Au_{25} clusters indicated that their luminescence decay traces showed unique ultrafast growth and decay kinetics that are absent in the larger Au clusters (44). A fast and slow luminescence decay of Au nanocrystals (NCs) was determined originating from recombination of the linear Au-S bond and the staple motif, respectively (45). It has been well-established that the luminescence of Au nanoclusters arose from the HOMO-LUMO gap (46), which was due to the interband transition between the 6sp conduction band and the filled 5d band (47, 48).

In this review, we will give a brief introduction on 1) the hydrogen reduction and molecular H_2 desorption from Pt_{13} , Pd_{13} and Pt/Pd alloy nanocluster surface investigated by ab initio molecular dynamics (AIMD) simulation, and 2) the photoexcitation, electron/hole relaxation and the absorption, excitation and emission spectra of a thiolate protected Au_{13} nanocluster calculated by ab initio electron dynamics (ED).

Electrical and Optical Properties of Pt_{13} and Pd_{13} Nanoclusters

The M_{13} ($\text{M} = \text{Pt}$ and Pd) metal nanocluster investigated has one metal atom in the center, coordinated with other twelve side metal atoms in an O_h point group symmetry. Pt and Pd have an electronic configuration of $[\text{Xe}]4\text{f}^{14}5\text{d}^96\text{s}^1$ and $[\text{Kr}]4\text{d}^{10}$, respectively. Each of the side metal atoms is hydrogenated by two hydrogen atoms ($\text{M}_{13}\text{H}_{24}$), as shown in Figure 1. A structural optimization shows that there is a slightly deformation of O_h to D_{4h} symmetry, indicating a lower energy of D_{4h} symmetry on the Pt_{13} cluster. On the other hand, the $\text{Pd}_{13}\text{H}_{24}$ nanocluster twists to lower the energy for stabilization, increasing the Pd-Pd bond distance up to 2.85 Å, longer than the Pt-Pt bond distance (2.72 Å). During the optimization a few of the H atoms are bridging the neighboring two Pt atoms by a longer Pt-H bond distance (1.76 Å), comparing to the isolated Pt-H bond length (1.58 Å). However, every two of the hydrogen on Pd atoms approach to each other and bond together, indicating a potentially higher catalytic property of Pd than Pt nanoclusters. The H-H bond distance in the optimized $\text{Pt}_{13}\text{H}_{24}$ nanocluster is well separated, but decreases to 0.86 Å in the $\text{Pd}_{13}\text{H}_{24}$ nanocluster, close to H-H bond length of dihydrogen at 0.75 Å, indicating a potentially more active surface chemistry on Pd than Pt nanocluster. Density of state (DOS) of both $\text{Pt}_{13}\text{H}_{24}$ and $\text{Pd}_{13}\text{H}_{24}$ nanoclusters is shown in Figure 2 and 3. There is very small

band gap between HOMO and LUMO, indicating a metal character of $M_{13}H_{24}$ nanoclusters. A band gap less than 0.06 eV is observed for $Pd_{13}H_{24}$ nanocluster, which is much smaller than that of $Pt_{13}H_{24}$ nanocluster.

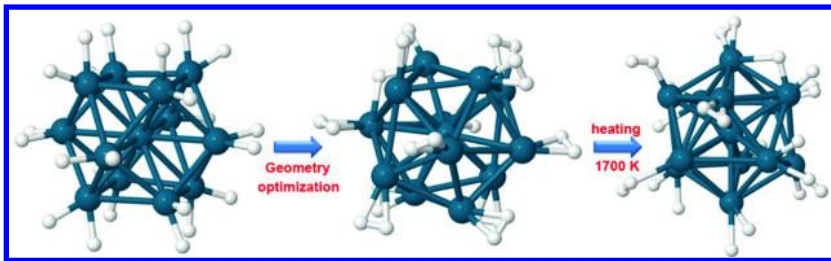


Figure 1. Geometry optimization and heat treatment of $Pd_{13}H_{24}$ cluster. The large and small balls represent the Pd and H atoms, respectively. Adapted with permission from ref (49). Copyright 2015 Taylor & Francis.

Charged Pt_{13} and Pd_{13} Nanoclusters

The investigated $M_{13}H_{24}$ nanoclusters are charged by certain amounts of elementary charges to see what effects the charging has on the properties of the metal nanocluster. The charged nanocluster is labeled as $M_{13}H_{24}^{n\pm}$ ($n = 1\sim 24$). Density of states (DOS) of the charged $Pt_{13}H_{24}^{n\pm}$ ($n = 0, 1$ and 2) nanoclusters are shown in Figure 2. The HOMO of one negative charged $Pt_{13}H_{24}$ nanocluster, $Pt_{13}H_{24}^-$, presents new electronic states at higher energy. Adding more electrons on the cluster, $Pt_{13}H_{24}^{2-}$, increases the orbital energy of HOMO dramatically, in favor of high intrinsic reactivity of the metallic sites (50). The orbital energy of HOMO of the positive charged models decreases with charges and the Fermi level shifts to -7.5 eV after two electrons are removed. Removing more electrons causes the crash of the nanocluster structure. The linear absorption spectra of the charged $Pt_{13}H_{24}$ nanocluster are also shown in Figure 2. Adding one electron to $Pt_{13}H_{24}$ model causes all the absorption bands turning sharp. In contrast to this, the absorption spectra of positively charged clusters ($Pt_{13}H_{24}^+$ and $Pt_{13}H_{24}^{2+}$) become much broader, due to the contributions of some new absorption bands. For example, a new absorption band appears at the low energy range (~ 0.5 eV) in $Pt_{13}H_{24}^+$ model. The absorption spectra of $Pd_{13}H_{24}^{n\pm}$ cluster show approximately five absorption bands before 2.5 eV (~ 500 nm), locating in the visible and IR spectral ranges. Positively charged clusters show only slightly blue shift for these five bands. But the negatively charged clusters present dramatic decrease of absorption intensity in the IR range. This observation can be explained as follows. When the electrons are removed, there are more upper HOMOs available to accept the excited electrons from lower level HOMOs, which is attributed to the new peaks in the IR range.

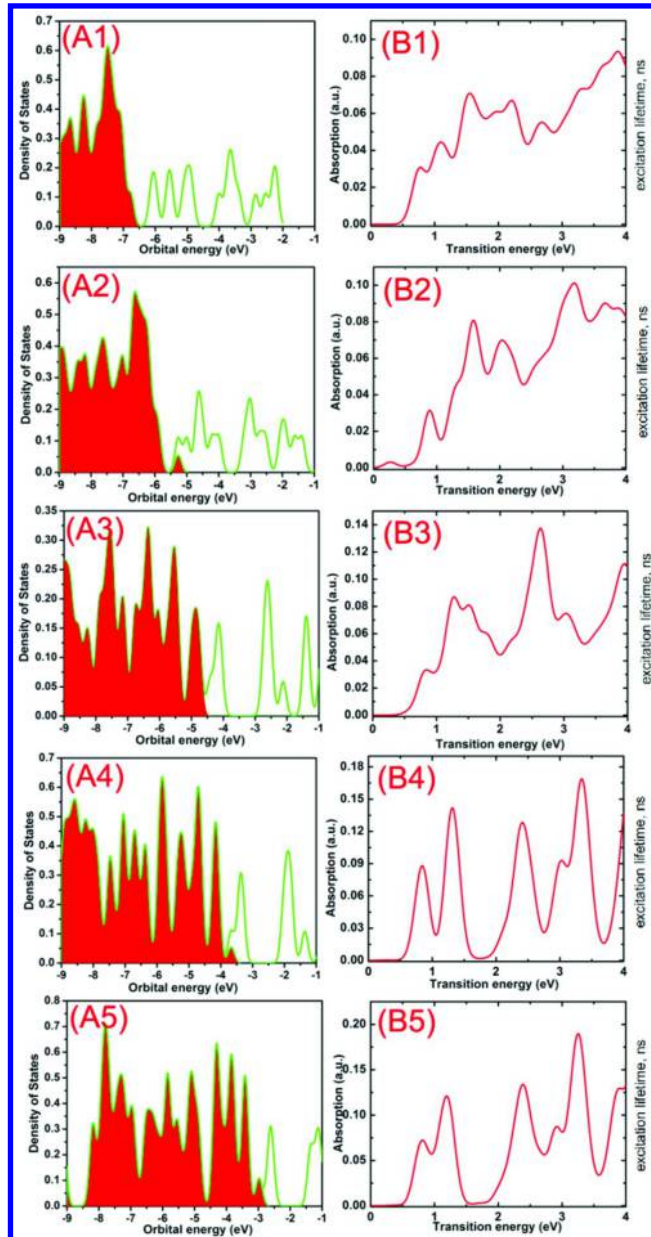


Figure 2. Left column: the density of states of $\text{Pt}_{13}\text{H}_{24}^{2+}$, $\text{Pt}_{13}\text{H}_{24}^+$, $\text{Pt}_{13}\text{H}_{24}$, $\text{Pt}_{13}\text{H}_{24}^-$ and $\text{Pt}_{13}\text{H}_{24}^{2-}$ models (from top to bottom). Filled area symbolizes filled orbitals. **Right column:** Computed linear absorption spectra for the same models. Adapted with permission from ref (20). Copyright 2013 American Chemical Society.

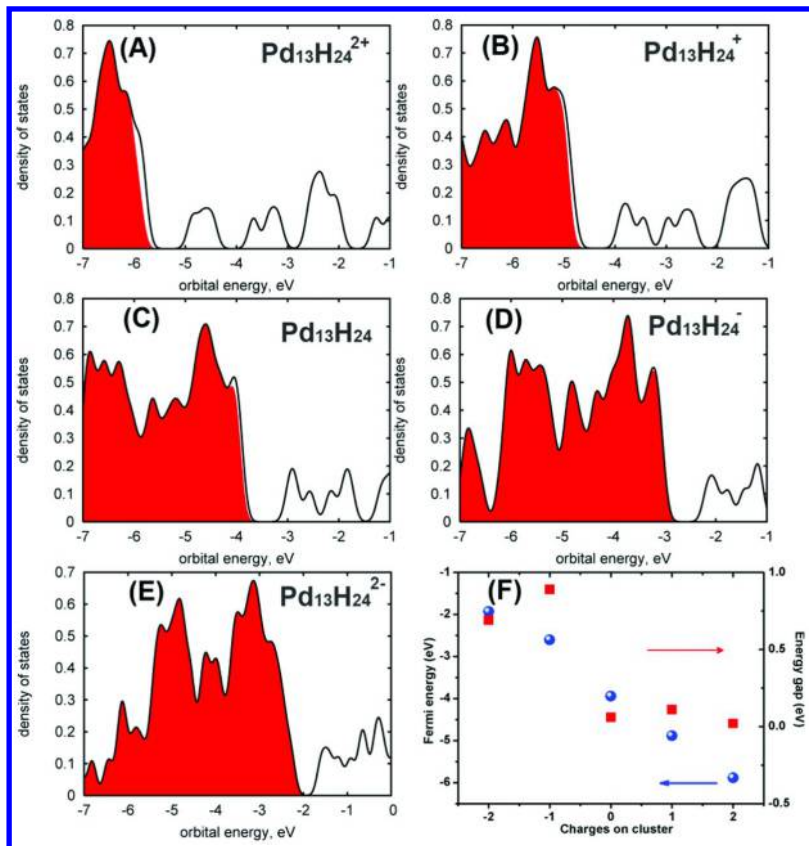


Figure 3. Density of states of $Pd_{13}H_{24}^{n\pm}$ ($n = 0, 1$ and 2) clusters (from A to E). Panel (F) summarizes the dependence of band gap and Fermi energy on total charges of $Pd_{13}H_{24}^{n\pm}$ clusters. Adapted with permission from ref (47). Copyright 2015 Taylor&Francis.

H₂ Desorption Catalytically from Metal Nanocluster Surface

Many catalytic reactions are carried out under elevated temperature. So it is interesting to investigate the changes of the electrical and structural properties of metal nanocluster during heat treatment, which also gives the information about thermal stability. During heat treatment, all the atoms gain certain velocities determined by the forces between atoms, which are transferred from their potentials. Ab initio molecular dynamics (AIMD) was simulated to model the change of the position of the atoms in metal nanocluster after heating and the whole trajectory is determined by the velocities of atoms at the initial time ($t = 0$). At each time step of the trajectory, the forces are determined according to the Hellman Feynman theorem (51). This simulation is to investigate the dynamics of interaction between hydrogen atoms and metal nanocluster catalyst, which

assigns non-zero momentum to each ion. Different heating temperatures generate different range of forces acting on the nuclei, which in turn produce different molecular dynamics trajectories.

Figure 1 represents the structure of $Pd_{13}H_{24}$ nanocluster before and after heating at 1700K. The frame metal atoms stay almost identical, but the H atoms undergo prominent migration. Some of the hydrogen atoms bond to each other and almost detach from the Pd nanocluster surface as a H_2 molecule. Those bonded hydrogen atoms are the clear evidence of the formation of a semi-bounded H_2 molecule, $Pd\cdots H-H$, on the surface of Pd nanocluster. Less migration and bonding of hydrogen atoms was observed in the $Pt_{13}H_{24}$ model, indicating less active hydrogen on Pt nanocluster surface (26).

During the AIMD simulation, one semi-bonded H–H group desorbs in a molecular form after 3 fs, as shown the snapshot image in Figure 4, representing the desorption of one H_2 molecule catalytically from the Pd nanocluster surface. The desorption rate can be estimated as $1/3\text{ fs}^{-1}$ accordingly. At 10 fs and 270 fs, another two and as many as seven H_2 molecules are formed and desorbed from the Pd_{13} nanocluster, respectively. The similar H_2 desorption behavior was also observed on the Pt_{13} nanocluster but after 1000 fs there are only four H_2 molecules that desorb, implying a less active surface of Pt than Pd nanocluster. As an example, a video showing the hydrogen desorption process can be viewed in the Supplementary Information. The results presented in Figure 4 illustrate a transition between high and low density of surface adsorbates. The number of surface hydrogen adsorbates decreases after each desorption event thus approaching to the low density surface coverage. These results evidence the lower desorption rate for lower surface coverage. An almost saturated hydrogen adsorbed Pt cluster has been reported (17), and in another literature, the H_2 absorption on Pt cluster surface was observed to occur in 10 fs by a Direct MD study, which is comparable to our work (52).

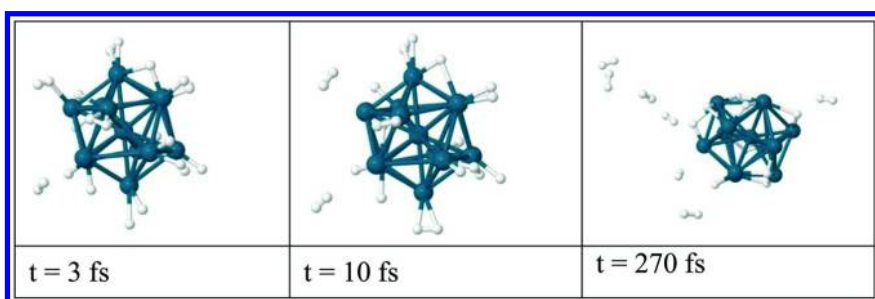
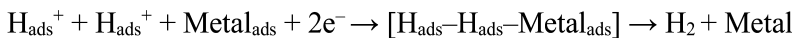


Figure 4. Snapshots of $Pd_{13}H_{24}$ nanocluster at different steps during AIMD process. Adapted with permission from ref (47). Copyright 2015 Taylor&Francis.

The energy required for H_2 molecules to desorb from metal catalyst is one of the concerns to many researchers. Figure 5 shows the time dependence on the total energy of $Pt_{13}H_{24}$ nanocluster in the steps when H_2 molecule desorbs. This diagram is closely related to a catalytic reaction, as described in ref (53),



If this applies to the H_2 desorption reaction catalytically, it can be described as



and the three configurations in Figure 5 can be considered as reactant, transition state and product, respectively. The geometry of intermediate state is determined by the configuration which has the maximum total energy during the desorption. Metal nanocluster act as the catalyst. The activation energy can be estimated as 0.51 eV, determined by the difference of energy between reactant and transition state.

It has to be point out that an exploration of the potential energy surface at zero temperature is a standard approach to explore a single desorption event in more details. An adequate method for determining an optimal path along potential energy surface is offered by Henkelman et. al in the Nudge Elastic Band method (54). The Nudge-Elastic Band (NEB) method has become a workhorse in determining the transition states (TS) and minimum-energy pathways (MEP) (55), especially when implemented within density-functional theory (DFT). However, our work focuses on a statistical approach, explicitly modeling finite temperature and multiple reactions running simultaneous in the same system.

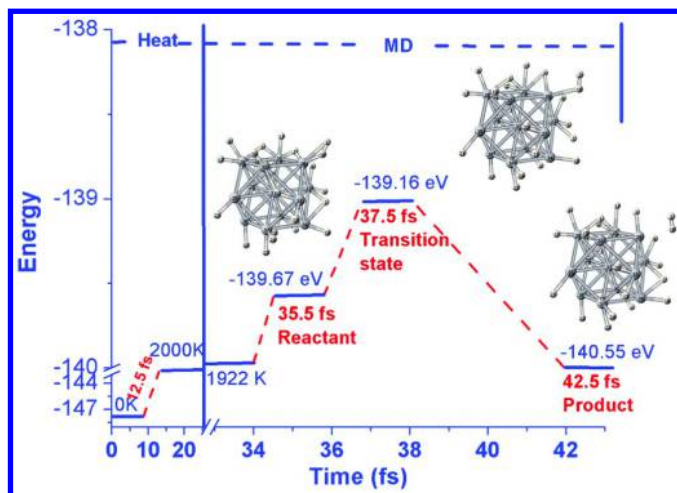


Figure 5. H_2 desorption pathway with time during AIMD process for $\text{Pt}_{13}\text{H}_{24}$ cluster model. The structures of the initial, intermediate, and final configurations are shown. The activation energy E is estimated as 0.51 eV as maximal fluctuation of total energy during desorptive AIMD trajectory.

H₂ Desorption Catalytically from the Charged Metal Nanocluster Surface

The dependence of heating temperature on the H₂ desorption rate over the charged Pt nanoclusters are shown in Figure 6.

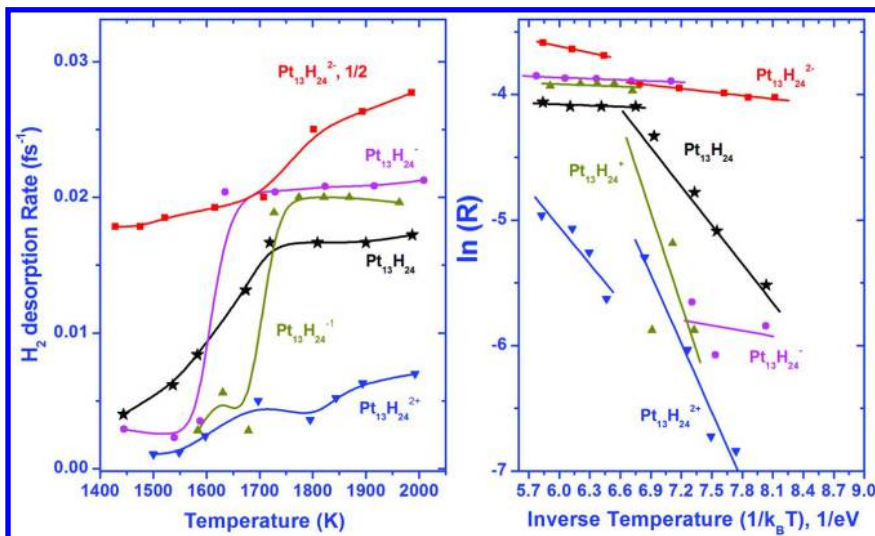


Figure 6. Heat treatment temperature dependence on the H₂ desorption rate on charged Pt nanoclusters (left panel). Same data in form of Arrhenius plot: logarithm of desorption rate versus inverse temperature. The slope of linear fit provides activation energy, \bar{E}_a , according to Arrhenius plot (right panel). Adapted with permission from ref (20). Copyright 2013 American Chemical Society.

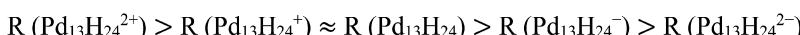
The result of the left panel in Figure 6 indicates a sequence of catalytic activity, Pt₁₃H₂₄²⁻ > Pt₁₃H₂₄⁻ > Pt₁₃H₂₄ > Pt₁₃H₂₄⁺ > Pt₁₃H₂₄²⁺. The maximum H₂ desorption rate found on Pt₁₃H₂₄²⁻ model at 1986 K is around 0.067 fs⁻¹, approximately corresponding to 0.61 ml/h per cluster, comparable to the experimental result of around 0.1~1.5 ml/h on Pt and RuO₂ co-deposited TiO₂ photocatalysts (56). The desorption rates of all the investigated models computed at different temperatures are analyzed and fitted to Arrhenius law, as shown in the right panel of Figure 6. The computed Arrhenius activation energy, \bar{E}_a , and average rates, \bar{R} , are calculated and summarized in Table 1. The average desorption rate and activation energies depend on cluster charges in a different manner. Higher average desorption rate corresponds lower activation energy. The computed Arrhenius activation energies \bar{E}_a are systematically lower than E_a (at 1800K) based on instantaneous change of total energy. But either way, the Pt₁₃H₂₄²⁻ model shows the highest desorption rate and correspondingly almost the

lowest activation energy. The linear fitting of desorption rate of $\text{Pt}_{13}\text{H}_{24}^{n\pm}$ models present two different slopes, which indicates that there might be two different activation barriers for H_2 desorption.

Table 1. H_2 Desorption Rate (at $\sim 1800\text{K}$) and Activation Energy of Various $\text{Pt}_{13}\text{H}_{24}^{n\pm}$ Models ($n = 0, 1$, and 2). Activation Energy Is Estimated Based on Jump of Total Energy at the Time of Desorption Event from the Beginning of AIMD. Computed Average Desorption Rate \bar{R} , and Average Activation Energy \bar{E}_a , as Function of Total Charge Modification for $\text{Pt}_{13}\text{H}_{24}^{n\pm}$ Clusters, Computed as a Slope of Arrhenius Plot, According to $\bar{E}_a = -k_B \frac{\ln R(T') - \ln R(T'')}{T'^{-1} - T''^{-1}}$. There Are Two Slopes of the Fitting Plots for the Clusters, Which Are Possibly Corresponding to Two Energy Barriers. Accordingly the Average Desorption Rate \bar{R} Is Also Separated into Two Values. Adapted with permission from ref (20). Copyright 2013 American Chemical Society.

Model	Charge	Desorption rate at $\sim 1800\text{ K}$ (fs^{-1})	Activation energy, E_a (eV)	$\bar{R} \times 10^{-3}$ (fs^{-1})	\bar{E}_a (eV)
$\text{Pt}_{13}\text{H}_{24}^{2+}$	+2	0.004	3.17	1.56/5.42	0.98/1.83
$\text{Pt}_{13}\text{H}_{24}^+$	+1	0.017	2.69	3.73/19.7	0.03/2.45
$\text{Pt}_{13}\text{H}_{24}^0$	0	0.018	2.23	6.19/16.1	0.03/1.03
$\text{Pt}_{13}\text{H}_{24}^-$	-1	0.021	0.87	2.90/20.7	0.03/0.13
$\text{Pt}_{13}\text{H}_{24}^{2-}$	-2	0.060	0.56	18.7/26.3	0.09/0.17

On the surface of Pd nanocluster total of seven H_2 molecules desorb from Pd surface in less than 300 fs. This is in great contrast to the desorption behavior of $\text{Pt}_{13}\text{H}_{24}$ cluster, where only four hydrogen molecules desorbed after 1000 fs under the same conditions. This is a strong indication that Pd_{13} nanocluster has better catalytic activity than Pt_{13} nanocluster. At ambient temperature (300 K) H_2 desorption has been obvious over all the Pd_{13} clusters, whereas for Pt_{13} cluster the "turn on" temperature activating the catalytic reaction has to be as high as 900 K. Of all the charged $\text{Pd}_{13}\text{H}_{24}$ clusters, the $\text{Pd}_{13}\text{H}_{24}^{2+}$ cluster presents the highest regular desorption rate (R) which follows the sequence of



This is also in contrast to the result of Pt_{13} nanocluster where $\text{Pt}_{13}\text{H}_{24}^{2-}$ shows the highest activity. The reason for this discrepancy is not quite clear yet.

Pd-Doped $\text{Pt}_{13}\text{H}_{24}$ Nanocluster

One of the Pt atoms in the $\text{Pt}_{13}\text{H}_{24}$ nanocluster was replaced by one Pd atom and the catalytic properties of the obtained $\text{Pt}_{12}\text{PdH}_{24}$ alloy nanocluster were investigated. The neutral $\text{Pt}_{13}\text{PdH}_{24}$ cluster presents the highest desorption rate

than any charged clusters. Neither positively nor negatively charging benefit the H₂ desorption on Pt₁₃PdH₂₄ cluster. Furthermore, a desorption rate comparison between Pt₁₃PdH₂₄ cluster and Pt₁₃H₂₄₂₋ cluster indicates that doping of one Pd atom into the Pt₁₃ cluster induces an increase of H₂ desorption rate to as high as 0.091 fs⁻¹. In Figure 7 three snapshots of AIMD process at 6, 7 and 17 fs show that the 1st H₂ desorption takes place at the Pd atom. This gives a clear view that Pd doping benefits the catalytic activity of Pt cluster.

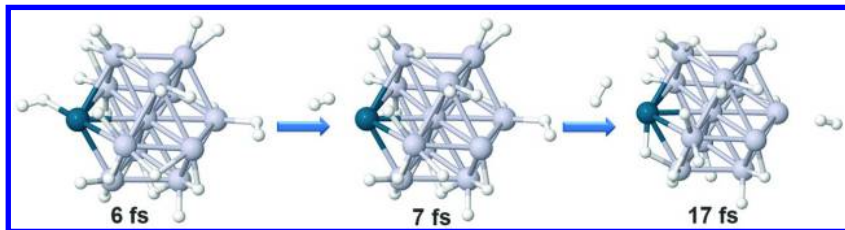
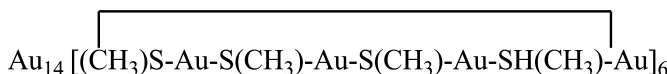


Figure 7. The snapshot images of Pt₁₂PdH₂₄ cluster structure during the AIMD process. The gray sphere is Pt atom, the white sphere is H atom and the dark cyan sphere is Pd atom.

Au Nanocluster Protected by Organo-Thiolate Ligand

The investigated thiolate protected Au nanocluster, Au₃₈(SCH₃)₂₄, has a structure as,



It has a core Au₁₃ cluster, protected by 6 cyclic [-CH₃-Au-]₄ oligomeric thiolate ligands (Figure 8), plus a balancing Au atom.

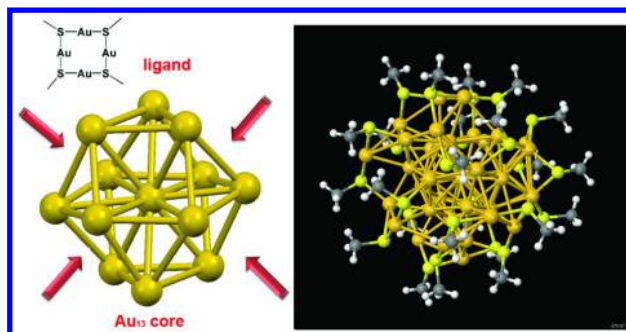


Figure 8. The structure of Au₁₃ core, thiolate ligand and Au₃₈(SCH₃)₂₄ nanocluster.

The Au core has a structure that is similar to Pt₁₃ and Pd₁₃ nanocluster, which is derived from the deformation of a truncated-octahedral face-centered-cubic structure to a disordered cluster core made of distorted pentagonal bipyramidal subunits, which was reported more stable than the original truncated-octahedral geometry (57). The Au atoms have the electron charges of ~ 5.8 (0.4 on the center Au core and 5.4 on the outer 24 Au atoms) and -5.8 on the 24 thiolate ligands. The binding energy between Au core and ligand was reported as 1.1 eV (58).

The DOS of Au₃₈(SCH₃)₂₄ nanocluster (not given) shows new bands at around -18.0 and -14.0 eV, which are absent in the DOS of core Au (54). These bands are formed from the thiolate ligand molecular orbitals. There is an upward shift of the Fermi energy by 2.2 eV after adding the thiolate ligands to the core Au. Some of the unfilled sub gaps below the Fermi energy of the Au core are filled after the thiolation by the ligands, most likely due to the charge redistribution between Au core and ligand shell. The calculated energy gap between the HOMO and LUMO states of Au₃₈(SCH₃)₂₄ and Au core are 0.29 and 0.11 eV, respectively.

To understand the correlation between the nanocluster structure and optical properties, the electronic structure, optical absorption spectrum of Au₃₈(SCH₃)₂₄ nanocluster, the energy of Kohn-Sham molecular orbitals, and the contributions of different atoms to the orbitals are shown in Figure 9. The electronic structure of Au₃₈(SCH₃)₂₄ indicates that the HOMO, LUMO and LUMO-1 are mainly composed of 5d and 6sp atomic orbitals of Au. From HOMO-1 to HOMO-8 the 5d orbitals of Au become dominant. LUMOs higher than LUMO+2 are mainly constructed by the 6sp orbitals of Au. The 3p orbitals of sulfur contribute significantly to the HOMO-2 and other lower HOMOs.

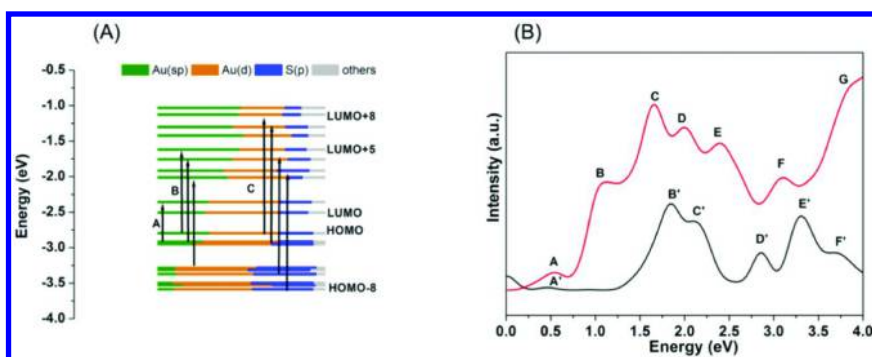


Figure 9. (A): Kohn-Sham orbital energy level diagram for the Au₃₈(SCH₃)₂₄ nanocluster. Each KS orbital indicates the relative contributions from the atomic orbitals of Au(6sp) in green, Au(5d) in orange, S(3p) in blue and others in light gray. (B): Calculated absorption spectra of Au₃₈(SCH₃)₂₄ (top) and core Au nanocluster (bottom). The peaks are broadened by a Lorentzian with a half-width of 0.01 eV. Adapted with permission from ref (59). Copyright 2015 Taylor & Francis.

The absorption spectrum of $\text{Au}_{38}(\text{SCH}_3)_{24}$ features a peak (A) at 0.54 eV, the first major peak (B) at 1.12 eV, and three other major peaks (C, D, E) at 1.66, 2.00 and 2.44 eV respectively, which is in agreement with the experimental result (60). The peak A corresponds to $d \rightarrow d$ (HOMO-1 \rightarrow LUMO+1) intraband transition, and the group peaks from 1.0 to 3.0 eV (peak B to D) originates from a $d \rightarrow sp$ interband transition. There are also two broad bands (F and G) from 3.0 to 4.0 eV. The absorption peaks of core Au nanocluster show the shift to higher energy, *e.g.*, from peak B to B'(C'), peak D to D' and peak E to E', which is agreement with the experimental results (61). This indicates that the HOMO, HOMO-1, HOMO-2 and LUMO+1 through LUMO+3 are composed of the atomic orbitals from the core Au atoms (42). But HOMO-4 through HOMO-8 may get contribution of the atomic orbitals from the atoms in the ligands, which gives the new absorption peak C after thiolate ligands are attached on the core Au surface.

Photoexcitation electron dynamics, after electrons are photoexcited from occupied orbitals to unoccupied orbitals is of important property to investigate. An insight of this electron dynamics will contribute to the better understanding of the optical properties of Au nanoclusters, together with the time-resolved emission and decay lifetime kinetics. When the investigated $\text{Au}_{38}(\text{SCH}_3)_{24}$ nanocluster is irradiated by light and photon is absorbed, an electron is excited from the occupied orbital a to higher unoccupied orbital b , *e.g.* from $a = \text{HO-18}$ to $b = \text{LU+17}$ orbital (HO and LU are the abbreviation of HOMO and LUMO), which corresponds to the absorption band G in the Figure 9 with the transition energy at 3.838 eV. The excitation energy for simulation was chosen based on two criteria; (i) efficient absorption at chosen energy and (ii) opportunity to explore larger number of photoexcitation decay channels. After the generation of the electron-hole pair, the nonradiative relaxation of the electron and hole to the LUMO and HOMO orbitals occurs due to the nonadiabatic electron-phonon process.

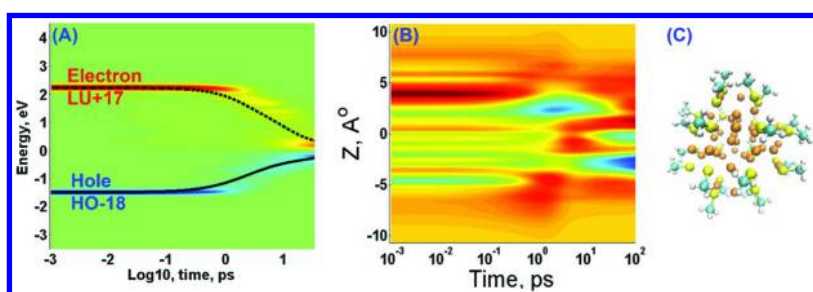


Figure 10. Electronic dynamics of $\text{Au}_{38}(\text{SCH}_3)_{24}$ nanocluster photoexcited at absorption band G (HO-18, LU+17). (A): The iso-contours of the population of charges. Red, green and blue colors encode excess, no change, and lack of electronic populations at given energy. (B): the evolution of the nonequilibrium charge density distribution projected onto the z direction. (C): $\text{Au}_{38}(\text{SCH}_3)_{24}$ nanocluster structure is shown in the same range in z-axis as panel (B). Adapted with permission from ref (58). Copyright 2015 Taylor&Francis.

The results of photo-induced electron dynamics are shown in Figure 10. Figure 10 (A) displays the iso-contours of the charge population, $\Delta n^{(a,b)}(\varepsilon, t)$. The iso-contours of the population, with red and blue color indicating gain and loss of charge density with respect to the equilibrium distribution, indicates that the nonradiative internal conversion of the photoexcited electron and hole finishes within around 30 ps. The average electron and hole dissipation rate constants, K_e and K_h , are 0.171 and 0.248 ps⁻¹, respectively. Table 2 summarizes the computational results on the electrons and holes dissipation process for different photo-excitations, corresponding to the different peaks in the calculated absorption spectra of Au₃₈(SCH₃)₂₄ and core Au nanocluster (Figure 9). The dissipation rates of holes are relatively higher than that of electrons for both the clusters $K_h > K_e$, i.e., $\tau_h < \tau_e$, which is ascribed to stronger nonadiabatic couplings in the valence band (VB) compared with that in the conduction band (CB).

The longer relaxation time of electrons will enhance the relative contribution of the photoexcited electrons to the luminescent emission. The evolution of the nonequilibrium charge density distribution projected onto the z direction is given in Figure 10 (B). At $t \sim 0.5$ ps when the relaxation of electrons and holes begins, the holes density at the top ligands increases and the electron density in the center Au core increases. This indicates a charge transfer from the thiolate ligand orbitals to the center Au cluster orbitals.

Table 2. Dynamics of Photoexcited Electron-Hole Pairs Corresponding to the Peaks in the Absorption Spectrum in the Au₃₈(SCH₃)₂₄ Nanocluster. Adapted with permission from ref (58). Copyright 2015 Taylor&Francis.

Absorption peak	A	B	C	D	E	F	G
Transition Energy (eV)	0.561	1.177	1.670	1.995	2.352	3.030	3.838
Oscillator Strength	0.246	0.705	0.996	0.424	0.507	0.206	0.366
Hole index (iH)	2	1	1	12	1	13	17
Electron orbital (iE)	2	6	9	4	15	11	18
K_e , ps ⁻¹	0.0957	0.102	0.127	0.110	0.169	0.146	0.171
K_h , ps ⁻¹	0.0917	0	0	0.230	0	0.230	0.248
K_e+K_h , ps ⁻¹	0.186	0.102	0.127	0.340	0.169	0.376	0.419

The computed emission spectra of thiolate-protected and bare Au nanoclusters triggered by photo-excitations of similar energies are compared. The dynamics of energy dissipation and relevant emission spectra are illustrated in Figure 11. Specifically, the instantaneous photoexcitation of the Au₃₈(SCH₃)₂₄/ Au core nanoclusters at transition energy of 3.838 eV / 3.717 eV, corresponding to absorption band G / F' in Figure 9 are followed by the excitation energy dissipation with time (Figure 11 (A) / (D)), monitored by time-resolved (Figure 11 (B) / (E)) and integrated (Figure 11 (C) / (F)) emission spectra. Figure 11

(A) shows that in thiolated Au nanocluster the excitation at around 3.838 eV, corresponding to the parent interband absorption from HOMO-17 to LUMO+18, has a non-radiative lifetime of 0.1 ps at the LUMO+18 orbital. From this time the electronic relaxation induced by the lattice vibrations occurs between 0.1 and 10 ps and stays at the edge of the band gap for longer than 100 ps. In the bare Au nanocluster, the excitation at around 3.717 eV, shown in Figure 11 (D), corresponding to the parent interband absorption from HOMO-4 to LUMO'+11, has a radiative lifetime of around 1.0 ps at the LUMO'+11 orbital, which is longer than that of the similar photo-excited state of the $\text{Au}_{38}(\text{SCH}_3)_{24}$ nanocluster. This is consistent with the larger nonradiative decay rate of electron for the $\text{Au}_{38}(\text{SCH}_3)_{24}$ than Au core nanocluster. After $t = 1.0$ ps the lattice vibration causes the nonradiative relaxation to the transitional energy at ~ 3.4 eV where the electronic energy stays at this state for almost 100 ps. Finally the energy dissipates at the edge of the band gap for longer than 200 ps. This strong radiative transition at ~ 3.4 eV, which is not observed for the $\text{Au}_{38}(\text{SCH}_3)_{24}$ nanocluster, indicates that the protective thiolate ligands contributes to the nonradiative energy dissipation of the $\text{Au}_{38}(\text{SCH}_3)_{24}$ nanocluster.

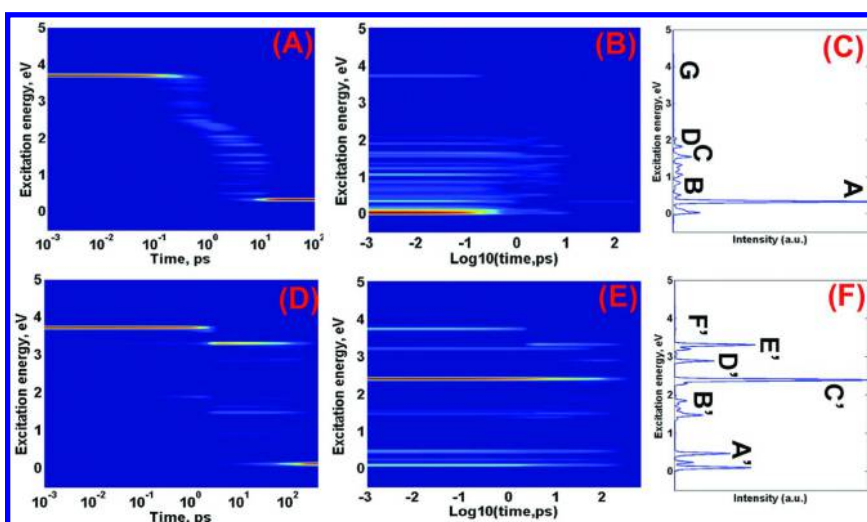


Figure 11. Simulated photoexcitation dynamics (A, D), emission dynamics (B, E) and integrated emission spectra (C, F) for thiolate protected Au (A-C) after photoexcited at 3.838 eV (peak G in Figure 9) of $\text{Au}_{38}(\text{SCH}_3)_{24}$ nanocluster and Au core (D-F) after photoexcited at 3.717 eV (peak F' in Figure 9) of Au core. (A): dynamics of the excitation energy dissipation with time. Color code: red \sim maximum population; navy blue \sim zero population. Initial excitation at $\hbar\Omega = 3.838$ eV evolves in time. At each subsequent instant of time excitation appears at lower energy finalizing at lowest available excitation. (B): calculated time-resolved emission spectrum. (C): Integrated emission spectrum. Adapted with permission from ref (58). Copyright 2015 Taylor&Francis.

The time-resolved emission spectra triggered by the instantaneous photoexcitation are compared in Figure 11 (B) and 11 (E). An emission signal at around 3.838 eV, corresponding to the parent interband absorption band G, disappears at around 0.1 ps, which indicates the beginning of the relaxation. There are also several additional emission bands at energy less than 2.0 eV. The time-resolved emission spectrum of the Au core, as shown in Figure 11 (E), presents a similar emission signal at 3.717 eV, due to the parent interband absorption. Likewise, this transition possess a lifetime of ~ 2 ps, longer than that of the $\text{Au}_{38}(\text{SCH}_3)_{24}$ nanocluster. There are many strong emission bands owning much longer lifetime with transition energy between 2.3 \sim 3.2 eV, and relatively less emission bands with transition energy lower than 2.0 eV. The band gap of the Au core cluster is smaller than 0.1 eV, so there are relatively more interband transitions, compared to the strong intraband transitions for the $\text{Au}_{38}(\text{SCH}_3)_{24}$ nanocluster. So these strong intraband transitions are from the contribution of the thiolate ligands.

Figure 11 (C) gives the representative integrated emission spectrum of the $\text{Au}_{38}(\text{SCH}_3)_{24}$ nanocluster after photoexcitation at 3.838 eV. The emission peaks are consistent with the emission features shown in Figure 11 (B). The strong bands at energy less than 0.3 eV are corresponding to the intraband optical transitions of photo-excited electrons or holes within the conduction band or valence band. The prominent emission band appears at around 2.0 eV (620 nm) and the first strong emission at 1.5 eV (820 nm), which are consistent with an experimental result where mercaptosuccinic acid protected Au_{38} nanocluster was etched by bovine serum albumin (62) and a phosphine/thiolate-protected Au_{24} nanocluster. Given the photoexcitation wavelength at 3.838 eV, this computed Stokes shift is also consistent with the experimental results. The integrated emission spectrum of the Au core shown in Figure 11 (F) presents the most strong emission band at 2.3 eV, corresponding to the intraband transition.

Conclusions and Perspectives

Catalytic reactions present a challenge to computational studies since the electronic structure and thus the bonding pattern changes qualitatively in the course of the simulation. Prezhdo et.al pioneered time-domain atomistic studies of the photo-induced electron dynamics (ED) at molecule/semiconductor interfaces and initiated the ab initio, time-domain studies of the photo-induced dynamics of excited charge carriers in semiconductor and metallic quantum dots (63, 64). Their nonadiabatic molecular dynamics simulations most closely mimic the complex coupled evolutions of charges, phonons, and spins as they occur in nature. Tretiak et.al has developed the excited molecular dynamics method to model photochemical time-dependent processes in extended molecular systems based on the quantum-chemical numerical computations. This technique combines semi-empirical Hartree-Fock computations with a time-dependent density matrix calculation of vertical optical excitations, using the ground-state single-electron density matrix as input (65, 66). In our work on the hydrogen reduction on metal cluster surface, the basic idea underlying our molecular dynamics simulation

method is to compute the forces acting on the nuclei from electronic structure calculations that are performed “on-the-fly” as the MD trajectory is generated (67–69). In our work on thiolate protected Au nanocluster, we applied ab initio electron dynamics (AIED) for interpreting photoexcitation and electron/hole relaxation of Au nanocluster. We simulated the relaxation rates of photo-excited electrons and holes in core and thiolate-protected Au nanoclusters by applying an *ab initio* treatment of the electronic states when the nonadiabatic transitions are induced by the vibrational dynamics. The on-the-fly nonadiabatic couplings are used as parameters to the Redfield theory, providing the dynamics of carriers and allowing for analysis of multiple nonradiative relaxation pathways.

Since the performance of a catalyst is a balance between the binding energy of adsorbates and the barriers of reaction. Our AIMD trajectories successfully simulate the fusion of two protons into one H₂ molecule accompanied by bond breaking between Pd and H₂. Furthermore, AIMD allows determining more details about catalysis, e.g. the most probable desorption site, the number of total H₂ molecules desorbed from the cluster. In this sense, this AIMD approach is more general and can be applied to simulate other reactions, such as fusion, fragmentation, etc. In the future work, the most challenging research interests will be on how to combine the simulation of photon absorption (70, 71), and charge transfer from a substrate to the surface of nanocatalyst (72, 73) and charge-facilitated surface reaction (26). One is able to complete the pathways of subsequent elementary processes contributing to the photocatalytic water splitting.

The computation results on thiolated protected Au nanoclusters laid out here provide a view for further understanding of the distinct electronic, optical and photochemical properties of stable Au nanoclusters. Generally the electronic properties during photon absorption and charge transfer can be calculated. One has to keep in mind that the electron excitation, energy dissipation, electron relaxation, which have been successfully calculated by our computation method, are crucial to the photochemistry. This should facilitate synthesis and practical application for catalysis, sensing, bio-labeling and molecular electronics.

Acknowledgments

Financial support by Guangdong Research Center of Engineering Technology for Wasterwater Treatment is acknowledged. Computational resources of USD (University of South Dakota) High Performance Computing facilities are gratefully acknowledged.

References

1. Aiken, J. D.; Finke, R. G. *J. Mol. Catal. A* **1999**, *145*, 1–44.
2. Kyriakou, G.; Boucher, M. B.; Jewell, A. D.; Lewis, E. A.; Lawton, T. J.; Baber, A. E.; Tierney, H. L.; Flytzani-Stephanopoulos, M.; Sykes, E. C. H. *Science* **2012**, *335*, 1209–1212.
3. Willets, K. A.; van Duyne, R. P. *Annu. Rev. Phys. Chem.* **2007**, *58*, 267–297.

4. Favier, F.; Walter, E. C.; Zach, M. P.; Benter, T.; Penner, R. M. *Science* **2001**, *293*, 2227–2231.
5. Murphy, C. J.; Sau, T. K.; Gole, A. M.; Orendorff, C. J.; Gao, J. X.; Gou, L. F.; Hunyadi, S. E.; Li, T. *J. Phys. Chem. B* **2005**, *109*, 13857–13870.
6. Hauck, T. S.; Jennings, T. L.; T., Y.; Kumarades, C.; Chan, W. C. W. *Adv. Mater.* **2008**, *20*, 3832–3838.
7. El-Sayed, I. H.; Huang, X. H.; El-Sayed, M. A. *Nano Lett.* **2005**, *5*, 829–834.
8. Farias, D.; Schilbe, P.; Patting, M.; Rieder, K. H. *J. Chem. Phys.* **1999**, *110*, 559–569.
9. Kajiwara, M.; Uemiya, S.; Kojima, T. *Int. J. Hydrogen. Energy* **1999**, *24*, 839–844.
10. Hansen, S.; Klahn, M.; Beweries, T.; Rosenthal, U. *ChemSusChem* **2012**, *5*, 656–660.
11. Chen, A.; Holt-Hindle, P. *Chem. Rev.* **2010**, *110*, 3767–3804.
12. Utschig, L. M.; Dimitrijevic, N. M.; Poluektov, O. G.; Chemerisov, S. D.; Mulfort, K. L.; Tiede, D. M. *J. Phys. Chem. Lett.* **2011**, *2*, 236–241.
13. Khoobiar, S. *J. J. Phys. Chem.* **1964**, *68*, 411–412.
14. Christmann, K. *Surf. Sci. Rep.* **1988**, *9*, 1–163.
15. Lozano, A.; Groß, A.; Busnengo, H. F. *Phys. Chem. Chem. Phys.* **2009**, *11*, 5814–5822.
16. Busnengo, H. F.; Dong, W.; Sautet, P.; Salin, A. *Phys. Rev. Lett.* **2001**, *87*, 127601.
17. Watari, N.; Ohnishi, S. *J. Chem. Phys.* **1997**, *106*, 7531–7540.
18. Roques, J.; Dufaure, C. L.; Mijoule, C. *J. Chem. Theory Comput.* **2007**, *3*, 878–884.
19. Meng, Q. G.; May, P. S.; Berry, M. T.; Kilin, D. *Int. J. Quantum Chem.* **2012**, *112*, 3896–3903.
20. Meng, Q. G.; Yao, H.; Kilin, D. In *Nanotechnology for Sustainable Energy*; Hu, Y. H., Burghaus, U., Qiao, S., Eds.; ACS Symposium Series 1140; American Chemical Society: Washington, DC, 2013; pp 173–185.
21. Sheppard, D.; Terrell, R.; Henkelman, G. *J. Chem. Phys.* **2008**, *128*, 134106.
22. Zhang, J.; Alexandrova, A. N. *J. Phys. Chem. Lett.* **2012**, *3*, 751–754.
23. Liu, P. *J. Phys. Chem. C* **2012**, *116*, 25337–25343.
24. Okamoto, Y. *Chem. Phys. Lett.* **2006**, *429*, 209–213.
25. Pijper, E.; Kroes, G. J.; Olsen, R. A.; Baerends, E. J. *J. Chem. Phys.* **2002**, *117*, 5885–5898.
26. Barrio, L.; Liu, P.; Rodríguez, J. A.; Campos-Martín, J. M.; Fierro, J. *J. Chem. Phys.* **2006**, *125*, 164715.
27. Yang, L.; DePristo, A. E. *J. Chem. Phys.* **1994**, *100*, 725–728.
28. Xu, W.; Schierbaum, K. D.; Geopol, W. *Int. J. Quantum Chem.* **1997**, *62*, 427–436.
29. Sun, Y.; Zhang, M.; Fournier, R. *Phys. Rev. B* **2008**, *77*, 075435–075442.
30. Kang, J. H.; Menard, L. D.; Nuzzo, R. G.; Frenkel, A. I. *J. Am. Chem. Soc.* **2006**, *128*, 12068–12069.
31. Singh, J.; Nelson, R. C.; Vicente, B. C.; Scott, S. L.; van Bokhoven, J. A. *Phys. Chem. Chem. Phys.* **2010**, *12*, 5668–5677.

32. Parker, J. F.; Fields-Zinna, C. A.; Murray, R. W. *Acc. Chem. Res.* **2010**, *43*, 1289–1296.

33. Price, R. C.; Whetten, R. L. *J. Am. Chem. Soc.* **2005**, *127*, 13750–13751.

34. Wu, Z.; Wang, M.; Yang, J.; Zheng, X.; Cai, W.; Meng, G.; Qian, H.; Wang, H.; Jin, R. *Small* **2012**, *8*, 2028–2035.

35. Shang, L.; Brandholt, S.; Stockmar, F.; Trouillet, V.; Burns, M.; Nienhaus, G. U. *Small* **2011**, *8*, 661–665.

36. Lee, D.; Donkers, R. L.; Wang, G.; Harper, A. S.; Murray, R. W. *J. Am. Chem. Soc.* **2004**, *126*, 6193–6199.

37. Jadzinsky, P. D.; Calero, G.; Ackerson, C. J.; Bushnell, D. A.; Kornberg, R. D. *Science* **2007**, *318*, 430–433.

38. Qian, H.; Eckenhoff, W. T.; Zhu, Y.; Pintauer, T.; Jin, R. *J. Am. Chem. Soc.* **2010**, *132*, 8280–8281.

39. Kilin, D.; Tsemekhman, K. L.; Kilina, S.; Balatski, A. V.; Prezhdo, O. V. *J. Phys. Chem. A* **2009**, *113*, 4549–4556.

40. Lopez-Acevedo, O.; Tsunoyamo, H.; Tsukuda, T.; Häkkinen, H.; Aikens, C. M. *J. Am. Chem. Soc.* **2010**, *132*, 8210–8218.

41. Aikens, C. M. *J. Phys. Chem. C* **2008**, *112*, 19797–19800.

42. Lopez-Acevedo, O.; Akola, J.; Whetten, R. L.; Grönbeck, H.; Häkkinen, H. *J. Phys. Chem. C* **2009**, *113*, 5035–5038.

43. Das, A.; Li, T.; Nobusada, K.; Zeng, Q.; Rosi, N. L.; Jin, R. *J. Am. Chem. Soc.* **2012**, *134*, 20286–20289.

44. Sajini Devadas, M.; Kim, J.; Sinn, E.; Lee, D.; Goodson, T., III; Ramakrishna, G. *J. Phys. Chem. C* **2010**, *114*, 22417–22423.

45. Shu, G. W.; Lin, C. C.; Chung, H. P.; Shen, J. L.; Lin, C. A. J.; Lee, C. H.; Chang, W. H.; Chan, W. H.; Wang, H. H.; Yeh, H. I.; Yuan, C. T.; Tang, J. *Appl. Phys. Lett.* **2009**, *95*, 261911.

46. Link, S.; Beeby, A.; FitzGerald, S.; El-Sayed, M. A.; Schaaff, T. G.; Whetten, R. L. *J. Phys. Chem. B* **2002**, *106*, 3410–3415.

47. Huang, T.; Murray, R. W. *J. Phys. Chem. B* **2001**, *105*, 12498–12502.

48. Wu, Z.; Jin, R. *Nano Lett.* **2010**, *10*, 2568–2573.

49. Meng, Q.; Chen, J.; Kilin, D. *Mol. Simul.* **2015**, *41*, 134–145.

50. Mager-Maury, C.; Bonnard, G.; Chizallet, C.; Sautet, P.; Raybaud, P. *ChemCatChem* **2011**, *3*, 200–207.

51. Feynman, R. P. *Phys. Rev.* **1939**, *56*, 340–342.

52. Ishikawa, Y.; Mateo, J. J.; Tryk, D. A.; Cabrera, C. R. *J. Phys. Chem. C* **2010**, *114*, 4995–5002.

53. Williams, V. R.; Mattice, W. L.; Williams, H. B. *Basic Physical Chemistry for the Life Sciences*; W. H. Freeman and Company: San Francisco, 1978; Chapter 6, pp 328–330.

54. Henkelman, G.; Jónsson, H. *J. Chem. Phys.* **2000**, *113*, 9901–9904.

55. Sheppard, D.; Xiao, P.; Chemelewski, W.; Johnson, D. D.; Henkelman, G. *J. Chem. Phys.* **2012**, *136*, 074103.

56. Borgarello, E.; Kiwi, J.; Pelizzetti, E.; Visca, M.; Grätzel, M. *Nature* **1981**, *289*, 158–160.

57. Garzón, I. L.; Rovira, C.; Michaelian, K.; Beltrán, M. R.; Ordejón, P.; Junquera, J.; Sánchez-Portal, D.; Artacho, E.; Soler, J. M. *Phys. Rev. Lett.* **2000**, *85*, 5250–5251.
58. Häkkinen, H.; Walter, M.; Grönbeck, H. *J. Phys. Chem. B* **2006**, *110*, 9927–9931.
59. Meng, Q.; Chen, J.; Kilin, D. *Mol. Phys.* **2015**, *113*, 408–417.
60. Tsunoyamo, H.; Nickut, P.; Negishi, Y.; K., A.-S.; Matsumoto, Y.; Tsukuda, T. *J. Phys. Chem. C* **2007**, *111*, 4153–4158.
61. Negishi, Y.; Takasugi, Y.; Sato, S.; Yao, H.; Kimura, K.; Tsukuda, T. *J. Am. Chem. Soc.* **2004**, *126*, 6518–6519.
62. Muhammed, M. A. H.; Verma, P. K.; Pal, S. K.; Retnakumari, A.; Koyakutty, M.; Nair, S.; Pradeep, T. *Chem. Eur. J.* **2010**, *16*, 10103–10112.
63. Prezhdo, O. V. *Acc. Chem. Res.* **2009**, *42*, 2005–2019.
64. Prezhdo, O. V.; Duncan, W. R.; Prezhdo, V. V. *Prog. Surf. Sci.* **2009**, *84*, 30–68.
65. Tretiak, S.; Saxena, A. R.; Martin, L.; Bishop, A. R. *Phys. Rev. Lett.* **2002**, *89*, 97402.
66. Tretiak, S.; Mukamel, S. *Chem. Rev.* **2002**, *102*, 3171–3212.
67. Car, R.; Parrinello, M. *Phys. Rev. Lett.* **1985**, *55*, 2471.
68. Kresse, G.; Furthmüller, J. *Phys. Rev. B* **1996**, *54*, 11169–11186.
69. Hafner, J. *J. Comput. Chem.* **2008**, *29*, 2044–2078.
70. Jensen, S.; Kilin, D. *Int. J. Quantum Chem.* **2012**, *112*, 3874–3878.
71. Zhang, Y.; Kilin, D. *Int. J. Quantum Chem.* **2012**, *112*, 3867–3873.
72. Inerbaev, T. M.; Kilin, D. *MRS Proc.* **2012**, *1390*, mrsf11-1390-i03-03.
73. Chen, J. C.; Schmitz, A.; Kilin, D. *Int. J. Quantum Chem.* **2012**, *112*, 3879–3888.

Chapter 12

Surface Photochemistry of Quantum Dot-Porphyrin Nanoassemblies for Singlet Oxygen Generation

Eduard Zenkevich^{*,1} and Christian von Borczyskowski²

¹Department of Information Technologies and Robototechnique,
National Technical University of Belarus, Prospect Nezavisimosti 65,
20013 Minsk, Belarus

²Institute of Physics, Center for Nanostructured Materials and Analytics,
Technische Universität Chemnitz, Reichenhainer Str. 70,
D-09107 Chemnitz, Germany

*E-mail: zenkev@tut.by.

This Chapter covers the basics of nanotechnology, focusing on hybrid organic-inorganic nanoassemblies based on self-assembly principles. Here, we are willing to discuss the formation principles and mechanisms of excitation energy relaxation being studied for nanoassemblies based on core/shell CdSe(ZnS) colloidal semiconductor quantum dots (QD) exhibiting size-dependent photophysical properties and surfacely activated by pyridyl-substituted porphyrins, H₂P (bulk solutions) in liquid solvents at 295 K (steady-state, picosecond time-resolved luminescence spectroscopy and single molecule spectroscopy). Upon formation of QD-H₂P nanoassemblies the QD photoluminescence (PL) is quenched as can be detected both via single particle detection and ensemble experiments in solution. PL quenching has been quantitatively assigned to FRET QD → H₂P (10-14%) and Non-FRET (86-90%) processes. Using near-IR photoluminescence measurements, we performed a quantitative comparative studying the efficiencies of the singlet oxygen generation by alone QDs and “QD-H₂P” nanoassemblies upon variation of the laser pulse energy. It was found that for QD-H₂P nanoassemblies the experimental efficiencies of singlet oxygen generation are

essentially higher with respect to those obtained for alone QDs. In the case of QD-H₂P nanoassemblies, it was proven also that the non-linear dependence of the efficiency of singlet oxygen generation on the laser pulse energy is caused by non-radiative intraband Auger processes, realized in QD counterpart. It has been found that values of FRET QD→H₂P efficiencies obtained via direct measurements of IR-emission of singlet oxygen at low laser excitation ($\Phi_{\text{IR}} = 0.12 \pm 0.03$) are in a good agreement with the corresponding FRET efficiencies found from the direct sensitization data for porphyrin fluorescence ($\Phi_{\text{FRET}} = 0.14 \pm 0.02$) in nanoassemblies. Such quantitative analysis was done for the first time and shows that namely FRET process QD→H₂P is a main reason of singlet oxygen generation by QD→H₂P nanoassemblies.

Introduction

Criteria for Photodynamic Therapy with QD-Based Nanoassemblies

Based on evident progress in the synthesis of colloidal semiconductor QDs with relatively narrow size distributions within a few percent, rational shape-engineering, compositional modulation, electronic doping, and tailored surface chemistries, these nanoobjects as well as nanoassemblies based on QDs and functionalized organic compounds (including proteins) have become an important class of naomaterials with great potential for applications ranging from electronic and optoelectronic devices (*1–10*) to material science (*11–15*), sensorics (*16–19*) and nanomedicine (*14, 20–30*). The science and technology of nearly all QD-based materials, drug delivery systems, diagnostic methods, controlled release systems, organic-inorganic nanoassemblies, etc., involve on every length scale, from the molecular to the macro, surface and interfacial phenomena that can be tuned by varying the surface and interfacial energy and by varying the specific chemical interactions and chemical groups populating such surfaces and interfaces.

A multidisciplinary and fast-evolving research area, nanomedicine presents new clinically relevant promises grounded in the disciplines of molecular biology, genomics, chemistry, and nanotechnology. With respect to QDs, in most cases the bottom-up formation of functional nanoassemblies is used. It is based on self-assembly approaches being the fundamental phenomenon that generates structural organization on all scales and may be realized in solutions and solid state via various basic interactions: hydrogen bonding, coordination bonding, electrostatic and donor-acceptor interactions, and metal-ion binding (*31*). The designed self-assembled interaction, the information necessary to initiate such a process, and the algorithm behind must be stored in the components, and must be operative via selective/specific interactions (*32*). What is now termed “non-covalent bottom up approach” has revolutionized traditional synthetic strategies, thus allowing the preparation of a variety of nanoobjects that are capable of selective recognition.

Spontaneous self-assembly, which occurs as a result of the complementarity of superstructure components, has enabled the preparation of QD-based architectures for possible biomedical applications (13, 14, 17, 20–22, 26, 28, 33, 34).

In this respect, nanoassemblies consisting of inorganic semiconductor QDs and photosensitizing organic molecules (ligands) covalently or non-covalently attached on their surface are considered as a perspective means to the selective destruction of malignant tissues, such as cancer cells, via the so-called photodynamic therapy (PDT) (35–46). It is well-documented (47), (48), that PTD is based on localized photo-induced generation of cytotoxic forms of molecular oxygen (available in a tissue under treatment) following the activation of a non-toxic photosensitizer (PS) with light. One mechanism for PDT (type I) involves the formation of free radical, the so-called “superoxide anion radical” (O_2^-). This process is connected with the photoinduced electron transfer and depends on redox properties of photosensitizer molecule (PS) and molecular oxygen. The second mechanism (type II) involves the photoinduced formation of triplet excited molecules of the photosensitizer (via non-radiative intersystem crossing process, $S_1 \sim T_1$) followed by the triplet-triplet energy transfer $^3PS \rightarrow ({}^3O_2)$. In the result, the formation of active singlet oxygen (1O_2) in a long-living ${}^1\Delta_g$ electronic state occurs. In the later case, realization of PDT relies on singlet oxygen, which is generally accepted as the main mediator of photocytotoxicity in PDT and causes oxidation and degradation of membranes of malignant cells. It is well known that since a direct excitation from the triplet ground state (3O_2) to the singlet excited state (1O_2) is forbidden by spin selection rules, oxygen is activated with a sequence of energy transfer events involving a photosensitizer.

The organic photosensitizers (PS) commonly used in PDT practice belong to the class of the biologically important tetrapyrrolic pigments, which may be accumulated in cancer tissues. They are known to efficiently populate the long-living triplet state and are therefore characterized by high efficiencies of singlet oxygen generation (47–50). Nowadays porphyrin-based sensitizers, in particular, chlorine e₆ (51–53) and its commercial derivatives are adopted and used in routine treatments (54, 55). These PSs typically require irradiation by a continuous wave (cw) laser radiation with spectral region of 410–700 nm which is defined by the absorption spectrum of the sensitizer. Development of alternative PSs are necessary to get more efficient singlet oxygen generation as well as to extend nomenclature of lasers used and to get deeper penetration into skin owing to shift operation wavelength towards long waves where skin is more transparent.

Potential candidates for new PDT photosensitizers should first of all feature efficient generation of singlet oxygen. For this to be possible a long living triplet state should exist with transition energy which is higher than the energy of excited singlet oxygen, $E({}^1\Delta_g) = 1.27 \mu$. Though photoinduced generation of singlet oxygen is the mandatory feature for every PDT sensitizer, there is a number of additional criteria which potential PDT sensitizer should meet for its applicability and efficiency in PTD treatment (35, 56): i) well defined chemical composition (dimers and oligomers presenting in case of many existing molecular photosensitizers are serious drawbacks); ii) absence of any dark toxicity, i.e. photosensitizer should be non-toxic until photon absorption occurred; iii) photosensitizer should be as selective as possible to the targeted tissues to

avoid damage of healthy cells (high selectivity remains a major challenge in PDT treatment (36)); iv) photosensitizer should be easily removed from the patient's body after treatment to avoid significant side post-treatment effects (for many existing PDT sensitizers, a patient needs to remain in low-level lights for several weeks to prevent excessive burning from the residual sensitizer); v) photosensitizer should not be hydrophobic since its agglomeration in aqueous solutions can drastically decrease singlet oxygen generation (many existing sensitizers are hydrophobic which results in decrease of ${}^1\text{O}_2$ quantum yield); vi) the photosensitizer should be photostable and strongly absorbing at the irradiation wavelength.

Unfortunately, even the most successful PSs, such as Photofrin, have major drawbacks: poor water-solubility, low selectivity, skin phototoxicity, and instability. Furthermore, their excitation wavelengths are not optimal for deep tissue penetration. In this respect, QDs have been established as powerful and versatile biological imaging probes which have high quantum yields, high photostability, large absorption coefficients, continuous absorption bands for multicolor capability, narrow and symmetric emissions, and many biofunctionalization strategies (20, 29, 35, 48, 56, 57). Though several examples of employing QDs for PDT have been described, their full capabilities have yet to be harnessed, and QD-photosensitizer conjugates are still an intriguing option for PDT applications.

In this Chapter we aim to consider perspectives of semiconductor quantum QDs as well as their nanoassemblies with organic porphyrin molecules (known PSs) for novel PDT photosensitizers capable to operate according to the above type II process. For PDT purposes, QDs seem to be attractive because of the following reasons (5, 12, 35, 43, 44, 56): (i) QDs are efficient photon harvesters, since their absorption spectra are comprise multiple excitonic transitions and are thus broader than the spectra of typical organic dyes used in PDT as well as are characterized by high molar decimal extinction coefficients in a wide spectral range; and (ii) the photon absorption of QDs can be tuned to the spectral transparency window of human skin. Although metallic QDs can be less toxic (58), semiconductor QDs have important advantages for medical applications (i.e. the ability to target drugs or imaging abilities (22, 23, 30, 59, 60)). Nevertheless, the direct measurements of the efficiencies of ${}^1\text{O}_2$ generation by semiconductor QDs are very rare or contradictory (35–37, 43, 61–63), thus QD full capabilities for PDT have yet to be harnessed.

Anchoring and Interaction of Potential Photosensitizers with QDs

Several concepts for the realization of QD-organic ligand nanoassemblies have been reported such as blends (64, 65), substitution of surfactant molecules by appropriate dyes (66), tailored polymer-dye shells (67–69), electrostatic interactions (70) or nanocomposites based on self-assembly processes (19, 42, 44, 71–75).

While quantum confinement is basically understood, the anchoring of functional organic molecules to tunable wide gap semiconductor colloidal QDs

using various approaches is still of considerable scientific and practical interest, as the particular chemical composition of the surfactant shell decisively affects the photophysical properties of the nanoassembly, especially the quantum yield of QD photoluminescence (PL). Colloidal QDs are bright emitters and characterized by a large absorption cross section (5, 12, 14). However, capping organic shells (including surfactants and dyes as organic ligands) have considerable impact on the optical properties of QDs (e.g. hot carrier relaxation, PL quantum yield and energy) as has been successfully studied experimentally and theoretically for several systems (75–85). QD PL efficiency has shown to be sensitive to the surrounding matrix also (86). In addition, it follows from theoretical considerations of QD structure and electronic properties (87–97) that organic ligands (depending on their concrete number, electronic properties and mobility on QD) may cause QD surface reconstruction, modify even on a single ligand base electronic states or electron-phonon coupling and hot carrier relaxation. Some of these effects including the influence of only one (or at least a few) ligand or surface attached dye molecules on surface states have been detected experimentally (75, 98).

Concerning PDT, clear potential advantages of nanoassemblies based on semiconductor QDs and organic PSs in comparison with individual organic PSs are as follows: (i) by choosing an appropriate material and size they can be excited in the whole visible region; (ii) they may target drugs of interest; (iii) they are used in optical imaging for studying the temporal and spatial dynamics of specific biomolecules and their interactions in real time, and, what is the most important, (iv) the non-radiative effective FRET QD→PS, depending on absorption/emission properties and intercenter distances and mutual geometry between coupled interacting QD-PS moieties. It should be mentioned also that when appropriately coated, CdSe-core QDs can be rendered nontoxic and used to track cell migration and reorganization *in vitro* (99) to play a key role to overcome many of the difficulties associated with traditional PDT. With respect to nanocomposites based on semiconductor QDs and tetrapyrrolic molecules this area has received much attention within last decade only (35–46, 59, 61, 62, 72, 100–109).

From the photochemical point of view, the generation of singlet oxygen by QD-PS bioconjugates should involve two steps. First, the energy transfer QD→PS should be organized resulting in PS S_1 -state formation followed by the non-radiative transition into PS triplet state T_1 via the intersystem crossing pathway. Second, the diffusionally controlled triplet-triplet energy transfer $PS(T_1) \rightarrow \text{oxygen}({}^3\text{O}_2)$ is realized resulting in ${}^1\text{O}_2$ generation in the surrounding media.

With respect to QD-PS nanoassemblies namely, a clear understanding of the reasons of QD PL quenching as well as the evaluation of energy transfer mechanisms and pathways involved in this two-step process is essential to the design and optimization of effective PDT drugs based on semiconductor QDs. As was outlined above, PL of colloidal QDs in solution are subject to various dynamic processes which are related to QD interface phenomena, attached ligand properties as well as temperature and polarity of the solvent. Thus, taking all these facts into account one should mention that, in reality, the quenching of QD

photoluminescence upon interaction with PS molecules serves as the indicator of the formation of the QD-PS nanoassembly. Nevertheless, the evaluation of the real reason of QD PL quenching in QD-PS nanoassemblies as well the role of the energy transfer in this case seems to not be a trivial question and thus needs a thorough experimental and theoretical verification for every system.

From this point of view, the Chapter provides a comprehensive description and a deeper discussion on all necessary steps what should be realized upon analysis of QD PL quenching processes in QD-PS nanoassemblies and corresponding efficiencies of the singlet oxygen generation. We will discuss experimental and theoretical results being obtained for nanocomposites based on highly monodisperse CdSe/ZnS QDs capped with n-trioctylphosphine oxide, TOPO (the diameters d_{CdSe} of QD vary between 2.1 and 5.2 nm, two capping ZnS monolayers were applied). In our studies, (5, 10, 15, 20)-tetra-meta-pyridyl-porphyrin $H_2P(m\text{-Pyr})_4$ was chosen as a functional organic ligand to be attached to QD surface because of two reasons. Firstly, we have shown that among a series of pyridyl-substituted free-base porphyrins, $H_2P(m\text{-Pyr})_4$ is characterized by the highest complexation constant (K_c 3×10^7 M⁻¹) and was found to exhibit the most effective PL quenching of the QD upon nanoassembly formation (72, 75, 100, 103, 104, 110–114). At ambient temperature in low-polar solutions (toluene, toluene-methylcyclohexane mixture), the self-formation of QD-porphyrin nanocomposites is realized via two-fold non-covalent ligating coordination $Zn\cdots N\text{-Pyr}$ of heteroatoms N (in two adjacent pyridyl rings of porphyrin molecule) with Zn^{2+} ions of ZnS core-shell (the so-called key-lock principle). Figure 1 shows a schematic presentation of such hetero nanoassemblies consisting of a QD with the tri-*n*-octyl phosphine oxide (TOPO) surfactant layer and one $H_2P(m\text{-Pyr})_4$ molecule attached via two meso-pyridyl rings nearly perpendicular to the QD surface. Secondly, according to our direct measurements in toluene (42, 44, 115) the quantum efficiency of singlet oxygen generation by $H_2P(m\text{-Pyr})_4$ molecules is relatively high ($\gamma_\Delta = 0.6$) what makes it as a good candidate for such experiments.

The details of experimental setup and measurements (steady-state and ps-ns time-resolved) as well as preparation procedures (sampling, titration, etc.) one may find in our previous publications (72, 74, 75, 100, 103, 104, 110–113).

Here, our discussion will be focused on the detailed photo-physical studies of excited states relaxation dynamics for QD-porphyrin nanoassemblies based on steady-state and PL picosecond time-resolved measurements as well as on the direct measurements of the efficiencies of the singlet oxygen (1O_2) generation by QDs alone and nanocomposites these what is the most interesting for PDT applications. In contrast to a lot of studies devoted to an optimization of QD-PS nanoassemblies with respect to high energy transfer efficiencies, we will quantitatively analyze of the reasons of QD PL quenching taking into account the competition of energy transfer events and other quenching processes. We will pay attention to not only the experimental elucidation of the efficiencies of 1O_2 generation by QD-porphyrin nanoassemblies but analyze some factors (i.e. oxygen concentration in solution, the energy of laser excitation) which may influence on this process in solutions. Finally, we will show that the

direct detection of the emission of singlet oxygen generated by QD-porphyrin nanoassemblies may be considered as an additional non-dependent route for the quantitative verification of the energy transfer realization in organic-inorganic nanostructures.

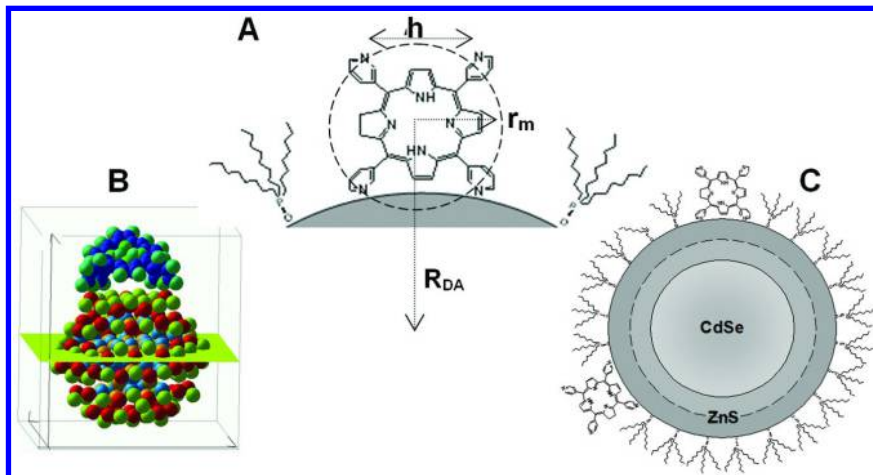


*Figure 1. Structural properties of nanoassemblies based on semiconductor CdSe/ZnS QDs capped with *n*-triptylphosphine oxide (TOPO) and H₂P(*m*-Pyr)₂ molecules. A: Schematic presentation of QD-porphyrin nanoassemblies. B: An optimized geometry for Cd₃₃Se₃₃ + H₂P(*m*-Pyr)₂ (B, optimization by HyperChem 7.0; simulations by *ab initio* density functional theory, DFT, with the VASP code (92)). C: the scales of CdSe core, ZnS shell, porphyrin and TOPO molecules corresponding to relative sizes of the main components of the arrays. The ZnS shell thickness for QDs was estimated on the basis of the thickness of one ZnS layer $l = 5 \text{ \AA}$; parameters for conical TOPO molecules $r_{bottom} = 5.5 \text{ \AA}$, $h_{con} = 9.9 \text{ \AA}$; $r_m = 7.5 \text{ \AA}$ is the radius of porphyrin molecule with opposite pyridyl rings having nitrogens in meta-positions, $h = 10 \text{ \AA}$ is the mean distance between meta-nitrogens of adjacent pyridyl rings (HyperChem 4.0, semiempirical method PM3). \mathbf{R}_{DA} is the intercenter between QD and porphyrin molecule. Based on experimental data (100) and quantum-chemical calculations (92) it has been proven that the attached porphyrin macrocycle is presumably perpendicular to QD surface.*

Spectral-Kinetic Manifestation of QD-Porphyrin Nanoassemblies Formation

As we have shown experimentally, the titration of CdSe/ZnS QD toluene solution by a comparable amount of meso-pyridyl substituted porphyrin molecules leads to the QD PL quenching manifesting in the relative PL intensity decrease and decay shortening (72, 74, 75, 100, 103, 104, 110–113). Noteworthy, in the concentration range $C = (0.5 \div 10) \times 10^{-7} \text{ M}$ being used in titration experiments in

toluene at ambient conditions, the PL dynamic quenching due to collisions of interacting moieties within ~20 ns (QD mean PL decay (72, 100, 116, 117) is low probable. Thus, the observed QD PL quenching has been interpreted as being due to the formation of nanoassemblies via anchoring porphyrin ligating molecules on the ZnS surface. In addition, the QD PL quenching efficiency and thus the probability to form QD-porphyrin nanoassemblies scales with the number of pyridyl rings having access to the QD surfaces, being the strongest one in the case of tetra-pyridyl substituted porphyrin $\text{H}_2\text{P}(\text{Pyr})_4$ (100). Figure 2 shows typical spectral transformations and time-resolved QD PL data as a function of added monomeric porphyrins $\text{H}_2\text{P}(\text{m-Pyr})_4$ at well defined molar ratios $x = [\text{H}_2\text{P}]/[\text{QD}]$. It is seen that upon increase of the molar ratio x , a linear increase of the porphyrin absorption bands takes place, whereas, in all cases, the QD absorption ($\lambda_{\text{max}} = 556$ nm) remains constant. On the contrary, the QD PL emission (at $\lambda_{\text{max}} = 585$ nm) is considerably quenched upon titration by $\text{H}_2\text{P}(\text{Pyr})_4$ molecules. Time-resolved PL measurements show that the emission of pure QDs without porphyrin ligand is characterized by a non-exponential decay (72, 100, 112, 116, 117). The interaction with anchored porphyrin molecules manifests itself in the appearance and rise of two additional short time components (~ 7 ns and ~ 700 ps) (72, 75, 112).

It should be mentioned also that for individual porphyrin molecules $\text{H}_2\text{P}(\text{m-Pyr})_4$ in non-degassed toluene at ambient temperature, the S_1 -state decay is $\tau_{\text{S}}^0 = 8.7$ ns as is well known for a lot of free-base porphyrin in such conditions (49). It follows from experimental data that the porphyrin fluorescence decay in QD-porphyrin nanoassemblies under study is not shortened. In contrast, being attached to QD surface, $\text{H}_2\text{P}(\text{m-Pyr})_4$ ligand is characterized by slightly increased S_1 -state decay $\tau_{\text{S}} = 9.5$ ns at the same excitation and detection conditions. This decay increase is also proves the formation of QD-porphyrin nanoassemblies and may be attributed to the screening action of a relatively large TOPO-capped QD subunit thus limiting the access of oxygen molecule (quencher of a porphyrin S_1 -state) to the excited extra-ligand. Such screening effects were found also in self-assembled porphyrin triads and pentads (110, 115, 118). In addition, absorption spectra of the QD-porphyrin nanoassemblies are essentially a linear combination of the corresponding QD and porphyrin $\text{H}_2\text{P}(\text{m-Pyr})_4$ ligand, with only small changes in wavelength maxima (blue shift by ~1.5 nm) and band intensities $\text{Q}(0,0)/\text{Q}(0,1)$ ratio for porphyrin counterpart (100, 104, 112, 113). It means that in the ground state the interaction between QD and porphyrin molecule(s) in nanoassemblies is weak, and they retain their individual identities.

All these facts indicate evidently that the formation of QD-porphyrin nanocomposites leads to the increase of the non-radiative relaxation channels in the excited states of QD namely while the fluorescence decay of the attached porphyrin is not shortened. Typically, the above PL quenching for QD counterpart being observed in numerous QD-dye nanocomposites is commonly interpreted as being due to the photoinduced charge transfer (CT) (23, 119–124) and/or to the dipole-dipole resonant energy transfer of Foerster type (FRET) $\text{QD} \rightarrow \text{dye}$ (18, 19, 22, 45, 68, 72, 74, 92, 100, 101, 112, 125–131). Usually in the FRET case, the direct verification of the energy transfer process as a real reason of PL quenching is the comparison of the experimental values of FRET efficiencies via the donor (QD) PL quenching and the sensitization of the acceptor (porphyrin) fluorescence.

Such a quantitative comparison has been carried out by us for QD-porphyrin (72, 100, 110, 113) and QD-perylene bisimide (74, 129) self-assembled nanostructures. Below, we are willing to discuss this question with respect to nanoassemblies based on TOPO-capped CdSe/ZnS QDs ($d_{\text{CdSe}} = 3.0 \text{ nm}$, 2 ZnS monolayers, $C_{\text{QD}} = 4 \times 10^{-7} \text{ M}$) and $\text{H}_2\text{P}(\text{m-Pyr})_4$ molecules in toluene at 295 K (see Figure 1), as far as these nanoassemblies have been the studied in the experiments with singlet oxygen detection which will be described later.

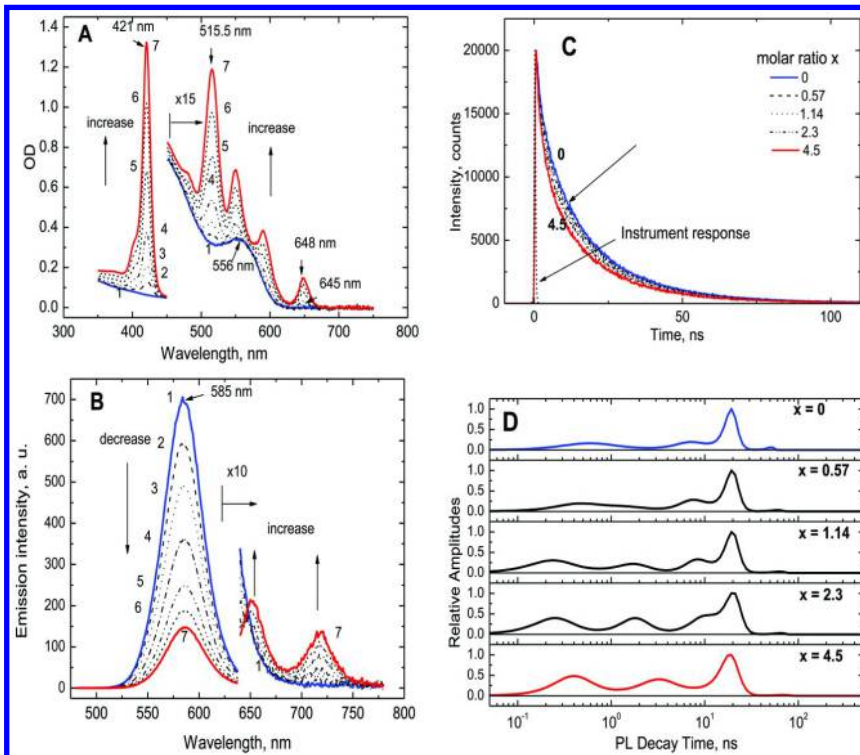


Figure 2. Absorption (A) and emission (B, $\lambda_{\text{ex}} = 465 \text{ nm}$) spectra as well as time-resolved PL traces (C, $\lambda_{\text{exc}} = 575 \text{ nm}$, $\lambda_{\text{em}} = 585 \text{ nm}$) and decay amplitude distributions (D) for CdSe/ZnS QD (diameter of CdSe core $d = 3.8 \text{ nm}$) upon titration by $\text{H}_2\text{P}(\text{m-Pyr})_4$ molecules in toluene at 295 K at sequence molar ratio x increase: 0.0(1); 1.15 (2); 2.3 (3); 4.5 (4); 9.1 (5); 13.5 (6); 17.8 (7)

Quantitative Analysis of QD Photoluminescence Quenching in Quantum Dot-Porphyrin Nanoassemblies

For nanoassemblies consisting of TOPO-capped CdSe/ZnS QDs ($d_{\text{CdSe}} = 3.0 \text{ nm}$, 2 ZnS monolayers, $C_{\text{QD}} = 4 \times 10^{-7} \text{ M}$) and $\text{H}_2\text{P}(\text{m-Pyr})_4$ molecules in toluene at 295 K, the direct comparison of QD PL quenching results and sensitization data for porphyrin fluorescence was carried out using a complete set of titration

points. Figure 3A collects the relative comparison of two dependences at the same experimental conditions ($\lambda_{\text{exc}} = 465$ nm): integrated fluorescence intensity of individual $\text{H}_2\text{P}(\text{m-Pyr})_4$ molecules as a function of the increased molar concentration of porphyrin (points 1), and enhanced integrated fluorescence intensity of $\text{H}_2\text{P}(\text{m-Pyr})_4$ molecules at the same molar concentrations of porphyrin but in the presence of CdSe/ZnS QDs of a given constant concentration (points 2).

It should be mentioned that according to our measurements the fluorescence quantum efficiency (ϕ) for attached $\text{H}_2\text{P}(\text{m-Pyr})_4$ molecules remains almost the same as that for free porphyrin. At the same time, Figure 3A shows that upon increasing the molar ratio x in solutions of QD-porphyrin nanoassemblies the integrated fluorescence intensities of $\text{H}_2\text{P}(\text{m-Pyr})_4$ ligand are noticeably larger than those being measured for individual porphyrin molecules at constant excitation conditions ($\lambda_{\text{ex}} = 465$ nm, the donor QD strong absorption). This finding reflects the existing of the sensitization (enhancement) effect that is typical for FRET phenomena. In addition, the fluorescence excitation spectrum of $\text{H}_2\text{P}(\text{m-Pyr})_4$ ligand in bioconjugate ($\lambda_{\text{reg}} = 719$ nm) provides the direct information about QD \rightarrow porphyrin FRET process (Fig. 3B). Nevertheless at a given molar ratio x , there is no full coincidence between absorption and fluorescence excitation spectra for “QD-porphyrin” bioconjugates. Thus, the realization of FRET with a quantum efficiency of 100% is not the case for the nanoassembly under study.

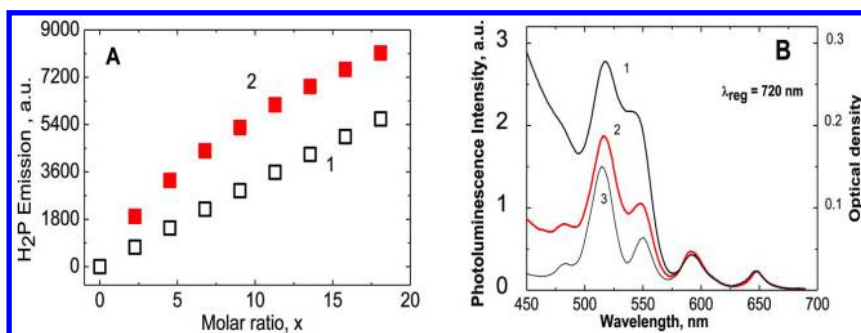


Figure 3. Porphyrin $\text{H}_2\text{P}(\text{m-Pyr})_4$ fluorescence intensities in toluene at two experimental conditions. A: Integrated fluorescence intensity of individual $\text{H}_2\text{P}(\text{m-Pyr})_4$ molecules (1) and enhanced integrated fluorescence intensity of $\text{H}_2\text{P}(\text{m-Pyr})_4$ in the presence of CdSe/ZnS QDs ($d_{\text{CdSe}} = 3.00$ nm/2 ZnS monolayers) (2) at the same molar concentrations of porphyrin and excitation conditions ($\lambda_{\text{exc}} = 465$ nm) for both cases. B: Comparison of the absorption spectrum (1) and porphyrin fluorescence excitation spectrum (2, $\lambda_{\text{reg}} = 720$ nm, corrected for excitation spectral response) for a solution of CdSe/ZnS QD with $\text{H}_2\text{P}(\text{m-Pyr})_4$ molecules at molar ratio $x = 4.0$; (3) is fluorescence excitation spectrum for alone porphyrin at the same $\text{H}_2\text{P}(\text{m-Pyr})_4$ concentration and experimental conditions as for case (2). A small tail rest of QD emission in the porphyrin fluorescence spectral range has been subtracted. Spectra (1), (2) and (3) are normalized with respect to the intensity of $Q(0,0)$ porphyrin band ($\lambda = 647$ nm).

Based on the experimental approach described in (68, 100, 132, 133), at every titration step we compared directly QD PL quenching efficiencies Φ_{QUENCH} with estimated FRET efficiencies Φ_{FRET} being obtained via porphyrin fluorescence sensitization effect. This estimation is based on the comparison of the absorption spectra of the QD-porphyrin mixture solution at every x ratio with the fluorescence excitation spectra of mixed solutions and individual porphyrin solutions at the same molar porphyrin concentration. QD PL quenching data as well as fluorescence excitation spectra (recorded at $\lambda_{\text{em}} = 720$ nm) have been obtained at every titration step. Experimental FRET efficiencies Φ_{FRET} have been calculated from the direct measurements of the corresponding intensities in fluorescence excitation spectra and optical densities (OD) in absorption spectra using the formula

$$\Phi_{\text{FRET}} = \left[\frac{I_{\text{DA}}(\lambda_{\text{ex}} = 465\text{nm}) - I_{\text{A}}(\lambda_{\text{ex}} = 465\text{nm})}{I_{\text{A}}(\lambda_{\text{ex}} = 590\text{nm})} \right] : \left[\frac{OD_{\text{DA}}(465\text{nm}) - OD_{\text{A}}(465\text{nm})}{OD_{\text{A}}(590\text{nm})} \right], \quad (1)$$

where, I_{DA} corresponds to the porphyrin fluorescence intensity at $\lambda_{\text{em}} = 651$ nm for QD-porphyrin nanoassemblies (that is for mixed solutions in the presence of both QD and $\text{H}_2\text{P}(\text{m-Pyr})_4$) whereas I_{A} is the fluorescence intensity of individual porphyrin at the same molar ratio at two different excitation wavelengths (465 and 590 nm). OD are the corresponding optical densities of the solution at given molar ratio x . The difference $[I_{\text{DA}}(\lambda_{\text{ex}} = 465\text{nm}) - I_{\text{A}}(\lambda_{\text{ex}} = 465\text{nm})]$ reflects the increase of the acceptor emission due to FRET. $\lambda_{\text{ex}} = 590$ nm corresponds to the wavelength, where the absorption of QD is negligible.

Figure 4 presents the comparison of QD PL quenching results and FRET values estimated via the porphyrin sensitization effect (Eq. 1) obtained for a given QD-porphyrin nanoassemblies in all experimental range of molar ratios x .

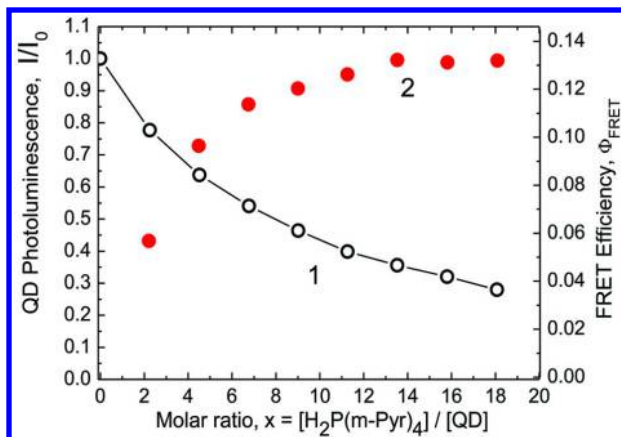


Figure 4. Comparison of QD PL quenching results I/I_0 (1, left scale) and Φ_{FRET} values (2, right scale) estimated via the porphyrin sensitization effect for QD-porphyrin nanoassemblies (CdSe/ZnS, $d_{\text{CdSe}} = 3.0$ nm, 2 ZnS monolayers, and $\text{H}_2\text{P}(\text{m-Pyr})_4$ porphyrin molecules) as function of the molar ratio $x = [\text{H}_2\text{P}(\text{m-Pyr})_4] / [\text{QD}]$ in toluene at 295 K.

It is evidently seen that at every molar ratio x , Φ_{FRET} values calculated from fluorescence enhancement (right scale) are significantly smaller than those estimated from QD PL quenching efficiency [$\Phi_{\text{QUENCH}} = 11(x)/I_0$]. In all titration range Φ_{FRET} values are of order 6 - 10 % and do not exceed 14 - 17 % even at high x values. It should be mentioned also that beginning from $x > 6$ there is a saturation tendency for experimental Φ_{FRET} values. Noteworthy, the same differences between Φ_{FRET} values (sensitization effect) and Φ_{QUENCH} efficiencies (quenching effect) have been observed for all QD-porphyrin bioconjugates based on $\text{H}_2\text{P}(\text{m-Pyr})_4$ porphyrin molecules and CdSe/ZnS QDs of various sizes (72, 100, 113). Thus, the obtained results demonstrate clearly that FRET is not a dominant reason of QD PL quenching in QD-porphyrin nanocomposites.

In fact, there have been numerous studies of energy transfer from semiconductor QDs to various acceptor organic ligands. Experimental results (18, 19, 22, 45, 68, 72, 74, 100, 112, 113, 123, 125, 129–131, 134–138) and theoretical considerations (92, 139) suggest nanocrystalline materials and organic-inorganic hybrids are best described in the weak coupling regime. The application of the weak coupling model arises due to the dissimilarity in the wave functions of the molecular orbitals in organic systems and band-like orbitals in nanocrystals that prevents traditional strong interactions. This allows the application of Foerster theory (140, 141) which typically is used at the limit of “localized oscillators” as a result of the electric dipole approximation. In this model FRET from a photoexcited donor (D) to a lower-energy acceptor (A) takes place due to the coupling of the dipole moment of an exciton in a D chromophore with absorbing transition in nearby A chromophores. The acceptor itself may relax to its ground state with or without photon emission. FRET rate constant k_{DA} for an isolated D - A pair at distance R_{DA} is expressed by

$$k_{DA} = \frac{1}{\tau_D^0} \cdot \frac{R_0^6}{R_{DA}^6} \quad (2)$$

where τ_D^0 is the emission decay of the individual donor, R_{DA} is the center-to-center distance of the idealized point dipoles. For QD-porphyrin nanoassemblies, the distance R_{DA} is the distance from the center of the CdSe/ZnS QD to the center of $\text{H}_2\text{P}(\text{m-Pyr})_4$ ligand assuming a perpendicular orientation of a porphyrin macrocycle with respect to QD surface (see Figure 1). R_0 is the critical Foerster radius which may be calculated as

$$(R_0^{\text{theor}})^6 = \frac{9000 \ln 10 k^2 \Phi_D^0}{128 \pi^5 n^4 N_A} \times \int_0^{\infty} f_D(v) \epsilon_A(v) \frac{dv}{v^4} \quad (3)$$

where $N_A = 6.022 \cdot 10^{23} \text{ M}^{-1}$ is Avogadro number. Φ_D^0 is the donor emission quantum yield in the absence of FRET, n is the refraction index of the solvent. Orientation factors $k^2 = [\cos(\mu_D, \mu_A) - 3 \cos(\mu_D, \mathbf{r}_{DA}) \cos(\mu_A, \mathbf{r}_{DA})]^2$, where (μ_D, μ_A) is the angle between transition dipole moment vectors of the D and A subunits, (μ_D, \mathbf{r}_{DA}) and (μ_A, \mathbf{r}_{DA}) denote the angles between the dipole vectors of D and A and the direction D→A, respectively. For a random static rigid distribution

of interacting dipoles $k^2 = 0.467$ (141) (for QD-porphyrin nanoassemblies in our case). Spectral overlap integral

$$J = \int_0^{\infty} f_D(v) \epsilon_A(v) \frac{dv}{v^4} \quad (4)$$

is calculated on the basis of experimental acceptor, A (porphyrin) absorption and donor, D (QD) PL spectra, where $\epsilon(v)$ corresponds to the A molar decimal extinction coefficient, $f_D(v)$ corresponds to the D quantum emission spectrum normalized to unity by area on a wave number scale. The calculated and experimentally determined parameters reflecting FRET for CdSe/ZnS QDs and $H_2P(m\text{-Pyr})_4$ molecules being used for nanoassembly formation are collected in Table 1.

It follows from data presented in Table 1 that according to theoretical estimations, if FRET is considered as the dominant reason of QD PL quenching, the theoretical FRET efficiency for pair interaction QD-one porphyrin molecule should be no less than

$$\Phi_{\text{FRET}}^{\text{theor}} = \left[1 + \left(\frac{R_{\text{DA}}}{R_0^{\text{theor}}} \right)^6 \right]^{-1} \sim 0.7 \div 0.8. \quad (5)$$

For a given nanoassembly, this theoretical estimation in the frame of common FRET model is in contradiction with experimental Φ_{FRET} values obtained using Eq. 1 (see curve 2 in Figure 4).

On the other hand, experimental total quenching rate constants k_q^{exper} for the QD PL quenching in QD-porphyrin nanoassemblies at a given molar ratio x have been estimated (without discrimination of FRET and possible non-FRET non-radiative relaxation channels) on the basis of equation

$$k_q^{\text{exper}} = \langle K_{\text{SV}}(x) \rangle / \langle \tau_D^0 \rangle, \quad (6)$$

where PL decay rate $1/\tau_D^0 = 6.8 \times 10^7 \text{ s}^{-1}$ for individual QD. In its turn, experimental Stern-Volmer mean rate constants $\langle K_{\text{SV}}(x) \rangle$ has been evaluated from the experimental PL quenching data plotted in Stern-Volmer representation (based on titration experiments) according to approach described by us in detail earlier (72, 112, 113).

From data presented in Table 1 it is evidently seen that in all titration range $k_q^{\text{exper}} < k_{\text{DA}}^{\text{theor}}$. It means that the typical FRET QD \rightarrow porphyrin process (with experimental quantum efficiency $\Phi_{\text{FRET}} \leq 0.12$ only) is realized in QD-porphyrin nanoassemblies under study but the main part of the QD PL quenching should be connected with the other reason. In addition, for TOPO-capped CdSe/ZnS QDs of a given size ($d_{\text{CdSe}} = 2.6 \text{ nm}$ and 2 ZnS monolayers), upon the replacement of $H_2P(m\text{-Pyr})_4$ molecules by $CuP(m\text{-Pyr})_4$ and tetrahydroporphyrin, THP(*m*-Pyr)₄ derivatives (thus changing the overlap integral $J(v)$ values by factor of 2.5) the quenching efficiency of QD PL remains nearly the same (103, 104). Thus, FRET QD \rightarrow porphyrin in “QD-porphyrin” bioconjugates is not the only one mechanism

of the total QD PL quenching. Nevertheless, in this case low FRET serves as indicator for the formation of the QD-porphyrin nanoassemblies.

Table 1. CdSe/ZnS QD ($d_{CdSe}=3.0$ nm, 2 ZnS monolayers) Properties and FRET Parameters for QD-Porphyrin Nanoassembly with the Donor-Acceptor Distance $R_{DA}=2.78$ nm (Molar Ratio $x = 4.0$, Toluene, Refractive Index $n = 1.4969$, $T=295$ K)

System	ϕ_D^0	$\bar{\alpha}_{\tau_D^0} \bar{n}$ ns	$J(\nu)$, $cm^3 M^{-1}$	R_0^{theo} , nm	k_{DA}^{theor} , s ⁻¹	k_q^{exper} , s ⁻¹
QD-H ₂ P	0.63	14.74	4.0×10 ⁻¹⁴	3.1	1.3×10 ⁸	(8±2)×10 ⁶

Notes: ϕ_D^0 and $\bar{\alpha}_{\tau_D^0} \bar{n}$ are QD PL quantum efficiency and mean decay, correspondingly, in the case of FRET absence. Non-exponential decay of QD PL has been fitted by three components $I(t) = A_1 \times \exp(-t/\tau_1) + A_2 \times \exp(-t/\tau_2) + A_3 \times \exp(-t/\tau_3)$, and the mean lifetime value has been calculated as $\bar{\alpha}_{\tau_D^0} \bar{n} = \sum(A_i \text{ times; } \tau_i^2) / \sum(A_i \times \tau_i)$. Intercenter distance R_{DA} has been estimated from structural and geometrical parameters for QD-porphyrin nanoassembly (see Figure 1). FRET theoretical rate constant k_{DA}^{theor} was calculated using Eq (2). Experimental total quenching rate constant k_q^{exper} for the QD PL quenching in QD-porphyrin nanoassemblies at a given molar ratio x has been estimated using equation (6).

The comparative titrations of the given CdSe/ZnS QD solutions by H₂P(m-Pyr)₄ molecules and tetrahydroporphyrin THP(m-Pyr)₄ ligands (holes acceptor) give the coincidental curves for QD PL quenching without changes of fluorescence parameters for THP(m-Pyr)₄ also (104). In addition, the coincidental QD PL quenching curves have been obtained when using di-pyridyl substituted ligands H₂P(m-Pyr)₂(Ph)₂ and electron acceptors, H₂P(m-Pyr)₂(Anthraquinone)₂ or H₂P(m-Pyr)₂(5FPh)₂, and the fluorescence of these electron acceptors being attached to QD surface was not quenched (103). Thus, non-dependence of QD PL quenching efficiency on redox properties of porphyrin ligands and the absence of the ligand fluorescence quenching in QD-porphyrin nanoassemblies rules out the dominant role of typical photoinduced charge transfer (PCT) processes with participation of molecular orbitals of porphyrin macrocycle (known for multiporphyrin self-assembled arrays (110, 118, 142, 143).

We have found for the first time that a mechanism clearly distinct from PCT and FRET may be responsible for ligand-induced QD PL quenching in QD-porphyrin nanocomposites (72, 113). This process is correlated with the extension of the exciton wave function beyond the interface between the QD and the attached porphyrin molecule. Based on comparison of experimental data and quantum mechanical calculations it follows that the specificity of the exciton non-radiative decay in QD-porphyrin nanoassemblies (that is QD PL non-FRET quenching) is connected with the charge tunneling through ZnS barrier in the conditions of quantum confinement. From the physico-chemical point of view, upon attachment of H₂P(m-Pyr)₄ molecule to QD surface, the electron wave function may be locally modified forming a surface local state(s) capable to trap

the electron of the photogenerated exciton. Thus, one point-like charge density perturbation caused by organic linker group or chromophore at QD interface forces the electron of the delocalized exciton of quantum dot to become localized. It should be stressed that the presently discussed mechanism for QD PL quenching is completely distinct from the known photoinduced charge transfer between interacting inorganic and organic counterparts.

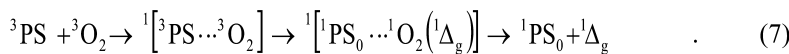
Based on these physical arguments, now we are capable to comparatively analyze the interaction of individual QDs and QD-porphyrin nanoassemblies with molecular oxygen in liquid solutions.

Experimental Studies of Singlet Oxygen Generation

Singlet Oxygen Generation by Alone CdSe/ZnS Quantum Dots

There are few reports in the literature on intrinsically inherent generation of singlet oxygen by QDs without any intermediate energy transfer process involved (61, 144). Lately superoxide generation by QDs has also been reported (145). Notably, the observed 5% efficiency of 1O_2 generation by bare quantum dots is one order of the magnitude lower than that known for molecular PDT sensitizers.

Typically in liquid solutions, the photosensitized production of active singlet oxygen (1O_2) in a long-living ${}^1\Delta_g$ electronic state is indeed a very general process via the interaction of a light-activated PS molecule with molecular oxygen, O_2 . In the result, the excited states of organic PS, particularly the longer-lived triplet T_1 -state, are efficiently quenched by O_2 . It is well-documented (146), that the process of T_1 -states quenching by O_2 is realized via non-radiative transitions between electronic states in an intermediate short-living weak collision complex formed as a result of a diffusional contact of a given excited organic molecule with an oxygen molecule. From this point of view and taking into account Wigner spin conservation rule (transitions between terms of the same multiplicity are spin-allowed) (147), the quenching of T_1 -state of the organic PS (3PS) followed by the formation of singlet oxygen, 1O_2 (or ${}^1\Delta_g$) may take place via one way:



From the considerations presented in literature (146, 148) it follows that in the case of porphyrins and chlorins as PSs, the relation k_{disks} is used (where k_{dis} is the rate constant of the collision complex dissociation, k_s is the bimolecular rate constant of S_1 -state quenching by O_2). In addition, reaction (7) of 1O_2 generation corresponds to the case when $k_T = (1/9)k_s$, where k_T is the bimolecular rate constant of T_1 -state quenching by molecular oxygen.

Below we shall discuss these quenching processes for individual QDs characterized by some features (see Figure 5 and Table 2). We have succeeded to detect surely the 1O_2 emission (spectra and kinetics generated with the quantum efficiency $\gamma_\Delta = 1.5\%$ by individual CdSe/ZnS QDs of two sizes ($d_{\text{CdSe}} = 2.5$ nm and 3.0 nm). In air-saturated toluene (1 atm of air), the 1O_2 emission decay was measured to be $\tau({}^1\Delta_g) = 30.0 \mu\text{s}$. These results coincide with the corresponding data obtained for alone CdSe QDs ($d_{\text{CdSe}} = 5$ nm) in oxygen-saturated toluene at

ambient temperature (γ_{Δ} 1.5%, $\tau(^1\Delta_g)$ = 28.5 μ s (61)). Table 2 shows that for CdSe/ZnS QDs with $d_{\text{CdSe}} = 5.2$ nm no singlet oxygen was observed when these QDs were excited at the same conditions. In the later case, it is necessary to bear in mind that in contrast to CdSe/ZnS QDs of smaller sizes ($d_{\text{CdSe}} = 2.5$ and 3.0 nm), quantum dots with $d_{\text{CdSe}} = 5$ nm are characterized by essentially lower PL quantum efficiency, caused by a lot of deep trap surface states with their low level emission detected by us in the red and IR spectral range overlapping with $^1\text{O}_2$ emission region. Correspondingly, these competitive PL quenching processes seem to be the main reason of the lack of the $^1\text{O}_2$ generation by large QDs in our case. In this respect it should be mentioned that no singlet oxygen generation was detected for alone water-soluble CdTe QDs (62, 149) and the reasons of that may be different from those discussed above.

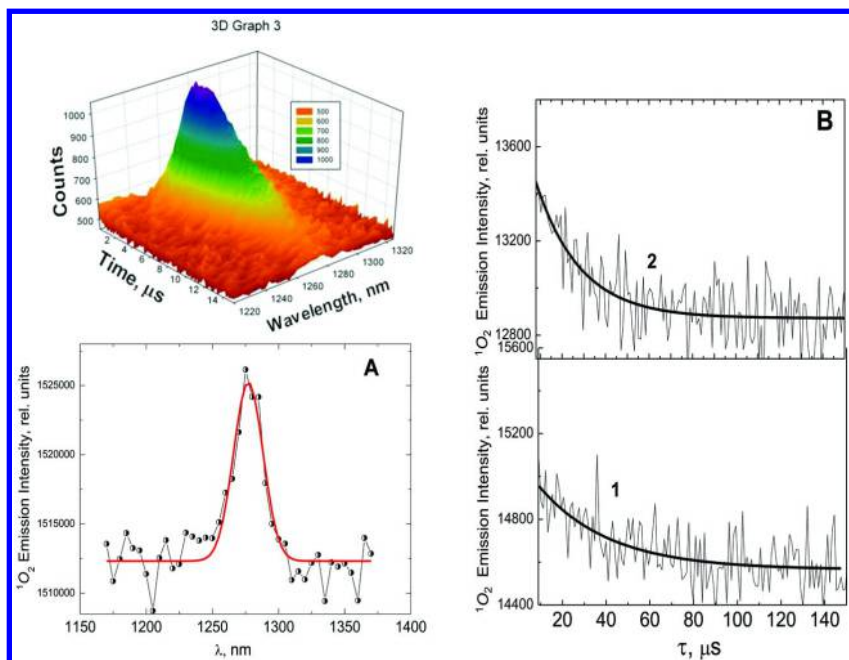


Figure 5. 3D presentation, spectrum of singlet oxygen $^1\text{O}_2$ emission (A) directly sensitized by CdSe/ZnS QDs (Hops Yellow, core diameter $d_{\text{CdSe}} = 3.0$ nm 2 ZnS monolayers) in air-saturated toluene, and $^1\text{O}_2$ sensitized luminescence decays in toluene solutions (B) in the presence of 1 atm of air (1) and 1 atm of pure oxygen (2).

Experimental results presented in Figure 5 and Table 2 show that for CdSe/ZnS QDs with $d_{\text{CdSe}} = 3.0$ nm, the 5-times increase of the dissolved oxygen concentration leads to the increase of the quantum efficiency γ_{Δ} by 1.7 times while the $^1\text{O}_2$ emission decay $\tau(^1\Delta_g)$ remains unchanged. Simple calculations using the formula $C = [(4\pi/3)R^3]^{-1}$, connecting the concentration C and mean distances R between molecules (150), show that the 5-times increase of C corresponds to

the increase of R by 1.7 times for dissolved oxygen molecules. The last value is in a good coincidence with the mentioned above increase of the quantum efficiency γ_Δ upon rise of the dissolved oxygen concentration. It means that the interaction of excited QD with molecular oxygen is realized via the diffusionally controlled formation of the short-living weak collision complex. At last, it should be noted that the 5-times increase of dissolved oxygen does not lead to the strong shortening of the mean decay $\bar{\tau}_D^0$ for the QD photoluminescence. In some extent, this fact reflects low γ_Δ values being measured for alone CdSe/ZnS QDs in toluene.

Table 2. TOPO Capped CdSe/ZnS QD Parameters and Their Quantum Efficiencies of Singlet Oxygen Generation in Toluene at 295 K

d_{CdSe} nm	$\lambda_{PL_{max}}$ nm	τ_i (ns), A_i	$\bar{\tau}_D^0 \bar{\eta}$ ns	ϕ_{D^0}	γ_Δ
2.5	540	$\tau_1 = 1.48$ ns, $A_1 = 0.022$ $\tau_2 = 9.73$ ns, $A_2 = 0.044$ $\tau_3 = 20.56$ ns, $A_3 = 0.023$	14.93	0.43	0.015±0.005
3.0	558	$\tau_1 = 0.54$ ns, $A_1 = 0.030$ $\tau_2 = 8.29$ ns, $A_2 = 0.024$ $\tau_3 = 16.71$ ns, $A_3 = 0.046$	14.74	0.63	0.015±0.005
3.0*)	558	$\tau_1 = 0.35$ ns, $A_1 = 0.018$ $\tau_2 = 6.21$ ns, $A_2 = 0.009$ $\tau_3 = 15.92$ ns, $A_3 = 0.026$	14.54	-	0.025±0.005
5.2	620	$\tau_1 = 0.93$ ns, $A_1 = 0.078$ $\tau_2 = 5.69$ ns, $A_2 = 0.037$ $\tau_3 = 20.76$ ns, $A_3 = 0.011$	11.74	0.075	--

Notes: In all cases experiments have been carried out at 1 atm. air, while for γ_Δ 1 atm. of pure oxygen has been used. ϕ_{D^0} is QD emission quantum efficiency. QD PL non-exponential decays $\bar{\tau}_D^0$ upon excitation at $\lambda_{exc} = 460$ nm have been fitted by $I(t) = \sum A_i \times \exp(-t/\tau_i)$, and the mean lifetime values have been calculated as $\bar{\tau}_D^0 \bar{\eta} = \sum (A_i \times \tau_i^2) / \sum (A_i \times \tau_i)$, upon fitting procedure weighted chi square values were in the range of $\chi^2 = 1.02 \div 1.13$. $\lambda_{PL_{max}}^{PL}$ is QD PL maximum. Quantum efficiencies of singlet oxygen generation γ_Δ have been measured with respect to a standard Pd-mesoporphyrin in toluene with $\gamma_\Delta = 1.0$ (49) (excitation at $\lambda_{exc} = 532$ nm, the singlet oxygen emission was detected at maximum with $\lambda_{max} = 1270$ nm). According to our measurements (151), the quantum efficiency of singlet oxygen generation by $H_2P(m\text{-Pyr})_4$ molecules $\gamma_\Delta = 0.6$.

Notably, like in our case, low efficiencies of 1O_2 sensitization were mentioned in literature also (35, 36, 61–63, 152). Some physical reasons of the low quantum efficiency of singlet oxygen generation by alone QDs in liquid solutions at ambient temperature may be considered in this respect. It is well documented (153, 154) that the lowest energy exciton (formed by the band-edge $1S(e) \rightarrow 1S_{3/2}(h)$ transition) is splitted into five sub-levels caused by the crystal shape asymmetry, the intrinsic crystal field (in hexagonal lattice structures), and the electron-hole exchange interaction. Two of the five states with lower energy, including the

ground state, are optically passive (a total angular momentum $N = 2$) and form the so-called “dark” exciton. The high-energy states being optically active (a total angular momentum $N = 1$) form the so-called “bright” exciton. According to theoretical considerations (153), the energy gap between the first optically active state and the optically forbidden ground exciton state is estimated by tens of milli-electron volts ($\sim 200 \text{ cm}^{-1}$) and increases with decreasing QD size, leading to an increase of the Stokes shift in PL spectra.

On the other hand, it is well documented the thermal redistribution of excitons between states with different total angular momentums ($N_m = 1^L$ and 2) is the main reason that leads to the strong temperature dependence of single-exciton intrinsic recombination dynamics in CdSe QDs (14, 154, 155). At low temperatures, exciton recombination occurs primarily via the low-oscillator-strength “dark” state and characterized by slow (submicrosecond to microsecond) PL decay. Upon temperature rise, the higher-oscillator-strength short-living “bright” states become thermally populated from the “dark” state, which leads to a faster PL dynamics. Finally, at sufficiently high temperatures (e.g. thermal energy kT is comparable or larger than the energy gap $\Delta E = E_{\text{bright}} - E_{\text{dark}}$) exciton population becomes distributed equally between the “bright” and “dark” states leading to the saturation of PL decay at a value of twice the bright-exciton lifetime (in the region of $\sim 20 \text{ ns}$ for CdSe QDs).

It follows from the analysis of the size dependence of the band-edge exciton splitting (fine structure) for hexagonal CdSe QDs (presented in (153)) that for CdSe/ZnS QDs with $d_{\text{CdSe}} = 3.0 \text{ nm}$ (discussed in details here) this energy distance $\Delta E = E_{\text{bright}} - E_{\text{dark}}$ is in the range of 30 meV ($\sim 240 \text{ cm}^{-1}$). As far as the transition from the ground to the “dark” state it is not observable in the QD steady-state absorption spectra, the low-oscillator-strength “dark” state is often referred as the “triplet” state (61). It is considered also (156, 157) that the exciton fine structure of QDs (discussed in (14, 153–155)) is an analogous spectral quantity to the singlet-triplet manifold of molecules. In this respect two principal features should be taken into account for QDs under study: i) at room temperature $\Delta E \sim 240 \text{ cm}^{-1}$ is comparable with $kT \sim 210 \text{ cm}^{-1}$, and “dark” states are shortened down to $\sim 15 \text{ ns}$ due to an effective thermal distribution between the “bright” and “dark” states; ii) both for “bright” exciton (a total angular momentum $N = 1$) and for “dark” exciton ($N = 2$), the reaction between molecular oxygen and QD in these states is not fully correspond to Wigner spin conservation rule. In addition, on the base of femtosecond time-resolved studies it has been suggested (61) that the low quantum efficiency of 1O_2 generation by alone QDs may be due to carrier trapping and non-radiative carrier recombination occurring on the early picosecond time scale. Then, like for organic PSs (146, 147) spin statistics also diminishes the fraction of the QD – 3O_2 contact complexes capable to generate singlet oxygen. At last, for some CdSe/ZnS QDs on the basis of PL decay time distribution analysis it was shown that trap or defect states exhibit at room temperature a lifetime of about 80 ns and are red shifted by about 110 meV ($\sim 890 \text{ cm}^{-1}$) (117, 156). Correspondingly, these states may effectively compete with 1O_2 generation by alone QDs.

Thus, the main conclusion which follows up from the obtained results and presented considerations is that at ambient temperature most of alone QDs are hardly perspective to the direct generation of singlet oxygen. Low singlet

oxygen yield observed to date for intrinsic QDs (without organic conjugates) prevents their immediate application in clinical practice. To summarize, the currently revealed low intrinsic QDs efficiency in singlet oxygen generation should be followed by the further extensive research towards understanding mechanisms of singlet oxygen generation and major influencing factors, first of all – size-dependent and composition-dependent singlet–triplet splitting of the lowest exciton state in QDs. Additionally, studies of possible size-dependent photoinduced Cd release in Cd-based QDs and their size-dependent photostability are mandatory to explore QD-based PTD feasibility to its fullest potential.

Singlet Oxygen Generation by QD-Porphyrin Nanoassemblies

It follows from the results presented and discussed above in this Chapter, that the formation of QD-(porphyrin)_n nanoassemblies by the attachment of $n \geq 1$ H₂P(m-Pyr)₄ molecules to one QD surface leads to its PL quenching. In a microscopic picture, each single act of the attachment opens a new competitive decay channel which is responsible for the QD PL quenching. In any titration experiment with use of steady-state optical spectroscopy, the QD total PL intensity $I(x)$ obtained from an ensemble of QD-(porphyrin)_n nanoassemblies with a static distribution of n at a given ratio x is the weighted sum of the contributions of each individual bioconjugate. Assuming a quasi-infinite number n^* of binding sites available for porphyrin molecules per one QD, the probability of the existence of QD-(porphyrin)_n nanoassembly with particular n porphyrin molecules at a given ratio x follows binomial or oftenly the Poisson distribution (described in (110, 118, 158–160)

$$P_n(x) = x_n \cdot \exp(-x) / n! , \quad (8)$$

provided n^* is quasi-infinite. This assumption holds also for finite n^* if a strong PL quenching (at equimolar ratio) is observed which was shown for the QD-porphyrin nanoassemblies earlier (100). Thus, the free porphyrin molecules are then subject to a redistribution over the free binding sites with respect to their availability, with the probability of filling a vacancy on a particular nanoassebly QD-(porphyrin)_n proportional to the probability of its occurrence in the ensemble. This partial redistribution picture occurred in a good agreement with the experimental results on time-resolved fluorometry of QD-(porphyrin)_n showing also that the fraction of porphyrin molecules remaining uncomplexed in solution increases with growing porphyrin-to-QD molar ratio x (100, 117). At last, comparing experimentally determined PL quenching rates k_q and calculations of the size-dependent exciton wave functions in the conditions of the spatial confinement, it was concluded that the attachment of only one porphyrin molecule induces a perturbation of the wave function which is accompanied by a strong increase of non-radiative decay rates (72, 113).

Thus, taking into account the experimental quenching data for QD-porphyrin nanoassemblies based on CdSe/ZnS QDs ($d_{CdSe}=3.0$ nm, 2 ZnS monolayers) and H₂P(m-Pyr)₄ molecules) (Figure 4), analysis of Poisson distribution in the molar ratio range of $0 \leq x \leq 10$ for the system under study (100, 112) as well as

PL quenching specificity for QD-porphyrin nanoassemblies (72, 113) we will analyze the singlet oxygen generation by the given nanoassemblies at the molar ratio $x = 4$ in toluene at ambient temperature. This nanoassembly with a given value $x = 4$ was prepared by one-step mixing. Firstly, calculations according to formula (8) show that at this molar ratio practically all porphyrin molecules are fixed on QD surface: e.g. $P_0(4)=0.02 \ll P_4(4)=0.2, P_5(4)=0.2$. Secondly, at this molar ratio PL quenching and FRET parameters are surely detected. Indeed, the experimental data were measured to be (Figure 4 and Table 1): the efficiency of QD PL quenching $I(x)/I_0 = 0.65$, QD emission decay shortening from $\bar{\tau}_{D^0} = 14.74$ ns down to $\bar{\tau}_{D^0} = 13.7$ ns, FRET efficiency $\Phi_{\text{FRET}} = 0.14 \pm 0.02$ as estimated using formula (1) from sensitization data for porphyrin fluorescence, as a real signature of FRET.

Figure 6 shows the comparative analysis of the singlet oxygen $^1\text{O}_2$ luminescence decays and intensities (pumped at $\lambda_{\text{exc}}=532$ nm, measured at $\lambda_{\text{reg}}=1270$ nm) sensitized by individual CdSe/ZnS QDs and alone $\text{H}_2\text{P}(\text{m-Pyr})_4$ molecules with respect to the corresponding kinetics being obtained for solutions of QD-porphyrin nanoassemblies with $x=4$ having the same molar concentrations of QDs and porphyrin molecules as well being excited at constant laser excitation conditions. Figure 6A evidently shows that upon laser excitation the QD-porphyrin nanoassemblies do indeed produce singlet oxygen with the higher efficiency in comparison with alone QDs at the same experimental conditions in air-saturated toluene. From the other hand, Figure 6B demonstrates that in these conditions, the efficiency of $^1\text{O}_2$ generation by the same QD-porphyrin nanoassembly is higher also than that measured for the solution of individual porphyrin molecules at the same molar concentration.

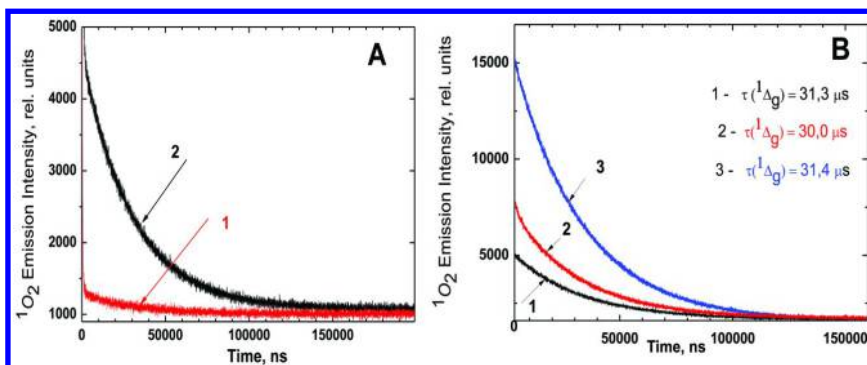


Figure 6. A: Comparative presentation of singlet oxygen $^1\text{O}_2$ luminescence decays sensitized by individual CdSe/ZnS QDs (1) with respect to those measured for QD-porphyrin nanoassemblies (2) at the same molar concentrations of QDs and laser excitation conditions. B: Decay kinetics of $^1\text{O}_2$ luminescence observed for alone $\text{H}_2\text{P}(\text{m-Pyr})_4$ molecules (1), QD-porphyrin nanoassemblies (2) at the same molar concentrations of porphyrin and Pd-mesoporphyrin as a standard (3) at fixed laser excitation conditions. The molar ratio $x = 4$ was constant in air-saturated toluene, laser excitation at $\lambda_{\text{exc}}=532$ nm, pulse duration $\Delta t_{1/2} = 0.7$ ns, pulse energy $E = 4 \mu\text{J}$, observation at $\lambda_{\text{reg}}=1270$ nm.

In all cases presented in Figure 6 the radiative relaxation of ${}^1\text{O}_2$ detected at $\lambda_{\text{reg}}=1270$ nm is characterized by the same decay value of $\tau({}^1\Delta_g) = 30\text{-}31\ \mu\text{s}$ that is typical for the singlet oxygen emission in non-polar liquid solutions (39, 40, 47, 61, 115).

From these findings one may conclude that QD-porphyrin nanoassemblies can produce ${}^1\text{O}_2$ more effectively with respect to their counterparts alone. Nevertheless, for clear understanding the role of FRET namely and pathways involved in the two-step process of singlet oxygen generation by the given nanoassemblies we have paid our attention to the quantitative comparison of the obtained experimental data. Before doing so, a test experiments were conducted to elucidate the role of excitation conditions in this case. The reason of that is explained by the fact that, typically, photoluminescence measurements are carried out at essentially lower excitation energies with respect to laser experiments being used for ${}^1\text{O}_2$ generation.

Figure 7 shows the experimental dependencies of the normalized emission intensities on the energy of laser excitation for QD-porphyrin nanoassemblies under study. CdSe/ZnS QDs and porphyrin $\text{H}_2\text{P}(\text{m-Pyr})_4$ molecules were dissolved air-saturated toluene. Notably, QD molar concentrations were the same in cases A and B, while in cases C and D porphyrin molar concentrations were kept equal. It is evidently seen that the QD PL intensity ($\lambda_{\text{em}}=558\ \text{nm}$) is not a linear function of the laser pulse energy E for alone QDs (A) as well as for QDs in QD-porphyrin nanoassemblies (B).

This non-linearity is more pronounced for alone QDs with respect to those in nanoassemblies. In the case of alone porphyrin solutions ($\lambda_{\text{em}}=720\ \text{nm}$) the above dependence is linear practically (C), while in contrast, this dependence for porphyrin counterpart in the QD-porphyrin nanoassembly is non-linear (D). The linear dependence (Figure 7C) for alone porphyrin solutions in the whole range of nanosecond laser energies (Figure 7C) is explained by the minor role of the singlet-singlet and triplet-triplet annihilation processes (49, 161, 162) at low solute concentrations ($\geq 10\text{-}510\div 6\ \text{M}$ in the given case). Non-linear dependence obtained for alone QDs (Figure 7A) reflects the well-documented pump-intensity dependence of the amplitudes of the single-exciton caused by non-radiative intraband Auger processes (14, 155). While the intrinsic mechanism for depopulation of singly excited exciton is radiative electron-hole recombination, the decay of multi-e-h pair states in QDs is dominated by non-radiative Auger processes mediated by Coulomb electron-electron interactions in the conditions of the spatial confinement (14, 155).

Auger recombination is a non-radiative process in which the e-h recombination energy is not emitted as a photon but instead is transferred to a third particle (an electron or a hole) that is re-excited to a higher-energy state thus leading to a decrease of QD photoluminescence intensities. The less pronounced non-linear dependence of QD PL intensity observed for QD-porphyrin nanoassemblies (Figure 7B) may be considered as a signature of the influence of two competing processes (dominant non-FRET and less effective FRET (72, 113)) leading to an additional quenching of singly excited exciton in QD. This conclusion is in agreement with other results showing that biexciton Auger recombination of CdTe QDs is a function not only the QD diameter but

strongly dependent on the QD surface trapping, capping reagents and/or surface conditions (163). In this respect, the non-linear dependence of fluorescence measured for porphyrin being attached to QD surface (Figure 7D) presents itself a direct proof of the realization of namely FRET process QD→porphyrin competing with both radiative electron-hole recombination and non-radiative Auger process in the conditions of powerful excitation.

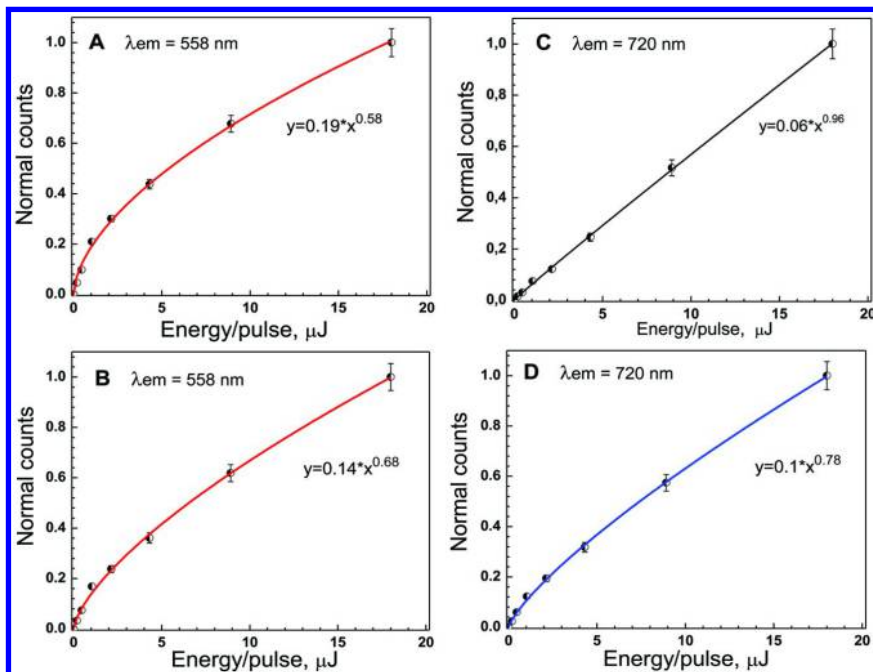


Figure 7. Dependencies of the normalized emission intensities on the energy of laser excitation for alone CdSe/ZnS QDs (A) and QDs in QD-porphyrin nanoassemblies (B) as well as for alone porphyrin H₂P(m-Pyr)₄ molecules (C) and those attached to QDs in nanoassemblies (D). In cases A and B QD molar concentrations were the same, in cases C and D porphyrin molar concentrations were kept equal. Experimental conditions: laser excitation $\lambda_{exc}=532$ nm, pulse duration $\Delta t_{1/2}=9$ ns, repetition rate $v=1$ kHz, mean maximal pulse energy $E=18$ μ J, laser beam size $d\leq 0.5$ mm. Experimental errors for intensity measurements were 5 % at high energies and up to 10 % at low energies.

The above results evidently show that the relative increase of the efficiency of 1O_2 generation by QD-porphyrin nanoassemblies with respect to that for alone QDs coincides with the observed sensitized increase of the fluorescence intensity for the attached porphyrins caused by FRET. Therefore, understanding and ultimately controlling the energy of laser excitation we have carried out the quantitative estimation of FRET efficiency in the bioconjugate based on singlet

oxygen generation experiments presumably. Optical densities of samples were less 0.2 at $\lambda_{exc}=532$ nm in order to exclude the inner filter effect. Because of an overlap of QD and porphyrin absorption spectra at $\lambda_{exc}=532$ nm, some amount of singlet oxygen detected for nanoassembly may arise via the direct excitation of porphyrin molecules attached to QD. Therefore (see Figure 6B), the intensities of 1O_2 emission at $\lambda_{reg}=1270$ nm were measured comparatively for alone $H_2P(m-Pyr)_4$ molecules (curve 1), QD-porphyrin nanoassemblies (curve 2) at the same molar concentrations of porphyrin as well as for Pd-mesoporphyrin as a standard (curve 3) at fixed laser excitation conditions. Correspondingly, in the case of FRET, the whole intensity I_{Δ}^{Σ} of singlet oxygen emission should be

$$I_{\Delta}^{\Sigma} = I_{\Delta}^A + I_{\Delta}^{DA} , \quad (9)$$

where I_{Δ}^A is 1O_2 emission intensity sensitized via direct excitation of acceptor A ($H_2P(m-Pyr)_4$ in the given case), and I_{Δ}^{DA} is an additional increase of 1O_2 emission intensity sensitized via FRET. It is clear that in the absence of FRET one should measure $I_{\Delta}^{\Sigma} = I_{\Delta}^A$. It is known that at low optical densities, the intensity of 1O_2 emission depends linearly on the fraction of absorbed exciting light by photosensitizer (49, 148). Based on these considerations, the expected increase of 1O_2 emission intensity sensitized via FRET in QD-porphyrin nanoassembly with the efficiency $\Phi_{FRET} = 1.0$ was evaluated using the following expression

$$(I_{\Delta}^{DA})_{max} = \frac{I_{\Delta}^0 \times \beta_{QD}}{\beta_0} \times \gamma_{\Delta}^A , \quad (10)$$

where I_{Δ}^0 is 1O_2 luminescence intensity sensitized by standard Pd-mesoporphyrin, $\gamma_{\Delta}^A = 0.6$ is the quantum efficiency of singlet oxygen generation by $H_2P(m-Pyr)_4$ molecules in toluene (151), $\beta_{QD} = (1 - 10^{-D_{QD}})$ is the fraction of exciting light being absorbed by QD in nanoassembly, $\beta_0 = (1 - 10^{-D_0})$ is the fraction of exciting light being absorbed by a standard, D_{QD} and D_0 are the corresponding optical densities of the samples at $\lambda_{exc}=532$ nm.

Finally, from experimental data (Figure 6B) using measured values I_{Δ}^{Σ} (curve 2), I_{Δ}^A (curve 1) and evaluated value via expression (10), one may obtain FRET efficiency in QD-porphyrin nanoassemblies derived from singlet oxygen generation experiments:

$$\Phi_{FRET}^{\Delta} = \frac{(I_{\Delta}^{\Sigma} - I_{\Delta}^A)}{(I_{\Delta}^{DA})_{max}} . \quad (11)$$

Our findings have shown that FRET quantum efficiency is $\Phi_{FRET}^{\Delta} = 0.07 \pm 0.03$ at maximal laser intensity ($E = 18 \mu J/pulse$) and rises up to $\Phi_{FRET}^{\Delta} = 0.12 \pm 0.03$ at lower excitation ($E \leq 4.5 \mu J/pulse$). The decrease of Φ_{FRET}^{Δ} values upon the laser intensity increase is caused by the influence of a non-radiative Auger recombination discussed above.

A principal result is that within the accuracy of the experiment, Φ_{FRET}^{Δ} values evaluated via 1O_2 emission measurements at low laser excitation, are in a good agreement with FRET efficiencies $\Phi_{FRET} = 0.14 \pm 0.02$ found from the direct sensitization data for porphyrin fluorescence in QD-porphyrin nanoassemblies

with molar ratio $x = 4$. The obtained good coincidence of experimental values Φ_{FRET} and $\Phi_{\Delta}^{\text{FRET}}$ (evaluated from principally different experimental approaches) may be considered as a real background permitting to conclude quantitatively that namely FRET process QD \rightarrow porphyrin is a reason of singlet oxygen generation by nanoassemblies under consideration. Thus, the full scheme of the processes leading to singlet oxygen generation by QD-porphyrin nanoassemblies may be presented by the following way:

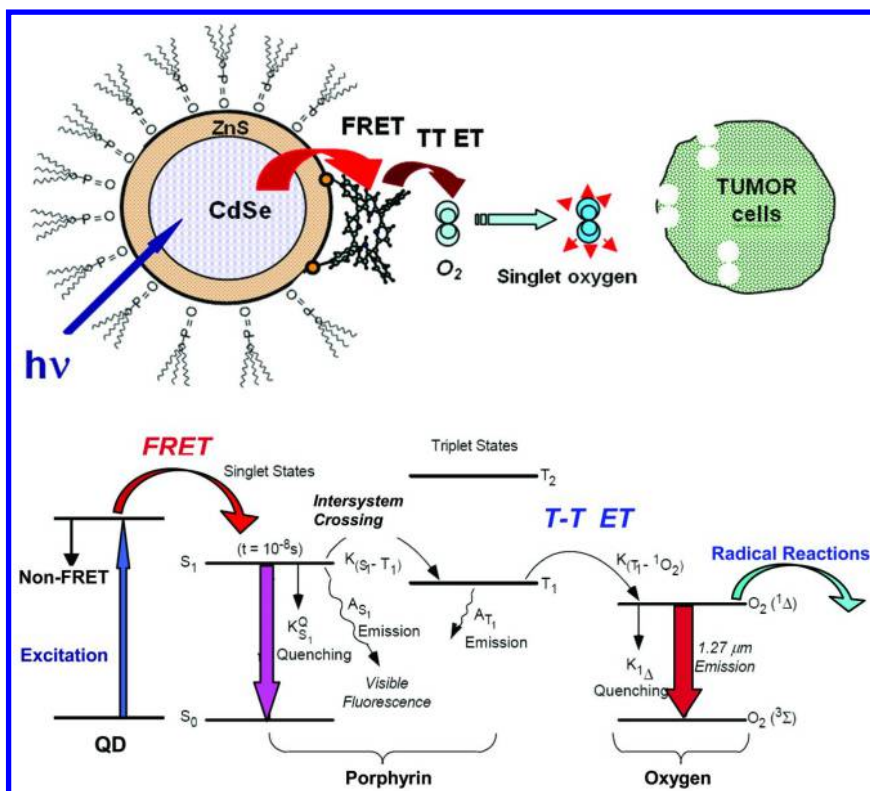


Figure 8. Schematic presentation of singlet oxygen formation (top) and full scheme of energy processes leading to singlet oxygen generation by QD-porphyrin nanoassemblies

To our knowledge, such an approach is a first example showing quantitatively the role of FRET effects in the singlet oxygen generation by QD – PS nanoassemblies. Nevertheless, it should be added also that a good operativity of QD-porphyrin nanoassemblies in potential PDT is connected with a reasonable increase of FRET efficiency and high light harvesting of the PS emission.

Conclusions

Basically, in this Chapter we have described excited states relaxation dynamics for nanoassemblies based on CdSe/ZnS QDs and tetra-meta-pyridyl substituted porphyrins and formed by the self-assembly ligation interactions in liquid solutions. In addition to fundamental results presented here, one of the methodological objectives of this Chapter is to show the reader the basic approaches what should be used to detect and discriminate the reasons of the emission quenching for interacting subunits in organic-inorganic nanoassemblies.

Herein we focused on a quantitative experimental analysis (steady-state and picosecond time-resolve measurements) of QD photoluminescence quenching caused by two main reasons: the electron tunneling in the conditions of quantum confinement (the efficiency of 0.85±0.90) as well FRET QD→porphyrin (the efficiency of 0.10±0.15). In addition, on the basis of near-IR photoluminescence measurements of singlet oxygen 1O_2 emission, we performed a comparative studying the efficiencies of 1O_2 generation by alone QDs and QD-porphyrin nanoassemblies upon variation of the laser pulse energy. It was shown that the experimental efficiencies γ^Δ of 1O_2 generation for QD-porphyrin nanoassemblies are essentially higher than those obtained for alone QDs. Taking into account experimental data and structure of excitonic states for QDs, it was concluded that at ambient temperature most of alone QDs are hardly perspective to the direct generation of singlet oxygen.

Finally, it has been found that FRET efficiencies $\Phi^{\Delta\text{FRET}} = 0.12 \pm 0.03$ obtained via the direct 1O_2 emission measurements at low laser excitation, are in a good coincidence with FRET efficiencies $\Phi_{\text{FRET}} = 0.14 \pm 0.02$ evaluated from the direct sensitization data for porphyrin fluorescence in nanoassemblies. Such quantitative analysis was done for the first time and shows that namely FRET process QD→porphyrin is a reason of singlet oxygen generation by QD-porphyrin nanoassemblies.

Concluding, some perspectives of the presented approach may be described as follows. It is well-known that porphyrin and chlorin derivatives present a variety of photochemical properties that have been much explored to obtain better photosensitizers for the PDT of cancer. Nevertheless, cited references and results discussed in this Chapter raise the hypothesis that QD-porphyrin nanoassemblies have a potential to be photosensitizers of a novel type. Furthermore, the other anchoring conditions (including covalent coupling) may be used in order to diminish the role of non-FRET quenching in QD-PS nanoassemblies. However, our species are not soluble in water, thus limiting biological applications. Having fully characterized these hybrid nanoassemblies in organic solvents, the next step should be devoted to translate these complexes to water. Water-soluble species with high 1O_2 quantum efficiency are critical for artificial biocompatibility materials used as drug delivery carriers and *in vivo* imaging. The other approach may be connected with using other types of water-soluble nanocarriers (quantum dots and quantum rods) and biologically compatible PSs (149), (39), (27, 38), (164), (165) which may be anchored to these carriers. Interestingly, QDs are one of the best energy donors via two-photon excitation (TPE), which possess a large two-photon absorption (TPA) cross section and the wavelength of the

maximum TPA can be adjusted via changing the size of the QDs (166, 167). In this respect, biocompatible CdSe QD-porphyrin nanoassemblies are capable to not only effective generation of singlet oxygen for PDT through TPE of the QDs by energy transfer, but are also considered as good candidates for “see and treat” PDT in live cell imaging when controlling the molar ratio of dye quenching QDs (43) or may be used for oxygen sensing over physiological oxygen ranges (45).

Acknowledgments

This work was funded by the Volkswagen Foundation (Priority Program “Physics, Chemistry and Biology with Single Molecules”), the German Science Foundation (Graduate College 826 “Accumulation of Single Molecules to Nanostructures”), the Belarussian State Programs for Scientific Research “Convergence 3.2.08 – Photophysics of Bioconjugates, Semiconductor and Metallic Nanostructures and Supramolecular Complexes and Their Biomedical Applications” as well as the Belarussian Foundation for Fundamental Research – Grant № Ф10CO-005 « Development and Studying Physico-Chemical Properties of Composite Materials Based on Semiconductor Nanocrystals and Functional Organic Ligands” and BRFRR Grant No. Ф10CO-005.

Tetra-meso-pyridyl substituted porphyrin has been synthesized and characterized by Dr. A.M. Shulga (B.I. Stepanov Institute of Physics, National Academy of Sciences, Minsk, Belarus). We thank Prof. Dr. S.V. Gaponenko (B.I. Stepanov Institute of Physics, National Academy of Sciences, Minsk, Belarus) for fruitful discussion. This review Chapter is in part based on experimental results contributed by Dr. Th. Blaudeck (Chemnitz University of Technology), Prof. F. Cichos (Leipzig University, Germany), Dr. E. Petrov (Dresden University of Technology, Germany) as well Dr. Habil. E.I. Sagun, Dr. V.N. Knyukshto, Dr. A.S. Stasheuski, Dr. V.A. Galievsky, and Dr. A.P. Stupak (B.I. Stepanov Institute of Physics, National Academy of Sciences, Minsk, Belarus).

References

1. Haghi, A. K.; Thomas, S.; Pourhashemi, A.; Hamrang, A.; Kłodzinska, E. *Nanomaterials and Nanotechnology for Composites: Design, Simulation and Applications*; Apple Academic Press: Waretown, NJ, 2015; 450 p.
2. Mello Donegá, C. *Nanoparticles*; Springer-Verlag: Berlin Heidelberg, 2014.
3. Rogers, B.; Adams, J.; Pennathur, S. *Nanotechnology: Understanding Small Systems*; Series: Mechanical and Aerospace Engineering; CRC Press: Boca Raton, 2014; 427 p.
4. *Springer Handbook of Nanomaterials*; Vajtai, R., Ed.; Springer-Verlag: Berlin-Heidelberg, 2013.
5. *Semiconductor Nanocrystal Quantum Dots: Synthesis, Assembly, Spectroscopy and Applications*; Rogach A. L., Ed.; Springer-Verlag: Wien, 2008.

6. Gur, L.; Fromer, N. A.; Chen, C.-P.; Kanaras, A. G.; Alivisatos, A. P. Hybrid Solar Cells with Prescribed Nanoscale Morphologies Based on Hyperbranched Semiconductor Nanocrystals. *Nano Lett.* **2007**, *7*, 409–411.
7. Liu, L.; Hensel, J.; Fitzmorris, R. C.; Li, Y.; Zhang, J. Z. Preparation and Photoelectrochemical Properties of CdSe/TiO₂ Hybrid Mesoporous Structures. *J. Phys. Chem. Lett.* **2010**, *1*, 155–160.
8. Etgar, L.; Park, J.; Barolo, C.; Nazeeruddin, Md. K.; Viscardi, G.; Graetzel, M. Design and Development of Novel Linker for PbS Quantum Dots/TiO₂ Mesoscopic Solar Cell. *ACS Appl. Mater. Interfaces* **2011**, *3*, 3264–3267.
9. Coe-Sullivan, S.; Woo, W. -K.; Steckel, J. S.; Bawendi, M.; Bulovic, V. Tuning the performance of hybrid organic/inorganic quantum dot light-emitting devices. *Org. Electron.* **2003**, *4*, 123–130.
10. Baldenebro-Lopez, J.; Flores-Holguin, N.; Castorena-Gonzalez, J.; Glossman-Mitnik, D.; Adegoke, O.; Nyokong, T. Molecular design of copper complexes as sensitizers for efficient dye-sensitized solar cells. *J. Photochem. Photobiol., A* **2013**, *267*, 58–66.
11. Kovalenko, M. V.; Manna, L.; Cabot, A.; Hens, Z.; Talapin, D. V.; Kagan, C. R.; Klimov, V. I.; Rogach, A. L.; Reiss, P.; Milliron, D. J.; Guyot-Sionnest, P.; Konstantatos, G.; Parak, W. J.; Hyeon, T.; Korgel, B. A.; Murray, C. B.; Heiss, W. Prospects of Nanoscience with Nanocrystals. *ACS Nano* **2015**, *9*, 1012–1057.
12. Gaponenko, S. V. *Introduction to Nanophotonics*; Cambridge University Press: Cambridge, 2010.
13. Nicolini, C. In *Nanotechnology and Nanobiosciences*; Series on Nanobiotechnology; Pan Stanford Publishing: Stanford, CA, 2010; Vol. 1, Chapter 1.
14. Klimov, V. *Nanocrystal Quantum Dots*; CRS Press LLC: Washington, 2010; p 410.
15. Schmitt, F. -J.; Maksimov, E. G.; Suedmeyer, H.; Jeyasangar, V.; Theiss, C.; Paschenko, V. Z.; Eichler, H. J.; Renger, G. Time resolved temperature switchable excitation energy transfer processes between CdSe/ZnS nanocrystals and phycobiliprotein antenna from *Acaryochloris marina*. *Photonics Nanostruct. Fundam. Appl.* **2011**, *9*, 190–195.
16. Frasco, M. F.; Chaniotakis, N. Semiconductor quantum dots in chemical sensors and biosensors. *Sensors* **2009**, *9*, 7266–7286.
17. Jin, Z.; Hildebrandt, N. Quantum dot nanoparticles for *in vitro* sensing. *Front. Nanosci.* **2012**, *4*, 291–306.
18. Lemon, C. M.; Curtin, P. N.; Somers, R. C.; Greytak, A. B.; Lanning, R. M.; Jain, R. K.; Bawendi, M. G.; Nocera, D. G. Metabolic Tumor Profiling with pH, Oxygen, and Glucose Chemosensors on a Quantum Dot Scaffold. *Inorg. Chem.* **2014**, *53*, 1900–1915.
19. Hadar, I.; Halivni, S.; Even-Dar, N.; Faust, A.; Banin, U. Dimensionality Effects on Fluorescence Resonance Energy Transfer between Single Semiconductor Nanocrystals and Multiple Dye Acceptors. *J. Phys. Chem. C* **2015**, *119*, 3849–3856.

20. Vo-Dinh, T. *Nanotechnology in Biology and Medicine: Methods, Devices, and Applications*; CRC Press: Boca Raton, 2007; 792 p.
21. Shatkin, J. A. *Nanotechnology: Health and Environmental Risks*, 2nd ed.; Perspectives in Nanotechnology; CRC Press: Boca Raton, 2012; 284 p.
22. Mattossi, H.; Palui, G.; Na, H. B. Luminescent quantum dots as platforms for probing in vitro and in vivo biological processes. *Adv. Drug Delivery Rev.* **2012**, *64* (2), 138–166.
23. Ji, X.; Makarov, N. S.; Wang, W.; Palui, G.; Robel, I.; Mattossi, H. Tuning the Redox Coupling between Quantum Dots and Dopamine in Hybrid Nanoscale Assemblies. *J. Phys. Chem. C* **2015**, *119*, 3388–3399.
24. Knowles, K. E.; Frederick, M. T.; Tice, D. B.; Morris-Cohen, A. J.; Weiss, E. A. Colloidal Quantum Dots: Think Outside the (Particle-in-a-)Box. *J. Phys. Chem. Lett.* **2012**, *3*, 18–26.
25. Cheng, Y.; Burda, C. Nanoparticles for Photodynamic Therapy. In *Nanoscience and Technology*; Elsevier: London, 2010.
26. Moyano, D. F.; Goldsmith, M.; Solfield, D. J.; Landesman-Milo, D.; Miranda, O. R.; Peer, D.; Rotello, V. M. Nanoparticle Hydrophobicity Dictates Immune Response. *J. Am. Chem. Soc.* **2012**, *134*, 3965–3967.
27. Rakovich, A.; Savateeva, D.; Rakovich, T.; Donegan, J. F.; Rakovich, Y. P.; Kelly, V.; Lesnyak, V.; Eychmueller, A. CdTe Quantum Dot/Dye Hybrid System as Photosensitizer for Photodynamic Therapy. *Nanoscale Res. Lett.* **2010**, *5*, 753–760.
28. Mocatta, D.; Cohen, G.; Schattner, J.; Millo, O.; Rabani, E.; Banin, U. Heavily doped semiconductor nanocrystal quantum dots. *Science* **2011**, *332*, 77–81.
29. M.-X. Zhao, M.-X.; Zeng, E.-Z. E.-Z. Application of functional quantum dot nanoparticles as fluorescence probes in cell labeling and tumor diagnostic imaging. *Nanoscale Res. Lett.* **2015**, *10*, 171.
30. Guo, W.; Sun, X.; Jacobson, O.; Yan, X.; Min, K.; Srivatsan, A.; Niu, G.; Kiesewetter, D. O.; Chang, J.; Chen, X. Intrinsically Radioactive [64Cu]CuInS/ZnS Quantum Dots for PET and Optical Imaging: Improved Radiochemical Stability and Controllable Cherenkov Luminescence. *ACS Nano* **2015**, *9*, 488–495.
31. Whitesides, G. M.; Grzybowski, B. Self-assembly at all scales. *Science* **2002**, *295*, 2418–2421.
32. Lehn, J.-M. Perspectives in supramolecular chemistry – from molecular recognition towards molecular information-processing and self-organization. *Angew. Chem., Int. Ed. Engl.* **1990**, *29*, 1304–1319.
33. Murcia, M. J.; Naumann, C. A. In *Nanotechnologies for the Life Sciences*; Kumar, C. R., Ed.; Willey-VCH Verlag GmbH & Co. KGaA: Weinheim, 2005; Vol. 1, pp 1–40.
34. Benyettou, I.; Milosevic, Y.; Lalatonne, F.; Warmont, R.; Assah, J.-C.; Olsen, M.; Jouaid, L.; Motte, C.; Platas-Iglesias, A.; Trabolsi, F. Toward theranostic nanoparticles: CB[7]-functionalized iron oxide for drug delivery and MRI. *J. Mater. Chem. B* **2013**, *1*, 5076–5082.
35. Bakalova, R.; Ohba, H.; Zhelev, Z.; Nagase, T.; Jose, R.; Ishikawa, M.; Baba, Y. Quantum Dot Anti-CD Conjugates: Are They Potential

Photosensitizers or Potentiators of Classical Photosensitizing Agents in Photodynamic Therapy of Cancer? *Nano Lett.* **2004**, *4*, 1567–1573.

36. Samia, A. C. S.; Dayal, S.; Burda, C. Quantum dot-based energy transfer: perspectives and potential for applications in photodynamic therapy. *Photochem. Photobiol.* **2006**, *82*, 617–625.
37. Ma, J.; Chen, J.-Y.; Idowu, M.; Nyokong, T. Generation of Singlet Oxygen via the Composites of Water-Soluble Thiol-Capped CdTe Quantum Dots-Sulfonatedaluminum Phthalocyanines. *J. Phys. Chem. B* **2008**, *112*, 4465–4469.
38. Rakovich, A.; Rakovich, T.; Kelly, V.; Lesnyak, V.; Eychmuller, A.; Rakovich, Y. P.; Donegan, J. F. Photosensitizer methylene blue–semiconductor nanocrystals hybrid system for photodynamic therapy. *J. Nanosci. Nanotechnol.* **2010**, *10*, 2656–2662.
39. Tsay, J. M.; Trzoss, M.; Shi, L.; Kong, X.; Selke, M.; Jung, M. E.; Weiss, S. Singlet Oxygen Production by Peptide-Coated Quantum Dot-Photosensitizer Conjugates. *J. Am. Chem. Soc.* **2007**, *129*, 6865–6871.
40. Juzenas, P.; Chen, W.; Sun, Y. P.; Coelho, M. A. N.; Generalov, R.; Generalova, N.; Christensen, I. L. Quantum dots and nanoparticles for photodynamic and radiation therapies of cancer. *Adv. Drug Delivery Rev.* **2008**, *60*, 1600–1614.
41. Kang, S.; Yasuda, M.; Miyasaka, H.; Umeyama, T.; Matano, Y.; Yoshida, K.; Isoda, S.; Imahori, H. Multiporphyrin-modified CdSe nanoparticles as efficient light-harvesting materials. *ChemSusChem* **2008**, *1*, 254–261.
42. Zenkevich, E. I.; Sagun, E. I.; Knyuksho, V. N.; Stasheuski, A. S.; Galievsky, V. A.; Stupak, A. P.; Blaudeck, T.; von Borczyskowski, C. Quantitative Analysis of Singlet Oxygen (${}^1\text{O}_2$) Generation via Energy Transfer in Bioconjugates Based on Semiconductor Quantum Dots and Porphyrin Ligands. *J. Phys. Chem. C* **2011**, *115*, 21535–21545.
43. Qi, Z.-D.; Li, D.-W.; Jiang, P.; Jiang, F.-L.; Li, Y.-S.; Liu, Y.; Wong, W.-K.; Chean, K.-W. Biocompatible CdSe quantum dot-based photosensitizer under two-photon excitation for photodynamic therapy. *J. Mater. Chem.* **2011**, *21*, 2455–2458.
44. Zenkevich, E. I.; Gaponenko, S. V.; Sagun, E. I.; von Borczyskowski, C. Bioconjugates based on semiconductor quantum dots and porphyrin ligands: properties, exci-ton relaxation pathways and singlet oxygen generation efficiency for PDT applications. *Rev. Nanosci. Nanotechnol.* **2013**, *2*, 184–207.
45. Lemon, C. M.; Karnas, E.; Bawendi, M. G.; Nocera, D. G. Two-Photon Oxygen Sensing with Quantum Dot-Porphyrin Conjugates. *Inorg. Chem.* **2013**, *52*, 10394–10406.
46. Zhdanova, K. A.; Bragina, N. A.; Bagratashvili, V. N.; Timashev, P. S.; Mironov, A. F. Noncovalent assemblies of CdSe semiconductor quantum dots and an amphiphilic long-chain meso-arylporphyrin. *Mendeleev Commun.* **2014**, *24*, 247–249.
47. Dougherty, T. J.; Gomer, C. J.; Henderson, B. W.; Jori, G.; Kessel, D.; Korbelik, M.; Moan, J.; Peng, Q. Photodynamic therapy. *J. Natl. Cancer Inst.* **1998**, *90*, 889–905.

48. *Biomedical Photonics Handbook*; Vo-Dinh, T., Ed.; CRC Press LLC: New York, 2003; pp 1872.
49. Zenkevich, E. I.; Sagun, E. I.; Knyukshto, V. N.; Shulga, A. M.; Mironov, A. F.; Efremova, O. A.; Bonnett, R.; Songca, S. P.; Kassem, M. M. Photophysical and photochemical properties of potential porphyrin and chlorin photosensitizers for PDT. *J. Photochem. Photobiol. B* **1996**, *33*, 171–180.
50. DeRosa, M. C.; Crutchley, R. J. Photosensitized singlet oxygen and its applications. *Coord. Chem. Rev.* **2002**, *233*, 351–371.
51. Gomer, C.; Ferrario, A. Tissue distribution and photosensitizing properties of mono-l-aspartyl chlorin e₆ in a mouse tumor model. *Cancer Res.* **1990**, *50*, 3985–3990.
52. Mironov A. F. Modern state of chemistry of photosensitizers on the base of porphyrins and related compounds. In *Successes of Chemistry of Porphyrins*; Golubchikov, O. A., Ed.; St-Petersburg University: St. Petersburg, Russia; 2004. Vol. 4, pp 271–291.
53. Isakau, H.; Parkhats, M.; Knyukshto, V.; Dzhagarov, B.; Petrov, E.; Petrov, P. Toward understanding the high PDT efficacy of chlorine e₆–polyvinylpyrrolidone formulations: photophysical and molecular aspects of photosensitizer–polymer interaction in vitro. *J. Photochem. Photobiol. B* **2008**, *92*, 165–174.
54. Pandey, R.; Zheng, G. Porphyrins as photosensitizers in photodynamic therapy. In *The Porphyrin Handbook*; Kadish, K. M., Smith, K. M., Guilard, R., Eds.; Academic Press: San Diego, 2000; Vol. VI, Chapter 43, pp 157–230.
55. Nyman, E.; Hynninen, P. Research advances in the use of tetrapyrrolic photosensitizers for photodynamic therapy. *J. Photochem. Photobiol. B* **2004**, *73*, 1–28.
56. Michalet, X.; Pinaud, F.; Bentolila, L.; Tsay, J.; Doose, S.; Li, J.; Sundaresan, G.; Wu, A.; Gambhir, S.; Weiss, S. Quantum dots for live cells, in vivo imaging, and diagnostics. *Science* **2005**, *307*, 538–544.
57. Bruchez, M.; Moronne, M.; Gin, P.; Weiss, S.; Alivisatos, A. P. Semiconductor nanocrystals as fluorescent biological labels. *Science* **1998**, *281*, 2013–2016.
58. Skrabalak, S. E.; Chen, J.; Sun, Y.; Lu, X.; Au, L.; Cobley, L. M.; Xia, Y. Gold Nanocages: Synthesis, Properties, and Applications. *Acc. Chem. Res.* **2008**, *41*, 1587–1595.
59. Frasco, M. F.; Vamvakaki, V.; Chaniotakis, N. Porphyrin decorated CdSe quantum dots for direct fluorescent sensing of metal ions. *J. Nanopart. Res.* **2010**, *12*, 1449–1458.
60. McDowell, M.; Wright, A. E.; Hammer, N. I. Semiconductor nanocrystals hybridized with functional ligands: new composite materials with tunable properties. *Materials* **2010**, *3*, 614–637.
61. Samia, A. C. S.; Chen, X.; Burda, C. Semiconductor Quantum Dots for Photodynamic Therapy. *J. Am. Chem. Soc.* **2003**, *125*, 15736–15737.

62. Shi, L.; Hernandez, B.; Selke, M. Singlet Oxygen Generation from Water-Soluble Quantum Dot-Organic Dye Nanocomposites. *J. Am. Chem. Soc.* **2006**, *128*, 6278–6279.

63. Wang, S.; Gao, R.; Zhou, F.; Selke, M. Nanomaterials and singlet oxygen photosensitizers: potential applications in photodynamic therapy. *J. Mater. Chem.* **2004**, *14*, 487–493.

64. Ginger, D. S.; Greenham, N. C. Photoinduced electron transfer from conjugated polymers to CdSe nanocrystals. *Phys. Rev. B* **1999**, *59*, 10622–10629.

65. Anni, M.; Manna, L.; Cigolani, R.; Valerini, D.; Creti, A.; Lomascolo, M. Förster energy transfer from blue-emitting polymers to colloidal CdSe/ZnS core shell quantum dots. *Appl. Phys. Lett.* **2004**, *85*, 4169–4171.

66. Sykora, M.; Petruska, M.; Alstrum-Acevedo, J.; Bezel, I.; Meyer, T.; Klimov, V. Photoinduced Charge Transfer between CdSe Nanocrystal Quantum Dots and Ru-Polypyridine Complexes. *J. Am. Chem. Soc.* **2006**, *128*, 9984–9985.

67. Potapova, I.; Mruk, R.; Hübner, C.; Zentel, R.; Basché, T.; Mews, A. CdSe/ZnS nanocrystals with dye-functionalized polymer ligands containing many anchor groups. *Angew. Chem.* **2005**, *117*, 2490–2493.

68. Clapp, A.; Medintz, I.; Mauro, J.; Fisher, B.; Bawendi, M.; Mattoussi, H. Fluorescence Resonance Energy Transfer between Quantum Dot Donors and Dye-Labeled Protein Acceptors. *J. Am. Chem. Soc.* **2004**, *126*, 301–310.

69. Morris-Cohen, A.; Donakowski, M. D.; Knowles, K.; Weiss, E. The Effect of a Common Purification Procedure on the Chemical Composition of the Surfaces of CdSe Quantum Dots Synthesized with Trioctylphosphine Oxide (TOPO). *J. Phys. Chem. C* **2010**, *114*, 897–906.

70. Orlova, A.; Gubanova, M.; Maslov, V.; Vinogradova, G.; Baranov, A.; Fedorov, A.; Gounko, L. Spectro-luminescent properties of the complexes formed by charged CdTe quantum dots and molecules of the tetrasulfophthalocyanin. *Optika i Spectroscopiya (in Russian)*. **2010**, *108*, 975–982.

71. Alivisatos, A. The use of nanocrystals in biological detection. *Nat. Biotechnol.* **2004**, *22*, 47–52.

72. Blaudeck, T.; Zenkevich, E. I.; Cichos, F.; von Borczyskowski, C. Probing Wave Functions at Semiconductor Quantum-Dot Surfaces by NON-FRET Photoluminescence Quenching. *J. Phys. Chem. C* **2008**, *112*, 20251–20257.

73. Zenkevich, E. I.; Stupak, A. P.; Kowerko, D.; von Borczyskowski, C. Influence of single dye molecules on temperature and time dependent optical properties of CdSe/ZnS quantum dots: ensemble and single nanoassembly detection. *Chem. Phys.* **2012**, *406*, 21–29.

74. Kowerko, D.; Krause, S.; Amecke, N.; Abdel-Mottaleb, M.; Schuster, J.; von Borczyskowski, C. Identification of different donor-acceptor structures via FRET in quantum-dot-perylene bisimide assemblies. *Int. J. Mol. Sci.* **2009**, *10*, 5239–5256.

75. Zenkevich, E.; Stupak, A.; Göhler, C.; Krasselt, C.; von Borczyskowski, C. Tuning Electronic States of a CdSe/ZnS Quantum Dot by Only One Functional Dye Molecule. *ACS Nano* **2015**, *9*, 2886–2903.

76. Empedocles, S. A.; Bawendi, M. G. Influence of Spectral Diffusion on the Line Shapes of Single CdSe Nanocrystallite Quantum Dots. *J. Phys. Chem. B* **1999**, *103*, 1826–1830.

77. Yu, W. W.; Wang, Y. A.; Peng, X. Formation and stability of size-, shape-, and structure-controlled CdTe nanocrystals: ligand effects on monomers and nanocrystals. *Chem. Mater.* **2003**, *15*, 4300–4308.

78. Müller, J.; Lupton, J. M.; Rogach, A. L.; Feldmann, J.; Talapin, D. V.; Weller, H. Monitoring surface charge migration in the spectral dynamics of single CdSe/CdS nanodot/nanorod heterostructures. *Phys. Rev. B* **2005**, *72*, 205339.

79. Gomez, D. E.; van Embden, J.; Mulvaney, P. Spectral diffusion of single semiconductor nanocrystals: the influence of the dielectric environment. *Appl. Phys. Lett.* **2006**, *88*, 154106.

80. Munro, A. M.; Ginger, D. S. Photoluminescence Quenching of Single Nanocrystals by Ligand Adsorption. *Nano Lett.* **2008**, *8*, 2585–2590.

81. Ji, X.; Copenhaver, D.; Sichmeller, C.; Peng, X. Ligand Bonding and Dynamics on Colloidal Nanocrystal at Room Temperature: The Case of Alkylamines on CdSe Nanocrystals. *J. Am. Chem. Soc.* **2008**, *130*, 5726–5735.

82. Smith, A. M.; Nie, S. Semiconductor nanocrystals: structure, properties, and band gap engineering. *Acc. Chem. Res.* **2010**, *43*, 190–200.

83. Fernee, M. J.; Plakhotnik, T.; Louyer, Y.; Littleton, B. N.; Potzner, C.; Tamarat, P.; Mulvaney, P.; Lounis, B. Spontaneous Spectral Diffusion in CdSe Quantum Dots. *J. Phys. Chem. Lett.* **2012**, *3*, 1716–1720.

84. Cui, J.; Beyler, A. P.; Bischof, T. S.; Wilson, M. W. B.; Bawendi, M. G. Deconstructing the photon stream from single nanocrystals: from binning to correlation. *Chem. Soc. Rev.* **2014**, *43*, 1287–1310.

85. Brown, P. R.; Kim, D.; Lunt, R. R.; Zhao, N.; Bawendi, M. G.; Grossman, J. C.; Bulovic, V. Energy Level Modification in Lead Sulfide Quantum Dot Thin Films through Ligand Exchange. *ACS Nano* **2014**, *8*, 5863–5872.

86. Leatherdale, C.; Bawendi, M. *Phys. Rev. B: Condens. Matter Mater. Phys.* **2001**, *B 63*, 165311–165315.

87. Puzder, A.; Williamson, A. J.; Zaitseva, N.; Galli, G.; Manna, L.; Alivisatos, A. P. The Effect of Organic Ligand Binding on the Growth of CdSe Nanoparticles Probed by Ab Initio Calculations. *Nano Lett.* **2004**, *4*, 2361–2365.

88. Rempel, J. Y.; Trout, B. L.; Bawendi, M. G.; Jensen, K. F. Density Functional Theory of Ligand Binding on CdSe (0001), (000 $\bar{1}$), and (11 $\bar{2}$ 0) Single Crystal Relaxed and Reconstructed Surfaces: Implications for Nanocrystalline Growth. *J. Phys. Chem. B* **2006**, *110*, 18007–18016.

89. Frenzel, J.; Joswig, J. O.; Seifert, G. Optical Excitations in Cadmium Sulfide Nanoparticles. *J. Phys. Chem. C* **2007**, *111*, 10761–10770.

90. Gomez-Campos, F. M.; Califano, M. Hole Surface Trapping in CdSe Nanocrystals: Dynamics, Rate Fluctuations, and Implications for Blinking. *Nano Lett.* **2012**, *12*, 4508–4517.

91. Califano, M.; Gómez-Campos, F. M. Universal Trapping Mechanism in Semiconductor Nanocrystals. *Nano Lett.* **2013**, *13*, 2047–2052.

92. Kilin, D. S.; Tsemekham, K.; Zenkevich, E. I.; Prezho, O. V.; von Borczyskowski, C. Ab initio study of transfer dynamics from a core-shell semiconductor quantum dot to a porphyrin sensitizer. *J. Photochem. Photobiol. A* **2007**, *190*, 342–351.

93. Kilina, S. V.; Ivanov, S.; Tretiak, S. Effect of Surface Ligands on Optical and Electronic Spectra of Semiconductor Nanoclusters. *J. Am. Chem. Soc.* **2009**, *131*, 7717–7726.

94. Kilina, S.; Velizhanin, K. A.; Ivanov, S.; Prezhdo, O. V.; Tretiak, S. Surface Ligands Increase Photoexcitation Rates in CdSe Quantum Dots. *ACS Nano* **2012**, *6*, 6515–6524.

95. Fischer, S. A.; Crotty, A. M. M.; Kilina, S. V.; Ivanov, S. A.; Tretiak, S. Passivating ligand and solvent contributions to the electronic properties of semiconductor nanocrystals. *Nanoscale* **2012**, *4*, 904–914.

96. Voznyy, O.; Sargent, E. H. Atomistic model of fluorescence intermittency of colloidal quantum dots. *Phys. Rev. Lett.* **2014**, *112*, 157401.

97. Frantsuzov, P. A.; Volkán-Kacscó, S.; Jankó, B. Universality of the Fluorescence Intermittency in Nanoscale Systems: Experiment and Theory. *Nano Lett.* **2013**, *13*, 402–408.

98. Schmidt, R.; Krasselt, C.; Göhler, C.; von Borczyskowski, C. The Fluorescence Intermittency for Quantum Dot Is Not Power-Law Distributed: A Luminescence Intensity Resolved Approach. *ACS Nano* **2014**, *8*, 3506–3521.

99. Derfus, A. M.; Chan, W. C. W.; Bhatia, S. N. Probing the cytotoxicity of semiconductor quantum dots. *Nano Lett.* **2004**, *4*, 11–18.

100. Zenkevich, E.; Cichos, F.; Shulga, A.; Petrov, E.; Blaudeck, T.; von Borczyskowski, C. Nanoassemblies designed from semiconductor quantum dots and molecular arrays. *J. Phys. Chem. B* **2005**, *109*, 8679–8692.

101. Dayal, S.; Krolycki, R.; Lou, Y.; Qiu, X.; Berlin, J. C.; Kenney, M. E.; Burda, C. Femtosecond time-resolved resonance energy transfer from CdSe nanoparticles to phthalocyanines. *Appl. Phys. B* **2006**, *84*, 309–315.

102. Zhang, X.; Liu, Z.; Ma, L.; Hossu, M.; Chen, W. Interaction of porphyrins with CdTe quantum dots. *Nanotechnology* **2011**, *22*, 195501.

103. Zenkevich, E. I.; Sagun, E. I.; Yarovoi, A. A.; Shulga, A. M.; Knyukshto, V. N.; Stupak, A. P.; von Borczyskowski, C. Photoinduced relaxation processes in complexes based on semiconductor nanocrystals CdSe and organic molecules. *Optika i Spectroscopiya (in Russian)*. **2007**, *103*, 998–1009.

104. Zenkevich, E. I.; Blaudeck, T.; Shulga, A. M.; Cichos, F.; von Borczyskowski, C. Identification and assignment of porphyrin-CdSe heteronanoassemblies. *J. Lumin.* **2007**, *122-123*, 784–788.

105. Lihitkar, N. B.; Singh, S. B.; Singh, J.; Srivastava, O. N.; Naik, R. H.; Kulkarni, S. K. Optical investigations of interaction between zinc tetra phenyl porphyrin and CdSe nanoparticles. *Chem. Phys. Lett.* **2009**, *483*, 227–232.

106. Jhonsi, M. A.; Rengnathan, R. Study on the photoinduced interaction between TGA capped CdTe quantum dots and certain porphyrins by using spectroscopic techniques. *J. Colloid Interface Sci.* **2010**, *344*, 596–602.

107. Maslov, V.; Orlova, A.; Baranov, A. Combination therapy: complexing of Qds with tetrapyrrolics and other dyes. In *Photosensitizers in Medicine, Environment, and Security*; Springer-Verlag: New York, 2012; 57 p.
108. Shibu, E. S.; Hamada, M.; Murase, N.; Biju, V. Nanomaterials formulations for photothermal and photodynamic therapy of cancer. *J. Photochem. Photobiol., C* **2013**, *15*, 53–72.
109. Oluwole, D. O.; Britton, J.; Mashazi, P.; Nyokong, T. Synthesis and photophysical properties of nanocomposites of aluminum tetrasulfonated phthalocyanine covalently linked to glutathione capped CdTe/CdS/ZnS quantum dots. *Synth. Met.* **2015**, *205*, 212–221.
110. Zenkevich, E.; von Borczyskowski, C. Photoinduced relaxation processes in self-assembled nanostructures: multiporphyrin complexes and composites “CdSe/ZnS quantum dot-porphyrin”. *Macroheterocycles* **2009**, *2*, 206–220.
111. Zenkevich, E. I.; von Borczyskowski, C. Self-organization principles in the formation of multiporphyrin complexes and “semiconductor quantum dot-porphyrin” nanoassemblies. *J. Porphyrins Phthalocyanines* **2014**, *18*, 1–19.
112. Blaudeck, Th. Self-Assembly of functionalized porphyrin molecules on semiconductor nanocrystal surfaces. Ph.D. Thesis, TU Chemnitz, Chemnitz, Germany, 2007.
113. Blaudeck, T.; Zenkevich, E.; Abdel-Mottaleb, M.; Szwakowska, K.; Kowerko, D.; Cichos, F.; von Borczyskowski, C. Formation principles and ligand dynamics for nanoassemblies of CdSe quantum dots and functionalized dye molecules. *ChemPhysChem* **2012**, *13*, 959–972.
114. Borczyskowski von, C.; Zenkevich, E. Formation principles and exciton relaxation in semiconductor quantum dot - dye nanoassemblies. In *Quantum Dot Molecules, Lecture Notes in Nanoscale Science and Technology 14*; Springer Series in Materials Science; Wu, J., Wang, Z. M., Eds.; Springer Science+Business Media: New York, 2014; Vol. 14 pp 77–148.
115. Sagun, E. I.; Zenkevich, E. I.; Knyukshto, V. N.; Shulga, A. M.; Starukhin, D. A.; von Borczyskowski, C. Interaction of multiporphyrin systems with molecular oxygen in liquid solutions: extra-ligation and screening effects. *Chem. Phys.* **2002**, *275*, 211–237.
116. Petrov, E. P.; Cichos, F.; Zenkevich, E.; Starukhin, D.; von Borczyskowski, C. Time resolved photoluminescence anisotropy of CdSe/ZnS nanoparticles in toluene at 300 K. *Chem. Phys. Lett.* **2005**, *402*, 233–238.
117. Petrov, E. P.; Cichos, F.; von Borczyskowski, C. Intrinsic photophysics of semiconductor nanocrystals in dielectric media: formation of surface states. *J. Lumin.* **2006**, *119-120*, 412–417.
118. Zenkevich, E.; von Borczyskowski, C. W. Formation principles and excited states relaxation in self-assembled complexes: multiporphyrin arrays and “semiconductor CdSe/ZnS quantum dot-porphyrin” nanocomposites. In *Handbook of Porphyrin Science with Application to Chemistry, Physics, Materials Science, Engineering, Biology and Medicine*; Kadish, K., Smith, K. M., Guilard, R., Eds.; World Scientific Publishing Co. Pte. Ltd.: Singapore, 2012; Vol 22, Chapter 104, pp 68–159.

119. Schmelz, O.; Mews, A.; Basché, T.; Herrmann, A.; Müllen, K. Supramolecular Complexes from CdSe Nanocrystals and Organic Fluorophor. *Langmuir* **2001**, *17*, 2861–2865.

120. Boulesba, A.; Issac, A.; Stockwell, D.; Huang, Z.; Huang, J.; Guo, J.; Lian, T. Ultrafast Charge Separation at CdS Quantum Dot/Rhodamine B Molecule Interface. *J. Am. Chem. Soc.* **2007**, *129*, 15132–15133.

121. Issac, A.; Jin, S.; Lian, T. Intermittent Electron Transfer Activity From Single CdSe/ZnS Quantum Dots. *J. Am. Chem. Soc.* **2008**, *130*, 11280–11281.

122. Lutich, A. A.; Jiang, G.; Susha, A. S.; Rogach, A. L.; Stefani, F. D.; Feldmann, J. Energy Transfer versus Charge Separation in Type-II Hybrid Organic–Inorganic Nanocomposites. *Nano Lett.* **2009**, *9*, 2636–2640.

123. Boldt, K.; Jander, S.; Hoppe, K.; Weller, H. Characterization of the Organic Ligand Shell of Semiconductor Quantum Dots by Fluorescence Quenching Experiments. *ACS Nano* **2011**, *5*, 8115–8123.

124. Ji, X.; Wang, W.; Mattoussi, H. Effects of separation distance on the charge transfer interactions in quantum dot-dopamine assemblies. *Phys. Chem. Chem. Phys.* **2015**, *17*, 10108–10117.

125. Clapp, A. R.; Medintz, I. L.; Fisher, B. R.; Anderson, G. P.; Mattoussi, H. Can Luminescent Quantum Dots Be Efficient Energy Acceptors with Organic Dye Donors? *J. Am. Chem. Soc.* **2005**, *127* (4), 1242–1250.

126. Roy, R.; Hohng, S.; Ha, T. A practical guide to single-molecule FRET. *Nat. Methods* **2008**, *5*, 507–516.

127. Basche, T.; Bottin, A.; Li, C.; Müllen, K.; Kim, J.-H.; Sohn, B.-H.; Prabhakaran, P.; Lee, K.-S. Energy and charge transfer in nanoscale hybrid materials. *Macromol. Rapid Commun.* **2015**, *36*, 1026–1046.

128. Lee, J.; Kim, H.-J.; Cheng, T.; Lee, K.; Kim, Ki-S.; Glotzer, S. C.; Kim, J.; Kotov, N. A. Control of Energy Transfer to CdTe Nanowires via Conjugated Polymer Orientation. *J. Phys. Chem. C* **2009**, *113*, 109–116.

129. Kowerko, D.; Schuster, J.; Amecke, N.; Abdel-Mottaleb, M.; Dobrawa, R.; Wuerthner, F.; von Borczyskowski, C. FRET and ligand related NON-FRET processes in single quantum dot-perylene bisimide assemblies. *Phys. Chem. Chem. Phys.* **2010**, *12*, 4112–4123.

130. Gerlach, F.; Täuber, D.; von Borczyskowski, C. Correlated blinking via time dependent energy transfer in single CdSe quantum dot-dye nanoassemblies. *Chem. Phys. Lett.* **2013**, *572*, 90–99.

131. Beane, G.; Boldt, K.; Kirkwood, N.; Mulvaney, P. Energy Transfer between Quantum Dots and Conjugated Dye Molecules. *J. Phys. Chem. C* **2014**, *118*, 18079–18086.

132. Zenkevich, E.; Shulga, A.; Chernook, A.; Gurinovich, G. Migration of energy of electronic excitation in the chemical dimers of the cyclopentaneporphyrins. *J. Appl. Spectr.* **1986**, *45*, 984–991.

133. Knowles, K.; Tice, D.; McArthur, E.; Solomon, G.; Weiss, E. Chemical Control of the Photoluminescence of CdEe Quantum Dot-Organic Complexes with a Series of Para-Substituted Aniline Ligands. *J. Am. Chem. Soc.* **2010**, *132*, 1041–1050.

134. Javier, A.; Yun, C. S.; Sorena, J.; Strouse, G. F. Energy Transport in CdSe Nanocrystals Assembled with Molecular Wires. *J. Phys. Chem. B* **2003**, *107*, 435–442.
135. Sitt, A.; Even-Dar, N.; Halivni, S.; Faust, A.; Yedidya, L.; Banin, U. Analysis of Shape and Dimensionality Effects on Fluorescence Resonance Energy Transfer from Nanocrystals to Multiple Acceptors. *J. Phys. Chem. C* **2013**, *117*, 22186–22197.
136. Halivni, S.; Sitt, A.; Hadar, I.; Banin, U. Effect of Nanoparticle Dimensionality on Fluorescence Resonance Energy Transfer in Nanoparticle-Dye Conjugated Systems. *ACS Nano* **2012**, *6*, 2758–2765.
137. Stewart, M. H.; Huston, A. L.; Scott, A. M.; Efros, A. L.; Melinger, J. S.; Gemmill, K. B.; Trammell, S. A.; Blanco-Canosa, J. B.; Dawson, P. E.; Medintz, I. L. Complex Förster Energy Transfer Interactions between Semiconductor Quantum Dots and a Redox-Active Osmium Assembly. *ACS Nano* **2012**, *6*, 5330–5347.
138. Sadhu, S.; Patra, A. A brief overview of some physical studies on the relaxation dynamics and Förster resonance energy transfer of semiconductor quantum dots. *ChemPhysChem* **2013**, *14*, 2641–2653.
139. Basko, D.; La Rocca, J. C.; Bassani, F.; Agranovich, V. M. Foerster energy transfer from a semiconductor quantum well to an organic material overlayer. *Eur. Phys. J. B* **1999**, *8*, 353–362.
140. Foerster, T. *Modern Quantum Chemistry*; Sinanoglu, O., Ed.; Academic Press: New York, 1965, p 93.
141. Agranovich, V. M.; Galanin, M. D. *Electronic Excitation Energy Transfer in Condensed Matter*; North-Holland Pub. Co.: Amsterdam, 1982.
142. Zenkevich, E. I.; von Borczyskowski, C.; Shulga, A. M.; Bachilo, S. M.; Rempel, U.; Willert, A. Self-assembled nanoscale photomimetic models: structure and related dynamics. *Chem. Phys.* **2002**, *275*, 185–209.
143. Zenkevich, E. I.; von Borczyskowski, C.; Shulga, A. M. Structure and excited states properties of mutiporphyrin arrays formed by supramolecular design. *J. Porphyrins Phthalocyanines* **2003**, *7*, 731–754.
144. Generalov, R.; Christensen, I.; Chen, W.; Sun, Y.-P.; Kristensen, S.; Juzenas, P. Generation of singlet oxygen and other radical species by quantum dot and carbon dot nanosensitizers. In *Photodynamic Therapy: Back to the Future*. *Proc. SPIE* **2009**, *7380*, 738072.
145. Cooper, D.; Dimitrijevic, N.; Nadeau, J. Photosensitization of CdSe/ZnS QDs and reliability of assays for reactive oxygen species production. *Nanoscale* **2010**, *2*, 114–121.
146. Gijzeman, O. L. J.; Kaufman, E.; Porter, G. *J. Chem. Soc., Faraday Trans. II* **1973**, *69*, 70.
147. McNaught, A. D.; Wilkinson, A. *IUPAC Compendium of Chemical Terminology*, 2nd ed.; Blackwell Scientific Publications: Oxford, 1997.
148. Dzhagarov, B. M.; Sagun, E. I.; Ganzha, V. A.; Gurinovich, G. P. Mechanism for triplet state quenching of chlorophyll and related substances with molecular oxygen. *Khim. Fiz.* **1987**, *6*, 919–928.

149. Wuister, S. F.; Swart, I.; Driel, F. V.; Hickey, S. G.; Donega., C. D. M. Highly Luminescent Water-Soluble CdTe Quantum Dots. *Nano Lett.* **2003**, *3*, 503–507.
150. Murov, S. L.; Carmichael, I.; Hug, G. L. *Handbook of Photochemistry*; Marcel Dekker: New York, 1993.
151. Sagun, E. I.; Zenkevich, E. I.; Knyuksho, V. N.; Shulga, A. M. Extra-ligation influence on spectral-kinetic characteristics and excited states quenching of multiporphyrin complexes by molecular oxygen. *Optika i Spectroskopiya (in Russian)*. **2011**, *110*, 251–265.
152. Medintz, I. L.; Stewart, M. H.; Trammell, S. A.; Susumi, K.; Delahanty, J. B.; Mey, B. C.; Melinger, J. S.; Blanco-Canosa, J. B.; Dawson, F. E.; Mattoussi, H. Quantum dot-dopamine bioconjugates: redox-coupled nanoassemblies for *in vitro* and intracellular pH sensing. *Nat. Mater.* **2010**, *9*, 676–684.
153. Efros, Al. L.; Rosen, M.; Kuno, M.; Nirmal, M.; Norris, D. J.; Bawendi, M. G. Band-edge exciton in quantum dots of semiconductors with a degenerate valence band: dark and bright exciton states. *Phys. Rev. B*. **1996**, *54*, 4843.
154. Efros A. L. In *Semiconductor and metal nanocrystals: synthesis and electronic and optical properties*; Klimov, V. I., Ed.; Marcel Dekker: New York, 2003; pp 103–141.
155. Klimov, V. I. Spectral and dynamical properties of multiexcitons in semiconductor nanocrystals. *Annu. Rev. Phys. Chem.* **2007**, *58*, 635–673.
156. Scholes, G. D.; Kim, J.; Wong, C. Y.; Huxter, V. M.; Nair, P. S.; Fritz, K. P.; Kumar, S. Nanocrystal Shape and the Mechanism of Exciton Spin Relaxation. *Nano Lett.* **2006**, *6*, 1765–1771.
157. Scholes, G. D.; Rumbles, G. Excitons in nanoscale systems. *Nat. Mater.* **2006**, *5*, 683–696.
158. Morris-Cohen, A. J.; Vasilenko, V.; Amin, V. A.; Reuter, M. G.; Weiss, E. A. Model for Adsorption of Ligands to Colloidal Quantum Dots with Concentration-Dependent Surface Structure. *ACS Nano* **2012**, *6*, 557–565.
159. Tachiya, M. Kinetics of quenching of luminescent probes in micellar systems. *J. Chem. Phys.* **1982**, *76*, 340–348.
160. Tachiya, M. Application of a generating function to reaction kinetics in micelles: kinetics of quenching of luminescent probes in micelles. *Chem. Phys. Lett.* **1975**, *33*, 289–292.
161. Gurinovich, G.; Zenkevich, E.; Sagun, E. Radiationless intermolecular energy transfer with participation of acceptor excited triplet states. *J. Lumin.* **1982**, *26*, 297–317.
162. Lakowicz, J. R. *Principles of Fluorescence Spectroscopy*, 2nd ed.; Kluwer Academic/Plenum Publishers: New York, 1999; p 245
163. Klimov, V.; Mikhailovsky, A.; McBranch, D.; Leatherdale, C.; Bawendi, M. Quantization of multiparticle Auger rates in semiconductor quantum dots. *Science* **2000**, *287*, 1011–1013.
164. Yang, C.; Chen, W.; Quang, B. B.; Xiang, G. Recent progress on the liposomes loaded with quantum dots. *Rev. Nanosci. Nanotechnol.* **2012**, *1*, 257–270.

165. Fakhar-e-Alam, M.; Kishwar, S.; Siddique, M.; Atif, M.; Nur, O.; Willander, M. The photodynamic effect of ZnO nanorods and their ligands with different photosensitizers. *Rev. Nanosci. Nanotechnol.* **2012**, *1*, 40–51.
166. Schmidt, M. E.; Blanton, S. A.; Hines, M. A.; Guyot-Sionnest, P. Size-dependent two-photon excitation spectroscopy of CdSe nanocrystal. *Phys. Rev. B: Condens. Matter.* **1996**, *53*, 12629–12632.
167. Pu, S. C.; Yang, M. J.; Hsu, C. C.; Lai, C. W.; Hsieh, C. C.; Lin, S. H.; Cheng, Y.-M.; Chou, P.-T. The empirical correlation between size and two-photon absorption cross section of CdSe and CdTe quantum dots. *Small* **2006**, *2*, 1308–1313.

Subject Index

C

Carrier relaxation in nanoparticles
introduction, 201
molecular dynamics (MD), 202
non-equilibrium Green's function
method (NEGF), 202
quantum dots (QDs), 202

Kohn-Sham orbitals, 203
DFT-based calculations, 206
Feynman diagrams, 208*f*
geometry optimization, 204
one-phonon emission rates, 209
phonon frequencies, 205
preliminary results, 209
 $\text{Si}_{38}\text{H}_{42}$ nanorod, atomistic model,
210*f*
single particle density and phonon
density, 210*f*
single-particle energy corrections, 207
two-phonon processes, 208

G

GaN-InN alloys
methodology
computational details, 190
GaN and InN:GaN, molecular
structure, 191*f*

results
decoherence correction, effect, 195
DISH algorithm, decoherence effects,
196*f*
electronic structure, 192
energy relaxation, 193
excitation energies, 194
non-zero nonadiabatic coupling
matrix, 194
partial densities, 192*f*
relaxation kinetics, 193*f*
stochastic interactions, 195
two-exponential decay kinetics, 194

I

Interfacial electron transfer in
porphyrin-sensitized solar cells,
169

methods

interfacial electron transfer
simulations, 173
molecular structure and absorption
spectra, 172
slab model optimization, 172

results
absorption spectra, 174
anatase, assemblies, 178*f*
characteristic interfacial electron
transfer, 182*t*
complexes 1-5, calculated excitations,
175*f*
dye-nanoparticle assemblies, 178
extended Hückel LUMO, 180*f*
geometric parameters, 175*t*
ground state structures, 174
Hückel energy levels, 179*f*
interfacial electron transfer
simulations, 180
Kohn-Sham HOMO-1, 176*f*
soret regions of 1, natural transition
orbitals, 177*f*
soret regions of 3, natural transition
orbitals, 177*f*
survival probability, 181*f*

L

Low-dimensional TiO_2 , electronic and
optical properties
introduction, 47
photocatalytic mechanism, schematic
diagram, 48*f*
photocatalytic processes, 49
reactive minority surfaces of anatase,
excitonic effects, 50
anatase TiO_2 surface with periodicity,
52*f*
macroscopic dielectric function, 53*f*
two-body electron-hole pair
correlation function, 54*f*
spatially confined systems, excitonic
effects, 55
energy values (eV), 58*f*
exciton spatial localization, analysis,
61
in-plane lattice parameters and film
formation energy, 57*t*

lepidocrocite sheets optical response, packing effect, 60^f
 macroscopic dielectric functions, imaginary part, 59^f
 planar 2D infinite sheet, perspective view, 56^f
 titania/graphene nanocomposites, optical features, 62
 band structures, 65^f
 chemical bond, role, 67
 dielectric function, imaginary part, 66^f
 graphene-TiO₂ bilayer nanocomposite models, 64^f

M

Metal ions, surface of TiO₂ nanorods, 103
 introduction, 104
 heteronanoocrystals, 106
 photoelectrode, irradiation, 104
 sensitized semiconductor particles, coupling, 106
 results, 107
 brookite TiO₂ nanocrystals, surface, 111
 charge transfer dynamics, 112
 identical geometry, 109
 TiO₂ nanorods, preparation, 108
 X-ray photoelectron spectroscopy (XPS), 110

Metal nanoclusters, optical, electrical and catalytic properties, 215
 charged metal nanocluster surface, 223
 cluster structure, images, 225^f
 desorption rate, 224^t
 heat treatment temperature, 223^f
 Pd-doped Pt₁₃H₂₄ nanocluster, 224
 charged Pt₁₃ and Pd₁₃ nanoclusters, 218
 clusters, density of states, 220^f
 H₂ desorption pathway, 222^f
 metal nanocluster surface, desorption, 220
 models, density of states, 219^f
 Nudge-Elastic Band (NEB) method, 222
 Pd₁₃H₂₄ nanocluster, snapshots, 221^f
 organo-thiolate ligand, 225
 Au₁₃ core, structure, 225^f
 Au₃₈(SCH₃)₂₄, electronic dynamics, 227^f
 correlation between nanocluster structure and optical properties, 226
 Kohn-Sham orbital energy level diagram, 226^f

photoexcitation dynamics (A, D), 229^f
 photoexcitation electron dynamics, 227
 photoexcited electron-hole pairs, 228^t
 thiolate-protected and bare Au nanoclusters, computed emission spectra, 228
 Pt₁₃ and Pd₁₃ nanoclusters, 217
 geometry optimization and heat treatment, 218^f

O

Oxygen and water adsorption on indium oxide (111) surface, theoretical modeling, 137
 computation details, 139
 results, 141
 bare stoichiometric, linear optical adsorption spectra, 146^f
 oxygen molecule adsorption energy, 143
 partial charge density, 145^f
 stoichiometric, total density of states, 144^f
 surface oxygen vacancy formation energies, 142^t
 (111)-terminated IO surface, top view, 142^f

P

Photovoltaic materials, density matrix treatment of optical properties density operator approach, 157
 rotating wave approximation (RWA), 159
 supercell, changes in photoinduced population, 160^f
 Drude-Lorentz photoconductivity equation, 162
 photoconductance, relative changes, 165^f
 introduction, 151
 energy levels, schematic representation, 154^f
 nanostructured semiconductor surfaces, photoexcitation, 152
 semiconductor slab, pictorial representation, 153^f
 nanostructured semiconductor surfaces, 154
 four Si layers, supercell, 155^f

optical and conductivity properties, 155
light absorbance, 156
photoexcited surfaces, charge carriers, 161

Q

Quantum dot-porphyrin nanoassemblies, 235
introduction
nanoassemblies, advantages, 239
nanoassemblies, structural properties, 241^f
organic photosensitizers (PS), 237
photodynamic therapy, 236
photodynamic therapy (PDT), 237
QD-porphyrin nanoassemblies, 240
QDs, photosensitizers, 238
relaxation dynamics, 240
semiconductor quantum QDs, perspectives, 238
tri-n-octyl phosphine oxide (TOPO) surfactant layer, 240
QD photoluminescence quenching, 243
CdSe/ZnS QD, properties, 248^t
comparative titrations, 248
donor emission quantum yield, 246
photoexcited donor, 246
porphyrin H₂P(m-Pyr)₄ fluorescence intensities, 244^f
QD PL quenching, 245^f
saturation tendency, 246
spectral overlap integral, 246
Stern-Volmer mean rate, 247
QD-porphyrin nanoassemblies, 253
Auger recombination, 255
FRET quantum efficiency, 257
normalized emission intensities, dependencies, 256^f
singlet oxygen, comparative presentation, 254^f
singlet oxygen formation, schematic presentations, 258^f
QD-porphyrin nanoassemblies formation, manifestation, 241
dipole-dipole resonant energy transfer, 242
molecules, adsorption and emission, 243^f
porphyrin molecules, 241
Singlet oxygen generation, experimental studies alone CdSe/ZnS quantum dots, 249
excitons, thermal redistribution, 252

parameters and quantum efficiencies, singlet oxygen, 251^t
QDs, ambient temperature, 252
spectrum of singlet oxygen, 3D presentation, 250^f

Quantum dots, 117

calculation plan, 121
assumption 1, 122
assumption 2, 122
assumption 3, 123
assumption 4, 123
quantum dot, 122^f
tetrahedral symmetry configuration, MnSe₄ fragment, 123^f
computational details, 123
CIS method, Optical spectra for (CdSe)₁₀, 124^f
optical spectrum, 124^f
introduction, 118
five-fold-degenerate energy levels, splitting, 119^f
light emission, 119^f
ligand field approach, 119
energy level diagram, 120^f
results
assumption 1, 125
assumption 2, 126
assumption 3, 128
assumption 4, 129
Cd₁₆Se₁₆, optical spectra, 126^f
Cd₂₄Se₂₄, optical spectra, 127^f
CdSe QDs, size-dependence, 127^f
energy difference, 131^f
energy difference, crossing point, 129^f
luminescence energies, 130^t
single electron energy states, 128^f
ZnS optical gap, size dependences, 130^f

S

Single crystal substrates, sensitization conjugated polymers, sensitizers, 21
ZnO(0001), AFM images, 22^f
covalently bound dyes, metal oxide dye sensitization
anatase TiO₂, dye sensitization, 14^f
doping density, 10
maximum IPCE values, plot, 12^f
N3 and G15 sensitized TiO₂ electrodes, current-voltage curves, 11^f
preparation of terraced single crystal substrates, methods, 8

rutile crystals, photograph, 11*f*
 SrTiO₃ and ALD deposited TiO₂ films, AFM images, 13*f*
 titanium dioxide, 8
 UV treatment/cleaning of TiO₂, 9
 dye sensitization, history, 1
 dye-sensitized single crystal electrode, rate processes, 3*f*
 semiconductor electrodes, photosensitization, 2
 SnS₂ crystal, photograph, 7*f*
 squaraine dye Bis(4-dimethylamino-2-dihydroxyphenyl)squareaine (1-1 OHSQ), AFM images, 5*f*
 van der waal surfaces, 3
 Vis-NIR absorption spectrum, 6*f*
 WSe₂ crystal, photocurrent response, 4*f*
 gallium phosphide sensitization, 36
 sensitized photocurrent response, time dependence, 36*f*
 other single crystal substrates, 19
 quantum dots, sensitizers, 23
 anatase (001) TiO₂ single crystal, IPCE spectra, 28*f*
 band gap PbS QDs, IPCE spectra, 35*f*
 colloidal quantum dots, deposition, 24
 electronic coupling, 30
 generation and collection, multiple exciton, 34
 illumination energy, APCE values, 35*f*
 IPCE spectra and photocurrent, 29*f*
 MPA-capped CdSe QDs, IPCE spectra, 32*f*
 near-IR, absorbing quantum dots, 33
 quantum dot stability, 30
 rutile TiO₂, AFM images, 27*f*
 TOP/TOPO-capped CdSe QDs, IPCE spectra, 26*f*
 ZnO, IPCE values, 31*f*
 ZnO single crystal electrodes, PbS QDs, and redox couples, band alignment, 33*f*
 single crystal sensitization studies, specialized techniques, 19
 attenuated reflection spectroscopy, schematic, 20*f*
 TiO₂ crystals, dye binding morphologies, 14
 atomically flat single crystal (110) rutile TiO₂, AFM images, 18*f*
 dye desorption rates, 16
 dye loading, 15
 N3 adsorption, isotherms, 17*f*
 N3 and generic thiacyanine dye sensitizers, molecular structure, 15*f*
 TiO₂, surface bound confirmations, 18*f*

T

TiO₂ mesoporous materials
 experimental section, 88
 introduction, 81
 coupled semiconductors, 82
 doped TiO₂ photocatalysts, 83
 dye-sensitized TiO₂ photocatalysts, 84
 TiO₂ photocatalysts, 85
 visible light use, 82
 water splitting reaction, importance, 82
 results
 as-synthesized mesoporous titania materials, powder X-ray diffractogram, 89*f*
 calcined mesoporous titanium dioxide, diffuse reflectance spectra, 93*f*
 calcined mesoporous titanium dioxides, powder X-ray diffractogram, 90*f*
 doped and non-doped mesoporous titania, H₂ evolution, 96*f*
 dye molecules, structures, 94*s*
 dye-sensitized mesoporous titania, H₂ evolution, 95*f*
 mesoporous titanium dioxide materials, structural properties, 91*f*
 mesostructured titania, transmission electron microscope image, 93*f*
 N₂ adsorption-desorption isotherm, 92
 nitrogen adsorption-desorption isotherms, 90*f*
 photocatalytic studies, 95
 physico-chemical characterization, 88
 rhodamine B, amount, 97*t*
 zeta potential versus pH, variation, 94*f*